Chemical Kinetics in Combustion and Reactive Flows

Modeling Tools and Applications

V. I. Naoumov, V. G. Krioukov,
A. L. Abdullin, and A. V. Demin

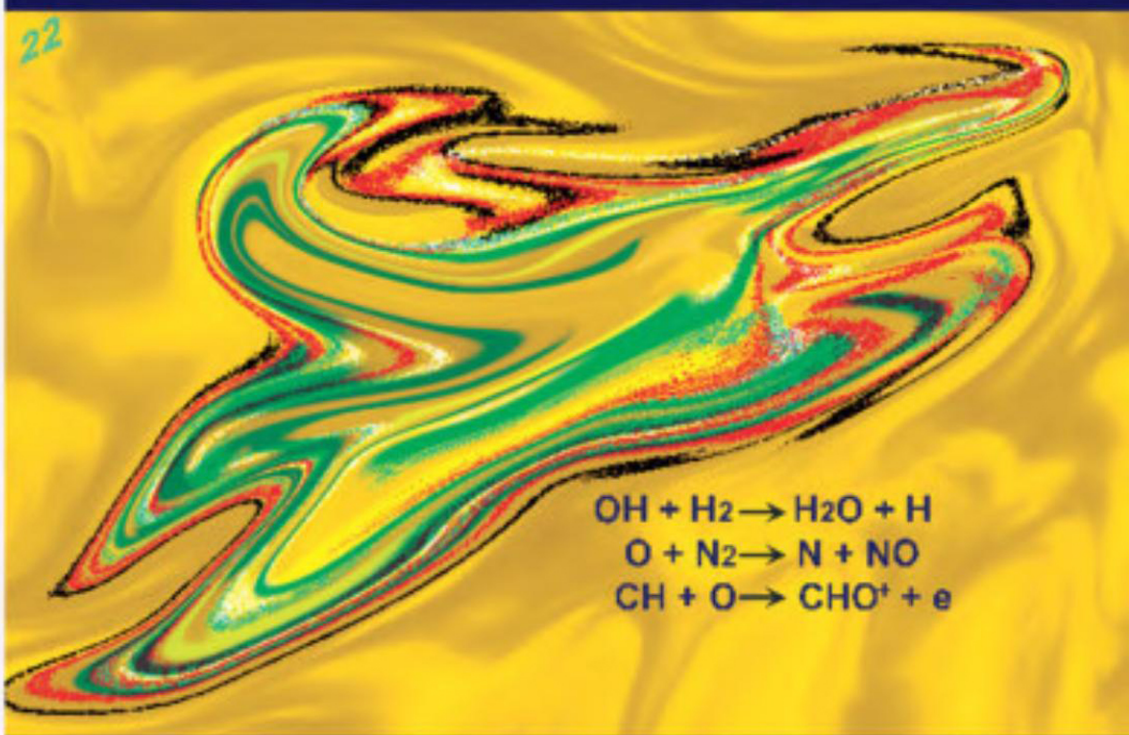

Chemical Kinetics in Combustion and Reactive Flows

Following elucidation of the basics of thermodynamics and detailed explanation of chemical kinetics of reactive mixtures, readers are introduced to unique and effective mathematical tools for the modeling, simulation, and analysis of chemical nonequilibrium phenomena in combustion and flows. The reactor approach is presented considering thermochemical reactors as the focal points. Novel equations of chemical kinetics compiling chemical thermodynamic and transport processes make reactor models universal and easily applicable to the simulation of combustion and flow in a variety of propulsion and energy generation units.

Readers will find balanced coverage of both fundamental material on chemical kinetics and thermodynamics, and detailed description of mathematical models and algorithms, along with examples of their application. Researchers, practitioners, lecturers, and graduate students will find this work valuable.

Dr. V. I. Naoumov is a professor of mechanical and aerospace engineering at the Central Connecticut State University, USA. His research interests are chemical kinetics, aerothermochemistry, and combustion in aerospace propulsion systems and automotive engines. He has 35 years of teaching experience, and in performing research for leading aerospace companies. Dr. Naoumov is Distinguished Scientist of the Russian Republic of Tatarstan and a recipient of the ASME 2018 Distinguished Engineer of the Year Award.

Dr. V. G. Krioukov is a professor of mechanical and aerospace engineering at the Kazan National Research Technical University, Russia. His research interests include chemical kinetics, combustion, and flows in propulsion and power generation systems. He has 40 years of teaching experience, and in performing research for leading Russian aerospace companies, and established the first mathematical modeling graduate program in Brazil. Dr. Krioukov is Distinguished Scientist of the Russian Republic of Tatarstan.

Dr. A. L. Abdullin is a vice president of the Academy of Sciences of the Republic of Tatarstan and professor and chair of the Department of Automotive Engines at the Kazan National Research Technical University, Russia. His areas of expertise are chemical kinetics, combustion, and reactive fluid systems. Dr. Abdullin is Distinguished Scientist of the Russian Republic of Tatarstan and recipient of the Gold Medal of the Society of Inventors of the Republic of Tatarstan.

Dr. A. V. Demin is a professor of the Engineering Ecology and Rational Nature Management Department at the Kazan State Power Engineering University, Russia. He does research in the fields of chemical kinetics, multiphase chemical nonequilibrium flows in aerospace propulsion systems, and internal combustion engines. Dr. Demin is an Honorary Worker of Higher Education, awarded by the Russian Ministry of High Education.

Downloaded from https://www.cambridge.org/core. Nottingham Trent University, on 17 Aug 2019 at 02:28:31, subject to the Cambridge Core terms of use, available at https://www.cambridge.org/core/terms. https://www.cambridge.org/core/product/00A104CC52C8272606D7CB8DEABFF53A

Downloaded from https://www.cambridge.org/core. Nottingham Trent University, on 17 Aug 2019 at 02:28:31, subject to the Cambridge Core terms of use, available at https://www.cambridge.org/core/terms. https://www.cambridge.org/core/product/00A104CC52C8272606D7CB8DEABFF53A

Chemical Kinetics in Combustion and Reactive Flows

Modeling Tools and Applications

V. I. NAOUMOV
Central Connecticut State University

V. G. KRIOUKOV
Kazan National Research Technical University

A. L. ABDULLIN
The Academy of Sciences of the Republic of Tatarstan

A. V. DEMIN
Kazan State Power Engineering University

CAMBRIDGE
UNIVERSITY PRESS

Downloaded from https://www.cambridge.org/core. Nottingham Trent University, on 17 Aug 2019 at 02:28:31, subject to the Cambridge Core terms of use, available at https://www.cambridge.org/core/terms. https://www.cambridge.org/core/product/00A104CC52C8272606D7CB8DEABFF53A

CAMBRIDGE
UNIVERSITY PRESS

University Printing House, Cambridge CB2 8BS, United Kingdom

One Liberty Plaza, 20th Floor, New York, NY 10006, USA

477 Williamstown Road, Port Melbourne, VIC 3207, Australia

314–321, 3rd Floor, Plot 3, Splendor Forum, Jasola District Centre, New Delhi – 110025, India

79 Anson Road, #06–04/06, Singapore 079906

Cambridge University Press is part of the University of Cambridge.

It furthers the University's mission by disseminating knowledge in the pursuit of education, learning, and research at the highest international levels of excellence.

www.cambridge.org
Information on this title: www.cambridge.org/9781108427043
DOI: 10.1017/9781108581714

© Viatcheslav I. Naoumov, Victor Krioukov, Airat Abdullin, and Alexey V. Demin 2019

This publication is in copyright. Subject to statutory exception and to the provisions of relevant collective licensing agreements, no reproduction of any part may take place without the written permission of Cambridge University Press.

First published 2019

Printed in the United Kingdom by TJ International Ltd, Padstow Cornwall

A catalogue record for this publication is available from the British Library.

Library of Congress Cataloging-in-Publication Data
Names: Naoumov, V. I., 1953– author.
Title: Chemical kinetics in combustion and reactive flows : modeling tools and applications / V.I. Naoumov, Central Connecticut State University, V.G. Krioukov, Kazan National Research Technical University, A.L. Abdullin, The Academy of Science of the Republic of Tatarstan, A.V. Demin, Kazan State Power Engineering University.
Description: Cambridge, United Kingdom ; New York, NY, USA : Cambridge University Press, 2019. | Includes bibliographical references and index.
Identifiers: LCCN 2019000334 | ISBN 9781108427043 (hardback)
Subjects: LCSH: Combustion–Mathematical models. | Chemical kinetics. | Turbulance.
Classification: LCC QD516 .N26 2019 | DDC 541/.361015118–dc23
LC record available at https://lccn.loc.gov/2019000334

ISBN 978-1-108-42704-3 Hardback

Cambridge University Press has no responsibility for the persistence or accuracy of URLs for external or third-party internet websites referred to in this publication and does not guarantee that any content on such websites is, or will remain, accurate or appropriate.

Downloaded from https://www.cambridge.org/core. Nottingham Trent University, on 17 Aug 2019 at 02:28:31, subject to the Cambridge Core terms of use, available at https://www.cambridge.org/core/terms. https://www.cambridge.org/core/product/00A104CC52C8272606D7CB8DEABFF53A

To our families for their support in all our endeavors.
To the Department 22 of the Kazan Aviation Institute,
one of the best Russian academic centers, where we worked
in the exciting atmosphere of creativity, integrity, and friendship.

Downloaded from https://www.cambridge.org/core. Nottingham Trent University, on 17 Aug 2019 at 02:30:18, subject to the Cambridge Core terms of use, available at https://www.cambridge.org/core/terms. https://www.cambridge.org/core/product/653E7A68184E3EEC292062B925ACBFEC

Downloaded from https://www.cambridge.org/core. Nottingham Trent University, on 17 Aug 2019 at 02:30:18, subject to the Cambridge Core terms of use, available at https://www.cambridge.org/core/terms. https://www.cambridge.org/core/product/653E7A68184E3EEC292062B925ACBFEC

Contents

Preface *page* xiii
Acknowledgments xix
Nomenclature xxi

Part I Basic Components of Chemical Nonequilibrium Models 1

1 Approaches to Combustion Simulation: Patterns, Models, and Main Equations 3
1.1 Standard Combustion Patterns 3
1.2 Basic Characteristics of Working Medium 10
1.3 Models of Chemical Equilibrium and Detailed Chemical Kinetics 16
1.4 Models of Instant Response, Global Kinetic Models, and Models of Nonequilibrium Chemical Kinetics 30
1.5 Application of Reactor Approach to the Simulation of Combustion and Reactive Flows 35

2 Governing Equations of Chemical Kinetics and Specific Features of Their Solution 41
2.1 Governing Equations of Chemical Kinetics and Accompanying Processes in the Reactors 41
2.2 Adaptation of Combustion Model to Heterogeneous Systems and Mass Exchange Reactions 50
2.3 Numerical Methods for Solving Reactor Model Equations 61
2.4 Structure and Main Stages of the Algorithm for Solving Reactor Model Equations 71
2.5 Verification of Single Reactor Models 89

3 Software Tools for the Support of Calculation of Combustion and Reacting Flows 95
3.1 Review of Features of Software Tools 95
3.2 Analysis of Thermodynamic Properties of Individual Substances 111
3.3 Sensitivity Analysis of Chemical Mechanisms in Combustion Chemistry 126

Downloaded from https://www.cambridge.org/core. Nottingham Trent University, on 17 Aug 2019 at 03:31:13, subject to the Cambridge Core terms of use, available at https://www.cambridge.org/core/terms. https://www.cambridge.org/core/product/E7259C6916AEFEA811228F2E47478781

3.4 Application of Evaluation of Eigenvalues to Combustion Analysis 140
3.5 Stand-Alone Methods of Reduction of Chemical Mechanisms 163
3.6 Combination of Reaction Mechanisms Reduction Methods 177

Part II Mathematical Modeling of Selected Typical Modes of Combustion 205

4 Laminar Premixed Flames: Simulation of Combustion in the Flame Front 207
4.1 Specific Features of Modeling 207
4.2 Convective Model of Combustion Processes in Laminar Flame Front and Impact of Diffusion 209
4.3 Application of Plug Flow Reactor to the Simulation of Combustion in the Premixed Laminar Flame 211
4.4 Examples of Numerical Simulation and Analysis 214

5 Droplets and Particles: Evaporation in High-Temperature Flow and Combustion in Boundary Layers 228
5.1 Peculiarities of Droplets Evaporation and Combustion 228
5.2 Application of Perfectly Stirred Reactor to the Simulation of Evaporation and Chemical Reacting of Dispersed Propellant: Governing Equations 231
5.3 Heat and Mass Transfer in Boundary Layer at Evaporation of Single Droplet 236
5.4 Peculiarities of Algorithm: Mathematical Model Testing 239
5.5 Numerical Simulation and Analysis of the Processes in Boundary Layers at Evaporation and Chemical Interaction 241

6 Models of Droplet Evaporation in Gas Flow 262
6.1 Classic Model of Droplet Evaporation in Reacting Gase Medium 263
6.2 Model of Droplet Evaporation in Reacting Gaseous Medium at High Pressures 266
6.3 Model of Evaporation of Multicomponent Fluid 273

Part III Simulation of Combustion and Nonequilibrium Flows in Propulsion and Power Generation Systems 281

7 Simulation of High-Temperature Heterogeneous Reacting Flows 283
7.1 Features of Physicochemical Processes in Combustion and Flow of Heterogeneous Mixtures 283
7.2 Model of Two-Phase Nonisothermal Jet in a Channel with Sudden Expansion 286
7.3 Multireactor Model of Reacting Flow 291
7.4 Numerical Study of Heterogeneous Reacting Flows 295

Downloaded from https://www.cambridge.org/core. Nottingham Trent University, on 17 Aug 2019 at 03:31:13, subject to the Cambridge Core terms of use, available at https://www.cambridge.org/core/terms. https://www.cambridge.org/core/product/E7259C6916AEFEA811228F2E47478781

8	**Simulation of Two-Phase Flows in Gas Generators of Liquid Propellant Rocket Engines**	310
	8.1 Physical Scheme and Mathematical Model of Two-Phase Flow in Gas Generators	310
	8.2 Kinetic Scheme of Soot Formation	320
	8.3 Testing the Reaction Mechanisms and Study of Soot Formation in Combustion and Flow of Methane–Oxygen Mixture in Two-Zone Gas Generator	323
	8.4 Numerical Study of Combustion and Flow of Unsymmetrical Dimethylhydrazine and Nitrogen Tetroxide in Liquid Propellant Rocket Engine Gas Generator	330
9	**Pressurization of Liquid Propellant Rocket Engine Tanks**	334
	9.1 Processes in Ullage of Liquid Propellant Tank	334
	9.2 Application of Reactor Approach to the Simulation of Pressurization	338
	9.3 Pressurizing Gas Flow and Heat and Mass Exchange in the Ullage	346
	9.4 Numerical Simulation and Optimization of Propellant Tank Pressurization	361
10	**Combustion and Ionization in Spark Ignition Engines**	380
	10.1 Ion Current as a Tool for Engine Performance Control: Specific Features of Ionization	380
	10.2 Model of Combustion: Governing Equations and Relations	382
	10.3 Ion Current Simulation	386
	10.4 Numerical Simulation of Combustion and Ionization	387
	References	397
	Index	418

Downloaded from https://www.cambridge.org/core. Nottingham Trent University, on 17 Aug 2019 at 03:31:13, subject to the Cambridge Core terms of use, available at https://www.cambridge.org/core/terms. https://www.cambridge.org/core/product/E7259C6916AEFEA811228F2E47478781

Downloaded from https://www.cambridge.org/core. Nottingham Trent University, on 17 Aug 2019 at 03:31:13, subject to the Cambridge Core terms of use, available at https://www.cambridge.org/core/terms. https://www.cambridge.org/core/product/E7259C6916AEFEA811228F2E47478781

Preface

The combustion and reactive flows analysis has demonstrated some new trends in the past several decades:

- in-depth study of the contribution of detailed chemical mechanisms to combustion performances
- a dramatic increase in the number of chemical reactions involved in the analysis of combustion and reactive flows
- the expansion of the range of problems and objects where mathematical models of combustion built around detailed chemical kinetics are applied (gasifiers, tube furnaces, fuel cells, ozone holes, etc.)
- development of mathematical model support tools: the comparison and transfer of data on species between various databases, sensitivity analysis, application of eigenvalues, reduction of reaction mechanisms, selection of the rate constants from experimental data, automatic control over the balance of chemical elements, etc.
- construction of highly sophisticated mathematical models and algorithms of combustion and reactive flows to provide the accurate and reliable prediction and optimization of operating performances of combustion devices.

However the development of such models is complicated by the necessity of integration therein and appropriate simulation of three complex phenomena – namely turbulent flow and interaction of multiphase media, heat and mass exchange between phases with due allowance for multidimensionality of these processes, and chemical interaction in the flow of reactants and combustion products. The multidimensional nature of the flows characteristic of propulsion and power generation systems, the presence of chemically and thermally nonhomogeneous regions, and complex mechanisms of chemical interaction in a gas phase under conditions sometimes far from chemical equilibrium render a detailed numerical simulation of the entire complex of aerothermochemical processes an extremely complex problem.

One of the governing of matters in simulation of such complex of processes consists in the selection of an approach and base models for their detailed simulation. At present two basic approaches may be isolated. In compliance with the first one, "gas-dynamic," physical schemes of processes are designed for multidimensional, mainly turbulent flows while 2-D and 3-D equations of nonreactive and reactive gas mixes motion are basic equations. Calculation algorithms comprise the procedures involving division of the solution region into finite elements, formation of finite-difference equations and

Downloaded from https://www.cambridge.org/core. Nottingham Trent University, on 17 Aug 2019 at 03:32:02, subject to the Cambridge Core terms of use, available at https://www.cambridge.org/core/terms. https://doi.org/10.1017/9781108581714.013

their solutions. To solve the combustion problems, the following approximations are used: eddy dissipation, flamelet, global reactions, or detailed chemical kinetics. The latter is used very seldom because of a considerable amount of calculations. The example of implementation of gas-dynamic approach is the FLUENT software tool.

The second one, the thermochemical or "reactor" approach, considers single reactors or sets of interconnected reactors as the focal points, while basic equations are detailed chemical kinetics equations. Calculation algorithms are built on implicit methods capable of solving stiff differential equations. This approach allows one to consider reactive systems involving hundreds of species and thousands of reactions. Reaction mechanisms can incorporate the nonstandard reactions of Landau–Teller, Troe, etc. Besides, it is possible to simulate two-temperature medium and surface kinetics reactions.Various tools are widely used in this approach for development of models of combustion and flow.Software tools CHEMKIN and KINETICUS are the examples of thermochemical or reactor approach implementation.

This book brought to public notice has been aimed at describing the thermochemical approach (hereinafter, the authors would use the "reactor" approach term) in case the constructing of numerical models rests on procedures and algorithms of detailed calculation of chemical composition and properties of combustions products in various types of reactors.

The gas-dynamic component of the models is designed on the basis of relatively simple working medium flow schemes, some assumptions for the formation of the system of integrated reactors, and a priori known data on the flow pattern features in working volumes of combustion and power generation systems.

Specific features of presentation consist in well-balanced description of both basic material on thermochemistry of high-temperature reactive mixtures and detailed description of unique models and algorithms for calculation of combustion and flow. Such approach makes the book material available for not only specialists in chemical thermodynamics and chemical kinetics, in application to combustion theory to combustion and flow problems solution, but also for graduate students who have limited knowledge in these fields and plan the in-depth study of aerothermochemistry and its application to the simulation of complex aerothermochemical processes. For this, in the authors' opinion, the reader should command, as a minimum, the entry graduate-level or graduate-level knowledge in thermodynamics, chemical thermodynamics, fluid mechanics, and heat and mass-transfer, as well as some skills in computational and numerical methods. However, the authors considered it apt to add the materials related to basic principles of chemical thermodynamics as well.

While considering the basis reactor schemes, equations, and algorithms, the reader learns the modeling tools that allow constructing far more complex mathematical models, algorithms, and computer codes. Besides, it helps to develop original invariant models of the processes including not only nonequilibrium chemical interaction in the gas phase but also mass exchange processes accompanying combustion and multiphase flows.

The book may well aid the creation, analysis, and application of proper models of combustion and flows in quite different high-temperature systems, provided the adequate original mathematical apparatus is used. Examples of constructing such

Downloaded from https://www.cambridge.org/core. Nottingham Trent University, on 17 Aug 2019 at 03:32:02, subject to the Cambridge Core terms of use, available at https://www.cambridge.org/core/terms. https://doi.org/10.1017/9781108581714.013

models, their use for the analysis, and the optimization of parameters of various high-temperature units are presented as well for all interested parties.

Structurally, the book is divided into three parts. Part I (Chapters 1–3) contains the required material from chemical thermodynamics, chemical kinetics, and fundamentals of combustion, and describes in detail the original basic mathematical models and algorithms for calculation of chemical nonequilibrium composition in separate idealized reactors. Special attention is given to the description of tools designed to maintain the chemical interaction and combustion simulation – that is, the presentation of information on thermodynamic properties of chemical species and the transfer of this information between different databases, sensitivity analysis, the application of eigenvalues, and the selection and reduction of reaction mechanisms. Examples of application of these tools to the analysis of combustion and chemical interaction problems in reactors and reacting flows are also given.

Part II (Chapters 4–6) describes the application of basis schemes, models and algorithms to simulation of separate standard physicochemical processes characteristic for high-temperature units – e.g., a model of combustion and nonequilibrium effects in the flame front, a novel model of vapor conversion and interaction under the conditions of chemical nonequilibrium in the boundary layer of a single droplet, and unique models of multifractional droplet evaporation and droplet evaporation at supercritical pressures. Every cited model is provided along with useful examples of its application.

Part III (Chapters 7–10) incorporates the set of applied models designed for the simulation of combustion processes and chemical nonequilibrium working medium flows in high-temperature unit – that is, combustion chambers for the generation of high-temperature gas, gas generators of liquid-propellant rocket engines, liquid-propellant rocket engine tanks, and internal combustion engines. These models are mainly multireactor systems and allow for, along with nonequilibrium variation of chemical composition, the important accompanying processes, such as evaporation, heat exchange, condensation, diffusion, the availability of turbulent flows and reverse flows, heat and mass exchange, ionization of combustion products, etc. The potential of these models and algorithms is verified by the examples of numerical analysis and optimization of the operating parameters of these units.

I. Basic Components of Chemical Nonequilibrium Models: Chapters 1–3

Chapter 1 illuminates main combustion schemes in idealized reactors and separate combustion process fragments in high-temperature units. The principal concepts of thermochemistry and thermodynamic properties of the working medium as well as the methods and procedures of their calculations are given. The structures and characteristics of most frequently used databases are described. The model and algorithm of calculation of chemical equilibrium systems are presented as well as the elements of detailed gas-phase chemical kinetics model along with corresponding equations in their traditional form. The other models of calculation of chemical composition are described as well – e.g., the instant response model, the global kinetic model, and the model of

Downloaded from https://www.cambridge.org/core. Nottingham Trent University, on 17 Aug 2019 at 03:32:02, subject to the Cambridge Core terms of use, available at https://www.cambridge.org/core/terms. https://doi.org/10.1017/9781108581714.013

nonequilibrium chemical kinetics. The reactor approach idea is presented while its applications to combustion and flow simulation are defined.

Chapter 2 derives in detail the chemical kinetics equations in exponential form for model reactors such as batch reactor, perfectly stirred reactor, and plug flow reactor. The concept is presented along with the examples of "accompanying" equations. The method of "large molecules" is described to allow extending the nonequilibrium models to heterogeneous systems. The procedure of mass exchange processes' presentation as "mass exchange reactions" is disclosed. Examples of the formation of these "reactions" and the determination of their "rate constants" are given. Classical and advanced explicit integration schemes of ordinary differential equations are proposed. Implicit schemes incorporating the Jacobian matrix are described (Gear, Pirumov, and spline integration). The algorithm for the formation of invariant computer codes for the calculation of chemical nonequilibrium systems is described. The structure of coordinating matrices, species enthalpy, and entropy presentation and the determination procedure of rate constants of reverse directions of chemical reactions are disclosed. Analytical formulas of the Jacobian matrix partial derivatives are obtained for their advantages to be analyzed. Separate single-reactor models have been verified.

Chapter 3 describes the procedure of conversion and comparison of thermodynamic properties of chemical species given in independent databases. Three databases, – IVTANTERMO, BURCAT, and TTR – are disclosed and compared. The algorithm of sensitivity coefficient determination to be applied to the perfectly stirred reactor is defined. Equations and procedure of analytical calculation of these coefficients are presented to allow analyzing the sensitivity nearby the "extinction line." The algorithm of chemical kinetics equations eigenvalue calculation is described. Relations between the nature of variation of these values and combustion stages have been established and applied to the batch reactor. The method for determination of integration steps at application of explicit schemes is proposed along with its application to the calculation of processes in specific high-temperature units. With the use of Jacobian eigenvalues applied to perfectly stirred reactor, the range of self-oscillation modes of pure kinetic nature was defined for complex reaction mechanisms. Three independent methods of reaction mechanism reduction – that is, the method of engagement with an adaptive threshold, the method of direct sounding, and the directed relation graph with error propagation method (DRGEP) – have been illuminated, along with the number of their efficient combinations that provides an automatic generation of reduced mechanisms. Examples are given for the efficient reduction of reaction mechanisms for "CH_4 + air" reacting systems for both rich and lean mixtures, as well as for propellants "O_2 + kerosene" and "unsymmetrical dimethylhydrazine + N_2O_4."

II. Mathematical Modeling of Selected Typical Modes of Combustion: Chapters 4–6

Chapter 4 describes the physical scheme, mathematical model, and algorithm of calculation of parameters in the premixed laminar flame front based on the front heat model

Downloaded from https://www.cambridge.org/core. Nottingham Trent University, on 17 Aug 2019 at 03:32:02, subject to the Cambridge Core terms of use, available at https://www.cambridge.org/core/terms. https://doi.org/10.1017/9781108581714.013

at increased pressures and using the basic model of plug flow reactor. The results of numerical experiments aimed at predicting the flame propagation rates of different propellants and ecological parameters prediction are presented.

Chapter 5 examines the dispersed fuel combustion problems and presents a model of chemical interaction and heat and mass exchange in the boundary layer on the basis of the reactor model at combustion of a single liquid droplet in a high-temperature reactive flow. The methodology of applying the perfectly stirred reactor scheme and the mathematical apparatus discussed in Part I in regard to the development of a model of chemical nonequilibrium evaporation and reacting in the boundary layer is described in detail. A detailed derivation of conservation equations characteristic of the process under consideration is given. Results of numerical analyses showing the mathematical model adequacy and cited along with the advantages of chemical nonequilibrium model application to simulation of the processes in the boundary layer at droplet evaporation under high temperatures of external flow are described.

Chapter 6 depicts several models of liquid droplet evaporation in a reactive gas-liquid flow at comparatively low temperatures of the flow when vapors failed to react within the boundary layer. The traditional Priem–Haidmann model of single-component liquid droplet evaporation at subcritical pressures is presented. Also, a novel droplet evaporation model at supercritical pressures proposed is, which – unlike traditional models – allows for nonuniform droplet heating over the radius. The third model is a unique one as well and simulates the multifractional liquid droplet evaporation. Its specific feature consists in the modeling of uneven evaporation of liquid fractions, which causes a stepwise increase in droplet temperature with its heating. Numerical analyses of multifractional propellant evaporation and evaporation at supercritical pressures are presented to underline the relevance of applying these nontraditional models to the creation of complex models of combustion and flow in high-temperature units.

III. Simulation of Combustion and Nonequilibrium Flows in Propulsion and Power Generation Systems: Chapters 7–10

Chapter 7 examines simulation of high-temperature heterogeneous reacting flows in combustion chambers at multifractional propellant droplet evaporation in the presence of recirculation using the multireactor scheme. A unique iteration algorithm is presented to allow a sequential cyclic solution of individual problems for the prediction of gas-dynamic parameters, properties of the dispersed evaporating multifractional liquid phase, and those of chemical interaction at conversion of reactants into combustion products. Examples of calculation are shown aiming to optimize the design and performance of combustion chambers of different propulsion and energy generation systems.

Chapter 8 presents the model for calculation of two-phase flows in gas generators of liquid-propellant rocket engines. It examines chemical nonequilibrium processes in the gas phase, droplet atomization polydispersity, slip velocity, and droplets' non-steady-state heating and evaporation at both subcritical and supercritical pressures, and it

Downloaded from https://www.cambridge.org/core. Nottingham Trent University, on 17 Aug 2019 at 03:32:02, subject to the Cambridge Core terms of use, available at https://www.cambridge.org/core/terms. https://doi.org/10.1017/9781108581714.013

considers the channels of the variable cross-section area. To calculate fuel-rich working medium properties at the combustion of hydrocarbon propellants, the authors worked out the kinetic mechanism supplemented by the original mechanism of soot participles formation via polyacetylenes and their radicals. The results of numerical experiments are given.

Chapter 9 describes the application of multireactor model to the creation of that for pressurization of liquid-propellant rocket engine tanks, and it presents the results on numerical analyses of complex set of aerothermochemical processes in the tank gas ullage. Whereas the comparatively low level of reacting medium temperature in the ullage, chemical nonequilibrium approach application is necessitated, which is confirmed by numerous results of numerical experiments analyzed in detail in the chapter. Cited material features a detailed mathematical description of complex schemes of gas flows in the ullage as well as heat and mass exchange processes and the analysis of their significant influence on the parameters of gas mixture in the ullage at the feeding of propellant into the thrust chamber of the rocket engine.

Chapter 10 describes the model of combustion and chemical nonequilibrium processes in spark ignition engines at the ignition and power stroke, with a focus on the combustion product ionization. The necessity of the application of chemical nonequilibrium model is caused by a notable effect of chemical nonequilibrium on the ionization of combustion products. The perfectly stirred reactors scheme and basic mathematical tools described in the first part of the book have shown their efficiency at simulation and predicting the ion current resulting from chemical and thermal ionization and its application for possible prediction of the engine working and ecological performances.

Downloaded from https://www.cambridge.org/core. Nottingham Trent University, on 17 Aug 2019 at 03:32:02, subject to the Cambridge Core terms of use, available at https://www.cambridge.org/core/terms. https://doi.org/10.1017/9781108581714.013

Acknowledgments

Work over the development of base reactor models, methods, algorithms, and other tools; their analysis; computer-code writing; their application to the development of applied models; and numerical analyses took several decades. For a number of reasons, not all applied models built around the base universal models and algorithms were included in this book. Particularly, multiple models and algorithms were omitted from the book scope: the model of calculation of ionized nonequilibrium heterogeneous flows in nozzles, the model of solid-propellant rocket engine thrust cut by coolant injection, the model of concurrent burnout of propellant and thermal insulation in the thrust chambers of solid propellant rocket engines, the model of low-emission pulverized coal burning in furnaces, the model of combustion processes in the combustion chamber of air jet engines, the model of two-dimensional axially symmetric chemical nonequilibrium reacting internal flows, and others.

Therefore, the authors consider their duty to mention their colleagues who provided invaluable contribution in creation of separate models, algorithms, computer programs, research and preparation of information for databases, and numerical analysis performance. We acknowledge with appreciation the following colleages who have contributed in these efforts: R. Khasanov, R. Iskhakova, I. Zenukov, R. Mukhammedzyanov, G. Glebov, T. Trinos, V. Kotov, R. Valeev, D. Sokolov, M. Nikandrova, V. Gasilin, K. Berezovskaia, and I. Safiullin, as well as untimely passing A. Senyukhin, R. Khairullin, and I. Naidyshev.

A number of developments presented in this book resulted from a close cooperation with the enterprises and research and development centers of the former Soviet Union, now related to ROSKOSMOS State Corporation, and with some other scientific centers and enterprises including those relating to automotive industry – e.g., the Kamsky Automobile Plant and the Swedish company MECEL-AB. The latest results included in this book were obtained thanks to financial support of the Russian Foundation for Basic Research and the Government of Tatarstan Republic. The authors are deeply indebted to these organizations.

Authors owe a debt of special gratitude to their Alma Mater, the Kazan Aviation Institute named after A. N. Tupolev (now Kazan National Research Technical University named after A. N. Tupolev) and to the first in the former Soviet Union Department of Rocket Engines, founded by the Rocketry Chief Designers S. Korolev and

Downloaded from https://www.cambridge.org/core. Nottingham Trent University, on 17 Aug 2019 at 03:29:50, subject to the Cambridge Core terms of use, available at https://www.cambridge.org/core/terms. https://www.cambridge.org/core/product/BE160A1F908CFE0F2D0EAE5DE2603349

V. Glushko, chaired lately by V. Alemasov, the Academician of the Russian Academy of Sciences, Twice the USSR State Prize Winner, who developed, along with his associates A. Tishin and A. Dregalin, the first in the Soviet Union methods, universal mathematical models, and software tools for the calculation of chemical equilibrium high-temperature systems. Exactly these persons made the authors of this book scientists and professionals in the field.

Downloaded from https://www.cambridge.org/core. Nottingham Trent University, on 17 Aug 2019 at 03:29:50, subject to the Cambridge Core terms of use, available at https://www.cambridge.org/core/terms. https://www.cambridge.org/core/product/BE160A1F908CFE0F2D0EAE5DE2603349

Nomenclature

Latin Letters

A_s^+	pre-exponential factor in Arrhenius equation written for forward direction of the s-th reversible chemical reaction, $s = 1 \ldots m_c$, depends on the order of reaction*
A_j	pre-exponential factor in Arrhenius equation written for the j-th chemical reaction, $j = 1 \ldots 2m_c + r_c$, depends on the order of reaction*
C_i	molar concentration of specie i, $gmol/cm^3$ or $kmol/m^3$
C_{pi}	molar specific heat at constant pressure of the specie i, $cal/(gmol \times \mathrm{K})$
c_{pi}	mass specific heat at constant pressure of the specie i, $J/(kg \times \mathrm{K})$
$\bar{C}_p = \sum_i C_{pi} r_i$	molar specific heat of mixture at constant pressure, $cal/(gmol \times \mathrm{K})$
$\bar{c}_p = \sum_i c_{pi} g_i$	mass specific heat of mixture at constant pressure, $J/(kg \times \mathrm{K})$
C	total molar concentration of gas mixture, mol/cm^3
c_{pV}	mass specific heat of vapor at constant pressure, $J/(kg \times \mathrm{K})$
$\bar{c}_{liq}$	average specific heat of liquid, $J/(kg \times \mathrm{K})$
$\bar{c}_{pq}$	average specific heat of the vapor of liquid component q at constant pressure, $J/(kg \times \mathrm{K})$
D_{im}	binary diffusion coefficient of the i-th substance in gas mixture, m^2/s
E_j	activation energy in Arrhenius equation written for the j-th chemical reaction, $j = 1 \ldots 2m_c + r_c$, $cal/gmol$
E_s^+	activation energy in Arrhenius equation written for forward direction of the s-th reversible chemical reaction, $s = 1 \ldots m_c$, $cal/gmol$
F	area, m^2
F_x	drag force acting on the droplet moving in gas flow, N
g_i	mass fraction of specie i
h	integration step, s or m

* Dimension of the reaction rate constant is defined by the reaction order:

- for zeroth-order reaction, $\left[k_j, A_j\right] = gmol/(cm^3 \times s)$
- for first-order reaction, $\left[k_j, A_j\right] = 1/s$
- for second-order reaction, $\left[k_j, A_j\right] = cm^3/(gmol \times s)$
- for third-order reaction, $\left[k_j, A_j\right] = cm^6/\left(gmol^2 \times s\right)$

(The units are *cm*, *gmol*, K, and *sec*.)

Downloaded from https://www.cambridge.org/core. Nottingham Trent University, on 17 Aug 2019 at 02:38:05, subject to the Cambridge Core terms of use, available at https://www.cambridge.org/core/terms. https://www.cambridge.org/core/product/702B9B43429471329E39FCB36C3C550A

h	convection heat transfer coefficient, $W/(m^2 \times \mathrm{K})$
H	total enthalpy, J
H_i	molar enthalpy of i-th specie, $J/kmol$ or $cal/gmol$
H_Σ	molar enthalpy of mixture, $J/kmol$
h_i	mass specific enthalpy of the i-th substance, J/kg
h_Σ	mass specific enthalpy of mixture, J/kg
h_{fuel}	enthalpy of fuel, J/kg
h_{ox}	enthalpy of oxidizer, J/kg
h_p	enthalpy of propellant, J/kg
h^+	specific enthalpy of reactants, J/kg
h_{liq}	specific enthalpy of liquid, J/kg
h_z	specific enthalpy of reacting mixture in the z-th reactor, J/kg
$\bar{h}$	average enthalpy of liquid, J/kg
h_g	specific enthalpy of gas, J/kg
h_d	enthalpy of liquid droplet, J/kg
J	Jacobian matrix
$\dot{J}$	mass flux, $kg/(m^2 \times s)$
$\dot{J}_V$	vapor mass flux from the droplet surface, $kg/(m^2 \times s)$
$\dot{J}_{qV}$	mass flux of the vapor of component q through the boundary layer, $kg/(m^2 \times s)$
k_m^o	mass stoichiometric ratio of propellant components (stoichiometric oxidizer- fuel ratio), $kg\ oxidizer/kg\ fuel$
k_m	mass ratio of propellant components (oxidizer-fuel ratio), $kg\ oxidizer/kg\ fuel$
k_s^+	rate constant of forward direction of the s-th reversible chemical reaction, $s = 1 \ldots m_c$, depends on the order of reaction*
k_s^-	rate constant of reverse direction of the s-th reversible chemical reaction, $s = 1 \ldots m_c$, depends on the order of reaction*
k_j	rate constant of the j-th reaction, $j = 1 \ldots 2m_c + r_c$, depends on the order of reaction*
K_s^c	equilibrium constant of s-th reaction based on molar concentrations, $\left(\frac{gmol}{cm^3}\right)^{\sum_i \left(\nu''_{is} - \nu'_{is}\right)}$
k	thermal conductivity, $W/(m \times \mathrm{K})$
$k_{i,}$	thermal conductivity of the i-th specie, $W/(m \times \mathrm{K})$
k_{gV}	average thermal conductivity of vapor–gas mixture in the boundary layer, $W/(m \times \mathrm{K})$
k_{liq}	thermal conductivity of liquid, $W/(m \times \mathrm{K})$
L_V	latent heat of evaporation, J/kg
L_{qV}	specific heat of evaporation of the q-th liquid component, J/kg
m_c	number of reversible reactions in reacting medium
M	mass, kg
$\dot{m}$	mass flow rate, kg/s
m_i^+, m_i^-	inflow and outflow of substance i, kg/s

Downloaded from https://www.cambridge.org/core. Nottingham Trent University, on 17 Aug 2019 at 02:38:05, subject to the Cambridge Core terms of use, available at https://www.cambridge.org/core/terms. https://www.cambridge.org/core/product/702B9B43429471329E39FCB36C3C550A

M_z	mass of reacting mixture in the z-th reactor, kg
n_a	number of atoms in reacting mixture
n_b	number of reacting substances (species)
n_s^+	temperature factor in Arrhenius equation written for the forward direction of the s-th reversible chemical reaction, $s = 1 \ldots m_c$
n_j	temperature factor in Arrhenius equation written for j-th chemical reaction, $j = 1 \ldots 2m_c + r_c$
n	number of integration step
Nu	Nusselt number
Nu_D	diffusion Nusselt number
Nu_T	thermal Nusselt number
n_z	total number of reactors
n_{sd}	the number of droplets groups in the droplet sizes distribution
n_q	number of the components in multicomponent droplet
p	pressure, Pa
p_i	partial pressure of the i-th substance in the gas mixture, Pa
p_{sat}	pressure of saturated vapor, Pa
Pr	Prandtl number
p_{Vsd}	vapor partial pressure above the surface of the sd-th group of droplets, Pa
$p_{V\infty}$	vapor partial pressure beyond the reduced film, Pa
Q	total heat transfer, J
$\dot{q}$	heat flux, W/m^2
q	heat flow rate, W
q	number of liquid fractions in multicomponent droplet
$R_0 = 8314.6$	universal gas constant, $J/(kmol \times \mathrm{K})$
$R_0 = 1.987$	universal gas constant, $cal/(gmol \times \mathrm{K})$
r_i	mole fraction of the i-th specie
r_i^+	mole fraction of the i-th substance in reactants
r_c	number of mass exchange reactions
Re	Reynolds number
R_d	droplet radius, m
R_{sd}	droplet radius of sd-th group of droplets, m
S_i^0	molar entropy of the specie i at $p = 1$ atm, $J/(kmol \times \mathrm{K})$ or $cal/(gmol \times \mathrm{K})$
Sc	Schmidt number
sd	number of the group of droplets
T	temperature, K
T_g	temperature of gas, K
T_{boil}	boiling temperature, K
T^+	temperature of reactants, K
T_d	temperature of droplet, K
T_{eq}	chemical equilibrium temperature, K

Downloaded from https://www.cambridge.org/core. Nottingham Trent University, on 17 Aug 2019 at 02:38:05, subject to the Cambridge Core terms of use, available at https://www.cambridge.org/core/terms. https://www.cambridge.org/core/product/702B9B43429471329E39FCB36C3C550A

T_f	temperature at the exit of the reactor or channel, K
T_∞	temperature of external gas flow, K
T_z	temperature of reacting mixture in the z-th reactor, K
T_0	initial temperature, K
T_{cr}	critical temperature, K
T_w	wall temperature, K
T_{gV}	average temperature of vapor–gas mixture in the boundary layer, K
T_{rf}	reference temperature, K
T_{sd}	temperature of the sd-th group of droplets, K
U	total internal energy, J
U_i	molar internal energy of the i-th substance, $J/kmol$
u_i	specific internal energy of the i-th substance, J/kg
V_g , u_g	velocity of gas, m/s
u_{sd}	velocity of sd-th group of droplets, m/s
V	volume, m^3
V_z	volume of z-th reactor, m^3
W_j	rate of the j-th reaction, $gmol/(cm^3 \times s)$
$W_{ij} = \left(\frac{dC_i}{d\tau}\right)_j$	rate of substance i concentration variation in j-th reaction, $gmol/(cm^3 \times s)$
x, y	coordinates, m
z	number of reactor

Greek Letters

$\alpha_{ox} = \frac{k_m}{k_m^o}$	oxidizer–fuel equivalence ratio
$\gamma_i \ = -ln\, r_i$	logarithm of mole fraction of the i-th specie
γ	relative variation of droplet volume at evaporation
δ	thickness of reduced film, m
ε/k	depth of the potential well in the Lennard–Jones potential
ζ_s	reduction threshold for substances
ζ_R	reduction threshold for reactions
ζ_d	reduction threshold of DRGEP method;
η_i	dynamic viscosity of the i-th substance, $N/(m^2 \times s)$
θ	parameter of approximation (θ = 0.4 . . . 0.5)
λ_i	eigenvalues of matrix
μ_i	molecular mass of the i-th specie, $kg/kmol$
μ_m, μ_g	average molecular mass, $kg/kmol$
μ_V	molecular mass of vapor, $kg/kgmol$
μ_q	molecular mass of the q-th liquid fraction, $kg/kmol$
ν_k	valence of the atomic element k
ν'_{is}	stoichiometric coefficient at i-th substance in forward direction of the s-th reversible chemical reaction

Downloaded from https://www.cambridge.org/core. Nottingham Trent University, on 17 Aug 2019 at 02:38:05, subject to the Cambridge Core terms of use, available at https://www.cambridge.org/core/terms. https://www.cambridge.org/core/product/702B9B43429471329E39FCB36C3C550A

ν''_{is}	stoichiometric coefficient at i-th substance in reverse direction of the s-th reversible chemical reaction
$\nu_{ij} = \nu''_{is} - \nu'_{is}$	difference of stoichiometric coefficients in the right-hand side and left-hand side for forward direction of the s-th reversible chemical reaction, $j = s$
$\nu_{ij} = \nu'_{is} - \nu''_{is}$	difference of stoichiometric coefficients in the right-hand side and left-hand side for reverse direction of the s-th reversible chemical reaction, $j = s + m_c$
ρ	density, kg/m^3
ρ_i	partial density of the i-th substance, kg/m^3
ρ_g	density of the gas phase, kg/m^3
ρ_V	vapor density, kg/m^3
ρ_q	density of the q-th liquid fraction, kg/m^3
ρ_{liq}	density of liquid,kg/m^3
σ_{im}	collision diameter of the Lennard–Jones potential
τ_f	integration interval or process time, s
τ_p	residence time, s
$\phi = \frac{k_m^o}{k_m}$	fuel–oxidizer equivalence ratio
$\Omega_j = W_j/C$	ratio of the j-th reaction rate to the total molar concentration,$1/s$
Ω_{im}	reduced collision integral for the i-th specie and mixture

Acronyms

PSR	perfectly stirred reactor
BR	batch reactor
PFR	plug flow reactor
SR	the system of interconnected reactors
LPRE	liquid-propellant rocket engine
SPRE	solid-propellant rocket engine
ABE	air-breathing engine
ICE	internal combustion engine
LM	large molecule
ODE	ordinary differential equations
DRG	Directed Relation Graph (method)
DRGEP	Directed Relation Graph with Error Propagation (method)

Downloaded from https://www.cambridge.org/core. Nottingham Trent University, on 17 Aug 2019 at 02:38:05, subject to the Cambridge Core terms of use, available at https://www.cambridge.org/core/terms. https://www.cambridge.org/core/product/702B9B43429471329E39FCB36C3C550A

Downloaded from https://www.cambridge.org/core. Nottingham Trent University, on 17 Aug 2019 at 02:38:05, subject to the Cambridge Core terms of use, available at https://www.cambridge.org/core/terms. https://www.cambridge.org/core/product/702B9B43429471329E39FCB36C3C550A

Part I

Basic Components of Chemical Nonequilibrium Models

Downloaded from https://www.cambridge.org/core. Nottingham Trent University, on 17 Aug 2019 at 02:47:29, subject to the Cambridge Core terms of use, available at https://www.cambridge.org/core/terms. https://www.cambridge.org/core/product/45923EF97F27DC6146EB97CD7DAC348D

Downloaded from https://www.cambridge.org/core. Nottingham Trent University, on 17 Aug 2019 at 02:47:29, subject to the Cambridge Core terms of use, available at https://www.cambridge.org/core/terms. https://www.cambridge.org/core/product/45923EF97F27DC6146EB97CD7DAC348D

1 Approaches to Combustion Simulation
Patterns, Models, and Main Equations

1.1 Standard Combustion Patterns

Combustion processes (that is, conversion of chemical energy of propellant components into thermal energy of combustion products) are typical for various engineering systems. Working volumes wherein these processes can occur may be represented by combustion chambers of liquid-propellant rocket engines (LPRE), solid-propellant rocket engines (SPRE), air-breathing engines (ABE) steam-gas generators, magneto-hydrodynamic generators (MHD generators), boiler furnaces of thermal electric power stations, and cylinders of internal combustion engines (ICEs) [1]. Besides, further conversion of combustion products with chemical conversions can proceed also in aircraft and rocket engine nozzles, ICE exhaust systems, LPRE gas ducts, etc.

Working volumes of these propulsion and power generation systems feature the availability of a multiphase working medium, a wide range of temperature variation (from hundreds to some thousands of degrees) and pressure (from several tenths of MPa to tens of MPa), chemical conversions not only in gas phase but in condensed phase as well, changes of parameters of state of working medium against the background of intraphase and interphase heat-and-mass transfer and multidimensional flow of working medium, a high degree of turbulence, and nonuniformity of parameters over the working volume. The history of these processes defines, in the end, the energetic and ecological characteristics of a particular propulsion and power generation system. One of the ways of simulating the latter consists in the development of mathematical models of combustion processes along with subsequent computational experiments [2].

Models of processes that occur in propulsion and power generation systems are usually based on mathematical models of some standard combustion modes for propellant components (oxidizer and fuel) in the working volumes. In the following paragraphs, some of these modes are considered in brief.

Combustion in homogeneous zones (Figures 1.1, 1.2, and 1.3). This is the simplest mode of combustion that can be considered as a process of conversion of ideally mixed reactants (propellant components) into combustion products in a sample reactor. Working medium composition and state parameters are uniform at any two points of a reactor but can vary in time [3, 4]. Heat exchange (Q – heat flow) of a reactor and an environment is also possible. Two patterns are most frequently used for simulation of combustion in homogeneous zones:

Downloaded from https://www.cambridge.org/core. Nottingham Trent University, on 17 Aug 2019 at 01:56:34, subject to the Cambridge Core terms of use, available at https://www.cambridge.org/core/terms. https://doi.org/10.1017/9781108581714.001

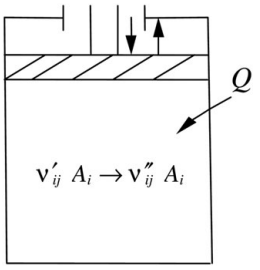

Figure 1.1 Combustion pattern in batch reactor. Q – heat flow.

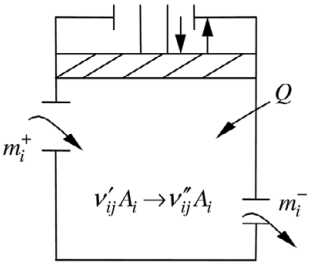

Figure 1.2 Combustion pattern in a perfectly stirred reactor (m_i^+ and m_i^- – mass flows at inlet and outlet).

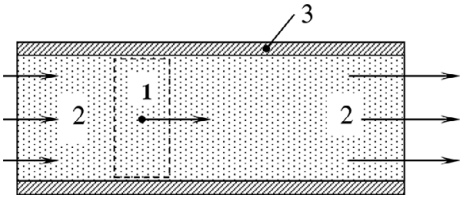

Figure 1.3 Combustion process in plug flow reactor (PFR): (1) moving batch reactor (BR); (2) one-dimensional gas flow; (3) tube wall.

1. Combustion in the batch reactor (BR; Figure 1.1) at no mass exchange with the environment ($m_i^+ = m_i^- = 0$). Problems usually solved in the framework of this procedure involve the assumption that the reactor originally houses the reactants that convert into chemically equilibrium combustion products at combustion.
2. Combustion in perfectly stirred reactor (PSR; Figure 1.2), with obligatory occurrence of mass exchange with environment ($m_i^+ \neq 0; m_i^- \neq 0$). Note here that reactants fed into the reactor are assumed to mix instantly with combustion products. It is usually assumed for the models using PSR [5] that $m_i^+ = m_i^-$ and variation of chemical composition of reacting mixture and state parameters proceed until a certain stationary state is reached, which can be both chemical equilibrium and chemical nonequilibrium.

Apart from these patterns, most frequently used is the approximation of moving BR – plug flow reactor (PFR; Figure 1.3) for simulation of combustion in one-dimensional

Downloaded from https://www.cambridge.org/core. Nottingham Trent University, on 17 Aug 2019 at 01:56:34, subject to the Cambridge Core terms of use, available at https://www.cambridge.org/core/terms. https://doi.org/10.1017/9781108581714.001

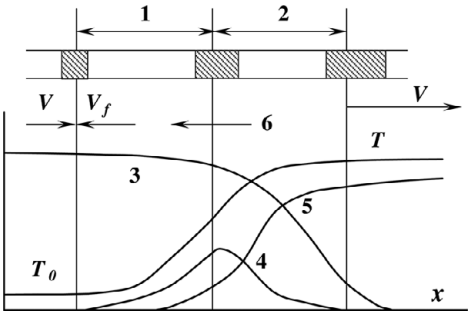

Figure 1.4 Flame front of premixed reactants: (1) heating zone; (2) combustion zone; (3) reactants; (4) intermediate substances; (5) combustion products; (6) heat transfer and diffusion.

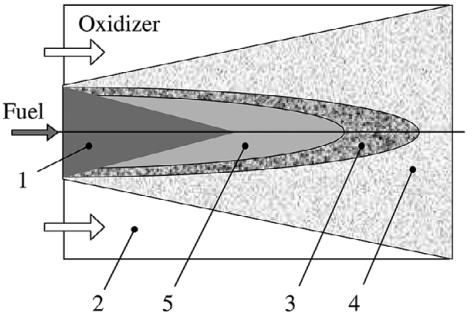

Figure 1.5 Diffusion combustion mode: (1) fuel; (2) oxidizer; (3) combustion zone; (4) nonuniform mixture of oxidizer and combustion products; (5) nonuniform mixture of fuel and combustion products.

reacting flows. In compliance with this procedure, it is assumed that neighboring moving working medium layers (volumes) are not mixed. Now, a thin layer of reacting gas (1) can be arbitrarily isolated, and combustion process can be described in said layer with application of the BRs moving at the gas velocity. In case the gas flow is transient, the combustion will be described by whatever system of BRs is used, while stationary flow may be represented by single BR using a reference system of coordinates.

Combustion in a flame front (deflagration) (Figure 1.4) occurs within a narrow zone, as premixed reactants being fed at its inlet while, at its outlet, combustion products are formed [6, 7]. The flame front is formed at the interaction of three phenomena: chemical reactions of combustion; heat transfer from combustion products to reactants; and diffusion of substances over the front (reactants diffuse with the flow, and combustion products diffuse against the flow). This interaction brings about the formation of a self-sustaining combustion zone displacing relative to fresh mixture at the flame speed (for example, $u_n \approx 1$ m/s). In turbulent flow, magnitude u_n increases notably because of the intensification of transport processes.

Diffusion combustion in parallel flows (Figure 1.5) originates when reactants are fed into the combustion zone separately and react with each other as they are being

Downloaded from https://www.cambridge.org/core. Nottingham Trent University, on 17 Aug 2019 at 01:56:34, subject to the Cambridge Core terms of use, available at https://www.cambridge.org/core/terms. https://doi.org/10.1017/9781108581714.001

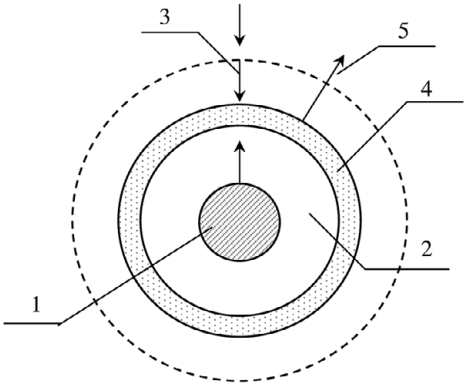

Figure 1.6 Combustion of a liquid fuel droplet in atmosphere of oxidizer: (1) droplet; (2) fuel vapor diffusion toward combustion zone; (3) oxidizer diffusion toward the combustion zone; (4) combustion zone; (5) combustion products diffusion toward the environment.

mixed [7]. Here, chemical reactions in the gas phase as well as diffusion and heat transfer are the governing processes that, unlike flame front, occur both along and across the flow. Several zones may be introduced in diffusion combustion: fuel; oxidizer; combustion zone; and zones of nonuniform mixes of propellant components with combustion products. The problem of simulation of this combustion process should be solved in at least a two-dimensional approximation. This is why it is more complicated than a deflagration mode.

Multiphase Combustion

Several combustion patterns may be introduced in this combustion mode subject to composition and properties of particles of liquid (or solid) phases. Some of them are considered in the following section on the assumption that phases are fixed relative to each other.

Combustion of a liquid fuel droplet in the atmosphere of oxidizer. The example of this pattern of combustion is shown in Figure 1.6 when droplets of fuel with inferior boiling temperature (for example, $T_{boil} \approx 500\,\text{K}$) are injected into oxidizing reacting medium (for example, $T_g > 1000$ K) to get gaseous products of their chemical interaction.

Combustion in this system occurs in some thin layer around the droplet. Gaseous oxidizer diffuses into said layer from the environment while vaporous of fuel diffuses from the droplet. Heat released at combustion propagates on both sides from the combustion layer to heat the oxidizer and to facilitate the droplet heating and evaporation [8].

Combustion of metal particles in the atmosphere of oxidizer. This combustion pattern is shown in Figure 1.7 [9]. A metal particle (for example, an aluminum particle) getting into the high-temperature oxidizing medium with temperature T_g converts into a liquid droplet (1) and, if T_g is higher than the metal ignition temperature ($T_{ign} = 2323$ K), then the combustion process proceeds at contact with gaseous oxidizer (2) to produce refractory oxides (for example, Al_2O_3). If T_g is lower than oxide boiling temperature

Downloaded from https://www.cambridge.org/core. Nottingham Trent University, on 17 Aug 2019 at 01:56:34, subject to the Cambridge Core terms of use, available at https://www.cambridge.org/core/terms. https://doi.org/10.1017/9781108581714.001

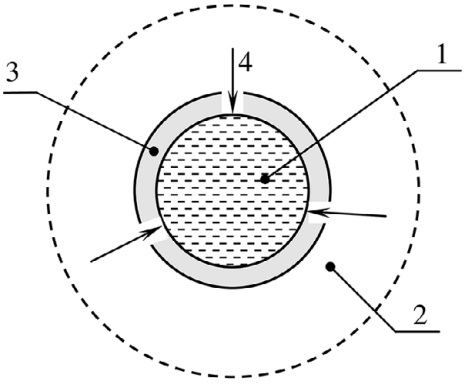

Figure 1.7 Combustion of metal particles in the atmosphere of oxidizer: (1) liquid metal; (2) oxidizing gas medium; (3) refractory oxide film; (4) fractures in oxide film.

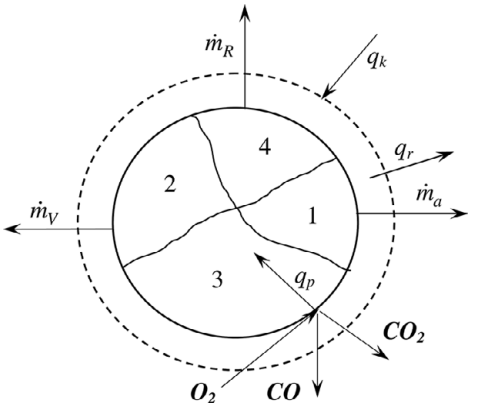

Figure 1.8 Coal particle structure and pattern of its combustion. (1) moisture; (2) volatile matters; (3) fixed carbon; (4) impurities; $\dot{m}_a, \dot{m}_V, \dot{m}_R$ – mass flows of steam, volatile matters, mineral impurities; q_k, q_r, q_p – heat flows from gas to particle (convection), radiative flow, heat flow into the particle.

T_{boil}, (for example, T_g = 2500 K, while T_{boil} = 3253 K), then it remains on the particle surface and forms the oxide film (3). Film thickness increases as combustion proceeds to impede oxidizer contact with the metal surface – hence, to retard the combustion process. However, thermal stresses originating in the oxide film cause fractures (4) through which the oxidizer penetrates the metal surface to make the combustion proceed.

Combustion of coal particles. Figure 1.8 shows the coal particle combustion process and processes that occur at the particle surface and in a boundary layer [10]. At particle heating, first, water contained therein is evaporated (flow $\dot{m}_a$). Then, volatile matters are formed (flow $\dot{m}_V$), carbon is ignited, and mineral impurities are released (flow $\dot{m}_R$). Here, particle temperature (T_p) increases and its density changes. Carbon combustion produces carbon monoxide (CO) and dioxide (CO_2); the ratio between the rates of

Downloaded from https://www.cambridge.org/core. Nottingham Trent University, on 17 Aug 2019 at 01:56:34, subject to the Cambridge Core terms of use, available at https://www.cambridge.org/core/terms. https://doi.org/10.1017/9781108581714.001

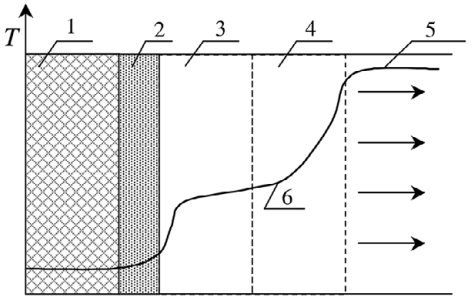

Figure 1.9 Combustion of solid-propellant grain: (1) solid-propellant grain; (2) reaction zone in condensed phase; (3) gasification zone; (4) zone of basic reactions; (5) zone of combustion products; (6) temperature variation.

formation of said substances depends on temperature T_p. Heat flow (q_p) for heating of the particle results from conversion of carbon into CO (or CO_2) on its surface. Multiple reactions – particularly, reactions of combustion of volatile matters – occur outside the particle (in the gas medium). The particles may be heated nonuniformly and are porous and nonspherical. The size of the particles may increase at the release of volatile matters. Heat exchange between particles and gases occurs via convection and radiation. The rates of volatile matter release and carbon are significantly different, but sometimes these processes can overlap.

Combustion of solid propellant (Figure 1.9). In this case, the fuel and oxidizer are in a solid phase and are almost perfectly stirred (in fact, a solid propellant could be treated as a monopropellant), and combustion occurs in the combustion zone similar in essence to the flame front of the premixed gaseous fuel and exider [11] with heat transfer from high-temperature combustion products to the solid-propellant grain. However, phase transitions (and possibly pyrolysis) of both the fuel and the oxidizer occur inside the combustion zone in addition to the processes inherent in a common flame front.

Detonation [12] is the mode of combustion of premixed reactants including the shock wave and zone of chemical conversions next thereto. Unlike flame front (deflagration), the detonation propagates at supersonic speed (V) while diffusion and heat transfer processes are of minor importance. Detonation is a self-sustaining process wherein a shock wave raises the temperature of reactants while the next chemical reactions maintain said shock wave. Figure 1.10 describes the distribution of basic flow parameters in the detonation wave. The motion rate starts to increase in the combustion zone to drop notably after the shock wave. Pressure distribution features an opposite dynamics while the temperature increases continuously. At detonation (unlike flame front), a significant nonequilibrium energy distribution over the degrees of freedom is observed at a certain section after the shock wave.

Combustion in high-temperature propulsion and power generation systems is normally a sophisticated process complicated by a nonuniform distribution of working medium parameters over the working volume, and it comprises several standard

Downloaded from https://www.cambridge.org/core. Nottingham Trent University, on 17 Aug 2019 at 01:56:34, subject to the Cambridge Core terms of use, available at https://www.cambridge.org/core/terms. https://doi.org/10.1017/9781108581714.001

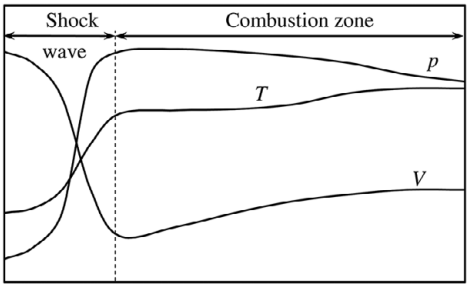

Figure 1.10 Variation of flow parameters at detonation.

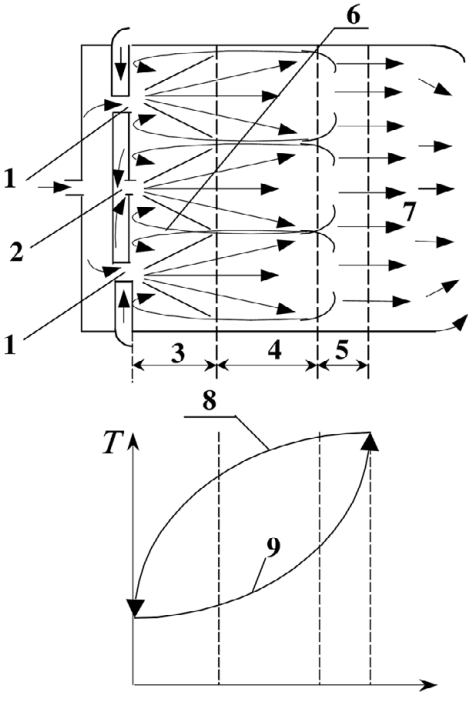

Figure 1.11 Diagram of processes in LPRE combustion chamber: (1) oxidizer injectors; (2) fuel injectors; (3) droplet formation zone; (4) evaporation and mixing zone; (5) combustion zone; (6) recirculation zone; (7) release of combustion products into a nozzle; (8) temperature of the reverse flow; (9) straight flow temperature.

patterns. Let us consider, for example, the processes in the LPRE combustion chamber [1] designed for the conversion of chemical energy of the propellant into thermal energy of combustion products (Figure 1.11). The combustion chamber's main unit is the injector plate composed of the set of fuel and oxidizer injectors; thereof, the injector plate design defines chamber efficiency. Immediately after injection of the components (fuel and oxidizer), different-diameter droplets are formed. These droplets drive the gas mixture located near the injector plate into the combustion zone.

Downloaded from https://www.cambridge.org/core. Nottingham Trent University, on 17 Aug 2019 at 01:56:34, subject to the Cambridge Core terms of use, available at https://www.cambridge.org/core/terms. https://doi.org/10.1017/9781108581714.001

High-temperature combustion products are fed from this zone, in their turn, to the injector plate to produce recirculating flows to maintain the combustion process. Moving droplets of liquid component evaporate, while vapors of fuel and oxidizer stir and react, and convert into combustion products. Thus, the following combustion processes in the LPRE combustion chamber are observed: combustion in the two-phase system; combustion in homogeneous zones; diffusion combustion. At the same time, the key method of maintaining the combustion is implemented by the flame front combustion mode with the replacement of molecular heat-and-mass transfer by the convective transfer.

1.2 Basic Characteristics of Working Medium

Working medium in propulsion and power generation systems, as a rule, is the mixture of individual substances with a predominance of the gas phase, but some of them can be in a condensed (liquid or solid) state. Such substances in combustion analysis are considered to be atoms, molecules, and radicals. Generally, let us identify them by index i, but in some formulas (related to the calculation of chemical equilibrium systems), index k is assigned to atoms while index q is assigned to radicals and molecules. Their composition is described by factors a_{kq}; for example, we obtain for a CO_2 molecule: $a_{C,CO_2} = 1\ a_{O,CO_2} = 2$. Let us denote the valence of atoms by symbol ν_k. Hereinafter, gas components and their mixtures will be considered as ideal gases.

Working medium gas phase composition is described by various magnitudes: C_i, n_i, p_i, p_i interrelated by following formulas:

$$C_i = n_i/V; \quad p_i = C_i R_0 T; \quad \rho_i = p_i \mu_i/(R_0 T); \quad i = 1 \ldots n_b, \tag{1.1}$$

where V is the volume occupied by the gas mixture; C_i, n_i, p_i, ρ_i, μ_i are partial molar concentration, number of moles in volume V, partial pressure, partial density, and molecular mass of i-th substance, respectively; R_0 is universal gas constant; T is temperature; n_b is number of reacting substances.

In many instances, working medium composition is described by relative magnitudes molar r_i or mass g_i fractions, as well as by mole-mass concentrations χ_i. At the variation of state parameters only, these magnitudes (unlike ρ_i, p_i, C_i) remain unchanged. These can vary if chemical reactions proceed in the system or if mass exchange processes occur between the gas and condensed phase or between the system and environment. For ideal gases, these relative values are defined by known formulas:

$$r_i = \frac{n_i}{N_m} = \frac{C_i}{C} = \frac{p_i}{p}; \quad g_i = \rho_i/\rho; \quad \chi_i = g_i/\mu_i, \tag{1.2}$$

where ρ is mixture density; N_m is total number of gas phase moles in volume V, $C = N_m/V$ is total molar concentration.

Average working medium gas phase molecular mass μ_g and interrelation between magnitudes r_i, g_i, χ_i are defined by formulas listed in the Table 1.1.

Downloaded from https://www.cambridge.org/core. Nottingham Trent University, on 17 Aug 2019 at 01:56:34, subject to the Cambridge Core terms of use, available at https://www.cambridge.org/core/terms. https://doi.org/10.1017/9781108581714.001

Table 1.1 Interrelation between magnitudes r_i, g_i, χ_i

–	r_i	g_i	χ_i
r_i	–	$g_i\mu_g/\mu_i$	$\chi_i\mu_i$
g_i	$r_i\mu_i/\mu_g$	–	$\chi_i\mu_i$
χ_i	r_i/μ_g	g_i/μ_i	–
μ_g	$\sum_i r_i\mu_i$	$1/\left(\sum_i g_i/\mu_i\right)$	$1/\sum_i \chi_i$

Content of l-th condensed substance is usually described by mole fraction z_l – defined by formula: $z_l = m_l/m$, where m_l is mass of condensed phase and m is total mass of working medium. Here, average mass fraction of a condensate equals $z_\Sigma = \sum_l z_l$. Every individual substance is described by the parameters of Lennard–Jones potential σ_j (collision diameter) and $(\varepsilon/k)_i$ (depth of potential well). These parameters are used for the calculation of transport coefficients η_i, λ_i, D_i (viscosity, thermal conductivity, diffusion). For example, coefficient of viscosity of i-th substance is defined by the following formula:

$$\eta_i = 26.7 \times 10^{-5} \frac{\sqrt{\mu_i T_i^*}}{\sigma_i^2 \Omega_i^{2,2*}}, \tag{1.3}$$

where $\Omega_i^{2.2*}$ is the collision integral, a function of reduced temperature $T_i^* = T/\left(\frac{\varepsilon}{k}\right)_i$. The detailed data on the calculation of transport coefficients are provided in [4, 13].

The major characteristics of individual substances in the combustion analysis are the following:

- molar characteristics: enthalpy (H_i); internal energy (U_i); specific heat at constant pressure (C_{pi}); specific heat at constant volume (C_{vi}); and corresponding
- mass characteristics: h_i, u_i, c_{pi} , c_{vi} , interrelated by molecular mass , for example, $H_i = \mu_i h_i$.

These values are continuous for gases, while for condensed substances, they are piecewise continuous functions of temperature. There are relationships between thermodynamic characteristics, for example:

$$C_{pi} = dH_i/dT; \quad U_i = H_i - R_0 T; \quad C_{pi} = C_{vi} - R_0. \tag{1.4}$$

Substance-specific heat (hence, an enthalpy change) is known to be defined from experimental data in dependence on temperature [4]. These data are sufficient for performing thermodynamic calculations for nonreactive mixes. But in the case of reacting systems, it is necessary to employ substance enthalpies referenced to some thermodynamic scale. Since chemical reactions do not exhibit the elements transmutation, absolute enthalpies of individual substances can be defined by the principle of "zero standard enthalpy of formation of naturally occurring elements" – which implies that, under standard (reference) conditions (T_0 = 298 K, p = 1 atm), the magnitudes of H_i of chemical elements, given at their stable state, equal zero. For example, $H_{O_2}(\text{gas}) = 0, H_C(\text{graphite}) = 0$, $H_{N_2}(\text{gas}) = 0$. Then, absolute enthalpy of i-th substance is defined by the formula:

Downloaded from https://www.cambridge.org/core. Nottingham Trent University, on 17 Aug 2019 at 01:56:34, subject to the Cambridge Core terms of use, available at https://www.cambridge.org/core/terms. https://doi.org/10.1017/9781108581714.001

$$H_i(T) = H_i^{298} + \int_{T_0}^{T} C_{pi}(t)\,dt + \sum_s \Delta H_s, \tag{1.5}$$

where H_i^{298} is a standard enthalpy of formation of i-th substance; $\sum_s \Delta H_s$ is the sum of heats of phase and polymorphic transitions.

In calculation of combustion, one of the necessary thermodynamic characteristics of every individual substance is molar entropy at p = 1 atm (S_i^0), which depends also on the temperature and requires some absolute scale. For chemically reacting systems, this scale is set proceeding from the third law of thermodynamics that postulates that at 0 K, entropy of whatever substance equals zero. Then, molar entropy of i-th substance is defined by the formula:

$$S_i^0(T) = S_i^{298} + \int_{T_0}^{T} \frac{C_{pi}(t)}{t}\,dt, \tag{1.6}$$

where S_i^{298} is entropy of i-th substance at T_0 = 298 K.

The information on temperature dependencies of $H_i(T)$ and $S_i^0(T)$ is usually tabulated [14, 15], but for the execution of numerical analyses (computations), it is convenient to represent these dependencies as polynomials with individual values of approximation coefficients for every substance and to be integrated in the substances databases, most widely known being the following:

1. **Database TTR** [13] including values $H_i(T), S_i^0(T), C_{pi}(T)$, described by the formula (for gases):

$$H_i = A_{Ii} + \sum_{q=1}^{7} a_{qi} x^q \quad x = 0.001T; \tag{1.7}$$

$$S_i^0 = A_{si} + 10^{-3} a_{1i}\,lnx + \sum_{q=2}^{7} \frac{q}{q-1} a_{qi} x^{q-1}; \tag{1.8}$$

$$C_{pi} = 10^{-3} \sum_{q=1}^{7} q a_{qi} x^{q-1}, \tag{1.9}$$

where A_{Si}, A_{Ii}, $a_{1i} \ldots a_{7i}$ are approximation coefficients in the temperature range T = 298 K … 5000 K, while for condensed substances, the similar relationships are used:

$$H_i = A_{I\,zi} + \sum_{q=1}^{3} a_{qzi} x^q; \quad x = 0.001T; \tag{1.10}$$

$$S_i^0 = A_{szi} + 10^{-3} a_{1zi}\,lnx + \sum_{q=2}^{3} \frac{q}{q-1} a_{qzi} x^{q-1}; \tag{1.11}$$

Downloaded from https://www.cambridge.org/core. Nottingham Trent University, on 17 Aug 2019 at 01:56:34, subject to the Cambridge Core terms of use, available at https://www.cambridge.org/core/terms. https://doi.org/10.1017/9781108581714.001

$$C_{pi} = 10^{-3} \sum_{q=1}^{3} q a_{qi} x^{q-1}, \tag{1.12}$$

for every z-th temperature subinterval.

2. **Database THERMO** [16, 17], wherein values H_i, S_i^0 for gases are calculated by the formulas:

$$\frac{H_i}{R_o T} = a_{1zi} + \frac{a_{2zi}}{2} T + \frac{a_{3zi}}{3} T^2 + \frac{a_{4zi}}{4} T^3 + \frac{a_{5zi}}{5} T^4 + \frac{a_{6zi}}{T}; \tag{1.13}$$

$$\frac{S_i^0}{R_o} = a_{1zi}\, lnT + a_{2zi} T + \frac{a_{3zi}}{2} T^2 + \frac{a_{4zi}}{3} T^3 + \frac{a_{5zi}}{4} T^4 + a_{7zi}; \tag{1.14}$$

$$\frac{C_p}{R_0} = a_{1zi} + a_{2zi} T + a_{3zi} T^2 + a_{4zi} T^3 + a_{5zi} T^4 \tag{1.15}$$

in two temperature intervals: $T = 298\ \text{K} \div T_1\ (z = 1)$; and $T = T_1 \div T_f\ (z = 2)$; $T_1 = 1000$ K; $T_f = 5000$ K or 6000 K. For condensed substances, values H_i, S_i^0 are calculated by formulas of the type (1.10; 1.11), but T_1 and T_f are defined by phase transition temperatures.

3. **Database IVTANTERMO** [18]. Values H_i, S_i^0 for both gaseous and condensed individual substances are represented by the formulas:

$$H_i = \Delta H_{fl}^o + 10^4 \left[-2a_{-2zi} x^{-1} - a_{-1zi} + a_{Lzi} x + a_{1zi} x^2 + 2a_{2zi} x^3 + 3a_{3zi} x^4 \right]; \tag{1.16}$$

$$S_i^0 = -a_{-2zi} x^{-2} + a_{Lzi}\, lnx + a_{0zi} + a_{Lzi} + 2a_{1zi} x + 3a_{2zi} x^2 + 4a_{3zi} x^3; \tag{1.17}$$

$$C_{pi} = 2a_{-2zi} x^{-2} + a_{Lzi} + 2a_{1zi} x + 6a_{2zi} x^2 + 12a_{3zi} x^3;\ x = 0.0001T\ z = 1 \div z_f, \tag{1.18}$$

in some temperature intervals (a_{-2zi}, … , a_{3zi} are approximation coefficients). Note here that the number of approximation intervals z_f may vary from $z_f = 1$ to $z_f = 6$, while magnitudes of T_f can make $T_f = 6000$ K, 10,000 K, or 20,000 K as a subject to a substance.

Important characteristics of reacting mixtures are constants of dissociation of individual substances into atoms based on partial pressures or concentrations [4, 13]:

$$K_q^p = \frac{\prod_k p_k^{a_{kq}}}{p_q}; \tag{1.19}$$

$$K_q^c = \frac{\prod_k C_k^{a_{kq}}}{C_q}, \tag{1.20}$$

where a_{kq} is the number of atoms of k-th type in q-th individual substance.

These constants correspond to so-called basic reactions of dissociation of molecules or radicals into the atoms. For example, for NH_3, these values correspond to the reaction of its dissociation into the atoms: $NH_3 \Leftrightarrow N + H + H + H$, while dissociation constant based on partial pressures is represented by

Downloaded from https://www.cambridge.org/core. Nottingham Trent University, on 17 Aug 2019 at 01:56:34, subject to the Cambridge Core terms of use, available at https://www.cambridge.org/core/terms. https://doi.org/10.1017/9781108581714.001

$$K^p_{NH_3} = \frac{p_N (p_H)^3}{p_{NH_3}}. \tag{1.21}$$

In the general case, dissociation constants for gaseous substances are functions of temperature and could be calculated by the following formula:

$$ln\, K^p_q = \frac{\sum a_{kq} S^0_k - S^0_q}{R_0} - \frac{\sum a_{kq} H_k - H_q}{R_0 T}. \tag{1.22}$$

It will be shown in Chapter 2 that constants of equilibrium for whatever reversible chemical reactions are easily defined from dissociation constants.

Major characteristics of reacting mixtures are mixture enthalpies (H_Σ,h_Σ), which, for ideal gases, are additive values to be defined by formula:

$$H_\Sigma = \sum_i H_i r_i \qquad h_\Sigma = \sum_i h_i g_i = \sum_i H_i r_i / \sum_i \mu_i r_i. \tag{1.23}$$

If the condensed phase is considered split into separate molecules [14], then Formulas (1.23) are valid for heterogeneous mixtures. Specific heats at constant pressure of the mixture of ideal gases are defined by the following relationships:

$$\bar{C}_p = \sum_i C_{pi} r_i; \qquad \bar{c}_p = \sum_i c_{pi} g_i = \sum_i C_{pi} r_i / \sum_i \mu_i r_i. \tag{1.24}$$

In a case of chemical equilibrium reacting mixtures, these specific heats are referred to as "frozen." Equilibrium combustion models assume that gaseous substances can dissociate at heating, which requires extra heat. This energy is frequently related to heat capacity, and, hereby, the concept of "equilibrium heat capacity" originates. The formula for its determination is provided in the papers Gordon et al. [16] and Alemasov et al. [13]. "Equilibrium" specific heats can be several times higher than that of "frozen" one. To describe chemically nonequilibrium processes, only "frozen" heat capacity is usually used, which hereinafter will be simply named as specific heat or heat capacity.

Units of high-temperature propulsion and power generation systems usually use two-component propellants : fuel and oxidizer. Prevalence of positive valence atoms is inherent in fuel while negative valence atoms prevail in oxidizer. Chemical composition of these components can be described in two ways:

- "Real" chemical formulas, for example, oxidizer – N_2O_4 (nitrogen tetroxide) and fuel – N_2H_4 (hydrazine)
- The conditional formula, for example, can be used to describe the components as follows: oxidizer – $N_{0.2}O_{0.4}$ – and fuel – $N_{20}H_{40}$ – i.e., the conditional formulas describe the ratio between atoms in every component (note that the conditional formula can be fully consistent with the real one).

The conditional formulas are used in equilibrium calculations while only "real" chemical formulas should be used in chemical kinetic models. In general, every component can be described by the following formulas: fuel – $\left[b_{1f} b_{2f} \ldots b_{kf} \ldots b_{n_a f}\right]$; oxidizer – $[b_{1ox}\, b_{2ox} \ldots b_{kox} \ldots b_{n_a ox}]$. For example, in the case of component $N_{0.2}O_{0.4}$,

Downloaded from https://www.cambridge.org/core. Nottingham Trent University, on 17 Aug 2019 at 01:56:34, subject to the Cambridge Core terms of use, available at https://www.cambridge.org/core/terms. https://doi.org/10.1017/9781108581714.001

we have $b_{Nox} = 0.2$; $b_{Oox} = 0.4$; $b_{Hox} = 0.0$; while for the $N_{20}H_{40}$ component, we get $b_{Nf} = 20$; $b_{Hf} = 40$; $b_{Of} = 0$. The concepts of stoichiometric ratio of components (κ_o is the mole stoichiometric ratio ; k_m^o is the mass stoichiometric ratio) are similarly defined by the following formulas:

$$\kappa_o = -\sum_{k=1}^{n_a} b_{kf}\,\nu_k \Big/ \sum_{k=1}^{n_a} b_{kox}\,\nu_k; \qquad k_m^o = \kappa_o \sum_{k=1}^{n_a} \mu_k b_{kox} \Big/ \sum_{k=1}^{n_a} \mu_k b_{kf}, \tag{1.25}$$

where μ_k and ν_k are molecular mass and valence of k-th type of atom, and n_a is the number of atoms in reacting mixture.

In reality, in combustion processes proceeding in the propulsion and power generation systems, the ratio between an oxidizer and fuel – oxidizer-to-fuel ratio (κ – mole ratio; k_m – mass ratio) – can notably differ from the stoichiometric oxidizer-to-fuel ratio. The following factors describe aforesaid difference:

– an excess of oxidizer (α_{ox} – equivalence ratio):

$$\alpha_{ox} = \frac{k_m}{k_m^o} = \frac{\kappa}{\kappa_o}, \tag{1.26}$$

(if, for example, $\alpha_{ox} > 1$, then the reacting system has the excess oxidizer and the mixture is called "a lean mixture");

– an excess of fuel (ϕ):

$$\phi = \frac{k_m^o}{k_m} = \frac{\kappa_o}{\kappa}, \tag{1.27}$$

(if $\phi > 1$, then the reacting system has the excess fuel, and mixture is called " a rich mixture").

Every component (as an individual substance) features some enthalpy. As a rule, components feature mass enthalpies h_f and h_{ox}. Then, using stoichiometric oxidizer-to-fuel ratio and equivalence ratio, an enthalpy (h_p) and conditional formula (b_{kp}) of a propellant could be defined. For example, for a known magnitude α_{ox}, we have

$$h_p = \frac{h_f + h_{ox}\alpha_{ox}k_m^o}{1 + \alpha_{ox}k_m^o}; \tag{1.28}$$

$$b_{kp} = b_{kf} + \alpha_{ox}\kappa_o b_{kox}. \tag{1.29}$$

The concept of heating values (calorific values) or heat of formation ΔH_a (highest) and ΔH_b (lowest) is frequently used instead of enthalpy for the fuels when an air is used as an oxidizer. Then, for calculation of fuel enthalpy, it is necessary, first of all, to define total enthalpy of combustion products (1.23) $h_\Sigma(298\,\mathrm{K})$ by their composition at $\alpha_{ox} = 1$ and T = 298 K, or using chemical equilibrium model. Then, knowing total enthalpy of combustion products, the fuel enthalpy can be calculated by the following formula:

$$h_f = \left(1 + k_m^0\right)h_\Sigma(298\mathrm{K}) + \Delta H_b - k_m^0 h_{ox}. \tag{1.30}$$

Downloaded from https://www.cambridge.org/core. Nottingham Trent University, on 17 Aug 2019 at 01:56:34, subject to the Cambridge Core terms of use, available at https://www.cambridge.org/core/terms. https://doi.org/10.1017/9781108581714.001

1.3 Models of Chemical Equilibrium and Detailed Chemical Kinetics

The major phenomenon that is inherent in the combustion is the process of chemical conversion in gas phase. Models describing the conversion, define the depth of simulation of the entire combustion process. The existing models of reacting medium can be divided into the following groups:

- instant response models (without consideration of dissociation)
- chemical equilibrium models
- global kinetic models
- formal chemical kinetics models
- nonequilibrium chemical kinetics models

This paragraph describes two of the groups – chemical equilibrium models and formal chemical kinetics models, which are considered as the basis for constructing mathematical models of combustion processes represented in the entire monograph. Section 1.4 will describe brief characteristics of other models – namely instant response models, global kinetic models, and models of nonequilibrium chemical kinetics.

1.3.1 Chemical Equilibrium Models.

The models of this type are used for solutions of a numerous scientific and engineering problems, because chemical equilibrium models describe the real processes with the sufficient accuracy or can be used as an initial approximation for more accurate models. The applications of equilibrium models to computers were concurrently developed in 1960s in both the former Soviet Union [13] and the USA [16]. They allowed computing of reacting systems of a very complex chemical composition. These models are applied for computation of combustion products' characteristics in cases where it is known that rates of chemical reactions are very high, and reacting systems (for example, combustion products at the exit of combustion chamber of Liquid Propellant Rocket Engine or combustion products in the primary zone of a gas turbine combustor) are in the chemical equilibrium state. Models developed in the USA were described in many papers, including Gordon et al. [16], Reynolds [19], and Warnatz et al. [20]. Thus, the fundamentals of the chemically equilibrium state computation model will be explained herein. This model was developed in the former Soviet Union by Alemasov et al. [13] as applied to BR at constant pressure and temperature (p,T = const). This computation aims at the analysis of the chemical composition of combustion products.

Problem specification and basic initial data include the following assumptions:

a. A set of reacting substances is already known and includes atomic components. For example, such substances for reacting system C + O + H can be the following species $CO, CO_2, H_2, O_2, H, H_2O$, and obligatorily include atoms C, O, and H.
b. For every substance, '*i*', following relations $H_i = f_i^H(T)$ *and* $S_i^0 = f_i^S(T)$, contained in a database of substances, are already known.
c. A reacting medium occupies volume V with already known parameters p, T = const.

Downloaded from https://www.cambridge.org/core. Nottingham Trent University, on 17 Aug 2019 at 01:56:34, subject to the Cambridge Core terms of use, available at https://www.cambridge.org/core/terms. https://doi.org/10.1017/9781108581714.001

d. All substances are in chemical equilibrium between each other and feature definite temperature and pressure.
e. Homogeneous and heterogeneous mixtures are assumed to consist of individual substances in an ideal state. Ideal gas law can be applied to separate gases, including ions and electron gas, as well as to a gas mixture as a whole.
f. An atomic composition of a mixture – for example, propellant conditional formula (b_{ip}) – is already known.
g. Partial pressures of substances (p_i) and some normalizing factor M_c are considered to be unknown.

Basic Equations

The model exploits the notion of "basic reaction" (Section 1.2). Then, one basic reaction can be referenced to every type of molecule or radical. This allows the developing of a universal model (and computation algorithm) wherein the relation (1.19) can be written for every non-atomic substance. Relations written for the set of substances make the first set of equations of the model and are referred to as dissociation equations:

$$\frac{\prod_k p_k^{a_{kq}}}{p_q} = K_q^p, \qquad q = 1, \ldots, n_v; \quad k = 1, \ldots, n_a, \tag{1.31}$$

where p_q – partial pressure of q-th molecular substance (including radicals); p_k – partial pressure of k-th atomic substance; p_i – generalized symbol for molecular and atomic substances ($i = 1 \ldots n_v + n_a$); K_q^p – dissociation constant of q-th substance calculated based on partial pressures, which is a known value; n_v, n_a – quantities of molecular and atomic substances, respectively).

The number of atoms of every type is not changed in chemically reacting medium (at the absence of mass exchange); therefore, for every chemical element the relationship of atom conservation could be represented as following:

$$\sum a_{kq} n_q + n_k \sim b_{kp}, \tag{1.32}$$

where n_k *and* n_q are numbers of moles of atomic and molecular substances in reacting volume.

Since it is known that $p_k \sim n_k$ and $p_q \sim n_{q_t}$, then it may be written as following:

$$\sum a_{kq} p_q + p_k \sim b_{kp}, \qquad k = 1, \ldots, n_a. \tag{1.33}$$

To transform these relations to equations, it is sufficient to multiply their right-hand sides by some unknown factor denoted as M_c. This results in following:

$$\sum a_{kq} p_q + p_k = M_c b_{kp}. \tag{1.34}$$

The number of these equations equals the number of atoms n_a.

Model includes the Dalton equation:

$$\sum_{i=1}^{n_b} p_i = p; \quad i = 1, \ldots, (n_v + n_a = n_b). \tag{1.35}$$

Downloaded from https://www.cambridge.org/core. Nottingham Trent University, on 17 Aug 2019 at 01:56:34, subject to the Cambridge Core terms of use, available at https://www.cambridge.org/core/terms. https://doi.org/10.1017/9781108581714.001

Table 1.2 Atomic composition of propellant components

Symbol of Atom	b_{kf}	b_{kox}	ν_k	μ_k
C	2	0	4	12
H	6	0	1	1
O	0	2	−2	16

Thus, for calculation of the chemical equilibrium composition of combustion products, it is required to solve the system $(n_v + n_a + 1)$ of algebraic equations (1.31), (1.34), and (1.35) with unknowns p_k, p_q, M_c.

Let us cite the example of the ;model for fuel "$C_2H_6 + O_2$" with $\alpha_{ox} = 1, p = 8$ atm, $h_f = -4100$ kJ/kg, $h_{ox} = 0$, assuming that reacting system comprises the substances: H, C, O, O_2, H_2, CH_4, CO, CO_2, H_2O, OH, C_2H_2.

Using Formula (1.25) and the atomic composition from Table 1.2, it is possible to define in a stepwise manner:

$$\kappa_o = -\frac{\sum b_{kf}\nu_k}{\sum b_{kox}\nu_k} = 3.5; \quad k_m^o = \kappa_o \sum_{k=1}^{n_a} \mu_k b_{kox} / \sum_{k=1}^{n_a} \mu_k b_{kf} = 3.5\frac{32}{30} = 3.73; \tag{1.36}$$

$$\begin{aligned} b_{\mathrm{H}_p} &= b_{\mathrm{H}_f} + \alpha_{ox}\kappa_o b_{\mathrm{H}_{ox}} = 6; \\ b_{\mathrm{C}_p} &= b_{\mathrm{C}_f} + \alpha_{ox}\kappa_o b_{\mathrm{C}_{ox}} = 2; \quad b_{\mathrm{O}_p} = b_{\mathrm{O}_f} + \alpha_{ox}\kappa_o b_{\mathrm{O}_{ox}} = 7. \end{aligned} \tag{1.37}$$

Now, the propellant conditional formula will be as follows: $C_2H_6O_7$.

Propellant enthalpy is defined by Formula (1.38):

$$h_p = \frac{h_f + h_{ox}\alpha_{ox}k_m^o}{1 + \alpha_{ox}k_m^o} = \frac{-4100 + 0 \times 1 \times 3.73}{1 + 1 \times 3.73} = -866.8[\mathrm{KJ/kg}]. \tag{1.38}$$

With the help of Formula (1.31) the dissociation equation for molecules and radicals can be easily written:

$$\mathrm{O_2} = \frac{p_{\mathrm{O}}^2}{p_{\mathrm{O_2}}} = K_{\mathrm{O_2}}^p; \quad \mathrm{H_2} \Rightarrow \frac{p_{\mathrm{H}}^2}{p_{\mathrm{H_2}}} = K_{\mathrm{H_2}}^p; \quad \mathrm{CH_4} \Rightarrow \frac{p_{\mathrm{C}}p_{\mathrm{H}}^4}{p_{\mathrm{CH_4}}} = K_{\mathrm{CH_4}}^p; \tag{1.39}$$

$$\mathrm{CO} \Rightarrow \frac{p_{\mathrm{C}}p_{\mathrm{O}}}{p_{\mathrm{CO}}} = K_{\mathrm{CO}}^p; \ \mathrm{CO_2} \Rightarrow \frac{p_{\mathrm{C}}p_{\mathrm{O}}^2}{p_{\mathrm{CO_2}}} = K_{\mathrm{CO2}}^p; \ \mathrm{OH} \Rightarrow \frac{p_{\mathrm{O}}p_{\mathrm{H}}}{p_{\mathrm{OH}}} = K_{\mathrm{OH}}^p; \tag{1.40}$$

$$\mathrm{H_2O} \Rightarrow \frac{p_{\mathrm{H}}^2 p_{\mathrm{O}}}{p_{\mathrm{H_2O}}} = K_{\mathrm{H_2O}}^p; \ \mathrm{C_2H_2} \Rightarrow \frac{p_{\mathrm{C}}^2 p_{\mathrm{H}}^2}{p_{\mathrm{C_2H_2}}} = K_{\mathrm{C_2H_2}}^p. \tag{1.41}$$

The equation of conservation of atoms is obtained with the help of Formula (1.34):

$$C \Rightarrow \ p_{\mathrm{CH_4}} + p_{\mathrm{CO}} + p_{\mathrm{CO_2}} + 2p_{\mathrm{C_2H_2}} + p_{\mathrm{C}} = 2M_c; \tag{1.42}$$

$$\mathrm{H} \Rightarrow \quad 2p_{\mathrm{H_2}} + 4p_{\mathrm{CH_4}} + 2p_{\mathrm{H_2O}} + p_{\mathrm{OH}} + 2p_{\mathrm{C_2H_2}} + p_{\mathrm{H}} = 6M_c; \tag{1.43}$$

$$\mathrm{O} \Rightarrow \quad 2p_{\mathrm{O_2}} + p_{\mathrm{CO}} + 2p_{\mathrm{CO_2}} + p_{\mathrm{H_2O}} + p_{\mathrm{OH}} + p_{\mathrm{O}} = 7M_c. \tag{1.44}$$

Downloaded from https://www.cambridge.org/core. Nottingham Trent University, on 17 Aug 2019 at 01:56:34, subject to the Cambridge Core terms of use, available at https://www.cambridge.org/core/terms. https://doi.org/10.1017/9781108581714.001

Dalton's law will be written as follows:

$$p_O + p_H + p_C + p_{O_2} + p_{H_2} + p_{CH_4} + p_{CO} + p_{CO_2} + p_{H_2O} + p_{OH} + p_{C_2H_2} = 8. \quad (1.45)$$

Method of Solving the Equations

Equations (1.31), (1.34), and (1.35) form the system of nonlinear algebraic equations (the system can be comprised from hundreds and thousands of equations). An algorithm of its solution without a series of preliminary transformations will be unstable for the following reasons:

- There is a possibility of great deviation of magnitudes of the roots of equations (they may differ from each other by 10^{30} times).
- Selected initial approximations of the magnitudes of unknowns are, as a rule, far from the roots of equations.

Under these conditions, the calculation procedure can bring about negative values of magnitudes $(p_k,\ p_q,\ M_c)$, which will stop or "cycle" the solution iteration process. For that reason, the convergence problems are specifically emphasized in a computation algorithm [13]. To rule out negative magnitudes, the replacement of variables is performed in the equations:

$$\gamma_k = ln\, p_k;\ \ \gamma_q = ln\, p_q;\ \ \gamma_c = ln\, M_c. \quad (1.46)$$

As the consequence, these equations are displayed as

$$F_q \equiv \gamma_q - \sum_k a_{kq}\gamma_k + ln\, K_q^p = 0;\ \ q = 1, \ldots, n_v; \quad (1.47)$$

$$F_k \equiv ln\left(\sum_q a_{kq}\, e^{\gamma_q} + e^{\gamma_k}\right) - \gamma_c - ln\, b_{kp} = 0; \qquad i = 1, \ldots, n_a; \quad (1.48)$$

$$F_c \equiv ln\left(\sum_i e^{\gamma_i}\right) - \ln p = 0; \qquad i = 1, \ldots, n_b. \quad (1.49)$$

To solve the system, (1.47–1.49), Newton's method with some modifications [13] was used for the reduction of computations and providing the reliability of results. Newton's method, based on the Taylor expansion, allows the changeover to the following iterative formula:

$$F_s^{(m+1)} = F_s^{(m)} + \sum_v \left(\frac{\partial F_s}{\partial \gamma_v}\right)\Delta\gamma_v; \qquad v, s \in k, q, c, \quad (1.50)$$

where $F_s^{(m)}$ – discrepancy of a previous iteration; $\partial F_s/\partial\gamma_v$ are derivatives calculated from the data of a previous iteration; $\Delta\gamma_v$ – sought increment; m – iteration number.

Assuming that new iteration will bring about the magnitude $F_s^{(m+1)} = 0$, it is possible to write the system of linear equations:

Downloaded from https://www.cambridge.org/core. Nottingham Trent University, on 17 Aug 2019 at 01:56:34, subject to the Cambridge Core terms of use, available at https://www.cambridge.org/core/terms. https://doi.org/10.1017/9781108581714.001

$$\sum_{v}\left(\frac{\partial F_s}{\partial \gamma_v}\right)_m x_v = -\delta_s^{(m)}, \tag{1.51}$$

where unknown increment $\Delta\gamma_v = x_v = \gamma_v^{(m+1)} - \gamma_v^{(m)}$; and $\delta_s^{(m)} \equiv F_s^{(m)}$.

This system should be solved to obtain increments x_s that will be used to find new approximation of the magnitudes of roots:

$$\gamma_s^{(m+1)} = \gamma_s^{(m)} + x_s, \tag{1.52}$$

Formulas (1.51–1.52) require allowing for generalizing the indices:

$$F_s = F_q; \quad x_s = x_q; \quad s = 1, \ldots, n_v; \quad q = 1, \ldots, n_v; \tag{1.53}$$

$$F_s = F_k; \quad x_s = x_k; \quad s = (n_v + 1, \ldots, (n_v + n_a); \quad k = 1, \ldots, n_a; \tag{1.54}$$

$$F_s = F_c; \quad x_s = x_c; \quad s = (n_v + n_a + 1). \tag{1.55}$$

Derivatives of the Jacobian matrix are given here:

$$\begin{aligned} &\frac{\partial F_q}{\partial \gamma_q} = 1; \quad \frac{\partial F_q}{\partial \gamma_k} = -a_{kq}; \quad \frac{\partial F_q}{\partial \gamma_c} = 0; \quad \frac{\partial F_k}{\partial \gamma_q} = \frac{a_{kq}}{B_k} e^{\gamma_q} = \frac{a_{kq}\, p_q}{B_k}; \\ &\frac{\partial F_k}{\partial \gamma_k} = \frac{e^{\gamma_q}}{B_k} = \frac{p_k}{B_k}; \quad \frac{\partial F_k}{\partial \gamma_c} = -1; \quad \frac{\partial F_c}{\partial \gamma_i} = \frac{1}{\sum\limits_q e^{\gamma_i}} \cdot e^{\gamma_i} = \frac{p_i}{\sum\limits_i p_i}; \quad \frac{\partial F_c}{\partial \gamma_c} = 0, \end{aligned} \tag{1.56}$$

where $B_k = \sum\limits_q a_{kq} p_q + p_k$.

Let us substitute Formula (1.56) into System (1.51) to obtain

$$x_q - \sum a_{kq} x_k = -\delta_q; \tag{1.57}$$

$$\sum a_{kq} p_q x_q + p_k x_k - B_k x_c = -\delta_k B_k; \tag{1.58}$$

$$\sum p_i x_i = -\delta_c \sum_i p_i; \quad i \in k, \; q. \tag{1.59}$$

Figure 1.12 shows the structure of a matrix of system factors (1.57–1.59) where "hollow" blocks correspond to zero values of derivatives. By using the Jacobian matrix features, it is possible to reduce the system of these equations from $(n_v + n_a + 1)$ to $(n_a + 1)$ equations. This reduced system is solved by the Gauss method. As a result, new magnitudes x_s are obtained.

To rule out divergence and cycling of iterations, it is expedient to use Formula (1.60) rather than Formula (1.52) for getting unknown magnitudes of computation:

$$\gamma_s^{(m+1)} = \gamma_s^{(m)} + \varsigma^{(m)} x_s, \tag{1.60}$$

where $\varsigma^{(m)}$ is an iteration step factor $\left(\varsigma^{(m)} \le 1\right)$.

There are various ways for defining the iteration step factor; one of them is given next:

Let p to be the iteration number and $\Delta = \sum \mid \delta_q \mid + \sum \mid \delta_k \mid + \mid \delta_c \mid$. Then, magnitude $\varsigma^{(m)}$ can be defined by the following relations:

Downloaded from https://www.cambridge.org/core. Nottingham Trent University, on 17 Aug 2019 at 01:56:34, subject to the Cambridge Core terms of use, available at https://www.cambridge.org/core/terms. https://doi.org/10.1017/9781108581714.001

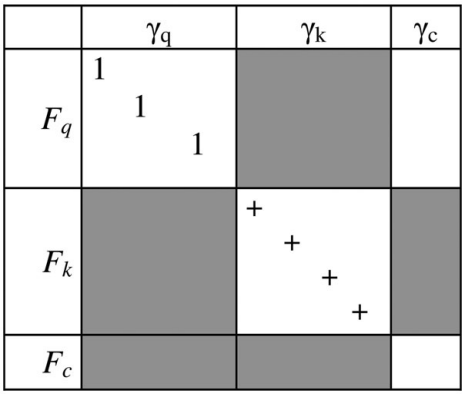

Figure 1.12 Structure of the Jacobian matrix (-non-null elements).

- if $m < 15$, then $\varsigma = \frac{0.3}{\Delta}$;
- if $\varsigma < 0.1$ and $m > 5$, then $\varsigma = 0.1$;
- if $m > 15$, then $\varsigma = \frac{m}{15} - 0.9$;
- if $\varsigma > 1$, then $\varsigma = 1$;
- if $m < 10$ and $\varsigma > 0.6$, then $\varsigma = 0.6$.

The accuracy of computation will be, as a rule, quite sufficient after getting $\max_s \mid \Delta\gamma_s \mid < 0.0001$. The initial approximation is usually selected in the following way:

$$p_k^o = p_q^o = \frac{p}{n_v + n_a}; \quad M_c^o = \frac{20p}{\mu_p}, \tag{1.61}$$

where μ_p is the conditional fuel molecular mass.

Simulation of Condensed Phase

Combustion products, apart from gaseous products, can also comprise of condensed substances calculated at chemical equilibrium with the help of strict thermochemical equations provided, for example, in Alemasov et al. [13].

In compliance with this "classical" approach, condensed phase originates when partial pressure becomes higher than the pressure of saturated vapors ($p_q > p_s^v$). In this case, partial pressure of a substance is considered equal to saturated vapor pressure ($p_q = p_s^v$), while the remaining part of substance forms the condensed phase. For example, for reacting mixture containing inter alia carbon substances CO_2, CO, C^* and C_s (vapor), the equation of conservation of carbon (C) atoms has the following form:

$$ln\left(P_{CO_2} + p_{CO} + p_{C_s} + p_{C^*}\right) - ln\, M_c - ln\, b_{C_p} = 0. \tag{1.62}$$

Downloaded from https://www.cambridge.org/core. Nottingham Trent University, on 17 Aug 2019 at 01:56:34, subject to the Cambridge Core terms of use, available at https://www.cambridge.org/core/terms. https://doi.org/10.1017/9781108581714.001

Besides, the following equation should be incorporated in mathematical model:

$$ln\, p_{C_s} = \frac{S^o_{C_s} - S^o_{C^*}}{R_o} - \frac{H_{C_s} - H_{C^*}}{R_o T}, \tag{1.63}$$

where * is the condensed phase index.

Formula (1.63) differs from standard equation of dissociation (1.47) and decreases the algorithm reliability since Newton's method converges poorly at "stick–slip" variation of unknown characteristics. Because of these problems, an alternative method of condensed phase prediction is sometimes used. Thus, the paper by Gordon et al. [16] used the concept of "single condensed molecule," given the assumption that condensate is contained in combustion products as separate molecules. However, this idea can be implemented only at minor amounts of condensate content, since its high concentration and dispersion result in a notable error at calculation.

This deficiency is eliminated in the method of "large molecules" proposed by Khudyakov in [21]. In compliance with this method, it is assumed that particles of condensed matter B_i are "large molecules" (LM) consisting of n^* condensate molecules (it is accepted that $n^* = 1000$). Note here that set of LM is considered to be a separate gaseous substance B^*_i governed by the ideal gas state equation but with thermodynamic properties (enthalpy and entropy) of the condensate.

Let's assume that condensed phase is distributed over the separate molecules condensed carbon C^*_1 (with parameters H^* and S^*) and is in equilibrium with gas phase (C_s). Then, in this case it is formally possible to write, in a compliance with (1.47), the equation of phase dissociation C^*_1 in phase C_s:

$$ln\, p_{C_s} - ln\, p_{C^*_1} = ln\, K_{C^*_1} = \frac{S^o_{C_s} - S^o_{C^*_1}}{R_o} - \frac{H_{C_s} - H^o_{C^*_1}}{R_o T}. \tag{1.64}$$

Equation (1.64) complies completely with the rules of dissociation equations formation to and provides a good convergence of the results and invariance of model for heterogeneous mixtures. However, if (1.63) is replaced by (1.64) in System (1.47), it is possible to get a significant error in the results because a magnitude of $ln\, p_{C^*_1}$ can be very high.

Now, assume that every condensed molecule consists of n^* molecules of the type C^* (that is, the condensed phase is represented by molecules of the type C^*_n). In this case we have $H_{C^*_n} = n^* H_{C*}$; $S^o_{C^*_n} = n^* S^o_{C^*}$ while molecule dissociation equation C^*_n can be written as follows:

$$n^* ln\, p_{C_s} - ln\, p_{C^*_n} = \frac{n^* S^o_{C_s} - n^* S^o_{C^*}}{R_o} - \frac{n^* H_{C_s} - n^* H_{C^*}}{R_o T}. \tag{1.65}$$

By dividing by n^*, we get

$$ln\, p_{C_s} - \frac{ln\, p_{C^*_n}}{n^*} = \frac{S^o_{C_s} - S^o_{C^*}}{R_o} - \frac{H_{C_s} - H_{C^*}}{R_o T}. \tag{1.66}$$

If $n^* \to \infty$, then Equation (1.64) will be identical to Equation (1.63) and at $n^* = 1000$, the error caused by summand $\frac{ln\, p_{C^*_n}}{n^*}$ becomes a negligible quantity.

Downloaded from https://www.cambridge.org/core. Nottingham Trent University, on 17 Aug 2019 at 01:56:34, subject to the Cambridge Core terms of use, available at https://www.cambridge.org/core/terms. https://doi.org/10.1017/9781108581714.001

1.3.2 Formal Chemical Kinetics

Basic Concepts and Laws

Unlike chemical equilibrium models, chemical kinetics allows for dynamics of a composition of a reacting mixture at limited reaction rates. Combustion in a gas medium is described by the set of chemical reactions that generally proceed at a time. Reactions that describe chemical transformations caused by collision of particles (atoms, radicals, molecules) are referred to as elementary reactions. A branch of theoretical chemical kinetics that deals with elementary reactions is called detailed (formal) chemical kinetics [2, 3, 20, 22, 23, 24]. Fundamentals of this theory are stated in this section. The reacting system (H + F) is being used as an accompanying example. Let us consider this system containing a priori the substances H_2 and F_2, which convert into combustion products in a combustion process. Chemical conversions of these reactants are described by the set of elementary reactions with rate constants listed in Table 1.3 (the units are cm, gmol, K, and sec), where k_s^+– rate constant of forward direction of reaction s; A_s^+, n_s^+, E_s^+– parameters of Arrhenius equation written for forward direction of reaction s; $\nu_{is}^{'}$, $\nu_{is}^{''}$ – stoichiometric coefficients of substance i in forward and reverse directions of reaction s, respectively.

To formalize the statement and writing of generalized equations, it is necessary to number the reacting medium substances. The latter are numbered in the example as follows: (1) H; (2) F; (3): H2; (4) F2; (5) HF. Index "*i*" will be used for substances while index "*s*" will be used for reactions. Let us describe the reacting medium properties and characteristics in compliance with detailed chemical kinetics.

1. Elementary reactions proceed in forward and reverse directions. For example, the R1 reaction (Table 1.4) equation in forward direction is written as follows: $2F + M \Rightarrow F_2 + M$; while in reverse direction we have $F_2 + M \Rightarrow 2F + M$.
2. Participation of i-th substance in s-th reaction is described by stoichiometric coefficients: $\nu_{is}^{'}$ in forward direction and $\nu_{is}^{''}$ in reverse direction. The Table 1.4 lists these coefficients for reacting system under consideration.
3. Catalytic particle (third body) M of vital role participates in some reactions. Let us consider reaction R3 as an example. In principle, it can proceed without particle M as well, that is, like:

Table 1.3 Approximate reaction mechanism for the system "F+H" ($s = 1...6$)

№ (Rs)	Reaction	Rate Constant $k_s^+ = A_s^+ T^{n_s^+} \, exp\left(-E_s^+/R_0T\right)$
R1	$2F + M \Leftrightarrow F_2 + M$	$1.1\times10^{18}\ T^{-1.0}$
R2	$2H + M \Leftrightarrow H_2 + M$	$1.38\times10^{20}\ T^{-1.5}$
R3	$F + H + M \Leftrightarrow HF + M$	$10^{19}\ T^{-1.0}$
R4	$F_2 + H \Leftrightarrow F + HF$	$1.26\times10^{14}\ \exp(-2400\ /R_0T)$
R5	$F + H_2 \Leftrightarrow H + HF$	$1.58\times10^{14}\ \exp(-1600\ /R_0T)$
R6	$F_2 + H_2 \Leftrightarrow H + HF$	$10^{13}\ \exp(-25{,}000\ /R_0T)$

Downloaded from https://www.cambridge.org/core. Nottingham Trent University, on 17 Aug 2019 at 01:56:34, subject to the Cambridge Core terms of use, available at https://www.cambridge.org/core/terms. https://doi.org/10.1017/9781108581714.001

Table 1.4 Coordination of stoichiometric coefficients and chemical reactions for the system (H+F)

	ν'_{is}					ν''_{is}				
	H	F	H_2	F_2	HF	H	F	H_2	F_2	HF
Reactions	(1)	(2)	(3)	(4)	(5)	(1)	(2)	(3)	(4)	(5)
R1. $2F + M \Leftrightarrow F_2 + M$	-	2	-	-	-	-	-	-	1	-
R2. $2H + M \Leftrightarrow H_2 + M$	2	-	-	-	-	-	-	1	-	-
R3. $F + H + M \Leftrightarrow HF + M$	1	1	-	-	-	-	-	-	-	1
R4. $F_2 + H \Leftrightarrow F + HF$	1	-	-	1	-	-	1	-	-	1
R5. $F + H_2 \Leftrightarrow H + HF$	-	1	1	-	-	1	-	-	-	1
R6. $F_2 + H_2 \Leftrightarrow HF + HF$	-	-	1	1	-	-	-	-	-	2

$$\text{R3a. } H + F \Rightarrow HF. \tag{1.67}$$

In this case, the high energy of atoms H and F will be absorbed by molecule HF to make it overexcited and dissociated quickly into atoms. However, at the moment of formation of this molecule, the third particle (whatever atom, radical, or molecule) can collide therewith to carry off the excess energy so that HF molecule becomes stable. Therefore, the R3 reaction is a real existing reaction while third body particle M is identified as any particle of a reacting system (in our example, $M \in H, H_2, F, F_2, HF$).

4. Every elementary reaction is described by the order equal to the sum of stoichiometric coefficients (the sum of particles involved in a single collision).

   A reaction can have different orders in forward and reverse directions. For example, the R2 reaction has third order in the forward direction and second order in the reverse direction.

   Three types of elementary reactions are most probable: mono-, bi-, and trimolecular. Sometimes, zero-order reactions could be also used. The flowing units – cm, gmol, and s – are traditional for chemical kinetics. Then, reaction rate features the unit $[W_s]$ = gmol/(cm^3 s). The dimension of the rate constant is defined by reaction order it is related to, namely:
   - for a zeroth-order reaction $[k_s] = \text{gmol}/(\text{cm}^3\text{s})$;
   - for a first-order reaction $[k_s] = 1/\text{s}$;
   - for a second-order reaction $[k_s] = \text{cm}^3/(\text{gmol s})$;
   - for a third-order reaction $[k_s] = \text{cm}^6/\left(\text{gmo1}^2\text{s}\right)$.

5. The rate of every elementary reaction is described by the substance concentration variation in this reaction per unit of time:

$$W_{is} = \left(\frac{dC_i}{d\tau}\right)_s. \tag{1.68}$$

In particular, variation rate of the content of substance H in reaction R4 is written in the following way:

Downloaded from https://www.cambridge.org/core. Nottingham Trent University, on 17 Aug 2019 at 01:56:34, subject to the Cambridge Core terms of use, available at https://www.cambridge.org/core/terms. https://doi.org/10.1017/9781108581714.001

$$W_{14} = \left(\frac{dC_H}{d\tau}\right)_4.$$

In the general case, the following reactions occur in reacting medium that comprises of the substances B_i:

$$\sum_i \nu'_{is} B_i \Leftrightarrow \sum_i \nu''_{is} B_i; \quad i = 1, \ldots, n_b \; s = 1, \ldots, m_c, \tag{1.69}$$

where n_b – number of reacting substances and m_c – number of reactions in reacting medium.

6. Formal kinetics exploits rate constants of both forward and reverse chemical reactions that are represented in Arrhenius form. For example, for forward direction,

$$k_s^+ = A_s^+ T^{n_s^+} \, exp\left(-E_s^+/R_0 T\right), \tag{1.70}$$

where A_s^+, n_s^+, E_s^+ are factors describing the forward direction of s-th reaction: pre-exponential factor (temperature-independent constant), temperature factor and activation energy , respectively.

Formula (1.70) defines the dimension A_s^+ by the reaction order, n_s^+ is a dimensionless unit, and E_s^+ features the units [cal/gmol], while universal gas constant R_0 =1.987 cal/(gmol·K). Magnitudes A_s^+, n_s^+, E_s^+ are usually defined empirically and in many respects depend on actual conditions of reaction occurrence and on the method of experimental data approximation [22, 23]. Therefore, in different published sources for the same reaction, these factors may notably differ (this relates in particular to magnitudes A_s^+, n_s^+).

The following laws act in detailed chemical kinetics.

Mass action law. In compliance with the law, the variation rate of the content of substance i in reaction j forward direction is written as follows:

$$W_{is}^+ = \left(\nu''_{is} - \nu'_{is}\right) k_s^+ \prod_p C_p^{\nu'_{is}} \cdot \quad i, p = 1 \ldots n_b. \tag{1.71}$$

That is, elementary chemical reaction rate varies with concentration of substances involved in the reaction in orders equal to stoichiometric coefficients. In particular, for rate of substance H (1) content variation in reaction R4, we have

$$W_{14}^+ = (-1) \times 1.26 \times 10^{14} \, exp\left(-2400/R_0 T\right) C_1 C_4. \tag{1.72}$$

A similar formula is valid for the reverse direction as well:

$$W_{is}^- = \left(\nu'_{is} - \nu''_{is}\right) k_s^- \prod_p C_p^{\nu''_{ps}}, \tag{1.73}$$

where k_s^+ and k_s^- – s-th reaction rate constants in forward and reverse directions, respectively.

Downloaded from https://www.cambridge.org/core. Nottingham Trent University, on 17 Aug 2019 at 01:56:34, subject to the Cambridge Core terms of use, available at https://www.cambridge.org/core/terms. https://doi.org/10.1017/9781108581714.001

Principle of independence of chemical reactions. The total rate of i-th substance content variation (W_i) is defined as the sum of rate variations of content of that substance in all elementary reactions that occur in a reacting medium:

$$W_i = \sum_s W_{is}^+ + \sum_s W_{is}^-; \quad i = 1 \ldots n_b \qquad s = 1 \ldots m_c. \tag{1.74}$$

For example, substance F_2 (4) content variation rate is described as follows:

$$W_4 = W_{41}^+ + W_{41}^- + W_{44}^+ + W_{44}^- + W_{46}^+ + W_{46}^-. \tag{1.75}$$

Principle of limiting transition. Rate constants of reversible elementary reaction s (k_s^+ and k_s^-) are interrelated by the ratio:

$$\frac{k_s^+}{k_s^-} = K_s^c, \tag{1.76}$$

where $K_s^c = f(T)$ – equilibrium constant of s-th chemical reaction .

This ratio represents a concordance of chemical equilibrium model (see Subsection 1.3.1) with detailed chemical kinetics. In this case, the results of chemical kinetic calculations, with time approaching infinity ($\tau \to \infty$), approach the data obtained from chemical equilibrium model.

In fact, at the chemical equilibrium state, we have the following formula for every reaction:

$$\mid \nu_{is}'' - \nu_{is}' \mid k_s^+ \prod_p C_{pe}^{\nu_{is}'} = \mid \nu_{is}' - \nu_{is}'' \mid k_s^- \prod_p C_{pe}^{\nu_{is}''} \quad i,\ p = 1 \ldots n_b; \quad s = 1 \ldots m_c, \tag{1.77}$$

where e – equilibrium concentration index.

Then, the following formula can be written for equilibrium constant:

$$\mid \nu_{is}'' - \nu_{is}' \mid k_s^+ \prod_p C_{pe}^{\nu_{is}'} = \mid \nu_{is}' - \nu_{is}'' \mid k_s^- \prod_p C_{pe}^{\nu_{is}''} \quad i, p = 1, \ldots, n_b \quad s = 1 \ldots, m_c, \tag{1.78}$$

This constant is known to be calculated by methods of chemical thermodynamics [4, 20] and to be approximated by a relation like $K_s^c = f_s(T)$. However, more expedient is the determination of equilibrium constants directly in the computation process with the application of data on constants of dissociation of the substance into atoms; see (1.19) and (1.20).

It can be shown that equilibrium constants of elementary reactions are the combinations of constants of dissociation of substances into atoms; see (1.20). The equilibrium constant is written as follows for arbitrary j-th elementary reaction:

$$K_s^c = \prod_i \left(K_i^c\right)^{\nu_{is}'} \Big/ \prod_i \left(K_i^c\right)^{\nu_{is}''}, \quad i = 1, \ldots, n_b \qquad s = 1, \ldots, m_c, \tag{1.79}$$

where dissociation constants based on concentrations K_s^c are computed for non-atomic substances by relationships:

Downloaded from https://www.cambridge.org/core. Nottingham Trent University, on 17 Aug 2019 at 01:56:34, subject to the Cambridge Core terms of use, available at https://www.cambridge.org/core/terms. https://doi.org/10.1017/9781108581714.001

$$K_i^c = K_i^p \left(R_o T\right)^{\left(1-\sum a_{ki}\right)}, \qquad i = 1, \ldots, n_b, \tag{1.80}$$

where K_i^p is defined by Formula (1.19), while for atomic substances, the accepted is $K_i^p = 1$.

Let us show the validity of Formula (1.79) for reaction (R4) $F_2 + H_2 \Leftrightarrow HF + HF$.

In compliance with (1.78), we have

$$K_{R4}^c = \frac{C_{e,\mathrm{HF}}\, C_{e,\mathrm{HF}}}{C_{e,\mathrm{F_2}}\, C_{e,\mathrm{H_2}}}. \tag{1.81}$$

Application of formulas in (1.20) brings about the following, for example, for substance HF: $C_{e,\mathrm{HF}} = \frac{C_{e,\mathrm{H}}\, C_{e,\mathrm{F}}}{K_{\mathrm{HF}}^c}$. Substitution of similar relations for remaining substances to (1.81) brings about

$$K_{R4}^c = \frac{C_{e,\mathrm{HF}}\, C_{e,\mathrm{HF}}}{C_{e,\mathrm{F_2}}\, C_{e,\mathrm{H_2}}} = \frac{\dfrac{C_{e,\mathrm{H}}\, C_{e,\mathrm{F}}}{K_{\mathrm{HF}}^c} \times \dfrac{C_{e,\mathrm{H}}\, C_{e,\mathrm{F}}}{K_{\mathrm{HF}}^c}}{\dfrac{C_{e,\mathrm{F}}\, C_{e,\mathrm{F}}}{K_{\mathrm{F_2}}^c} \times \dfrac{C_{e,\mathrm{H}}\, C_{e,\mathrm{H}}}{K_{\mathrm{H_2}}^c}}. \tag{1.82}$$

Now, allowance for equal number of atomic concentrations in the numerator and denominator (since the number of atoms in chemical reactions does not vary) brings about, finally,

$$K_{R4}^c = \frac{\dfrac{C_{e,\mathrm{H}}\, C_{e,\mathrm{F}}}{K_{\mathrm{HF}}^c} \dfrac{C_{e,\mathrm{H}}\, C_{e,\mathrm{F}}}{K_{\mathrm{HF}}^c}}{\dfrac{C_{e,\mathrm{F}}\, C_{e,\mathrm{F}}}{K_{\mathrm{F_2}}^c} \dfrac{C_{e,\mathrm{H}}\, C_{e,\mathrm{H}}}{K_{\mathrm{H_2}}^c}} = \frac{K_{\mathrm{F_2}}^c\, K_{\mathrm{H_2}}^c}{K_{\mathrm{HF}}^c\, K_{\mathrm{HF}}^c}. \tag{1.83}$$

Equations describing the rate of variation of substances concentrations at any moment are called kinetic equations or *equations of chemical kinetics*. These equations in the formal chemical kinetics model are formed due to the principle of independence of elementary chemical reactions; that is, for the chemical process proceeding at constant volume for i-th substance, it can be written:

$$\frac{dC_i}{d\tau} = W_i = \sum_{s=1}^{m_c} W_{is}^{+} + \sum_{s=1}^{m_c} W_{is}^{-}; \quad i = 1, \ldots, n_b; \qquad s = 1, \ldots, m_c. \tag{1.84}$$

Allowing for mass action law (1.71) and (1.73), Equation (1.84) can be rewritten in the following way:

$$\frac{dC_i}{d\tau} = \sum_{s=1}^{m_c} \left(\nu_{is}'' - \nu_{is}'\right) k_s^{+} \prod_{k=1}^{n_b} C_k^{\nu_{ks}'} + \sum_{s=1}^{m_c} \left(\nu_{is}' - \nu_{is}''\right) k_s^{-} \prod_{k=1}^{n_b} C_k^{\nu_{ks}''}. \; i,k = 1, \ldots, n_b; \; j = 1, \ldots, m_c. \tag{1.85}$$

The equations in (1.85) are valid at absence of substance supply into the volume and substance discharge and allow defining at any time the concentration of i-th substance related to this equation.

Downloaded from https://www.cambridge.org/core. Nottingham Trent University, on 17 Aug 2019 at 01:56:34, subject to the Cambridge Core terms of use, available at https://www.cambridge.org/core/terms. https://doi.org/10.1017/9781108581714.001

For example, the following equations shown above for constant volume (V = const) may be written for reacting system (H, F, F_2, H_2, HF):

$$\frac{dC_{\mathrm{H}}}{d\tau} = -2k_2^+ C_{\mathrm{H}}^2 C + 2k_2^- C_{\mathrm{H}_2} C - k_3^+ C_{\mathrm{F}} C_{\mathrm{H}} C + k_3^- C_{\mathrm{HF}} C - k_4^+ C_{\mathrm{F}_2} C_{\mathrm{H}} + k_4^- C_{\mathrm{F}} C_{\mathrm{HF}} + 2k_5^+ C_{\mathrm{F}} C_{\mathrm{H}_2}^2 - 2k_5^- C_{\mathrm{H}} C_{\mathrm{HF}}, \tag{1.86}$$

$$\frac{dC_{\mathrm{F}}}{d\tau} = -2k_1^+ C_{\mathrm{F}}^2 C + 2k_1^- C_{\mathrm{F}_2} C - k_3^+ C_{\mathrm{F}} C_{\mathrm{H}} C + k_3^- C_{\mathrm{HF}} C + 2k_4^+ C_{\mathrm{F}}^2 C_{\mathrm{H}} - 2k_4^- C_{\mathrm{F}} C_{\mathrm{HF}} - k_5^+ C_{\mathrm{F}} C_{\mathrm{H}_2} + k_5^- C_{\mathrm{H}} C_{\mathrm{HF}}, \tag{1.87}$$

$$\frac{dC_{\mathrm{F}_2}}{d\tau} = +k_1^+ C_{\mathrm{F}}^2 C - k_1^- C_{\mathrm{F}_2} C - k_4^+ C_{\mathrm{F}_2} C_{\mathrm{H}} + k_4^- C_{\mathrm{F}} C_{\mathrm{HF}} - k_6^+ C_{\mathrm{F}_2} C_{\mathrm{H}_2} + k_6^- C_{\mathrm{HF}}^2, \tag{1.88}$$

$$\frac{dC_{\mathrm{H}_2}}{d\tau} = +k_2^+ C_{\mathrm{H}}^2 C - k_2^- C_{\mathrm{H}_2} C - k_5^+ C_{\mathrm{F}} C_{\mathrm{H}_2} + k_5^- C_{\mathrm{H}} C_{\mathrm{HF}} - k_6^+ C_{\mathrm{F}_2} C_{\mathrm{H}_2} + k_6^- C_{\mathrm{HF}}^2, \tag{1.89}$$

where C – a total concentration of a mixture.

Databases of parameters of reactions – apart from those of the first, second, and third orders – frequently include the Lindemann reactions [24] and its more accurate representation – i.e., "Troe" reactions [4] called "the pressure-dependent reactions" or "variable-order reactions." They usually imitate the decomposition of polyatomic molecules brought about by the collision with the third body M and are formally written as follows:

$$\mathrm{A} + (\mathrm{M}) \Leftrightarrow \mathrm{B} + \mathrm{D} + (\mathrm{M}). \tag{1.90}$$

Such notation means that, for example, at high pressures, this reaction is the first-order reaction:

$$\mathrm{A} \Leftrightarrow \mathrm{B} + \mathrm{D}. \tag{1.91}$$

Meanwhile, at low pressures, it is the second-order reaction:

$$\mathrm{A} + \mathrm{M} \Leftrightarrow \mathrm{B} + \mathrm{D} + \mathrm{M}. \tag{1.92}$$

But, as Lindemann proposed, the reaction (1.90) is a summarized one and can be represented by two elementary reactions:

$$\mathrm{A} + \mathrm{M} \underset{k_1^- \leftarrow}{\overset{\rightarrow k_1^+}{\rightleftharpoons}} \mathrm{A}^* + \mathrm{M}, \tag{1.93}$$

and

$$\mathrm{A}^* \underset{k_2^- \leftarrow}{\overset{\rightarrow k_2^+}{\rightleftharpoons}} \mathrm{B} + \mathrm{D}, \tag{1.94}$$

which follow laws of chemical kinetics, and their rate constants k_1^+, k_1^-, k_2^+, k_2^- depend only on the temperature.

Downloaded from https://www.cambridge.org/core. Nottingham Trent University, on 17 Aug 2019 at 01:56:34, subject to the Cambridge Core terms of use, available at https://www.cambridge.org/core/terms. https://doi.org/10.1017/9781108581714.001

However, if these reactions are formally combined into a single reaction (with exclusion of excited molecule A*), then it is possible to obtain the reaction

$$\mathrm{A} \underset{k_{ef}^{-} \leftarrow}{\overset{\rightarrow k_{ef}^{+}}{}} \mathrm{B} + \mathrm{D}. \tag{1.95}$$

Rate constants of this reaction depend on both temperature and pressure. The decomposition rate from Formula (1.95) is reported in terms of

$$W = k_{ef}^{+} C_{\mathrm{A}}. \tag{1.96}$$

Application of Formulas (1.93) and (1.94) to the rate constant k_{ef}^{+} gives

$$k_{ef}^{+} = \frac{k_2^{+} k_1^{+} C}{k_1^{-} C + k_2^{+}} = f(T,\ p), \tag{1.97}$$

where $C = p/(R_0 T)$.

However, this constant is a formal one (nonphysical), and representation of Reaction (1.95) does not yet define the order of this reaction. Particularly at high pressures ($p \to \infty$), we can obtain the following from (1.97):

$$k_{ef}^{+} = \frac{k_2^{+} k_1^{+}}{k_1^{-}}, \tag{1.98}$$

wherefrom

$$W = \frac{k_2^{+} k_1^{+}}{k_1^{-}} C_{\mathrm{A}}, \tag{1.99}$$

which depicts Reaction (1.95) as a monomolecular that proceeds in forward direction.

But at low pressures, ($p \to 0$) follows from (1.97):

$$k_{ef}^{+} = k_1^{+} C, \tag{1.100}$$

wherefrom $W = k_1^{+} C\ C_{\mathrm{A}}$, which depicts Reaction (1.95) in its forward direction as bimolecular one.

As shown earlier, Reaction (1.90) is not a new type of reactions, but represents a set of two elementary reactions. If somewhat credible thermodynamic properties are attributed to substance A* (excited state of molecules A) and entered in the database of these substances, then the Lindemann reaction can be represented by two elementary pressure-independent reactions.

By now, multitude gas phase elementary reactions have been analyzed and described. These are accumulated in multiple databases [25, 26, 27, 28, 29] and, as a rule, feature similar structures of the type: "Symbolic notation of the reaction; Arrhenius parameters (A_s^{+}, n_s^{+}, E_s^{+}); temperature interval, reference to publications" (for instance, see Table 1.5).

For reactions involving the third body (M), catalytic efficiencies of individual substances are frequently cited.

Downloaded from https://www.cambridge.org/core. Nottingham Trent University, on 17 Aug 2019 at 01:56:34, subject to the Cambridge Core terms of use, available at https://www.cambridge.org/core/terms. https://doi.org/10.1017/9781108581714.001

Table 1.5 An excerpt from database of reactions [27]

CH2O+O=HCO+OH	1.80E+13	0.0	3080.0
HCO+O2=HO2+CO	7.58E+12	0.0	410.0
HCO+M=H+CO+M	1.86E+17	–1.0	17,000.0
H2O/5.0/ H2/1.87/ CO2/3.0/			
CO/1.87/ CH4/2.81/			
HCO+OH=H2O+CO	1.00E+14	0.0	0.0

Such databases include, as a rule, "Troe" reactions with structure that differs from that of standard elementary reaction. Many data bases are specialized: [27] – reactions of heavy hydrocarbons; [29] – reactions in the medium: C+ H+ O+ N; [26] – reactions of sulfur-bearing substances: S + H + O + N, etc. Usually, such databases contain also data on thermodynamic properties of included in reaction mechanisms substances represented by polynomials. Computer codes for computation of chemical nonequilibrium processes such as, for example, CHEMKIN [5], KINTECUS [30], and FLUENT [31] incorporate their own databases. Since one and the same reaction might have been analyzed by various scientists, various values of Arrhenius factors could be observed.

1.4 Models of Instant Response, Global Kinetic Models, and Models of Nonequilibrium Chemical Kinetics

The previous section presented the peculiarities of chemical equilibrium models and formal (equilibrium) chemical kinetics models in detail that made the basis of described mathematical models of combustion and chemical nonequilibrium flows. Brief characteristics of other known models of reacting systems will be given also.

1.4.1 Models of Instant Response without Dissociation

These models are the simplest out of the models of the calculation of composition of combustion products [11]. They are based on the equation of conservation of atoms; therefore, the number of atoms in combustion products should equal the number of corresponding atoms in reactants.

Assume that it is necessary to calculate combustion products composition for some propellant of conditional formula $\left[b_{1p}b_{2p}\ldots b_{kp}\ldots b_{n_ap}\right]$. Let's accept symbol b_{mp} for the designation of number of atoms of m type, the quantity of which is maximum in the conditional formula. Then, let us define the set of accountable substances in combustion products $B_i(i = 1 \ldots n_a)$ and designate their mole fractions via r_i (unknown values). Then, proceeding from the atoms conservation equation, it can be written:

$$\frac{\sum\limits_i a_{ki}r_i}{\sum\limits_i a_{mi}r_i} = \frac{b_{kp}}{b_{mp}};\quad i = 1, \ldots,\ n_a;\qquad k = 1, \ldots,\ n_a(k \neq m). \tag{1.101}$$

Downloaded from https://www.cambridge.org/core. Nottingham Trent University, on 17 Aug 2019 at 01:56:34, subject to the Cambridge Core terms of use, available at https://www.cambridge.org/core/terms. https://doi.org/10.1017/9781108581714.001

The number of these equations equals $(n_a - 1)$. Complement the preceding equations with normalizing equation $\sum_i r_i = 1$ to obtain the system of equations composed by n_a linear equations for them to be solved for r_i determination.

A simpler version of instant response model [32] considers oxidizer, fuel, and combustion products to be three individual substances without chemical formulas but with known stoichiometric ratio of components k_m^0. Then, the conversion of components into combustion products is displayed by the following scheme:

Combustion products + fuel + oxidizer → Combustion products + fuel for $k_m < k_m^0$; Combustion products + oxidizer for $k_m > k_m^0$

With mass fractions g_f, g_{ox}, g_{cp} (fuel, oxidizer, and combustion products mass fractions in reacting mixture), the aforesaid scheme can be rewritten for the case $k_m > k_m^0$ in the following form:

$$g_{cp}^v + g_f^v + g_{ox}^v \equiv g_{cp}^v + g_f^v + k_m g_f^v \Rightarrow \quad g_{cp}^w + g_{ox}^w, \tag{1.102}$$

where

$$g_{cp}^w = g_{cp}^v + g_f^v\left(1 + k_m^0\right); \qquad g_{ox}^w = g_f^v\left(k_m - k_m^0\right). \tag{1.103}$$

While for the case $k_m < k_m^0$,

$$g_{cp}^v + g_f^v + g_{ox}^v \equiv g_{cp}^v + g_f^v + k_m g_f^v \Rightarrow \quad g_{cp}^w + g_f^w, \tag{1.104}$$

$$\text{where } g_{cp}^w = g_{cp}^v + k_m g_f^v\left(1 + 1/k_m^0\right);\ g_f^w = g_f^v\left(1 - k_m/k_m^0\right), \tag{1.105}$$

v and w are indices of the system initial and final states.

Models of this type are widely used for prediction of the parameters of high-temperature propulsion and power generation units, particularly for the simulation of multidimensional reacting flows, but are less suitable for the description of chemical nonequilibrium reacting flows and the prediction of combustion products' ecological performances [33, 34].

1.4.2 Global Chemical Kinetics

This approach (like formal chemical kinetics) assumes that reactions proceed at a finite rate, but chemical conversions are described by simple mechanisms, neglecting the complex nature of chemical mechanisms and chemical kinetics laws [33]. The simplest scheme is described by the reaction, "fuel + oxidizer → combustion products." For example,

$$C_3H_8 + 5O_2 \rightarrow 3CO_2 + 4H_2O. \tag{1.106}$$

Downloaded from https://www.cambridge.org/core. Nottingham Trent University, on 17 Aug 2019 at 01:56:34, subject to the Cambridge Core terms of use, available at https://www.cambridge.org/core/terms. https://doi.org/10.1017/9781108581714.001

The global chemical kinetics uses reaction rate constants written in terms of the Arrhenius equation form, while reaction rate is described by equation:

$$W = AT^n \, exp\left(-\frac{E}{R_0 T}\right) C_{\mathrm{A}}^{\alpha} C_{\mathrm{B}}^{\beta} \ldots, \tag{1.107}$$

where A, n, E, α, β are selected from experimental data or by approximation of results obtained from formal chemical kinetics. Note here that parameters α and β can have fractional values. For instance, the following formula was obtained for Reaction (1.106) [35]:

$$W = 8.6 \times 10^{12} \, exp\left(-\frac{30000}{R_0 T}\right) C_{\mathrm{C_3H_8}}^{0.1} C_{\mathrm{O_2}}^{1.65}. \tag{1.108}$$

The research [36] proposed the following formula for the reaction of combustion of methane in the air:

$$W = 1.92 \times 10^{18} \, exp\left(-\frac{31200}{R_0 T}\right) C_{\mathrm{CH_4}}^{0.42} C_{\mathrm{O_2}}^{0.84}, \tag{1.109}$$

which approximates the result of effect of 40 elementary reactions.

The global chemical kinetic approach is mainly used in the combustion analysis of complex (two- or three-dimensional) reacting flows. In this case, the problems inherent in formal chemical kinetics models are avoided since there is no necessity in solving the stiff and intricate equations like (1.85). This allows one to concentrate on other combustion process phenomena such as diffusion, turbulence, and nonuniformity of parameters [37].

Global kinetics is applicable in situations when a detailed mechanism is very complex or unknown. Then, proceeding from experimental data – e.g., combustion products' formation rate and reactants 'decay rate, depending on concentrations, state parameters, etc. – it is possible to get global reactions and their rates. Frequently, such situations originate in the analysis of combustion on solid surfaces (combustion of solid fuel, combustion of coal particles). For example, the following reactions for pyrolysis of hydrocarbons contained in coal were proposed in [38]:

$$\text{"Carbon"}(C) \leftarrow \text{heavy hydrocarbons} \rightarrow \text{volatile matters}\ (V), \tag{1.110}$$

where

$$C = (1 - \alpha_1)k_1 + (1 - \alpha_2)k_2; \quad V = \alpha_1 k_1 + \alpha_2 k_2; \tag{1.111}$$

C, V – carbon and volatile matters formation rates.

Rate constants in (1.111) are defined by the equations:

$$k_1 = 2 \times 10^5 \, exp\left(-\frac{104.6 \times 10^6}{R_0 T}\right); \qquad \alpha_1 = 0.4; \tag{1.112}$$

$$k_2 = 1.3 \times 10^7 \, exp\left(-\frac{167.4 \times 10^6}{R_0 T}\right); \quad \alpha_2 = 0.8. \tag{1.113}$$

Downloaded from https://www.cambridge.org/core. Nottingham Trent University, on 17 Aug 2019 at 01:56:34, subject to the Cambridge Core terms of use, available at https://www.cambridge.org/core/terms. https://doi.org/10.1017/9781108581714.001

Thus, global kinetic approach boasts the advantages compared with formal chemical kinetics for combustion analysis in working volumes of propulsion and power generation systems for accounting of inhomogeneity of reacting mixtures. However, for the computation of detailed combustion characteristics – for example, to predict concentration of harmful matters and determine the limits of stable combustion – it is necessary to use formal chemical kinetics.

1.4.3 Nonequilibrium Chemical Kinetics

This model is used if the equilibrium energy distribution over the degrees of freedom of molecules and atoms is disturbed. For instance, after a shock wave passes through the mixture of a gaseous fuel and oxidizer, thermal equilibrium (Maxwell distribution) over translational and rotational degrees of freedom of molecules is settled in several collisions. Yet, for settlement of equilibrium over vibrational degrees of freedom, hundreds and thousands of collisions are required. Under these conditions ,the application of formal chemical kinetics model can lead to significant errors [35].

Ionization-chemical interaction of electrons, ions, and neutral particles occurs in weakly ionized plasma. But, in connection with the notable difference in masses of electrons and other particles in plasma, the state of a two-temperature medium is settled frequently: one is the temperature for electrons, and the other one is for ions and neutral particles [39]. In this case, nonequilibrium chemical kinetics that can allow for these effects is also used for the simulation.

However, this approach is more complicated compared to formal chemical kinetics and used only in such situations when formal kinetics causes significant errors in calculation of combustion processes parameters. Theoretical fundamentals of nonequilibrium chemical kinetics are stated, for instance, in the following papers [35, 40, 41].

More current papers, for example, [42], describe thermal nonequilibrium processes for chemically reacting systems in the framework of one of the two following approaches; i.e.,

a. **“Mode” kinetics**. In this case, in the absence of equilibrium between translational and vibrational degrees of freedom of molecules of reactants (but with maintained Boltzmann distribution of molecules over vibrational degrees of freedom), the reaction is simulated by two- or multiple-temperature models. Introduction of second temperature (vibrational temperature of vibrationally excited molecules) into physical–mathematical models of processes that occur in thermally nonequilibrium conditions allows the description of chemical interaction in more adequate way.
b. **“Level” kinetics**. It is used given the absence of the Boltzmann distribution for the simulation of reactions with the description of population of specific vibrational energy levels.

Both approaches at the analysis of mode and level kinetics feature major problems related to the knowledge of coefficients in appropriate equations, i.e., magnitudes of rate

Downloaded from https://www.cambridge.org/core. Nottingham Trent University, on 17 Aug 2019 at 01:56:34, subject to the Cambridge Core terms of use, available at https://www.cambridge.org/core/terms. https://doi.org/10.1017/9781108581714.001

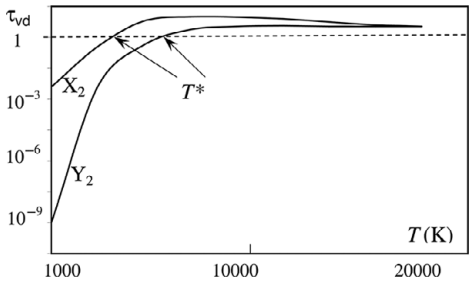

Figure 1.13 Relation between vibrational relaxation time and the distinctive time of dissociation reaction for two analyzed molecules X_2 and Y_2.

constants of vibrational energy exchange and chemical reactions. If separate *j*-th reaction with one nonequilibrium vibrationally excited reactant is isolated from all processes occurring in the medium, and one temperature T_v describing the vibrational energy of the excited particle (reactant of the *j*-th reaction) is isolated, apart from gas temperature T in the medium, the rate constant of this reaction will be the function of two temperatures $k_s = k_s(T, T_v)$. In the case of multi-temperature kinetics, the rate constant is described by formula $k_s = k_s(T, T_{vm})$ where T_{vm} is the set of vibrational temperatures.

In this situation, relationship $k = k_s(T, T_v)$ is obtained from the rate constant of the same reaction $k_s^0(T)$ analyzed in chemically nonequilibrium medium, but with allowance for deviation from thermal equilibrium. This deviation is described by a special multiplier called a nonequilibrium factor, $Z_s(T,\ T_v)$, incorporated in the formula: $k_s(T, T_v) = z_s(T, T_v)k_s^0(T)$. By definition, at $T_V \to T_t$, nonequilibrium factor $Z_s(T, T_v) \to 1$.

The necessity in dual-temperature analysis originates when characteristic scale (duration in time) of analyzed phenomenon, time of vibrational relaxation, and distinctive time of chemical reaction render comparable. The example of such a situation is the flow downstream the front of extremely strong shock wave (Figure 1.13).

Temperature T^* is a boundary magnitude dividing the temperature ranges wherein the mode $(T_v < T^*)$ or level $(T_v > T^*)$ approach is used with notable adequacy. These estimates allow concluding the following:

– The solution of thermal nonequilibrium kinetics in mode approximation is more justified at low magnitudes of translational temperature of gas.
– The necessity of level kinetics application rises with the increase in translational temperature.

The chemical reaction rate constant in the level approximation is represented by the function of translational temperature and vibrational level number $k(T, m)$ of excited molecule. The notion of the relative level factor is introduced for every rate constant model:

$$G(m,\ m^*,\ T) = \frac{k(m, T)}{k(m^*, T)}, \tag{1.114}$$

Downloaded from https://www.cambridge.org/core. Nottingham Trent University, on 17 Aug 2019 at 01:56:34, subject to the Cambridge Core terms of use, available at https://www.cambridge.org/core/terms. https://doi.org/10.1017/9781108581714.001

as the function of integer argument m with parameters m^* and T, where T is gas temperature, and m and m^* are numbers of vibrational levels of dissociating molecule.

At present, data on factors $Z_s(T, T_v)$ and $G(m,\ m^*, T)$, hence on nonequilibrium kinetics processes' rate constants, are based mainly on the analysis of experimental results. Their theoretical determination is carried out by very complex algorithms, which require a massive amount of computations on supercomputers. That is why these computations are possible only for the simple reacting systems.

It should be noted also that nonequilibrium chemical kinetic models used for conditions of disturbance of equilibrium distribution of energy over the degrees of freedom, despite the potentially high accuracy of obtained results are, as a rule, implemented in computer codes that have low efficiency in terms of practical applications, which becomes apparent in the instability of the computational process and significant limitations of the areas of application.

1.5 Application of Reactor Approach to the Simulation of Combustion and Reactive Flows

At present, two approaches have to be adopted for the development of mathematical models of combustion and flow: gas-dynamic and reactor approaches.

The gas-dynamic approach is based on classical equations of motion, conservation of mass, and energy. With the progress in numerical methods and computer engineering, this approach developed in the line of calculation of two- and three- dimensional flows with subsequent allowance for turbulence. Then, after practical mastering of this field, the researchers came to the scene with the analyses of flow with due allowance for combustion processes [2, 33]. Note here that classical equations of motion are supplemented by terms that allow for combustion effects and, besides, equations of variation of concentration of the reacting substance are introduced. The structure of the said extra terms and equations is defined by the model of variation of chemical composition. Besides, models of "instant response" and "global chemical kinetics" are widely used for solving two- and three-dimension combustion problems. Thus, for example, [43] developed a two-dimensional mathematical model of the processes in chambers of complex geometry, which comprises the Navier–Stokes equations, conservation of mass, energy, and variation of concentration of substances. Calculation of combustion is based on the instant response model. Similarly, in the research of [37], a three-dimensional model was developed for the prediction and analysis of flow characteristics in an aluminum smelting furnace. Methane and oxygen were propellant components while a global kinetic two-stage mechanism was used for calculation of combustion:

$$CH_4 + 1,5O_2 \Rightarrow CO + 2H_2O; 2CO + O_2 \Rightarrow 2CO_2. \tag{1.115}$$

At the same time, only few papers, for example, [44] and [45] integrate two- or three-dimensional models of the flow with detailed chemical kinetics (Figure.1.14).

One of such papers by [44] described the model of three-dimensional flow with 28 substances and 55 chemical reactions using the resources of several R&D centers,

Downloaded from https://www.cambridge.org/core. Nottingham Trent University, on 17 Aug 2019 at 01:56:34, subject to the Cambridge Core terms of use, available at https://www.cambridge.org/core/terms. https://doi.org/10.1017/9781108581714.001

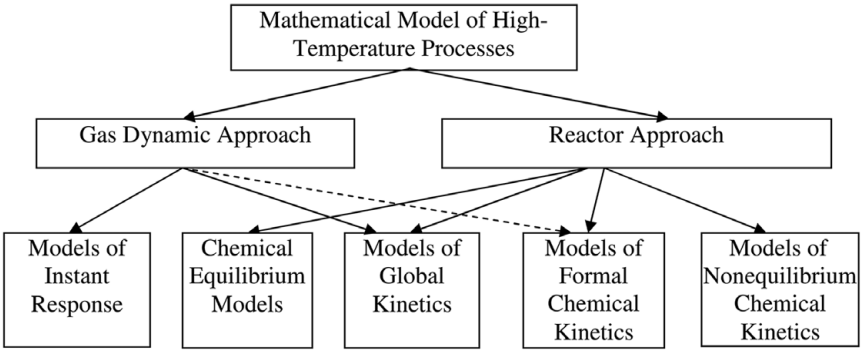

Figure 1.14 Diagram of combustion models application illustrates the gas-dynamic and reactor approaches.

since an extremely large scope of computations is required to this end. Authors noted the significant problems of providing nonnegativity of low concentrations of reacting substances and preserving the quantity of atoms, along with providing acceptable calculation time for the solution of stiff equations and maintaining sufficient accuracy of calculations. Katta and Roquemore [45] developed the model of two-dimensional chemically nonequilibrium flow of preliminary stirred components H_2 + air in a cylindrical combustion chamber with reverse flow. The reacting system comprised 11 substances and 20 reactions. The authors also pointed out the significant time of calculation.

The reactor approach is based on equations of formal chemical kinetics in zero-dimensional state (for example, Eq. (1.85)). This approach to the simulation of combustion processes has emerged earlier than gas-dynamic approach. It aimed at analyzing an increasingly complex reacting systems and developing the methods of integration of stiff chemical kinetics equations [2, 5]. This made it possible to create algorithms invariant with respect to the set of reacting substances and mechanisms of chemical reactions, and computer codes for combustion processes' computation. Thus, for example, the paper [46] disclosed the formation of a detailed mechanism for combustion of kerosene and *n*-decane (with a complex stage of their pyrolysis), including 193 substances and 1085 reactions. For the analysis and substantiation of the, self-created invariant computer code was used [47]. Processes of combustion of nitroamine single-component fuel with elementary composition H-N-O-C were simulated in the study [48]. This research aimed at analyzing the initial stage of ignition and stability of combustion of the aforesaid propellant. Combustion was assumed to proceed in a single adiabatic reactor; the reacting medium included 38 individual substances and 700 elementary reactions. The authors used their own invariant computer codes for numerical analyses.

The options of employment of gas-dynamic approach and reactor approach are presented in the Figure 1.14. It is important to point out some limitations of the employment of the observed models:

Downloaded from https://www.cambridge.org/core. Nottingham Trent University, on 17 Aug 2019 at 01:56:34, subject to the Cambridge Core terms of use, available at https://www.cambridge.org/core/terms. https://doi.org/10.1017/9781108581714.001

- Models of instant response are practically not in use today in the reactor approach.
- Chemical equilibrium models are not in use in the gas-dynamic approach since they require a considerable amount of calculations.
- Models of nonequilibrium chemical kinetics are very complex, and could be in use for relatively simple reacting systems, but operating at very high temperatures (up to 12,000 K), containing as a rule ionized mixtures [39].

At the same time, the evolution of computers and progress in the development of methods and algorithms of "multidimensional" chemical kinetics will lead to the expansion of the area of the application of the combined gas-dynamic and chemical kinetics approaches [49].

At present, the reactor approach is being developed in the direction of accounting for nonuniformity of characteristics of real working volumes. For example, the kinetic mechanism allowing for 107 substances and 642 reactions was developed and used in the study [50] of the processes in gas generator (rich mixture of hydrocarbons with oxygen). The gas generator mathematical model included two PSRs. The influence of droplets evaporation on combustion products was allowed for via the reduction in time of reacting mixture in the second reactor.

The greater number of reactors (up to 100) was included in the combustion model for the preliminary stirred mixture ($CH_4 + O_2 + N_2 + NO_2$) in laminar flame front [51]. The reacting medium was simulated by more than 20 substances participating in 200 elementary reactions. This research aimed at analyzing NO_2 in a rather complex reacting medium.

The fundamental concept of the reactor approach is in separation of the working volume being simulated into reactors (homogeneous zones) with uniform distribution of parameters over every separate reactor. The geometry of reactors is assumed to be defined by calculation by traditional equations of motion [2], semiempirical equations of the theory of jets [52] or even by some empirical relationships [53]. Given that basically every reactor can be associated with a single finite element in FEA, we arrive at a merging of gas-dynamic and reactor approaches. However, in the case of multidimensional flows, it results in a giant amount of computations in the framework of a formal chemical kinetics. In compliance with the reactor approach, it is rational to consider the single reactor (R) not as BR (Figure 1.1) or PSR (Figure 1.2) but as some combination thereof, i.e., as a variable-volume homogeneous reacting system. The latter allows heat-and-mass exchange with the environment (or with neighboring reactors), varying the state parameters (temperature, mass, and pressure) in time and, even, motion. The reactor (R) or system of reactors (SR) boast a notable more expanded field of applications than BR, PFR, or PSR, as shown in the following examples.

1. Steady-state flow of high-temperature reacting combustion products over the Laval nozzle (Figure 1.15a) can be considered to be the motion of thin layers of gas pushed out in series and not mixing with each other. Assuming one-dimensional flow, let us isolate a sufficiently thin layer/volume moving at the gas rate. This and similar volumes can be interpreted as PFR (moving BR) with variable parameters. The following variation of parameters of each of these reactors, that is, by constructing an appropriate

Downloaded from https://www.cambridge.org/core. Nottingham Trent University, on 17 Aug 2019 at 01:56:34, subject to the Cambridge Core terms of use, available at https://www.cambridge.org/core/terms. https://doi.org/10.1017/9781108581714.001

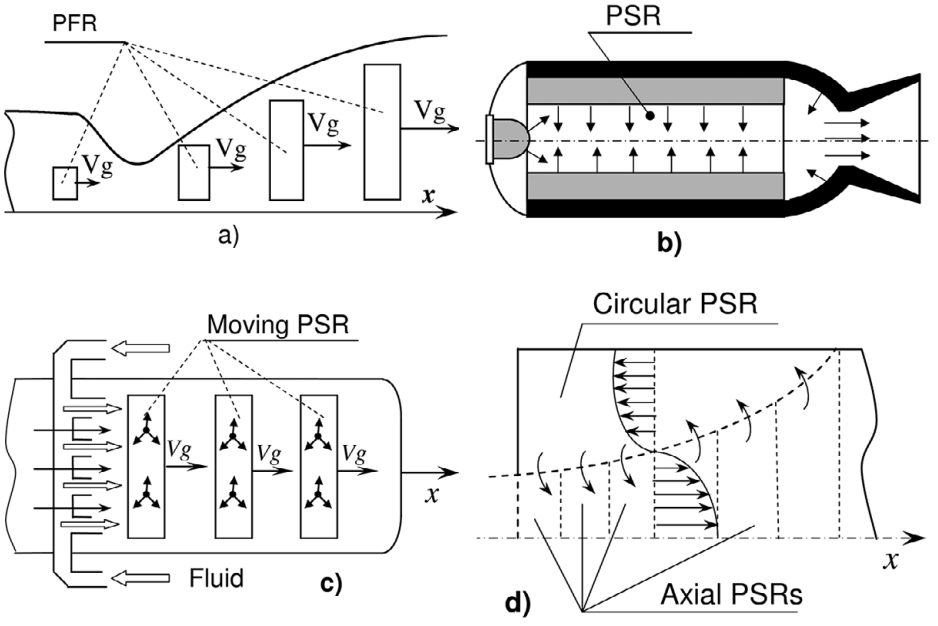

Figure 1.15 Application of the reactor approach to the simulation of combustion and flow.

mathematical model, it is possible to predict and analyze the major parameters of nozzle processes. In particular, in the case of heterogeneous combustion products, it is possible to estimate the mutual influence of gas phase chemical nonequilibrium and the velocity (temperature) nonequilibrium of the condensate; nonequilibrium of condensation and crystallization processes; influence of the electrons and ions thermal emission on electrophysical characteristics of combustion products.

2. Transient processes in the Solid Propellant Rocket Engine at start-up and thrust cutoff conditions can be simulated with the help of the stationary PSR model. These conditions are known to exhibit a notable influence of chemical nonequilibrium on in-chamber parameters. With allowance for low velocity of combustion products in the chamber and uniform pressure distribution, the entire chamber may be considered a PSR (Figure 1.15b). Using an appropriate relationship for simulation of fuel regression rates, coolant evaporation (if the coolant is injected into the combustion chamber in order to cut off the thrust), heat exchange, etc., it is possible to create a mathematical model for processes that proceed in the combustion chamber. Even such an approximated zero-dimensional pattern allows estimating chemical nonequilibrium effects at mixing the combustion products of igniter and main propellant grain at start-up as well as the interaction of coolant vapors, propellant combustion products, and internal thermal insulation at thrust cutoff stage.

3. Reacting gas-fluid flows (gas flow with fluid droplets) are inherent in the processes in multiple high-temperature units – gas generators, afterburners, chambers with generator gas afterburning, chemical neutralizers, units of chemical technology, etc. – which differ from similar devices in that notable bulk of fuel (oxidizer) or ballasting component

Downloaded from https://www.cambridge.org/core. Nottingham Trent University, on 17 Aug 2019 at 01:56:34, subject to the Cambridge Core terms of use, available at https://www.cambridge.org/core/terms. https://doi.org/10.1017/9781108581714.001

gasification products are injected into a chemically reacting gas mixture. A model of the process in a gas generator is shown in Figure 1.15c. An extraction of a rather thin layer of a dispersed gas–fluid mixture displacing at the gas rate (but not at the rate of the liquid) allows for simulating this layer (except for droplets contained therein) with the help of a moving PSR. Models of moving PSR, gas-dynamic relationships for two-phase flows and equations that define the droplets evaporation and heating rates allow a prediction and analysis of the major properties of the working medium – for example, the gas phase chemical composition, its temperature, and droplet evaporation time. Note here that it is possible to allow for such phenomena as chemical nonequilibrium, liquid phase polydispersity, evaporation, and nonequilibrium two-velocity effects in gas-liquid flow.

4. Flow patterns with sudden expansion and, respectively, with recirculation zone formation are inherent in combustion chambers of gas turbine engines, rocket engines running on "liquid + liquid" (liquid fuel and liquid oxidizer), and "gas + liquid" (gaseous fuel/oxidizer and liquid oxidizer/fuel) schemes. For the prediction and analysis of parameters of such flows, it is required to apply complex two-dimensional (for axially symmetric channels) patterns. However, using the pattern wherein the zone of recirculation is simulated by circular PSR while combustion products flow along the axis (main zone) is simulated by the system of PSR (sPSR) to allow the construction of the quasi-two-dimensional flow models with recirculation (Figure 1.15d). Such a model is to be complemented with the equations of motion for gas and liquid phases, and relationship for determination of reactor boundaries, evaporation model, and other correlations to allow simulation of the combustion zone parameters in both the recirculation zone and core flow. Usually, the non-stationary PSR model is used (unless the steady state is reached).

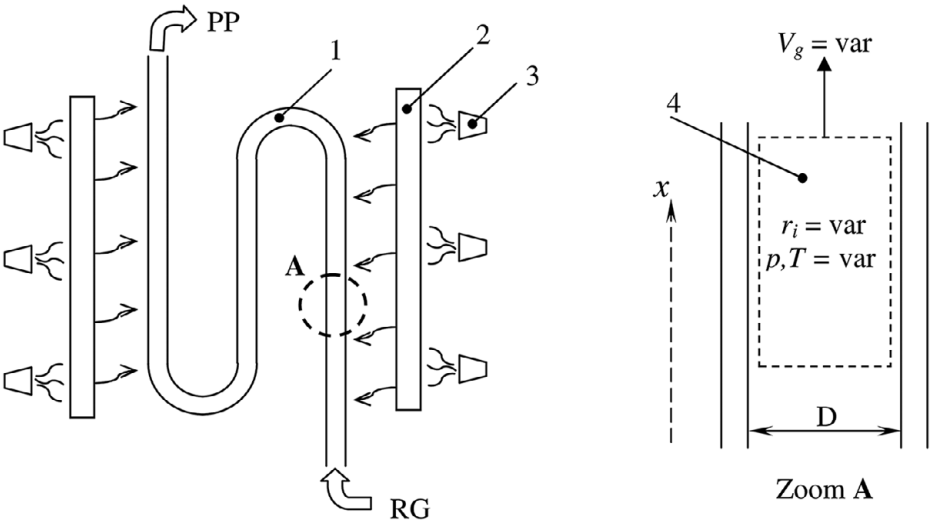

Figure 1.16 Diagram of radiant tubular furnace:
(1) tubular coil; (2) emitting shield; (3) gas burners; (4) moving BR; RG – gaseous reactants (C_2H_6 + steam H_2O); PP – pyrolysis products.

Downloaded from https://www.cambridge.org/core. Nottingham Trent University, on 17 Aug 2019 at 01:56:34, subject to the Cambridge Core terms of use, available at https://www.cambridge.org/core/terms. https://doi.org/10.1017/9781108581714.001

As a rule, PFR represents a steady-state flow without mixing neighboring layers. Reactants (fuel and oxidizer, or a single-component substance), both gaseous and liquid, are fed to the inlet of such units. Combustion (pyrolysis) of these substances converts them into multicomponent combustion products (homogeneous or heterogeneous) with the release of a certain amount of heat (at combustion) or with heat absorption (at pyrolysis). For example, ethylene production industrial furnaces (Figure 1.16) [54] exploit ethane (C_2H_6) as the main reactant, which decomposes at its flow in tube 1 according to the reaction $C_2H_6 \rightarrow C_2H_4 + H_2$. This process proceeds with absorption of significant amount of heat transferred from the shields heated by gas burners. Actually, the pyrolysis mechanism comprises hundreds of elementary reactions, CH_4, C_3H_8, soot, etc.

Practically crucial problems for solving of which the patterns of reactors and systems of reactors can be used are not limited to the examples described in this chapter and will be disclosed in Chapters 4–10.

Downloaded from https://www.cambridge.org/core. Nottingham Trent University, on 17 Aug 2019 at 01:56:34, subject to the Cambridge Core terms of use, available at https://www.cambridge.org/core/terms. https://doi.org/10.1017/9781108581714.001

2 Governing Equations of Chemical Kinetics and Specific Features of Their Solution

2.1 Governing Equations of Chemical Kinetics and Accompanying Processes in the Reactors

Equations of gas-phase chemical kinetics (1.85) (see Section 1.3) are valid for a constant volume (V = const) BR, while occurring a reversible chemical reactions. However, in the general case, it is desirable to allow for volume variation (V = var) in the reactor R, or in an assumed reactor of the system of reactors (SR), as well as in occurrences of irreversible reactions herein, feed and discharge of substances and surface reactions [5]. Such reactions reflect the change in gas mass and its composition in the reactor due to a number of processes (for example, evaporation, condensation, combustion of metals and coal, absorption, etc.).

In the general case [3, 4], the equations of chemical kinetics are defined as follows:

$$\frac{1}{V}\frac{dn_i}{d\tau} = \sum_s \left(\nu''_{is} - \nu'_{is}\right) k_s^+ \left(\prod_p C_p^{\nu'_{ps}}\right) C^{m_s} + \sum_s \left(\nu'_{is} - \nu''_{is}\right) k_s^- \left(\prod_p C_p^{\nu''_{ps}}\right) C^{m_s} + \sum_{q_+}^{r^+} \Phi_{iq_+}^+ - \sum_{q_-}^{r^-} \Phi_{iq_-}^-,\ i,p = 1, \ldots, n_b;\ s = 1, \ldots, m_c;\ q^+ = 1, \ldots, r^+;\ q^- = 1, \ldots, r^-, \tag{2.1}$$

where C is the overall molar concentration of gas mixture; C_p is the partial molar concentration of specie p in the gas mixture; m_s is the attribute of third body in the reaction (m_s = 1 means reaction occurrence with the presence of third body; otherwise, m_s = 0); $\sum_{q_+}^{r^+} \Phi_{iq_+}^+$, $\sum_{q_-}^{r^-} \Phi_{iq_-}^-$ are sums of sources and sinks of i-th specie in the reactor; r^+, r^- are the number of sources and sinks, respectively ($r_c = r^+ + r^-$).

In Equations (2.1) rate constants k_s^+ and k_s^- represent forward and reverse directions of reactions and interrelate in the form of $k_s^- = k_s^+/K_s$ (where K_s is the constant of equilibrium of s-th reversible reaction)

Because of an arbitrary way of the notation of the source (sinks) terms, the form of equations creates difficulties in developing the algorithms and computer codes invariant with respect to the reacting medium. The acceptable method for avoiding this problem consists in the application of conditional reactions of "mass supply" and "mass discharge" ("mass exchange reactions") [8, 55, 56] to identify mass exchange processes:

Downloaded from https://www.cambridge.org/core. Nottingham Trent University, on 17 Aug 2019 at 01:58:27, subject to the Cambridge Core terms of use, available at https://www.cambridge.org/core/terms. https://doi.org/10.1017/9781108581714.002

$$\sum_i \nu'_{is} B_i \Rightarrow \sum_i \nu''_{is} B_i. \qquad s = (m_c + 1) \ldots (m_c + r_c). \tag{2.2}$$

Similar to the reversible chemical reactions, mass exchange reactions will be described by the rate constant written in compliance with the rules of formal chemical kinetics [7, 23].

Section 2.2 describes the method of the formalization of mass exchange processes in the reactor with the help of such reactions and methods of construction of their rate constants. Note that such an approach sometimes is not rational or even possible. To simplify the conversion of Equations (2.1), let us assume that we managed to represent all source and sink terms as the mass exchange reactions that obey the kinetic laws. Besides, to simplify the notation, each reversible chemical reaction (1.69) will be considered a combination of two irreversible reactions, and the following designations will be introduced:

$$\begin{aligned}
&\nu_{ij} = \nu''_{is} - \nu'_{is}; \quad n_{ij} = \nu'_{is}, \quad \text{if} \quad j = s, \quad \text{and} \quad s = 1, \ldots, m_c, \\
&\nu_{ij} = \nu'_{is} - \nu''_{is}; \quad n_{ij} = \nu''_{is}, \quad \text{if} \quad j = s + m_c, \quad \text{and} \quad s = 1, \ldots, m_c, \\
&\nu_{ij} = \nu''_{is} - \nu'_{is}; \quad n_{ij} = \nu'_{is}, \quad \text{if} \quad j = s + m_c, \quad \text{and} \quad s = (m_c + 1), \ldots, (m_c + r_c).
\end{aligned} \tag{2.3}$$

In compliance with accepted designations, forward directions of chemical reactions have indices $j = 1, \ldots, m_c$; reverse directions have indices $j = (m_c+1), \ldots, 2m_c$; and mass exchange reaction indices are $j = 2m_c+1, \ldots, 2m_c+r_c$.

Allowing for (2.2) and (2.3), Equations (2.1) may be written for reactor R as follows:

$$\frac{1}{V}\frac{dn_i}{d\tau} = \sum_j \nu_{ij} k_j \left(\prod_p C_p^{n_{pj}} \right) C^{m_j}. \quad i, p = 1, \ldots, n_b; \quad j = 1, \ldots, 2m_c + r_c. \tag{2.4}$$

Equations (2.4) feature the form simplified compared to (2.1) and allow for both chemical and nonchemical ways of varying the gas mixture composition. Further conversion of Equation (2.4) consists in involvement of relative concentrations r_i or g_i. Thus, by using the relations $n_i = N_m r_i$; $C_i = p r_i/(R_0 T)$, where N_m is the total number of moles in volume V, we obtain

$$\begin{aligned}
\frac{1}{V}\frac{dn_i}{d\tau} &= \frac{1}{V}\left(r_i \frac{dN_m}{d\tau} + N_m \frac{dr_i}{d\tau} \right) = \sum_j \nu_{ij} k_j \left(\frac{p}{R_0 T} \right)^{m_j} \prod_p r_p^{n_{pj}} \left(\frac{p}{R_0 T} \right)^{n_{pj}} \\
&= \sum_j \nu_{ij} k_j \left(\frac{p}{R_0 T} \right)^{\sum_p n_{pj} + m_j} \prod_p r_p^{n_{pj}}. \qquad i, p = 1, \ldots, n_b.
\end{aligned} \tag{2.5}$$

The number of Equations (2.5) equals the number of substances in the reacting mixture – i.e., n_b. Summation of all these equations over i gives

$$\begin{aligned}
&\sum_i \frac{r_i}{V}\frac{dN_m}{d\tau} + \sum_i \frac{N_m}{V}\frac{dr_i}{d\tau} = \frac{1}{V}\frac{dN_m}{d\tau} + \frac{N_m}{V}\frac{d\left(\sum_i r_i\right)}{d\tau} = \frac{1}{V}\frac{dN_m}{d\tau} \\
&= \sum_q \sum_j \nu_{qj} k_j \left(\frac{p}{R_0 T} \right)^{\sum_p n_{pj} + m_j} \prod_p r_p^{n_{pj}}. \quad p, q = 1, \ldots, n_b.
\end{aligned} \tag{2.6}$$

Downloaded from https://www.cambridge.org/core. Nottingham Trent University, on 17 Aug 2019 at 01:58:27, subject to the Cambridge Core terms of use, available at https://www.cambridge.org/core/terms. https://doi.org/10.1017/9781108581714.002

Let us introduce the notation $\overline{m_j} = m_j + \sum_p n_{pj} - 1$ and substitute $\frac{dN_m}{d\tau}$, expressed via (2.6), in (2.5). Then, we obtain

$$r_i \sum_q \sum_j \nu_{qj} k_j \left(\frac{p}{R_0 T}\right)^{\sum_p n_{pj}+m_j} \prod_p r_p^{n_{pj}} + \frac{N_m}{V}\frac{dr_i}{d\tau} = \sum_j \nu_{ij} k_j \left(\frac{p}{R_0 T}\right)^{m_j} \prod_p r_p^{n_{pj}} \left(\frac{p}{R_0 T}\right)^{n_{pj}}. \tag{2.7}$$

Substituting the equality $N_m/V = p/(R_0 T)$ into Equation (2.7) we obtain

$$\frac{dr_i}{d\tau} = \sum_j \nu_{ij} k_j \left(\frac{p}{R_0 T}\right)^{\bar{m}_j} \prod_p r_p^{n_{pj}} - r_i \sum_q \sum_j \nu_{qj} k_j \left(\frac{p}{R_0 T}\right)^{\bar{m}_j} \prod_p r_p^{n_{pj}} \equiv f_i^r. \tag{2.8}$$

Let us perform similar derivations using mass fractions (g_i), with allowance for

$$n_i \mu_i = g_i M_m; \quad \rho = \frac{M_m}{V} = p\mu_g/(R_0 T), \tag{2.9}$$

where M_m is the gas mass in the reactor, and $\mu_g = \sum_i r_i \mu_i$ is the molecular mass of the mixture in the reactor.

Then, by multiplying every i-th Equation (2.4) by molecular mass μ_i, we obtain

$$\begin{aligned}\frac{\mu_i}{V}\frac{dn_i}{d\tau} = \frac{1}{V}\frac{d(g_i M_m)}{d\tau} = \frac{M_m}{V}\frac{dg_i}{d\tau} + \frac{g_i}{V}\frac{dM_m}{d\tau} &= \mu_i \sum_j V_{ij} k_j \left(\frac{p}{R_0 T}\right)^{m_j} \prod_p \left(\frac{g_p \mu_g}{\mu_p}\right)^{n_{pj}} \left(\frac{p}{R_0 T}\right)^{n_{pj}} \\ &= \mu_i \sum_j \nu_{ij} k_j \left(\frac{p\mu_g}{R_0 T}\right)^{\left(m_j + \Sigma n_{pj}\right)} (\mu_g)^{-m_j} \prod_p \left(\frac{g_p}{\mu_p}\right)^{n_{pj}}.\end{aligned} \tag{2.10}$$

By summing all Equations (2.10), we obtain

$$\frac{M_m}{V}\frac{d(\sum g_i)}{d\tau} + \frac{\sum g_i}{V}\frac{dM_m}{d\tau} = \frac{1}{V}\frac{dM_m}{d\tau} = \sum \mu_i \sum_j \nu_{ij} k_j \left(\frac{p\mu_g}{R_0 T}\right)^{\left(m_j + \Sigma n_{pj}\right)} (\mu_g)^{-m_j} \prod_p \left(\frac{g_p}{\mu_p}\right)^{n_{pj}}. \tag{2.11}$$

By substituting the right-hand side of Equation (2.11) into Equation (2.10) instead of the term $\frac{1}{V}\frac{dM_m}{d\tau}$, we obtain

$$\begin{aligned}\frac{M_m}{V}\frac{dg_i}{d\tau} + g_i \sum \mu_i \sum_j \nu_{ij} k_j \left(\frac{p\mu_g}{R_0 T}\right)^{\left(m_j + \sum n_{pj}\right)} (\mu_g)^{-m_j} \prod_p \left(\frac{g_p}{\mu_p}\right)^{n_{pj}} \\ = \mu_i \sum_j \nu_{ij} k_j \left(\frac{p\mu_g}{R_0 T}\right)^{\left(m_j + \sum n_{pj}\right)} (\mu_g)^{-m_j} \prod_p \left(\frac{g_p}{\mu_p}\right)^{n_{pj}}.\end{aligned} \tag{2.12}$$

Moving the second term of Equation (2.12) to the right-hand side with due allowance for $\rho = \frac{M_m}{V} = p\mu_g/(R_0 T)$, we obtain the equation of chemical composition variation derived in terms of mass fractions:

Downloaded from https://www.cambridge.org/core. Nottingham Trent University, on 17 Aug 2019 at 01:58:27, subject to the Cambridge Core terms of use, available at https://www.cambridge.org/core/terms. https://doi.org/10.1017/9781108581714.002

$$\frac{dg_i}{d\tau} = \mu_i \sum_i \nu_{ij} k_j p^{\bar{m}_j} \mu_g^{-m_j} \prod_p \left(\frac{g_p}{\mu_p}\right)^{n_{pj}} - g_i \sum_q \mu_q \sum_j \nu_{gj} k_j \rho^{\bar{m}_j} \mu_g^{-m_j} \prod_p \left(\frac{g_p}{\mu_p}\right)^{n_{pj}} \equiv f_i^g, \tag{2.13}$$

where $i, q, p = 1, \ldots, n_b$; $j = 1, \ldots, (2m_c + r_c)$; M_m is the working medium mass in volume V, and μ_g is the average molecular mass of the gas.

These equations at application of mole-mass concentrations $\chi_i = g_i/\mu_i$ are represented by

$$\frac{d\chi_i}{d\tau} = \sum_j \nu_{ij} k_j \rho^{\bar{m}_j} \left(\sum_p \chi_p\right)^{m_j} \prod_p \chi_p^{n_{pj}} - \chi_i \sum_q \mu_q \sum_j \nu_{qj} k_j \rho^{\bar{m}_j} \left(\sum_p \chi_p\right)^{m_j} \prod_p \chi_p^{n_{pj}}. \tag{2.14}$$

Equations (2.8, 2.13, 2.14) are valid for BR at variables T, p, V, and M_m. The mass of the gas M_m may vary in this reactor due to evaporation, condensation, combustion of liquid or solid particles in the reactor, and even the interaction of particles of the material of which the wall is fabricated from with gas medium, etc. If mass of the gas in the reactor does not vary ($dM_m/d\tau = 0$), then, with due allowance for the relation (2.11), Equation (2.13) is simplified as follows:

$$\frac{dg_i}{d\tau} = \mu_i \sum_j \nu_{ij} k_j \rho^{\bar{m}_j} \mu_g^{-m_j} \prod_p \left(\frac{g_p}{\mu_p}\right)^{n_{pj}}. \tag{2.15}$$

Equations (2.8, 2.13, 2.14) are valid at no occurrence of chemical conversions too. Gas phase composition in such an eventuality varies due to substance supply and discharge; this process is simulated by summands that describe mass exchange reactions.

In principle, the same equations describe the processes in PSR (Figure 1.2), but it is irrational to simulate the supply of reactants and discharge of products (m^+, m^- are mass flows at the inlet and outlet of the reactor, respectively) by mass exchange reactions, since it would be required to include multiple extra mass supply reactions (the number of such reactions equals that of substances). Therefore, corresponding summands should be reflected in the equations of chemical kinetics. Then, extra summands will appear in Equations (2.8, 2.13, 2.14). Let us cite the deriving of equations for PSR with application of molar fractions. In compliance with [3, 4] the initial form of these equations with allowance for Formula (2.3) will be written as follows:

$$\frac{1}{V}\frac{dn_i}{d\tau} = \sum_j \nu_{ij} k_j \left(\prod_p C_p^{n_{pj}}\right) C^{m_j} + W_i^+ - W_i^-; \qquad i, p = 1 \ldots n_b;\ j = 1 \ldots 2m_c; \tag{2.16}$$

where W_i^+, W_i^- are rates of origination and decay of i-th substance caused by the flows of substances m^+ and m^- in the reactor unit volume.

Downloaded from https://www.cambridge.org/core. Nottingham Trent University, on 17 Aug 2019 at 01:58:27, subject to the Cambridge Core terms of use, available at https://www.cambridge.org/core/terms. https://doi.org/10.1017/9781108581714.002

These rates are described by the formulas:

$$W_i^+ = \frac{m^+ g_i^+}{\mu_i V} = \frac{m^+ r_i^+ p \mu_g}{\mu^+ M_m R_0 T} = \frac{p r_i^+ \mu_g}{\mu^+ \tau_p R_0 T}; \tag{2.17}$$

$$W_i^- = \frac{m^- r_i p}{M_m R_0 T}; \quad i = 1 \ldots n_b, \tag{2.18}$$

where $\tau_p = M_m/m^+$ is the residence time, and r_i^+ are mole fractions of the reactants.

Replacing W_i^+, W_i^- in compliance with Equations (2.17) and (2.18) and allowing for $C = p/(R_0 T)$; $C_i = r_i C$ and $n_i = r_i N_m$, we now obtain from Equation (2.16):

$$\frac{1}{V}\frac{dn_i}{d\tau} = \frac{N_m}{V}\frac{dr_i}{d\tau} + \frac{r_i}{V}\frac{dN_m}{d\tau} = \sum_j \nu_{ij} k_j \left(\frac{p}{R_0 T}\right)^{m_j + \sum n_{pj}} \prod_p r_p^{n_{pj}} + \frac{p r_i^+ \mu_g}{\mu^+ \tau_p R_0 T} - \frac{m^- r_i p}{M_m R_0 T}. \tag{2.19}$$

By summing Equations (2.19) with due allowance for $\sum r_i = 1$ and $\sum \frac{dr_i}{d\tau} = 0$, we obtain

$$\frac{1}{V}\frac{dN_m}{d\tau} = \sum_q \sum_j \nu_{qj} k_j \left(\frac{p}{R_0 T}\right)^{m_j + \sum n_{pj}} \prod_p r_p^{n_{pj}} + \sum_q \frac{p r_q^+ \mu_g}{\mu^+ \tau_p R_0 T} - \frac{m^- p}{M_m R_0 T} \quad q, p = 1 \ldots n_b. \tag{2.20}$$

By replacing the relation $\frac{1}{V}\frac{dN_m}{d\tau}$ in Equations (2.19), we now obtain from Equations (2.20):

$$\frac{N_m}{V}\frac{dr_i}{d\tau} + r_i \left(\sum_q \sum_j \nu_{qj} k_j \left(\frac{p}{R_0 T}\right)^{m_j + \sum n_{pj}} \prod_p r_p^{n_{pj}} + \sum_q \frac{p r_q^+ \mu_g}{\mu^+ \tau_p R_0 T} - \frac{m^- p}{M_m R_0 T} \right) = \sum_j \nu_{ij} k_j \left(\frac{p}{R_0 T}\right)^{m_j + \sum n_{pj}} \prod_p r_p^{n_{pj}} + \frac{p r_i^+ \mu_g}{\mu^+ \tau_p R_0 T} - \frac{m^- r_i p}{M_m R_0 T}. \tag{2.21}$$

By keeping the relation $\frac{N_m}{V}\frac{dr_i}{d\tau}$ only in the left-hand side of Equation (2.21), we obtain

$$\frac{N_m}{V}\frac{dr_i}{d\tau} = \sum_j \nu_{ij} k_j \left(\frac{p}{R_0 T}\right)^{m_j + \sum n_{pj}} \prod_p r_p^{n_{pj}} + \frac{p r_i^+ \mu_g}{\mu^+ \tau_p R_0 T} - \frac{m^- r_i p}{M_m R_0 T} - r_i \left(\sum_q \sum_j \nu_{qj} k_j \left(\frac{p}{R_0 T}\right)^{m_j + \sum n_{pj}} \prod_p r_p^{n_{pj}} + \sum_q \frac{p r_q^+ \mu_g}{\mu^+ \tau_p R_0 T} \right) + \frac{m^- r_i p}{M_m R_0 T}. \tag{2.22}$$

Summands $\frac{m^- r_i p}{M_m R_0 T}$ may be cancelled to write the following with allowance for $N_m/V = p/(R_0 T)$:

$$\frac{dr_i}{d\tau} = \sum_j \nu_{ij} k_j \left(\frac{p}{R_0 T}\right)^{m_j + \sum n_{pj} - 1} \prod_p r_p^{n_{pj}} + \frac{r_i^+ \mu_g}{\mu^+ \tau_p} - r_i \left(\sum_q \sum_j \nu_{qj} k_j \left(\frac{p}{R_0 T}\right)^{m_j + \sum n_{pj} - 1} \prod_p r_p^{n_{pj}} + \sum_q \frac{r_q^+ \mu_g}{\mu^+ \tau_p} \right); \quad i, p, q = 1 \ldots n_b; \; j = 1 \ldots 2m_c. \tag{2.23}$$

Downloaded from https://www.cambridge.org/core. Nottingham Trent University, on 17 Aug 2019 at 01:58:27, subject to the Cambridge Core terms of use, available at https://www.cambridge.org/core/terms. https://doi.org/10.1017/9781108581714.002

It is easy to see that Equations (2.19) contain the summand describing the gas mixture discharge from the reactor while Equations (2.23) do not include this summand. Equations (2.19) describe the rate of variation of the number of moles of i-th substance caused by flow rate m^-; Equations (2.23) describe the variation of relative values (mole fractions), and the convective flow from the reactor does not affect the variation of these values because convective mass discharge occurs proportionally to the concentration of substances in the reactor.

At combustion simulation, it is frequently necessary to consider the PSR under steady-state conditions. In this case, the equation becomes algebraic and is written in the following form:

$$\sum_j \nu_{ij} k_j \left(\frac{p}{R_0 T}\right)^{m_j + \sum n_{pj} - 1} \prod_p r_p^{n_{pj}} + \frac{r_i^+ \mu_g}{\mu^+ \tau_p} - r_i \left(\sum_q \sum_j \nu_{qj} k_j \left(\frac{p}{R_0 T}\right)^{m_j + \sum n_{pj} - 1} \prod_p r_p^{n_{pj}} + \sum_q \frac{r_q^+ \mu_g}{\mu^+ \tau_p} \right) = 0. \tag{2.24}$$

Such nonlinear equations are solved by approximate methods (for example, by the Newton method [2, 5]), but the iterative process of the solution diverges frequently. It requires to get back to the transient form (2.23) and calculate steady-state parameters by numerical integration of differential equations. Like in the case of BR, equations of chemical kinetics, the latter for PSR may be described via changes of mass fractions (g_i) and mole-mass concentrations (χ_i). But, herein, equations of the type (2.8) and (2.23) are solely used for inambiguity of the mathematical description of diverse models.

As was shown in the Section 1.1, the steady-state one-dimensional reacting gas flow is described by a single displacing BR, that is, PFR, Figure 1.3. Then, by using the operator transform $\frac{d}{d\tau} = V_g \frac{d}{dx}$, we obtain, for example, from Relations (2.8), the chemical kinetics equations for PFR in the following form:

$$\frac{dr_i}{dx} = \frac{1}{V_g} \left(\sum_j \nu_{ij} k_j \left(\frac{p}{R_0 T}\right)^{\bar{m}_j} \prod_p r_p^{n_{pj}} - r_i \sum_q \sum_j \nu_{qj} k_j \left(\frac{p}{R_c T}\right)^{\bar{m}_j} \prod_p r_p^{n_{pj}} \right). \tag{2.25}$$

Equations (2.8, 2.23, 2.25) are nonlinear ordinary differential equations (ODE) to be integrated by numerical methods only. Note here that minor values of r_i can render negative due to errors in finite-difference approximation, which are of no physical sense. At the same time, placing the constraints on minimum concentrations (for example, $r_i \geq 10^{-7}$) may bring about erroneously high reaction rates with the involvement of radicals, the dummy supply of substances in the reacting mixture, and, hence, the distortion of the combustion parameters. Besides, allowance for minor concentrations is necessary to solve environmental problems when contaminants of minimum concentration notably affect the environment. Problems with minor concentrations may be avoided at the stages of development of the algorithms or computer codes, but our experience showed that it is more convenient to introduce another form of chemical kinetic equations with the following substitution: $\gamma_i = -ln\, r_i$. Then, for example, equation (2.8) takes on the following form:

Downloaded from https://www.cambridge.org/core. Nottingham Trent University, on 17 Aug 2019 at 01:58:27, subject to the Cambridge Core terms of use, available at https://www.cambridge.org/core/terms. https://doi.org/10.1017/9781108581714.002

$$\frac{d\gamma_i}{d\tau} = -e^{\gamma_i} \sum_j \nu_{ij} k_j \left(\frac{p}{R_0 T}\right)^{\bar{m}_j} exp\left(-\sum_p n_{pj}\gamma_p\right) + \sum_q \sum_j \nu_{qj} k_j \left(\frac{p}{R_0 T}\right)^{\bar{m}_j} exp\left(-\sum_p n_{pj}\gamma_p\right) \equiv f_{\gamma i}, \tag{2.26}$$

where $i, p, q = 1, \ldots, n_b$, $j = 1, \ldots, 2m_c + r_c$.

The notation of this equation may be formally simplified:

$$\frac{d\gamma_i}{d\tau} = -e^{\gamma_i} \sum_j \nu_{ij}\Omega_j + \sum_q \sum_j \nu_{qj}\Omega_j \equiv f_{\gamma i}, \tag{2.27}$$

where

$$\Omega_j = k_j \left(\frac{p}{R_o T}\right)^{\bar{m}_j} exp\left(-\sum_p n_{pj}\gamma_p\right). \tag{2.28}$$

This term may be treated as the rate of j-th reaction relative to the total molar concentration – i.e., $\Omega_j = W_j/C$.

Similarly, one can obtain the following equations for PSR:

$$\frac{d\gamma_i}{d\tau} = -e^{\gamma i}\left(\sum_j \nu_{ij}\Omega_j + \frac{r_i^+ \mu_g}{\mu^+ \tau_p}\right) + \sum_q \sum_j \nu_{qj}\Omega_j + \sum_q \frac{r_q^+ \mu_g}{\mu^+ \tau_p} \equiv f_{\gamma i}. \tag{2.29}$$

At similar substitution, Equation (2.14) will take on the form:

$$\frac{d\gamma_{ix}}{d\tau} = -e^{\gamma_{ix}} \sum_j \nu_{ij} k_j p^{\bar{m}_j} \left(\sum_p e^{-\gamma_{px}}\right)^{m_j} exp\left(-\sum_p n_{pj}\gamma_{px}\right) + \sum_q \mu_q \sum_j \nu_{qj} k_j \rho^{\bar{m}_j} \left(\sum_p e^{-\gamma_{px}}\right)^{\bar{m}_j} exp\left(-\sum_p n_{pj}\gamma_{px}\right), \tag{2.30}$$

where $\gamma_{ix} = -ln\chi_i$.

Hereinafter, for inambiguity of mathematical description of diverse models, only equations of the type (2.27, 2.29) will be used, and they are called "the chemical kinetics equations of exponential form."

Equations (2.27) are written for single reactor R. In the simulation of reacting volume by the system of reactors SR composed by N interrelated reactors, the variation of chemical composition will be described by analogy with (2.27) by the following equations:

$$\frac{d\gamma_{iz}}{d\tau} = -e^{r_{iz}} \sum_j \nu_{ij} k_{jz} \left(\frac{p}{R_0 T_Z}\right)^{\bar{m}_j} exp\left(-\sum_p n_{pj}\gamma_{pz}\right) + \sum_q \sum_j \nu_{qj} k_{jz} \left(\frac{p}{R_0 T_Z}\right)^{\bar{m}_j} exp\left(-\sum_p n_{pj}\gamma_{pz}\right), \tag{2.31}$$

where $z = 1, \ldots, n_z$ and n_z is the number of reactors in this system.

Downloaded from https://www.cambridge.org/core. Nottingham Trent University, on 17 Aug 2019 at 01:58:27, subject to the Cambridge Core terms of use, available at https://www.cambridge.org/core/terms. https://doi.org/10.1017/9781108581714.002

Combustion processes occurring in high-temperature units of real propulsion and power generation systems (combustion chamber, gas generators, nozzles, furnaces) are complex for mathematical simulation since they incorporate multiple interacting phenomena (chemical reactions, turbulence, diffusion, heat and mass transfer, release of energy) [8]. As a rule, in mathematical reactor models, along with chemical kinetics equations, the other relations used as well are referred to hereinafter as "accompanying equations." In particular, many models [57] use calorific equation relating enthalpy, temperature, and composition of the reacting mixture:

$$\text{a) } h_\Sigma = \sum_i H_i r_i \Big/ \sum_i \mu_i r_i \quad \text{or} \quad \text{b) } h_\Sigma = \sum_i h_i g_i \tag{2.32}$$

$$\text{or c) } H_\Sigma = \sum_i H_i r_i, \tag{2.33}$$

where h_Σ, H_Σ are mass and molar enthalpy of the mixture in reactor, and h_i, H_i are mass and molar enthalpy of i-th substance.

These equations do not depend on the reactor type but h_Σ, H_Σ may vary subject to external conditions (for example, because of heat supply, presence of inlet flows, surface reactions, etc.). In particular, for stationary PSR with heat supply (q_m) per unit mass of reactants inlet flow, it can be written:

$$h^+ + q_m = h_\Sigma = \sum_i h_i g_i, \tag{2.34}$$

where h^+ is mass specific enthalpy of reactants.

In the case of PFR simulating, for example, one-dimensional reacting flow in the Laval nozzle, we have the following equation:

$$h^* - V_g^2/2 = h_\Sigma = \sum_i H_i r_i \Big/ \sum_i \mu_i r_i, \tag{2.35}$$

where h^* is stagnation enthalpy of the flow, and V_g is flow velocity.

Calorific equations in the form (2.34, 2.35) thus render the equations of energy for the simulated reactor.

Most applied problems use equations of energy in differential form with explicit operator $dT/d\tau$ [5]. For example, for adiabatic BR ($h_\Sigma = const$) at constant pressure ($p = const$) we differentiate Equation (2.32b) to get

$$\frac{dh_\Sigma}{d\tau} = \sum_i \frac{dh_i}{dT}\frac{dT}{d\tau} g_i + \sum_i h_i \frac{dg_i}{d\tau} = 0. \tag{2.36}$$

Now, following therefrom with allowance for $c_{pi} = dh_i/dT$ (where c_{pi} is isobaric mass specific heat of i-th substance) allows us to obtain

$$\frac{dT}{d\tau} = -\frac{\sum_i h_i \frac{dg_i}{d\tau}}{\sum_i c_{pi} g_i} = -\frac{1}{c_{p\Sigma}} \sum_i h_i f_i^g, \tag{2.37}$$

Downloaded from https://www.cambridge.org/core. Nottingham Trent University, on 17 Aug 2019 at 01:58:27, subject to the Cambridge Core terms of use, available at https://www.cambridge.org/core/terms. https://doi.org/10.1017/9781108581714.002

where $c_{p\Sigma}$ is the isobaric specific heat of the mixture, and f_i^g is the right-hand side of Equation (2.13).

Similarly, proceeding from Equation (2.33), we can obtain

$$\frac{dT}{d\tau} = -\frac{\sum_i H_i \frac{dr_i}{d\tau}}{\sum_i C_{pi} r_i} = -\frac{1}{C_{p\Sigma}} \sum_i H_i f_i^r, \tag{2.38}$$

where $C_{p\Sigma}$ is the isobaric molar specific heat of the mixture, f_i^r is the right-hand side of Equation (2.8).

Apart from the energy equations, mathematical models of processes in high-temperature units may incorporate the other relations as well. For example, the model of ethane pyrolysis tube furnace [54] (Figure 1.16) may include the following equations and relations:

1. Chemical kinetics equations in exponential form (2.26)
2. Heat transfer equation in the following form

$$\frac{dq_m}{dx} = \frac{\alpha_\Sigma \pi D}{\dot{m}} (T_w - T) \equiv f_q, \tag{2.39}$$

   where q_m is external heat flow per unit of mass, $\dot{m}$ is total mass flow rate (vapor plus reactants), D is tube inner diameter, T_w is wall temperature, and α_Σ is total coefficient of heat transfer to the gas flow;
3. Equation of motion in the following form:

$$\frac{dp}{dx} = -\frac{p\mu_g V_g}{R_0 T} \left(\frac{dV_g}{dx} + \frac{\xi V_g}{2D} \right), \tag{2.40}$$

   where ξ is the hydraulic loss factor.
4. Energy equation for PFR in the following form:

$$\left(h_0^* + q_m - V_g^2/2 \right) \mu_g = \sum_i H_i r_i, \tag{2.41}$$

   where h_0^* is stagnation mass specific enthalpy of reactants

5) Flow rate equation:

$$V_g - \frac{4\dot{m} R_0 T}{\pi D^2 p \mu_g} = 0. \tag{2.42}$$

Such mathematical model permits allowance for the following phenomena:

- Process of ethane pyrolysis (in the framework of detailed chemical kinetics).
- Heat transfer from the tube walls to the reacting mixture.
- Pressure drop caused by hydrodynamic drag.
- Heat absorption due to endothermic reactions.

Downloaded from https://www.cambridge.org/core. Nottingham Trent University, on 17 Aug 2019 at 01:58:27, subject to the Cambridge Core terms of use, available at https://www.cambridge.org/core/terms. https://doi.org/10.1017/9781108581714.002

Note here that the model described above was constructed given the following assumptions:

– There is steady-state one-dimensional flow in the tube.
– Local losses of pressure are included in total pressure losses.

Unknown parameters in presented model of tube furnace are $q_m,\ p,\ T,\ V_g$.

2.2 Adaptation of Combustion Model to Heterogeneous Systems and Mass Exchange Reactions

2.2.1 Adaptation of Combustion Model to Heterogeneous Systems

The calculation of the composition of heterogeneous combustion products is known to evoke definite problems [13, 58]. One of the ways of their elimination in calculation of chemical equilibrium consists in the application of the model of large molecules (LM; see Section 1.3). At this point, the condensed substances may be considered as "gaseous" to allow the chemically equilibrium calculations involving these condensed substances to be executed by the gas-phase model algorithm. For example, for condensed phase molecule Al_2O_3 at n^* = 1000, one has $a_{ki}^* = (2000; 3000)$; i.e., the chemical formula of large molecule of this substance may be written as $Al_{2000}O_{3000}$, hereinafter referred to as $Al_2O_3^*$.Then the magnitudes of thermodynamic functions for large molecules should be determined by the formulas: $H_i^* = H_i n^*; S_i^{0^*} = S_i^0 n^*$ (where $H_i; S_i^0$ are molar enthalpy and entropy of i-th substance in condensed state), while LM dissociation constants can be calculated by Relations (1.22), the gaseous substance dissociation constants are defined from

$$ln K_i^{p^*} = \frac{\sum\limits_k a_{ki}^* S_k^o - S_i^{o^*}}{R_0} - \frac{\sum\limits_k a_{ki}^* H_k - H_i^*}{R_0 T}. \tag{2.43}$$

Note here that reacting medium may include both regular (gaseous) molecules and "large molecules" of the same substance. As a result, equilibrium equations for gaseous and condensed substances may be written in the framework of LM method in the same form. In solving many practical problems, the aforesaid approach is extended to the other relationships such as conservation equations, energy equations, etc.

This allows applying the calculation algorithm written for homogeneous combustion products, without notable alterations, to heterogeneous mixes to simplify the chemical equilibrium calculation significantly. Thereby, it is reasonable enough to attempt applying the LM method to the simulation of processes in chemically nonequilibrium systems when basic assumptions of this method – equality of temperatures and rates of gas and condensed phases, and small size of condensate particles – are close to the reality.

These assumptions may be used in the simulation of processes proceeding in LPRE fuel tanks, modeling flows of combustion products with condensed particles of extremely small sizes in the nozzles, numerical study of physicochemical conversion

Downloaded from https://www.cambridge.org/core. Nottingham Trent University, on 17 Aug 2019 at 01:58:27, subject to the Cambridge Core terms of use, available at https://www.cambridge.org/core/terms. https://doi.org/10.1017/9781108581714.002

of propellant in fuel conversion zones of various combustion chambers, etc. The LM method may also be applied to intermediate products and end products of combustion in condensed phase.

To adapt the LM method to calculation of chemically nonequilibrium processes, it is at least necessary to

- Include reactions of some sort involving LMs in the chemical mechanism.
- Provide for compliance of corrections instilled in the set of equations of chemical kinetics (2.4) with the main provisions of chemical kinetics.
- Derive the formulas for constants of velocities of reactions involving LM "gas."
- Allow for features of the LM "gas" thermodynamic properties.

The mechanism of the formation of reactions involving LMs should be accounted for to a definite extent. For example, several formal options involving a large molecule may be assumed for the condensation process. Some of them are analyzed in [55]. Thus, the following procedure of presenting the reaction of deposition of B_2O_3 gaseous molecules on the surface of condensed particles of $B_2O_3^*$ may be used (at $n^* = 1000$):

$$(B_2O_3)_1 \Leftrightarrow 0.001B_2O_3^*. \tag{2.44}$$

The fractional value of the coefficient in the right-hand side is caused by the necessity in satisfaction of balance of the species in this reaction. Certain singularity of its notation results from the requirement of coherence between LM method assumptions and basic provisions of formal chemical kinetics. The phrase from earlier citing the necessity of the allowance for the condensation mechanism in presenting the reaction with the application of the LM method may be described as follows.

At extremely high temperatures ($T > 3000$ K) in reducing reacting media, the reaction $CO + CO \Rightarrow C + CO_2$ proceeds with the formation of elemental carbon with its further condensation (carbon black as the aggregate of atoms C and H is formed at lower temperatures). If the condensation stage is very fast, then LMs of the condensate may be included in the reacting medium (C^* with the number of common molecules $n^* = 1000$) and represent the reaction of condensed carbon formation as follows:

$$\text{a)}\ CO + CO \underset{k_a^-}{\overset{k_a^+}{\Leftrightarrow}} 0.001C^* + CO_2, \tag{2.45a}$$

or in the form:

$$\text{b)}\ CO + CO + C^* \underset{k_b^-}{\overset{k_b^+}{\Leftrightarrow}} 1.001C^* + CO_2. \tag{2.45b}$$

Proceeding from whatever mechanism of LM formation, one should introduce corrections to the set of equations of chemical composition variation in compliance with the provisions of formal chemical kinetics. Thus, if the ordinary gas-phase mechanism of chemical conversions is supplemented with the reaction (2.45a), then it is necessary to

- supplement the CO concentration variation equation with the following expression:

Downloaded from https://www.cambridge.org/core. Nottingham Trent University, on 17 Aug 2019 at 01:58:27, subject to the Cambridge Core terms of use, available at https://www.cambridge.org/core/terms. https://doi.org/10.1017/9781108581714.002

$$-2k_a^+ C_{CO}^2 + 2k_a^- C_{CO_2} C_{C*}^{0.001} \tag{2.46}$$

– supplement the CO_2 concentration variation equation with the following expression:

$$k_a^+ C_{CO}^2 - k_a^- C_{CO_2} C_{C*}^{0.001} \tag{2.47}$$

– supplement the composition variation equation with the following equation:

$$dC_{C^*}/d\tau = \left(k_a^+ C_{CO}^2 - k_a^- C_{CO_2} C_{C^*}^{0.001}\right) 0.001 \tag{2.48}$$

At application of invariant programs [5; 30; 59], these supplements to chemical kinetics equations will be effected automatically.

For reactions involing the LMs, it is necessary to preset or to calculate, in some manner, one of the reaction rate constants. In some cases, it seems quite possible. For example, at the simulation of processes for which the condensed phase – i.e., LM gas – is known to be in equilibrium with some aggregate of gas substances or with one of them. Thus, the particles of condensed water (H_2O) can be in reacting system in equilibrium with its vapor. Then, for example, for reaction,

$$H_2O \Leftrightarrow (1/n^*)H_2O^*, \tag{2.49}$$

it is in fact necessary to set a known large value of velocity constant sufficient for, practically preventing practically the shift of this reaction from equilibrium. In many cases, a real value of the reaction rate constant involving LM can be defined with the help of the theory of condensation. Nevertheless, setting of the reaction rate constants with LM involved requires a practical experience like the task of reaction notation. However, these complexities are compensated by the fact that after their solution, appropriate equations are automatically allowed for in right-hand sides of Equations (2.4).

Note here that the equilibrium constant of reaction involving the LM can be described, by analogy with Formula (1.79), by the combination of the constants of dissociation (LM gas included) into atoms. For example, we have for Reaction (2.45a):

$$K_a = C_{CO_2} C_{C^*}^{0.001} / C_{CO}^2 = \left(K_{CO}^p\right)^2 (R_0 T)^{0.999} \Big/ \left(K_{CO_2}^p \left(K_{C^*}^p\right)^{0.001}\right) \tag{2.50}$$

where constant $K_{C^*}^p$ is calculated from Relation (2.43).

Eventually, in the application of some invariant program for the calculation of the combustion process in gas-phase reaction mediums [5, 30, 56], it is possible to simulate combustion in the system including condensed substances. Here, it should be allowed for the fact that reference data on the values of molar enthalpy, entropy, and specific heat of condensed substances should be multiplied by the number of molecules (n^*) that form the LMs.

In creating the algorithm of calculation, some difficulties are caused by the discontinuity in the relations $H_i = f_i(T)$ for large molecules originating due to polymorphic

Downloaded from https://www.cambridge.org/core. Nottingham Trent University, on 17 Aug 2019 at 01:58:27, subject to the Cambridge Core terms of use, available at https://www.cambridge.org/core/terms. https://doi.org/10.1017/9781108581714.002

conversions or phase transitions of condensate substances. One of the ways for overcoming said difficulties consists in the application of a piecewise approximation of the relation $K_i^p = f_i(T)$ at the application of reference values H_{rfi}, S^0_{rfi}, T_{rf}. It is expedient to combine the intervals of this approximation with linearization intervals of the relation $H_i = f_i(T)$ (see Section 2.4).

2.2.2 Simulation of Mass Exchange Processes

Composition variation equations (2.2, 2.8, 2.26) obtained in Section 2.1 stipulate for the inclusion of ordinary chemical reaction rate summands and mass exchange reaction summands, in their right-hand sides. The following types of mass exchange processes are characteristic of the combustion:

1. mass exchange caused by convective gas transfer from one reactor into another or convective gas exchange between the reactor and environment;
2. mass exchange caused by phase transitions within one reactor (evaporation of liquid phase contained therein, condensation of gas-phase substances inside the reactor and on the surfaces of its walls, adsorption, absorption, sublimation, thermoelectronic emission, etc.);
3. mass exchange caused by concentration diffusion of separate substances contained in reacting mixture their flowing through the membranes, etc.

Application of these conditional reactions simplifies the simulation of processes in reactors (BR, PFR, PSR) at the mass feed and discharge in combustion. Mathematical models and algorithms become more flexible with respect to mass exchange process inside the reactors, between reactors, and between reactors and the environment. For this, the "mass exchange reactions" should be described by a symbolic form of chemical reactions and correspond to the law of mass action.

For example, in the simulation of fluid droplet evaporation inside the reacting system, the vapor formation rate (that of mass feed) does not frequently depend on the vapor concentration in the reactor. This allows considering the mass feed to be the result of an occurrence of a certain hypothetical zero-order reaction. At the same time, it is frequently assumed that in the simulation of condensation, the rate of i-th component discharge from the reactor depends on its concentration at the first stage, which allows identifying this type of mass discharge as the first-order hypothetical reaction (refer to Subsection 1.3.2).

These properties permit imparting the "source" and "sink" terms in Equations (2.1) the form of standard components of the equations of chemical kinetics. Then, these summands render formally indistinguishable from the other terms to allow add them to the sum given in sigma notation. For this, the kinetic mechanism should be supplemented with "mass exchange" reactions (2.2) corresponding formally to regular chemical reactions. It is obvious that the rate constants of such reactions feature a specific form characteristic of the mass transfer particular conditions and differing, in a general case, from the standard Arrhenius equation. Let us consider some distinctive examples of mass exchange reactions and notation of their rates constants:

Downloaded from https://www.cambridge.org/core. Nottingham Trent University, on 17 Aug 2019 at 01:58:27, subject to the Cambridge Core terms of use, available at https://www.cambridge.org/core/terms. https://doi.org/10.1017/9781108581714.002

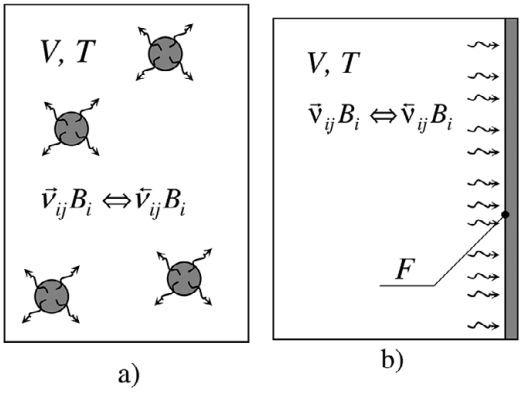

Figure 2.1 Schemes of evaporation (a) and condensation (b) in BR (F is the cold surface whereon condensation occurs).

Evaporation of liquid individual substance B_i. Let us consider BR (Figure 2.1a) of volume V containing N_p small drops of substance B_i uniformly distributed over this volume. Let us assume that the evaporation rate of every drop with mass m_p is described by the following relation [8, 32]:

$$\frac{dm_p}{d\tau} = \frac{D_{im}S_p p\mu_i}{\delta R_0 T_p} ln\left(1 - \frac{p_{sat}(T_p)}{p}\right) \equiv f_{pi}, \tag{2.51}$$

where δ is reduced film depth around the particle; D_{im} is the coefficient of binary diffusion; S_p, T_p are the surface area and particle temperature, respectively; and p_{sat} is pressure of saturated vapors.

In case evaporation rate weakly depends on concentration of substance in the reactor, then the evaporation process may be described by one zero-order reaction $\rightarrow B_i$ [60]. At determining the rate constant k_i^+ let us allow for the fact that overall evaporation rate of substance B_i will be written as $f_{pi}N_p$, while the reacting medium volume will be

$$V_r = V - V_p N_p, \tag{2.52}$$

where V_p is the volume of a single particle.

Then the mass exchange reaction rate (velocity of B_i substance emergence in gas unit volume) will be

$$W_i^+ = \frac{f_{pi}N_p}{(V - N_p V_p)\mu_i}. \tag{2.53}$$

Since the proposed reaction is of "zero order," then one can obtain that $k_i^+ = W_i^+$.

Condensation of substance B_s. (Figure 2.1b) Oversaturated vapor of k-th metal with concentration C_k is formed in reacting medium that fills the BR to generate the

Downloaded from https://www.cambridge.org/core. Nottingham Trent University, on 17 Aug 2019 at 01:58:27, subject to the Cambridge Core terms of use, available at https://www.cambridge.org/core/terms. https://doi.org/10.1017/9781108581714.002

condensing metal flow $\dot{m}$(kg/s) to the cold surface F that can be determined by the formula [61]:

$$\dot{m} = \frac{\beta F\sqrt{R_0 T\mu_k}(C_k - C_{sat})}{(1-0.4\beta)\sqrt{2\pi}}, \tag{2.54}$$

where β is the dimensionless coefficient of condensation; C_{sat} is the concentration of saturated vapor at the surface F.

If magnitude C_{sat} is neglected because of the low temperature of the surface F, then Formula (2.54) acquires the form:

$$\dot{m} = \frac{\beta F\sqrt{R_0 T\mu_k}C_k}{(1-0.4\beta)\sqrt{2\pi}}. \tag{2.55}$$

Now, the mass discharge reaction rate (the rate of B_s substance escaping from the reactor unit volume) is defined by the formula:

$$W_s^- = -\frac{\dot{m}}{V\mu_k} = -\frac{\beta F\sqrt{R_0 T}C_k}{(1-0.4\beta)V\sqrt{2\pi\mu_k}}. \tag{2.56}$$

This magnitude corresponds to the first-order reaction ($B_k \rightarrow$) with the rate constant

$$k_k^+ = \frac{\beta F\sqrt{R_0 T}}{(1-0.4\beta)V\sqrt{2\pi\mu_k}}. \tag{2.57}$$

Substance diffusion into reactor through the membrane. In some cases, the process of individual substances feeding into the reactor should be described by more than one mass exchange reaction. This may be caused by the difference in concentrations leading to concentration diffusion of one or several individual substances, their feed in or discharge from the reactor (the phenomenon characteristic of, for example, the membrane technology), etc.

At mass exchange between the reactor and environment via the membrane (Figure 2.2), permeable for substance B_i, the rate of its flow through the membrane

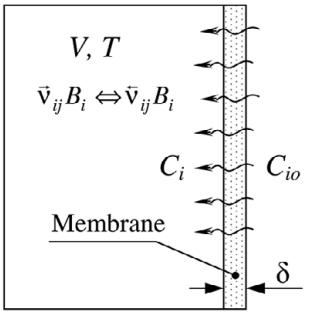

Figure 2.2 Scheme of individual substance diffusion into the reactor through the membrane.

Downloaded from https://www.cambridge.org/core. Nottingham Trent University, on 17 Aug 2019 at 01:58:27, subject to the Cambridge Core terms of use, available at https://www.cambridge.org/core/terms. https://doi.org/10.1017/9781108581714.002

(J_i) depends on the difference in concentrations of this substance on both sides of the membrane and is defined by the formula [8, 62],

$$J_i = \frac{D_{ef}}{\delta_m} F(C_{ie} - C_i), \tag{2.58}$$

where D_{ef} is the coefficient of diffusion, δ_m is membrane thickness, F is the membrane area, and C_{ie} is the molar concentration of i-th substance in external medium (C_{ie} = const).

Then the rate of *i-th* substance appearance in the reactor unit volume will be

$$W_i = \frac{D_{ef}}{V\delta_m} F(C_{ie} - C_i). \tag{2.59}$$

For this rate it is impossible to choose the only mass exchange reaction corresponding to the law of action masses. But if one decomposes the right-hand side of (2.59) into two summands,

$$W_i = \frac{D_{ef}}{V\delta_m} FC_{ie} - \frac{D_{ef}}{V\delta_m} FC_i, \tag{2.60}$$

the overflowing processes may be described by two reactions:

(a) zero-order reaction: $\rightarrow \mathrm{B_i}$ with the rate:

$$W_i^+ = \frac{D_{ef}}{V\delta_m} FC_{ie} \tag{2.61}$$

and rate constant $k_i^+ = W_i^+$;

(b) first-order reaction: $\mathrm{B_i} \rightarrow$ with the rate:

$$W_i^- = \frac{D_{ef}}{V\delta_m} FC_i = k_i^- C_i \tag{2.62}$$

and rate constant $k_i^- = D_{ef}F/(V\delta_m)$.

These reactions obey the action mass law and may be included in the mechanism of reactions along with ordinary elementary gas-phase reactions.

Combustion of carbon particles in the air medium. Figure 2.3 shows the scheme of carbon particles' combustion in BR in the oxidizer medium (air). The reactor of volume V contains N_p particles, and combustion rate ($\dot{m}_p$) of every particle is described by the formula [63]:

$$\dot{m}_p = A_k \, exp\left(-\frac{E_k}{R_0 T_p}\right) p_{\mathrm{O_2}}^{0.5} A_p, \tag{2.63}$$

where $p_{\mathrm{O_2}}$ is partial pressure of oxygen in gas (of "atm" dimension for this formula), A_p is the carbon particle surface area, and A_k, E_k are parameters defined experimentally.

Downloaded from https://www.cambridge.org/core. Nottingham Trent University, on 17 Aug 2019 at 01:58:27, subject to the Cambridge Core terms of use, available at https://www.cambridge.org/core/terms. https://doi.org/10.1017/9781108581714.002

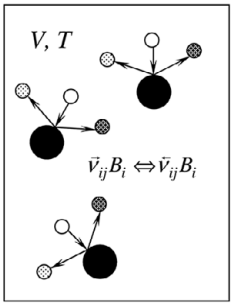

Figure 2.3 Scheme of carbon combustion by the model.

According to this model, when a O_2 molecule hits the surface of a carbon particle, it can interact with carbon to form a CO_2 or CO molecule (Figure 2.3) (depending on temperature T_p); then the resulting molecule goes into the gaseous medium. This process is described by the following reaction equation:

$$\mathrm{C} + \left(\frac{1+\varphi}{2}\right)\mathrm{O_2} \rightarrow \varphi\mathrm{CO_2} + (1-\varphi)\mathrm{CO}, \tag{2.64}$$

where φ is the degree of CO_2 formation.

To determine the values of φ the following relation is used in Reaction (2.64):

$$\frac{1-\varphi}{\varphi} = A_c \, exp\left(-\frac{E_c}{R_0 T_p}\right), \tag{2.65}$$

where coefficients A_c, E_c are also given in [63].

Neglecting the volume of particles in the reactor allows one to obtain carbon combustion rate easily:

$$\dot{m}_\mathrm{C} = N_p A_p A_k \, exp\left(-\frac{E_k}{R_0 T_p}\right) p_{\mathrm{O_2}}^{0.5}. \tag{2.66}$$

Therefrom, we obtain for the rate of carbon combustion in reacting medium unit volume:

$$W_\mathrm{C} = \frac{N_p}{V} A_p A_k \, exp\left(-\frac{E_k}{R_0 T_p}\right) p_{\mathrm{O_2}}^{0.5}, \tag{2.67}$$

where combustion rate has the dimension [kg/(m^3s)].

However, chemical-kinetic calculations use concentrations of substances, not partial pressure. This is why it is necessary to substitute p_{O_2} for C_{O_2} in Equation (2.67) to obtain

$$W_\mathrm{C} = \frac{N_p A_p}{V} A_k \, exp\left(-\frac{E_k}{R_0 T_p}\right) \left(C_{\mathrm{O_2}} R_0 T_g\right)^{0.5}. \tag{2.68}$$

Relation (2.68) is written in SI system and should be transformed in that traditionally used in chemical kinetics (gmol, cm, s, and calorie). By performing appropriate

Downloaded from https://www.cambridge.org/core. Nottingham Trent University, on 17 Aug 2019 at 01:58:27, subject to the Cambridge Core terms of use, available at https://www.cambridge.org/core/terms. https://doi.org/10.1017/9781108581714.002

transforms (with allowance for 1 kmol being equal to 1000 gmol; 1m = 100 cm; 1 atm. = 101352 Pa, R_0 = 8314.6 J/(kmol K)), we obtain the relationship for the rate of carbon combustion by reaction (2.64) in the unit volume in the following form:

$$W_{\mathrm{C}} = 0.001 \frac{N_p A_p}{V \mu_{\mathrm{c}}} A_k \sqrt{82.06} T_g^{0.5} \, exp\left(-\frac{E_k}{R_0 T_p}\right) C_{\mathrm{O}_2}^{0.5} \tag{2.69}$$

where C_{O_2} is given in gmol/cm^3, while W_{C} is given in gmol/(cm^{3}s) and μ_{c} is the molecular mass of carbon.

This expression may be interpreted as the rate of a certain chemical reaction of the 0.5 order. Then, we can write

$$W_{\mathrm{C}} = k_{\mathrm{C}} C_{\mathrm{O}_2}^{0.5}, \tag{2.70}$$

where k_{C} is defined by the expression:

$$k_{\mathrm{C}} = 9.06 \times 10^{-3} \frac{N_p A_p}{V \mu_{\mathrm{c}}} A_k T_g^{0.5} \, exp\left(-\frac{E_k}{R_0 T_p}\right). \tag{2.71}$$

Now it is necessary to determine symbolic formulas for mass exchange reactions that describe the O_2 absorption and CO and CO_2 formation, and to define the appropriate rate constants. For this, known value k_C, laws of chemical kinetics, and expression for reaction of surface combustion (2.64) will be used. This reaction shows that, along with each burned out gram-mole of carbon, $1 + \varphi/2$ gram-moles of O_2 disappears from gas phase, and simultaneously φ gram-moles of CO_2 and $(1 - \varphi)$ gram-moles of CO appear. Now, allowing for (2.70), it is possible to determine the following reaction rates:

$$W_{\mathrm{O}_2} = -\left(\frac{1+\varphi}{2}\right) k_{\mathrm{C}} C_{\mathrm{O}_2}^{0.5}; \quad W_{\mathrm{CO}_2} = \varphi k_{\mathrm{C}} C_{\mathrm{O}_2}^{0.5}; \quad W_{\mathrm{CO}} = (1-\varphi) k_{\mathrm{C}} C_{\mathrm{O}_2}^{0.5}. \tag{2.72}$$

These rates should be included as additional summands in equations of chemical kinetics for O_2, CO_2, and CO. Let us assume that the mechanism of elementary chemical reactions additionally incorporates the mass exchange reactions

$$0.5\mathrm{O}_2 \xrightarrow{k_1} 0.5\mathrm{CO}_2; \qquad 0.5\mathrm{O}_2 \xrightarrow{k_2} \mathrm{CO} \tag{2.73}$$

with rate constants $k_1 = 2\varphi k_{\mathrm{C}}$; $k_2 = (1 - \varphi) k_{\mathrm{C}}$.

Let us verify if the rates obtained from notations (2.73) match with Formulas (2.72). It is obvious that ,in compliance with the laws of chemical kinetics, one can obtain from (2.73):

$$W'_{\mathrm{CO}_2} = 0.5 k_1 C_{\mathrm{O}_2}^{0.5} = \varphi k_{\mathrm{C}} C_{\mathrm{O}_2}^{0.5}, \tag{2.74}$$

$$W''_{\mathrm{CO}} = k_2 C_{\mathrm{O}_2}^{0.5} = (1-\varphi) k_{\mathrm{C}} C_{\mathrm{O}_2}^{0.5}, \tag{2.75}$$

which agrees with W_{CO_2} and W_{CO} in (2.72). Similarly, we obtain for O_2:

$$W'_{\mathrm{O}_2} + W''_{\mathrm{O}_2} = -0.5 \times 2\varphi k_{\mathrm{C}} C_{\mathrm{O}_2}^{0.5} - 0.5(1-\varphi) k_{\mathrm{C}} C_{\mathrm{O}_2}^{0.5} = -\left(\frac{1+\varphi}{2}\right) k_{\mathrm{C}} C_{\mathrm{O}_2}^{0.5}, \tag{2.76}$$

Downloaded from https://www.cambridge.org/core. Nottingham Trent University, on 17 Aug 2019 at 01:58:27, subject to the Cambridge Core terms of use, available at https://www.cambridge.org/core/terms. https://doi.org/10.1017/9781108581714.002

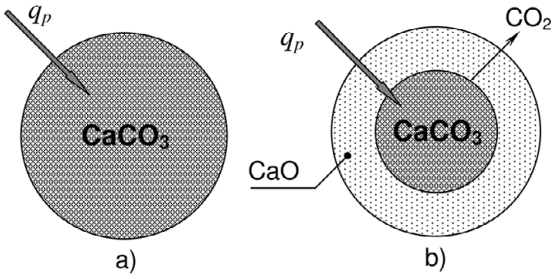

Figure 2.4 Scheme of calcium carbonate particles calcination.

that agrees with W_{O_2}. Thus, the forms of mass exchange reactions (2.73) have been selected properly.

Calcination of $CaCO_3$ particles. In some high-temperature units [64, 65, 66], small amount of calcium carbonate fine particles $CaCO_3$ are fitted in combustion zone (Figure 2.4a), which are converted at high temperatures into aggregates of microparticles CaO (Figure 2.4b).

These aggregates facilitate removal of harmful substances from combustion products. Since $CaCO_3$ particles are fitted in small amounts, then it may be assumed, for simplification, that condensed particles $CaCO_3^*, CaO^*$ are separate molecules (i.e., $n^* = 1$), while calcination occurs in the reaction: [67]

$$CaCO_3^* \xrightarrow{k_{Ca}^+} CaO^* + CO_2 \tag{2.77}$$

This reaction may be interpreted as an elementary reaction that obeys the action mass law. Then it may be included in the mechanism of ordinary chemical reactions. However, for this, it is necessary to determine the appropriate rate constant k_{Ca}^+. Empirical data cited in papers [68, 69] serves well to this end. The example of determination of rate constant k_{Ca}^+ with the use of empirical equation obtained in these papers is given as follows:

$$x_{Ca} = 1 - \left(1 - \frac{k_m}{d_{Ca}^{0.55}}\tau\right)^3, \tag{2.78}$$

where x_{Ca} is the CaO^* formation degree; $k_m = 10.303\ exp\left(-10980/T_g\right)$ is the coefficient of calcination rate; d_{Ca} is the initial diameter of $CaCO_3$ particle; r_{CaO} is the mole fraction of CaO; $r^0_{CaCO_3}$ is the initial mole fraction of $CaCO_3$ in the reacting medium.

Performing the substitution

$$y = 1 - x_{Ca} = 1 - r_{CaO}/r^0_{CaCO_3} = r_{CaCO_3}/r^0_{CaCO_3} = C_{CaCO_3}/C^0_{CaCO_3}. \tag{2.79}$$

where y is the degree of $CaCO_3$ decomposition in Equation (2.79),

we now obtain

$$y^{\frac{1}{3}} = 1 - \frac{k_m}{d_{Ca}^{0.55}}\tau. \tag{2.80}$$

Downloaded from https://www.cambridge.org/core. Nottingham Trent University, on 17 Aug 2019 at 01:58:27, subject to the Cambridge Core terms of use, available at https://www.cambridge.org/core/terms. https://doi.org/10.1017/9781108581714.002

To get the reaction rate constant (2.77), first represent the relation (2.80) in the form of an ordinary differential equation,

$$\frac{dy}{d\tau} = -Ay^{\alpha}, \tag{2.81}$$

where A, α are unknown constants.

By solving Equation (2.81), we obtain

$$\frac{y^{1-\alpha}}{1-\alpha} + C = -A\tau, \tag{2.82}$$

where

$$y^{1-\alpha} = -C(1-\alpha) - A(1-\alpha)\tau. \tag{2.83}$$

Formulas (2.80) and (2.83) will be identical if

$$C = -3; \qquad \alpha = 2/3; \qquad A = 3k_m/d_{\mathrm{Ca}}^{0.55}. \tag{2.84}$$

Substitute found values C, α and A in (2.81) and perform inverse interchange of y from Relation (2.79), to obtain

$$\frac{d\left(\frac{C_{\mathrm{CaCO_3}}}{C^0_{\mathrm{CaCO_3}}}\right)}{d\tau} = -\frac{3k_m}{d_{\mathrm{Ca}}^{0.55}}\left(\frac{C_{\mathrm{CaCO_3}}}{C^0_{\mathrm{CaCO_3}}}\right)^{2/3}. \tag{2.85}$$

Take the value $C^0_{\mathrm{CaCO_3}}$ out the differential sign into right-hand side of (2.85) to then be multiplied and divided by $C_{\mathrm{CaCO_3}}$:

$$\frac{dC_{\mathrm{CaCO_3}}}{d\tau} = -\frac{3k_m}{d_{\mathrm{Ca}}^{0.55}}\left(\frac{C_{\mathrm{CaCO_3}}}{C^0_{\mathrm{CaCO_3}}}\right)^{2/3}\frac{C_{\mathrm{CaCO_3}}}{C_{\mathrm{CaCO_3}}}C^0_{\mathrm{CaCO_3}}. \tag{2.86}$$

Now simplify the result to get

$$\frac{dC_{\mathrm{CaCO_3}}}{d\tau} = -\frac{3k_m}{d_{\mathrm{Ca}}^{0.55}}\left(\frac{C^0_{\mathrm{CaCO_3}}}{C_{\mathrm{CaCO_3}}}\right)^{1/3}C_{\mathrm{CaCO_3}}. \tag{2.87}$$

Equation (2.87) defines the degree of $CaCO_3$ decomposition in compliance with reaction (2.77). Consider it as the first-order reaction to get the formula for determination of the rate constant of this reaction:

$$k^{+}_{\mathrm{Ca}} = 30.909d_{\mathrm{Ca}}^{-0.55}\,exp\left(\frac{-21817}{R_0T}\right)\left(\frac{C^0_{\mathrm{CaCO_3}}}{C_{\mathrm{CaCO_3}}}\right)^{1/3}, \tag{2.88}$$

which allows us to incorporate it in the mechanism of elementary chemical reactions.

Cited examples display that mass exchange reactions bring about the simplification of the notation of chemical kinetics reactions because there is no need to write the members that reflect mass exchange processes independently or to render them

Downloaded from https://www.cambridge.org/core. Nottingham Trent University, on 17 Aug 2019 at 01:58:27, subject to the Cambridge Core terms of use, available at https://www.cambridge.org/core/terms. https://doi.org/10.1017/9781108581714.002

absolutely uniform for both gas-phase and multiphase reacting mixtures. As a result, the obtained uniformity simplifies the creation of the algorithm and allows its application for the simulation of processes in various high-temperature units irrespective of the character of the mass exchange processes that occur therein.

In compliance with technology of the simulation of the mass transfer by mass exchange reactions, the basic mechanism of chemical conversions in the gas phase should be supplemented by a set of such reactions. This technique allows us to preserve the invariance of algorithm and computer code with respect to gas medium. Summands in chemical kinetics equations resulting from these reactions should comply, by their form, with the laws of formal chemical kinetics – including, at the same time, the data on mass flows obtained from equations such as (2.51), (2.54), (2.58), (2.63), and (2.78).

2.3 Numerical Methods for Solving Reactor Model Equations

2.3.1 Description of Reactor Model Equations

It follows from the Section 2.1 that the reactor model can be described by the system of differential-algebraic equations:

$$\frac{d\gamma_i}{d\tau} = f_{\gamma i}\left(\langle\gamma_p\rangle, \langle\xi_t, \xi_\omega\rangle\right); \quad i = 1 \ldots .n_b; \quad p = 1 \ldots n_b; \tag{2.89}$$

$$\frac{d\xi_t}{d\tau} = f_{\xi t}\left(\langle\gamma_p\rangle, \langle\xi_t, \xi_\omega\rangle\right); \quad t = 1 \ldots d; \quad \omega = 1 \ldots c; \tag{2.90}$$

$$F_\omega \equiv F\left(\langle\gamma_p\rangle, \langle\xi_t, \xi_\omega\rangle\right) = 0, \tag{2.91}$$

where $\gamma_i = -ln(r_i)$; ξ_t, ξ_ω are desired unknown magnitudes (except for chemical composition of reacting mixture) – parameters of accompanying processes; and d, c are the number of differential and algebraic equations describing the accompanying processes in the reactor.

In most cases, algebraic equations may be represented in differential form. For example, the energy equation for adiabatic BR may be written in both algebraic (2.33) and differential (2.38) form. This is why, for further analysis given in this section, let us assume that the reactor model is described by ordinary differential equations (ODE). These equations are nonlinear and include obligatory the equations of a detailed chemical kinetics – for example, as (2.29), which are stiff and complicated [2, 70] and require an attentive selection of a finite difference scheme at constructing the calculation algorithm.

It is known that in the numerical integration of differential equations, both accuracy and stability of solution should be guaranteed. In the case of non-stiff systems, admissible integration step size, as a rule, is limited by the required accuracy of calculation, while in the case of stiff systems, the step size is also limited by stability. Let us consider a linear ODE system for evaluation of the integration step size:

Downloaded from https://www.cambridge.org/core. Nottingham Trent University, on 17 Aug 2019 at 01:58:27, subject to the Cambridge Core terms of use, available at https://www.cambridge.org/core/terms. https://doi.org/10.1017/9781108581714.002

$$\frac{dz_i}{d\tau} = -C_{ij}z_j = f_i\left(\langle z_j \rangle\right) \quad i, j = 1, \ldots, m, \tag{2.92}$$

where C_{ij} is the positively definite matrix [70], and z_i is the vector of unknowns.

Let us write in index less (matrix) form:

$$\frac{dz}{d\tau} = -Cz. \tag{2.93}$$

For illustration of stiffness, this ODE system can be represented after a series of linear transforms (see [71]):

$$\frac{dy}{d\tau} = -Dy, \tag{2.94}$$

where $D = diag(\lambda_1, \lambda_2, \ldots, \lambda_m)$ is the diagonal matrix, λ_i is matrix C eigenvalues (then $\lambda_i > 0$), and y is linear functions of vector z. Therefore, peculiarities revealed for analysis of (2.94) will be extended to the system of equations (2.92) or (2.93) as well.

Evidently, the analytical solution of (2.94) will be written as follows:

$$y_i = exp\,(-\lambda_i \tau), \tag{2.95}$$

whence it follows that at $\tau \to \infty$, value $y_i \to 0$.

Let us solve the set of equations (2.94) numerically applying the Euler explicit finite-difference scheme:

$$y_{i,n+1} = y_{i,n} + hf_i\left(\langle y_j \rangle\right) \tag{2.96}$$

with arbitrarily selected integration step h (assuming all values $y_i(0) > 0$).

For the first and n-th steps, we have

$$y_1 = y_0 - hDy_0 = (I - hD)y_0, \quad y_{n+1} = y_n - hDy_n = (I - hD)y_n, \tag{2.97}$$

whence executing recurrent substitutions after making the n-th step, we have

$$y_{n+1} = (I - hD)^n y_0, \tag{2.98}$$

where I is the unit matrix.

Since matrix $(I - hD)$ is a diagonal matrix with elements $d_j = (1 - h\lambda_i)$, then matrix $(I - hD)^n$ is also diagonal with elements $d_i^n = (1 - h\lambda_i)^n$. It is obvious that, at $\mid d_i \mid > 1$, the element value $y_{i,n+1}$ will increase with every step (that is, the solution will be "unstable"), while in compliance with Formula (2.95), it should approach zero. Therefore, at the application of the Euler explicit finite-difference scheme, the integration step should be limited by $\mid 1 - h\lambda_i \mid < 1$ for all elements of matrix $(I - hD)$. Representing this condition by

$$\mid 1 - h\lambda_{max} \mid < 1 \text{ where } \lambda_{max} = max(\lambda_1, \lambda_2, \ldots \lambda_m), \tag{2.99}$$

one obtains $h\lambda_{max} < 2$ – i.e., to provide for stability of calculation by the Euler explicit scheme, integration step h should be selected with allowance for constraint:

$$h < 2/\lambda_{max}. \tag{2.100}$$

Downloaded from https://www.cambridge.org/core. Nottingham Trent University, on 17 Aug 2019 at 01:58:27, subject to the Cambridge Core terms of use, available at https://www.cambridge.org/core/terms. https://doi.org/10.1017/9781108581714.002

Then it follows from (2.95) that all values of y_i will approach zero, but at different rate (subject to λ_i). The most slowly varying component will be $y_i \equiv y(\lambda_{min})$, where $\lambda_{min} = min(\lambda_1, \lambda_2, \ldots, \lambda_m)$ – i.e., the length of required integration step is inversely proportional to λ_{min}. If λ_{max} and λ_{min} differ but insignificantly, the required number of integration steps could be relatively small, since $y(\lambda_{max})$ and $y(\lambda_{min})$ will approach zero at approximately equal rates. In such cases, the system (2.93) or (2.94) is not considered a stiff one. However, in many applied analyses, the values λ_{max} and λ_{min} differ by hundreds, thousands, and more times. Then the number of required integration steps becomes extremely high, since integration interval should be set very large (because of the small value of λ_{min}), while the integration step should be selected very small (because of the great value of λ_{max}).

Problems of this sort are called stiff [71], and a special parameter (stiffness) is introduced for them and defined by the relation:

$$Jt = \frac{\lambda_{max}}{\lambda_{min}}. \tag{2.101}$$

Now let us apply the implicit Euler scheme to the same equation:

$$y_{i,n+1} = y_{i,n} + hf\left(\left\langle y_{j,n+1}\right\rangle\right). \tag{2.102}$$

This will have the following form at solving the system of equations (2.94):

$$y_1 = y_0 - hDy_1 \quad y_{n+1} = y_n - hDy_{n+1}, \tag{2.103}$$

whence one can write

$$y_1 = y_0(I + hD)^{-1}. \tag{2.104}$$

After execution of n-th step, we have

$$y_{n+1} = (I + hD)^{-n} y_0. \tag{2.105}$$

Matrix $(I + hD)$ is the diagonal matrix as well as matrix $(I + hD)^{-1}$ inverse thereof with elements $d_i = (1 + h\lambda_i)^{-1}$ – which, irrespective of values h and λ_i ($\lambda_i > 0$), are always smaller than unity. Therefore, in compliance with Formula (2.105), all values of y_i approach zero, and there are no constraints with respect to stability per integration step irrespective of the stiffness degree (it is obvious that integration step constraints in terms of accuracy are remained).

The given analysis is valid for nonlinear ODEs as well:

$$\frac{dx_i}{d\tau} = f_i\left(\left\langle x_j\right\rangle\right) \quad i, j = 1, \ldots, m. \tag{2.106}$$

And in certain zones $(\tau \pm \Delta\tau)$, it is such that nonlinear members will exercise negligibly small influence on the solution. For this, it is necessary to decompose the right-hand sides of Equations (2.106) into Taylor series with elimination of nonlinear summands, which brings, at n-th step to the system of linear ODEs,

Downloaded from https://www.cambridge.org/core. Nottingham Trent University, on 17 Aug 2019 at 01:58:27, subject to the Cambridge Core terms of use, available at https://www.cambridge.org/core/terms. https://doi.org/10.1017/9781108581714.002

$$\frac{dx_i}{d\tau} = f_i\left(\left\langle x_i^n \right\rangle\right) + \sum \left(\frac{\partial f_i}{\partial x_j}\right)_n \left(x_i^{n+1} - x_i^n\right), \tag{2.107}$$

where $\left(\frac{\partial f_i}{\partial x_j}\right)$ represents elements of the Jacobian matrix calculated at the beginning of *n-th* step of integration.

This makes the system of nonlinear ODEs represented over the entire integration range by the system of linear ODE (2.107) valid for local zones of this interval. Therefore, the concept of stiffness may be extended to nonlinear ODEs as well; herewith, stiffness may vary over the integration interval length. Cited examples with application of two versions of Euler method indicate that ODE numerical analysis procedures may be divided into two large groups:

- Explicit methods (they may be iterative but without the inversion of matrices)
- Implicit methods (applying the matrix inversion procedures).

2.3.2 Application of Explicit Methods for Solution of Stiff Differential Equations

Methods of the solution of ODE have been developed and used for more than hundred years, yet at present, new schemes of numerical integration are being developed. Their advantages consist of the small scope of calculations and simple programming. Reviews of these methods are given in many papers and monographs (see, for example, [72, 73]). Of these methods, the best known are

- One-step methods of Runge–Kutta [74]
- Multi-step methods of Adams. [75]

Some of these methods are described next.

Fourth-order Runge–Kutta method. Among one-step difference methods, this method is a "classical" one. Here, the unknown function *y(x)* used in the equation (for better visual clarity, the methods are described here for a single equation)

$$\frac{dy}{dx} = f(x, y) \tag{2.108}$$

is approximated by the Taylor series wherein the series members remain, up to the fourth order. Accuracy of this method features the order h^5, and the following sequence of calculations is performed:

$$\begin{aligned} &k_1 = hf(x_n, y_n); \quad k_2 = hf\left(x_n + \frac{h}{2}, y_n + \frac{k_1}{2}\right); \\ &k_3 = hf\left(x_n + \frac{h}{2}, \ y_n + \frac{k_2}{2}\right); \quad k_4 = hf(x_n + h, \ y_n + k_3); \\ &y_{n+1} = y_n + \frac{1}{6}(k_1 + 2k_2 + 2k_3 + k_4). \end{aligned} \tag{2.109}$$

Stability constraint for this method is described by the condition [71]:

$$h_{RK} < \frac{2.8}{\lambda_{max}}. \tag{2.110}$$

Downloaded from https://www.cambridge.org/core. Nottingham Trent University, on 17 Aug 2019 at 01:58:27, subject to the Cambridge Core terms of use, available at https://www.cambridge.org/core/terms. https://doi.org/10.1017/9781108581714.002

Multi-step Adams methods. In the general case, Adams schemes are described as follows:

$$y_{n+k} = h\beta_k f_{n+k} + \sum_{j=0}^{k-1} \left(h\beta_j - \alpha_j y_{n+j}\right), \tag{2.111}$$

where k is the number of steps used in the method; and α_j, β_j, β_k are coefficients to guarantee the approximation accuracy.

To calculate the values y_{n+k}, it is necessary to know these values at the previous points of the finite-difference mesh, namely:

$$(x_n, y_n), \left(x_{n+1}, y_{n+1}\right), \ldots., \left(x_{n+k-1}, y_{n+k-1}\right) \tag{2.112}$$

spaced apart by integration step h – i.e., the computer memory should store the results of calculation at previous steps.

Adams methods may be divided into two groups:

– Explicit methods of Adams–Bashforth [2]
– Iterative methods of Adams–Multon [2].

At the beginning of integration, these methods exploit one-step schemes to "pick up" the number of points required for the start of finite-difference scheme. Adams methods require smaller scope of calculations than Runge–Kutta methods but larger memory capacity at comparable accuracy.

Methods of Adams–Bashforth of the first to fourth orders, inclusive, are described by the formulas:

$$\begin{aligned}
y_{n+1} &= y_n + hf_n, \\
y_{n+2} &= y_{n+1} + \frac{h}{2}\left(3f_{n+1} - f_n\right), \\
y_{n+3} &= y_{n+2} + \frac{h}{12}\left(23f_{n+2} - 16f_{n+1} + 5f_n\right), \\
y_{n+4} &= y_{n+3} + \frac{h}{24}\left(55f_{n+3} - 59f_{n+2} + 37f_{n+1} - 9f_n\right),
\end{aligned} \tag{2.113}$$

where $f_{n+j} \equiv f\left(x_{n+j}, y_{n+j}\right)$.

For increase in stability, the Adams–Multon method includes the iterative calculation of the unknown value y_{n+k} with its preliminary calculation by the Adams–Bashforth method. For example, the series of formulas is used for the first-order scheme:

$$u_{n+1} = y_n + hf_n, \qquad f_{n+1} = f(x_{n+1}, u_{n+1}), \qquad y_{n+1} = y_n + \frac{h}{2}\left(f_{n+1} + f_n\right). \tag{2.114}$$

For second- through fourth-order schemes, Adams–Multon methods are described by the formulas:

$$\begin{aligned}
y_{n+2} &= y_{n+1} + \frac{h}{12}\left(5f_{n+2} + 8f_{n+1} - f_n\right), \\
y_{n+3} &= y_{n+2} + \frac{h}{24}\left(9f_{n+3} + 19f_{n+2} - 5f_{n+1} + f_n\right), \\
y_{n+4} &= y_{n+3} + \frac{h}{720}\left(251f_{n+4} + 646f_{n+3} - 264f_{n+2} - 106f_{n+1} - 19f_n\right).
\end{aligned} \tag{2.115}$$

Downloaded from https://www.cambridge.org/core. Nottingham Trent University, on 17 Aug 2019 at 01:58:27, subject to the Cambridge Core terms of use, available at https://www.cambridge.org/core/terms. https://doi.org/10.1017/9781108581714.002

Integration step constraints in terms of stability for methods of Adams–Bashforth and Adams–Multon are defined by the conditions [76]:

$$h_{AB} < \frac{0.3}{\lambda_{max}}; \quad h_{AM} < \frac{3}{\lambda_{max}}. \tag{2.116}$$

As follows from (2.110) and (2.116), "classical" explicit methods feature low levels of stability. However, these schemes are significantly simpler that implicit schemes (exploiting matrix inversion procedures), which is why the attempts extending the range of explicit schemes stability are not ceasing. Lately, a notable advance has been reached in this direction [77, 78, 79, 80, 81], and the area of application of explicit methods continues to extend.

In compliance with the paper [81], there are two basic approaches to the construction of explicit methods for the solution of stiff equations. The first approach proceeds from the extension of the stability range and is implemented for Runge–Kutta methods [78, 79]. The second approach is built around the following provisions:

- Evaluation of maximum absolute values of eigenvalues of the Jacobian matrix (λ_{max} and eigenvalues close thereto) – i.e., the detection of the stiff spectrum
- Subsequent stabilization of the calculation scheme at obtained points of the stiff spectrum – i.e., the minimization of stability polynomial values $P(h\lambda)$ at these points (2.120).

The eigenvalues evaluation procedure may be "implicit" in these methods – i.e., these values are not directly calculated, but a numerical interval, which is narrow enough, is defined, wherein the stiff spectrum points are located. Consider the examples of implementation of these approaches.

Lebedev–Medovikov second-order method [78]. The explicit second-order-accuracy scheme with time-varying steps based on the first approach is proposed in the paper [78] for solving ODE stiff systems:

$$\begin{aligned} Y_0 &= y_0 \\ U_{i+1/2} &= Y_i + h\,\alpha_{i+1} f(t_i, Y_i); \quad t_{i+1/2} = t_i + h\,\alpha_{i+1}; \end{aligned} \tag{2.117}$$

$$\begin{aligned} Y_{i+1} &= U_{i+1} + h\,\nu_{i+1}\,\alpha_{i+1}\left(f\left(t_{i+1/2}, U_{i+1/2}\right) - f(t_i, Y_i)\right) \\ &= U_{i+1} - \nu_{i+1}\left(U_{i+1} - 2\,U_{i+1/2} + Y_i\right); \quad i = 0, \ldots, s-1; \end{aligned} \tag{2.118}$$

$$\begin{aligned} Y_{i+1} &= U_{i+1} + h\,\nu_{i+1}\,\alpha_{i+1}\left(f\left(t_{i+1/2}, U_{i+1/2}\right) - f(t_i, Y_i)\right) \\ &= U_{i+1} - \nu_{i+1}\left(U_{i+1} - 2\,U_{i+1/2} + Y_i\right); \quad i = 0, \ldots, s-1; \end{aligned} \tag{2.119}$$

$y_1 = Y_s$ if s is even,

$y_1 = Y_{s-1} + h\alpha_s f(t_{s-1}, Y_{s-1})$ if s is odd,

where y_0, y_1 are values of y at the integration step beginning and end; Y, U are intermediate values of unknown obtained at iterations; and s is the number of iterations per integration step.

Values of α_i, ν_i are defined in the calculation of stability function (polynomial) roots. This function is described as follows:

$$P_s(\lambda h) = \prod_{i=1}^{s/2}\left[(1 - \alpha_i \lambda h)^2 - \nu_i \alpha_i^2 (\lambda h)\right]. \tag{2.120}$$

Downloaded from https://www.cambridge.org/core. Nottingham Trent University, on 17 Aug 2019 at 01:58:27, subject to the Cambridge Core terms of use, available at https://www.cambridge.org/core/terms. https://doi.org/10.1017/9781108581714.002

In the method proposed by the authors, it is necessary and sufficient to obey following equalities:

$$2\sum_{i=1}^{s/2}\alpha_i = 1; \qquad 2\sum_{i<j}^{s/2}\alpha_i\alpha_j + \sum_{i=1}^{s/2}\alpha_i^2(1-\nu) \quad = \frac{1}{2}; \tag{2.121}$$

If one assume

$$\begin{aligned} \alpha_i &= \frac{1/w_j + 1/w_{j+1}}{2}; \quad j = 2i, \\ \nu_i &= 1 - \frac{4/w_j w_{j+1}}{1/w_j + 1/w_{j+1}}; \quad i = 1, \ldots, s/2, \end{aligned} \tag{2.122}$$

where w_j represents roots of polynomial (2.120), then, substituting the value ν_i from (2.122) in (2.121), the set of equations is obtained to relate these roots. Thus, the problem of difference scheme construction is reduced to the determination of polynomial (2.120) – i.e., to the calculation of values α_i, ν_i. The integration step in the explicit iteration scheme proposed by the authors has the following constraints:

$$h_{ex}(C) \le 0.814s^2/\lambda_{max}. \tag{2.123}$$

For example, at the number of iterations $s = 5$, one can obtain the size of a stable step $h_{ex}(C) \le 20.3/\lambda_{max}$, which is notably larger than that in Runge–Kutta method.

Three-stage, one-step Skvortsov method. This method implements the second method described in the paper [81]. The main concept consists of the minimization of stability polynomial $P(h\lambda_1)$ in the area of λ_1. (where λ_1 is a negative number with an absolute value larger by far than the other eigenvalues). Then integration may be performed with the step significantly larger than the minimum time constant ($\tau = 1/\lambda_1$). To implement the approach, it is necessary to possess the estimate of maximum of absolute value of eigenvalues of Jacobian matrix. Such estimate can be obtained on the basis of power method built around Formulas (2.121; 2.122) with the help of data obtained at preliminary stages of the one-step method. The paper discusses the three-stage, one-step method, its stages being implemented by the formulas

$$\begin{aligned} &k_0 = f(x_0, y_0); \\ &u_1 = y_0 + hk_0; \quad k_1 = f(x_1, u_1); \\ &u_2 = u_1 + h\alpha(k_1 - k_0); \quad k_2 = f(x_1, u_2), \end{aligned} \tag{2.124}$$

where α is a relatively small constant (for example, $\alpha = 10^{-3}$); and k, u are intermediate values of derivatives and unknowns.

One may write for linear ODE:

$$k_1 - k_0 = (hA)^2 h^{-1} y_0; \;\; k_2 - k_1 = \alpha(hA)^3 h^{-1} y_0. \tag{2.125}$$

A nonlinear function may be described by linear relation in the case of the nonlinear system at smooth function f and sufficiently small h to use Formulas (2.124) to write the approximate equality:

$$k_1 - k_0 \approx hAk_0; \quad k_2 - k_1 = \alpha(hA)^2 k_0, \tag{2.126}$$

where $A = \frac{\partial f}{\partial y}$ is the Jacobian matrix calculated at the initial point.

Downloaded from https://www.cambridge.org/core. Nottingham Trent University, on 17 Aug 2019 at 01:58:27, subject to the Cambridge Core terms of use, available at https://www.cambridge.org/core/terms. https://doi.org/10.1017/9781108581714.002

Relations (2.125) and (2.126) allow to apply the powerful method to get the estimate of the eigenvalues of matrix hA. Denote the i-th component of vector k (i.e., the value of vector k corresponding to the i-th unknown) via $k^{(i)}$ and then estimate z_1 of maximum absolute value of the eigenvalue of matrix hA over the i-th component with allowance for (2.124) and (2.126) [81]. This results in

$$z_1 = \frac{b}{a}; \quad a = \alpha\left(k_1^{(i)} - k_0^{(i)}\right); \quad b = k_2^{(i)} - k_1^{(i)}. \tag{2.127}$$

The final formula for the step of integration over the i-th component (i.e., the value of vector k corresponding to the i-th unknown) is expressed as follows:

$$y_1^{(j)} = u_1^{(i)} + hc\left(k_1^{(i)} - k_0^{(i)}\right), \tag{2.128}$$

where c is the "adjustable" parameter. Its value is calculated for each i-th component subject to magnitude z_1.

This relationship is set proceeding from the condition of supporting the highest accuracy of non-stiff components and fast prevention of stiff component influence on the numerical analysis process.

In the case of non-stiff components – i.e., at $|z_1 \leq 1.6|$, assuming that $c = 1/2 + z_1/6$, one can get the following:

$$y_1^{(i)} = y_0^{(i)} + h\left(k_0^{(i)} + \frac{1}{2}\left(k_1^{(i)} - k_0^{(i)}\right) + \frac{1}{6\alpha}\left(k_2^{(i)} - k_1^{(i)}\right)\right). \tag{2.129}$$

This formula guarantees the second-order accuracy for nonlinear systems.

For stiff components at $z_1 \leq 1.6$, $c = -1/z_1 - 1/z^2$ is assumed, which makes stability function (2.120) equal to zero at $z = z_1$. For stiff components at $z_1 > 1.6$, $c = 1.23/z_1$ is assumed.

Cited formulas and constants preset therein provide for a correct character of numerical solution and continuous dependence of parameter c on z_1 and $1/z_1$. The paper [81] does not set explicitly the conditions of integration step limitation by stability of the type (2.123). However, the given examples indirectly indicated that this approach guarantees the stability approximately eight times higher than that resulting from the application of the Runge–Kutta explicit method.

2.3.3 Implicit Method for Solving Stiff Differential Equations

Despite the aforementioned advantages of explicit schemes, because of their high stiffness, the overwhelming majority of reactor analyses are based on implicit difference methods. They are more complex but, on the whole, require a smaller scope of calculations and are easily spread to differential-algebraic equations. Let us describe some implicit schemes.

Gear's method [82, 83]. This method is frequently used in reactor analyses and incorporated in a widely used software tool for solving complex chemical kinetics problems, CHEMKIN [5]. It is based on two difference schemes. In case equations

Downloaded from https://www.cambridge.org/core. Nottingham Trent University, on 17 Aug 2019 at 01:58:27, subject to the Cambridge Core terms of use, available at https://www.cambridge.org/core/terms. https://doi.org/10.1017/9781108581714.002

$dy/dt = f(t,\ y)$ are non-stiff in some segment of integration, then the iterative Adams–Multon scheme is used:

$$y_n^{(m+1)} = y_{n-1} + h\beta_0 f\left(t_n, y_n^{(m)}\right) + h\sum_{l=1}^{k-1}\beta_l f(t_{n-l}, y_{n-l}) = a_n + h\beta_0 f\left(t_n, y_n^{(m)}\right), \quad (2.130)$$

where β_0, β_l are coefficients that guarantee the accuracy of approximation.

In case equations become sufficiently stiff, the implicit scheme is used with application of the Jacobian matrix and the Newton iterative process:

$$P\left[y_n^{(m+1)} - y_n^{(m)}\right] = y_n^{(m)} - a_n - h\beta_0 f\left(t_n, y_n^{(m)}\right), \quad (2.131)$$

where $P = I - h\beta_0 J$, m is the iteration step number, and

$$J = \left\{\frac{\partial f}{\partial y}\right\} \quad (2.132)$$

is a Jacobian matrix.

Unlike the classical Newton method, matrix P remains invariable in all iterations of integration step. Besides, it can remain unchanged at several further steps as well unless a satisfactory convergence of the iteration process is held. This procedure is called a "scheme with frozen Jacobian." It is known that 80% of calculations in reactor analyses fall on calculations of partial derivatives and matrix calculations; this is why the increase in the number of iterations at the integration step is compensated with usury with the decrease in the number of Jacobian matrix recalculations at the integration step.

To refine the Gear's method, it seems expedient to replace the Adams–Multon scheme with one of the improved schemes, [78] or [81], which feature stability several times higher than that of the former. Besides, these schemes are the so-called self-starting schemes – i.e., unlike the Adams–Multon scheme, they require no application of a one-step method to start the calculation.

Pirumov's method [84, 85]. This method known also as the θ-method exploits differential equations represented in every integration step in the form (in terms of chemical kinetics equations (2.27)):

$$F_i^{n+1} \equiv \gamma_i^{n+1} - \gamma_i^n - h_n\left(\theta f_i\left(<\gamma_k^n>\right) + (1-\theta) f_i\left(<\gamma_k^{n+1}>\right)\right) = 0; \quad i,\ k = 1,\ \ldots, n_b, \quad (2.133)$$

where $\langle\gamma_k\rangle \equiv \gamma_1,\ \gamma_2,\ \ldots,\ \gamma_{nb}$, θ is the parameter of approximation ($\theta = 0.4 \ldots 0.5$), h_n is the integration step, and n is the integration step number.

Note here that differential equations of accompanying processes may also be described as (2.133), while algebraic equations – for example, (2.91) – remain unchanged. For example, for analysis of adiabatic BR including equations (2.29, 2.32), unknowns γ_i^{n+1}, T^{n+1} are determined from the relations

$$x_k^{n+1,m+1} = x_k^{n+1,m} - \Delta x_k^{m+1};\ k = 1,\ \ldots,\ (n_b + 1), \quad (2.134)$$

Downloaded from https://www.cambridge.org/core. Nottingham Trent University, on 17 Aug 2019 at 01:58:27, subject to the Cambridge Core terms of use, available at https://www.cambridge.org/core/terms. https://doi.org/10.1017/9781108581714.002

where m is the iteration number, while Δx_k^{m+1} is determined in the analysis of the system of linear equations,

$$\left[\frac{\partial F_i}{\partial x_k}\right]\Delta x_k^{m+1} = -F_i^m, \tag{2.135}$$

where $x_k = \gamma_q$, T; $i, k = 1, \ldots, (n_b + 1)$; $q = 1, \ldots, n_b$.

In analysis of the system (2.135) used is the scheme of the frozen Jacobian matrix and LU decomposition [70] of Jacobian matrix wherein it is decomposed into two triangular matrices (L_{is} is lower and U_{sk} is upper; $s = 1, \ldots, n_b + 1$) so that $[\partial F_i/\partial x_k] = L_{is}U_{sk}$. Unknown discrepancies Δx_k^{m+1} are defined in two steps:

1. system $L_{is}y_s = -F_i^m$ is solved to determine y_s.
2. system $U_{sk}\Delta x_k^{m+1} = y_s$ is solved to determine Δx_k^{m+1}.

Note here that LU decomposition requires the number of calculation approximately three times smaller than matrix inversion.

Iteration in the current step of integration will be performed unless the relative change of Δx_k^{m+1} is less than a preset value. A version of the Newton scheme with matrices L_{is} and U_{sk} "frozen" in several integration steps [85] is employed, which notably decreases the calculation time.

Method of spline approximation [86, 87] .

Some models use the scheme of spline approximation of unknowns in every integration step instead of finite-difference approximation (2.133). This procedure, proposed in the paper [88] for analysis of stiff equations, is called the spline-integration method. Here, magnitude γ_i is approximated in every integration step $(\tau_n, \ldots, \tau_{n+1})$ by quadratic polynomial,

$$\gamma_i^{n+1}(\tau) = \tilde{a}_i^{n+1} + \tilde{b}_i^{n+1}\tau + \tilde{c}_i^{n+1}\tau^2; \;\; i = 1, \ldots, n_b, \tag{2.136}$$

or, in dimensionless form,

$$\gamma_i^{n+1}(\bar{\tau}) = a_i^{n+1} + b_i^{n+1}\bar{\tau} + c_i^{n+1}\bar{\tau}^2, \tag{2.137}$$

where $\bar{\tau} = (\tau - \tau_n)/h_n$; $0 \le \bar{\tau} \le 1$; $\gamma_i^{n+1}(0) = \gamma_i^n$; $\gamma_i^{n+1}(1) = \gamma_i^{n+1}$ are magnitudes γ_i at the start and end of $(n+1)$-th integration step; and $a_i^{n+1}, b_i^{n+1}, c_i^{n+1}$ are unknown coefficients of polynomial.

It is assumed in the first two steps that values of unknown γ_i and its derivative at the boundary of integration steps are equal – i.e., the following relations are valid:

$$\gamma_i^n(1) = \gamma_i^{n+1}(0); \qquad \frac{\partial \gamma_i^n(1)}{\partial \tau} = \frac{\partial \gamma_i^{n+1}(0)}{\partial \tau}, \tag{2.138}$$

therefrom, in compliance with (2.137), we obtain

$$a_i^{n+1} = a_i^n + b_i^n + c_i^n; \quad b_i^{n+1} = \left(b_i^n + 2c_i^n\right)\frac{h_n}{h_{n-1}}. \tag{2.139}$$

That is, at the start of iteration on the interval $(\tau_n, \ldots, \tau_{n+1})$ values of coefficients a_i^{n+1}, b_i^{n+1} are determined unambiquously. Thus, coefficients c_i^{n+1} only remain unknown while Equations (2.137) may be written as follows:

Downloaded from https://www.cambridge.org/core. Nottingham Trent University, on 17 Aug 2019 at 01:58:27, subject to the Cambridge Core terms of use, available at https://www.cambridge.org/core/terms. https://doi.org/10.1017/9781108581714.002

$$\frac{d\left(a_i^{n+1}+b_i^{n+1}\bar{\tau}+c_i^{n+1}\bar{\tau}^2\right)}{d\bar{\tau}}=h_n\frac{d\gamma_i^{n+1}}{d\tau}=h_nf_i(<\gamma_k>)=h_nf_i\left(<a_k^{n+1}+b_k^{n+1}\bar{\tau}+c_k^{n+1}\bar{\tau}^2>\right), \tag{2.140}$$

where $h_n=\tau_{n+1}-\tau_n$; $i=1,\ldots,n_b$.

Allowing for the fact that Equations (2.140) are written for the point τ_{n+1} (i.e., $\bar{\tau}_{n+1}=1$), one obtains the following system instead of (2.133):

$$F_i^{n+1}\equiv b_i^{n+1}+2c_i^{n+1}-h_nf_i\left(<c_k^{n+1}>\right)=0. \tag{2.141}$$

The initial iteration in the integration step $(n+1)$ is determined from the expression

$$c_{i,0}^{n+1}=c_i^n(h_n/h_{n-1})^2, \tag{2.142}$$

which is obtained from the equality of second derivatives γ_i over τ at the boundary of intervals $(\tau_{n-1},\ \ldots,\tau_n)$ and $(\tau_n,\ \ldots,\tau_{n+1})$. In the next steps after the estimation of $a_i^{n+1},b_i^{n+1},c_i^{n+1},\gamma_i^{n+1}$, coefficient b_i^{n+1} is corrected by interpolation of relations $\gamma_i(\tau)$ over the points $\gamma_i^{n-2},\gamma_i^{n-1},\gamma_i^n$:

$$b_i^{n+1}=(q_i+2s_i(h_{n-2}+h_{n-1}))/h_n, \tag{2.143}$$

where $s_i=\left(\frac{h_{n-1}}{h_n}\left(\gamma_i^n-\gamma_i^{n-1}\right)-\gamma_i^{n-1}+\gamma_i^{n-2}\right)/\left(h_{n-1}^2+h_nh_{n-2}\right);q_i=\left(\gamma_i^{n-1}-\gamma_i^{n-2}-s_ih_{n-1}^2\right)/h_{n-1}$.

2.4 Structure and Main Stages of the Algorithm for Solving Reactor Model Equations

Along with the numerical method, the algorithm for solving reactor model equations should comprise additional procedures required for construction of invariant programs that follow:

- Sequence of operation with substance and reaction databases
- Conversion of symbolic and numeric data obtained from these databases into numeric arrays to construct the chemical kinetics equations
- Relating the thermodynamic properties of substances with chemical-kinetic parameters and characteristics
- Automatic calculation of reverse reaction rate constants proceeding from the limiting transition principle
- Procedure of extending the algorithm over heterogeneous system
- Calculation of Jacobian matrix partial derivatives
- Procedure of integration step variation.

2.4.1 Structure of Files and Governing Matrices

Reactor models described earlier as well as algorithms and corresponding computer codes are invariant. Therefore, the calculation of a particular reacting system requires a significant amount of data on the reacting medium. This information includes

Downloaded from https://www.cambridge.org/core. Nottingham Trent University, on 17 Aug 2019 at 01:58:27, subject to the Cambridge Core terms of use, available at https://www.cambridge.org/core/terms. https://doi.org/10.1017/9781108581714.002

Table 2.1 Fragment of reacting medium archives REAS

$O_2 + H_2 + Al$				Reacting medium code (KC)
H, O, H_2, O_2, OH, H_2O, Al, Al_2O, Al_2O_3*				← Set of substances
O_2+H_2 = OH + OH	12.403	0	39,000	← Equation of reaction and lgA^+,n^+,E^+
H_2 + OH = H_2O + H	13.382	0	5200	— // —
H + O_2 = OH + O	14.3	0	16,700	— // —
OH + OH = H_2O + O	13.159	0	0	— // —
O + O + M = O_2 + M	15.258	0	0	— // —
H +M + OH = H_2O + M	16.559	0	0	— // —
→ H_2O	0	0	0	← Reaction of mass feed
$Al_2O + O_2 \rightarrow Al_2O_3$*	0	0	0	← Reaction involving large molecular (LM)

- Data on thermodynamic and thermophysical properties of every substance of reacting medium
- Data on every reaction in reaction mechanism.

At present, multiple databases have been developed for both substances [13, 14, 17, 18, 89] and chemical reactions [26, 27, 28, 29]. The application of these databases makes it possible to form a specific reacting medium – that is, to provide the data on thermophysical and thermodynamic properties of the required set of substances and parameters of selected kinetic mechanism. For example, the symbolic form of the reacting system substances could be used directly for the readout of information on their thermodynamic and thermophysical properties from the database. Chemical mechanisms may be selected from the database with the help of unique numbers of chemical reactions compiled in the appropriate initial data file. However, this reacting medium formation method causes a significant increase of the scope of the data in the file of initial data. The most acceptable and friendly procedure of reacting medium formation consists of the application of the "reacting medium code" concept proposed in the CHEMKIN software tool [5]. Here, only this code should be presented in the initial data file. Sets of substances and reactions describing this medium are automatically selected from adequately structured archives by this code. Previous developments of the reactor approach exploit this concept, too, and use a similar algorithm for selection of substances and reactions [56, 59]. This algorithm operates with three data archives: reacting medium – file REAS (Table 2.1); gaseous substances – file INDG (Table 2.2); condensed substances – file INDK (Table 2.3).

Table 2.1 comprises the code line (KC), the line of the set of substances (B_i, B_i^*) of the simulated reacting medium, and the mechanism of chemical reactions. This mechanism includes the symbolic notation of every reaction and coefficients A_j^+, n_j^+, E_j^+ of the Arrhenius equation for the calculation of rate constants for forward directions of reactions. The reacting system code in this example is the notation O_2+H_2 +Al. The computer code reads, according to this notation, the symbols of substances and lines of reactions. Numbers are assigned to substances and reactions as they are read off – i.e., $(H \rightarrow 1, O \rightarrow 2 \ldots Al_2O_3^* \rightarrow 9)$ for substances, and $(O_2 + H_2 = OH + OH \rightarrow (1) \ldots A1_2O + O_2 \rightarrow Al_2O_3^* \rightarrow (8))$ for reactions. Note here that reaction 7 is the mass

Downloaded from https://www.cambridge.org/core. Nottingham Trent University, on 17 Aug 2019 at 01:58:27, subject to the Cambridge Core terms of use, available at https://www.cambridge.org/core/terms. https://doi.org/10.1017/9781108581714.002

Table 2.2 Excerpt from gaseous substance archive INDG

		H			Substance symbol
0.100799E1	0.212000E1	0.505399E3	0.334136E2	0.506386E5	μ, σ, ε/κ, A_S, A_I
0.497335E4	−0.705296E1	0.464247E1	−0.162989E1	0.312332E0	a_1, a_2, a_3, a_4, a_5
−0.50786E1	0.121980E2	1	300	5000	a_6, a_7, ν_k, T_{min},T_{max}
		H_2			Substance symbol
0.201600E1	0.293399E1	0.340999E2	0.407824E2	−0.211948E4	μ, σ, ε/κ, A_S, A_I
0.747623E4	−0.113302E4	0.107003E4	−0.375279E3	0.698089E2	a_1, a_2, a_3, a_4, a_5
−0.671189E1	0.262211E0	0	300	5000	a_6, a_7, ν_k, T_{min},T_{max}
		E (electron)			Substance symbol
0.548900E-3	0.100000E1	0.100000E3	0.110090E2	−0.145737E4	μ, σ, ε/κ, A_S, A_I
0.497337E4	−0.707358E1	0.466014E1	−0.163756E1	0.314094E0	a_1, a_2, a_3, a_4, a_5
−0.30991E-1	0.122919E-2	0	300	5000	a_6, a_7, ν_k, T_{min},T_{max}

Table 2.3 Excerpt from condensed substance archive INDK

Al_2O_3*	101.96		!Substance symbol, μ
900.	2326.	6000.	! T_1, T_2, T_3
0.765385E01	0.396356E02	0.486349E02	! A_{S1}, A_{S2}, A_{S3}
−0.404692E06	−0.409829E06	−0.402946E06	! A_{I1}, A_{I2}, A_{I3},
0.748686E04	0.262364E05	0.389306E05	! a_{11}, a_{12}, a_{13}
0.249092E05	0.168176E04	−0.133173E00	! a_{21}, a_{22}, a_{23}
−0.966457E04	0.549886E02	0.997356E02	! a_{31}, a_{32}, a_{33}
0.554300E04	0.554300E04	0.554300E04	! b_{01}, b_{02}, b_{03}
−0.108000E04	−0.108000E04	−0.108000E04	! b_{11}, b_{12}, b_{13}

feed reaction (Section 2.2) and, in this particular case, describes the evaporation of the water into the reacting medium, while reaction 8 involves LM of Al_2O_3*. Rate constants of reactions 7 and 8 are calculated in integration by Formulas (2.51) or with help of models of the type [9].

Table 2.2 uses the example of three substances to show that the archive of gaseous substances includes the following information: molecular mass μ; Lennard–Jones potential parameters σ, ε/κ; approximating coefficients A_S, A_I, a_1, a_2, a_3, a_4, a_5, a_6, a_7 from the database of TTR (item 1.2); valence for atoms ν_k; temperature interval T_{min}, T_{max} of approximating coefficients application.

Table 2.3 uses the example of one substance to show that the condensed substance archive comprises the following data: molecular mass μ; approximating coefficients A_{Sz}, A_{Iz}, a_{1z}, a_{2z}, a_{3z}, b_{1z}, b_{2z} from the database of TTR (Section 1.2), where z is the number of temperature interval; and b_{1z}, b_{2z} are the coefficients for linear approximation of condensate density.

Downloaded from https://www.cambridge.org/core. Nottingham Trent University, on 17 Aug 2019 at 01:58:27, subject to the Cambridge Core terms of use, available at https://www.cambridge.org/core/terms. https://doi.org/10.1017/9781108581714.002

Table 2.4 Structure of matrix N_R.

Symbol	H	O	H_2	O_2	OH	H_2O	Al	Al_2O	Al_2O_3*
Number of substance (***i***)	(1)	(2)	(3)	(4)	(5)	(6)	(7)	(8)	(9)
Number of reactions (***s***)	2	3	1	1	1	2	0	8	8
involving *i*-th substance	3	4	2	3	2	6	0	0	0
	6	5	0	5	3	7	0	0	0
	0	0	0	8	4	0	0	0	0
	0	0	0	0	6	0	0	0	0

Table 2.5 Structure of matrix N_V

Symbol	H	O	H_2	O_2	OH	H_2O	Al	Al_2O	Al_2O_3*
Number of substance (***i***)	(1)	(2)	(3)	(4)	(5)	(6)	(7)	(8)	(9)
Stoichiometric coefficients	1	1	−1	−1	2	1	0	−1	1
(ν_{ij})	−1	1	−1	−1	−1	1	0	0	0
	−1	−2	0	1	1	1	0	0	0
	0	0	0	−1	−2	0	0	0	0
	0	0	0	0	−1	0	0	0	0

Table 2.6 Structure of matrix N_S

Reactions	Forward Direction						Reverse Direction						Mass Exchange	
s	1	2	3	4	5	6	1	2	3	4	5	6	7	8
j	1	2	3	4	5	6	7	8	9	10	11	12	13	14
n_{ij}	1	1	1	2	2	1	2	1	1	1	1	1	0	1
	1	1	1	0	0	1	0	1	1	1	0	0	0	1
	0	0	0	0	0	0	0	0	0	0	0	0	0	0
Numbers of substances	3	3	1	5	2	1	5	1	2	2	4	6	6	4
involved in *j*-th reaction	4	5	4	0	0	5	0	6	5	6	0	0	0	8
	0	0	0	0	0	0	0	0	0	0	0	0	0	0
m_j	1	1	1	1	2	2	1	1	1	1	1	1	−1	1

The enumeration of substances and reactions allows one to automatically structure the three coordinating matrices to form the right-hand sides of the chemical kinetics equations. Such matrices for reacting medium $O_2 + H_2 + Al$ are shown in the Tables 2.4, 2.5, and 2.6.

Table 2.4 shows the matrix N_R, the columns of which specify the reaction numbers for every substance involved therein. For example, atom O is involved in reactions 3, 4, and 5. Table 2.5 shows matrix N_V, the columns of which specify corresponding

Downloaded from https://www.cambridge.org/core. Nottingham Trent University, on 17 Aug 2019 at 01:58:27, subject to the Cambridge Core terms of use, available at https://www.cambridge.org/core/terms. https://doi.org/10.1017/9781108581714.002

stoichiometric coefficients ν_{ij} for every substance that appears in Formulas (2.3) and Equations (2.4). For instance, the same atom O presents in the reactions 3, 4, and 5 with stoichiometric coefficients $\nu_{ij} = 1; 1; -2$ respectively.

Table 2.6 shows matrix N_S with stoichiometric coefficients n_{ij}, numbers of substances involved in j-th reaction, and values of exponents $\bar{m}_j$ used in Equations (2.26, 2.28). For example, forward direction reaction $H + O_2 \Leftrightarrow O + OH\,(s = 3, j = 3)$ involves substances (1) = H and (4) = O_2, while reverse direction reaction (s = 3, j = 9) involves substances (2) = O and (5) = OH.

It is shown that coordinating matrices N_R, N_V, N_S comprise redundant information; i.e., the amount of data exceeds one required for formation of right-hand sides of the equations. But on the other hand, the proposed structure of these matrices significantly simplifies the search for and selection of data on substances and reactions, thus reducing calculation time.

2.4.2 Representation of Enthalpy, Entropy, and Equilibrium Constants

Analysis of reactor problems requires multiple calculations of enthalpies and entropies H_i, S_i^0 of reacting medium individual substances depending on temperature (hereinafter, let us assume that $T_g \equiv T$ for simplification of notation). For their calculation polynomial approximating Formulas (1.7–1.9) are used for gaseous substances, and (1.10–1.12) are used for condensed substances. Though these formulas are simple, the amount of enthalpy and entropy calculations is great. This is why polynomial formulas for enthalpies and entropies H_i, S_i^0 are replaced by piecewise linear relationships in limited intervals of temperatures $T_{rf} \pm \Delta T$ to reduce the amount of calculations, covering a wide range of possible temperatures T (Figure 2.5) of reacting mixtures. For this, H_i, S_i^0 values are first calculated at three reference points ($T_{rf} + \Delta T, T_{rf}$, and $T_{rf} - \Delta T$) by Formulas (1.7–1.12). Since, as combustion proceeds, temperature T_g can

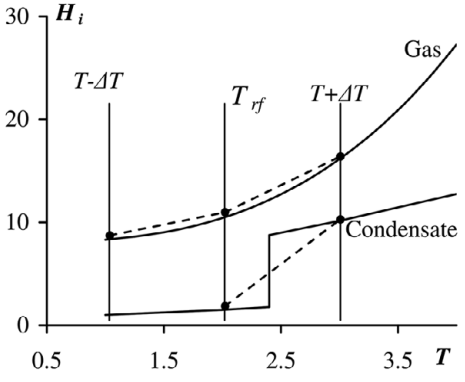

Figure 2.5 Diagram of linearization of individual substance enthalpy dependence of temperature.

Downloaded from https://www.cambridge.org/core. Nottingham Trent University, on 17 Aug 2019 at 01:58:27, subject to the Cambridge Core terms of use, available at https://www.cambridge.org/core/terms. https://doi.org/10.1017/9781108581714.002

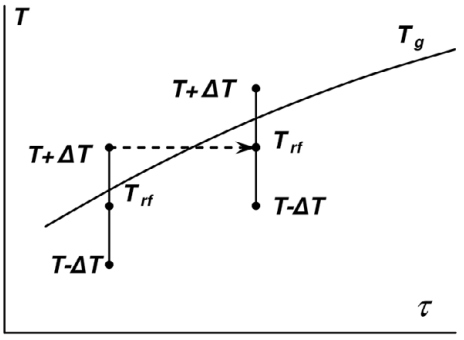

Figure 2.6 Illustration of $(T_{rf} \mp \Delta T)$ linearization interval shift at reacting medium temperature variation.

fall beyond the linearization interval limits, this interval shifts to allow one to determine the new reference point (Figure 2.6) by Formulas (1.7–1.12).

Enthalpy and entropy values are defined proceeding from reference values by the following formulas:

$$H_i = H_{rfi} + C_{pi}^{\pm}\left(T - T_{rf}\right), \tag{2.144}$$

$$S_i^0 = S_{rfi}^0 + \left[\left(S_{rfi}^0 - S_{\pm i}^0\right)/\Delta T\right]\left(T - T_{rf}\right), \tag{2.145}$$

$$C_{pi}^{\pm} = \mid H_{rf\,i} - H_{\pm i} \mid /\Delta T, \tag{2.146}$$

where $H_{\pm i} = H_{rfi}^{T+\Delta T}$ or $H_{rfi}^{T-\Delta T}$ $S_{\pm i}^0 = S_{rfi}^{0,T+\Delta T}$ or $S_{rfi}^{0,T-\Delta T}$; $H_{rf\,i}$ is the reference value of i-th substance molar enthalpy, $H_{rfi}^{T+\Delta T}$, $H_{rfi}^{T+\Delta T}$ are the reference values of enthalpy at $T_{rf} + \Delta T$ and $T_{rf} - \Delta T$, respectively; $S_{rfi}^{0,T+\Delta T}$, $S_{rfi}^{0,T-\Delta T}$ are the reference values of entropy at $T_{rf} + \Delta T$ and $T_{rf} - \Delta T$, respectively; T_{rf} is the reference value of temperature; and $C_{pi}^{\pm}$ is the reference value of average molar specific heat in linearization interval.

Experience in application of such linearization has proven with accuracy sufficient for applications that this interval ΔT may be taken equal as $\Delta T = 50\,\mathrm{K} \ldots 100\,\mathrm{K}$. Note here that discontinuous enthalpy changes in phase transitions points for condensed substances (Figure 2.5) are replaced in linearization by linear segments with steep slope. Such replacement causes a certain error in obtained results, but in practical applications, the error is not that significant, and its influence can be reduced, if necessary, by decreasing the linearization interval (ΔT). Besides, experience in operation with applied programs incorporating the relationships (2.144–2.146) has proven that discontinuity in heat capacities existing on boundaries of linearization intervals brings, in fact, no influence on either convergence or accuracy of the results of the calculation [57].

Downloaded from https://www.cambridge.org/core. Nottingham Trent University, on 17 Aug 2019 at 01:58:27, subject to the Cambridge Core terms of use, available at https://www.cambridge.org/core/terms. https://doi.org/10.1017/9781108581714.002

Given the linearization, the relationship (2.32) takes the following form:

$$h_\Sigma = \sum_i H_i r_i / \sum_i \mu_i r_i = \sum_i \left(H_{rf\,i} + C_{pi}^{\pm}(T - T_{rf}) \right) r_i / \sum_i \mu_i r_i, \tag{2.147}$$

wherefrom one can obtain

$$h_\Sigma \sum_i \mu_i r_i = \sum_i H_{rf\,i} r_i + (T - T_{rf}) \sum_i C_{pi}^{\pm} r_i. \tag{2.148}$$

now, after some simple transforms, the equation of the form required for application of Newton method can be obtained:

$$F_T \equiv T - T_{rf} - \sum_i (h_\Sigma \mu_i - H_{rfi}) r_i / \sum_i C_{pi}^{\pm} r_i = 0, \tag{2.149}$$

which hereinafter will be called the "calorific" or "energy" equation.

Rate constants for forward and reverse directions of reversible *s-th* reactions in the framework of formal chemical kinetics should satisfy the principle of limiting transition (1.76). The equilibrium constant contained therein to define k_s^- can be preliminary approximated by some relationship like $K_s = f_s(T)$. However, it is more expedient to define equilibrium constants directly in calculations with application of data on constants of dissociation of substances into atoms (1.19, 1.20). This results in a lower load of random access memory since the number of reacting components is usually notably less than the amount of chemical reactions corresponding thereto.

Equilibrium constant K_s is written by analogy with (1.79, 1.80) in the following form for the arbitrary elementary reversible *s*-th reaction:

$$K_s = \prod_i (K_i^p)^{\nu'_{is}} \Bigg/ \left[\prod_i (K_i^p)^{\nu''_{is}} (R_0 T)^{\sum_i (\nu''_{is} - \nu'_{is})} \right], \tag{2.150}$$

where constants of dissociation based on pressure K_i^p are described by relationships (1.19).

These constants can be calculated in temperature range $\{(T_{rf} - \Delta T) \ \ldots \ (T_{rf} + \Delta T)\}$ by Formulas (1.22) for reference points $T_{rf} - \Delta T; T_{rf}; T_{rf} + \Delta T$ and interpolated over these points with a sufficient degree of accuracy by the Arrhenius equation:

$$lnK_i^p = lnA_i^p + n_i^p lnT - E_i^p/(R_0 T), \tag{2.151}$$

where A_i^p, n_i^p, E_i^p are coefficients of interpolation.

Such notation of dissociation constants K_i^p results, finally, in the Arrhenius form of equilibrium constants calculated by concentrations K_s, hence, rate constants of reverse reactions as well. This can be shown as follows:

Downloaded from https://www.cambridge.org/core. Nottingham Trent University, on 17 Aug 2019 at 01:58:27, subject to the Cambridge Core terms of use, available at https://www.cambridge.org/core/terms. https://doi.org/10.1017/9781108581714.002

$$
\begin{aligned}
K_s &= \prod_i (K_i^p)^{\nu'_{is}} \Big/ \left[\prod_i (K_i^p)^{\nu''_{is}} (R_0T)^{\sum_i (\nu''_{is}-\nu'_{is})} \right] \\
&= \frac{\prod_i \left(A_i^p T^{n_i^p} \, exp\left(-E_i^p/(R_0T)\right) \right)^{\nu'_{is}}}{(R_0T)^{\sum_i (\nu_{is}-\nu'_{is})} \prod_i \left(A_i^p T^{n_i^p} \, exp\left(-E_i^p/(R_0T)\right) \right)^{\nu''_{is}}} \\
&= \frac{\left(\prod_i (A_I^p)^{\nu'_{is}} \right) T^{\left(\sum_i n_i^p \nu'_{is} \right)} \, exp\left(-\sum_i \nu'_{is} E_i^p/(R_0T) \right)}{(R_0T)^{\left(\sum_i (\nu''_{is}-\nu'_{is}) \right)} \left(\prod_i (A_i^p)^{\nu''_{is}} \right) T^{\left(\sum_i n_i^p \nu''_{is} \right)} \, exp\left(-\sum_i \nu''_{is} E_i^p/(R_0T) \right)} \\
&= A_s^e T^{n_s^e} \, exp\left(-E_s^e/(R_0T)\right),
\end{aligned}
\tag{2.152}
$$

where

$$
A_s^e = \prod_i (A_i^p)^{\nu'_{is}} \Big/ \left(R_0^{\left(\sum_i (\nu'_{is}-\nu''_{is}) \right)} \prod_i (A_i^p)^{\nu''_{is}} \right), \tag{2.153}
$$

$$
n_s^e = \sum_i n_i^p \nu'_{is} - \sum_i n_i^p \nu''_{is} - \sum_i \left(\nu''_{is} - \nu'_{is} \right), \tag{2.154}
$$

$$
E_s^e = \sum_i \nu'_{is} E_i^p - \sum_i \nu''_{is} E_i^p. \tag{2.155}
$$

Now, one obtains

$$
k_s^- = \frac{k_s^+}{K_s} = \frac{A_s^+ T^{n_s^+} \, exp\left(-E_s^+/(R_0T)\right)}{A_s^e T^{n_s^e} \, exp\left(-E_s^e/(R_0T)\right)} = A_s^- T^{n_s^-} \, exp\left(-E_s^-/(R_0T)\right) \ , \tag{2.156}
$$

where $A_s^- = A_s^+/A_s^e$; $n_s^- = n_s^+ - n_s^e$; $E_s^- = E_s^+ - E_s^e$

Thus, by calculating K_j via constants of substance dissociation into atoms, using coefficients of approximating polynomials A_s, A_1, a_1, . . . , a_7 of Formulas (1. 7–1.12), symbolic notation of the reaction and coefficients A_s^+, n_s^+, E_s^+ for rate constant of forward reaction, it is possible to define, without extra initial data, the Arrhenius form of rate constant of reverse reaction k_s^-, which unifies and simplifies the algorithm and corresponding computer code.

2.4.3 Determination of Jacobian Matrix Partial Derivatives

Basic equations used in independent reactor problems (BR, PSR), models of typical combustion modes (see Chapters 4–6), and applied models (see Chapters 7–10) are chemical kinetics equations and the calorific (energy) equation. This monograph

Downloaded from https://www.cambridge.org/core. Nottingham Trent University, on 17 Aug 2019 at 01:58:27, subject to the Cambridge Core terms of use, available at https://www.cambridge.org/core/terms. https://doi.org/10.1017/9781108581714.002

employs chemical kinetics equation in exponential form: (2.26) for BR, (2.29) for PSR, and (2.149) for the calorific equation. These equations are known to be stiff and, at present, require implicit methods with the application of the Jacobian matrix for their solution. The structure of this matrix for independent reactor analyses (2.26; 2.149) and (2.29; 2.149) are shown in Figure 2.2. To comply with the most important condition $\sum_i r_i = 1$, one of chemical kinetics equations in the system using Equation (2.26), or in the system using Equation (2.29), the corresponding substance with maximum concentration is replaced by the so-called normalizing equation:

$$F_{na} \equiv 1 - \sum_i e^{-\gamma_i} = 0. \tag{2.157}$$

Models described in this monograph exploit Pirumov's scheme (θ-method) [85] or spline-integration scheme [86]. An important fragment of these methods consists in the calculation of the matrix partial derivatives that can be defined numerically or analytically. The procedure of their numerical determination [5] is widely used, since it is easily algorithmized and, in fact, rules out crude errors. However, the analytical calculation of the Jacobian matrix partial derivatives features its intrinsic advantages, i.e.,

– Fewer calculations are required (particularly, for equations in exponential form).
– An accurate calculation of the Jacobian matrix brings about (at "frozen" scheme) a reduced number of iterations at integration step and Jacobian matrix recalculations.
– The analytical calculation of derivatives in "boundary" zones (nearby the combustion extinction line) [90] or nearby bifurcation points [91] allow one to get closer to these singularities, which makes it possible to reveal the reacting system characteristics in these zones more accurately.

Therefore, analyses described in the monograph accentuate the analytical calculation of partial derivatives. Next, the derivation of derivatives (Figure 2.7) is described for the

	γ_k	T
$F_{\gamma i}$	$\partial F_{\gamma i}/\partial \gamma_k$	$\frac{\partial F_{\gamma i}}{\partial T}$
F_z	$\partial F_z/\partial \gamma_k$	0
$F_{\gamma i}$	$\partial F_{\gamma i}/\partial \gamma_k$	$\frac{\partial F_{\gamma i}}{\partial T}$
F_T	$\partial F_T/\partial \gamma_k$	$\frac{\partial F_T}{\partial T}$

Figure 2.7 Structure of Jacobian matrix for calculation of combustion in single reactor.

Downloaded from https://www.cambridge.org/core. Nottingham Trent University, on 17 Aug 2019 at 01:58:27, subject to the Cambridge Core terms of use, available at https://www.cambridge.org/core/terms. https://doi.org/10.1017/9781108581714.002

BR model and a version of Pirumov's scheme application. In compliance with this scheme, Equations (2.26) take the following form:

$$F_{\gamma_i}^{n+1} = \gamma_i^{n+1} - \gamma_i^n - h\left(\theta f_{\gamma i}\left(<\gamma_k^n>, T^n\right) + (1-\theta) f_{\gamma i}\left(<\gamma_k^{n+1}>, T^{n+1}\right)\right) = 0; \quad i, \ k = 1, \ldots, n_b; \tag{2.158}$$

where

$$f_{\gamma_i} \equiv -e^{\gamma_i} \sum_j \nu_{ij}\Omega_j + \sum_q \sum_j \nu_{qj}\Omega_j; \tag{2.159}$$

$$\Omega_j = k_j \left(\frac{p}{R_0 T}\right)^{\bar{m}_j} exp\left(-\sum_p n_{pj}\gamma_p\right) \quad i, k, p, q = 1, \ldots, n_b; \ j = 1, \ldots, 2m_c; \ + r_c. \tag{2.160}$$

It is obvious that algebraic equation (2.149) remains unchanged.

Values with index n in relationship (2.158) are considered constant, hence, derivatives $\frac{\partial F_{\gamma_i}}{\partial \gamma_k}$ have the form:

$$\frac{\partial F_{\gamma_i}}{\partial \gamma_k} = \delta_i^k - h(1-\theta)\frac{\partial f_{\gamma i}}{\partial \gamma_k}, \tag{2.161}$$

where δ_i^k is the Kronecker symbol.

Let us find the derivative $\frac{\partial f_{\gamma_i}}{\partial \gamma_k}$, but first, let us calculate the derivative of the expression

$$f_{\gamma_i 1} \equiv -e^{\gamma_i} \sum_j \nu_{ij}\Omega_j \tag{2.162}$$

or

$$f_{\gamma_i 1} \equiv -e^{\gamma_i} \sum_j \nu_{ij} k_j \left(\frac{p}{R_0 T}\right)^{\bar{m}_j} exp\left(-\sum_p n_{pj}\gamma_p\right). \tag{2.163}$$

Differentiation gives

$$\frac{\partial f_{\gamma_i 1}}{\partial \gamma_k} = -\delta_i^k e^{\gamma_i} \sum_j \nu_{ij}\Omega_j - e^{\gamma_i} \sum_j \nu_{ij} k_j \left(\frac{p}{R_0 T}\right)^{\bar{m}_j} \frac{\partial}{\partial \gamma_k}\left(exp\left(-\sum_p n_{pj}\gamma_p\right)\right). \tag{2.164}$$

Expand the last derivative to obtain

$$\frac{\partial}{\partial \gamma_k}\left(exp\left(-\sum_p n_{pj}\gamma_p\right)\right) = -exp\left(-\sum_p n_{pj}\gamma_p\right) n_{kj}. \tag{2.165}$$

Substitute (2.165) in (2.164) to get

$$\frac{\partial f_{\gamma_i 1}}{\partial \gamma_k} = -\delta_i^k e^{\gamma_i} \sum_j \nu_{ij}\Omega_j + e^{\gamma_i} \sum_j \nu_{ij} k_j \left(\frac{p}{R_0 T}\right)^{\bar{m}_j} exp\left(-\sum_p n_{pj}\gamma_p\right) n_{kj}. \tag{2.166}$$

Downloaded from https://www.cambridge.org/core. Nottingham Trent University, on 17 Aug 2019 at 01:58:27, subject to the Cambridge Core terms of use, available at https://www.cambridge.org/core/terms. https://doi.org/10.1017/9781108581714.002

Allow for (2.160) to write

$$\frac{\partial f_{r_i 1}}{\partial \gamma_k} = -\delta_i^k e^{r_i} \sum_j \nu_{ij}\Omega_j + e^{\gamma_i} \sum_j \nu_{ij} n_{kj}\Omega_j. \tag{2.167}$$

Further, lets us simplify to obtain

$$\frac{\partial f_{\gamma_i 1}}{\partial \gamma_k} = -e^{\gamma_i} \sum_j \nu_{ij}\left(\delta_i^k - n_{kj}\right)\Omega_j. \tag{2.168}$$

For the addend (double sum) of the Expression (2.159), let us perform similar transforms to get

$$\frac{\partial}{\partial \gamma_k}\left(\sum_q \sum_j \nu_{qj}\Omega_j\right) = \sum_q \sum_j \nu_{qj} n_{kj}\Omega_j. \tag{2.169}$$

Substitute (2.168) and (2.169) in (2.161) to get finally

$$\frac{\partial F_{\gamma i}}{\partial \gamma_k} = \delta_i^k + h(1-\theta)\left[e^{\gamma_i} \sum_j \nu_{ij}\left(\delta_i^k - n_{kj}\right)\Omega_j - \sum_p \sum_j \nu_{pj} n_{kj}\Omega_j\right]. \tag{2.170}$$

For derivative $\frac{\partial F_{\gamma_i}}{\partial T}$, we initially have

$$\frac{\partial F_{\gamma i}}{\partial T} = -h(1-\theta)\frac{\partial f_{\gamma i}}{\partial T}. \tag{2.171}$$

Let us rewrite Expression (2.163), replacing rate constant k_j with its Arrhenius representation:

$$f_{\gamma_i 1} \equiv -e^{\gamma_i} \sum_j \nu_{ij}\Omega_j = -e^{\gamma_i} \sum_j \nu_{ij} A_j T^{n_j} \, exp\left(-\frac{E_j}{R_0 T}\right)\left(\frac{p}{R_0 T}\right)^{\bar{m}_j} exp\left(-\sum_p n_{pj}\gamma_p\right). \tag{2.172}$$

Then, differentiation of this expression allow us to obtain

$$\begin{aligned}\frac{\partial f_{\gamma_i 1}}{\partial T} = -e^{\gamma_i}\Bigg\{ & \sum_j \nu_{ij} A_j \left(\frac{n_j}{T}\right) T^{n_j} \, exp\left(-\frac{E_j}{R_0 T}\right)\left(\frac{p}{R_0 T}\right)^{\bar{m}_j} exp\left(-\sum_p n_{pj}\gamma_p\right) \\ & + \sum_j \nu_{ij} A_j T^{n_j}\left(\frac{E_j}{R_0 T^2}\right) exp\left(-\frac{E_j}{R_0 T}\right)\left(\frac{p}{R_0 T}\right)^{\bar{m}_j} exp\left(-\sum_p n_{pj}\gamma_p\right) \\ & + \sum_j \nu_{ij} A_j T^{n_j} \, exp\left(-\frac{E_j}{R_0 T}\right)\left(-\frac{\bar{m}_j}{T}\right)\left(\frac{p}{R_0 T}\right)^{\bar{m}_j} exp\left(-\sum_p n_{pj}\gamma_p\right)\Bigg\}\end{aligned} \tag{2.173}$$

Let us allow, for (2.160), to reduce Formula (2.173) to the following form:

$$\frac{\partial f_{\gamma_i 1}}{\partial T} = -e^{\gamma_i}\left\{\sum_j \nu_{ij}\Omega_j \frac{n_j}{T} + \sum_j \nu_{ij}\Omega_j\left(\frac{E_j}{R_0 T^2}\right) + \sum_j \nu_{ij}\Omega_j\left(-\frac{\bar{m}_j}{T}\right)\right\}, \tag{2.174}$$

Downloaded from https://www.cambridge.org/core. Nottingham Trent University, on 17 Aug 2019 at 01:58:27, subject to the Cambridge Core terms of use, available at https://www.cambridge.org/core/terms. https://doi.org/10.1017/9781108581714.002

whence we obtain

$$\frac{\partial f_{\gamma_i 1}}{\partial T} = -e^{\gamma_i} \sum_j \nu_{ij} \Omega_j \left(\frac{n_j - \bar{m}_j}{T} + \frac{E_j}{R_0 T^2} \right). \tag{2.175}$$

By making the similar transforms for double sum of expression (2.159) and allowing for (2.170), we obtain finally

$$\frac{dF_{yi}}{\partial T} = h(1-\theta) \left[e^{\gamma_i} \sum_j \nu_{ij} \Omega_j \left(\frac{n_j - \bar{m}_j}{T} + \frac{E_j}{R_0 T^2} \right) - \sum_p \sum_j \nu_{pj} \Omega_j \left(\frac{n_j - \bar{m}_j}{T} + \frac{E_j}{R_0 T^2} \right) \right]. \tag{2.176}$$

Let us take into account that for derivatives of the energy equations (2.149) with respect to concentrations:

$$\frac{dr_i}{d\gamma_i} = -\, exp\,(-\gamma_i) = -r_i, \tag{2.177}$$

and

$$(T - T_{rf}) \sum_i C_{pi}^{\pm} r_i = \sum_i \left(h_\Sigma \mu_i - H_i^{rf} \right) r_i. \tag{2.178}$$

Differentiation of the expression (2.149) allows us to get

$$\frac{\partial F_T}{\partial \gamma_k} = \left[\left(h_\Sigma \mu_k - H_k^{rf} \right) r_k \left(\sum_q C_{pq}^{rf} r_q \right) - C_{pk}^{rf} r_k \left(\sum_i \left(h_\Sigma \mu_i - H_i^{rf} \right) r_i \right) \right] \Big/ \left(\sum_q C_{pq}^{rf} r_q \right)^2. \tag{2.179}$$

Replacement with application of (2.178) allows to obtain

$$\frac{\partial F_T}{\partial \gamma_k} = \left[\left(h_\Sigma \mu_k - H_k^{rf} \right) r_k \sum_q C_{pq}^{rf} r_q - C_{pk}^{rf} r_k (T - T_{rf}) \sum_i C_{pi}^{rf} r_i \right] \Big/ \left(\sum_q C_{pq}^{rf} r_q \right)^2. \tag{2.180}$$

Making cancellation allows us to get finally

$$\frac{\partial F_T}{\partial \gamma_k} = \left[\left(h_\Sigma \mu_k - H_k^{rf} \right) r_k - C_{pk}^{rf} r_k (T - T_{rf}) \right] \Big/ \sum_q C_{pq}^{rf} r_q. \tag{2.181}$$

The other Jacobian matrix partial derivatives are (Figure 2.7):

$$\frac{\partial F_{na}}{\partial \gamma_k} = e^{-\gamma_k}; \frac{\partial F_T}{\partial T} = 1; \frac{\partial F_{na}}{\partial T_g} = 0.$$

For BR model, in the case of spline-integration scheme application (refer to item 2.3), instead of unknowns γ_i^{n+1}, values c_i^{n+1} become unknowns, and chemical kinetics equations (in a difference form) will be written as follows:

$$F_{ci}^{n+1} \equiv b_i^{n+1} + 2C_i^{n+1} - h_{n+1} f_{ci}(< c_k^{n+1} >) = 0, \tag{2.141}$$

Downloaded from https://www.cambridge.org/core. Nottingham Trent University, on 17 Aug 2019 at 01:58:27, subject to the Cambridge Core terms of use, available at https://www.cambridge.org/core/terms. https://doi.org/10.1017/9781108581714.002

while energy equation (2.149) does not vary, if we allow for

$$\gamma_i^{n+1} = a_i^{n+1} + b_i^{n+1} + c_i^{n+1},\ d\gamma_i/dc_i = 1. \tag{2.182}$$

Hereupon the derivatives of Expression (2.141) with respect to concentrations will take the form

$$\frac{\partial F_{ci}}{\partial c_k} = 2\delta_i^k + h_{n+1}\left[e^{\gamma_i}\sum_j \nu_{ij}\left(\delta_i^k - n_{kj}\right)\Omega_j - \sum_p\sum_j \nu_{pj}n_{kj}\Omega_j\right], \tag{2.183}$$

while temperature derivatives do not vary.

PSR-reactor model (2.29) meant for a version of Pirumov's scheme application incorporate analytical partial derivatives with respect to concentrations in following form:

$$\frac{\partial F_{\gamma i}}{\partial \gamma_k} = \delta_i^k + h_n(1-\theta)\left[\delta_i^k e^{\gamma_j}\left(\sum_j \nu_{ij}\Omega_j + \frac{r_i^+\mu_\Sigma}{\mu^+\tau_p}\right) - e^{\gamma_j}\left(\sum_j \nu_{ij}n_{kj}\Omega_j + \frac{r_i^+\mu_k r_k}{\mu^+\tau_p}\right) + \sum_q\left(\sum_j \nu_{qj}n_{kj}\Omega_j + \frac{r_q^+\mu_k r_k}{\mu^+\tau_p}\right)\right]. \tag{2.184}$$

PSR-reactor models for a version of the spline-integration scheme application, incorporate analytical partial derivatives with respect to concentrations in following form:

$$\frac{\partial F_{ci}}{\partial c_k} = 2\delta_i^k + h_{n+1}\left[\delta_i^k e^{\gamma_j}\left(\sum_j \nu_{ij}\Omega_j + \frac{r_i^+\mu_\Sigma}{\mu^+\tau_p}\right) - e^{\gamma_j}\left(\sum_j \nu_{ij}n_{kj}\Omega_j + \frac{r_i^+\mu_k r_k}{\mu^+\tau_p}\right) + \sum_q\left(\sum_j \nu_{qj}n_{kj}\Omega_j + \frac{r_q^+\mu_k r_k}{\mu^+\tau_p}\right)\right], \tag{2.185}$$

where γ_i is replaced by Formula (2.182).

The other partial derivatives for single reactors (Figure 2.7) remain unchanged for both numerical schemes and these reactors. It should be noted that partial derivatives in exponential form (2.26, 2.29) require fewer calculations than analytical derivatives for equations of the traditional type, since terms Ω_j calculated in determination of right-hand side terms of Equations (2.26, 2.29) are used.

Models of typical combustion forms (Chapters 4–6) and applied models (Chapters 7–10) are more complex than those of single reactors, since they include some additional equations describing the accompanying processes reflecting the specific features of typical combustion forms or design and the operation of high-temperature units under consideration. For these models, it also makes sense to use the analytical calculation of partial derivatives. Often, their calculation can be simplified by isolating slightly varying complexes in "accompanying" equations that should be recalculated at every integration step but could be considered constant in the calculation of partial derivatives. Besides, it can be defined from the physical scheme or results of analysis of equations that the variation of some derivatives slightly depends on the variation of working medium composition and even temperature. In such cases, appropriate

Downloaded from https://www.cambridge.org/core. Nottingham Trent University, on 17 Aug 2019 at 01:58:27, subject to the Cambridge Core terms of use, available at https://www.cambridge.org/core/terms. https://doi.org/10.1017/9781108581714.002

equations may be excluded from an implicit scheme and integrated in parallel with the main calculation by a somewhat explicit scheme. Then these equations may not be integrated in the Jacobian matrix.

The model of ethane pyrolysis (Equations 2.25 and 2.39–2.42) in a tubular furnace [54] may be considered as an example. By applying the finite-difference Pirumov's scheme (θ-method) to this model, we obtain the following relationships:

1. Chemical kinetics equations for PFR (2.25) in exponential form

$$F_{\gamma i} \equiv \gamma_i^{n+1} - \gamma_i^n - h\left(\theta f_{\gamma i}^n - (1-\theta) f_{\gamma i}^{n+1}\right) = 0; \quad i,\ k = 1, \ldots, n_b, \tag{2.186}$$

where $f_{\gamma_i} \equiv \frac{1}{V_g}\left(-e^{\gamma_i}\sum_j \nu_{ij}\Omega_j + \sum_q \sum_j \nu_{qj}\Omega_j\right)$;

2. Energy equation for PFR (2.41) descried in the form

$$F_T \equiv T - T_{rf} - \sum_q \left(\left(h_0^* + q_m - V_g^2/2\right)\mu_q - H_q^{rf}\right) r_q \Big/ \sum_q C_{pq}^{rf} r_q = 0; \tag{2.187}$$

3. Heat transfer equation (2.39) represented in the form

$$F_q \equiv q_m^{n+1} - q_m^n - h\left(\theta f_q^n + (1-\theta) f_q^{n+1}\right) = 0, \tag{2.188}$$

where $f_q = \frac{\alpha_\Sigma \pi D}{\dot{m}}(T_w - T)$; α_Σ is the total heat transfer coefficient to gas flow calculated by the formula $\alpha_\Sigma = \bar{k}_g Nu/D$,
where $Nu = 0.021\,Re^{0.8}Pr^{0.4}$ [62], *Re, Pr* are Reynolds and Prandtl numbers, respectively, and $\bar{k}_g$ is the average thermal conductivity of the gas;

4. Flow rate equation (2.42), represented as follows:

$$F_w \equiv V_g - \frac{4\dot{m}R_0 T}{\pi D^2 p \mu_g} = 0; \tag{2.189}$$

5. Equation of motion (2.40):

$$\frac{dp}{dx} = -\frac{p\mu_g V_g}{R_0 T}\left(\frac{dV_g}{dx} + \frac{\xi V_g}{2D}\right) \equiv f_p$$

represented as follows:

$$F_p \equiv p^{n+1} - p^n - h\left(\theta f_p^n + (1-\theta) f_p^{n+1}\right) = 0. \tag{2.190}$$

Pressure variation over the furnace length depends weakly on the stiff parameters (pyrolysis products composition and temperature). Therefore, Equation (2.190) may be omitted from the implicit scheme but integrated in the form (2.40) in the explicit scheme (for example, by the Runge–Kutta method). Then the set of equations (2.186–2.189) and the appropriate Jacobian matrix shown in Figure 2.8 will be incorporated in Pirumov's implicit scheme. Besides, heat transfer coefficient value α_Σ varies insignificantly in the process of integration. This is why this coefficient may be considered

Downloaded from https://www.cambridge.org/core. Nottingham Trent University, on 17 Aug 2019 at 01:58:27, subject to the Cambridge Core terms of use, available at https://www.cambridge.org/core/terms. https://doi.org/10.1017/9781108581714.002

	γ_k	T	q_m	V_g
$F_{\gamma i}$	$\partial F_{\gamma i}/\partial \gamma_k$	$\frac{\partial F_{\gamma i}}{\partial T}$	$\frac{\partial F_{\gamma i}}{\partial q_m}$	$\frac{\partial F_{\gamma i}}{\partial V_g}$
F_z	$\partial F_z/\partial \gamma_k$	0	0	0
$F_{\gamma i}$	$\partial F_{\gamma i}/\partial \gamma_k$	$\frac{\partial F_{\gamma i}}{\partial T}$	$\frac{\partial F_{\gamma i}}{\partial q_m}$	$\frac{\partial F_{\gamma i}}{\partial V_g}$
F_T	$\partial F_T/\partial \gamma_k$	$\frac{\partial F_T}{\partial T}$	$\frac{\partial F_T}{\partial q_m}$	0
F_q	0	$\frac{\partial F_q}{\partial T}$	$\frac{\partial F_q}{\partial q_m}$	0
F_w	$\partial F_w/\partial \gamma_k$	$\frac{\partial F_w}{\partial T}$	0	$\frac{\partial F_w}{\partial V_g}$

Figure 2.8 Structure of Jacobian matrix for calculation of pyrolysis in tubular furnace.

constant in the derivation of partial derivatives, though at every integration step it should be recalculated.

2.4.4 Selection of Integration Step

Combustion processes are known to proceed very slowly (for example, at the radicals accumulation stage) or very quickly (at the thermal explosion stage) [20]. Therefore, the integration step can vary in simulation some million times. Thus, the integration step prediction in calculations makes an important procedure of the entire algorithm facilitating the optimization of amount of calculations. In the solution of stiff problems, this procedure should be formed with due allowance for the maintenance of accuracy and stability of calculation. Moreover, schemes with "frozen" Jacobian require additional analysis and the establishment of an optimal ratio between step size, number of iterations per a step, and number of Jacobian recalculations. For example, the attempt to perform calculations with maximum possible step can result in the need in too-frequent recalculation of Jacobian, which is a rather time-consuming operation.

Many authors [77] consider that step selection for rather complex combustion models has no unambiguous solution and that it is possible to construct a sufficiently reliable and efficient step-size prediction procedure proceeding only from multiple numerical experiments. On the basis of our own experience in simulation of high-temperature processes [56, 59], it is possible to make recommendations on the formation of such procedure for numerical schemes with "frozen" Jacobian:

– The increase in step (usually a twofold increase) is permitted only at simultaneous fulfillment of several conditions and at a high degree of "reliability" – i.e., at sufficient confidence that at the next two integration steps no step division will be required.

Downloaded from https://www.cambridge.org/core. Nottingham Trent University, on 17 Aug 2019 at 01:58:27, subject to the Cambridge Core terms of use, available at https://www.cambridge.org/core/terms. https://doi.org/10.1017/9781108581714.002

- Step division (usually halving) should be performed given at least one of the permissible conditions are not met as well as at origination of symptoms of divergence in the Newton iteration process.
- At reaching extremely low concentrations (for example, $r_i < 10^{-30}$), the appropriate chemical kinetics equation should be replaced by equation $d\gamma_i/d\tau = 0$, which prevents further decreasing of concentration.
- It is necessary to control the crossing by any unknown magnitude of its zero value that, for instance, occurs frequently with reacting system enthalpy and to interrupt the magnitude variation verification at the integration step.
- At the first integration step, the initial discrepancies in algebraic equations (for example, $F_{na,}$ F_T, see Figure 2.7) should be several times smaller than a preset accuracy of the termination of iterations ε_N; otherwise, "infinite" division of the first step is possible.
- It is advisable to reasonably minimize the number of recalculations of Jacobian, which is attained by controlled formal "delays" in step duplication and by increasing the permissible number of iterations in the Newton method.

On the basis of these recommendations, integration step selection procedures have been formed in the models of typical combustion modes (Chapters 4–6) and applied models (Chapters 7–10), each with its peculiarities. These procedures are practically identical in single reactor analyses (for instance, for BR and PSR). As an example, let us cite the integration step selection procedure for such analyses exploiting Pirumov's scheme.

In reactor analyses, apart from the main parameters ($x_i \in \gamma_i, T_g$), the following will be calculated:

- Number of iterations at *n-th* step of integration J_n
- Maximum relative variation of values of unknowns x_i between iterations at this step (convergence criterion)

$$\varepsilon = \max_i \left|\Delta x_i^{n+1}/x_i^n\right|; \quad i = 1, \ \ldots, n_b \tag{2.191}$$

- Maximum relative variation of values of unknowns x_i at integration step (convergence criterion)

$$\Delta = \max_i \mid \left(x_i^{n+1} - x_i^n\right)/x_i^n \mid \tag{2.192}$$

- Number of steps (K_J) performed without recalculation of Jacobian matrix.

Integration step and, hence, the scope and accuracy of calculations are controlled by the following parameters:

- Δ_x – maximum admissible value of magnitude Δ
- ε_N – maximum admissible value of magnitude ε

Downloaded from https://www.cambridge.org/core. Nottingham Trent University, on 17 Aug 2019 at 01:58:27, subject to the Cambridge Core terms of use, available at https://www.cambridge.org/core/terms. https://doi.org/10.1017/9781108581714.002

- J_h – maximum admissible number of iterations at integration step
- J_p – admissible number of iterations without recalculation of Jacobian matrix
- K_{ds} – minimum necessary number of iteration steps (for doubling of step) performed without recalculation of Jacobian.
- The magnitude of the iteration step is defined by the following conditions:
- Iterations at the integration step are completed if $J_n > J_h$ or $\varepsilon \leq \varepsilon_N$.
- The matrix of partial derivatives is recalculated at *n-th* step if $J_n > J_p$.
- Doubling of integration step h occurs at the joint fulfillment of the following conditions:

$$J_h \leq J_p; \quad \varepsilon \leq \varepsilon_N; \quad K_J > K_{ds}; \quad \Delta \leq \Delta_x.$$

- Fragmentation of the integration step occurs if one of the conditions, $\varepsilon > 3\varepsilon_N$ or $\Delta > 3\Delta_x$, is fulfilled (if iterations are completed) or at quitting the iteration cycle (if the maximum of the discrepancies exceeds the prescribed limit).

  In all other cases, the integration step h remains unchanged.

Long-term testing of Pirumov's method for different types of analysis and different sets of initial data makes it possible to develop the following recommended values of step variation parameters:

$$\Delta_x = 0.005; \varepsilon_N = 10^{-5} \ldots 10^{-7}; J_h = 12; J_2 = 3; J_p = 7. \tag{2.193}$$

2.4.5 Scheme of Calculation Algorithm for Reactor Analysis

Following stages of the reactor problem solution given in Subsections 2.3.3 and 2.4.1–2.4.4, it is possible to form the block diagram of algorithm that complies with single rectors and reflects (mainly) the algorithms of the typical modes of the combustion and applied reactor models given in Chapters 4–10.

This block diagram is shown in Figure 2.9, where functions of blocks are differentiated as follows:

- Block B1 reads off information from initial file containing KC (reacting medium code), initial values of unknowns (T_0, r_{i0},), parameters p,τ_f (integration interval), h_0 (initial integration step), and calculation control parameters.
- Block B2 reads off by code KC the information on preset reacting medium (symbols of the set of substances B_i, B_i^*; symbolic notations of the reactions and coefficients of Arrhenius equation) from file REAS, its structure being shown in Table 2.1.
- Block B3 reads off data on approximating coefficients for calculation of thermophysical and thermodynamic properties of substances from files INDG (Table 2.2) and INDK (Table 2.3) by symbols of substances B_i, B_i^*.

Downloaded from https://www.cambridge.org/core. Nottingham Trent University, on 17 Aug 2019 at 01:58:27, subject to the Cambridge Core terms of use, available at https://www.cambridge.org/core/terms. https://doi.org/10.1017/9781108581714.002

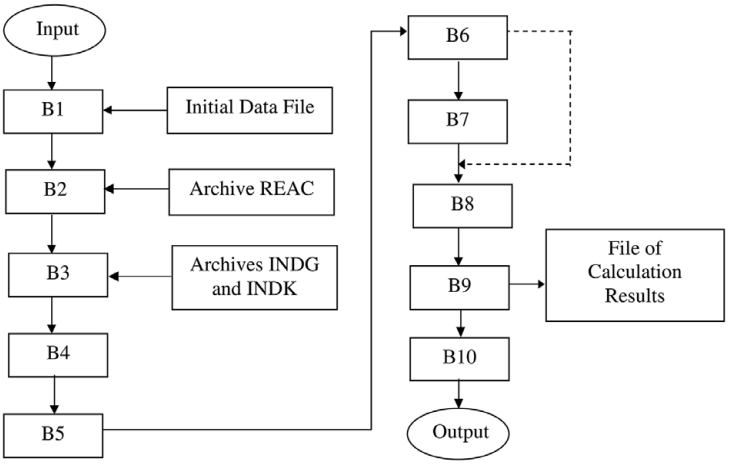

Figure 2.9 Diagram of algorithm for calculation of processes in single reactor.

- Block B4 performs a linguistic analysis of symbolic data, assigns numbers to reactions and substances, performs checks for errors in notation of reactions, and forms coordinating matrices for calculation of right-hand sides of chemical kinetics equations (Tables 2.4, 2.5, 2.6).
- Block B5 implements calculation of chemically equilibrium states (Subsection 1.3.1), if necessary.
- Block B6 executes preliminary calculations required for chemically nonequilibrium calculation and defines reference parameters H_i^{rf}, S_{rfi}^0, C_i^{rf}, rate constants of reverse directions of chemical reactions k_s^-, and rate constants of "mass exchange" reactions. These are calculated at the beginning of integration of the system of equations and in the cases when temperature T_g falls beyond the limits of the linearization interval (Subsection 2.4.2).
- Block B7 calculates partial derivatives of Jacobian matrix (Subsection 2.4.2) and its *LU* decomposition (Subsection 2.3.3) in cases when matrix recalculation is required.
- Block B8 implements at every integration step the calculation of chemically nonequilibrium composition of reacting mixture and its temperature by Equations (2.26, 2.149) or (2.29, 2.149) in a single reactor by Pirumov's scheme (2.133) or by the spline-integration method (2.141)
- Block B9 estimated subsequent integration step following procedure described in Subsection 2.4.4.
- Block 10 performs the final calculations; determines the process global characteristics (for example, degree of the shift from chemical equilibrium), general indices of calculation (number of integration steps, number of steps fragmentations, number of recalculations of Jacobian matrix, etc.), and error indices; and writes the calculation results to the output file.

Downloaded from https://www.cambridge.org/core. Nottingham Trent University, on 17 Aug 2019 at 01:58:27, subject to the Cambridge Core terms of use, available at https://www.cambridge.org/core/terms. https://doi.org/10.1017/9781108581714.002

2.5 Verification of Single Reactor Models

The previously described reactor approach to simulation of chemically nonequilibrium processes including universal basic mathematical models, procedures, and algorithms for the computation of combustion product composition makes a tool for the formation of applied models, algorithms, and computer codes that allow for multiple accompanying processes and are used for prediction and optimization of combustion and flows of reacting multiphase systems as well as working parameters of diverse propulsion and power generation systems, which is illustrated in Chapters 4–10.

However, the description of universal models built around the BR, PFR, and PSR – as well as the illustration of their application – might be incomplete without the comparison with similar models using these single reactor schemes such as, for example, the tools described in [5, 92, 93].

The description of CHEMKIN software package [5] represents the guidelines for the computation of combustion in adiabatic BR. The mathematical apparatus and corresponding gas-phase utility package [5] differ from the other software in the following aspects:

- CHEMKIN uses a TERMO-type database for information about species [16], as distinct from the TTR database [13].
- The traditional form of chemical kinetics equations is used in CHEMKIN, as opposed to exponential form of these equations.
- For integration of equations, the CHEMKIN uses the Gear's procedure, which – unlike Pirumov's method – is implemented in the proposed mathematical model and algorithms realized in the software package.

This is why the comparison of computation results with those obtained by application of GASPHASE is of interest. The reacting medium – including H, O, N, H_2, O_2, OH, HO_2, HO, H_2O, N_2, NO, and 23 reactions (see [5]) at 1 atm and 1000 K – is taken as the example.

The mixture's basic composition features the following concentrations of reactants – i.e., $r_{H_2} = 0.244$, $r_{O_2} = 0.732$ and $r_{N_2} = 0.024$. Figures 2.10 and 2.11 show the variations of reacting mixture temperature and composition versus time calculated with application of both software packages. The computation results are shown to be very close despite the aforesaid differences.

Paper [92] dealing with the analysis of hydrogen + air combustion for the gas turbine conditions cites, apart other results, the numerical analysis of ignition process with the help of adiabatic BR. Computations have been performed by software package [92] while the reacting medium has been represented by the mechanism [94] designed for a wide range of variation of thermodynamic and working parameters, namely T = 298 K–3000 K; p = 0.3 . . . 87 atm; $\alpha_{ox} = 0.2 \ldots 4.0$. The mechanism contained 19 reactions, including two "Troe" reactions (9a, 9b; 15a, 15b) and 8 species (Table 2.7). Each of the

Downloaded from https://www.cambridge.org/core. Nottingham Trent University, on 17 Aug 2019 at 01:58:27, subject to the Cambridge Core terms of use, available at https://www.cambridge.org/core/terms. https://doi.org/10.1017/9781108581714.002

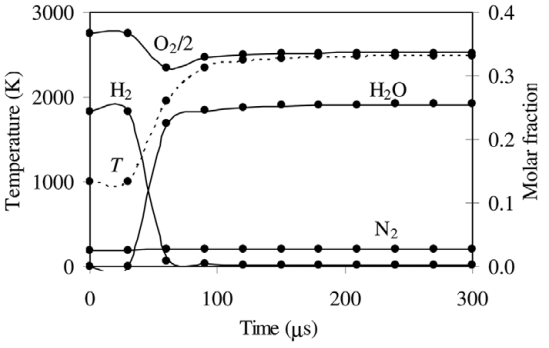

Figure 2.10 Mole fractions of species H_2, O_2, H_2O, N_2 (——), and temperature (·····) versus time in BR: (——), (·····) – computations made with application of the authors' software package; (●) – [5]. Courtesy of ANSYS, Inc

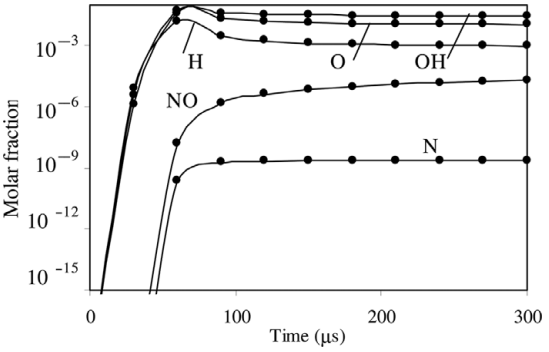

Figure 2.11 Mole fractions of species NO, H, O, OH, N in BR: (——) - computations made with application of the authors' software package; (●) – [5]. Courtesy of ANSYS, Inc

reactions, $HO_2 + HO_2 = H_2O_2 + O_2$ and $H_2O_2 + OH = H_2O + HO_2$, is formally by two reactions (14*p,q* and 19*p,q*, respectively) for better accuracy of rate constant calculation.

Results of comparison between computations by two models are given in Figures 2.12, 2.13, and 2.14 for the following conditions, i.e. T = 900 K and 1300 K; p = 17 atm; $\alpha_{ox} = 2.0$. Note here that calculations presented in [92] didn't include variation in temperature, which was preliminary estimated in [92] by the CHEMKIN software package. This is likely to bring about a certain discrepancy between compared results. If one allows for the fact that the characteristics of ignition are very sensitive to the variation of reacting medium parameters, then it may be concluded that the data obtained in application of these two models are close enough.

It is obvious that there is a notable difference between combustible mixture ignition times – i.e., at T_0 = 1300 K ($\tau_z \approx 3\mu s$) and T_0 = 900 K ($\tau_z \approx 10,000\,\mu s$). To explain this effect, it is necessary to allow for the following:

Downloaded from https://www.cambridge.org/core. Nottingham Trent University, on 17 Aug 2019 at 01:58:27, subject to the Cambridge Core terms of use, available at https://www.cambridge.org/core/terms. https://doi.org/10.1017/9781108581714.002

Table 2.7 Mechanism of the hydrogen + air combustion reactions. (A^+, n^+, E^+ – Arrhenius coefficients for forward direction of reaction)

No.	Reaction	A^+	n^+	E^+
1	$H + O_2 = O + OH$	$3.548 \cdot 10^{15}$	−0.406	16,599
2	$O + H_2 = OH + H$	$5.080 \cdot 10^{04}$	2.670	6290
3	$OH + H_2 = H_2O + H$	$2.160 \cdot 10^{08}$	1.510	3430
4	$O + H_2O = OH + OH$	$2.970 \cdot 10^{06}$	2.020	13,400
5	$H_2 + M = 2H + M$	$4.581 \cdot 10^{19}$	−1.400	104,380
6	$O + O + M = O_2 + M$	$6.166 \cdot 10^{15}$	−0.500	0
7	$O + H + M = OH + M$	$4.710 \cdot 10^{18}$	−1.000	0
8	$H + OH + M = H_2O + M$	$3.802 \cdot 10^{22}$	−2.000	0
9a	$H + O_2 + = HO_2$ (k_∞)	$1.475 \cdot 10^{12}$	0.60	0
9b	$H + O_2 + M = HO_2 + M$ (k_0)	$6.366 \cdot 10^{20}$	−1.72	525
10	$HO_2 + H = H_2 + O_2$	$1.660 \cdot 10^{13}$	0.0	823
11	$HO_2 + H = OH + OH$	$7.079 \cdot 10^{13}$	0.0	295
12	$HO_2 + O = OH + O_2$	$3.251 \cdot 10^{13}$	0.000	0
13	$HO_2 + OH = H_2O + O_2$	$2.891 \cdot 10^{13}$	0.0	−497
14p	$HO_2 + HO_2 = H_2O_2 + O_2$	$4.198 \cdot 10^{14}$	0.0	11,982
14q	$HO_2 + HO_2 = H_2O_2 + O_2$	$1.300 \cdot 10^{11}$	0.0	−1629
15a	$H_2O_2 = OH + OH$ (k_∞)	$2.951 \cdot 10^{14}$	0	48,430
15b	$H_2O_2 + M = OH + OH + M$ (k_0)	$1.202 \cdot 10^{17}$	0	45,500
16	$H_2O_2 + H = H_2O + OH$	$2.410 \cdot 10^{13}$	0.0	3970
17	$H_2O_2 + H = HO_2 + H_2$	$4.819 \cdot 10^{13}$	0.0	7950
18	$H_2O_2 + O = HO_2 + OH$	$9.550 \cdot 10^{06}$	2.000	3970
19p	$H_2O_2 + OH = H_2O + HO_2$	$1.000 \cdot 10^{12}$	0.0	0
19q	$H_2O_2 + OH = H_2O + HO_2$	$5.794 \cdot 10^{14}$	0.0	9557

k_∞– rate constants for "Troe" reactions (see Section 1.3) 9a, 15a (high pressures);
k_0– rate constants for "Troe" reactions 9b, 15b (low pressures).

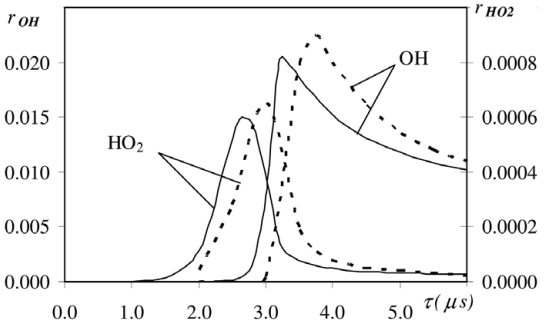

Figure 2.12 Variation of mole fractions of species OH, HO_2 in the ignition zone of the hydrogen+ air mixture versus time at $T_0 = 1300$ K; $p = 17$ atm, $\alpha_{ox} = 2.0$; (—) – computations performed with application of the authors' software package; (—) – [92]. Reprinted from *Combustion and Flame*, J. Ströhle, and T. Myhrvold, "Reduction of a Detailed Reaction Mechanism for Hydrogen Combustion under Gas Turbine Conditions," vol. 144, pp. 545–557, 2006, Copyright (2006), with permission from Elsevier

Downloaded from https://www.cambridge.org/core. Nottingham Trent University, on 17 Aug 2019 at 01:58:27, subject to the Cambridge Core terms of use, available at https://www.cambridge.org/core/terms. https://doi.org/10.1017/9781108581714.002

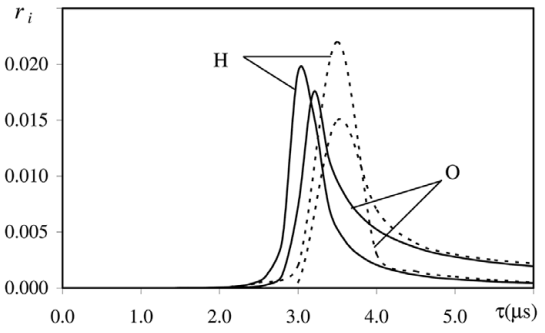

Figure 2.13 Variation of mole fractions of species O, H in the ignition zone of the hydrogen + air mixture versus time at T_0 = 1300 K; p = 17 atm, $\alpha_{ox} = 2.0$; (—) – computations performed with application of the authors' software package; (—) – [92]. Reprinted from *Combustion and Flame*, J. Ströhle, and T. Myhrvold, "Reduction of a Detailed Reaction Mechanism for Hydrogen Combustion under Gas Turbine Conditions," vol. 144, pp. 545–557, 2006, Copyright (2006), with permission from Elsevier

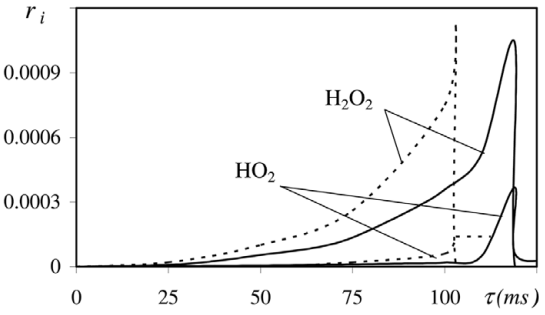

Figure 2.14 Variation of mole fractions of species H_2O_2, HO_2 in the ignition zone of the hydrogen + air mixture versus time at T_0 = 900 K; p = 17 atm, $\alpha_{ox} = 2.0$; (—) – computations performed with application of the authors' software package; (—) – [92]. Reprinted from *Combustion and Flame*, J. Ströhle, and T. Myhrvold, "Reduction of a Detailed Reaction Mechanism for Hydrogen Combustion under Gas Turbine Conditions," vol. 144, pp. 545–557, 2006, Copyright (2006), with permission from Elsevier

– Active radicals O, H, OH, if contained in a notable amount, provoke the occurrence of chain reactions, which results, in fact, in the instant hydrogen burnout.
– Species HO_2, H_2O_2 tie up these radicals to facilitate the inhibition of combustion but, at the increase in temperature, get easily decomposed.

Thus, at T_0 = 1300 K, species HO_2, H_2O_2, though are readily formed, aredecomposed at once, which is why the growth of O, H, OH occurs with subsequent heat explosion (Figures 2.12; 2.13). However, at T_0 = 900 K, species HO_2, H_2O_2 neutralize these radicals and, hence, whilst temperature in the reactor does not rise to a certain level, the concentration of radicals O, H, OH remains very low ($r_i < 10^{-8}$) and combustion fails to start (Figure 2.14).

Downloaded from https://www.cambridge.org/core. Nottingham Trent University, on 17 Aug 2019 at 01:58:27, subject to the Cambridge Core terms of use, available at https://www.cambridge.org/core/terms. https://doi.org/10.1017/9781108581714.002

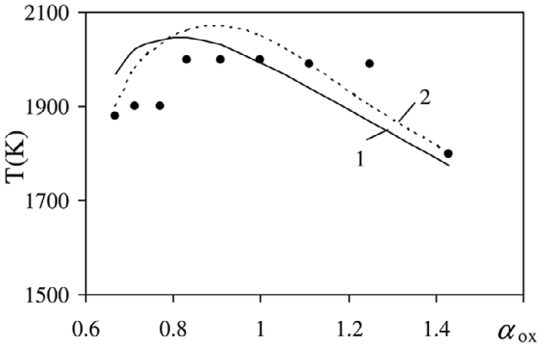

Figure 2.15 Change in steady-state temperature in PSR subject to α_{ox}
1 – computations made with application of the authors' software package; 2 – theoretical results [93]; ● – experimental data [93]. Reprinted from *Combustion and Flame*, P. Glarborg, J. A. Miller, and R. J. Kee, "Kinetic Modeling and Sensitivity Analysis of Nitrogen Oxide Formation in Well-Stirred Reactors," vol. 65, pp. 177–202, 1986, Copyright (1986), with permission from Elsevier

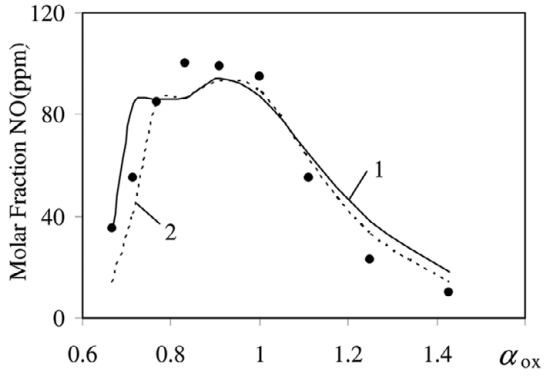

Figure 2.16 Variation in steady-state NO concentration in PSR subject to α_{ox}
1- computations performed with the help of the authors' software package; 2 – theoretical results [93]; ● – experimental data [93]. Reprinted from *Combustion and Flame*, P. Glarborg, J. A. Miller, and R. J. Kee, "Kinetic Modeling and Sensitivity Analysis of Nitrogen Oxide Formation in Well-Stirred Reactors," vol 65, pp. 177–202, 1986, Copyright (1986), with permission from Elsevier

The feature of the reaction mechanism given in Table 2.7 consists in that the reactions 9 and 15 (Troe reactions) are notable therein.

In the case of the PSR model, the results have been compared with those given in [93] wherein the methane + air mixture was analyzed with due allowance for the formation of nitrogen-containing compounds. The mechanism developed in [93] included 213 reactions. In the comparison, in fact, the same mechanism with extraction of some insignificant hydrocarbon reactions and with replacement of some rate constants was used, involving nitrogen species by similar rate constants from the database [26], which

Downloaded from https://www.cambridge.org/core. Nottingham Trent University, on 17 Aug 2019 at 01:58:27, subject to the Cambridge Core terms of use, available at https://www.cambridge.org/core/terms. https://doi.org/10.1017/9781108581714.002

brought about the mechanism including 204 reactions. The comparison was performed under the following conditions: $\alpha_{ox} = 0.6 \ldots 1.5$; $p = 1\,\text{atm}$; $T^{+} = 464\,\text{K}$; $\tau_p = 2ms$. The results are shown in Figures 2.15 and 2.16.

It is obvious that there are some discrepancies between computations made and the data borrowed from [93], which can be explained by both aforesaid differences in the reaction mechanisms and application of different databases of thermodynamic properties of individual species.

Downloaded from https://www.cambridge.org/core. Nottingham Trent University, on 17 Aug 2019 at 01:58:27, subject to the Cambridge Core terms of use, available at https://www.cambridge.org/core/terms. https://doi.org/10.1017/9781108581714.002

3 Software Tools for the Support of Calculation of Combustion and Reacting Flows

3.1 Review of Features of Software Tools

3.1.1 Problems of Simulation and Relevance of Software Tools Development

Modern kinetic mechanisms are intricate and can comprise tens of substances and hundreds of reactions [46, 95, 96]. For example, paper [97] deals with low-temperature decomposition of hydrocarbons to analyze the combustion mechanism totaling 340 substances and 3400 reactions. The authors of [98] exploited the combustion mechanism including 120 substances and 721 reactions for simulation of *n*-decane ignition. In the calculation of the oxidation of hydrocarbons described in [99], a mechanism comprising 71 substances and 417 reactions was analyzed.

Equations of chemical kinetics describing such transformations are stiff and cumbersome. For example, the reacting system analyzed in [100] is described by 88 ordinary differential equations. The left-hand side of each of these equations includes, on average, 24 nonlinear summands; therefore, programming of equations solving requires a significant amount of time. Besides, at even minor changes in the reaction mechanism, it is necessary to correct the computer program, while the probability of program errors is extremely high. Therefore, to create the opportunity of calculations with application of complex reaction mechanisms, as far back as the 1980s, development of invariant computer programs has been initiated [101, 102]. These computer programs along with models of reacting systems in application to idealized reactors composed the "cores" of invariant software packages.

However, in time, and with the accumulation of experience, various support software units are added to these cores to allow

- evaluation of the influence of properties of substances and reactions on characteristics of reacting systems
- control over adequacy and increase in validity of calculation results
- simplification of formation and optimization of reaction mechanisms
- evaluation of the efficiency of calculation schemes

Such support units facilitate the detection of most important stages of kinetic mechanisms, the accurate interpretation of reacting medium characteristics, a more reliable calculation of rate constants, integration scheme selection, determination of the degree of the shift from chemical equilibrium, etc. Experience has shown that

Downloaded from https://www.cambridge.org/core. Nottingham Trent University, on 17 Aug 2019 at 02:05:11, subject to the Cambridge Core terms of use, available at https://www.cambridge.org/core/terms. https://doi.org/10.1017/9781108581714.003

application of similar software tools significantly raises the efficiency of mathematical simulation of combustion and pyrolysis [2, 99, 103] and increases the quality of numerical analyses. Therefore, the development of traditional and new software tools as well as embedding them in complex invariant computer programs of high-temperature process calculation is an urgent problem.

Known invariant software packages based on reactor schemes such as CHEMKIN [5; 102] and KINTECUS [30] already contained some software tools, but as new versions were developed, extra software blocks were built in these systems.

The CHEMKIN Collection is composed of long-standing developments and generalized methods and algorithms used for the calculation of chemical reacting systems; the first version of the collection was brought forward in 1980. This first version was formed as the invariant one with respect to reacting medium. Reaction mechanisms used rate constants written in Arrhenius form while the chemical mechanisms were kept in a database of chemical reactions. Both reversible and nonreversible reactions were written in symbolic form. Separate archives incorporated the database of substances of structure identical to that of thermodynamic and thermophysical properties of the type: BURCAT [17] , THERMO [16], and MARINOV [27]. Chemical kinetics equations were used in a traditional form. The algorithm of their solution used the set of Adam's methods [2, 104] or Gear's methods with application of the Jacobian [105].

The next versions (CHEMKIN II and CHEMKIN III) expanded the potential of this package, particularly as follows:

- Tools for the description of pressure-dependent reactions (Troe reactions, item 1.3, [106]) and reactions in the Landau–Teller form for vibration energy transfer were added.
- Possibilities were provided for indication of more than one expression of the rate of chemical reaction and for explicit computation of the rate of the reverse direction of reversible chemical reaction in Arrhenius form.
- The applicability of the CHEMKIN Collection was notably expanded by incorporating global reaction kinetics; new options allowed the specification of the orders of reactions for every substance and the adoption of fractional stoichiometric coefficients.

The package is built around the GAS_PHASE_KINETICS computer program composed by flexible and high-capacity tools for incorporating complex chemical kinetics in the simulation of reactor processes. This package consists of two main components: a preprocessor and a library of calculation subprograms. The preprocessor reads off a symbolic description of the chemical reactions mechanisms set by the user. The mechanisms comprise the data on substances as well as descriptions of rate constants. The preprocessor output generates the arrays used by the library of subprograms. Models built around the GAS_PHASE_KINETICS are widely used for the development and optimization of combustion and chemical reacting systems and also comprise the possibility of the simulation of two-temperature plasma medium.

In addition, the CHEMKIN collection contains some "ready to use" invariant computer programs, for example:

Downloaded from https://www.cambridge.org/core. Nottingham Trent University, on 17 Aug 2019 at 02:05:11, subject to the Cambridge Core terms of use, available at https://www.cambridge.org/core/terms. https://doi.org/10.1017/9781108581714.003

- the AURORA program, intended for the simulation of transition processes in PSR, including the interaction of plasma with gas and surface reactions
- the CRESLAF program, designed for the simulation of chemically reacting laminar flows and boundary layers in cylindrical and flat channels
- the PASR program, designed for the calculation of mixing and chemical kinetic processes in partially mixed reacting media in reactors
- the PLUG program, designed for the simulation of processes in BR with allowance for gas-phase and surface reactions
- the PREMIX program, designed for the simulation of stationary laminar flame of premixed components
- the SURFTTERM program, which defines thermochemical, transport, and kinetic data for gas-phase and heterogeneous reacting systems

The CHEMKIN Collection also comprises some software tools, for example:

- the calculation of chemical equilibrium states
- the calculation of thermodynamic and thermophysical characteristics of reacting systems
- the calculation of sensitivity coefficients of reactions rate constants

KINTECUS package. Like the CHEMKIN package, KINTECUS [30] is the invariant one and includes some "ready to use" programs as well as software tools. The package is oriented to development of chemical mechanisms and calculations using the reactor approach. It can use thermodynamic databases of the THERMO and BURCAT types.

KINTECUS allows simulation of the processes in following reactors: isothermic; nonisothermal; adiabatic with constant volume; adiabatic at constant pressure (with variable volume); and processes with preset variation of volume (simulation of the reciprocating engine stroke), temperature, concentration of substances, etc. Data for calculations are stored in three archives: electronic table of reactions, electronic table of substances, and electronic table of parameters. Besides, KINTECUS can simultaneously uses several thermodynamic databases of the CHEMKIN type and allows the use of supplementary substances from adjacent thermodynamic databases. The algorithm for the integration of chemical kinetics equations in KINTECUS calculates Jacobian analytically. This is very useful for the simulation of complex kinetic mechanisms since usually applied finite difference methods can cause errors of zeroing or overflow. The package can use fractional coefficients for substances, which is necessary, for example, at the simulation of consequent decomposition of complex hydrocarbons [25, 27]. Several heterogeneous reactions can also be simulated wherein gaseous substances can be included in the condensed phase, per contra. This possibility allows simulating the combustion in gas–liquid systems [8, 101].

The package comprises some set of software blocks including such that allow its sufficiently wide application: the possibility to select reaction rate constants, initial concentrations, Lindemann and Troe parameters in pressure-dependent rate constants [24]; third-body efficiencies [28], initial temperature, residence time, energy of activation, and many other parameters describing the reacting system.

Downloaded from https://www.cambridge.org/core. Nottingham Trent University, on 17 Aug 2019 at 02:05:11, subject to the Cambridge Core terms of use, available at https://www.cambridge.org/core/terms. https://doi.org/10.1017/9781108581714.003

The package has the following features:

- It helps perform the uncertainty analysis to calculate real-life averaged behaviors with confidence bands/standard deviations of chemical system given Gaussian/Poisson deviations
- The package allows sensitivity analysis of chemical composition and temperature on the basis of both global and local normalized sensitivity coefficients. These sensitivity coefficients are used in the procedure of reaction mechanism reduction to identify which reactions are the main "sources and sinks" of substances (i.e., they require precise rate constants) and which can have notably approximate values of such constants;
- It incorporates the software tool, ATROPOS, allowing the reduction of complex reaction mechanisms to a reasonable set of essential substances and reactions without significant loss in the accuracy of the simulation.
- The package includes an "analyzer" for automatic control over the balance of chemical elements and charge. This procedure significantly increases the rate of detection of errors in the reaction mechanism writing, particularly when this mechanism has significant dimension.
- It ncludes the set of procedures for the calculation of eigenvalues and eigenvectors of Jacobian, which in principle allows one ot analyze the combustion process stability both for simple and complex reacting systems.

Theoretical elaborations of combustion problems were shown to frequently use software tools in both chemical system-oriented computer codes and invariant software. These frequently used tools include procedures of the exchange of data on substances between databases [107, 108], methods of sensitivity analysis [109, 110, 111], the application of eigenvalues [112, 113], and reaction mechanism reduction algorithms [114, 115, 116]. Some of them are described in brief in the following subsections.

3.1.2 Databases of Thermodynamic Properties of Individual Substances

Invariant programs and program packages for the calculation of combustion, as a rule, incorporate their own databases of individual substances. These databases include molecular mass μ, Lennard–Jones potential parameters σ, ε/κ, and dependencies of enthalpy and entropy on temperature $H = f(T)$ and $S_o = f(T)$ in polynomial form. Usually, these data are borrowed from universal databases: TTR [13], IVTANTHERMO [18], and BURCAT [17], or specialized databases such as [16, 27]. These databases undergo continuous correction such as obtaining data on new substances and updating data on existing ones

For example, [117] displays the results obtained with the help of one and the same computer code but at application of various databases of substances. Figure 3.1 shows the variations in concentrations of OH and NH in O-N-H-Ar in the reacting medium during its combustion in the Butch reactor. Calculations have been performed in terms of the CHEMKIN program with an alternate application of different databases [102, 118, 119]. It is obvious that variation of OH concentration is not practically affected by the type of database but the latter brings about a notable influence on NH radical concentration.

Downloaded from https://www.cambridge.org/core. Nottingham Trent University, on 17 Aug 2019 at 02:05:11, subject to the Cambridge Core terms of use, available at https://www.cambridge.org/core/terms. https://doi.org/10.1017/9781108581714.003

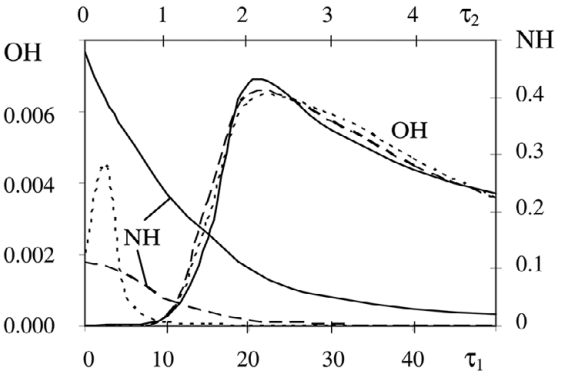

Figure 3.1 Variation of concentrations of substances OH and NH in reacting medium (O-N-H-Ar) at application of different databases: (—), Chemkin, 1980; (- -), UCID-17833; (– –), JANAF, 1985; OH, (mole fractions) = $f(\tau_1)$, NH (ppm) = $f(\tau_2)$, τ_1 and τ_2 in ms. Reprinted from *Combustion and Flame* R. J. Martin and N. J. Brown, "The Importance of Thermodynamics to the Modeling of Nitrogen Combustion Chemistry" vol 78, pp. 365–376, 1989, Copyright (1989), with permission from Elsevier

A case in point in this respect is the TTR database that used a tabulated handbook [120] and the IVTANTHERMO database based on handbooks [15; 121]. Comparison of the content of these databases reveals the "evolution" of data on substances and accidental errors (Section 3.2).

Paper [122] is dedicated specially to the search of errors in the databases brings in the notion "quality of thermodynamic data," which means the errors in the calculation of thermodynamic functions and values of thermochemical properties. These errors can deeply influence the results of simulation of processes accompanied by physical and chemical transforms; therefore, the analysis of data quality and the search for erroneous values are considered urgent measures. The quality of information in databases can be significantly improved if a computer-aided control procedure is used built around some set of rules presented by the authors.

A comparison of thermodynamic data stored in two databases is cited as an example of data quality evaluation. One of them is called a database of comparison while another one is referred to as a database under analysis. The latter was one of the earliest versions of HTU database [107]. This database was collected from different sources and was not coordinated in terms of the basic laws of thermodynamics. The IVTANTHERMO database [18] was considered the database of comparison.

In their analysis, the authors [122] compared the values of the following thermodynamic characteristics:

- $\Delta H_f^0(298.15)$ – standard enthalpy of formation of a compound from the elements
- $C_p^0(298.15)$ – heat capacity at constant pressure at standard conditions
- $S^0(298.15)$ – entropy at standard conditions
- $\Phi^0(T)$ – reduced Gibbs energy at $T = 1000$ K

Downloaded from https://www.cambridge.org/core. Nottingham Trent University, on 17 Aug 2019 at 02:05:11, subject to the Cambridge Core terms of use, available at https://www.cambridge.org/core/terms. https://doi.org/10.1017/9781108581714.003

The difference in thermodynamic properties is rather great for many substances. For example, the difference in enthalpy of formation exceeds 100 kJ/mole for 40 substances. For other properties, the difference is greater than 20 J/(mole K): in specific heat, for 33 substances; in entropy, for 65 substances; in Gibbs energy, for 66 substances.

The results of the performed analysis made authors reveal errors of two types: random and object-caused errors. Random errors are caused by misprints or errors in data sources, misleading use of published data, or errors in data incorporated into database. Object-caused errors feature different origins; therefore, they could be hardly classified. Nevertheless, these errors may include the following:

- the application of obsolete data at availability of new data
- the application of unreliable data evaluation methods or those of evaluation with the help of obsolete data
- the application of the results of only one experimental study, which is poorly correlated with more reliable data for similar substances
- the application of oversimplified assumption $C_p(T) = const$ in a broad range of temperatures

The cited examples illustrate that the application of erroneous and unreliable data could bring about grave errors in thermodynamic calculations. In addition, it follows Section 1.2 that the data on properties of substances in universal databases [13, 17, 18] is presented in different units, thermodynamic scales and polynomial forms.

To solve any applied problem, it is frequently necessary to engage data on substances from different databases in the analysis. For example, papers [100, 123] wherein a complex medium is simulated – i.e., "Coal + Air + $CaCO_3$" – represent the reacting system composed first by 46 substances taken from the TTR database [13]. Then, it proved necessary to increase the number of reactions and substances. These substances (absent from the TTR database) were kept in the databases [18; 26], but to include them in the computer program's working database, it proved necessary to re-approximate the enthalpy and entropy as a functions of temperature in order to evaluate the errors and to manually enter the array of numerical data. This is why the problem of developing the tool for online comparison of properties and conversions of polynomial forms for their inclusion in the computer program's working database is quite an important one.

3.1.3 Methods of Analysis and Calculation of Sensitivity Coefficients

An important tool used in simulation of combustion processes is the analysis of reacting medium temperature and composition sensitivity relative to the chemical reaction rate constants [2]. These constants are known to be represented as approximating formulas derived from experiments or fundamental calculations. They can notably depend on temperature and sometimes on pressure as well. Their values are frequently defined with significant errors of up to the second to third order [3, 25, 35]. The complexity of many proposed mechanisms of chemical reactions causes bottlenecks in the evaluation of the way an ambiguity in chemical reaction rate constants affects the calculated values of concentrations and temperatures. From there, the following problems spring up:

Downloaded from https://www.cambridge.org/core. Nottingham Trent University, on 17 Aug 2019 at 02:05:11, subject to the Cambridge Core terms of use, available at https://www.cambridge.org/core/terms. https://doi.org/10.1017/9781108581714.003

- influence of the rate constant variation on fundamental parameters of combustion process
- determination of rates for which notable errors are permitted in the rate constants
- revealing the reactions that require determination of constant k_s with minimum error

These problems are solved with the help of sensitivity analysis. The development of mechanisms of such analysis has been initiated decades ago, and the results are published in numerous papers [2, 93, 110, 124, 125, 126]. As of today, two classes of sensitivity analysis methods have been developed: global and local.

Global or stochastic methods [125, 127, 128] allow for the influence of parameters varying simultaneously in some range of values. The apparent sensitivity analysis method for this class consists in repeated integration of ordinary differential equations with different values of parameters. This allows one to define the region of the solution in some preset space of parameter variation. However, this method becomes cumbersome with the increase in independent variables. Global methods are used to calculate the averaged sensitivity characteristics that perform quantitative determination of major deviations of parameters. However, these methods are rarely used thus far in chemical kinetics and the simulation of combustion processes due to the complexity of chemical reaction mechanisms now used.

Local or deterministic methods provide the data on how ambiguity in one parameter – for example, k_s – influences the calculated values of any one of the dependent variables – for example, r_i, T. Local sensitivity analysis consists in the calculation and interpretation of sensitivity coefficients. There are local methods [111, 129] of so-called direct solution wherein proper sensitivity coefficients are considered to be dynamic variables, and, collaterally with the solution of the main system of equations, differential equations describing the variation of these coefficients are integrated. Better known are methods [96, 103], intended for calculations of the first-order sensitivity coefficients with the application of the finite-difference approach. They consist in the independent variation of every parameter k_s and in the calculation of the deviation of any characteristic of combustion caused by this variation.

One of the most known among these methods is based on the calculation of PSR characteristics with the determination of sensitivity coefficients – that is, $\partial r_i/\partial k_s, \partial T/\partial k_s$ type derivatives at the reactor's steady-state condition for every reaction of the reactions mechanism. Usually, these coefficients are defined numerically with a preliminary calculation of two stationary states with different values of k_s.

This approach is used in both traditional and modern developments. In particular, sensitivity coefficients in the CHEMKIN Collection [2] are defined for the model of reactor including the following relations:

$$\frac{dY_i}{d\tau} = \frac{1}{\tau_p}\left(Y_i - Y_i^+\right) + \frac{\dot{\omega}_i \mu_i}{\rho} \equiv f_{Yi}, \quad i = 1, \ldots, n_b, \tag{3.1}$$

$$c_p \frac{dT}{d\tau} = \frac{1}{\tau_p}\sum_i Y_i^+\left(h_i^+ - h_i\right) - \sum_i \frac{h_i \dot{\omega}_i \mu_i}{\rho} - \frac{Q}{\rho V} \equiv f_T, \tag{3.2}$$

Downloaded from https://www.cambridge.org/core. Nottingham Trent University, on 17 Aug 2019 at 02:05:11, subject to the Cambridge Core terms of use, available at https://www.cambridge.org/core/terms. https://doi.org/10.1017/9781108581714.003

where Y_i, Y_i^+ are mass fractions of the i-th substance in the reactor and at its inlet, respectively; $\dot{\omega}_i$ is the rate of formation of the i-th substance in chemical reactions; μ_i is the molecular mass of the i-th substance; ρ, c_p are the density and specific heat capacity of the mixture; and n_b is the number of substances in reacting medium.

Equations (3.1) and (3.2) with some initial conditions are integrated until the stationary state described by the formulas,

$$f_{Yi} = 0, \quad f_T = 0, \tag{3.3}$$

which are the functions of each rate constant.

In particular, for the s-th reaction, allowing for $Y_i = Y_i(k_s)$ and $T = T(k_s)$, one can write

$$f_{Yi}(Y_i(k_s), T(k_s), k_s) = 0, \quad f_T(Y_i(k_s), T(k_s), k_s) = 0. \tag{3.4}$$

Differentiating Equations (3.4) over k_s, one get

$$\sum_i \frac{\partial f_{Yi}}{\partial Y_i}\frac{\partial Y_i}{\partial k_s} + \frac{\partial f_{Yi}}{\partial T}\frac{\partial T}{\partial k_s} = -\frac{\partial f_{Yi}}{\partial k_s} \quad , \quad \sum_i \frac{\partial f_T}{\partial Y_i}\frac{\partial Y_i}{\partial k_s} + \frac{\partial f_T}{\partial T}\frac{\partial T}{\partial k_s} = -\frac{\partial f_T}{\partial k_s} \tag{3.5}$$

After numerical determination of derivatives,

$$\frac{\partial f_{Yi}}{\partial Y_i}, \frac{\partial f_{Yi}}{\partial T}, \frac{\partial f_{Yi}}{\partial k_s}, \frac{\partial f_T}{\partial Y_i}, \frac{\partial f_T}{\partial T}, \tag{3.6}$$

Equations (3.5) become the system of algebraic linear equations of the $(n_b + 1)$ order. At solving this system, sensitivity coefficients $\partial Y_i/\partial k_s, \partial T/\partial k_s$ are defined but only for a single s-th reaction. For example, if the chemical interaction mechanism includes 200 reactions, then, to define all sensitivity coefficients, it is necessary to solve System (3.5) 200 times with the preliminary numerical determination of derivatives (3.6), which requires a significant amount of calculations. Besides, for determination of these derivatives, it is required to preset the values of increments: $\Delta\gamma_i, \Delta T, \Delta k_s$. Selection of these increments makes a step intuitive to a considerable extent, and can hardly be algorithmized [30], particularly for invariant computer codes.

3.1.4 Application of Eigenvalues to Combustion Problems and Procedure of Their Calculation

For the solution of a series of problems related to the mathematical simulation of combustion, "eigenvalues and eigenvectors" of chemical kinetics equations are also used. In connection with the complexity of calculations, this tool is used mainly for simple (model) reacting systems [24, 90, 91]. In addition, while solving some problems, significant difficulties sometimes arise in calculating eigenvalues [70]. However, up to now, in connection with evident efficiency of the tool under analysis, not a few publications came to light wherein eigenvalues were used for the solution of actual problems of combustion. Basically, they are used for the following:

Downloaded from https://www.cambridge.org/core. Nottingham Trent University, on 17 Aug 2019 at 02:05:11, subject to the Cambridge Core terms of use, available at https://www.cambridge.org/core/terms. https://doi.org/10.1017/9781108581714.003

– calculation of chemical kinetics equations stiffness [2, 81, 85]
– reduction of reaction mechanisms [90, 130]
– determination of combustion instability regions [91]

The role of eigenvalues in the problems of ODE stiffness calculations (including the chemical kinetics equations) and in selection of numerical schemes has been shown in Section 2.3, while Subsection 3.1.5 will display the application of eigenvalues for the reduction of reaction mechanisms. Let us consider, as an example, the application of eigenvalues to problems of determination of combustion instability regions.

Chemical Oscillation: Brusselator

An example of relation between specific modes of chemical processes and eigenvalues is given in monograph [131] describing the set of reactions (bryusselyator):

$$\mathrm{A} \xrightarrow{k_1} \mathrm{X}, \quad \mathrm{B} + \mathrm{X} \xrightarrow{k_2} \mathrm{Y} + \mathrm{D}, \quad 2\mathrm{X} + \mathrm{Y} \xrightarrow{k_3} 3\mathrm{X}, \quad \mathrm{X} \xrightarrow{k_4} \mathrm{E}, \tag{3.7}$$

wherein it is assumed that reactants A and B exist in tangible excess while their concentrations may be considered invariable, and substances D and E are not involved in any chemical reactions; (k_1, k_2, k_3, k_4 are rate constants).

Appropriate kinetic equations can be written as follows (refer to Section 1.3):

$$\frac{dC_\mathrm{X}}{dt} = k_1 C_\mathrm{A} - k_2 C_\mathrm{B} C_\mathrm{X} + k_3 C_\mathrm{X}^2 C_\mathrm{Y} - k_4 C_\mathrm{X}, \tag{3.8}$$

$$\frac{dC_\mathrm{Y}}{dt} = k_2 C_\mathrm{B} C_\mathrm{X} - k_3 C_\mathrm{X}^2 C_\mathrm{Y}, \tag{3.9}$$

where C_X, C_Y, C_A, C_B are the concentration of substances X, Y, A, B; t is time. These equations can be reduced to dimensionless form with the minimum number of control parameters. For this, it is necessary now move to new variables, $x = (k_3/k_4)^{1/2} C_\mathrm{X}$, $y = (k_3/k_4)^{1/2} C_\mathrm{Y}$.

Then Equations (3.8) and (3.9) will take the form

$$\frac{dx}{d\tau} = \dot{x} = a - (b+1)x + x^2 y, \tag{3.10}$$

$$\frac{dy}{d\tau} = \dot{y} = bx - x^2 y, \tag{3.11}$$

where $a = \left(k_1^2 k_3 / k_4^3\right)^{1/2} C_\mathrm{A}$, $b = (k_2/k_4) C_\mathrm{B}$.

It should be pointed out that variables x, y and parameters a, b can take on only positive values. As a result, a dynamic second-order system is obtained with two control parameters a and b.

At zeroing the derivatives $\frac{dx}{d\tau}$, $\frac{dy}{d\tau}$, it is easy to define the state of equilibrium:

$$x_p = a; \quad y_p = {}^{b}\!/_{a}, \tag{3.12}$$

which corresponds to stationary proceeding of chemical reaction, when concentrations of reacting substances are invariable. However, conditions of instability can be defined

Downloaded from https://www.cambridge.org/core. Nottingham Trent University, on 17 Aug 2019 at 02:05:11, subject to the Cambridge Core terms of use, available at https://www.cambridge.org/core/terms. https://doi.org/10.1017/9781108581714.003

for the bryusselyator – i.e., the conditions of self-excitation of auto-oscillation. For this, minor deviations from the state of equilibrium are set in the following form:

$$x = a + \xi, \quad y = {}^{b}/_{a} + \eta, \tag{3.13}$$

and System (3.10, 3.11) is linearized. Then, for example, one obtains from Equation (3.10):

$$\begin{aligned} \frac{d(a+\xi)}{d\tau} = \frac{d\xi}{d\tau} &= a - (b+1)(a+\xi) + (a+\xi)^2\left({}^{b}/_{a} + \eta\right) \\ &= -b\xi - \xi + 2b\xi + \frac{b}{a}\xi^2 + a^2\eta^2 + 2a\eta\xi + \xi^2\eta. \end{aligned} \tag{3.14}$$

At linearization, summands may be neglected wherein variables ξ, η feature the second order. Similarly, Equation (3.11) is transformed. As a result, we obtain the system of linear ordinary differential equations.

$$\frac{d\xi}{d\tau} = (b-1)\xi + a^2\eta \tag{3.15}$$

$$\frac{d\eta}{d\tau} = -b\xi - a^2\eta. \tag{3.16}$$

Then, in compliance with [132] and assuming ξ, η is proportional to $exp\,(\lambda t)$, a characteristic equation is formed:

$$(\lambda - b + 1)\left(\lambda + a^2\right) = -a^2 b. \tag{3.17}$$

Following eigenvalues are the roots of (3.17):

$$\lambda = -\frac{a^2 - b + 1}{2} \pm \sqrt{\frac{(a^2 - b + 1)^2}{4} - a^2 b}. \tag{3.18}$$

At $b_c = a^2 + 1$, an imaginary solution results: $\lambda = \pm ia\sqrt{b_c}$. Then, in compliance with the theory of linear differential equations with constant coefficients, the solution of the initial Equations (3.8) and (3.9) will be cyclic (auto-oscillating).

Auto-Oscillations in a Flow Reactor with Two-Step Sequential Reaction

Paper [91] describes mathematical simulation of dynamic behavior of PSR wherein proceeds two-stage sequential reaction $A \xrightarrow{k_1} B \xrightarrow{k_2} C$ (assuming the excess of initial substance). Both stages of combustion are exothermic. The kinetic model is reduced to the system of three ordinary differential equations in dimensionless variables with the use of the Damkeller (Da) number, which characterizes the substance residence time in the reactor, and the Semenov (Se) number, which describes the possibility of thermal explosion [8]. The region of auto-oscillations was revealed in the Da–Se parametric space (limit cycles). Calculations have shown that the auto-oscillation region is closed and features a lenticular shape. Results given in the paper [91] show that with the increase in criterion Se, the oscillation period, as well as maximum amplitude of

Downloaded from https://www.cambridge.org/core. Nottingham Trent University, on 17 Aug 2019 at 02:05:11, subject to the Cambridge Core terms of use, available at https://www.cambridge.org/core/terms. https://doi.org/10.1017/9781108581714.003

temperature, decreases. With the increase in criterion Da, the auto-oscillation period increases, and the maximum amplitude of temperature decreases.

Brief Data on the Procedure of Eigenvalue Calculations

Obtaining eigenvalues is a complex problem that requires a great scope of calculations. For example, the inversion of the n_b –size matrix requires approximately $(n_b)^3$ arithmetic operations while the search of eigenvalues for this matrix demands about $(n_b)^4$ operations [70, 73]. Besides, the calculation of these magnitudes needs a joint application of some cumbersome algorithms [133, 134] with no confidence in a successful solution of the problem for arbitrary matrix. Let us bring brief data on procedures of eigenvalue calculations with the help of handbook [70].

Matrix **A**, sized to *N***N*, has eigenvector $\boldsymbol{x}$ and corresponding eigenvalue λ when the following relation obeyed:

$$\mathbf{A}\mathbf{x}_R = \lambda \mathbf{x}_R \quad \text{or} \quad \mathbf{x}_L \mathbf{A} = \lambda \mathbf{x}_L, \tag{3.19}$$

where $\mathbf{x}_R, \mathbf{x}_L$ are the right and eigenvectors, respectively.

The following equality is valid for eigenvalues:

$$\det |\mathbf{A} - \lambda \mathbf{I}| = 0, \tag{3.20}$$

where det is the matrix determinant and **1** is the unit matrix.

If one expands this expression, the polynomial relative to λ of *N* order will results, its roots making the eigenvalues. For the small matrix, these values are easily defined by the solution of algebraic equations [135], but for matrices of the fifth order and higher, methods of computational mathematics are used.

Eigenvalues of real asymmetric matrices may be either real or pairs of complex conjugate numbers. These are defined by matrix diagonalization – i.e., by application of some transforms during which matrix eigenvalues do not vary while matrix elements (apart from diagonal elements) are zeroed. Such transforms are called "similarity transformations" and are performed by the formula:

$$\mathbf{A} \rightarrow \mathbf{Z}^{-1}\mathbf{A}\mathbf{Z}, \tag{3.21}$$

where **Z** is the transforming matrix, while the main used algorithms differ by procedures of transforming matrix formation.

Real asymmetric matrices in a general case can be "diagonalized" to one element (λ, a real number) or to the system of small blocks (2∗2) arranged in diagonal, all other elements being zero. Each of these blocks corresponds to a complex conjugate pair of eigenvalues.

The main strategy of almost all modern eigenvalues and eigenvectors calculation methods consists in that matrix **A** is reduced to diagonal form by the chain of similarity conversions (rotations):

$$\mathrm{A} \rightarrow \mathrm{P}_1^{-1}\mathrm{A}\,\mathrm{P}_1 \rightarrow \mathrm{P}_2^{-1}\mathrm{P}_1^{-1}\mathrm{A}\,\mathrm{P}_1\mathrm{P}_2 \rightarrow \mathrm{P}_3^{-1}\mathrm{P}_2^{-1}\mathrm{P}_1^{-1}\mathrm{A}\,\mathrm{P}_1\mathrm{P}_2\mathrm{P}_3 \ \text{ etc.} \tag{3.22}$$

At such transforms of the initial matrix eigenvalues do not vary.

Downloaded from https://www.cambridge.org/core. Nottingham Trent University, on 17 Aug 2019 at 02:05:11, subject to the Cambridge Core terms of use, available at https://www.cambridge.org/core/terms. https://doi.org/10.1017/9781108581714.003

There are two different approaches to implementing this strategy. The first approach consists in construction of individual matrices $\mathbf{P}_i$ as explicit "elementary" transformers designed for special problems, for example, for zeroing of a particular off-diagonal element (Jacobian transformation) or a total column or total row (Householder transformation). In a general case, the finite chain of similar transforms cannot diagonalize the matrix, and, therefore, after a finite number of rotations, it is necessary to complete the analysis with the help of the other algorithms.

The other approach exploits the methods of *factorization,* when matrix **A** *can be decomposed* **to** the product of left-hand and right-hand factors $\mathbf{F}_R$ and $\mathbf{F}_L$, respectively. Then,

$$\mathbf{A} = \mathbf{F}_L\mathbf{F}_R, \tag{3.23}$$

or, equivalently, $\mathbf{F}_L^{-1}\mathbf{A} = \mathbf{F}_R$. If these factors are multiplied in reverse order and Formula (3.23) is used, we get $\mathbf{F}_R\mathbf{F}_L = \mathbf{F}_L^{-1}\mathbf{A}\mathbf{F}_L$, which is immediately recognized as the matrix A similarity transform with transforming matrix $\mathbf{F}_L$. Frequently, both approaches work well in combination with each other, and modern methods exploit this possibility. The main used algorithms are described in detail in papers [70, 133, 134]. Let us present their brief characteristics.

Jacobian transforms. This method consists of a chain of orthogonal matrix similarity transforms. Every transform (*Jacobian rotation*) is a plane turn aiming at zeroing one of the off-diagonal elements of the matrix. Serial transforms do not conserve preset zero elements but, nevertheless, off-diagonal elements become smaller and smaller unless the matrix renders a diagonal one to the accuracy of computer zero.

The *Givens reduction* is a modification of Jacobian method. Rather than reducing the matrix to diagonal form continuously, this process terminates when the matrix is tridiagonal one. This allows the procedure termination per finite steps, unlike the Jacobian method, which requires an indefinite number of iterations for convergence purposes.

Householder method. This method is the as stable as the Givens reduction but requires two times fewer operations. The basic transformer is the Householder matrix **P** of the following form:

$$\mathbf{P} = \mathbf{I} - \mathbf{w}\mathbf{w}^{\mathrm{T}} \tag{3.24}$$

where **w** is a real vector such that $|\mathbf{w}|^2 = 1$.

When a tridiagonal matrix or Hessenberg matrix obtained (Figure. 3.2), one of the following procedures is used to get eigenvalues.

Direct calculation of characteristic polynomial roots (3.20). This problem for tridiagonal matrix can be calculated with the help of recursion procedure [136].

Algorithms QR and QL. The main idea of the QR algorithm consists in that any real matrix can be presented in the following form: **A = QR**, where **Q** is an orthogonal matrix, while **R** is an upper triangular matrix. However, if these algorithms are applied directly to initial matrix **A,** then a considerable number of arithmetic operations will be required to get values of λ. In the case of the tridiagonal matrix or Hessenberg form matrix, this number decreases significantly, which renders algorithms QR and QL highly efficient.

Downloaded from https://www.cambridge.org/core. Nottingham Trent University, on 17 Aug 2019 at 02:05:11, subject to the Cambridge Core terms of use, available at https://www.cambridge.org/core/terms. https://doi.org/10.1017/9781108581714.003

$$\begin{vmatrix} + & + & + & + & + & + \\ + & + & + & + & + & + \\ 0 & + & + & + & + & + \\ 0 & 0 & + & + & + & + \\ 0 & 0 & 0 & + & + & + \\ 0 & 0 & 0 & 0 & + & + \end{vmatrix}$$

Figure 3.2 Matrix structure of Hessenberg form.

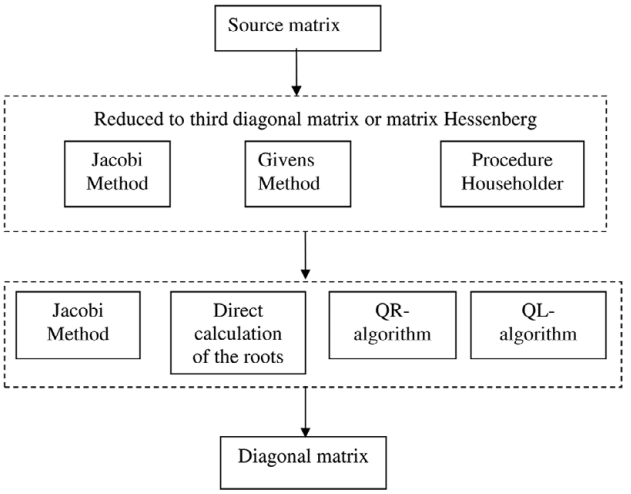

Figure 3.3 Scheme of eigenvalues calculations.

Figure 3.3 shows possible sequences of the application of different algorithms at the definition of eigenvalues.

3.1.5 Methods of Reduction of Kinetic Mechanisms

The main concept of complex kinetic mechanism reduction rests on the quite justified assumption that many reactions and substances can be withdrawn from the complete mechanism without damaging the results of calculations in the region of interest for a researcher of the variation of parameters of the reacting mixture. Then, after execution of the procedure of reduction, possibilities of simulation of multidimensional reacting flows increase significantly. Besides, the main schemes of reactants (or propellant components) conversion into combustion products are revealed. The term "reduction" can hereinafter be interpreted as an *automatic* reduction of reaction mechanisms unlike an *expert* one [99]. By now, many methods have been developed for mechanism

Downloaded from https://www.cambridge.org/core. Nottingham Trent University, on 17 Aug 2019 at 02:05:11, subject to the Cambridge Core terms of use, available at https://www.cambridge.org/core/terms. https://doi.org/10.1017/9781108581714.003

reduction, all of them being practically oriented to some reactor scheme of combustion (BR, PSR, or PFR).

The diversity of reduction methods should be pointed out. Reduction methods differ not only in algorithms but in the formulation of the problem as well. This feature results from the fact that the problem of reduction is a "reverse" one and it is practically impossible to form a single optimum reduced mechanism [97]. Because of the diversity of the proposed methods, their classification has not been established yet; in addition, reduction algorithms usually include several methods of their reduction. We can propose to distinguish the three following groups of existing methods:

- methods of reaction rates analysis [95, 97, 99, 137]
- methods using eigenvalues [90, 112, 130]
- methods operating with preformed tabulated data of equilibrium calculations [114, 138, 139, 140]

Methods of reaction rate analysis are included in many popular procedures of mechanism reduction. First, the set of "target" substances (t-substances) is preliminary established and might not be removed from the reaction mechanism, since t-substances are used for the evaluation of the errors due to mechanism reduction. In contrast to "target," substances, "nontarget" species might be removed from mechanism. Let's call these substances "sounded" (examined). Also, reduction thresholds for substances (ζ_s) and for reactions (ζ_R) should be specified. If the error is due to the elimination of certain species or if the reaction is higher than the prescribed threshold, the sounded species or reactions cannot be removed.

Then velocities of substance concentration variation ($\dot{\omega}_i$) and elementary reaction rates (W_{ij}) are used to evaluate the influence of every sounded substance on the concentration of the t-substance. This evaluation can, for example, be executed by the formula:

$$\delta_{ti} = \left| \frac{r_t(C) - r_t(i)}{r_t(C)} \right| \leq \zeta_s \quad t \in (\text{target substances}), \tag{3.25}$$

where δ_{ti} is the relative deviation by the t-th substance because of elimination of specie i; and $r_t(C), r_t(i)$ are mole fractions of t-substances defined by the complete mechanism (C-mechanism) and by the mechanism excluding the i-substance, respectively.

If this influence is smaller than the preset threshold, then the i-th substance and the corresponding j-th reactions with their involvement (designated as $R_s(i)$) are removed out from the mechanism. However, this mechanism may still contain redundant reactions. Therefore, it is possible to analyze this mechanism to rule out such reactions with the help of the formula,

$$\delta_{tj} = \left| \frac{r_t(C) - r_t(j)}{r_t(C)} \right| \leq \zeta_R, \tag{3.26}$$

where δ_{tj} is the relative deviation by the t-th substance because of the elimination of the s-th reaction, and $r_t(s)$ is the mole fractions of t-substances defined by the mechanism with the excluded s-reaction.

Downloaded from https://www.cambridge.org/core. Nottingham Trent University, on 17 Aug 2019 at 02:05:11, subject to the Cambridge Core terms of use, available at https://www.cambridge.org/core/terms. https://doi.org/10.1017/9781108581714.003

A popular method of reduction is the DRG method (directed relation graph method) [141] exploiting the concept of "species coupling efficiency" between the t -substance and every i-th substance ($t \neq i$). This parameter is defined by the formula,

$$B_{ti} = \frac{\sum_s abs\{\nu_{ts}(W_s - W_{s+m_c})\}_i}{\sum_s abs\{\nu_{ts}(W_s - W_{s+m_c})\}} \qquad s = 1 \ldots m_c, \tag{3.27}$$

where the denominator is the sum of the absolute differences of all rates of forward and reverse chemical reactions involving the t-th substance while the numerator is the sum of the absolute differences of all rates of forward and reverse chemical reactions involving both the t-th and the i-th substance.

If magnitude B_{it} for every target substance is smaller than the preset threshold, then the i-th substance and all reactions $R_s(i)$ are excluded from the mechanism. The DRG method is developed into the DRGEP method (directed relation graph error propagation method [142]), described in the Section 3.5.

Methods using eigenvalues. Paper [90] develops a two-parametric algorithm of combustion process calculation for conditions of ignition and extinction of the reacting mixture. The algorithm uses the PSR scheme and includes a series of calculation options: sensitivity analysis, evaluation of solution stability, determination of critical points, reduction of reaction mechanisms, and calculation of stability criterion. At the mechanism reduction step, the authors [90] use the PCA method (principal component analysis method) based on the calculation and analysis of eigenvalues and eigenvectors or the sensitivity matrix (**S**). In compliance with the PCA method, at the highest eigenvalues of the product ($\mathbf{S}^{\mathrm{T}}\cdot\mathbf{S}$) considered are the most important eigenvectors ($\bar{V}$). Eigenvalues of larger modulo $\bar{V}$ indicate the important reactions.

The reaction is considered an important one if the eigenvector element value in the dominant eigenvalue is larger than a certain threshold – for example, ($\bar{V}_i \geq 0.2$).

The other method – the CSP method (computational singular perturbation method) [130] – uses the algebra of eigenvalues and vectors for the reduction of complex mechanisms of reactions. This reduction is performed in the framework of PSR scheme, the equation for which is presented in a general form:

$$\frac{d\bar{C}}{d\tau} = \bar{g}(< \bar{C} >), \tag{3.28}$$

where $\bar{C}$ is the vector of concentrations of substances in the reacting mixture and $\bar{g}(< \bar{C} >)$ is the right-hand side of chemical kinetics equations.

By differentiating Equations (3.28), one obtains

$$\frac{d\bar{g}}{dt} = \frac{\partial \bar{g}}{\partial \bar{C}}\frac{dY}{d\tau} = \bar{J}\,\bar{g}, \tag{3.29}$$

where $\bar{J}$ is the Jacobian for which it is required to define eigenvalues and eigenvectors.

This Jacobian can be decomposed into three matrices:

$$\overline{\overline{J}} = \left(\overline{\overline{A}}\right)^{-1}\overline{\overline{\Lambda}}\,\overline{\overline{A}}, \tag{3.30}$$

where $\overline{\overline{A}}$ is the matrix of eigenvectors and $\overline{\overline{\Lambda}}$ is the diagonal matrix of eigenvalues.

Downloaded from https://www.cambridge.org/core. Nottingham Trent University, on 17 Aug 2019 at 02:05:11, subject to the Cambridge Core terms of use, available at https://www.cambridge.org/core/terms. https://doi.org/10.1017/9781108581714.003

If the i-th eigenvalue (λ_i) is a large negative number, then the appropriate mode tends very quickly to zero, an, if only one substance is related with this mode, then this substance can be presented as the function of the other substances. Then one equation from the system (3.28) corresponding to this substance and all reactions involving it can be excluded from the mechanism. To determine the other substances of this type, there are special procedures based on the search and analysis of the fastest reactions. The algorithm proposed by the authors allows operating with complex eigenvalues. It is pointed out that at the decrease in residence time (τ_p), the number of such values increases. The method proposed by the authors was successfully tested for reacting systems "H_2 + air" and "CH_4 + air."

Methods operating with tabulated data of equilibrium calculations. Paper [138] proposes the ILDM method (intrinsic low dimensional manifolds), which uses the idea of a partial chemical equilibrium relative to substances – parameters. A homogeneous reacting system described by the following equations is considered:

$$\frac{\partial \phi_i}{\partial t} = W_i \quad i = 1, \ldots, n_b, \tag{3.31}$$

where W_i is the rate of variation of the concentration of the i-th substance, n_b is the quantity of reacting substances, $\phi_i = Y_i/M_i$ is the number of moles in unit of mass, Y_i is the mass fraction, and M_i is the molecular mass of i-th substance, respectively.

First, these equations are presented on the basis of the eigenvalues of matrix $\partial W(\phi^0)/\partial\phi$. Then, eigenvalues of Jacobian $\partial W(\phi^0)/\partial\phi$ are calculated by analogy with the CSP method. For these eigenvalues λ_i, relaxation times $\tau_i = 1/|\mathrm{Re}(\lambda_i)|$ are defined (where Re is the real part of λ_i). Substances in amount of n_u associated with the greatest values of τ_i (n_u = 1 ... 3) are defined as "control parameters," and their variation is described by Equations (3.31). The other substances in the amount of ($n_e = n_b - n_u$) are considered as existing in chemical equilibrium with "control parameters." Before the execution of calculations, a database is first formed (collector), which contains the following relations in tabulated form:

$$\phi_k = f(\phi_u), \tag{3.32}$$

where ϕ_k are the concentrations of substances in equilibrium with concentrations $\phi_u (u = 1, \ldots, n_u)$ of "control parameters."

To fill this collector, it is necessary to execute multiple chemical equilibrium calculations for all physically reasonable values of concentrations ϕ_u. In particular, the paper [114] gives univariate reduced scheme (n_u= 1) for the reacting system "H_2 + air." The system contains two elements, O and H, along with individual substances O_2, H_2, OH, H_2O, etc., corresponding to these elements. Nitrogen-contained substances are not allowed for, since molecular nitrogen is considered an inert substance. The number of H_2O (ϕ_{H_2O}) moles is used as the control parameter. The concentration of the other substances is defined by equations of their dissociation and by equations of conservation of chemical elements (see Subsection 1.3.1).

The aforementioned methods of reduction have been used for some reacting systems, in particular, "H_2 + O_2" [143], "H_2 + air" [144], "Heavy hydrocarbons + air" [33], "H_2S + air" [115], "CH_4 + air" [137], "Kerosene-type surrogate fuel + air" [99], etc.

Downloaded from https://www.cambridge.org/core. Nottingham Trent University, on 17 Aug 2019 at 02:05:11, subject to the Cambridge Core terms of use, available at https://www.cambridge.org/core/terms. https://doi.org/10.1017/9781108581714.003

Table 3.1 Polynomial form, computing origin (T_{rf} – reference temperature) and units of enthalpy in E- and R-databases

Data base	Type of data base	Enthalpy polynomial form	Number of formula	Reference temperature T_{rf}(K)	Units
IVTAN (IVT)	E	$H = a_0 + 10^4\left[\begin{array}{l}-2a_{-2}x^{-1} - a_{-1} + a_L x \\ +a_1x^2 + 2a_2x^3 + 3a_{3i}x^4\end{array}\right]$	(1.16)	298	$\frac{J}{gmol}$
BURCAT (BUR)	E	x = 0.0001T $\frac{H}{R_o T} = a_1 + \frac{a_2}{2}T + \frac{a_3}{3}T^2 + \frac{a_4}{4}T^3 + \frac{a_5}{5}T^4 + \frac{a_6}{T}$	(1.13)	298	$\frac{J}{kgmol}$
TTR	R	$H = A_I + \sum_{q=1}^{7} a_q x^q$ x = 0.001T	(1.7)	293	$\frac{cal}{gmol}$

3.2 Analysis of Thermodynamic Properties of Individual Substances

Thermodynamic properties of individual substances (Subsection 3.1.2) have a significant impact on the characteristics of combustion. Usually, at the simulation of combustion and reacting flows, these properties are represented by custom working databases using polynomials adopted from widespread databases like THERMO (BURCAT [17], LEEDs [26], CHEMKIN [5]), IVTANTERMO [18], and TTR [13]. Since polynomial forms of these databases differ (see Table 3.1), a certain tool of prompt comparison of properties and polynomial form conversion is required to incorporate them in the working database of a custom program. The authors of the monograph created this relatively simple tool (algorithm and CONVER computer code), which can be used for the analysis in solving following problems:

- expansion of the custom working database (we'll name it "R") by substances available in widespread databases
- comparison of thermodynamic properties in the custom database with higher-quality data of widespread databases (we'll name them "E")
- influence of the discrepancy in data on substances contained in different databases on the results of high-temperature process calculations

Here, one of the versions of such tools is described, and we'll assume that IVTANTERMO [18] and BURCAT [17] are E-databases while the TTR database [13] is an R-database.

3.2.1 Algorithm of Conversion of Polynomials of Thermodynamic Properties of Individual Substances

The proposed tool, CONVER code, is based on the algorithm of polynomial conversion that comprises the following block (steps):

B1. The following information is read off from the E-database according to the substance's chemical formula for all temperature subintervals (indices: *in* is the start of the subinterval, *f* is the end of the subinterval):

Downloaded from https://www.cambridge.org/core. Nottingham Trent University, on 17 Aug 2019 at 02:05:11, subject to the Cambridge Core terms of use, available at https://www.cambridge.org/core/terms. https://doi.org/10.1017/9781108581714.003

Table 3.2 Approximation coefficients for three temperature subintervals for calculation of thermodynamic properties of CO_2 (IVT)

T_{in}(K)	T_f(K)	a_0	a_L	a_{-2}	a_{-1}	a_1	a_2	a_3
298	1500	264.54	26.202	−0.00085	0.10473	255.82	−484.38	517.14
1500	6000	336.42	56.814	−0.03092	2.19535	21.096	−17.443	8.68598
6000	10,000	408.31	118.67	−0.4418	14.899	−115.29	53.923	−10.636

Table 3.3 Approximation coefficients for two temperature subintervals for calculation of thermodynamic properties of CO_2 (BUR)

T(K)	a_1 = 0.46365E+01	a_2 = 0.27414E-02	a_3 = -0.99589E-06	a_4 = 0.16039E-09
200 . . . 1000	a_5 = −0.91619E-14	a_6 = 0.49025E+05	a_7 = −0.19349E+01	
T(K)	a_1 = 0.23568E+01	a_2 = 0.89841E-02	a_3 = −0.71221E-05	a_4 = 0.24573E-08
1000 . . . 6000	a_5 = −0.14288E-12	a_6 = 0.48372E+05	a_7 = 0.99009E+01	

– magnitudes T_{in}, T_f, a_0, a_L, a_{-2}, a_{-1}, a_1, a_2, a_3 are read off from the IVT database;
– magnitudes T_{in}, T_f, a_1, a_2, a_3, a_4, a_5, a_6, a_7 are read off from the BUR database (see 1.13; 1.14).

For example, see Tables 3.2 and 3.3 for the coefficients are read off from the IVT database for CO_2.

B2. For each subinterval, the number of temperature steps is preset and the set of temperatures for the entire interval T_k, ($k = 1 \ldots m_z$,) is formed, $m_z = \left(\sum_1^t k_i + 1\right)$, where t – the number of temperature subintervals, k_i – temperature steps number in each subinterval.

B3. Calculation of parameter ΔE describing the discrepancy in enthalpy values at various reference temperatures in databases $E(T_{E,0})$ and $R(T_{R,0})$. For IVR database it is necessary to calculate the magnitudes:

$$F_j = 10^4\left[-2a_{-2}X_j^{-1} + a_{-1} + a_2X_j + a_1X_j^2 + 2a_2X_j^3 + 3a_3X_j^4\right] \quad j = 1,2 \qquad (3.33)$$

at $X_1 = 10^{-4}T_{E,0}$; $X_2 = 10^{-4}T_{R,0}$.

For the BUR database, the magnitudes,

$$F_j = R_0T_j\left[a_1 + \frac{a_2}{2}T_j + \frac{a_3}{3}T_j^2 + \frac{a_4}{4}T_j^3 + \frac{a_5}{5}T_j^4\right] \qquad j = 1,2, \qquad (3.34)$$

should be calculated at $T_1 = T_{E,0}$; $T_2 = \cdot T_{R,0}$.

Then the discrepancy in enthalpy values will be defined by the formula:

$$\Delta E_s = F_2 - F_1. \qquad (3.35)$$

B4. Parameters H_k^E, S_{0k}^E are calculated for each values of T_k defined at step B2 by Relationships (1.16) and (1.17) for IVT-database and by (1.13, 1.14) for the BUR database.

B5. Recalculation of enthalpy and entropy in compliance with the temperature initial values and dimensions adopted in the R-database:

Downloaded from https://www.cambridge.org/core. Nottingham Trent University, on 17 Aug 2019 at 02:05:11, subject to the Cambridge Core terms of use, available at https://www.cambridge.org/core/terms. https://doi.org/10.1017/9781108581714.003

$$\frac{H_k^E + \Delta E_s}{W} \Rightarrow H_k^R, \quad \frac{S_{0k}^E}{W} \Rightarrow S_{0k}^R, \tag{3.36}$$

where, for the IVT database, $W = 4.184$, while for the BUR database, $W = 4184$.

B6. The Chebyshev method [73, 145] is used to calculate the approximating polynomials of the TTR database form from obtained tabulated values $H_k^R = f_H(T_k), S_{0k}^R = f_S(T_k)$:

- for gas substances: a_0, a_s, a_1, $a_2 \ldots a_7$ (see 1.7, 1.8)
- for condensed substances: a_0, a_s, a_1, a_2, a_3 (see 1.10, 1.11) at every temperature subinterval

B7. The obtained approximation coefficients are used to calculate the enthalpy and entropy values $H_k^R = f_H(T_k)$and $S_{0k}^R = f_S(T_k)$, respectively, for every value of T_k.

B8. Reapproximation errors $\varepsilon_k^H, \varepsilon_k^S$ between E- and R-databases are defined by formulas:

$$\varepsilon_k^H = \frac{\left|H_k^R - H_k^E\right|}{C_{pk}^E}, \quad \varepsilon_k^S = \frac{\left|\left(S_{0k}^R - S_{0k}^E\right)T_k\right|}{C_{pk}^E}, \tag{3.37}$$

where $k = 1 \ldots m_z$,

as well as average errors:

$$\bar{\varepsilon}_H = \sum_k \varepsilon_k^H / m_z, \quad \bar{\varepsilon}_S = \sum_k \varepsilon_k^S / m_z. \tag{3.38}$$

These magnitudes feature the temperature dimension (K) and make a definite contribution to errors of combustion products chemical composition and temperature (T_g) calculation. Let us, for example, obtain from reapproximation the values $\bar{\varepsilon}_H(CO_2) = 5$ K and assume for other combustion product substances $\bar{\varepsilon}_H = 0$ K, while the working medium composition include $r_{CO_2} = 20\%$. Then adiabatic temperature (T_g) will be defined with the error $\delta T_g \approx 5 * 0.2 = 1$ K. Therefore, if one assumes that arithmetic average values $\bar{\varepsilon}_H(CO_2) = 5$ K, then for most calculations, reapproximation results may be assumed to be correct and used in the R-database for application in combustion process calculation programs.

The described algorithm was used to create the CONVER computer code.

Influence of Calculation Accuracy on Approximation Coefficients

The Chebyshev method (step B6) is the main part of this algorithm whereby tabulated data of temperature ($x_k = 0.001T_k$) and enthalpy (H_k) set at points k are used to define approximation coefficients a_i of polynomial (1.7); that is

$$[x_k, H_k] \Rightarrow H(x) = \sum_{i=0}^{n} a_i x^i, \tag{3.39}$$

where $n = 7$ for gas substances and $n = 3$ for condensed substances.

Downloaded from https://www.cambridge.org/core. Nottingham Trent University, on 17 Aug 2019 at 02:05:11, subject to the Cambridge Core terms of use, available at https://www.cambridge.org/core/terms. https://doi.org/10.1017/9781108581714.003

Chebyshev polynomials have the following form:

$$\begin{aligned} &g_0(x) = 1, \quad g_1(x) = x, \\ &g_2(x) = 2x^2 - 1; \quad g_3(x) = 4x^3 - 3x. \\ &\cdots\cdots\cdots\cdots\cdots\cdots\cdots\cdots\cdots\cdots \\ &g_{n+1}(x) = 2xg_n(x) - g_{n-1}(x). \end{aligned} \tag{3.40}$$

On the basis of these polynomials, the relation $H(x, a')$ may be written as follows:

$$H(x, a') = \sum_{i=0}^{n} a'_i g_i(x), \tag{3.41}$$

where a'_i are "intermediate" approximation coefficients.

To determine them, it is required to solve the system of linear equations:

$$A_{iq}a'_q = B_i \qquad i, q = 0, \ldots, n, \tag{3.42}$$

$$A_{iq} \equiv \left(g_i, g_q\right) = \frac{1}{m_z + 1}\sum_{k=0}^{m_z} g_i(x_k)g_q(x_k) \quad k = 1, \ldots, m_z, \tag{3.43}$$

$$B_i \equiv (g_i, H) = \frac{1}{m_z + 1}\sum_{k=0}^{m_z} g_i(x_k)H(x_k). \tag{3.44}$$

After solving System (3.42), the values a'_i can easily be recalculated to coefficients a_i used in the working database by reducing the similar summands or using a recurrent procedure [146].

Preliminary calculations have shown that matrix A_{iq} can be ill conditioned, bringing about errors in the calculation of coefficients a_i. The main factor influencing these errors is likely to be the number of significant digits (N_c) allowed in the calculations. The role of this factor may be evaluated by mathematical experiment. Digits N_c are known to differ in translators from Fortran and C++ languages [147, 148]. Therefore, errors in the calculation of coefficients a_i may be revealed by comparing the results of the calculations performed by different versions of the CONVER program written in different languages. The following statements are obvious:

- At single precision, for ill-conditioned matrix A_{iq} values of coefficients a_i obtained by different versions can be dissimilar.
- At double precision, even for ill-conditioned matrix A_{iq} coefficients a_i in various versions of CONVER code will be equal.

This is why four versions of CONVER code were developed:

- with single precision (in Fortran (AF1) and C^{++} (AC1))
- with double precision (Fortran (AF2) and C^{++} (AC2))

All versions are based on the above algorithm, which compiles the consequence of blocks B1–B8.

On using these versions, test calculations on re-approximation of data from the THERMO database [16] to polynomial form of the TTR database were performed to

Downloaded from https://www.cambridge.org/core. Nottingham Trent University, on 17 Aug 2019 at 02:05:11, subject to the Cambridge Core terms of use, available at https://www.cambridge.org/core/terms. https://doi.org/10.1017/9781108581714.003

Table 3.4 Coefficients of re-approximation (THERMO ⇒ TTR) for substances H_2O and NO in temperature interval $T = 300$ K . . . 6000 K

H_2O	$10^{-5}a_1$	$10^{-4}a_1$	$10^{-3}a_2$·	$10^{-4}a_3$·
AC1	−0.60077	0.77361	−0.23521	0.16747
AF1	−0.60078	0.77413	−0.24629	0.16852
	$10^{-3}a_4$	$10^{-3}a_5$	$10^{-2}a_6$	$10^{-1}a_7$
AC1	−0.80102	0.18547	−0.21921	0.10569
AF1	−0.80621	0.18683	−0.22103	0.10666
NO	$10^{-5}a_1$	$10^{-4}a_1$	$10^{-3}a_2$·	$10^{-4}a_3$·
AC1	0.19919	0.60671	0.15681	−0.04581
AF1	0.19920	0.60621	0.15794	−0.04691
	$10^{-3}a_4$	$10^{-1}a_5$	a_6	a_7
AC1	0.07327	−0.49383	−0.11892	0.02640
AF1	0.07873	−0.63961	−0.07863	0.01573

Table 3.5 Coefficients of re-approximation (THERMO⇒ TTR) for substances SiO_2^* in three temperature intervals

300 K– 847 K	AF1	AC1	AF2	AC2
a_S10^{-2}	0.058094	0.058067	0.058349	0.058349
a_l10^{-6}	−0.219755	−0.219755	−0.21976	−0.21976
a_l10^{-5}	0.032225	0.032216	0.03234	0.03234
$a_2{\cdot}10^{-4}$	1.45689	1.45717	1.4546	1.4546
a_310^{-3}	−4.78180	−4.78387	−4.7673	−4.7673
847 K – 1000 K	AF1	AC1	AF2	AC2
a_S10^{-2}	0.047670	−0.031870	0.25431	0.25431
a_l10^{-6}	−0.218093	−0.216557	−0.22210	−0.22210
a_l10^{-5}	0.010822	−0.039375	0.14144	0.14144
a_210^{-4}	1.52962	2.07526	.11309	.11309
a_310^{-3}	−5.08680	−7.05929	0.02449	0.02449
1000 K – 1696 K	AF1	AC1	AF2	AC2
a_S10^{-2}	0.254220	0.252499	0.25324	0.25324
a_l10^{-6}	−0.222112	−0.222052	−0.22208	−0.22208
a_l10^{-5}	0.141539	0.140139	0.14074	0.14074
a_210^{-4}	0.114314	0.124890	0.12035	0.12035
a_310^{-3}	0.014209	−0.011933	−0.00077	−0.00077

identify the difference between coefficients a_i determined by these computer codes. Some samples are listed in Tables 3.4 and 3.5. Approximation coefficients $a_0, a_1 \ldots, a_7$ for gas substances H_2O and NO in the interval $T = 200 \ldots 6000$ K calculated by computer codes AF1 and AC1 are shown in table 3.4. It is obvious that the difference is insignificant for coefficients a_0, a_1, a_2, a_3, a_4 compared to a significant difference for coefficients a_5, a_6 and a_7, which indicates "degradation" of conditionality of the system of equations (3.42).

Downloaded from https://www.cambridge.org/core. Nottingham Trent University, on 17 Aug 2019 at 02:05:11, subject to the Cambridge Core terms of use, available at https://www.cambridge.org/core/terms. https://doi.org/10.1017/9781108581714.003

In the case of condensed substances, the difference in coefficients can become all the more notable. Table 3.5 lists the coefficients of re-approximation a_s, a_I, $a_{1,}$ a_2, a_3 defined by four computer codes: AF1, AC1, AF2, and AC2 for substance SiO_2^* in the intervals: $T = 200 \ldots 847$ K, $T = 847 \ldots 1000$ K, and $T = 1000 \ldots 1600$ K. Apparently, the difference between coefficients obtained by computer codes AF1, AC1 is significant, particularly in the interval $T = 847 \ldots 1000$ K. However, the difference between coefficients a_2, a_3 is more notable than that for coefficients a_I, a_1. At the same time, the coefficients defined by double-precision computer codes (AF2 and AC2) are, in fact, identical. Therefore, for further calculations, computer code AF2 or AC2 was used.

Using computer code AF2, the conversion of polynomials was performed for more than 50 substances from every E-database. Some results of errors in conversion of polynomials from the IVTANTERMO database to the working database are shown in Figures 3.4 – 3.6.

Figure 3.4 shows the dependence of errors $\varepsilon_k^H, \varepsilon_k^S$ on the temperature of gaseous H_2O. These errors are not greater than 1 K in the selected temperature range (298–6000 K) with the maximum in the area of low temperatures.

Figures 3.5 and 3.6 show the dependence of errors $\varepsilon_k^H, \varepsilon_k^S$ on temperature in two intervals for condensed substance $Fe_2O_3^*$. The maximum value of errors ε^S, ε^H reaches 1.5 K in the range from 300 K to 400 K (Figure 3.6) at average values $\bar{\varepsilon}_H$, $\bar{\varepsilon}_S$ = 0.4 K.

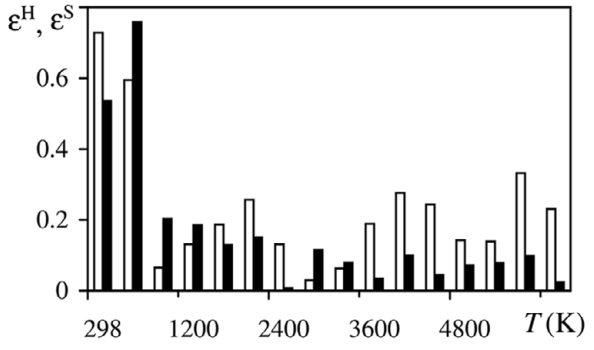

Figure 3.4 Dependence of errors ε^S (□) and ε^H (■) on temperature in the range of ($T = 298 \ldots$ 6000 K) for H_2O (gas).

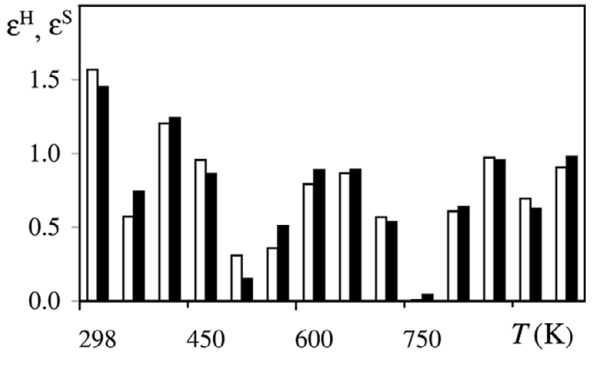

Figure 3.5 Dependence of errors ε^S (□) and ε^H (■) on temperature in the range of ($T = 298 \ldots$ 955 K) for condensed substance $Fe_2O_3^*$.

Downloaded from https://www.cambridge.org/core. Nottingham Trent University, on 17 Aug 2019 at 02:05:11, subject to the Cambridge Core terms of use, available at https://www.cambridge.org/core/terms. https://doi.org/10.1017/9781108581714.003

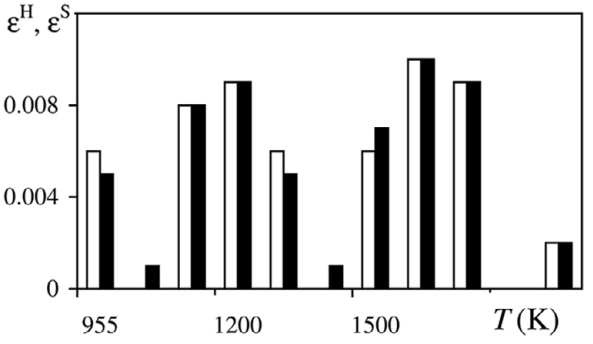

Figure 3.6 Dependence of errors ε^S (□) and ε^H (■) on temperature in the range of (T = 955 . . . 1812 K) for condensed substance $Fe_2O_3^*$.

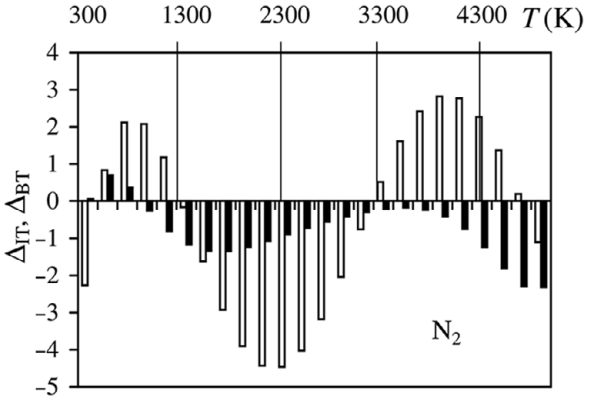

Figure 3.7 Discrepancies Δ_{IT} (□) and Δ_{BT} (■) obtained for N_2.

Similar results were obtained for all analyzed substances. The average error of re-approximation for gases is in permissible limits and does not exceed 1 K. However, for condensed substances higher errors $\bar{\varepsilon}_H$ and $\bar{\varepsilon}_S$ are observed than those for gases, particularly, in the first temperature interval corresponding to relatively low temperatures.

3.2.2 Comparison of Commonly Used Databases: Main Substances in Combustion Products

Widely used databases [5, 13, 17, 18, 26] are known to have higher credibility among combustion process analysts who, as a rule, assume that data in various databases on one and the same substance are identical and not corrected from time to time. Analysis of publications shows that in some cases, these data could differ and be corrected now and then. The developed tool including CONVER code and associated computer programs allow an online detection of such discrepancies. The following are some results of the comparison of data in known databases (TTR, IVTANTERMO [IVT], and BURCAT [BUR]) for typical stable gaseous substances of combustion products. This comparison was performed in the temperature range T = 300 . . . 5000 K, while Figures 3.7–3.15 show the discrepancies between the databases (Δ_{IT}– between IVT and TTR; Δ_{BT} - between BUR and TTR). These discrepancies were calculated by the formulas

Downloaded from https://www.cambridge.org/core. Nottingham Trent University, on 17 Aug 2019 at 02:05:11, subject to the Cambridge Core terms of use, available at https://www.cambridge.org/core/terms. https://doi.org/10.1017/9781108581714.003

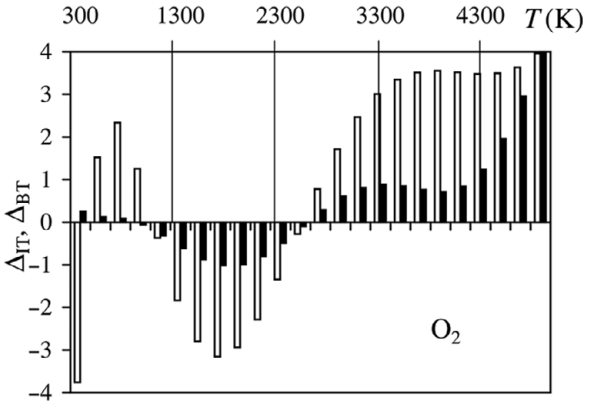

Figure 3.8 Discrepancies Δ_{IT} (□) and Δ_{BT} (■) obtained for O_2.

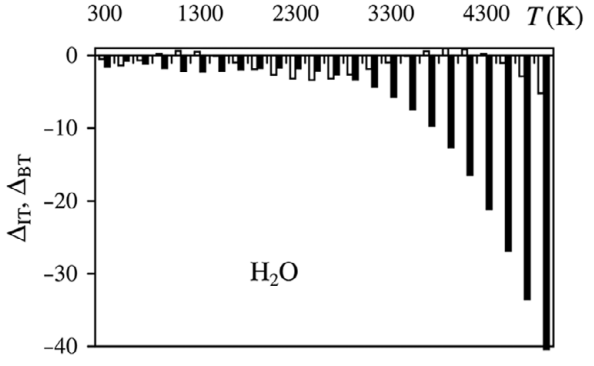

Figure 3.9 Discrepancies Δ_{IT} (□) and Δ_{BT} (■) obtained for gaseous H_2O.

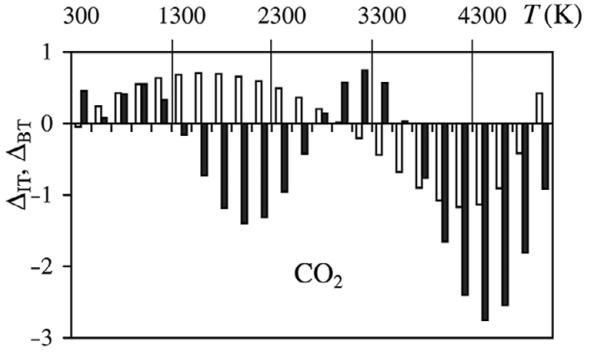

Figure 3.10 Discrepancies Δ_{IT} (□) and Δ_{BT} (■) obtained for CO_2.

$$\Delta_{IT} = \frac{H(\mathrm{IVT}) - H(\mathrm{TTR})}{C_p(\mathrm{TTR})} \quad \text{and} \quad \Delta_{BT} = \frac{H(\mathrm{BUR}) - H(\mathrm{TTR})}{C_p(\mathrm{TTR})}. \tag{3.45}$$

and, by analogy with errors ε_H, have an impact on the temperature T_g. They can be both positive and negative, which allows an easy evaluation of the difference

Downloaded from https://www.cambridge.org/core. Nottingham Trent University, on 17 Aug 2019 at 02:05:11, subject to the Cambridge Core terms of use, available at https://www.cambridge.org/core/terms. https://doi.org/10.1017/9781108581714.003

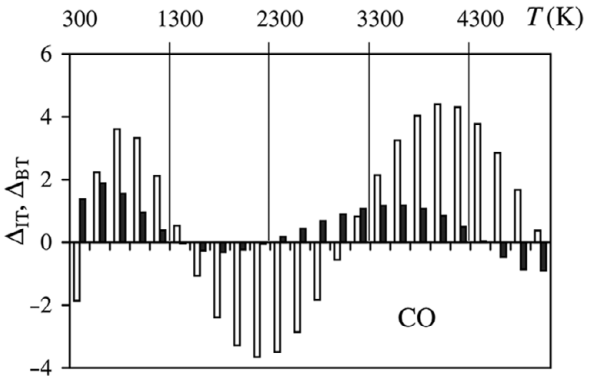

Figure 3.11 Discrepancies Δ_{IT} (□) and Δ_{BT} (■) obtained for CO.

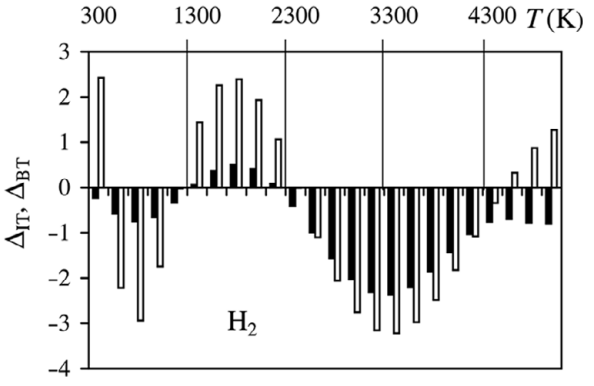

Figure 3.12 Discrepancies Δ_{IT} (□) and Δ_{BT} (■) obtained for H_2.

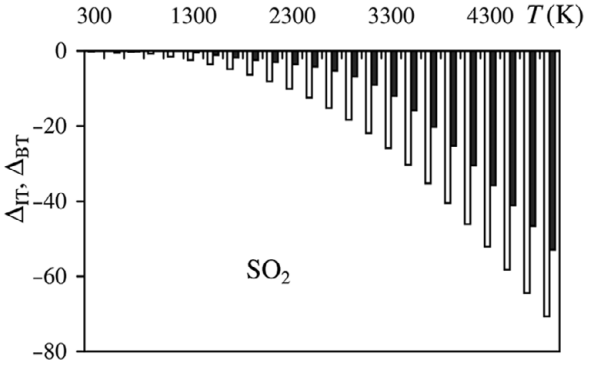

Figure 3.13 Discrepancies Δ_{IT} (□) and Δ_{BT} (■) obtained for SO_2.

between IVT and BUR databases. Re-approximation errors (ε^H) for these substances made according to the CONVER program did not exceed 2 K. Therefore, if discrepancies (Δ_{IT}, $\Delta_{BT} < 5$ K) are insignificant, let us relate them to re-approximation errors.

Downloaded from https://www.cambridge.org/core. Nottingham Trent University, on 17 Aug 2019 at 02:05:11, subject to the Cambridge Core terms of use, available at https://www.cambridge.org/core/terms. https://doi.org/10.1017/9781108581714.003

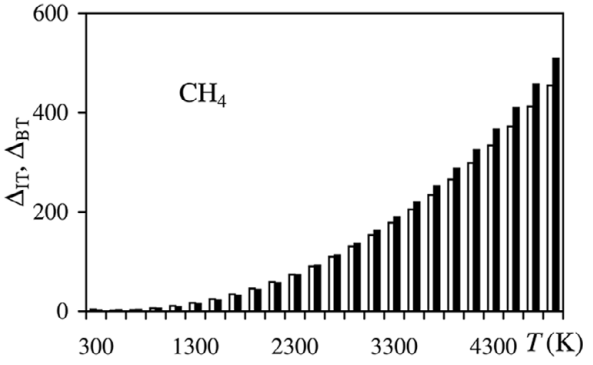

Figure 3.14 Discrepancies Δ_{IT} (□) and Δ_{BT} (■) obtained for CH_4.

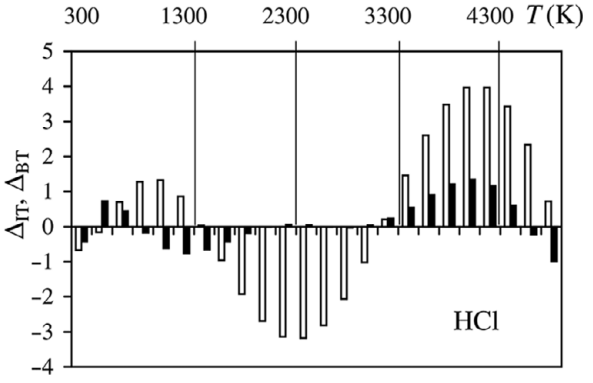

Figure 3.15 Discrepancies Δ_{IT} (□) and Δ_{BT} (■) obtained for HCl.

Figure 3.7 displays discrepancies Δ_{IT} and Δ_{BT} for molecular nitrogen (N_2). It is obvious that for all three databases, these discrepancies are, in fact, not greater than re-approximation errors. It means that thermodynamic properties of N_2 were initially determined correctly and, therefore, are not adjusted for a long time. Similar conclusions may be made for molecular oxygen (O_2) from the results shown in Figure 3.8.

Figure 3.9 gives the values Δ_{IT} and Δ_{BT} for gaseous H_2O. Apparently, discrepancies for this substance in the range of 300 . . . 3500 K between these databases are not large, but a notable difference appears between the data (IVT, TTR) and (TTR, BUR) that reaches 40 K for a temperature of 4900 K. Basically, this discrepancy is not significant for the calculation of the combustion and high-temperature flows, since at $T > 3500$ K, the water content in combustion products is low because of dissociation.

For substances CO_2, CO, and H_2 (Figures 3.10, 3.11, and 3.12) the differences between databases (IVT, TTR, BUR) are insignificant and do not exceed 4 K. It is known that at combustion of hydrocarbon fuels in the air, substances N_2, O_2, H_2O, CO_2, CO, H_2 make up 95% of the combustion products. Since the errors caused by ambiguities in determination of thermodynamic properties of these substances are minor, then one may conclude that the results of hydrocarbon fuel combustion process calculations performed for various bases will bring about close results.

Downloaded from https://www.cambridge.org/core. Nottingham Trent University, on 17 Aug 2019 at 02:05:11, subject to the Cambridge Core terms of use, available at https://www.cambridge.org/core/terms. https://doi.org/10.1017/9781108581714.003

Figure 3.13 displays, as an example, the discrepancies Δ_{IT} and Δ_{BT} for substance SO_2. These discrepancies increase with increase in temperature to reach at $T = 4900$ K the values $\Delta_{IT} = -70$ K and $\Delta_{BT} = -50$ K. At the same time, the difference between modern databases makes $\Delta_{IT} - \Delta_{BT} = -20$ K. This means that the data initially obtained for SO_2 [120] were corrected. Now, these data are reliable, and it is recommended to use the data from IVT or BUR databases for this substance.

Notably higher discrepancies (up to $\Delta_{IT} \approx \Delta_{BT} \approx 500$ K at 4900 K) are obtained for methane (Figure 3.14). Obtained distributions show that these discrepancies result from the difference in specific heat that for CH_4 is notably higher in the IVT and BUR databases as compared with the TTR database. At the same time, the difference $\Delta_{IT} - \Delta_{BT}$ is minor ($\approx$20 K at $T = 3300$ K); therefore, it is necessary to use later data from the IVT or BUR databases.

In the case of substance HCl, a component of solid propellant combustion products (Figure 3.15), only minor discrepancies are observed ($max(\Delta_{IT}) \approx 4$ K, $max(\Delta_{BT}) \approx 3$ K), which do not fall beyond the limits of re-approximation errors.

These examples allow a conclusion that the created computer code CONVER is a useful tool for prompt replenishment of working databases by thermodynamic properties of substances and improvement of their quality.

3.2.3 Comparison of Commonly Used Databases: Atoms and Radicals in Combustion Products

The following are some results of the comparison of thermodynamic properties from widely used databases (TTR, IVT, BUR) for some atoms and radicals in combustion products. Re-approximation errors (ε^H) obtained with the help of the CONVER program did not exceed 3 K either. Comparison was performed in the range of temperature $T = 300 \ldots 5000$ K, while Figures 3.16–3.24 show the discrepancies between the databases.

Figure 3.16 displays discrepancies Δ_{IT} and Δ_{BT} for hydrogen atom H. It follows from these figures that these discrepancies increase with the increase in temperature to reach, at $T = 4900$ K, the values $\Delta_{IT} = 60$ K and $\Delta_{BT} = 60$ K. However, the difference between

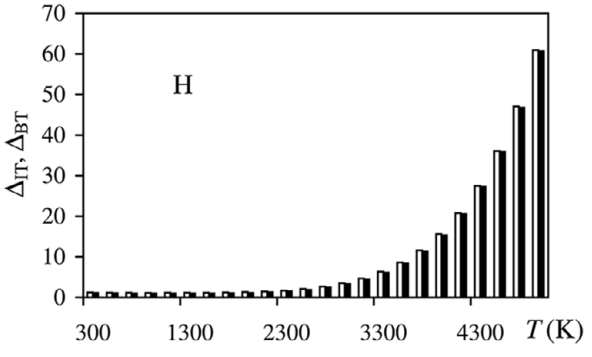

Figure 3.16 Discrepancies Δ_{IT} (□) and Δ_{BT} (■) obtained for atom H.

Downloaded from https://www.cambridge.org/core. Nottingham Trent University, on 17 Aug 2019 at 02:05:11, subject to the Cambridge Core terms of use, available at https://www.cambridge.org/core/terms. https://doi.org/10.1017/9781108581714.003

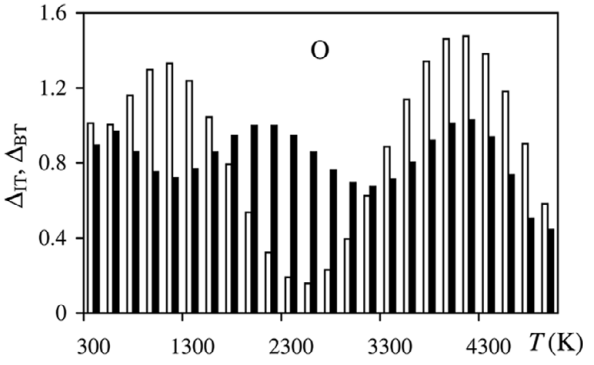

Figure 3.17 Discrepancies Δ_{IT} (□) and Δ_{BT} (■) obtained for O.

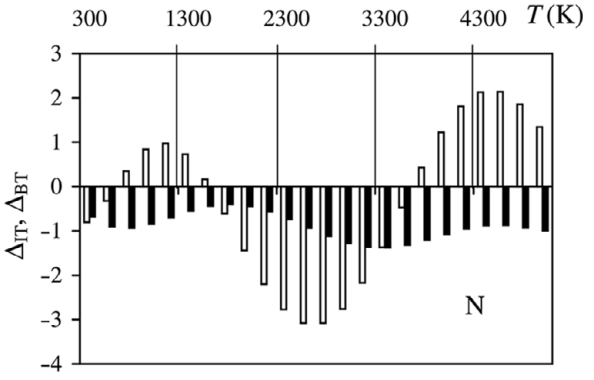

Figure 3.18 Discrepancies Δ_{IT} (□) and Δ_{BT} (■) obtained for N.

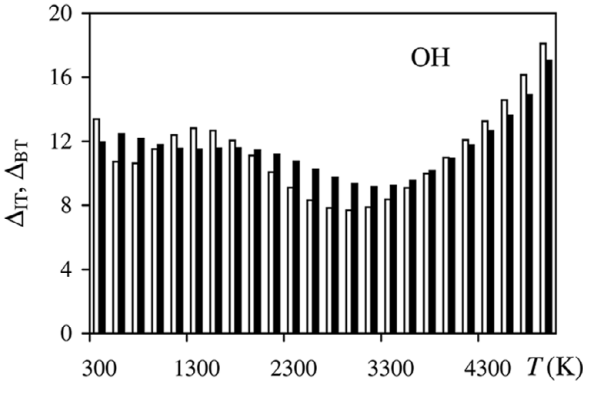

Figure 3.19 Discrepancies Δ_{IT} (□) and Δ_{BT} (■) obtained for OH.

values Δ_{IT} and Δ_{BT} is negligibly small, which means that data on thermodynamic properties of the H atom were corrected in modern databases.

In the case of atoms of oxygen (O) and nitrogen (N) (Figures 3.17 and 3.18) the difference between databases (IVT, TTR, BUR) are insignificant and do not exceed 4 K, which does not fall beyond the limits of re-approximation errors.

Downloaded from https://www.cambridge.org/core. Nottingham Trent University, on 17 Aug 2019 at 02:05:11, subject to the Cambridge Core terms of use, available at https://www.cambridge.org/core/terms. https://doi.org/10.1017/9781108581714.003

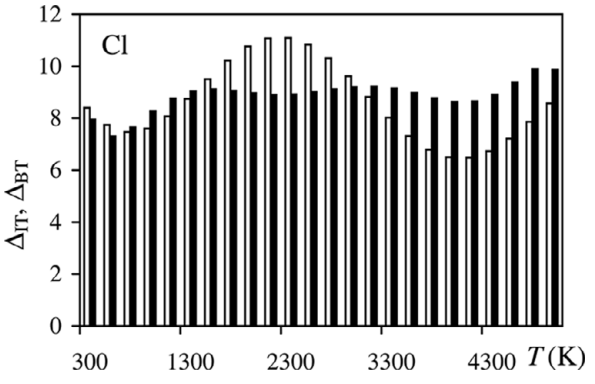

Figure 3.20 Discrepancies Δ_{IT} (□) and Δ_{BT} (■) obtained for Cl.

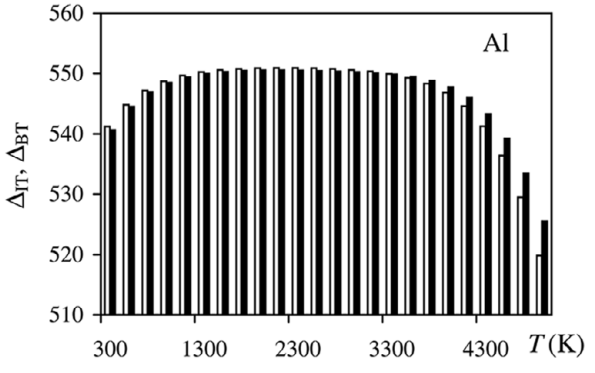

Figure 3.21 Discrepancies Δ_{IT} (□) and Δ_{BT} (■) obtained for Al.

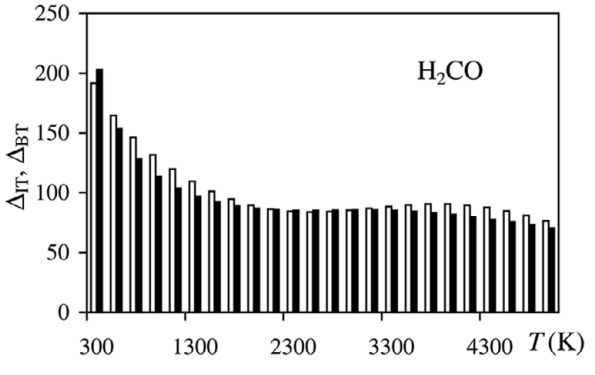

Figure 3.22 Discrepancies Δ_{IT} (□) and Δ_{BT} (■) obtained for H_2CO.

Figures 3.19 and 3.20 show the discrepancies Δ_{IT} and $\Delta_{BT}$for radical OH and atom Cl, respectively. It is obvious that, in the case of these substances, discrepancies in the databases do not exceed 18 K, and discrepancies between the IVT and BUR databases are only 2 K.

Downloaded from https://www.cambridge.org/core. Nottingham Trent University, on 17 Aug 2019 at 02:05:11, subject to the Cambridge Core terms of use, available at https://www.cambridge.org/core/terms. https://doi.org/10.1017/9781108581714.003

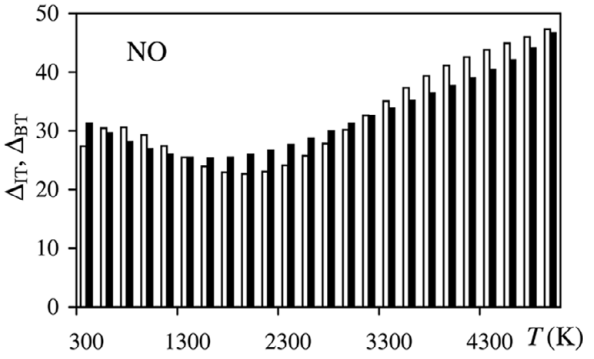

Figure 3.23 Discrepancies Δ_{IT} (□) and Δ_{BT} (■) obtained for NO.

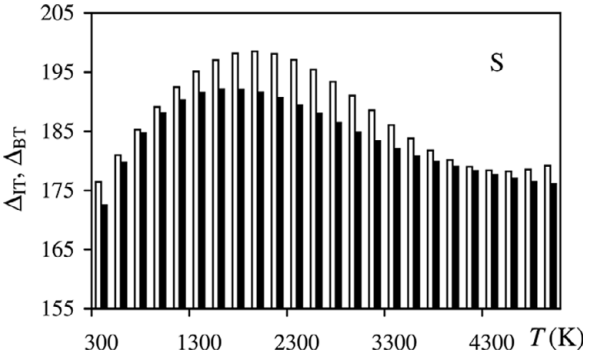

Figure 3.24 Discrepancies Δ_{IT} (□) and Δ_{BT} (■) obtained for S.

Figure 3.21 displays discrepancies atom Al. It is seen from this figure that there are notable discrepancies between data of databases IVT and BUR with the data of database TTR ($\Delta_{IT} \approx 550$ K). The character of histogram $\Delta_{IT}, \Delta_{BT} = f(T)$ shows that this discrepancy results from the great difference in the heat of the formation of this atom. But, at the same time, this difference between databases IVT and BUR is only 5 . . . 10 K.

In the case of radical H_2CO (Figure 3.22), discrepancies reach high magnitudes ($\approx$ 200K) at $T = 300$ K and then drop down to ≈ 80 K at $T = 5000$ K. Minor discrepancies between databases IVT and BUR (≈ 8 K) should be pointed out at both high and low temperatures.

Figure 3.23 displays notable discrepancies between Δ_{IT} and Δ_{BT} for radical NO, which reach the values of ≈ 50 K, yet this difference in the case of this substance between databases IVT and BUR makes only ≈ 5 K.

For atom S (Figure 3.24), the differences in databases IVT, TTR, and BUR reach $\approx$ 200 K at $T = 2000$ K, while at initial and final temperature values are in the limits of $\approx$ 180 K. However, modern databases IVT and BUR feature minor discrepancies for this atom.

Downloaded from https://www.cambridge.org/core. Nottingham Trent University, on 17 Aug 2019 at 02:05:11, subject to the Cambridge Core terms of use, available at https://www.cambridge.org/core/terms. https://doi.org/10.1017/9781108581714.003

The analysis of the results shown in Figures 3.7–3.24 allows the following conclusions:

– During the last decades (the TTR database was formed in the 1960s), databases of thermodynamic properties were refined for many substances (both stable and intermediate), and in many cases, these refinements proved to be more significant.
– Modern databases display insignificant discrepancies for almost all tested substances, which confirms their high quality.

It makes sense to evaluate the influence of discrepancies (Δ_{IT}, Δ_{BT}) in the case of some substances (with allowance for their actual content) on temperature and other properties of combustion products.

This influence can be evaluated by simple relationships:

$$\delta T_{IT}(i) = |\Delta_{IT}| r_i, \quad \delta T_{BT}(i) = |\Delta_{IB} - \Delta_{IT}| r_i, \tag{3.46}$$

where r_i is the "estimation" mole fraction of the i-th substance in combustion products of propellants obtained from the analysis of numerical data from the handbook [21, 149, 150, 151, 152, 153, 154] and monograph [155]; $\delta T_{IT}(i), \delta T_{BT}(i)$ are errors in combustion product temperature allowing for "estimation" content of the i-th substance resulting from discrepancies between databases TTR, IVT and IVT, BUR. As shown in preceding histograms, values $\delta T_{BT}(i)$ are insignificant, while estimates $\delta T_{IT}(i)$ are notably larger and shown in Tables 3.6 and 3.7.

Analysis of these tables allows one to conclude that discrepancies between modern databases IVT and BUR and the earlier database TTR are notably greater with respect to atoms and radicals than to stable substances of combustion products. However, the content of atoms and radicals in combustion products is basically insignificant.

Table 3.6 Discrepancies between databases $\Delta_{IT}$and possible errors δT in combustion product temperature for stable substances of combustion products

Species	Δ_{IT} for 2300 K	r_i	δT_{2300}	Δ_{IT} for 4000 K	r_i	δT_{4000}
N_2	4	0.7	2.8	3	0.5	1.5
CO_2	2	0.1	0.2	3	0.1	0.3
H_2O	5	0.2	1.0	40	0.1	4
CO	3	0.2	0.6	4	0.05	0.2
AlCl	150	0.02	3	150	0.02	3
CH_4	50	0.05	2.5	300	0.005	1.5
H_2	3	0.2	0.6	3	0.2	0.6
HBO_2	80	0.1	8	50	0.2	10
HCl	3	0.2	0.6	4	0.2	0.8
O_2	4	0.2	0.8	4	0.1	0.4
SO_2	10	0.1	1.0	50	0.05	2.5

Downloaded from https://www.cambridge.org/core. Nottingham Trent University, on 17 Aug 2019 at 02:05:11, subject to the Cambridge Core terms of use, available at https://www.cambridge.org/core/terms. https://doi.org/10.1017/9781108581714.003

Table 3.7 Discrepancies between databases Δ_{IT} and possible errors δT in combustion products temperature for atoms and radicals

Species	Δ_{IT} for 2300 K	r_i	δT_{2300}	Δ_{IT} for 4000 K	r_i	δT_{4000}
H	2	0.01	0.02	20	0.2	4
O	1	0.02	0.02	1.5	0.2	0.3
N	4	0.0001	0	2	0.01	0.02
OH	10	0.01	0.1	12	0.1	1.2
Cl	10	0.01	0.1	12	0.01	0.12
HCO	2000	0.0001	0.2	1000	0.001	1.0
Al	550	0.01	5.5	500	0.05	25
CH_3	250	0.001	0.25	150	0.01	1.5
H_2CO	200	0.001	0.2	80	0.001	0.08
NO	30	0.001	0.03	40	0.01	0.4
AlO	700	0.001	0.7	500	0.01	5
NO_2	20	0.01	0.2	140	0.001	0.14
S	200	0.01	2	180	0.05	9
HO_2	200	0.01	2	100	0.001	0.1

This is why possible errors in combustion product temperatures δT (at temperature levels of 2300 K and 4000 K) are, in the general case, insignificant; the maximum error makes 25 K for atom Al at $T = 4000$ K).

Hence, the data of chemical equilibrium calculations (proceeding from the TTR database in the 1960s [13, 120]) may be used as before, but with caution in science and engineering. Nevertheless, to increase the quality of working databases, a critical analysis should be performed with the help of a tool similar to CONVER code, and at notable discrepancies in whatever substance, it is expedient to replace polynomials of thermodynamic properties with newer and more reliable data.

3.3 Sensitivity Analysis of Chemical Mechanisms in Combustion Chemistry

Sensitivity analysis of reacting medium composition and temperature with respect to constants of chemical reaction rates makes it one of important tools used in combustion process analysis [2, 103]. Calculation of sensitivity coefficients is frequently used for the analysis of the following problems: the influence of rate constant variation on combustion characteristics and detection of reactions for which it is necessary to define such constants with minimum error, etc. Sensitivity analysis is also used as one of the steps in the procedure for reaction mechanism reduction [90; 110].

One of the known approaches to determining sensitivity coefficients rests on the calculation of PSR characteristics with the numerical study of these coefficients for the

Downloaded from https://www.cambridge.org/core. Nottingham Trent University, on 17 Aug 2019 at 02:05:11, subject to the Cambridge Core terms of use, available at https://www.cambridge.org/core/terms. https://doi.org/10.1017/9781108581714.003

steady state of the reactor. The proposed algorithm exploits the same approach but with analytic determination of sensitivity coefficients.

3.3.1 Sensitivity Coefficient Computing Technique

The chemical kinetics equations for PSR used for calculation of sensitivity coefficients are derived in Section 2.1 and have the following form:

$$\frac{d\gamma_i}{d\tau} = -e^{\gamma i}\left(\sum_j \nu_{ij}\Omega_j + \frac{r_i^+\mu_g}{\mu^+\tau_p}) + \sum_q\sum_j \nu_{qj}\Omega_j + \sum_q \frac{r_q^+\mu_g}{\mu^+\tau_p} \equiv f_{\gamma i}, \tag{2.29}$$

where $\Omega_j = k_j\left(\frac{P}{R_oT}\right)^{\bar{m}_j} exp\left(-\sum_p n_{pj}\gamma_p\right)$; is the relative rate of j -reaction:

$$\bar{m}_j = m_j + \sum n_{pj} - 1, \gamma_i = -ln\, r_i, \quad j = 1, \ldots, 2m_c.$$

Forward reactions have the numbers $j = 1, \ldots, m_c$, while reverse reactions have the numbers $j = m_c + 1, \ldots, 2m_c$.

Let us assume that irreversible and mass exchange reactions are absent. The energy equation (assuming the adiabatic reactor) is used in an integral form:

$$T - T_{rf} - \sum_i \left(h\mu_i - H_i^{rf}\right) r_i \Big/ \sum_i C_{pi}^{rf} r_i \equiv F_T = 0 \qquad i = 1, \ldots, n_b. \tag{2.149}$$

Thus, the reactor model is described by Equations (2.29) and (2.149) with unknowns γ_i and T, which should be determined for the steady-state condition, and then the sensitivity coefficients should be calculated. The calculation algorithm uses the spline-integration method [86].

Sensitivity coefficients are defined for the steady-state reactor when left-hand side terms of Equation (2.29) equal zero. Parameters for which sensitivity is analyzed are rate constants of forward directions of chemical reactions $k_s^+ (s = j = 1 \ldots m_c)$ because rate constants of reverse reactions k_s^- are calculated by Formula (1.76) and are not independent parameters. Then, by analogy with Equations (3.5),

$$\sum_k \frac{\partial f_{\gamma i}}{\partial \gamma_k}\frac{\partial \gamma_k}{\partial k_s^+} + \frac{\partial f_{\gamma i}}{\partial T}\frac{\partial T}{\partial k_s^+} = -\frac{\partial f_{\gamma i}}{\partial k_s^+} \qquad i,k = 1, \ldots, n_b; s = 1, \ldots, m_c, \tag{3.47}$$

$$\sum_k \frac{\partial F_T}{\partial \gamma_k}\frac{\partial \gamma_k}{\partial k_s^+} + \frac{\partial F_T}{\partial T}\frac{\partial T}{\partial k_s^+} = -\frac{\partial F_T}{\partial k_s^+}, \tag{3.48}$$

where unknown are $\frac{\partial \gamma_k}{\partial k_s^+}$, $\frac{\partial T}{\partial k_s^+}$ in the amount of $(n_b + 1)$ for every s-th reversible reaction.

However, as shown in [93], it is more convenient to use sensitivity coefficients in the following form:

$$R_{is} = \frac{\partial lnr_i}{\partial lnk_s^+} = -\frac{k_s^+\partial \gamma_k}{\partial k_s^+}; \quad R_{Ts} = \frac{\partial lnT}{\partial lnk_s^+} = \frac{k_s^+\partial T}{T\partial k_s^+} \tag{3.49}$$

Downloaded from https://www.cambridge.org/core. Nottingham Trent University, on 17 Aug 2019 at 02:05:11, subject to the Cambridge Core terms of use, available at https://www.cambridge.org/core/terms. https://doi.org/10.1017/9781108581714.003

These coefficients evaluate the variation of r_i and T, if rate constants k_s^+ increase by a factor of $e = 2.7183$. Allowing for Formula (3.49), the system of linear equations (3.47, 3.48) may be written as follows:

$$\begin{aligned}\sum_k \frac{\partial f_{\gamma i}}{\partial \gamma_k}\left(k_s^+ \frac{\partial \gamma_k}{\partial k_s^+}\right) + \frac{\partial f_{\gamma i}}{\partial T}\left(k_s^+ \frac{\partial T}{\partial k_s^+}\right) = -k_s^+ \frac{\partial f_{\gamma i}}{\partial k_s^+} \\ \sum_k \frac{\partial F_T}{\partial \gamma_k}\left(k_s^+ \frac{\partial \gamma_k}{\partial k_s^+}\right) + \frac{\partial F_T}{\partial T}\left(k_s^+ \frac{\partial T}{\partial k_s^+}\right) = -k_s^+ \frac{\partial F_T}{\partial k_s^+}\end{aligned}, \tag{3.50}$$

where unknown are $X_s \equiv [X_{is}, X_{Ts}] \equiv \left[k_s^+ \frac{\partial \gamma_k}{\partial k_s^+}, k_s^+ \frac{\partial T}{\partial k_s^+}\right]$,
or are in the form

$$AX_s = B_s, \tag{3.51}$$

where $A = \begin{bmatrix} \frac{\partial f_{\gamma i}}{\partial \gamma_k} & \frac{\partial f_{\gamma i}}{\partial T} \\ \frac{\partial F_T}{\partial \gamma_k} & \frac{\partial F_T}{\partial T} \end{bmatrix}$ and $B_s = \left[-k_s^+ \frac{\partial f_{\gamma i}}{\partial k_s^+}, -k_s^+ \frac{\partial F_T}{\partial k_s^+}\right]$.

Unlike [5, 93], the proposed computing technique for coefficients R_{is} and R_{Ts}, matrix A and vector B_s are determined analytically. The following formulas were derived in Subsection 2.4.3 from Equation (2.149):

$$\frac{\partial F_T}{\partial \gamma_k} = \left[\left(h\mu_k - H_k^{rf}\right) r_k - C_{pk}^{rf} r_k \left(T - T_{rf}\right)\right] \Big/ \sum_q C_{pq}^{rf} r_q, \tag{2.181}$$

$$\frac{\partial F_T}{\partial T} = 1. \tag{3.52}$$

The analytical expression for the determination of derivative $\frac{\partial f_{\gamma i}}{\partial \gamma_k}$ for PSR was obtained on deriving Formula (2.184) and was the part of this formula described as follows:

$$\frac{\partial f_{\gamma i}}{\partial \gamma_k} = -\delta_i^k e^{\gamma i}\left(\sum_j \nu_{ij}\Omega_j + \frac{r_i^+ \mu_g}{\mu^+ \tau_p}\right) + e^{\gamma i}\left(\sum_j \nu_{ij} n_{kj}\Omega_j + \frac{r_i^+ \mu_k r_k}{\mu^+ \tau_p}\right) - \sum_q \left(\sum_j \nu_{qj} n_{kj}\Omega_j + \frac{r_q^+ \mu_k r_k}{\mu^+ \tau_p}\right). \tag{3.53}$$

At the determination of derivative $\frac{\partial f_{\gamma i}}{\partial T}$, let us assume rate constant k_s^+ to be an independent parameter, hence for derivative $\frac{\partial \Omega_j}{\partial T}$, we have preliminarily

$$\frac{\partial \Omega_j}{\partial T} = \Omega_j \frac{\partial\left(ln\Omega_j\right)}{\partial T} = \Omega_j \frac{\partial\left(lnk_s^+ + \bar{m}_j ln(P/R_0 T) - \sum n_{pj}\gamma_p\right)}{\partial T} = -\Omega_j \frac{\bar{m}_j}{T}. \tag{3.54}$$

Now, finally, we get

$$\frac{\partial f_{\gamma i}}{\partial T} = e^{\gamma i}\left(\sum_j \nu_{ij}\Omega_j \frac{\bar{m}_j}{T}\right) - \sum_q \sum_j \nu_{qj}\Omega_j \frac{\bar{m}_j}{T}. \tag{3.55}$$

On derivation of the expression for derivatives $\frac{\partial f_{\gamma i}}{\partial k_s^+}$, it is necessary to allow for the fact that, for the forward direction of s-th reversible reaction,

Downloaded from https://www.cambridge.org/core. Nottingham Trent University, on 17 Aug 2019 at 02:05:11, subject to the Cambridge Core terms of use, available at https://www.cambridge.org/core/terms. https://doi.org/10.1017/9781108581714.003

$$\frac{\partial \Omega_s}{\partial k_s^+} = \frac{\partial \left(k_s^+ (P/(R_o T))^{\bar{m}_s} \, exp\left(-\sum n_{ps}\gamma_p\right)\right)}{\partial k_s^+} = \frac{\Omega_s}{k_s^+}, \tag{3.56}$$

while for the reverse direction of this reaction,

$$\frac{\partial \Omega_{s+m_c}}{\partial k_s^+} = \frac{\partial \left(k_s^+ / K_s (P/(R_o T))^{\bar{m}_{s+m_c}} \, exp\left(-\sum n_{p,s+m_c}\gamma_p\right)\right)}{\partial k_s^+} = \frac{\Omega_{s+m_c}}{k_s^+}. \tag{3.57}$$

Hence, we obtain

$$\frac{\partial f_{\gamma i}}{\partial k_s^+} = -e^{\gamma i}\left(v_{is}\frac{\Omega_s}{k_s^+} + v_{i,s+m_c}\frac{\Omega_{s+m_c}}{k_s^+}\right) + \sum_q \left(v_{qs}\frac{\Omega_s}{k_s^+} + v_{q,s+m_c}\frac{\Omega_{s+m_c}}{k_s^+}\right). \tag{3.58}$$

Continuing the derivation and allowing for $v_{i,s+m_c} = -v_{is}$; $\sum v_{q,s+m_c} = -\sum v_{qs}$, we get

$$\begin{aligned}\frac{\partial f_{\gamma i}}{\partial k_s^+} &= -\frac{e^{\gamma i}}{k_s^+} v_{is}(\Omega_s - \Omega_{s+mc}) + \frac{1}{k_s^+}\left(\Omega_s \sum_q v_{qs} - \Omega_{s+mc}\sum_q v_{qs}\right) \\ &= \frac{\Omega_s - \Omega_{s+mc}}{k_s^+}\left(-e^{\gamma i} v_{is} + \sum_q v_{qs}\right).\end{aligned} \tag{3.59}$$

Then vector $B_s \equiv [B_{is}, B_{Ts}]$has the following form:

$$B_{is} = -k_s^+ \frac{\partial f_{\gamma i}}{\partial k_s^+} = (\Omega_s - \Omega_{s+m_c})\left(e^{\gamma_i} v_{is} - \sum_q v_{qs}\right). \tag{3.60}$$

Finally, it is obvious that $B_{Ts} = \frac{\partial F_T}{\partial k_s^+} = 0$.

Solving the system of linear equations (3.50) allows us to get the roots X_s wherefrom sensitivity coefficients are determined:

$$R_{is} = -X_{is}; \quad R_{Ts} = X_{Ts}/T \qquad i = 1, \ldots, n_b. \tag{3.61}$$

Analysis of Formula (2.29) with respect to the elements of the main diagonal ($i = k$) of matrix A allows one to make the conclusion that

- The first summand $exp\,(\gamma_i)\left(\sum v_{ij}\Omega_j + \frac{r_i^+ \mu_g}{\mu^+ \tau_p}\right)$ including the differences $\Delta\Omega_s = \Omega_s - \Omega_{s+m_c}$ may equal zero.
- The second and third summands do not include these differences and are finite (other than zero), even at chemical equilibrium.

Thus, diagonal elements are not equal to zero, and, with a certain confidence, it may be concluded that matrix A is not singular. Then, for conditions of chemical equilibrium with allowance for vector $\bar{B}_s = 0$ (see [3.60]), the following statement may be formulated: "At chemical equilibrium, sensitivity coefficients $R_{is} = R_{Ts} = 0$." This conclusion is also confirmed by the fact that, at chemical equilibrium, the combustion products' chemical composition is the function of equilibrium constants (K_s), while these remain invariable in compliance with (2.152) on varying k_s^+. The computer code

Downloaded from https://www.cambridge.org/core. Nottingham Trent University, on 17 Aug 2019 at 02:05:11, subject to the Cambridge Core terms of use, available at https://www.cambridge.org/core/terms. https://doi.org/10.1017/9781108581714.003

RIS (the algorithm scheme is shown in the Figure 2.9) was supplemented by the module of calculation of sensitivity coefficients formed in compliance with described algorithm.

For comparison of the scope of calculations at numerical and analytical determination of sensitivity coefficients, let us point out that relationships $f_{\gamma i}$ (2.29) include summands $v_{ij}\Omega_j$ and sum them up. It is obvious that computing one value of $\Omega_j = k_j\left(\frac{P}{R_0T}\right)^{\bar{m}_j} exp\left(-\sum_p n_{pj}\gamma_p\right)$ or one reaction rate W_j requires a greater number of arithmetical operations than all adding operations. Therefore, on comparing the scope of calculations, we'll allow only for the number of Ω_j calculations at numerical and analytical approaches. Without deriving the general formula, let us give one example for the reacting medium described by $n_b = 20$ substances and $m_c = 80$ reactions. Assume also that every reaction includes four substances on average. Then, at numerical determination of sensitivity coefficients,

- First, it is necessary to calculate $2m_c = 160$ values of Ω_j to determine $f_{\gamma i}(\gamma_k)$.
- For elements $\partial f_{\gamma i}/\partial\gamma_k$ of matrix A with allowance for the formula $\frac{\partial f_{\gamma i}}{\partial\gamma_k} = \frac{f_{\gamma i}(\gamma_k+\Delta\gamma_k)-f_{\gamma i}(\gamma_k)}{\Delta\gamma_k}$, it is necessary to calculate the other $4m_c = 320$ values of $\Omega_j(\gamma_k + \Delta\gamma_k)$.
- For elements $\partial f_{\gamma i}/\partial T$ of matrix A with allowance for the formula $\frac{\partial f_{\gamma i}}{\partial T} = \frac{f_{\gamma i}(T+\Delta T)-f_{\gamma i}(T)}{\Delta T}$, it is necessary to calculate an extra 160 values of $\Omega_j(T + \Delta T)$, because all values of Ω_j depend on temperature.
- For vectors B_s, it is necessary to calculate an extra $2m_c = 160$ values of $\Omega_j\left(k_s^+ + \Delta k_s^+\right)$ with allowance for $\frac{\partial f_{\gamma i}}{\partial k_s^+} = \frac{f_{\gamma i}\left(k_s^+ + \Delta k_s^+\right)-f_{\gamma i}\left(k_s^+\right)}{\Delta k_s^+}$.

Hence, it follows that this example of numerical calculation of sensitivity coefficients requires the determination of 160 + 320 + 160 + 160 = 800 values of Ω_j. Meanwhile, at analytical determination, it is necessary to calculate 160 values of Ω_j all together. Thus, the advantage of analytical determination of sensitivity coefficients with respect to the number of calculations is obvious.

3.3.2 Comparison with Data of Other Studies

To substantiate the validity of RIS computer code, the latter was compared with the results obtained with the help of the well-known Aurora computer program [5]. It should be pointed out that, unlike RIS,

- Aurora employs a traditional form of chemical kinetics equations.
- Aurora employs different database of substances (with the other form of polynomials $H_i = f(T);\ S_i^0 = f(T);$).
- Energy equation is used in differential form.
- Partial derivatives of the Jacobian matrix and sensitivity coefficients are defined numerically.

Downloaded from https://www.cambridge.org/core. Nottingham Trent University, on 17 Aug 2019 at 02:05:11, subject to the Cambridge Core terms of use, available at https://www.cambridge.org/core/terms. https://doi.org/10.1017/9781108581714.003

Table 3.8 Mechanism of reactions for H + O medium

№	Reactions	lgA_s^+	n_s^+	E_s^+
1	$H + O_2 = O + OH$	16.707	−0.82	16,510
2	$H_2 + O = H + OH$	10.255	1.00	8830
3	$H_2 + OH = H_2O + H$	9.079	1.30	3630
4	$OH + OH = H_2O + O$	8.778	1.30	0
5	$H + OH + M = H_2O + M$ H_2O / 20	23.875	−2.60	0
6	$O_2 + M = O + O + M$	11.279	0.50	95,560
7	$H_2 + M = H + H + M$ H_2O / 6 / H / 2 / H_2 / 3	12.342	0.50	92,600
8	$H_2 + O_2 = OH + OH$	13.230	0.00	47,780
9	$H + O_2 + M = HO_2 + M$ H_2 / 3 / H_2O / 21/ O_2/ 0 / N_2/ 0	18.322	−1.00	0
10	$H + O_2 + O_2 = HO_2 + O_2$	19.826	−1.42	0
11	$H + O_2 + N_2 = HO_2 + N_2$	19.826	−1.42	0
12	$HO_2 + H = H_2 + O_2$	13.398	0.00	700
13	$HO_2 + H = OH + OH$	14.398	0.00	1900
14	$HO_2 + O = OH + O_2$	13.681	0.00	1000
15	$HO_2 + OH = H_2O + O_2$	13.699	0.00	1000
16	$HO_2 + HO_2 = H_2O_2 + O_2$	12.301	0.00	0
17	$H_2O_2 + M = OH + OH + M$	17.079	0.00	45,500
18	$H_2O_2 + H = HO_2 + H_2$	12.230	0.00	3750
19	$H_2O_2 + OH = H_2O + HO_2$	13.000	0.00	1800

Table 3.9 Composition and temperature of reacting mixture in the reactor for steady-state mode [5], Courtesy of ANSYS, Inc.

Program	T_f	r_O	r_{O_2}	r_{H_2}	r_{OH}	r_{OH_2}	r_{H_2O}	$r_{H_2O_2}$
Aurora*	1429	0.632^{-2}	0.263^{-1}	0.872^{-1}	0.565^{-2}	0.126^{-4}	0.2156	0.192^{-4}
RIS*	1426	0.619^{-2}	0.262^{-1}	0.867^{-1}	0.630^{-2}	0.117^{-4}	0.2152	0.173^{-4}

* Subscript following the number means its order. For example: $0.632^{-2} = 0.632 \cdot 10^{-2}$.

Comparison was made for reacting medium H + O including nine substances (O, O_2, H, H_2, OH, H_2O, HO_2, H_2O_2, and N_2) and 19 reactions listed in the Table 3.8 wherein symbols and numbers between / symbols mean the substance and the degree of its catalyticity. For example, fragment /H_2O/21/ in reaction 9 means that substance H_2O features catalytic efficiency 21 higher than generalized catalytic particle M.

Comparative calculation was performed for the following initial data: $\tau_p = 0.3 * 10^{-4} s$; $T^+ = 298\,\mathrm{K}$; $p = 10^5 \mathrm{Pa}$; $\tau_f = 10\tau_p$, where $\tau_f$is the reactor operation time, and chemical composition of the reactants at the entrance of the reactor: $r^+_{N_2} = 0.5563$; $r^+_{O_2} = 0.1305$; $r^+_{H_2} = 0.3132$. Initial composition of the reacting mixture in the reactor corresponded to equilibrium state of combustion products. Table 3.9 lists

Downloaded from https://www.cambridge.org/core. Nottingham Trent University, on 17 Aug 2019 at 02:05:11, subject to the Cambridge Core terms of use, available at https://www.cambridge.org/core/terms. https://doi.org/10.1017/9781108581714.003

Table 3.10 Sensitivity coefficients R_{is}, R_{Ts}(computer programs RIS and Aurora [5], Courtesy of ANSYS, Inc.)

№	Reaction	Computer Code	Sensitivity coefficients (R_{is}, R_{Ts})							
			O	O_2	H_2	OH	HO_2	H_2O	H_2O_2	T_f
1	$H + O_2 = O + OH$	RIS	0.44	−0.32	−0.18	0.34	−0.34	0.06	0.39	0.02
		Aurora	0.41	−0.29	−0.17	0.31	−0.31	0.05	0.37	0.02
2	$H_2 + O = H + OH$	RIS	−0.13	−0.09	−0.08	0.13	−0.11	0.02	0.11	0.01
		Aurora	−0.14	−0.10	−0.08	0.14	−0.12	0.03	0.12	0.02
3	$H_2 + OH = H_2O + H$	RIS	0.01	−0.15	−0.12	−0.06	−0.15	0.04	−0.21	0.01
		Aurora	0.03	−0.15	−0.13	−0.08	−0.16	0.04	−0.24	0.01
4	$OH + OH = H_2O + O$	RIS	−0.03	−0.01	−0.01	0.03	−0.01		0.03	
		Aurora	−0.02			0.02			0.02	
5	$H + OH + M = H_2O + M$	RIS	−0.05	−0.05	−0.01	0.05	−0.13	0.02	−0.07	0.03
		Aurora	−0.04	−0.04		0.05	−0.11	0.02	−0.08	0.03
7	$H_2 + M = H + H + M$	RIS	−0.06	−0.04	0.01	0.07	−0.14	0.02	−0.06	0.04
		Aurora	−0.06	−0.04		0.07	−0.14	0.02	−0.07	0.05
9	$H + O_2 + M = HO_2 + M$	RIS		−0.13	−0.05	0.18	0.59	0.03	0.06	0.05
		Aurora		−0.14	−0.06	0.19	0.58	0.04	0.05	0.05
11	$H + O_2 + N_2 = HO_2 + N_2$	RIS		−0.03	−0.01	0.03	0.12	0.01	0.01	0.01
		Aurora		−0.03	−0.01	0.04	0.11			0.01
12	$HO_2 + H = H_2 + O_2$	RIS	−0.01	0.01	0.01	−0.02	−0.11		−0.02	
		Aurora		0.02		−0.02	−0.11		−0.02	
13	$HO_2 + H = OH + OH$	RIS	0.01	−0.02	−0.01	0.02	−0.85		0.02	
		Aurora	0.01	−0.02	−0.01	0.02	−0.85		0.02	
17	$H_2O_2 + M = OH + OH + M$	RIS					0.01		0.83	
		Aurora							0.82	
18	$H_2O_2 + H = HO_2 + H_2$	RIS							−0.36	
		Aurora							−0.37	
19	$H_2O_2 + OH = H_2O + HO_2$	RIS							−0.43	
		Aurora							−0.40	

steady-state values r_i and T_f in the reactor obtained with the help of programs Aurora and RIS. With regard to the fact that calculations were performed with different databases of substances ("Aurora" program used BURCAT database [17], while RIS used the TTR database [13]), a good correspondence of calculation results obtained with the help of these programs was demonstrated.

Table 3.10 shows the comparison of sensitivity coefficients for selected reacting medium. Reactions 6, 8, 10, 14, 15, and 16 with values $|R_{is}| < 0.02$, and $|R_{Ts}| < 0.02$ in both computer programs are not given. Blank cells in the table mean that the values of appropriate sensitivity coefficients $abc(R_{is})$ and $abc(R_{Ts})$ are less than 0.01. On comparing the values of coefficients R_{is}, R_{Ts} allows concluding that the Aurora and RIS programs output very close results despite the differences in databases of substances, and those coefficients R_{is}, R_{Ts} in the Aurora programs are defined numerically unlike the RIS computer code.

Downloaded from https://www.cambridge.org/core. Nottingham Trent University, on 17 Aug 2019 at 02:05:11, subject to the Cambridge Core terms of use, available at https://www.cambridge.org/core/terms. https://doi.org/10.1017/9781108581714.003

Note here that the advantage of the presented model consists in analytical determination of these coefficients, which provides for their more precise calculation, notable decrease in the scope of calculations, and higher reliability of getting the results at approaching to the areas of instability.

3.3.3 Sensitivity Coefficients Dependence on Residence Time of Reacting Mixture H + S + O + (N) in the Reactor

The developed program was used to perform numerical analyses for reacting medium H + S + O + (N) under the following conditions: reactants – "H_2S + air"; $T^+ = 298$ K; $p = 10^5$ Pa; ($q_m = 0$); equivalence ratio based on fuel/oxidizer mass ratio $\phi_{fu} = 1/\alpha_{ox}$ = 1.0 … 0.667; and τ_p = var. The initial mechanism of reactions adopted from [25, 26], including 121 reactions and 25 substances (for exclusion of explicitly unimportant reactions), was reduced by the "engagement method" [115] to 33 reactions (Table 3.11 used the following dimensions: calorie, gram mole, centimeter, second) and substances (S, S_2, H, H_2, O, O_2, H_2O, OH, HS, H_2S, SO, SO_2, HS_2, HSO). Nitrogen was considered an inert gas. Calculations were performed at the variation of τ_p from very high values (areas of stable combustion) to those corresponding to the extinction zone.

Results of the calculation (temperature and chemical composition) at chemical equilibrium and under conditions of stable combustion (S1, S2) and near the extinction area (F1, F2) at ϕ_{fu} = 1.0 (stoichiometric mixture) and at ϕ_{fu} = 0.667, respectively, are shown in Table 3.12. Let us first discuss the results obtained for the stoichiometric mixture at stable combustion ($\tau_p = 10^{-3}s;$) in steady-state mode (S1). Here, we'll operate with forward (Ω_s) and reverse (Ω_{s+mc}) relative reaction rates of the reaction mechanism (1n … 33n) shown in Figure 3.25.

Temperature of combustion products at this mode is significant (T_g = 2093 K) while concentration of radicals O, H, OH is high (10^{-3} … $2{\cdot}10^{-3}$). These radicals reliably maintain the combustion process. Therefore, the rate of oxygen (O_2) consumption in the reactions 24n and 30n is high with its further conversion into H_2O and SO_2. Reactant H_2S participates in reactions 1n … 8n but is consumed in reaction 4n only with formation of radical HS and molecular hydrogen (H_2). Further, the diagram of reaction rates (Figure 3.25) shows that radicals HS create atoms S and radicals SO in reactions 9n and 10n. At the same time, atoms S are converted into radicals SO in reactions 13n and 14n. At the end of the conversion of sulfur compounds, radials SO are converted into the product of complete combustion SO_2 in compliance with reactions 23n and 24n. The other product of complete combustion, H_2O, is formed mainly due to reaction 23n. Stable combustion proceeds actively with low content of reactants in the reactor, which is at the same time higher than that at chemical equilibrium (see Table 3.12).

With residence time decreasing (because of increase in consumption of reactants or because of reactor volume reduction), combustion mode approaches the "extinction line" to make temperature T_g drop there, but combustion still persists. Combustion

Downloaded from https://www.cambridge.org/core. Nottingham Trent University, on 17 Aug 2019 at 02:05:11, subject to the Cambridge Core terms of use, available at https://www.cambridge.org/core/terms. https://doi.org/10.1017/9781108581714.003

Table 3.11 Mechanism of reactions adopted for the "H_2S + air" mixture

No.	Reactions	lgA_s^+	n_s^+	E_s^+
1n	$H_2S + M = H_2 + S + M$	24.20	−2.61	44,800
2n	$H_2S + SO_2 = H_2 + S + SO_2$	25,16	−2.61	44,800
3n	$H_2S + H_2O = H_2 + S + H_2O$	25.16	−2.61	44,800
4n	$H_2S + H = HS + H_2$	7.079	2.10	700
5n	$H_2S + O = HS + OH$	7.87	1.75	2920
6n	$H_2S + OH = HS + H_2O$	12.43	0	0
7n	$H_2S + S = HS + HS$	13.92	0	7400
8n	$H_2S + S = HS_2 + H$	13.30	0	7400
9n	$S + H_2 = HS + H$	14.15	0	19,400
10n	$HS + O = SO + H$	14.00	0	0
11n	$HS + OH = H_2O + S$	13.00	0	0
12n	$HS + O_2 = HSO + O$	13.28	0	17,883
13n	$S + OH = SO + H$	13.60	0	0
14n	$S + O_2 = SO + O$	6.72	1.81	600
15n	$2HS = S_2 + H_2$	12.00	0	0
16n	$HS + S = S_2 + H$	13.00	0	0
17n	$S_2 + M = 2S + M$	13.68	0	77,095
18n	$S_2 + H + M = HS_2 + M$	16.00	0	0
19n	$S_2 + O = SO + S$	13.00	0	0
20n	$HS_2 + H = S_2 + H_2$	7.08	2.10	700
21n	$HS_2 + OH = S_2 + H_2O$	12.432	0	0
22n	$HS_2 + S = S_2 + HS$	13.92	0	7400
23n	$SO + OH = SO_2 + H$	17.03	−1.35	0
24n	$SO + O_2 = SO_2 + O$	3.88	2.37	2980
25n	$2SO = SO_2 + S$	12.30	0	4000
26n	$HSO + H = H_2O + S$	9.20	1.37	−340
27n	$HSO + O_2 = SO_2 + OH$	12.00	0	9935
28n	$S + OH = HS + O$	11.80	0.50	8010
29n	$HS + O_2 = SO + OH$	12.00	0	10,000
30n	$H + O_2 = O + OH$	16.71	-0.82	16,510
31n	$H_2 + O = H + OH$	10.25	1.00	8830
32n	$H_2 + OH = H_2O + H$	9.08	1.3	3630
33n	$OH + OH = H_2O + O$	8.79	1.30	0

ceases at crossing this line. The calculation displayed that, at $\tau_p = 0.306 * 10^{-3} s$ (mode F1), the combustion still persists, while at $\tau_p = 0.304 * 10^{-3} s$, it ceases. It follows from Table 3.12 that the temperature in the reactor at this mode is notably lower than the equilibrium temperature (T_g = 1750 K), while the concentration of active particles H, O, OH is significantly lower (approximately in 10 times) than that at S1 mode. At the same time, the concentration of sulfur substances (S, HS, SO) is notably higher. A significant amount of nonreacted reactants ($H_2S \approx 1\%$; $O_2 \approx 3\%$) escape the reactor.

Figure 3.26 shows the values of forward (Ω_s) and reverse (Ω_{s+m_c}) relative reaction rates for this mode. This diagram shows that reactant H_2S is consumed in not only treaction 4n but the reactions 5n and 6n as well with the formation of radical HS, hydrogen (H_2), and water H_2O. At F1 mode, the water is formed, but mainly in reaction

Downloaded from https://www.cambridge.org/core. Nottingham Trent University, on 17 Aug 2019 at 02:05:11, subject to the Cambridge Core terms of use, available at https://www.cambridge.org/core/terms. https://doi.org/10.1017/9781108581714.003

Table 3.12 Temperature and chemical composition of combustion products (r_i) in PSR at various residence times τ_p and ratios of reactants*

$1/\alpha_{ox}$	$\phi_{fu} = 1.0$			$\phi_{fu} = 0.667$		
Mode	Chemical equilibrium	S1	F1	Chemical equilibrium	S2	F2
τ_p(sec)	∞	10^{-3}	0.306^{-3}	∞	1.2^{-3}	0.457^{-3}
T(K)	2092.7	1979.4	1750.4	1622.8	1577.5	1061.1
S	0.3386^{-5}	0.1288^{-3}	0.2034^{-3}	0	0.1765^{-4}	0.4585^{-4}
H	0.1337^{-3}	0.1612^{-2}	0.1513^{-3}	0.1199^{-6}	0.7762^{-3}	0.5433^{-5}
H_2	0.1993^{-2}	0.9701^{-2}	0.1473^{-1}	0.2990^{-5}	0.1329^{-2}	0.2007^{-5}
O	0.4824^{-4}	0.3285^{-3}	0.8542^{-4}	0.4929^{-5}	0.1381^{-2}	0.1049^{-4}
O_2	0.1320^{-2}	0.8449^{-2}	0.3469^{-1}	0.6681^{-1}	0.6689^{-1}	0.1229
H_2O	0.1279	0.1174	0.1045	0.8911^{-1}	0.8560^{-1}	0.5578^{-1}
OH	0.1139^{-2}	0.2389^{-2}	0.4332^{-3}	0.1750^{-3}	0.2733^{-2}	0.1162^{-3}
HS	0.2308^{-5}	0.2095^{-3}	0.1735^{-2}	0	0.2461^{-4}	0.9139^{-3}
H_2S	0.5488^{-6}	0.2180^{-3}	0.7315^{-2}	0	0.2284^{-3}	0.3082^{-1}
SO	0.1180^{-2}	0.6214^{-2}	0.6850^{-2}	0.7568^{-6}	0.7366^{-3}	0.1792^{-2}
SO_2	0.1294	0.1226	0.1011	0.8920^{-1}	0.8792^{-1}	0.4448^{-1}

* Superscript following the number indicates the number order. For example, $0.1993^{-2} = 0.1993*10^{-2}$

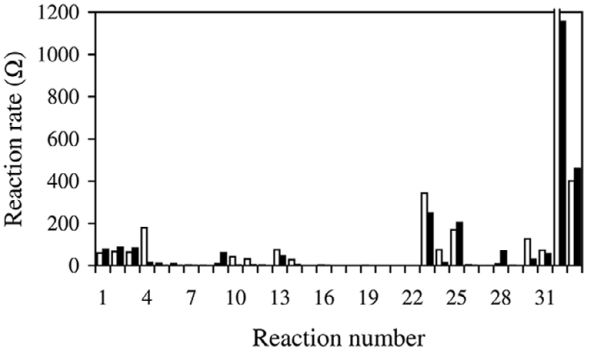

Figure 3.25 Diagram of relative reaction rates Ω_s(□) and Ω_{s+m_c}(■) at stable combustion, mode S1 ($\phi_{fu} = 1.0$, $\tau_p = 10^{-3}s$; $p = 10^5$ Pa). Numbers of the reactions comply with Table 3.11.

32n and partially in the reaction 6n. Formation of SO radical n (via intermediate substances *S*, HS) proceeds at high velocity in the reactions 10n, 11n, 13n, and 14n, but the conversion of these radicals into sulfur dioxide (SO_2) retards. This is why the concentrations of intermediate substances S, HS, and SO become higher than that at stable combustion.

After calculation of steady-state combustion in the reactor, sensitivity coefficients of composition and temperature (R_{is}, R_{Ts}) are calculated relative to rate constants k_s^+. These coefficients calculated for steady-state modes S1 and F1 are shown in the Figures 3.27 and 3.28.

Downloaded from https://www.cambridge.org/core. Nottingham Trent University, on 17 Aug 2019 at 02:05:11, subject to the Cambridge Core terms of use, available at https://www.cambridge.org/core/terms. https://doi.org/10.1017/9781108581714.003

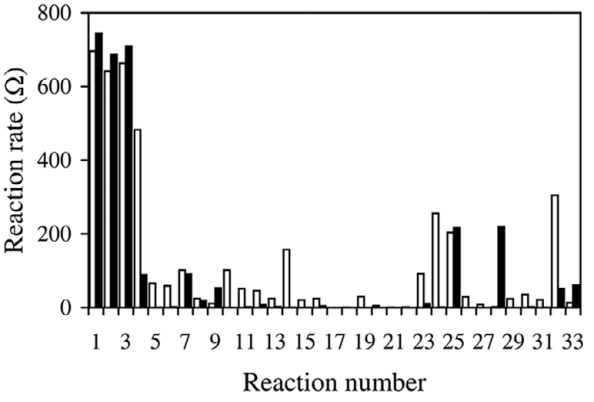

Figure 3.26 Diagram of relative reaction rates Ω_s(□) and Ω_{s+m_c}(■) in the extinction zone, mode F1 (ϕ_{fu} = 1.0, $\tau_p = 0.306{*}10^{-3}s$; $p = 10^5$ Pa). Numbers of the reactions comply with Table 3.11.

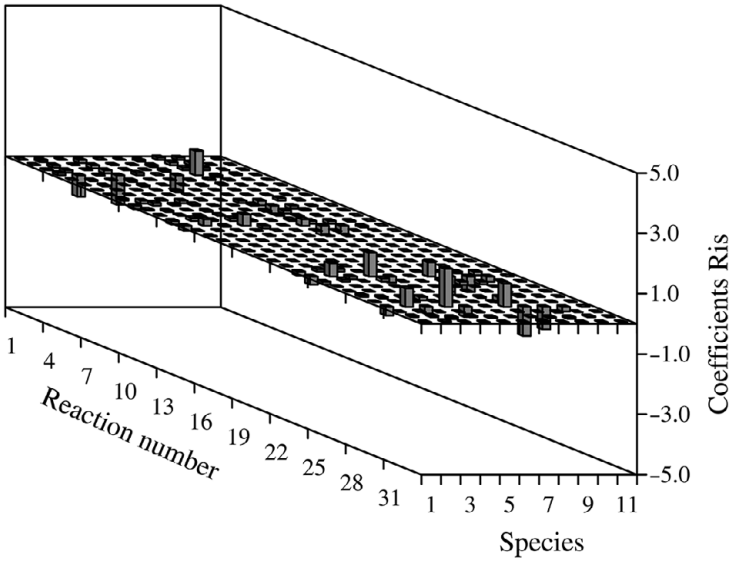

Figure 3.27 Diagram of sensitivity coefficients for substances R_{is} at stable combustion (ϕ_{fu} = 1.0, $\tau_p = 10^{-3}s$; $p = 10^5$ Pa). Substances: (1) S, (2) H, (3) H_2, (4) O, (5) O_2, (6) H_2O, (7) OH, (8) HS, (9) H_2S, (10) SO, (11) SO_2. Coefficients for substances S_2, HS_2, HSO are not shown. Numbers of the reactions comply with Table 3.11.

Figure 3.27 shows the diagram of coefficients R_{is} (apart from substances S_2, HS_2, and HSO) for the region of stable combustion at ϕ_{fu} = 1.0 and $\tau_p = 10^{-3}s$.

Apparently, these coefficients are mainly, low, though for some substances of minor concentrations upsurges of values R_{is} are observed (for example, $R_{\mathrm{HS},4} = 0.804$ at $r_{\mathrm{HS}} = 0.2{*}10^{-3}$; $R_{\mathrm{O},30} = 1.27$ at $r_{\mathrm{O}} = 0.3{*}10^{-3}$). For main substances in combustion products (SO_2 and H_2O), sensitivity coefficients are small ($R_{\mathrm{SO}_2,s}, R_{\mathrm{H_2O,s}} \leq 0.013$), which stipulates for low sensitivity coefficients for temperature $R_{Ts} \leq 0.007$. On interpreting these results, it

Downloaded from https://www.cambridge.org/core. Nottingham Trent University, on 17 Aug 2019 at 02:05:11, subject to the Cambridge Core terms of use, available at https://www.cambridge.org/core/terms. https://doi.org/10.1017/9781108581714.003

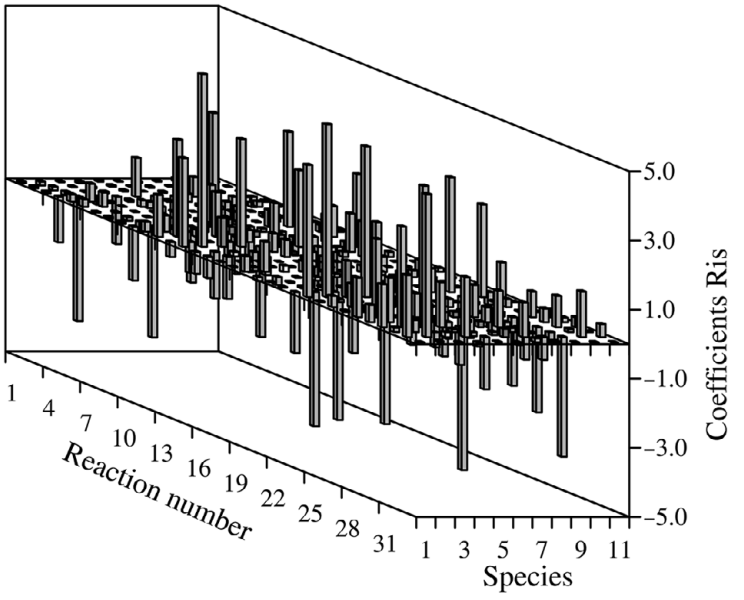

Figure 3.28 Diagram of sensitivity coefficients for substances R_{is} in extinction region (ϕ_{fu} = 1.0, $\tau_p = 0.306{*}10^{-3}s$; p = 10^5 Pa). Substances and reactions are enumerated as in Figure 3.27.

should be noted that at finite residence time ($\tau_p \neq \infty$), the reacting system shifts from equilibrium, and the difference $|\Delta\Omega_s| = |\Omega_s - \Omega_{s+m_c}| > 0$ exists for every reaction. Then

$$B_{is} = (\Omega_s - \Omega_{s+m_c}) \cdot \left(v_{is}\, exp\,(\gamma_i) - \sum_q v_{qs} \right) \neq 0, \tag{3.62}$$

hence, coefficients R_{is}, R_{Ts} become non-zero as well. It follows from the diagram of relative reaction rates Ω_s, Ω_{s+m_c} (Figure 3.25) that the following reactions proceed in the system:

- "slow" reactions (5n 6n, 7n, 12n, 15n, etc.) for which $\Omega_s \approx 0, \Omega_{s+m_c} \approx 0$, wherefrom small values of R_{is} result
- "fast" reactions (1n, 2n, 3n, 25n, 31n, 32n, etc.) with large values of Ω_s, Ω_{s+m_c}, but for which $\Omega_s \approx \Omega_{s+m_c}$, wherefrom minor values of R_{is} as well
- nonequilibrium reactions (9n, 10n, 11n, 13n, 14n, 23n, etc.) with a large difference $\Delta\Omega_s = \Omega_s - \Omega_{s+m_c}$ that can also bring about high values of R_{is}

Besides, for low concentration, cofactor $\left(v_{is}\, exp\,(\gamma_i) - \sum_q v_{qs} \right)$ in (3.62) becomes significant. For example, for substance HS, we obtain the value $e^{\gamma_{\mathrm{HS}}} = 1/r_{\mathrm{HS}} \approx 3300$, which facilitates an increase in coefficients $R_{\mathrm{HS},s}$.

Numerical calculations have indicated that at the decrease in τ_p, the sensitivity coefficients raise notably and can reach high values near the extinction region. This is shown in 3-D diagram of coefficients R_{is} (Figure 3.28, F1 mode). Apparently, in this

Downloaded from https://www.cambridge.org/core. Nottingham Trent University, on 17 Aug 2019 at 02:05:11, subject to the Cambridge Core terms of use, available at https://www.cambridge.org/core/terms. https://doi.org/10.1017/9781108581714.003

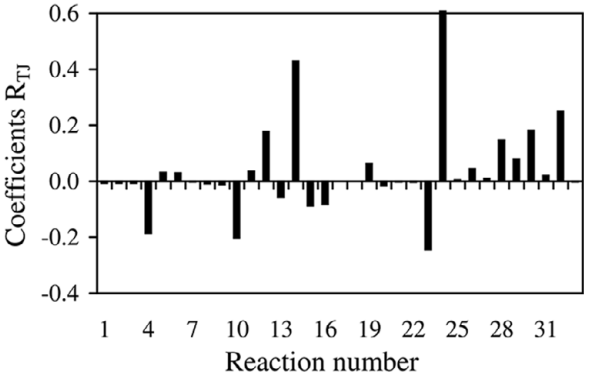

Figure 3.29 Diagram of sensitivity coefficients for temperature R_{Ts} in the extinction region (ϕ_{fu} = 1.0, $\tau_p = 0.306{*}10^{-3}s$; p = 10^5 Pa). Numbers of the reactions comply with Table 3.11.

case, the absolute values of many coefficients become very high (for example, $R_{\mathrm{H},24} = 9.86$; $R_{\mathrm{O}_2,14} = 2.61$; $R_{\mathrm{H_2S},4} = 2.42$). Besides, these coefficients increase significantly for the main substances in combustion products ($\max R_{\mathrm{SO}_2,s} = 0.999$, $\max R_{\mathrm{H_2O},s} = 0.5$), which causes high values of R_{Ts} (Figure.3.29). Note here that coefficients R_{Ts} describe both heat of s-th reaction and its rate in steady-state mode. Their positive values indicate exothermicity of the reaction forward direction.

To explain the effect of the increase in values of R_{is} (F1 mode), it is necessary to allow for the fact that in steady-state mode, the term $e^{\gamma i}\left(\sum_j \nu_{ij}\Omega_j + \frac{r_i^+ \mu_\Sigma}{\mu^+ \tau_p}\right)$ in Relationship (2.29) equals zero. Hence, in the equations written for reactants (i = H_2S, O_2, when $r_i^+ > 0$) with increasing τ_p, the modulus of the sum $\sum_j \nu_{ij}\Omega_j$ should increase. This sum includes forward and reverse relative reaction rates (Ω_s, Ω_{s+m_c}) involving reactants; therefore, for their increase, corresponding differences $\Delta\Omega_s = \Omega_s - \Omega_{s+m_c}$, an increase is required. This property confirms the magnitudes of Ω_s, Ω_{s+m_c} for all reactions shown in Figure 3.26 (F1 mode). Comparison with the data of diagram for steady-state mode (Figure 3.25) reveals a notable increase in $\Delta\Omega_s$for reactions of decomposition of H_2S (reactions 4n, 5n, 6n) and O_2 (reactions 12n, 14n, 24n). The influence of this increase is transferred to the other reactions of the system, which also causes the increase of corresponding differences $|\Delta\Omega_s|$. As a result, in compliance with (3.62), the magnitudes of B_{is} increase; hence, sensitivity coefficients increase as well.

Similar results (coefficients R_{is}, R_{Ts}) at the reduction in residence time have been obtained for other values of equivalence ratio based on fuel/oxidizer mass ratio in the range of ϕ_{fu} = 1.0 . . . 0.667. In particular, Figures 3.30 and 3.31 show 3-D diagrams of coefficients R_{is} (ϕ_{fu}= 0.667) for conditions of stable combustion ($\tau_p = 1.2{*}10^{-3}s$) and at the extinction region boundary ($\tau_p = 0.357{*}10^{-3}s$). In this region, values R_{is} can be very high, including those for the main substances of combustion products ($\max R_{\mathrm{SO}_2,s} = 6.54$; $\max R_{\mathrm{H_2O},s} = 4.41$) and temperature ($maxR_{Ts} = 3.82$).

Downloaded from https://www.cambridge.org/core. Nottingham Trent University, on 17 Aug 2019 at 02:05:11, subject to the Cambridge Core terms of use, available at https://www.cambridge.org/core/terms. https://doi.org/10.1017/9781108581714.003

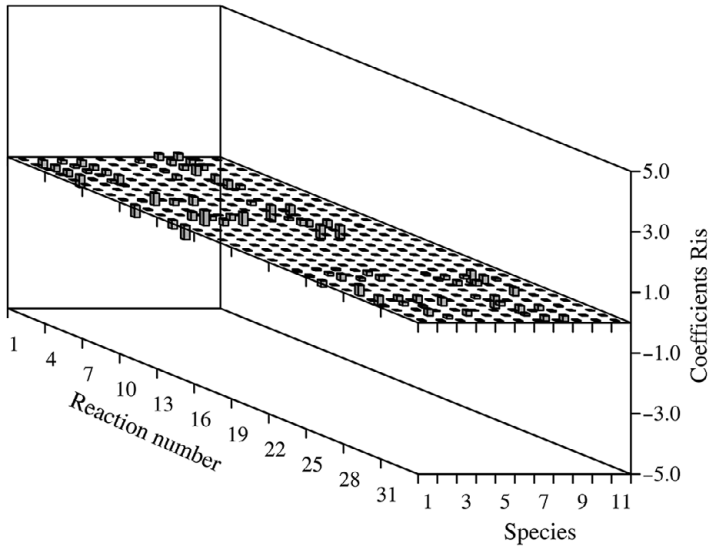

Figure 3.30 Diagram of sensitivity coefficients for substances R_{is} at stable combustion ($(\phi_{fu} = 0.667, \tau_p = 1.2{*}10^{-3}s;\ p = 10^5$ Pa). Substances and reactions are enumerated as in Figure 3.27.

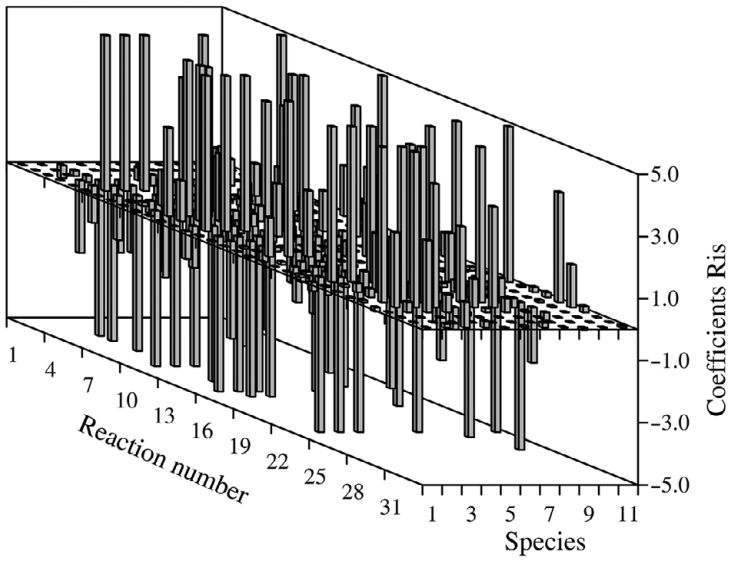

Figure 3.31 Diagram of sensitivity coefficients for substances R_{is} in the extinction region $\phi_{fu} = 0.667, \tau_p = 0.357{*}10^{-3}s;\ p = 10^5$ Pa. Substances and reactions are enumerated as in Figure 3.27.

Downloaded from https://www.cambridge.org/core. Nottingham Trent University, on 17 Aug 2019 at 02:05:11, subject to the Cambridge Core terms of use, available at https://www.cambridge.org/core/terms. https://doi.org/10.1017/9781108581714.003

3.4 Application of Evaluation of Eigenvalues to Combustion Analysis

The calculation of eigenvalues as a tool for combustion processes analysis is now used for solving the following problems:

- the selection of the methods for kinetic equation integration [2, 156, 157]
- the reduction of reaction mechanism [30, 130]
- the analysis of unstable combustion modes [90, 91]

Based on the material of monograph [70], one of the versions of this tool has been composed of a separate module to be incorporated in reactor models and, concurrently with the basic calculation, to define the variation of eigenvalues. In this paragraph, this tool is used for the identification of relations of the most important eigenvalues with combustion stages in the reactors, determination of potential number of integration steps by explicit schemes at calculation of processes in BR, using as an example the analysis of chemical nonequilibrium flows in the nozzles of rocket engines.

3.4.1 Algorithm for Calculation of Eigenvalues of Equations of Chemical Kinetics

While analyzing the combustion processes, eigenvalues (λ_i) are usually calculated for the Jacobian matrix constructed from the right-hand sides of chemical kinetics equations (2.27) and (2.29). Elements of this matrix $\frac{\partial f_i^\gamma}{\partial \gamma_k}$ for all types of the reactors (PSR, BR, and PFR) are defined during the integration of these equations by the algorithm described in Subsection 2.4.3. For example, these elements have the following form in the calculation of processes in BR:

$$J_{ik}^{\gamma} = \frac{\partial f_i^{\gamma}}{\partial \gamma_k} = e^{\gamma_i} \sum_j \nu_{ij} \left(\delta_i^k - n_{kj}\right) \Omega_j - \sum_p \sum_j \nu_{pj} n_{kj} \Omega_j, \;\; i,k,p = 1, \ldots, n_b, \;\; j = 1, \ldots, 2m_c \tag{3.63}$$

It is apparent that Formula (3.63) is a part of relationship (2.170) and requires no extra calculations to obtain the basic matrix.

Chemical kinetics equations are known to be nonlinear, and magnitudes λ_i may vary significantly while calculating them. Fortunately, the calculation of the Jacobian matrix (and, hence,J_{ik}^{γ}) is performed at some sets of steps stipulated for by the algorithm. At these points, eigenvalues may be calculated concurrently with the Jacobian recalculation to form the pattern of λ_i in the simulation of combustion process.

As shown in Figure 3.3, there are many ways of λ_i calculation, but recommendations of [70] isolate a successive application of Householder's procedure and the QR algorithm as the most preferable. Besides, the Jacobian asymmetry makes it expedient to build the so-called balancing procedure in the formed algorithm. The thing is that Householder's and QR algorithm procedures are efficient for symmetric matrices but can result in significant errors in the λ_i determination for asymmetric matrices. It is

Downloaded from https://www.cambridge.org/core. Nottingham Trent University, on 17 Aug 2019 at 02:05:11, subject to the Cambridge Core terms of use, available at https://www.cambridge.org/core/terms. https://doi.org/10.1017/9781108581714.003

apparent that matrix J^{γ}_{ik} (3.63) is asymmetric – that is, $\frac{\partial f^{\gamma}_i}{\partial \gamma_k} \neq \frac{\partial f^{\gamma}_k}{\partial \gamma_i}$. The asymmetric matrix in many practical applications can be very sensitive to minor changes in matrix elements that can cause notable errors. Therefore, many analysts recommend performing the asymmetric matrix "balancing" procedure before application of the basic algorithm to reduce aforesaid sensitivity. The symmetric matrix has no need in such procedure since it has been at first balanced.

Errors in the set of eigenvalues are normally proportionate to the matrix Euclidean norm:

$$E_N = \sqrt{\sum_j \sum_i a_{ij}}, \tag{3.64}$$

where a_{ij} are matrix elements; $i = 1 \ldots n$; $j = 1 \ldots n$; n is the matrix order.

The idea of balancing [70] consists in the application of similarity transformation (Subsection 3.1.4) so that corresponding rows and columns would have the comparable norms, that is, $E_{ri} \approx E_{cj}$ where the norm for rows is defined as

$$E_{ri} = \sqrt{\sum_i a_{ij}}, \tag{3.65}$$

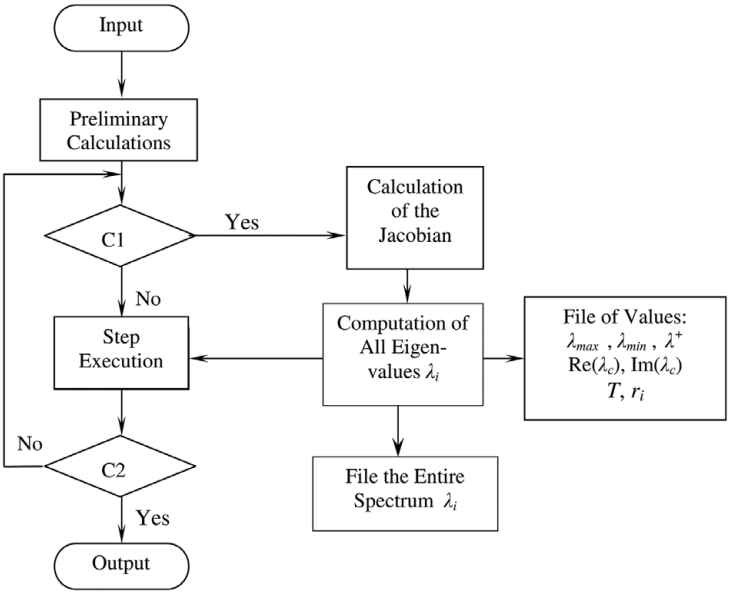

Figure 3.32 Block diagram for determination of eigenvalues at computing the combustion processes. C1 – is it necessary to recompute Jacobian? C2 – is the final value of integration interval reached? [156]. From A. L. Abdullin, V. I. Naoumov, and V. G. Krioukov, "Evaluation of Eigenvalues for the Analysis of Combustion and Chemical Non-equilibrium Flows," AIAA SciTech Forum. 55th AIAA Aerospace Science Meeting, AIAA 20017–0662, pp. 1–12, Grapevine, TX, 2017, reprinted by permission of the American Institute of Aeronautics and Astronautics, Inc

Downloaded from https://www.cambridge.org/core. Nottingham Trent University, on 17 Aug 2019 at 02:05:11, subject to the Cambridge Core terms of use, available at https://www.cambridge.org/core/terms. https://doi.org/10.1017/9781108581714.003

while the norm for columns has the following form:

$$E_{ci} = \sqrt{\sum_i a_{ij}}, \tag{3.66}$$

Thereby, the general matrix norm will decrease with eigenvalues remaining invariable. Reasoning from the data described earlier, the eigenvalue calculation procedure was formed including the procedures of balancing, Householder's, and the QR algorithm. These procedures are integrated into one module built in the general scheme of computing the processes in the reactor as it is shown in Figure 3.32.

The developed tool and corresponding module can be applied not only for the comparison of explicit and implicit schemes but for analysis of the problems of combustion instability and reduction of reaction mechanisms. This is why it defines the whole range of eigenvalues (including complex ones), which is stored in a separate archive in case the Jacobian is recalculated. Besides, the following most important eigenvalues are archived separately:

- maximum in absolute values among negative λ_{max}
- minimum in absolute values among negative λ_{min}
- maximum among positive λ^+
- maximum in absolute value of real part among complex values $\mathrm{Re}|\lambda_c|$
- maximum in absolute value of imaginary part λ_c, designated as $\mathrm{Im}|\lambda_c|$

3.4.2 Evolution of Eigenvalues in the Calculation of Combustion in Batch Reactor

Reacting System "CH_4 + Air"

The developed procedure of eigenvalue evolution determination is used as an example in the computation of "CH_4 + air" mixture ignition in adiabatic BR in the range of equivalence ratio variation α_{ox} = 0.6 ... 1.5 at p = 1 atm; T_0 = 1500 K. Adopted mechanism of reaction comprises 28 specie (C, H, O, N, N_2, O_2, OH, H_2, H_2O, HO_2, H_2O_2, HCO, HC_2O, CO, CO_2, CH, CH_2, CH_3, CH_4, CH_2O, CH_3O, C_2H, C_2H_2, C_2H_3, C_2H_4, C_2H_5, C_2H_6, C_2H_2O) and 131 reaction [93].

Figures 3.33–3.35 show the variation of mixture temperature in the reactor and variation of eigenvalues λ_{max}, λ_{min}, λ^+, λ_c at different α_{ox}. The results are presented on the reduced time scale $\tau_{rel} = \tau/\tau_{dm}$, where τ_{dm} is the maximum rate of temperature variation defined by the formula $\tau_{dm} = \tau\left(\frac{dT}{d\tau} = max\right)$. Temperature increase for all modes starts within the zone $\tau_{rel} \approx 1$.

In the analysis of eigenvalues variation (Figure 3.33), the integration interval may be divided into four zones/subintervals:

1. τ_{rel} = 0, ... ,0.004. This subinterval (not shown in Figure 3.33 because of its extremely low value, but given in Table 3.13) is described by very high values of $\lambda_{max} \approx 10^{13}$, which then decrease abruptly (Table 3.13). This effect results from a significant internal mismatch of formally preset initial chemical composition of the reacting system. For all these species, except for reactants, initial values

Downloaded from https://www.cambridge.org/core. Nottingham Trent University, on 17 Aug 2019 at 02:05:11, subject to the Cambridge Core terms of use, available at https://www.cambridge.org/core/terms. https://doi.org/10.1017/9781108581714.003

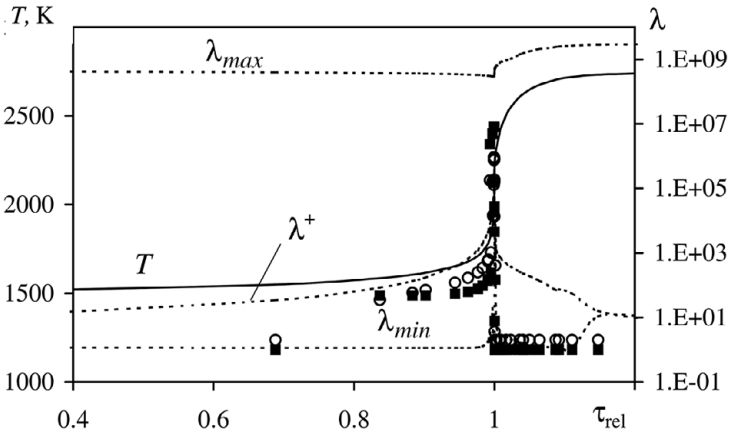

Figure 3.33 Evolution of the basic eigenvalues at "CH_4 + air" mixture combustion, α_{ox} = 1.0; (τ_{dm}= 14780μs); T_0 = 1500 K; ■ — Re$|\lambda_c|$, ○ -Im$|\lambda_c|$ [156]. From A. L. Abdullin, V. I. Naoumov, and V. G. Krioukov, "Evaluation of Eigenvalues for the Analysis of Combustion and Chemical Non-equilibrium Flows," AIAA SciTech Forum. 55th AIAA Aerospace Science Meeting, AIAA 20017–0662, pp. 1–12, Grapevine, TX, 2017, reprinted by permission of the American Institute of Aeronautics and Astronautics, Inc

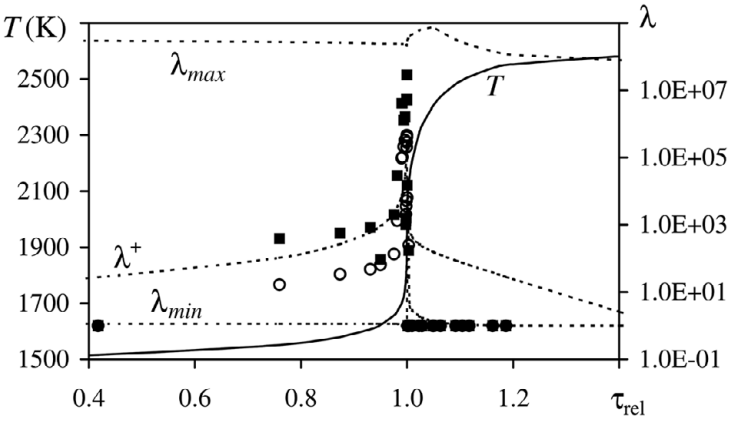

Figure 3.34 Evolution of eigenvalues for "CH_4 + air" reacting medium, α_{ox} = 1.5; (τ_{dm}= 10836μs); T_0 = 1500 K; ■ – *Re*$|\lambda_c|$, O –*Im*$|\lambda_c|$[156]. From A. L. Abdullin, V. I. Naoumov, and V. G. Krioukov, "Evaluation of Eigenvalues for the Analysis of Combustion and Chemical Non-Equilibrium Flows," AIAA SciTech Forum. 55th AIAA Aerospace Science Meeting, AIAA 20017–0662, pp. 1–12, Grapevine, TX, 2017, reprinted by permission of the American Institute of Aeronautics and Astronautics, Inc

$r_i^0 = 10^{-15}$ have been set, since while applying of chemical kinetics equations in exponential form, one cannot set the zero values ($r_i^0 = 0$). These features provoke very high artificial stiffness and very small initial integration steps. However, during a very short time, this artificial stiffness diminishes vanishes while reaching the natural balance of specie concentrations.

Downloaded from https://www.cambridge.org/core. Nottingham Trent University, on 17 Aug 2019 at 02:05:11, subject to the Cambridge Core terms of use, available at https://www.cambridge.org/core/terms. https://doi.org/10.1017/9781108581714.003

Table 3.13 Variation of eigenvalues λ_{max}, λ_{min}, λ^+, at initial step of calculation [156],* from A. L. Abdullin, V. I. Naoumov, and V. G. Krioukov, "Evaluation of Eigenvalues for the Analysis of Combustion and Chemical Non-equilibrium Flows," AIAA SciTech Forum. 55th AIAA Aerospace Science Meeting, AIAA 20017–0662, pp. 1–12, Grapevine, TX, 2017, reprinted by permission of the American Institute of Aeronautics and Astronautics, Inc.

$\tau(\mu s)$	λ_{max}	λ_{min}	λ^+
2.80^{-8}	8.69^{+12}	9.18^{-8}	6.85^{+1}
5.08^{-7}	1.69^{+12}	9.18^{-8}	6.85^{+1}
4.09^{-6}	2.42^{+11}	9.18^{-8}	6.85^{+1}
3.28^{-5}	3.08^{+10}	9.18^{-8}	6.84^{+1}
2.62^{-4}	4.04^{+9}	9.18^{-8}	6.81^{+1}
1.77^{-3}	1.07^{+9}	9.18^{-8}	6.65^{+1}
3.87^{-3}	5.07^{+8}	9.18^{-8}	6.43^{+1}

* Superscript at the number means the exponent, for example: $2.8^{-8} = 2.8\times10^{-8}$

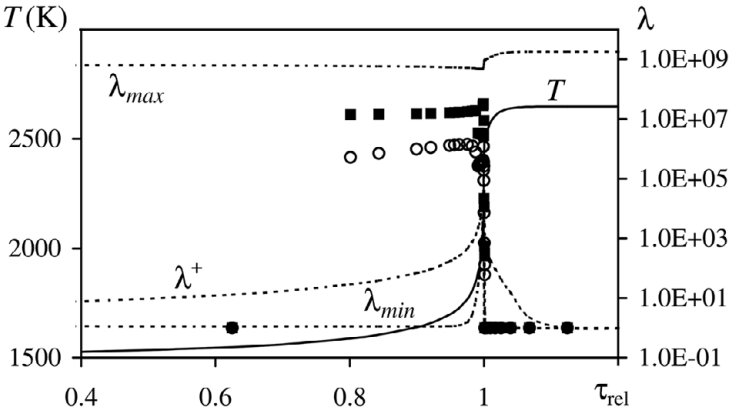

Figure 3.35 Evolution of eigenvalues for "CH_4 + air" reacting medium, $\alpha_{ox} = 0.6$; (τ_{dm}= 19,500μs); T_0 = 1500 K; ■ – $Re|\lambda_c|$, O –$Im|\lambda_c|$[156]. From A. L. Abdullin, V. I. Naoumov, and V. G. Krioukov, "Evaluation of Eigenvalues for the Analysis of Combustion and Chemical Non-Equilibrium Flows," AIAA SciTech Forum. 55th AIAA Aerospace Science Meeting, AIAA 20017–0662, pp. 1–12, Grapevine, TX, 2017, reprinted by permission of the American Institute of Aeronautics and Astronautics, Inc

2. τ_{rel}= 0.004 . . . 0.70 (Figure 3.33). This subinterval corresponds to the stage of accumulation of intermediate species (atoms and radicals) at, in fact, invariable temperature (see Table 3.14). For example, at the increase in temperature by 10 K only, mole fractions of atoms and radicals will increase by 7–10 orders compared with starting values.

Here one can observe the invariability of value $\lambda_{max} \approx 10^9$ and zero values of λ_{min} (this is likely to arise from considering the N_2 as an inert agent). Positive eigenvalue λ^+ plays here a special role. It reflects the exponential rise of some eigenvector (in our case, of some linear combination of concentrations). If λ^+ is small with respect to λ_{max}, then

Downloaded from https://www.cambridge.org/core. Nottingham Trent University, on 17 Aug 2019 at 02:05:11, subject to the Cambridge Core terms of use, available at https://www.cambridge.org/core/terms. https://doi.org/10.1017/9781108581714.003

Table 3.14 Variation of mole fractions of the basic atoms and radicals at the stage of their accumulation*

$\tau(s)$	T(K)	H	O	OH	CH_3	CH_2O	C_2H_4
0	1500	0.1^{-14}	0.1^{-14}	0.1^{-14}	0.1^{-14}	0.1^{-14}	0.1^{-14}
0.001	1501	0.821^{-7}	0.720^{-7}	0.375^{-7}	0.490^{-4}	0.848^{-4}	0.279^{-4}
0.002	1503	0.131^{-6}	0.101^{-6}	0.550^{-7}	0.607^{-4}	0.318^{-3}	0.183^{-3}
0.004	1510	0.175^{-6}	0.123^{-6}	0.702^{-7}	0.681^{-4}	0.849^{-3}	0.581^{-3}
0.006	1519	0.234^{-6}	0.151^{-6}	0.895^{-7}	0.766^{-4}	0.142^{-2}	0.103^{-2}
0.008	1531	0.338^{-6}	0.199^{-6}	0.123^{-6}	0.897^{-4}	0.215^{-2}	0.162^{-2}

* Superscript at the number means the exponent, for example: $0.821^{-7} = 0.821 \cdot 10^{-7}$

the influence of this rise is insignificant. However, the value of λ^+ increases to 10^2 in this subinterval and keeps on increasing further, which indicates the possible subsequent variations in the state of analyzed reacting system.

3. $\tau_{rel} = 0.7 \ldots 1.20$. This subinterval corresponds to heat explosion with a narrow zone of temperature rise and notable change in concentrations of all species. Value of λ_{max} increases approximately 10 times and stabilizes thereafter, which is caused by a sharp increase in temperature. The value of λ_{min} first does not vary ($\lambda_{min} \approx 0$), then increases to reach the maximum ($\lambda_{min} \approx 10^3$) to abruptly decrease at the subinterval end. This "spike" is likely to be caused by the change in mole fraction of inert N_2 owing to the increase in total number of reacting mixture moles. Besides, at this stage, the positive eigenvalue reaches the maximum ($\lambda^+ \approx 10^5$), and complex numbers $\lambda_c = Re(\lambda_c) \pm Im(\lambda_c)$ originate with high absolute values. These numbers display the possibility of the emergence of some oscillation phenomena at this stage of combustion.

4. $\tau_{rel} = 1.2 \ldots 1.60$. At the final subinterval (approaching chemical equilibrium), the value of λ_{max} practically does not vary. Complex eigenvalues λ_c vanish, while λ^+ approaches zero. All eigenvalues should be real and negative after sufficient time is expired.

Figures 3.34 and 3.35 display also the evolution of eigenvalues λ_{max}, λ_{min}, λ^+, and λ_c for the other values of α_{ox}. These data allows one to make the following conclusions:

- Changes in eigenvalues for different α_{ox} are similar;
- Like in the case of $\alpha_{ox} = 1.0$, it is possible to consider four typical subintervals – i.e., the setting of natural balance of species concentrations, the accumulation of radicals (increase in λ^+), heat explosion (origination of λ_c), approaching equilibrium ($\lambda^+, \lambda_c \to 0$).
- Magnitudes λ^+ at all values of α_{ox} reach their maximum magnitudes in the heat explosion zone.
- At deviation from stoichiometry, the zone of notable complex values (λ_c) expands.

Reacting System "H_2S +Air"

For conditions of "H_2S (hydrogen sulphide) + air" mixture ignition in adiabatic BR, the module of eigenvalues calculation was used to calculate the variation of the matrix J^{γ}_{ik} eigenvalues. To solve this problem, the full (not reduced) chemical mechanism was

Downloaded from https://www.cambridge.org/core. Nottingham Trent University, on 17 Aug 2019 at 02:05:11, subject to the Cambridge Core terms of use, available at https://www.cambridge.org/core/terms. https://doi.org/10.1017/9781108581714.003

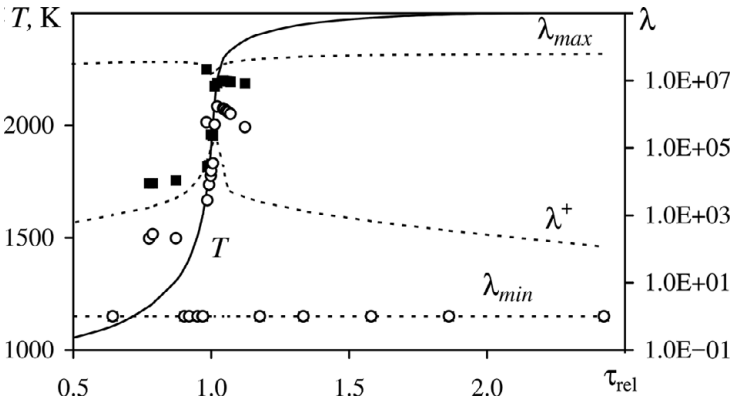

Figure 3.36 Evolution of eigenvalues for reacting medium, "H_2S + air," α_{ox} = 1.0; (τ_{dm}= 490μs); T_0 = 1000 K; ■ – $Re|\lambda_c|$, O –$Im|\lambda_c|$.

adopted from the papers [26; 110], which included 25 species (S, S_2, H, H_2, O, O_2, N, N_2, H_2O, OH, H_2O_2, HO_2, HS, H_2S, SO, SO_2, HS_2, SO_3, HO_2S, HO_3S, HOS, HSO, H_2O_2S, H_2SO, H_2OS, HSO_2, and H_2S_2) and 121 reactions. The calculations are performed in the range of change in the excess equivalence ratio α_{ox} = 0.6 . . . 1.5 at p = 1 atm; T_0 = 1000 K. Figure 3.36 displays the variation of temperature and eigenvalues at α_{ox} = 1.0 subject to reduced coordinate (τ_{rel}) at τ_{dm}= 490μs. The maximum temperature at the combustion final stage is about 2500 K. By analogy with the "CH_4 + air"combustion, the eigenvalue variation may be divided into four sub-intervals – i.e., establishment of the natural balance of species concentrations, the accumulation of intermediate species, heat explosion zone, and approaching chemical equilibrium. Hydrogen sulphide combustion in air is approximately accompanied the identical nature of the process and eigenvalues behavior to those of the methane combustion:

- The value of λ_{max} does not practically change with the change in temperature (and does not even reflect the rise in the heat explosion zone).
- The value of $\lambda_{min} \approx 0$, which is caused by availability of nitrogen considered to be the inert specie.
- The value of λ^+ increases at accumulation of intermediate species to reach its peak in the heat explosion zone.
- The complex values of λ_c arise ahead of the heat explosion zone and reach the peaks therein and then vanish.

The availability of notable "irregularity" in evolution of complex eigenvalues should be underlined.

Figures 3.37 and 3.38 show the temperatures and variation of eigenvalues for α_{ox} = 1.5 and α_{ox} = 0.6. Note that with the increase in α_{ox} the time of reaching the heat explosion "center" (τ_{dm}) decreases, but the pattern of the evolution does not vary. Only the areas of large values of complex numbers λ_c expand somewhat.

Downloaded from https://www.cambridge.org/core. Nottingham Trent University, on 17 Aug 2019 at 02:05:11, subject to the Cambridge Core terms of use, available at https://www.cambridge.org/core/terms. https://doi.org/10.1017/9781108581714.003

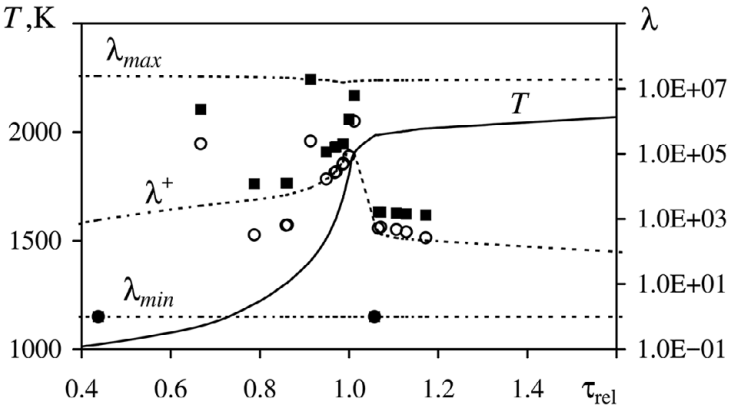

Figure 3.37 Evolution of eigenvalues for reacting medium, "H_2S + air," α_{ox} = 1.5; (τ_{dm}= 392μs); T_0 = 1000 K; ■ – $Re|\lambda_c|$, O –$Im|\lambda_c|$.

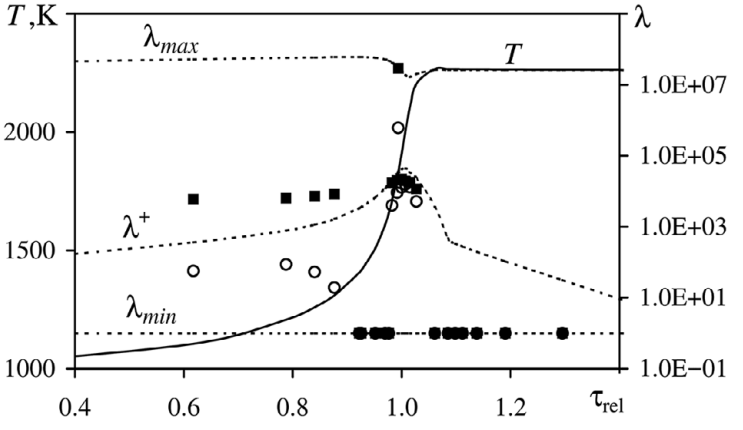

Figure 3.38 Evolution of eigenvalues for reacting medium, "H_2S + air," α_{ox} = 0.6; (τ_{dm}= 655μs); T_0 = 1000 K; ■ – $Re|\lambda_c|$, O –$Im|\lambda_c|$.

3.4.3 Comparison of Number of Integration Steps for Explicit and Implicit Finite Difference Schemes in Ignition Calculation

The explicit schemes of the solution of stiff differential equations are known to have the integration step constraints imposed by stability conditions. For instance, the following constraints are applied to Euler's and the Runge–Kutta methods:

$$h_E \leq 2/\lambda_{max}; \;\; h_{RK} \leq 2.8/\lambda_{max}. \tag{2.110}$$

While calculating the combustion with the help of detailed chemical kinetics equations, these constraints result in a very small integration step. However, because of the simplicity of implementation of explicit procedures, attempts to expand the region of

Downloaded from https://www.cambridge.org/core. Nottingham Trent University, on 17 Aug 2019 at 02:05:11, subject to the Cambridge Core terms of use, available at https://www.cambridge.org/core/terms. https://doi.org/10.1017/9781108581714.003

their stability do not cease. For example, the paper [157] proposes the second-order explicit methods with the constraints:

$$h_c \leq 0.81q^2/\lambda_{max}, \tag{2.123}$$

where q is the number of iterations at making the step, which allows the integration of the stiff equations with the notably larger step (at $q = 5$, one gets $h_c \leq 20.3/\lambda_{max}$). Thus, the area of application of explicit methods expands to make the following problems acquire a practical interest:

– determination of the list of reacting media and state parameters permitting the application of advanced explicit methods;
– determination of the possibility of increasing the explicit methods stability for deeper penetration into the analysis of stiff equations of chemical kinetics.

To evaluate the chances for application of explicit schemes, it is necessary to define, by some method, the number on integration steps for such schemes (K_1) in the combustion analysis. It is apparent that the "direct method" of analysis with application of the somewhat explicit method is not acceptable, since the number of integration steps may be extremely great (up to 10^8 and greater), which will cause a vast amount of computations. This is why this research employs another K_1 calculation technique using the tool for the determination of the Jacobian matrix (J^{γ}_{ik}) eigenvalues (λ_i). The maximum modulo thereof (λ_{max}) allows defining the local magnitude of integration step (h_{ex}) using the explicit scheme. Then, during calculation of the combustion process by the implicit scheme [85, 86], it is possible to define eigenvalues simultaneously for the entire combustion process and then to estimate the total number of integration steps. The corresponding relationship can be easily derived from Formulas (2.110). For example, while applying the Runge–Kutta method to some elementary quantum of time Δt, one gets

$$\Delta K_1 = \frac{\Delta t}{h_{RK}} = \frac{\Delta t}{2.8}\lambda_{max}, \tag{3.67}$$

wherefrom follows

$$K_1 = \frac{1}{2.8}\int_0^{t_f} \lambda_{max}(t)dt, \tag{3.68}$$

where t_f is the time duration of process.

Hereinafter, let us consider the number K_1 being calculated for the application of the Runge–Kutta method. Besides, for definiteness, let us assume that if, in some calculation, $K_1 > 100{,}000$ is predicted, then the explicit method is not recommended for analysis of this problem (or one with close parameters).

Calculations of this type have been made for reacting mixture "CH_4 + air" in BR for various values of α_{ox} and p at initial temperature $T_0 = 1700$ K. Figure 3.39 shows the results at $\alpha_{ox} = 1$ and $p = 1$ atm. Let us describe them by stages of combustion process.

Downloaded from https://www.cambridge.org/core. Nottingham Trent University, on 17 Aug 2019 at 02:05:11, subject to the Cambridge Core terms of use, available at https://www.cambridge.org/core/terms. https://doi.org/10.1017/9781108581714.003

Table 3.15 Variation of step size (h_{ex}, h_{im}) and magnitudes of (K_1, K_2) at explicit and implicit schemes at the first stage of combustion [156]* from A. L. Abdullin, V. I. Naoumov, and V. G. Krioukov, "Evaluation of Eigenvalues for the Analysis of Combustion and Chemical Non-Equilibrium Flows," AIAA SciTech Forum. 55th AIAA Aerospace Science Meeting, AIAA 20017–0662, pp. 1–12, Grapevine, TX, 2017, reprinted by permission of the American Institute of Aeronautics and Astronautics, Inc.

$\tau(s)$	λ_{max}	h_{ex}	h_{im}	K_1	K_2
0.4^{-14}	0.14^{15}	2.0^{-14}	0.2^{-14}	0.203	4
0.6^{-13}	0.16^{14}	1.75^{-13}	0.16^{-13}	0.765	16
0.92^{-10}	0.187^{11}	1.5^{-10}	0.16^{-10}	2.79	60
0.107^{-6}	0.528^{9}	0.53^{-8}	0.838^{-8}	22.1	165
0.66^{-6}	0.51^{9}	0.54^{-8}	1.67^{-8}	123	231
0.121^{-5}	0.509^{9}	0.54^{-8}	6.7^{-8}	223	260
0.222^{-5}	0.509^{9}	0.54^{-8}	13.4^{-8}	406	275

* Superscript at the number means the exponent, for example: $0.4^{-14} = 0.4 \times 10^{-14}$

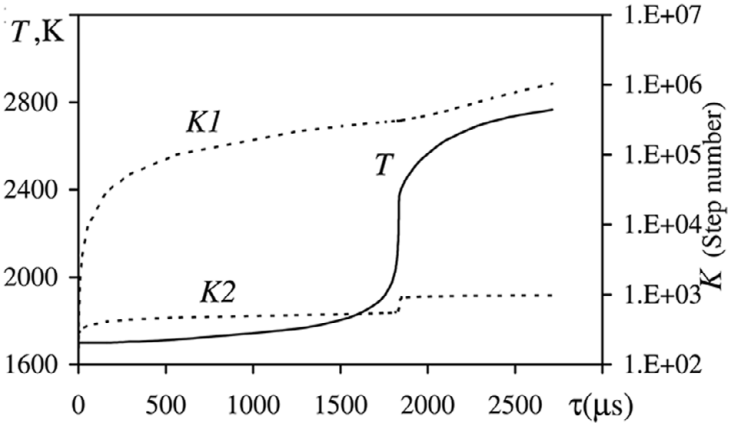

Figure 3.39 Variation of reacting medium temperature (T) and integration steps number at $\alpha_{ox} = 1.0$; $p = 1$ atm; $T_0 = 1700$ K (basic mode); K_1 – explicit scheme; K_2 – implicit scheme [156]. From A. L. Abdullin, V. I. Naoumov, and V. G. Krioukov, "Evaluation of Eigenvalues for the Analysis of Combustion and Chemical Non-Equilibrium Flows," AIAA SciTech Forum. 55th AIAA Aerospace Science Meeting, AIAA 20017–0662, pp. 1–12, Grapevine, TX, 2017, reprinted by permission of the American Institute of Aeronautics and Astronautics, Inc

The first stage is described by extremely high artificial stiffness ($\lambda_{max} = 10^{15}$), but the numbers of steps K_1 and K_2 at this stage are comparable (see Table 3.15). This results from the following:

– The integration step size at the explicit scheme is defined from Relationship (2.110).
– The integration step size at the implicit scheme is set extremely low ($h_{im} \approx 10^{-15}$s) at first, and its increase is possible according to the algorithm (see Subsection 2.4.4) only after several steps are taken.

Downloaded from https://www.cambridge.org/core. Nottingham Trent University, on 17 Aug 2019 at 02:05:11, subject to the Cambridge Core terms of use, available at https://www.cambridge.org/core/terms. https://doi.org/10.1017/9781108581714.003

This brings about an unexpected result in the first subinterval when $K_1 \approx K_2 \approx 300$ steps.

In the radicals accumulation subinterval, the temperature remains, in fact, invariable, and λ_{max} varies insignificantly. Then, at the implicit scheme, the integration proceeds with large steps, and the number increases insignificantly (from 300 to 500 steps). However, at the explicit scheme, the value K_1 increases from 300 to 300,000 because of the subinterval's large length and small size of step h_{ex}.

At the heat explosion subinterval, the value of λ_{max} increases notably as well. Therefore, the step should reduce at explicit scheme while the number of steps (K_1) should increase significantly. Step h_{im} decreases also, and the number of steps K_2 increases from 500 to 800 at the implicit scheme, owing to a dramatic increase in concentration and temperature.

In approaching the equilibrium subinterval, the value of λ_{max} remains high while the temperature and composition vary insignificantly; therefore:

- The calculation takes only 200 steps by the implicit scheme.
- To reach chemical equilibrium by the explicit scheme, $5*10^5$ additional steps should be made.

Therefore, calculation of this mode by explicit scheme is inefficient and involves the problems, even with due allowance for the progress in the increase of explicit scheme stability. For example, with a tenfold increase in stability – in compliance with Formula (2.123) – the number of integration steps at the explicit scheme will increase approximately 100 times as compared with the implicit scheme.

Similar results are obtained in the comparison of explicit and implicit schemes for the other α_{ox} as well as the interval of $\alpha_{ox} = 0.6 \ldots 1.5$ at $p = 1$ atm for reacting system "CH_4 + air." At the same time, at high α_{ox}, it is possible to perform calculations by the explicit scheme as well. For example, Figure 3.40 shows the changes in magnitudes T, K_1, K_2, with time at $\alpha_{ox} = 8.0$ (other parameters being equal to those given in Figure 3.39). The total number of steps in the calculation by implicit scheme K_2 = 1000 steps, while at integration by explicit scheme, $K_1 \approx 100,000$ steps, which allows one to apply this scheme and, all the more, the advanced explicit methods as well. The decrease in K_1 is caused by low temperature ($T \approx 2000\,K$) of reacting system, which results in the decrease in reaction rates and, correspondingly, to the decrease in λ_{max}.

Figure 3.41 demonstrates the influence of pressure on magnitudes K_1 and K_2 at keeping the other parameters invariable. At pressure p = 0.1 atm, the following total values have been obtained: $K_1(f) = 5{\cdot}10^6$ steps and $K_2(f)$ = 1000 steps. A notable increase in the number of steps $K_2(f)$ = 1000 steps. proved unexpected compared with the basic mode (Figure 3.39) at the decrease in pressure. It is known that at the decrease in pressure, the reaction rate drops and, accordingly, λ_{max} decreases; hence, the stiffness of equations decreases as well. On the other hand, the time of ignition renders about 10 times higher, which results in the increase in total number of integration steps. This result could hardly be foreseen if eigenvalues λ_{max} were calculated for few specific points. However, being aware of the entire path of its variation, the value of K_1 is defined sufficiently accurately. A similar calculation made for p = 10 atm outputs the

Downloaded from https://www.cambridge.org/core. Nottingham Trent University, on 17 Aug 2019 at 02:05:11, subject to the Cambridge Core terms of use, available at https://www.cambridge.org/core/terms. https://doi.org/10.1017/9781108581714.003

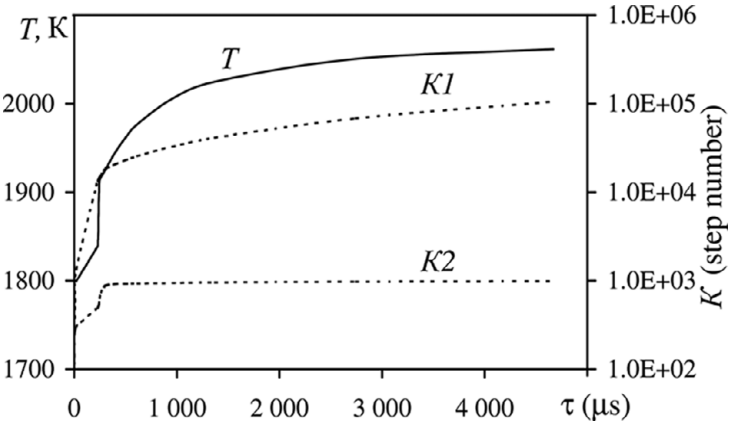

Figure 3.40 Variation of reacting medium temperature and integration steps number at combustion process at $\alpha_{ox} = 8.0$; $p = 1$ atm; $T_0 = 1700$ K. K_1 – explicit scheme; K_2 – implicit scheme [156]. From A. L. Abdullin, V. I. Naoumov, and V. G. Krioukov, "Evaluation of Eigenvalues for the Analysis of Combustion and Chemical Non-Equilibrium Flows," AIAA SciTech Forum. 55th AIAA Aerospace Science Meeting, AIAA 20017–0662, pp. 1–12, Grapevine, TX, 2017, reprinted by permission of the American Institute of Aeronautics and Astronautics, Inc

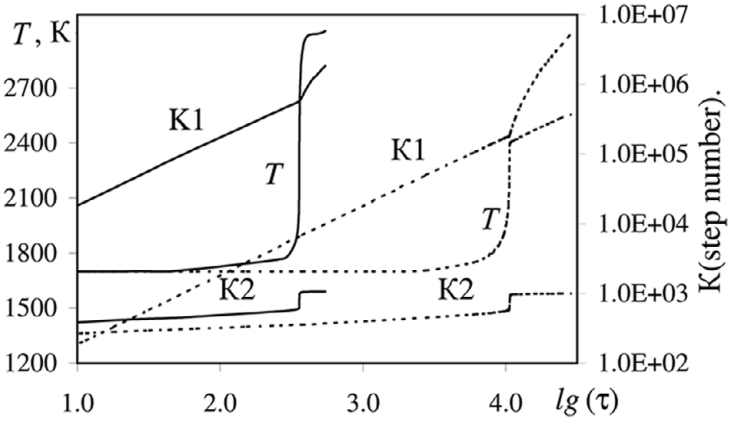

Figure 3.41 Variation of reacting medium temperature and integration step number at combustion process calculation at $\alpha_{ox} = 1.0$; $T_0 = 1700$ K. K_1 – explicit scheme; K_2 – implicit scheme; (— $p =$ 0.1 atm; — $p = 10$ atm.) [156]. From A. L. Abdullin, V. I. Naoumov, and V. G. Krioukov, "Evaluation of Eigenvalues for the Analysis of Combustion and Chemical Non-Equilibrium Flows," AIAA SciTech Forum. 55th AIAA Aerospace Science Meeting, AIAA 20017–0662, pp. 1–12, Grapevine, TX, 2017, reprinted by permission of the American Institute of Aeronautics and Astronautics, Inc

following values: $K_1(f) \approx 10^6$ steps, while $K_2(f) \approx 1000$ steps, which means that the number of steps $K_1(f)$ virtually does not increase compared with the basic mode. The same resulted from the influence of aforementioned opposite factors – that is, an increase in λ_{max} and a decrease in the integration interval.

Downloaded from https://www.cambridge.org/core. Nottingham Trent University, on 17 Aug 2019 at 02:05:11, subject to the Cambridge Core terms of use, available at https://www.cambridge.org/core/terms. https://doi.org/10.1017/9781108581714.003

3.4.4 Comparison of Explicit and Implicit Finite Difference Schemes in Calculation of Nonequilibrium Flows in the Nozzles

It is known that a significant chemical nonequilibrium can occur in nozzles of aerospace propulsion systems, caused by a drastic decrease in combustion product temperature over the nozzle length, high flow velocities, and, hence, comparatively small residence time of combustion products. Proper simulation of chemical nonequilibrium flow allows one to determine the working medium chemical composition, including harmful species, combustion products electrophysical characteristics, and the losses of specific impulse because of the shift from chemical equilibrium. This problem has been considered in many publications [56, 158, 159, 160, 161]. It has been shown, for example, that for conventional liquid rocket propellants, chemical kinetics equations at high temperatures and pressures at the entrance to the nozzle ($p_{oc} \approx 100$ atm.; $T_{oc} \approx 3000$) K are very stiff. This is why the application of explicit schemes of the Runge–Kutta type can lead to extremely small integration steps, especially at the initial stage of integration. At the same time, there are no estimates of the total number of potential integration steps ($K_1(f)$) in a case of the explicit schemes application. This is why it is not perfectly clear to what extent the advance in the development of stable explicit methods [78, 157] will allow their application to the simulation of high-temperature flows in the nozzles. To solve this problem, the tool for the calculation of eigenvalue variation is incorporated (see Figure 3.32) into the computer code for analyzing the inverse problem of the nozzle [162]. The mathematical model comprises the following equations:

– equations of chemical kinetics for PFR, obtained from (2.25):

$$\frac{d\gamma_i}{dx} = \frac{1}{V_g}\left(-e^{\gamma_i}\sum \nu_{ij}\Omega_j + \sum\sum \nu_{qj}\Omega_j\right) \equiv f_i^{\gamma};\ i,p,q = 1,\ldots,n_b;\ j = 1,\ldots,2m_c, \tag{3.69}$$

where $\Omega_j = k_j\left(\frac{p}{R_0T}\right)^{\bar{m}_j} exp\left(-\sum_p n_{pj}\gamma_p\right);\ \bar{m}_j = m_j + \sum n_{pj} - 1;\ \gamma_i = -ln\ r_i$

– equations of motion and energy:

$$\frac{dV_g}{dx} = \frac{R_0T}{V_g\sum_i r_i\mu_i}\varphi'(x); \quad h_{oc} - \frac{V_g^2}{2} = \frac{\sum_i H_i r_i}{\sum_i r_i\mu_i}; \tag{3.70}$$

where V_g is the gas velocity h_{oc} is mass specific enthalpy at the entrance to the nozzle

– the closure equation of the relationship $p = p(x)$ in the following form:

$$\varphi(x) = -ln\ (p/p_{oc}).$$

The calculation algorithm is based on Pirumov's method [85]. N The results of the application of this model for the calculation of nonequilibrium processes in LPRE and SPRE are given next.

Downloaded from https://www.cambridge.org/core. Nottingham Trent University, on 17 Aug 2019 at 02:05:11, subject to the Cambridge Core terms of use, available at https://www.cambridge.org/core/terms. https://doi.org/10.1017/9781108581714.003

Potential of Explicit Schemes in the Calculation of Nonequilibrium Processes in LPRE Nozzles

A comparison of the efficiency of explicit and implicit schemes in their application to the calculation of flows in LPRE nozzles has been made for combustion products of propellants "kerosene + O_2" (hereinafter, LRP1) and "nitrogen tetroxide (NT, N_2O_4) + unsymmetrical dimethylhydrazine (UDMH – $H_2N_2(CH3)2$)" (hereinafter, LRP2). Calculations have been made for nozzles with throat radiuses (r_m) of 0.006 m to 0.06 m and a nozzle geometric degree of expansion (the ratio of the nozzle exit area to the throat area) of f_a = 53 at the following parameters: equivalence ratio $\alpha_{ox} = 1.0$, pressure at the entrance to the nozzle p_{oc} = 20 ... 100 atm. Note here that the nozzle shape does not vary, but its length increases with the increase in radius. For LRP1, the reacting medium comprises 16 species and 47 reactions adopted from the paper [93], while for LRP2, the reacting medium comprises 26 species and 82 reactions adopted from the same paper. Combustion products have been assumed to be still at chemical equilibrium in the nozzle convergent portion up to the cross section where $x_{rel} = x/r_m = 10.9$ and the velocity reaches about 100 m/s. Then, for calculation, a model of chemical nonequilibrium flows is used.

The results of the calculations for both propellants are shown in Table 3.16 and in Figures 3.42 and 3.43. Figure 3.42 shows variation of values K_2 and J_2 (the number of integration steps by the implicit scheme and the number of recalculations of the Jacobian, respectively) over the nozzle relative length. The total number of steps of integration by implicit scheme $K_2(f) \approx 330$, of which 130 steps relate to the nozzle subsonic section. The vertical line at initial section is caused by setting a very small initial integration step for reliability of the calculations.

Weak and irregular dependence of values of $K_2(f)$ on governing parameters T_{oc}, p_{oc}, r_m is observed, although the losses of specific impulse ξ_{dq} differ significantly (Table 3.16). The magnitude of J_2 is more sensitive to variation of these parameters. It changes by about two times at the variation of λ_{max} by 100 times in the region under analysis.

Table 3.16 Comparison of explicit and implicit finite difference schemes of calculation of chemical nonequilibrium flows in LPRE nozzles (h_{fuel}, h_{ox} – enthalpy of fuel and oxidizer; M – Mach number); ξ_{dq}- coefficient of losses because of chemical noneqilibrium*

Propellant characteristics	p_{oc} (atm)	T_{oc}(K)	$r_m(m)$	$\xi_{dq}(\%)$	$K_1(M<1)$	$K_1(M>1)$	K_2	J_2
Kerosene + O_2 (LPR1)	100	3740	0.06	1.07	0.233^{+10}	0.029^{+10}	330	109
h_{fuel} = −1948 kJ/kg			0.006	2.31	0.245^{+9}	0.017^{+9}	296	77
h_{ox} = −398 kJ/kg	20	3496	0.06	2.82	0.533^{+9}	0.028^{+9}	335	61
			0.006	5.08	0.500^{+8}	0.058^{+8}	290	48
NT + UDMH (LPR2)	100	3461	0.06	1.06	0.644^{+9}	0.035^{+9}	315	82
h_{fuel} = 823,6 kJ/kg			0.006	2.35	0.625^{+8}	0.04^{+8}	329	51
h_{ox}= −212,5 kJ/kg	20	3280	0.06	3.11	0.158^{+9}	0.009^{+9}	285	51
			0.006	5.27	0.153^{+8}	0.007^{+8}	294	37

* Superscript at the number means the exponent, for example: $0.233^{+}10 = 0.233 \cdot 10^{+10}$

Downloaded from https://www.cambridge.org/core. Nottingham Trent University, on 17 Aug 2019 at 02:05:11, subject to the Cambridge Core terms of use, available at https://www.cambridge.org/core/terms. https://doi.org/10.1017/9781108581714.003

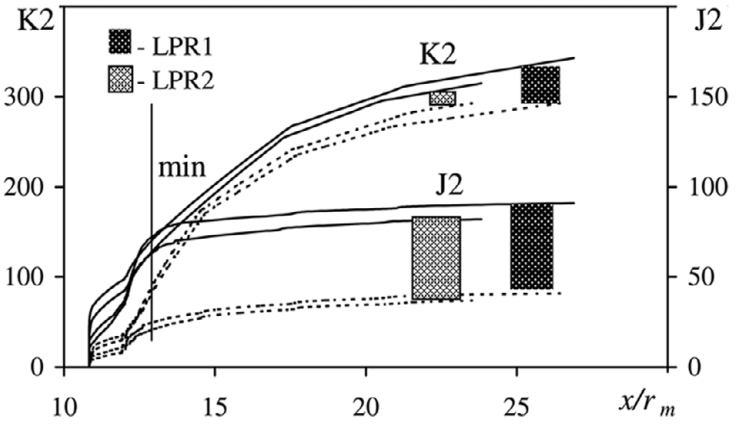

Figure 3.42 Variation of K_2 and J_2 over the nozzle relative length (propellants LRP1 and LRP2); — (p_{oc} = 100 atm., r_m = 0.06 m); — (p_{oc} = 20 atm, r_m = 0.006 m).

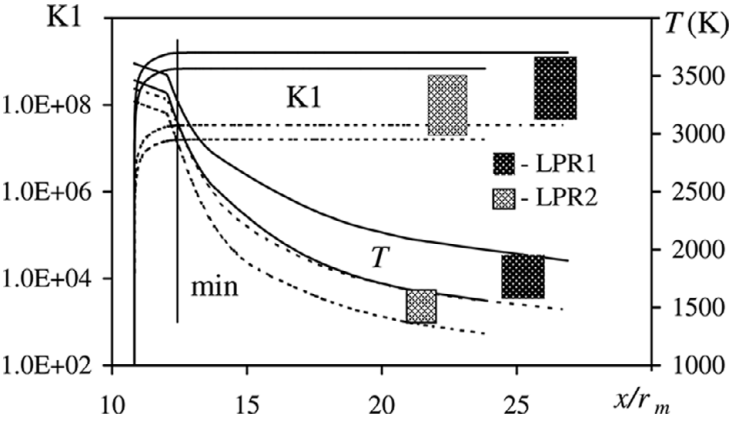

Figure 3.43 Variation of K_1 and temperature over the nozzle relative length (propellants LRP1 and LRP2); — (p_{oc} = 100 atm., r_m = 0.06 m); — (p_{oc} = 20 atm., r_m = 0.006 m).

Figure 3.43 shows variation in combustion product temperature and K_1 value (explicit Runge–Kutta scheme of the fourth order) subject to relative length x_{rel}. It is apparent that the number of steps $K_1(f)$ is extremely great and sensitive to governing parameters T_{oc}, p_{oc}, r_m. For example, in the case of LRP1 (T_{oc} = 3740 K), the maximum value of $K_1(f)$ equals 2.6×10^9, while for LRP2 (T_{oc} = 3461 K), $K_1(f)$ makes 0.7×10^9. With a decrease in p_{oc}, the number of steps $K_1(f)$ decreases, owing to the decrease in λ_{max}, while at a decrease in r_m, it occurs due to the reduction of the integration interval. At a simultaneous p_{oc} fivefold decrease and r_m tenfold decrease, in the region under analysis, $K(f) = 16 \times 10^6$ steps, which is also a very high value. It should be pointed out that the main volume of calculations is performed for the subsonic section of the nozzle (see Figure 3.43). It means that the parameters in this region are close to equilibrium values. Therefore, it is frequently assumed that chemical equilibrium is retained to the nozzle

Downloaded from https://www.cambridge.org/core. Nottingham Trent University, on 17 Aug 2019 at 02:05:11, subject to the Cambridge Core terms of use, available at https://www.cambridge.org/core/terms. https://doi.org/10.1017/9781108581714.003

throat (minimum cross section), and the nonequilibrium model can be exploited starting from the nozzle throat. This assumption lets one reduce the number of steps K_1 (for these particular conditions) by approximately a factor of 10 (Table 3.16). However, in this case also, the number of potential steps of integration K_1 (M > 1) remains very significant, and even the advanced explicit schemes [157] may hardly be applied the solution of this problem. Thus, explicit schemes used for calculation of chemical nonequilibrium process in LPRE can not compete thus far with implicit methods.

Potential of Explicit Schemes in the Calculation of Nonequilibrium Processes in SPRE Nozzles

The efficiency of explicit and implicit schemes in the case of SPRE nozzles has been evaluated for the following propellants:

– SP1 ($C_{10.8760}H_{46.546}O_{25.806}AL_{9.665}CL_{1.517}N_{6.781}$ – metalized propellant)
– SP2 ($C_{23.498}H_{30.259}O_{34.190}N_{10.011}$ – nitrocellulose propellant)

The reacting medium for SP1 propellant included 33 species and 6 reactions adopted from the papers [25, 93], while that for SP2 comprises 20 species and 48 reactions adopted from the same papers. It is apparent that the versions of SP1 calculation are "stiffer" than those for SP2. Calculations were performed at the following parameters: $p_{oc} = 20 \ldots 70$ atm., $r_m = 0.005 \ldots 0.05$ m and geometric degree of expansion $f_a = 33.9$. The model of chemical nonequilibrium flows is used downstream of cross section $x_{rel} = 2.2$. The results of the calculations are listed in Table 3.17 and Figures 3.44 and 3.45.

For both versions of calculations (Table 3.17), notable losses caused by chemical nonequilibrium are characteristic; that is, the composition of combustion products at the nozzle exit deviates from the chemical equilibrium. Particularly, in SP2 version, the composition is "frozen," even at the subsonic section, while the chemical equilibrium calculation predicts its further notable change.

Figure 3.44 shows the variation of values K_2 and J_2 over the nozzle relative length. Values of $K_2(f)$ are small: in the case of SP1, $K_2(f) \approx 250$ on average, while for the SP2

Table 3.17 Comparison of explicit and implicit finite difference schemes of calculation of chemical nonequilibrium processes in SPRE nozzles (h_p – propellant enthalpy)*

Propellant characteristics	p_{oc} (atm)	T_{oc}(K)	r_m	ξ_{dq}(%)	K_1(M < 1)	K_1(M > 1)	K_2	J_2
Propellant SP1	70	3638	0.05	1.84	0.423^{+8}	0.025^{+8}	345	79
$h_p = -1046$ kJ/kg			0.005	2.19	0.410^{+7}	0.010^{+7}	235	44
	20	3495	0.05	2.30	0.134^{+8}	0.005^{+8}	255	50
			0.005	3.27	0.131^{+7}	0.003^{+7}	230	41
Propellant SP2	70	2361	0.05	2.82	0.145^{+7}	0.003^{+7}	499	39
$h_p = -1964$ kJ/kg			0.005	2.88	0.155^{+6}	0.003^{+6}	472	31
	20	2357	0.05	2.54	0.469^{+6}	0.015^{+6}	493	33
			0.005	2.51	0.456^{+5}	0.017^{+5}	417	28

* Superscript at the number means the exponent, for example: $0.233^{+}10 = 0.233 \cdot 10^{+10}$.

Downloaded from https://www.cambridge.org/core. Nottingham Trent University, on 17 Aug 2019 at 02:05:11, subject to the Cambridge Core terms of use, available at https://www.cambridge.org/core/terms. https://doi.org/10.1017/9781108581714.003

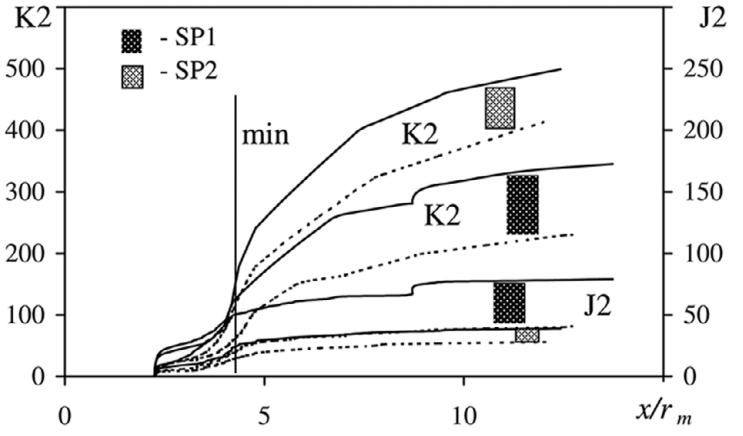

Figure 3.44 Variation of K_2 and J_2 over the nozzle relative length (propellants SP1 and SP2); — (p_{oc} = 70 atm., r_{m} = 0.05 m); — (p_{oc} = 20 atm., r_{m} = 0.005 m).

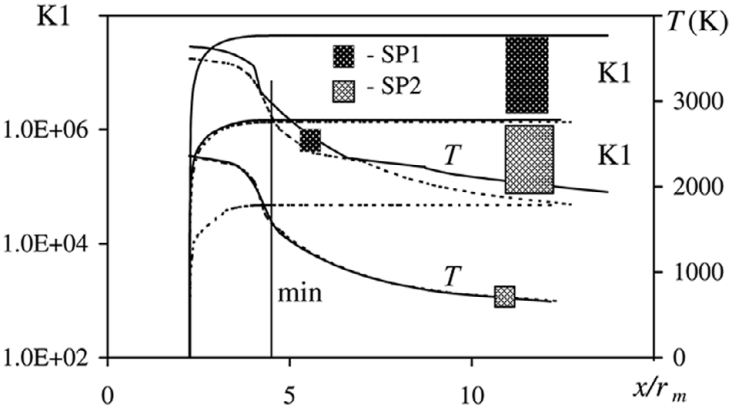

Figure 3.45 Variation of K_1 and temperature over the nozzle relative length (propellants SP1 and SP2); — (p_{oc} = 70 atm., r_{m} = 0.05 m); — (p_{oc} = 20 atm., r_{m} = 0.005 m).

version, $K_2(f) \approx 400$. Thus, calculation of a less "stiff" reacting system (the higher the temperature, the "stiffer" the system of equations) requires more integration steps. This feature results from the peculiarities of the algorithm exploiting the scheme with the "frozen" Jacobian. It follows from Table 3.17 that the Jacobian in the SP2 version recalculates notably less frequently than in the SP1 version. This feature of the scheme with the "frozen" Jacobian results in a larger number of integration steps. It should be noted that in the case of the SP1 version, a multiple division of the integration step occurs in the phase transition region of $Al_2O_3^*$ from a liquid state to a solid state. This feature is described by the break in the diagrams of variation of K_2 and J_2.

Figure 3.45 displays the variation of combustion products temperature and values of K_1 (explicit scheme) for both propellants subject to x_{rel}. It is apparent that the number of steps $K_1(f)$ is very great and sensitive to governing parameters T_{oc}, p_{oc}, r_{m}. The SP1

Downloaded from https://www.cambridge.org/core. Nottingham Trent University, on 17 Aug 2019 at 02:05:11, subject to the Cambridge Core terms of use, available at https://www.cambridge.org/core/terms. https://doi.org/10.1017/9781108581714.003

version, despite higher temperature T_{oc} (compared with the SP2 version) features the number of steps K_1 10 times smaller. With a decrease in pressure p_{oc} and radius r_{m}, K_1 decreases approximately pro rata with the product $p_{oc} \times r_{\text{m}}$. The majority of the calculations are performed for the nozzle subsonic section (see Figure 3.43). If chemical equilibrium is assumed to be retained to the minimum section, then the number of steps by the explicit scheme will decrease by 20 . . . 40 times (Table 3.17). Then, even for the calculation of chemical nonequilibrium flows of SP1 combustion products, the advanced explicit schemes are likely to be used. The SP2 reacting medium features stiffness ≈ 50 times less than that for the SP1 version, and the advanced schemes may be applied to the entire length of the nozzle.

The performed numerical calculations of eigenvalues with the application of the developed module of eigenvalues calculation have displayed that

– Explicit schemes (including advanced ones) are unacceptable for nozzles of typical LPRE because of extremely big number of integration steps.
– Explicit scheme are acceptable (owing to lower stiffness of chemical kinetic equations) at SPRE nozzle smaller sizes and lower pressures as well as at relatively low temperatures of working medium.

3.4.5 Pulse Combustion and Eigenvalues

It is known that a pulsating combustion is observed and frequently used in combustion units. Analysis of this type of combustion is described in multiple publications related, for example, to pulsations in combustion chambers of rocket engines [160], pulse-combustion boilers [163], solid industrial waste smokeless busting [164, 165], etc. These publications consider the combustion process to be a source of mechanical or thermal energy that, influenced by gas pulsations, acquires a periodic component, without which the pulsating combustion mode is impossible. However, the combustion process can possess an inherent instability – for example, the flame front hydrodynamic instability [166] or kinetic instability of the chemical reactions at the interaction of fuel and oxidizer. "The analytical model" for the computation of instable combustion (including the pulsating combustion) in PSR is proposed in the paper [91], while the reacting medium is described by only two reactions. But in the case of actual reacting systems described by complex chemical mechanisms, the pulsating combustion areas may be theoretically revealed only by numerical analysis [167, 168] on the basis of invariant computer programs of combustion calculation.

This procedure is applied herein for the detection of pulsating combustion modes in PSR for the "CH_4 + air" reacting system. Calculations have been performed in the area of "extinction line" (extinction of combustion) to reveal several such modes. The description and analysis of one of them are given in the following paragraphs.

Calculation has been made for PSR by the RISAV program for "CH_4 + air" propellant at the following values of the equivalence ratio, residence time, and pressure – i.e., $\alpha_{ox} = 0.66$; $\tau_p = 163\ \mu s$; $p = 16$ atm. The value of the heat feed (Q_s) per the unit of mass of incoming reactants $Q_s = 153$ kJ/kg – see Formula (2.34) – has been selected

Downloaded from https://www.cambridge.org/core. Nottingham Trent University, on 17 Aug 2019 at 02:05:11, subject to the Cambridge Core terms of use, available at https://www.cambridge.org/core/terms. https://doi.org/10.1017/9781108581714.003

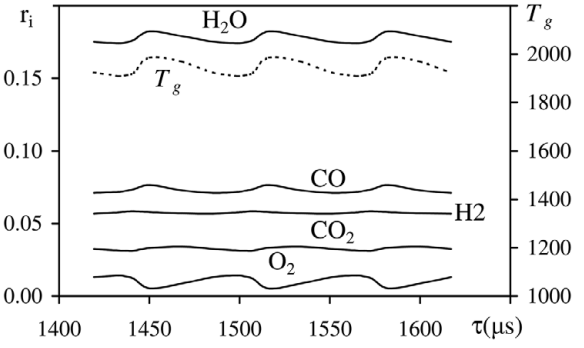

Figure 3.46 Variation of temperature T_g and concentrations of substances H_2O, CO, H_2, CO_2, O_2 at $\alpha_{ox} = 0.66$; $\tau_p = 163\,\mu s$; p = 16 atm.

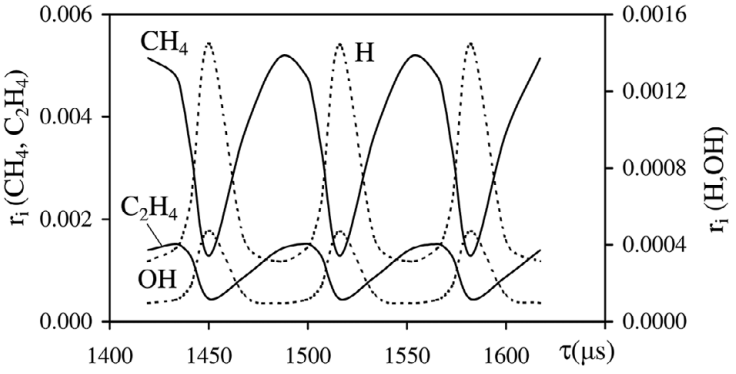

Figure 3.47 Variation of concentrations of substances CH_4, H, C_2H_4, OH at $\alpha_{ox} = 0.66$; $\alpha_{ox} = 0.66$; $\tau_p = 163\,\mu s$; p = 16 atm.

so that the chemical equilibrium temperature T_{eq} (that is, the temperature in the reactor at $\tau_p \to \infty$ reaches the value of 2050 K). Reactants enter the reactor with the following parameters: $T_{in} = 298$ K; $r_{CH_4} = 0.1361$; $r_{O_2} = 0.1814$; $r_{N_2} = 0.6825$. The mechanism of reactions taken mainly from the paper [93] includes 47 reactions and 28 substances. The initial composition of the reacting mixture and temperature in the reactor have been set to chemical equilibrium at T_{eq} = 2050 K, while thereafter, as thermodynamic processes occur therein, parameters of combustion products approach their steady-state values. This calculation has brought about a self-oscillating steady-state mode with the oscillation period $\tau_{ps} = 68\,\mu s$. The variation of the temperature and combustion products main substances concentrations are shown in Figures 3.46 and 3.47, and Table 3.18 lists the minimum and maximum values of these pulsation characteristics.

It is seen that notable self-oscillations are observed in this mode. Temperature pulsates synchronously with the concentrations of combustion products stable components H_2O and CO_2, since the main heat release is caused by the reaction of formation of these substances.

Downloaded from https://www.cambridge.org/core. Nottingham Trent University, on 17 Aug 2019 at 02:05:11, subject to the Cambridge Core terms of use, available at https://www.cambridge.org/core/terms. https://doi.org/10.1017/9781108581714.003

Table 3.18 Characteristics of pulsating values at $\alpha_{ox} = 0.66$; $\tau_p = 163\ \mu s$; $p = 16$ atm

	T_g(K)	r_{H_2O} (%)	r_{CO_2} (%)	r_{H_2} (%)	r_{O_2} (%)	r_{CO} (%)	r_{CH_4} (%)	$r_{C_2H_2}$ (%)
Max	1986	18.24	3.405	5.858	1.421	7.664	0.5170	0.734
Min	1909	17.41	3.125	5.690	0.872	7.113	0.1286	0.670
δ(%)	3.9	4.55	8.22	2.87	38.63	7.19	75.12	8.72
abs(Δ)	77	0.83	0.28	0.17	0.55	0.55	0.388	0.064

Variation of concentrations of CH_4 and O_2 reactants are opposite in phase with pulsations of H_2O and CO_2 concentration that causes the maintaining of self-oscillations. A very significant amplitude of the pulsations of reactants with respect to their average concentrations should be pointed out. Besides, amplitudes of pulsation of intermediate substances, H and OH, are also high (approximately 70% with respect to maximum values).

It is known that the oscillations of parameters in mathematical models are likely to result from instability of numerical schemes or errors in the algorithm or software. This is why for confirmation of the validity of analysis, a determination of eigenvalues is frequently used. The character of solving the system of ordinary differential equations is known to be defined by eigenvalues of the Jacobian matrix, and forming the set of said values for different solutions, self-oscillating components can be identified. Let us remember that the chemical kinetics equations (2.29) are nonlinear ones – that is, eigenvalues of the Jacobian matrix may be variable – but for a rather small time interval, these equations may be linearized to write their general solution as follows:

$$r_q = A_q + \sum_{k=1}^{n_b} a_k \, exp\,(\lambda_k t), \tag{3.71}$$

where A_q, a_k are some constants, λ_k are eigenvalues, and t is time.

At changing over to the other time interval, values of A_q, a_k, λ_k will vary in a general case. Eigenvalues of λ_k are known to be negative, positive, and complex, and they are known to define the behavior of the solution (in our case, mole fractions r_q). The correlation between these values and the character of solving the linear ordinary differential equations is shown in the Table 3.19.

With all negative λ_k, the concentrations monotonically and asymptotically approach some equilibrium values (Version 1). Then, let us consider all negative λ_k for all other versions except for those specially mentioned. If the spectrum of eigenvalues includes at least one positive, then we have an ever-increasing solution (Version 2). If this spectrum has at least one pair of complex-conjugate eigenvalues (i.e., $\lambda = \alpha \pm i\beta$), then

– At $\alpha < 0$, the solution will be oscillatory damping (Version 3).
– At $\alpha > 0$, the solution will be oscillatory diverging.

Finally, if the spectrum has at least one pair of imaginary eigenvalues (i.e., $\lambda = \alpha \pm i\beta$) –solely an imaginary part of the complex number – then the solution will be self-oscillating with a constant amplitude (Version 4).

Downloaded from https://www.cambridge.org/core. Nottingham Trent University, on 17 Aug 2019 at 02:05:11, subject to the Cambridge Core terms of use, available at https://www.cambridge.org/core/terms. https://doi.org/10.1017/9781108581714.003

Table 3.19 Correlation between eigenvalues and character of solving the linear ordinary differential equations

Eigenvalues	Behavior of solution	Eigenvalues	Behavior of solution
Version 1: $\lambda < 0$	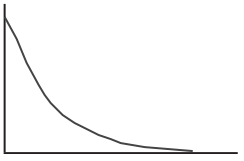	Version 3: $\lambda = \alpha \pm i\beta$, $\alpha < 0$	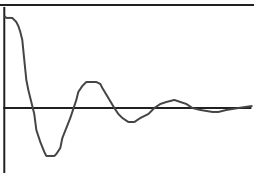
Version 2: $\lambda > 0$	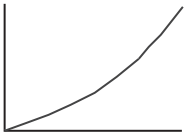		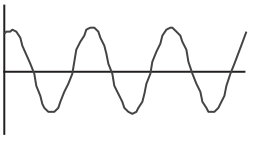

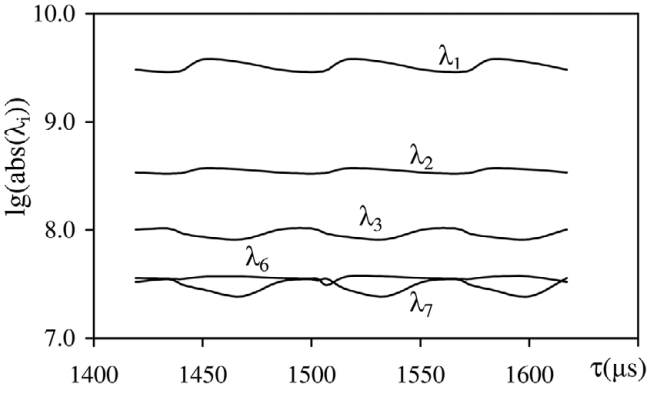

Figure 3.48 Variation of eigenvalues of λ_1, λ_2, λ_3, λ_6, λ_7 at $\alpha_{ox} = 0.66; \tau_p = 163\,\mu s$; p = 16 atm.

Versions of the solution behavior listed in the Table 3.18 are valid for linear ordinary differential equations and can be served as possible guidelines for nonlinear equations when eigenvalues vary during calculation. For the latter to be determined, the computer code is provided with the set of calculation of the entire spectrum of these values by the scheme shown in Figure 3.32, while the main results of the variation in eigenvalues are shown in Figures 3.48–3.50.

Twenty-eight eigenvalue variation curves (corresponding to the number of substances) have been defined, and eigenvalues are ranked by absolute value from abs $(\lambda_k) = 10^{10}$ to abs$(\lambda_k) = 10^2$. Figure 3.48 shows the variation of eigenvalues of λ_1, λ_2, λ_3, λ_6, and λ_7. These values oscillate but are real and negative, which is why they do not identify the self-oscillating behavior of the solution. The values of $\lambda_{12} \ldots \lambda_{18}$ and $\lambda_{21} \ldots \lambda_{28}$ are also real and negative. Figure 3.49 shows the change in eigenvalues of $\lambda_{4,5}$ and $\lambda_{8,9}$. The values are complex and conjugate, of the type

Downloaded from https://www.cambridge.org/core. Nottingham Trent University, on 17 Aug 2019 at 02:05:11, subject to the Cambridge Core terms of use, available at https://www.cambridge.org/core/terms. https://doi.org/10.1017/9781108581714.003

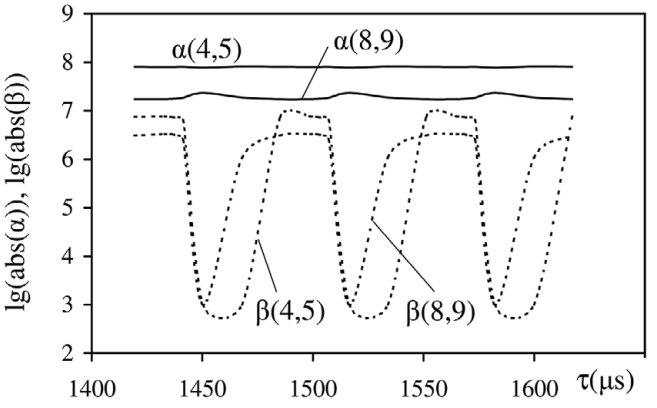

Figure 3.49 Variation of eigenvalues $\lambda_{4,5}$ and $\lambda_{8,9}$ at $\alpha_{ox} = 0.66; \tau_p = 163\,\mu s$; p = 16 atm.

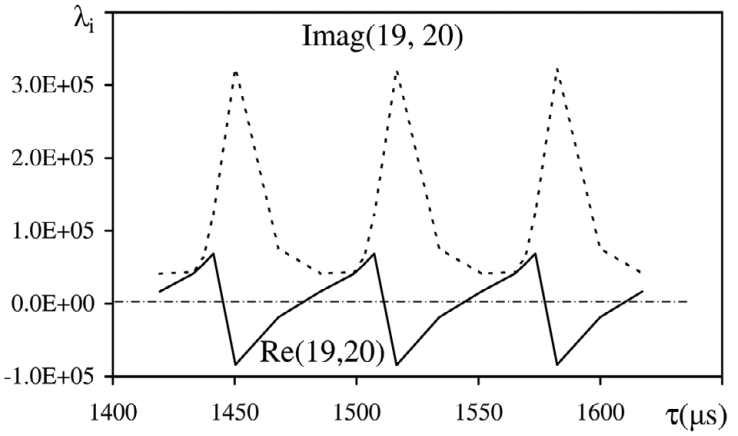

Figure 3.50 Variation of complex-conjugate eigenvalues $\lambda_{19,20}$ at $\alpha_{ox} = 0.66; \tau_p = 163\,\mu s$; p = 16 atm.

$\lambda = \alpha \pm i\beta$, but the values of real parts α are negative. The same behavior is characteristic of $\lambda_{10,11}$. Solutions identified by these eigenvalues are recurrent (Version 3) but do not describe the combustion process self-oscillations, since these are damping.

Figure 3.50 shows the variation of two remaining complex-conjugate values of $\lambda_{19,20}$. It is clear that they are not imaginary, which may identify self-oscillations (see Version 4). However, it is readily defined that real parts of these eigenvalues (α) during one period are both negative and positive.

At negative $\alpha = Re(\lambda_{19,20})$, the behavior features a damping character while at positive values, it features an increasing character. Note that this combination of parameters α causes the periodicity of the solution and in the considered example brings about the pulsations of combustion. Figure 3.50 allows one to make the conclusion

Downloaded from https://www.cambridge.org/core. Nottingham Trent University, on 17 Aug 2019 at 02:05:11, subject to the Cambridge Core terms of use, available at https://www.cambridge.org/core/terms. https://doi.org/10.1017/9781108581714.003

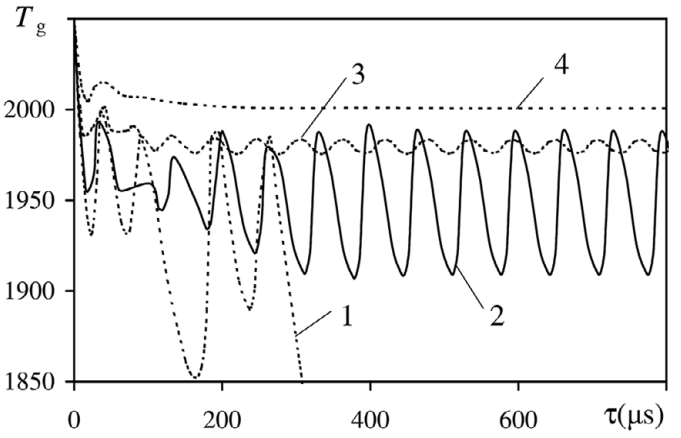

Figure 3.51 Character of "CH_4 + air" combustion in PSR at $\alpha_{ox} = 0.66$ p = 16 atm and different times of residence: 1) ($\tau_p = 150\,\mu s$); (2) ($\tau_p = 163\,\mu s$); (3) ($\tau_p = 200\,\mu s$); (4) ($\tau_p = 300\,\mu s$).

about equality of areas under negative and positive; therefore, the average value of α equals zero ($\bar{\alpha} = 0$) on the average within the period, which corresponds to Version 4 – that is, it corresponds to the periodic behavior.

If parameters α_{ox} and p preserved and residence time τ_p varies, the combustion conditions may vary. The preceding example describes the mode approximating to the attenuation line that isolates the combustion area from the noncombustion area [90]. Figure 3.51 shows the temperature variation T_g in reactor at differentτ_p. In all calculations, the gas initial composition and initial temperature in the reactor existed at chemical equilibrium at T_{eq} = 2050 K. At the mode-settling stage, irregular oscillations have been observed, caused by the combined effect of the following factors: the feed of reactants into the reactor, their mixing with chemical equilibrium mixture present in the reactor, and proceed of chemical reactions. Then, as the initial reacting medium is replaced, the influence of the initial composition in the reactor vanishes to set the steady-state vibrations (pulsations).

The presented temperature variations show that

- At $\tau_p = 150$ μs, combustion terminates after several oscillations.
- The pulsating mode at $\tau_p = 163$ μs already gets into the combustion area (replicates the cited example).
- At an increase in the residence time of up to $\tau_p = 200\,\mu s$ (i.e., at the displacement from the point of steady-state combustion in the reactor from the attenuation line – see Subsection 3.6.1, Figure 3.50) inside the combustion zone, pulsations originate as well, but of notably smaller amplitude.
- At $\tau_p = 300$ μs after the settling stage ends, combustion proceeds without pulsations.

Downloaded from https://www.cambridge.org/core. Nottingham Trent University, on 17 Aug 2019 at 02:05:11, subject to the Cambridge Core terms of use, available at https://www.cambridge.org/core/terms. https://doi.org/10.1017/9781108581714.003

At the same time, the entire spectrum of Jacobian matrix eigenvalues (3.63) has been defined for each of this calculation. Note here that

– In self-oscillating mode at $\tau_p = 200\,\mu s$, the complex-conjugate values with the real part (α) sign variation have been revealed (as at $\tau_p = 163\,\mu s$);
– In the steady-state section at $\tau_p = 300\,\mu s$ (i.e., without self-oscillations), no positive values have been revealed among real parts of λ_k (Version 1), while all real parts (α) among complex $\lambda = \alpha \pm i\beta$ have been negative (Version 3).

The obtained results have shown that the aids of eigenvalues may be used for confirmation of the validity of the calculations.

3.5 Stand-Alone Methods of Reduction of Chemical Mechanisms

The problem of the reduction of chemical mechanisms relates to the class of inverse problems [97, 169] and, in the case of a complex reacting system, has, as a rule, no unambiguous solution – i.e., a single, optimum reduced mechanism can hardly be obtained. This problem may be divided into two mechanism reduction problems:

1. A reduction in the framework of detailed chemical kinetics – the development of a skeleton mechanism to make the reduced mechanism obey the kinetic laws for it to be used in invariant programs, as shown in [5, 30].
2. A detailed mechanism reduction by its reducing to some global reactions [137], the application of the local equilibrium principle [20, 90, 138], or the preliminary derivation of approximating formulas for the simulation of some sub-mechanisms [143], etc.

The developments illuminated in this section relate to the first reduction problem. This problem may have various statements that differ in the fields of application, basic schemes, set of target characteristics, and ranges of reacting system parameters. Therefore, for one and the same reacting system, reduced mechanisms may differ notably in size and structure.

By now, a diversity of reduction methods and some versions of every method have been developed. Many reaction mechanism algorithms combine a few methods [90, 99, 130]. Every reduction technique is applied within the framework of some basic scheme of combustion computation (PSR, BR, PFR). Reduced mechanisms obtained by one procedure only for different basic schemes can differ significantly.

Practically all publications related with the development of the reaction mechanism reduction use the concept "target species." The difference in concentrations of these species characterize the deviation of the reduced mechanism from the initial complete mechanism (or C-mechanism). Target species cannot be removed during reduction unlike the other tested species.

The reduction mechanism procedures use usually the indices (thresholds) of reduction while an individual threshold is set for each reduction method used in the algorithm. The higher this threshold, the more notable is the reduction of the C-mechanism.

Downloaded from https://www.cambridge.org/core. Nottingham Trent University, on 17 Aug 2019 at 02:05:11, subject to the Cambridge Core terms of use, available at https://www.cambridge.org/core/terms. https://doi.org/10.1017/9781108581714.003

The resultant reduced mechanism may be developed for a single point in the region of change of the parameters of interest (for example,T_0, p). This mechanism will be called a local reduced mechanism (L-mechanism). The problem of reduction may be solved for a certain region as well. Then the obtained mechanism will be called a global mechanism (G-mechanism). Normally, it is formed by combining L-mechanisms.

As a rule [97], the reduction procedure includes two steps – i.e.,

– First, processes are calculated by the basic scheme with archiving necessary data, including intermediate results.
– Then, archived data are processed in compliance with the applied reduction methods.

Analyses described herein use the other approach, whereby the reduction mechanism formation algorithm is built into the chemical kinetics equations integration procedure while the reduction procedure is implemented for preset points of combustion process parameter variation (for example, at the points of the Jacobian recalculation).

Basic data are normally set as [30; 97]:

– a complete mechanism of chemical reaction (C-mechanism) for the analyzed reacting mixture, for which it is necessary to create the reduced mechanism in the framework of detailed chemical kinetics
– a basic scheme of combustion computation (PSR, BR, PFR, etc)
– a set of target species, which may be reactants that form the two-component propellant composed by fuel and oxidizer, main combustion products, and species of interest for the analyst
– reduction indices (thresholds) for reaction mechanism fragments to be ruled out;
– points or regions for the application of the reduced mechanism

3.5.1 Engagement Method with Adaptive Threshold

One of the apparent mechanism reduction methods consists in the analysis of chemical reaction rates for each species and the deletion of reactions that do not affect the total rate of the formation of this species. For example, if for some j-th reaction appearing in Equation (1.84), the following relation is obeyed for i-th species:

$$\nu_{ij} W_j \geq \zeta_z \sum \nu_{ij} W_j \tag{3.72}$$

then the j-th reaction is included in the reduced mechanism.

The engagement method has been developed on the basis of this approach [170]. The selection procedure starts from one of target species while involving (engaging) step-by-step those of the analyzed species and reactions that satisfy Relation (3.72). Let us use the chemical kinetics equations in Exponential Form (2.29) and relative rates Ω_j (2.28) appearing in the equation. This algorithm is described in the following paragraphs in the application to local reduced mechanism (L-mechanism) development.

Note here that every s-th reversible reaction in the right-hand sides of Equations (2.29), under the sign of sum $\sum \nu_{ij}\Omega_j$ is described by two summands: $\nu_{ij}\Omega_j$ ($j = s$, for

Downloaded from https://www.cambridge.org/core. Nottingham Trent University, on 17 Aug 2019 at 02:05:11, subject to the Cambridge Core terms of use, available at https://www.cambridge.org/core/terms. https://doi.org/10.1017/9781108581714.003

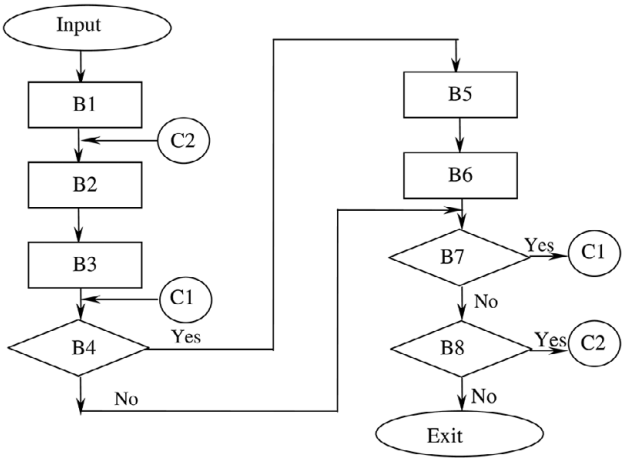

Figure 3.52 Block diagram of L-mechanism creation.

the forward direction), $\nu_{ij}\Omega_j$ ($j = s + m_c$, for the reverse direction). If the contribution of these summands is significant, then the s-th reaction shall be included in the L-mechanism. This contribution can be defined by various methods, for example, with respect to maximum absolute value ($\max\left|\nu_{ij}\Omega_j\right|$) or to sum $\sum_s abs\{\nu_{is}(\Omega_s - \Omega_{s+m_c})\}$. Index ζ_z defines the degree of reduction of the C-mechanism. At $\zeta_z = 0$, the reduced mechanism is equivalent to the C-mechanism. The larger the ζ_z, the smaller the number of reactions that will be included in L-mechanism.

The scheme of L-mechanism creation is given in Figure 3.52 and includes the following blocks:

B1. Initial data. These data comprise the all information required for computation of processes in the reactor and include the initial value of the mechanism reduction exponent (ζ_{z0}) and symbols of the target species. At first, the L-mechanism only includes the target species and no reactions.

B2. Analysis of the i-th specie. All reactions wherein this specie is involved are selected for each i-th specie included in the L-mechanism.

B3. Computation of the sum of absolute values of the difference in the rates of all reactions involving i-th specie:

$$\Omega_i^{\Sigma} = \sum_s abs\{\nu_{ij}(\Omega_s - \Omega_{s+m_c})\}. \tag{3.73}$$

B4. Selection of reactions. Reactions that satisfy the following inequality are selected from those involving i-th specie:

$$abc[\nu_{is}(\Omega_s - \Omega_{s+m_c})] \geq \zeta_{zi}\Omega_i^{\Sigma}\ s = 1, \ldots, m_c. \tag{3.74}$$

B5. Inclusion of the reactions. Every reaction selected in block B4 is included in the L-mechanism if not included earlier.

Downloaded from https://www.cambridge.org/core. Nottingham Trent University, on 17 Aug 2019 at 02:05:11, subject to the Cambridge Core terms of use, available at https://www.cambridge.org/core/terms. https://doi.org/10.1017/9781108581714.003

B6. Inclusion of species. Every specie from each selected in block B4 of the reaction is included in the L-mechanism if not included earlier. Assume, for example, that in the analysis of specie CH_2 in block B4, the following reaction has been selected:

$$CH_2 + O_2 \Leftrightarrow CO + H_2O. \tag{3.75}$$

Then, Reaction (3.75) and species O_2, H_2O, CO are included in the L-mechanism; that is, specie CH_2 initiates inclusion (engagement) in this mechanism of some reactions and species from the C-mechanism.

B7. Checking of reactions. The availability of reactions selected in block B4 but not yet analyzed in block B5 is checked. If no such reactions are available, then control is transmitted to block B8.

B8. Checking of species. Species included in the L-mechanism but not analyzed in block B2 are checked for availability. If such species are available (preset in basic data or included in L-mechanism in block B6), then control is transmitted to block B2 with subsequent transfer to blocks B3–B7. If all species included in the L-mechanism have already been analyzed in these blocks, then the L-mechanism is considered created. The reactions and species of the C-mechanism not engaged are considered insignificant for combustion mode under consideration and excluded from the analysis and use in the combustion model.

The application of this method to reacting systems H–O–S and C–H–O–(N) indicates that this method requires a small number of calculations and can be easily integrated in algorithms and programs of computation of chemical nonequilibrium processes.

However, as experience has shown, the original version of this method at invariable threshold $\zeta_{zi} = K_i \zeta_{z0}$ (when $K_i = 1$) has a significant disadvantage consisting in that the "linking force" between the target and "engaged" species is not allowed for. In this case, the reduced mechanism may incorporate insignificant reactions along with species that feature next to no influence on the combustion process. Therefore, the algorithm and corresponding computer code have been complemented with the block for computation of such "linking forces," which computes the influence coefficients K_i allowing for the effects of reactions on the target specie.

To clarify this situation, let us consider a model reacting system at p, T = const described by the reactions:

R1, R2 – reactions involving hydrogen (H) with high reaction rates (W_{R1}, W_{R2})
R3 – reaction H + Cl = HCl with the rate $W_{R3} = 0.08\, W_\Sigma(\mathrm{H})$
R4, R5 – reactions involving hydrogen (H) with low rates (W_{R4}, W_{R5})
R6 – reaction Cl + O_2 = ClO + O with rate $W_{R6} = 0.3\, W_\Sigma(\mathrm{Cl})$
R7, R8 – reactions involving chlorine (Cl) with rates
$W_{R7} = 0.1\, W_\Sigma(\mathrm{Cl})$, $W_{R8} = 0.06\, W_\Sigma(\mathrm{Cl})$
Assume the following:

– Hydrogen is the target specie while chlorine is that being tested.
– The engagement method is used at coefficient $K_i = 1$.

Downloaded from https://www.cambridge.org/core. Nottingham Trent University, on 17 Aug 2019 at 02:05:11, subject to the Cambridge Core terms of use, available at https://www.cambridge.org/core/terms. https://doi.org/10.1017/9781108581714.003

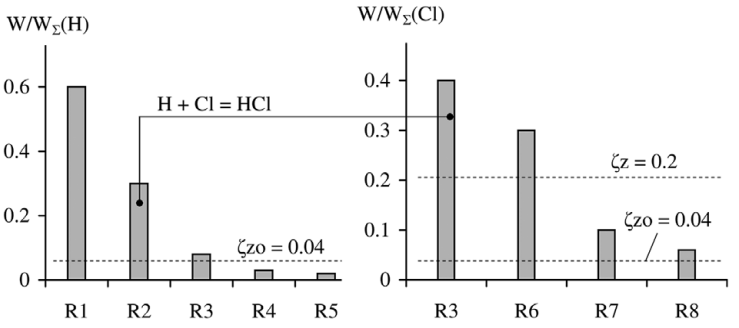

Figure 3.53 Diagrams of reaction velocities and engagement procedure at invariable and adaptive thresholds.

– The total rates of hydrogen and chlorine are interrelated by the relationship:

$$W_\Sigma(\mathrm{H}) = 5\,W_\Sigma(\mathrm{Cl}) \tag{3.76}$$

– The initial threshold $\zeta_{z0} = 0.04$.

Let us consider the procedure of analyzing the rates of hydrogen and its influence on engagement of chlorine.

Figure 3.53a shows the diagram of rates $W_{Ri}(\mathrm{H})$, which indicates the reactions R1, R2, and R3 will be included in the reduced mechanism. In compliance with reaction R3, specie Cl will be engaged; therefore, the specie should be analyzed later; the graph of the velocities of reactions the specie is involved in is shown in Figure 3.53b. It is apparent from this graph that at $\zeta_{zi} = K_i\zeta_{zo} = 0.04$, reactions R6, R7, and R8 will be engaged, although it is obvious that reactions R7 and R8 will bring about a quite insignificant influence on the target specie, H. It is obvious that it is necessary to allow for low influence of chlorine on the hydrogen formation rate and to increase the threshold at analyzing the rates $W_{Ri}(\mathrm{Cl})$, which allows setting the coefficient K_{Cl} equal to 5 with The application of Formula (3.76). Then the adaptive threshold will make $\zeta_{zi} = 5\,\zeta_{zo}$ and, in compliance with Figure 3.47b, reactions R7 and R8 will not be included in the reduced mechanism. To identify the influence of the tested specie on the target specie, it is expedient, by analogy with [97, 141, 142], to use the aforementioned concept of the linking force. These values in this example will be inversely proportional to coefficient K_{Cl}. Applying the relative rates Ω_x for the general case, the linking force between the k-th target specie and the i-th tested specie will be defined by the formula:

$$\Phi_{ik} = \left(\frac{\Delta f_k^i}{f_k} \Big/ \frac{\Delta f_i}{f_i}\right), \tag{3.77}$$

where $f_i = \sum \nu_{ij}\Omega_j = f_i(r_1, r_2 \ldots r_k \ldots r_i \ldots r_n)$, $f_k = \sum \nu_{kj}\Omega_j = f_k(r_1, r_2 \ldots r_k \ldots r_i \ldots r_n)$,

Downloaded from https://www.cambridge.org/core. Nottingham Trent University, on 17 Aug 2019 at 02:05:11, subject to the Cambridge Core terms of use, available at https://www.cambridge.org/core/terms. https://doi.org/10.1017/9781108581714.003

$$\Delta = \delta r_i = 0.001\, r_i, \quad \Delta f_i = f_i^{\Delta} - f_i, \quad \Delta f_k = f_k^{\Delta} - f_k,$$

$$f_i^{\Delta} = f_i(r_1, r_2 \ldots r_k \ldots (r_i + \Delta) \ldots r_n), \quad f_k^{\Delta} = f_k(r_1, r_2 \ldots r_k \ldots (r_i + \Delta) \ldots r_n)$$

To elucidate Formula (3.77), let's derive the expression for the computation of the link force between Cl and H, on using the previously mentioned example with reaction rates (W) and assuming that only reactions R3 and R6 occur in the system. For total velocities of variation of Cl and H concentrations, one now obtains

$$W_{\Sigma}(\mathrm{Cl}) = -k_3^{+} C_{\mathrm{H}} C_{\mathrm{Cl}} + k_3^{-} C_{\mathrm{HCl}} - k_6^{+} C_{\mathrm{O2}} C_{\mathrm{Cl}} + k_6^{-} C_{\mathrm{ClO}} C_{\mathrm{O}} \tag{3.78}$$

$$W_{\Sigma}(\mathrm{H}) = -k_3^{+} C_{\mathrm{H}} C_{\mathrm{Cl}} + k_3^{-} C_{\mathrm{HCl}} \tag{3.79}$$

Let's assume that $\Delta = 0.001 C_{\mathrm{Cl}}$. Then, it results for incremented velocities:

$$W_{\mathrm{Cl}}^{\Delta} = -k_3^{+} C_{\mathrm{H}} (C_{\mathrm{Cl}} + \Delta) + k_3^{-} C_{\mathrm{HCl}} - k_6^{+} C_{\mathrm{O2}} (C_{\mathrm{Cl}} + \Delta) + k_6^{-} C_{\mathrm{ClO}} C_{\mathrm{O}} \tag{3.80}$$

$$W_{\mathrm{H}}^{\Delta} = -k_3^{+} C_{\mathrm{H}} (C_{\mathrm{Cl}} + \Delta) + k_3^{-} C_{\mathrm{HCl}}. \tag{3.81}$$

Whence it follows:

$$\Delta W_{\mathrm{Cl}} = \; W_{\mathrm{Cl}}^{\Delta} - W_{\mathrm{Cl}} = -k_3^{+} C_{\mathrm{H}} \Delta - k_6^{+} C_{\mathrm{O2}} \Delta \tag{3.82}$$

$$\Delta W_{\mathrm{H}} = -k_3^{+} C_{\mathrm{H}} \Delta. \tag{3.83}$$

Now, for the link force ($\Phi_{\mathrm{Cl,H}}$) between the tested species (Cl) and the target specie (H), the following formula results:

$$\Phi_{\mathrm{Cl,H}} = \; \frac{k_3^{+} \Delta C_{\mathrm{H}}}{k_3^{+} C_{\mathrm{H}} \Delta - k_6^{+} C_{\mathrm{O2}} \Delta} \cdot \frac{W_{\mathrm{Cl}}}{W_{\mathrm{H}}}. \tag{3.84}$$

The entire set of values of Φ_{ik} forms the matrix of forces of the direct links between the target and tested species of the following dimension: $i = 1 \ldots n_b$; $k = 1 \ldots n_t$. Values of Φ_{kk} are formally taken to be the unit. Every matrix i-th line has n_t values from which it is necessary to determine the maximum value of the link force $G_i = \max\limits_{k \in 1 \ldots n_t} (\Phi_{ik})$. By this value, the influence coefficient is calculated (by the formula,$K_i = 1/G_i$), and then, by the formula $\zeta_{zi} = K_i \zeta_{z0}$, the adaptive threshold is calculated. This method requires the minor computations and can relatively simply be integrated in the models using PSR, BR, and PFR. The engagement method with the adaptive threshold is, in fact, identical to the known DRG method [141].

As an example, let us consider the results of reaction mechanism reduction for the mixture "CH_4+ air" (28 species and 131 reactions; see item Section 3.4). The creation of the reduced mechanism has been performed for the PSR scheme at $\alpha_{ox} = 1.0$; $T_0 = 2700$ K; $p = 1$ atm. Residence time $\tau_p = 0.39 \times 10^{-4}$ sec . Specie N_2 is considered inert. The preset set of target species is composed of CH_4, O_2, CO_2, H_2O, and, formally, N_2. Threshold values vary in the range of $\zeta_{z0} = 0.01 \ldots 0.04$. The reactor is other than adiabatic while T_0 is the temperature of equilibrium composition (i.e., the temperature at $\tau_p = \infty$). At $\tau_p = 0.39 \times 10^{-4}$ sec , the temperature T_f = 2345 K settles in the reactor. Table 3.20 displays the fragment of matrix Φ_{ik} (for 11 species out of 28, including four target species).

Downloaded from https://www.cambridge.org/core. Nottingham Trent University, on 17 Aug 2019 at 02:05:11, subject to the Cambridge Core terms of use, available at https://www.cambridge.org/core/terms. https://doi.org/10.1017/9781108581714.003

Table 3.20 Fragment of the matrix Φ_{ik} of direct linking forces for reacting system "CH_4 + air"*

Specie	Target species				Link force
	O_2	H_2O	CO_2	CH_4	G_i
H	0.163^{-1}	0.862^{-1}	0.161^{-1}	0.366^{-3}	0.862^{-1}
O	0.990^{-2}	0.541^{-1}	0.382^{-4}	0.749^{-4}	0.541^{-1}
O_2	1.00	0.921^{-3}	0.111^{-2}	0.00	1.00
OH	0.508^{-2}	0.841^{-1}	0.554^{-2}	0.165^{-3}	0.841^{-1}
H_2	0.196^{-4}	0.133	0.175^{-15}	0.691^{-4}	0.133
H_2O	0.802^{-4}	1.00	0.00	0.367^{-3}	1.00
CO	0.120^{-3}	0.259^{-6}	1.00	0.00	1.00
CO_2	0.109^{-3}	0.000	1.00	0.00	1.00
CH_3	0.593^{-6}	0.131^{-4}	0.00	0.639^{-4}	0.639^{-4}
CH_4	0.00	0.338	0.00	1.00	1.00
CH_2O	0.240^{-9}	0.128^{-3}	0.402^{-10}	0.00	0.128^{-3}

* Superscript at the number means its order, for example: $0.366^{-3} = 0.366 \cdot 10^{-3}$.

Note here that the values of the linking forces do not depend on the threshold value. Then, applying the formula,

$$abc[\nu_{is}(\Omega_s - \Omega_{s+m_c})] \geq K_i \zeta_{z0} \Omega_i^{\Sigma} \quad s = 1, \ldots, \ m_c, \tag{3.85}$$

important species and reactions are selected to the L-mechanism.

The created L-mechanisms for various values of $\zeta_{z0}$are listed in Table 3.21. The first column lists the reaction numbers for the basic mechanism. The symbol + indicates which reactions of the mechanism L ($\zeta_{z0} = 0.01$) have been included in the reduced mechanisms with the higher initial threshold. With the increase in this threshold, the L-mechanism size decreases. This example shows that

- Mechanism L ($\zeta_{z0} = 0.01$) includes 18 species (C, H, O, N, N_2, O_2, OH, H_2, H_2O, HO_2, HCO, CO, CO_2, CH, CH_2, CH_3, CH_4, CH_2O) and 34 reactions.
- Mechanism L ($\zeta_{z0} = 0.02$) includes 18 species (the same species) and 29 reactions.
- Mechanism L ($\zeta_{z0} = 0.04$) includes 16 species (the same species except for HO_2 and CH) and 19 reactions.

Table 3.22 shows the composition of basic species in combustion products at PSR exit at various thresholds. It is apparent that with the increase in ζ_{z0}, errors in the composition defined by the following formula increase:

$$\delta r_i = \left| \frac{r_i(\mathrm{C}) - r_i(\mathrm{L})}{r_i(\mathrm{C})} \right| \tag{3.86}$$

where $r_i(\mathrm{C}), r_i(\mathrm{L})$ are the mole fractions of the i-th specie at the reactor exit obtained by C- and L-mechanisms, respectively. On the average, the following errors result: $\delta r_i\,(\zeta_{z0} = 0.01) = 1\%$;

$$\delta r_i\,(\zeta_{z0} = 0.02) = \ 3\% \quad \delta r_i\,(\zeta_{z0} = 0.04) = \ 10\%.$$

Downloaded from https://www.cambridge.org/core. Nottingham Trent University, on 17 Aug 2019 at 02:05:11, subject to the Cambridge Core terms of use, available at https://www.cambridge.org/core/terms. https://doi.org/10.1017/9781108581714.003

Table 3.21 Reduced local mechanisms for reacting system "CH_4 + air" at various threshold values ζ_{z0} (№ (C) – numbers of reactions in C-mechanism)

№(C)	$\zeta_{z0} = 0.01$	0.02	0.04	№(C)	$\zeta_{z0} = 0.01$	0.02	0.04
1	$N + N = N_2$	+	+	36	$CH_3 + OH = CH_2O + H_2$		
2	$H + O_2 = O + OH$	+	+	45	$CH_2O + H = HCO + H_2$	+	+
3	$H_2 + O = H + OH$	+	+	46	$CH_2O + O = HCO + OH$	+	
4	$H_2 + OH = H_2O + H$	+	+	47	$CH_2O + OH = HCO + H_2O$	+	+
5	$OH + OH = H_2O + O$	+	+	48	$HCO + M = CO + H + M$	+	+
6	$H + OH + M = H_2O + M$	+		49	$HCO + H = CO + H_2$	+	+
10	$H + H + H_2O = H_2 + H_2O$			50	$HCO + O = CO + OH$	+	+
13	$H + O_2 + M = HO_2 + M$	+		51	$HCO + O = CO_2 + H$	+	+
15	$HO_2 + H = OH + OH$	+		52	$HCO + OH = CO + H_2O$	+	
24	$CO + OH = CO_2 + H$	+	+	55	$CH_2 + O = CO + H + H$	+	+
27	$CH_4 + H = CH_3 + H_2$	+	+	56	$CH_2 + O = CO + H_2$	+	
28	$CH_4 + O = CH_3 + OH$	+	+	58	$CH_2 + OH = CH_2 + H$	+	
29	$CH_4 + OH = CH_3 + H_2O$	+	+	59	$CH_2 + OH = CH + H_2O$	+	
32	$CH_3 + H = CH_2 + H_2$	+		68	$CH + H = C + H_2$		
33	$CH_3 + O = CH_2O + H$	+	+	69	$CH + O = CO + H$		
34	$CH_3 + O = CH_2 + OH$			77	$C + OH = CO + H$	+	+
35	$CH_3 + OH = CH_2 + H_2O$	+	+	78	$C + O_2 = CO + O$	+	

Table 3.22 Comparison of chemical composition of combustion products (r_i) at PSR exit (steady-state mode) for target and basic (significant) tested species for C-mechanism and for reduced mechanisms with different values of ζ_{z0}^*

		Reduced mechanisms		
Specie (r_i)	C-mechanism	$\zeta_{z0} = 0.01$	$\zeta_{z0} = 0.02$	$\zeta_{z0} = 0.04$
O_2	0.0283	0.0284	0.0292	0.0311
H_2O	0.1363	0.1362	0.1331	0.1250
CO_2	0.0435	0.0433	0.0418	0.0381
CH4	0.2051^{-4}	0.2036^{-4}	0.1886^{-4}	0.1549^{-4}
H_2	0.0228	0.0229	0.0239	0.0264
OH	0.0210	0.0211	0.0219	0.0240
CO	0.0459	0.0460	0.0471	0.0500
O	0.0108	0.0109	0.0121	0.0153
H	0.0179	0.0181	0.0201	0.0259
CH_2O	0.2988^{-4}	0.2986^{-4}	0.2943^{-4}	0.2671^{-4}

* Superscript at the number means its order, for example: $0.2051^{-4} = 0.2051 \cdot 10^{-4}$

3.5.2 Method of Direct Sounding of Species and Reactions

This method uses a trivial concept of mechanism reduction [169] and comprises the following steps;

Downloaded from https://www.cambridge.org/core. Nottingham Trent University, on 17 Aug 2019 at 02:05:11, subject to the Cambridge Core terms of use, available at https://www.cambridge.org/core/terms. https://doi.org/10.1017/9781108581714.003

- Combustion process computation by the basic reaction mechanism
- Removal of some reaction or some specie from this mechanism (along with the reactions wherein this specie is involved)
- Combustion process computation by the "truncated" reaction mechanism
- Comparison of two obtained results against themselves

If the comparison displays insignificant variations (for example, concentrations of target species), then the removed fragment of the reaction mechanism should not be returned in the mechanism and vice versa (the fragment should be returned in the case of significant changes). It is apparent that this method requires a significant number of computations and should be used in combination with the other reduction methods. It can hardly be used for BR and PFR. However, the method of the direct sounding of species and reactions is probably a reliable one as to the quality of reduction; therefore, one can try applying it to the PSR model when performing the reduction procedure for the steady-state case. This state is described by algebraic equations:

$$F_{\gamma i} \equiv -e^{\gamma i}\left(\sum_j \nu_{ij}\Omega_j + \frac{r_i^+\mu_g}{\mu^+\tau_p}\right) + \sum_q\sum_j \nu_{qj}\Omega_j + \sum_q \frac{r_q^+\mu_g}{\mu^+\tau_p} = 0 \qquad (3.87)$$

$$F_T \equiv T - T_{rf} - \sum_i \left(h\mu_i - H_i^{rf}\right) r_i \Big/ \sum_i C_{pi}^{rf} r_i = 0 \qquad i = 1, \ldots, n_b \qquad (2.149)$$

In the computation of the processes in the reactor with the basic mechanism, the steady state is defined during a long procedure of integration of Equations (2.29) and (2.149) with respect to time by the algorithm described in Subsection 2.4.5. Proceeding from this state to evaluate the influence of, for example, the s-th reaction, it is sufficient to zero the rate constants values k_s^+, k_s^- and then solve the system of algebraic equations (3.87), for example, by the Newton method. The solution of Equations (2.29) and (2.149) obtained for the basic mechanism is a good starting approximation for solving the same equations with zeroed constants k_s^+, k_s^-; therefore, iterations in the Newton method converge quickly. The paper [171] presented a two-step algorithm of reduction by the method of direct sounding of the species and reactions with the preliminary application of the engagement method at a low invariable threshold, ζ_{z0}.

At the first "sounding and selecting the species" step, the influence of every i-th specie with concentration $r_i \leq 10^{-3}$ and not included in the list of target species on the main parameters of the process is defined and, given the insignificant influence, then the i-th specie and appropriate reactions $R_s(i)$ are excluded from the mechanism. This influence is evaluated by a stepwise reduction of all constants $k_s^+(i), k_s^-(i)$ of reactions $R_s(i)$ by the following relations:

$$ln\, k_s^{+,m+1} = ln\, k_s^{+,m}(i) - h_m \;; \quad ln\, k_s^{-,m+1} = ln\, k_s^{-,m}(i) - h_m. \qquad (3.88)$$

Reduction step h_m (where m is the step number) is specified to be small to provide for reliability of computations, and then is exponentially increased. If at some step the following ratio is reached,

Downloaded from https://www.cambridge.org/core. Nottingham Trent University, on 17 Aug 2019 at 02:05:11, subject to the Cambridge Core terms of use, available at https://www.cambridge.org/core/terms. https://doi.org/10.1017/9781108581714.003

$$\delta_{ki} = \max \left| \frac{\gamma_k(\mathrm{LE}) - \gamma_{ki}(h_m)}{\gamma_k(\mathrm{C})} \right| \geq \zeta_v, \tag{3.89}$$

where $k \in$ (target species), δ_{ki} is the maximum relative deviation of k-th specie concentration; $\gamma_k(\mathrm{C})$, $\gamma_{ki}(h_m)$ are logarithms of target species concentrations defined by the C-mechanism at step h_m; ζ_v is the threshold for exclusion of species; LE are the results obtained after application of engagement method – then, further reduction of constants ceases and specie i is remained in the reaction mechanism. If upon reaching $\sum_m h_m > 20$ (that is, constants $k_s^+(i), k_s^-(i)$ are decreased by e^{20} times) the relation $\sum_s \delta_s < \zeta_v$ is obeyed, then the i-th specie and reactions $R_s(i)$ are removed from the mechanism, which results in the LS-mechanism. However, this mechanism still may contain a reactions of insignificant influence.

This is why the second "reaction sounding and selecting" procedure is performed. The technique of this analysis is similar to that used in the first procedure. Computations are performed for the steady-state condition with a stepwise reduction of rate constants k_s^+, k_s^- for the analyzed s-th reaction. The obtained mechanism is called the LF-mechanism.

The sounding method is included in the invariant scheme for computing the process in PSR called the RISZSR, which allows the generation of the reduced mechanisms. As an illustration, the following are results of reaction mechanism reduction for mixture "CH_4 + air" under conditions of the previous example (see Subsection 3.5.1) at $\zeta_{z0} = 0.01$; $\zeta_v = 0.01$; $\zeta_R = 0.01$ (the threshold for exclusion of reactions); K_i = 1. Table 3.23 lists the mole concentrations of the target and some important species, the maximum errors, the amounts of species, and the number of reactions remaining after every reduction step. It is apparent that the most significant reduction occurs at the engagement step. Note here that chemical composition deviation from the basic mechanism is at a minimum:

Table 3.23 Comparison of composition (r_{ib} – mole fractions) of combustion products at PSR exit (steady-state mode) for target and basic (significant) tested species for C-mechanism and for reduced mechanisms with different values of ζ_{z0}(sounding method)*

Specie (r_{ib})	C-mechanism	Method of engagement	Sounding of species	Sounding of reactions
O_2	0.0283	0.0284	0.0295	0.0310
H_2O	0.1364	0.1361	0.1317	0.1255
CO_2	0.0435	0.0433	0.0412	0.0383
CH_4	0.2051^{-4}	0.2034^{-4}	0.1854^{-4}	0.1796^{-4}
H_2	0.0228	0.0229	0.0243	0.0262
OH	0.0210	0.0211	0.0223	0.0238
CO	0.0459	0.0459	0.0477	0.0499
Error (%)	0	0.09	1.76	4.14
Reactions	131	50	21	11
Species	28	19	13	13

* Superscript at the number means its order, for example: $0.2051^{-4} = 0.2051 \cdot 10^{-4}$

Downloaded from https://www.cambridge.org/core. Nottingham Trent University, on 17 Aug 2019 at 02:05:11, subject to the Cambridge Core terms of use, available at https://www.cambridge.org/core/terms. https://doi.org/10.1017/9781108581714.003

Table 3.24 The local reduced mechanism of the "CH_4 + air" mixture combustion by the method of direct sounding of species and reactions (№ (C) – reaction number in C-mechanism)

№ (C)	Reactions	№ (C)	Reactions
2	$H + O_2 = O + OH$	29	$CH_4 + OH = CH_3 + H_2O$
4	$H_2 + OH = H_2O + H$	33	$CH_3 + O = CH_2O + H$
5	$OH + OH = H_2O + O$	47	$CH_2O + OH = HCO + H_2O$
6	$H + OH + M = H_2O + M$	48	$HCO + M = CO + H + M$
24	$CO + OH = CO_2 + H$	49	$HCO + H = CO + H_2$
27	$CH_4 + H = CH_3 + H_2$		

$$\delta(\mathrm{C},\mathrm{Z}) = \max \left| \frac{\gamma_k(\mathrm{C}) - \gamma_k(\mathrm{Z})}{\gamma_k(\mathrm{C})} \right| = 0.09\% \tag{3.90}$$

where $k \in$ (target species).

This is caused by the fact that at $\alpha_{ox} = 1.0$ and sufficiently high temperature (T_f = 2345 K), the complex hydrocarbons compounds are, in fact, not formed, which excludes their influence on combustion process. At the species sounding step (V is the symbol of the sounding of species method), the other six species and 29 reactions are removed from the mechanism while the error increases up to $\delta(\mathrm{C},\mathrm{V}) == 1.76\%$. Finally, at the reactions sounding step (R is the symbol of the sounding of reactions method), an additional 10 reactions are removed from the mechanism, but the error in this case approaches $\delta(\mathrm{C},\mathrm{R}) = 4.14\%$.

Finally, the reduced mechanism is shown in the Table 3.24. It comprises the species H, O, N_2, O_2, OH, H_2, H_2O, HCO, CO, CO_2, CH_3, CH_4, CH_2O. This mechanism is effective (closed); that is, it converts reactants CH_4 and O_2 into the basic combustion products (H_2O, CO_2). In particular, it easily reveals that methane (CH_4) is converted into CO_2 by the following basic scheme:

$$CH_4 \rightarrow CH_3 \rightarrow CH_2O \rightarrow HCO \rightarrow CO \rightarrow CO_2. \tag{3.91}$$

3.5.3 Directed Relation Graph with Error Propagation Method

As stated in Section 3.1, the reaction mechanism reduction problem is an inverse problem. This is why by now many reduction procedures have been developed. One of the most efficient is the directed relation graph with error propagation (DRGEP) method [142]. This algorithm is similar to DRG method [141], yet operates not only by direct links but by intermediate links between the target and remaining species as well. The DRGEP method is based on Dijkstra's problem and algorithm [172] adapted to the search of reduced reaction mechanisms. Let us clarify the core of the problem.

Let us have a directed graph with nodes and weighed arcs (paths) described by some dimensional units (for example, the length) connecting said nodes (Figure 3.54). For a given source node in the graph, Dijkstra's problem consists in determination of the shortest path between that node and all others while Dijkstra's algorithm reveals these

Downloaded from https://www.cambridge.org/core. Nottingham Trent University, on 17 Aug 2019 at 02:05:11, subject to the Cambridge Core terms of use, available at https://www.cambridge.org/core/terms. https://doi.org/10.1017/9781108581714.003

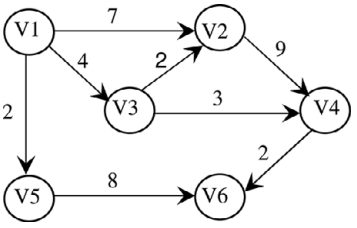

Figure 3.54 Example of oriented graph with weighed paths.

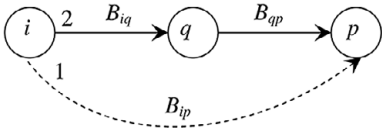

Figure 3.55 Fragment of reactions graph with weighed paths. (1) direct link; (2) link through intermediate node.

paths. Given the availability of all necessary data, it can help, for example, to define the better sequence of roads to get from one city to any city from multiple others, or what countries are the most profitable importers of oil, etc. Figure 3.54 shows the example of a "weighed graph" with six nodes and eight paths while the numbers of paths represents distances between the nodes.

There are several different paths between the same nodes, and a straight path will not necessarily be the shortest one. For example, the straight path from node V1 to node V2 equals 7 units, while through V3, it equals 6 units. Let the node V1 be the starting point. Then it is evident that the shortest distances to the other paths are as follows:

1. to V2 (V1 → V3 → V2); L = 6
2. to V3 (V1 → V3) L = 4
3. to V4 (V1 → V3 → V4) L = 7
4. to V5 (V1 → V5) L = 2
5. to V6 (B1 → V3 → V4 → V6) L = 9

This comparatively simple example makes the problem solution obvious, but Dijkstra's algorithm is a universal tool to be applied to graphs of whatever complexity.

The DRGEP method graph nodes correspond to species while the paths stand for links between them. The "force of link" between species is assigned to each path, and these forces should be evaluated qualitatively. There may be one straight path between two any species and several paths via a number of intermediate species (Figure 3.55). The primary purpose of the DRGEP method is the determination of the most important links between the target (k) species and other (i) species. If any i-th specie exercises an insignificant influence on each of the target species, this specie is removed from the mechanism.

Starting points at computation of links are the target species nodes. In compliance with [142], the force of the direct link between whatever two species i and p will be defined by the formula

Downloaded from https://www.cambridge.org/core. Nottingham Trent University, on 17 Aug 2019 at 02:05:11, subject to the Cambridge Core terms of use, available at https://www.cambridge.org/core/terms. https://doi.org/10.1017/9781108581714.003

$$B_{ip} = \frac{G_{ip}}{F_i} = \frac{\sum_s abs\{\nu_{is}(\Omega_s - \Omega_{s+m_c})\}_p}{\sum_s abs\{\nu_{is}(\Omega_s - \Omega_{s+m_c})\}}, \tag{3.92}$$

where $s = 1 \ldots m_c$; $i, p = 1 \ldots n_b$; $F_i = \sum_s abs\{\nu_{is}(\Omega_s - \Omega_{s+m_c})\}$ is the sum of differences of absolute values of the rates of all forward and reverce reactions involving i-th specie; and $G_{ip} = \sum_s abs\{\nu_{is}(\Omega_s - \Omega_{s+m_c})\}_p$ is the sum of differences of absolute values of the rates of all forward and reverse reactions involving both i-th and p-th substances specie.

At $i = p$, the value of $B_{ip} = 1$ while, in a general case, these values are in the range of $0 \leq B_{ip} \leq 1$ and related with other paths of the reactions graph. Given the availability of intermediate nodes (species), the force of link between species is defined by the product for forces of the links of connecting paths. For example, for the fragment of the graph (Figure 3.55), one obtains

$$B_{ip}^{(2)} = B_{iq}B_{qp}. \tag{3.93}$$

By applying Dijkstra's procedure, it is possible to define the most significant link between substances i and p. However, Dijkstra's algorithm operates with positive numbers only and uses the operations of addition. This is why it is necessary to make the conversion:

$$F_{ip} = -ln\, B_{ip}. \tag{3.94}$$

Then Dijkstra's algorithm may be applied to every target specie. Now, matrix Z_{ik}^d of dimension $\{i = 1 \ldots n_b.; k = 1 \ldots m_t\}$ will result. By applying the matrix inversion procedure, one can obtain $Z_{ik} = exp\left(-Z_{ik}^d\right)$ – the desired matrix of the most important links between the i-th specie and all target species. Now, select the greatest number $G_i^d = max(Z_{ik})$ from each i-th row to get the factor of the i-th specie influence on target species. If G_i^d is smaller than the preset threshold – i.e., $G_i^d \leq \zeta_d$ – then the i-th specie will be removed from the mechanism being reduced together with appropriate reactions.

The results of reaction mechanism reduction by the DRGEP method at $\zeta_d = 0.01 \ldots 0.04$ for the "CH_4 + air" reacting mixture under conditions used in previous examples (Subsections 3.5.1 and 3.5.2) are given next. Table 3.25 lists the forces of link of some important species with target species and factors of G_i^d (the column for nitrogen (N_2) is not shown, since the latter is the inert specie).

The analysis of this table allows one to make the following conclusions:

- Radical OH matters very much in the conversion of reactants into combustion products;
- Methane is decomposed, in fact, only via reactions with the CH_3 radical formation;
- Atom C, as well as radicals HO_2 and CH, brings about a weak influence on the combustion process.

Table 3.26 lists the following parameters: composition of the combustion products, the average error in chemical composition ($\bar{\delta}$) resulting from mechanism reduction, and

Downloaded from https://www.cambridge.org/core. Nottingham Trent University, on 17 Aug 2019 at 02:05:11, subject to the Cambridge Core terms of use, available at https://www.cambridge.org/core/terms. https://doi.org/10.1017/9781108581714.003

Table 3.25 Fragment of matrix Z_{ik} of the most important links between *i-th* and target species*

	Target species				
Specie	O_2	H_2O	CO_2	CH_4	G_i^d
C	0.0105	0.753^{-2}	0.0234	0.836^{-2}	0.0234
H	0.966	0.603	0.982	0.597	0.982
O	0.959	0.509	0.477	0.458	0.959
O_2	1.00	0.333	0.302	0.239	1.00
OH	0.943	1.00	0.908	0.631	1.00
H_2	0.275	0.247	0.280	0.367	0.367
H_2O	0.419	1.00	0.403	0.514	1.00
HO_2	0.0389	0.0179	0.0163	0.0113	0.0389
CO	0.241	0.150	0.921	0.149	0.921
CO_2	0.0863	0.0915	1.00	0.0577	1.00
CH	0.0136	0.0288	0.0131	0.0172	0.0288
CH_3	0.278	0.320	0.215	1.00	1.00
CH_4	0.139	0.265	0.118	1.00	1.00
CH_2O	0.253	0.260	0.273	0.389	0.389

* Superscript at the number means its order, for example: $0.753^{-2} = 0.753 \cdot 10^{-2}$

Table 3.26 Key parameters of the starting and reduced mechanisms for various values of threshold ζ_d (DRGEP method); r_i – mole fractions of reacting mixture in the reactor*

		Reduced mechanisms			
Specie (r_i)	C-mechanism	$\zeta_d = 0.01$	$\zeta_d = 0.02$	$\zeta_d = 0.03$	$\zeta_d = 0.04$
O_2	0.0283	0.0283	0.0283	0.0287	0.0293
H_2O	0.1364	0.1363	0.1363	0.1349	0.1326
CO_2	0.0434	0.0434	0.0434	0.0428	0.0416
CH_4	0.2051^{-4}	0.2045^{-4}	0.2045^{-4}	0.1971^{-4}	0.1851^{-4}
H_2	0.0228	0.0229	0.0229	0.0233	0.0241
OH	0.0210	0.0211	0.0211	0.0214	0.0221
CO	0.0458	0.0459	0.0459	0.0464	0.0473
Error (%)	0	≈ 0.2	≈ 0.2	≈ 1.2`	≈ 5.0
Reactions	131	64	64	52	45
Species	28	18	18	16	15

* Superscript at the number means its order, for example: $0.2051^{-4} = 0.2051 \cdot 10^{-4}$

the number of reactions and species in the L-mechanism. It is apparent that at stoichiometric conditions and high temperatures, hydrocarbons like CH_3O, C_2H, C_2H_2, C_2H_3, C_2H4, C_2H_5, C_2H_6, and C_2H_2O are contained in extremely low concentrations. This is why they do not affect the combustion process and are removed from the basic mechanism at even at an insignificant threshold, $\zeta_d = 0.01$. Note here that the average error, $\bar{\delta}$, is very small. The next nominees for removal in compliance with Table 3.25 are the C atom as well as HO_2 and CH radicals. However, at $\zeta_d = 0.02$, they remain in the

Downloaded from https://www.cambridge.org/core. Nottingham Trent University, on 17 Aug 2019 at 02:05:11, subject to the Cambridge Core terms of use, available at https://www.cambridge.org/core/terms. https://doi.org/10.1017/9781108581714.003

L-mechanism; therefore, at this threshold, the reacting mixture composition and reaction mechanism do not change (see fourth column of Table 3.26).

Atom C and radical CH are removed from the previous L-mechanism at threshold $\zeta_d = 0.03$ in compliance with Table 3.25. Then, 16 species and 52 reactions remain in the mechanism $\mathrm{L}(\zeta_d = 0.03)$. The value of the average error becomes as high as$\bar{\delta} = 12\%$. One more radical, HO_2, and seven reactions are removed at the threshold $\zeta_d = 0.04$. However, the results of computations obtained by the mechanism $\mathrm{L}(\zeta_d = 0.04)$ display a significant error.

Note here that after application of the DRGEP method, many reactions still remain in reduced mechanisms, including those of low importance. This is why it is worthwhile to use this method with the subsequent application of other procedures aimed at removing the reactions.

3.6 Combination of Reaction Mechanisms Reduction Methods

It follows from Section 3.5 that stand-alone methods (see [99, 142]) fail to sufficiently reduce chemical mechanisms; therefore, it is expedient to use them in combination with other procedures. Therefore the following algorithms are used in practice (see [90, 97, 98]), compiling various reduction methods. The methods and algorithms are the following:

- sequential application of engagement and sounding methods
- DRGEP method and engagement method with adaptive threshold

Let us consider the application of these methods and algorithms to different basic schemes and direct them toward the creation of global reduced mechanisms (G-mechanisms). Note here that such mechanisms can be multidimensional. For example, it is possible to set a problem to develop the aforesaid G -mechanism for some type of a high-temperature unit (furnace, gas generator, nozzle, etc.) for a prescribed range of the variation of parameters – e.g., α_{ox}, p, T, etc. To simplify the interpretation and comprehension of this approach, let us consider only one-dimensional G-mechanisms that focus on some temperature range at the preset values of α_{ox} and p.

3.6.1 Technique of Creation of G-Mechanism for PSR by Sequential Application of Engagement and Sounding Method

Let us analyze the creation of reduced mechanisms for steady-state modes of the PSR model. These modes are described by algebraic equations:

$$F_{\gamma i} \equiv -e^{\gamma i}\left(\sum_j V_{ij}\Omega_j + \frac{r_i^+\mu_g}{\mu^+\tau_p}\right) + \sum_q \sum_j \nu_{qj}\Omega_j + \sum_q \frac{r_q^+\mu_g}{\mu^+\tau_p} = 0, \tag{3.87}$$

$$F_T \equiv T - T_{rf} - \sum_i \left(\left(h_p + q_m\right)\mu_i - H_i^{rf}\right) r_i \Big/ \sum_i C_{pi}^{rf} r_i = 0 \quad i = 1, \ldots, n_b \tag{3.95}$$

Downloaded from https://www.cambridge.org/core. Nottingham Trent University, on 17 Aug 2019 at 02:05:11, subject to the Cambridge Core terms of use, available at https://www.cambridge.org/core/terms. https://doi.org/10.1017/9781108581714.003

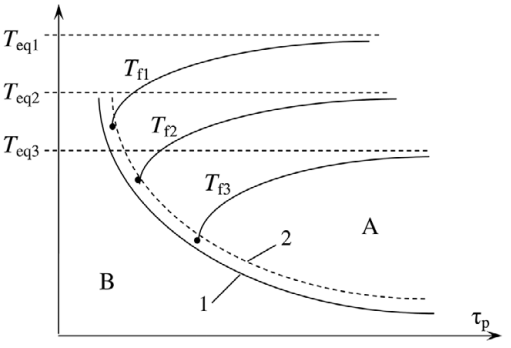

Figure 3.56 Variation of temperatures T_f subject toτ_p and heat flow q_m; (1) extinction line; (2) region adjacent to the extinction line; A – combustion region; B – non-combustion region; $T_{f1}(q_m > 0)$, $T_{f2}(q_m = 0)$, $T_{f3}(q_m < 0)$ – lines of steady-stage modes temperatures.

where $h_p = \frac{h_c + h_{ox}\,\alpha_{ox} k_m^o}{1+\alpha_{ox} k_m^o}$ is the enthalpy of propellant (reactants) and q_m is the external heat flow relative to unit mass of the flow entering the reactor (at $q_m = 0$ the process in reactor is adiabatic one).

Ceteris paribus, steady-state modes depend on the residence time τ_p and q_m. In $\tau_p - T$ coordinates at $q_m = const$, these modes (Figure 3.56) correspond to the points on the lines $T_{f1}(q_m > 0)$, $T_{f2}(q_m = 0)$, T_{f3} $(q_m < 0)$. At the increase in τ_p, the temperature of combustion products (T_f) in the reactor verges to that of chemical equilibrium T_{eq}, which can be predicted by the chemical equilibrium model (see Section 1.3). At the decrease in τ_p, the steady-state mode temperature drops to the so-called "extinction line," which separates combustion region A from noncombustion region B. It is evident from Figure 3.56 that a certain value of τ_{ex} corresponds to each temperature T_{eq} while at $\tau_q < \tau_{ex}$ combustion ceases and the value of T_f drops in a stepwise manner to the temperature of reactants. Basically, to create the G-mechanism as the function of temperature only (Gt-mechanism), it is necessary to perform calculations within the limits of the entire region A with the creation of the L-mechanism for each selected point (T_{eq},τ_p) and then to combine the L-mechanisms. The publications [90; 130] display that the scope of the calculations may be significantly reduced if these are made in the region adjacent to the extinction line. It is assumed that the Gt-mechanism obtained for this region covers L-mechanisms inside region A.

In the selection of points for the creation of L-mechanisms, it is necessary to first define the temperature interval for the Gt-mechanism and the step of ΔT temperature variation. Let us define this interval $(T_{eq,1} \ldots T_{eq,a} \ldots T_{eq,nv})$ by equilibrium temperatures (Figure 3.56). For every $T_{eq,a}$, it is required to calculate the value of q_m (3.95). For this, the chemical eqilibrium calculation should be first performed at p, $T_{eq,a} = const$ with the calculation of the value of ennthalpy of combustion products $h\left(T_{eq,a}\right)$. Now, the heat flow q_m is calculated by the formula:

$$q_m(v) = h\left(T_{eq,a}\right) - h_p. \tag{3.96}$$

Downloaded from https://www.cambridge.org/core. Nottingham Trent University, on 17 Aug 2019 at 02:05:11, subject to the Cambridge Core terms of use, available at https://www.cambridge.org/core/terms. https://doi.org/10.1017/9781108581714.003

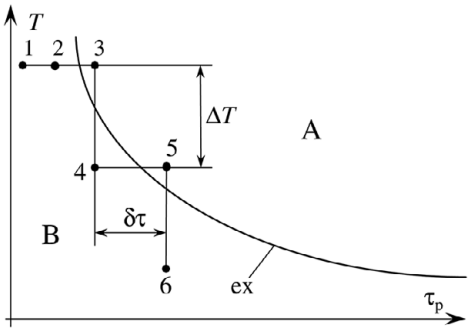

Figure 3.57 Dependence of temperatures T_f on residence time; *ex* – extinction line; A – combustion region, B – extinction zone; 3, 5 – points of calculation for L-mechanism creation.

This heat flow allows the reaching of the temperature $T_{eq,a}$ in the reactor at $\tau_p \to \infty$.

To perform calculations of PSR steady-state modes with the further addition of the reduction technique, it is necessary to know the values of $\tau_{ex}(a)$ close to the extinction line. However, these values are primarily unknown, and their search should be included in the general algorithm of reduction. The initial chemical composition of the gas in the reactor required for the calculation of the PSR steady-state mode normally is set as equilibrium at the temperature $T_{eq,a}$. This is allowed for to form the following algorithm of Gt-mechanism creation in a single PSR:

1. The following initial data are set: the complete mechanism (C-mechanism); reduction region parameters $T_{eq,1}, \Delta T, T_{eq,na}$; thresholds ζ_{z0}, ζ_v, ζ_R; the set of target species; the initial value of residence time τ_{p0} set as known to be existing in noncombustion region B; some increment $\delta\tau_p = \tau_{p,i+1}/\tau_{p,i}$ (for example, $\delta\tau_p = 1.1$).
2. The calculation for the G-mechanism is performed at τ_{p0}; in this case, combustion fails (see Figure 3.51), which is defined by a notable decrease in temperature in the reactor. Calculation is ceased, and the L-mechanism is not formed.
3. Residence time increases $\tau_{p,2} = \tau_{p,1}\delta\tau_p$, and calculation is reiterated at $T_{eq,0}$. If the system still exists in region B (point 2, Figure 3.57), then the new value of $\tau_{p,3} = \tau_{p,2}\delta\tau_p$ is defined to perform calculation for point 3.
4. If the calculation is carried out to some steady state with the formation of combustion products, it means that the reacting system is in combustion region A, and then the L-mechanism is created. Creation of this mechanism is described in Subsection 3.5.2. It is apparent that in this case, the algorithm comprises three steps: engagement method (with constant threshold), species, and reaction sounding. The reduction process starts from the C-mechanism at every selected point.
5. The new value of $T_{eq,2} = T_{eq,1} - \Delta T$ is defined to make system go to point 4.
6. The calculation is performed at point 4; if no ignition occurs, then residence time increases $\tau_{p,4} = \tau_{p,3}\delta\tau_p$ to make system go to point 5. In case this point is located

Downloaded from https://www.cambridge.org/core. Nottingham Trent University, on 17 Aug 2019 at 02:05:11, subject to the Cambridge Core terms of use, available at https://www.cambridge.org/core/terms. https://doi.org/10.1017/9781108581714.003

in region A, a new L-mechanism is created for it, and a new value of $T_{eq,3} = T_{eq,2} - \Delta T$(point 6) is defined, and so on, unless temperature $T_{eq,na}$ is reached with appropriate increase in τ_p.

3.6.2 Example of Creation of Gt-Mechanism for PSR

The described method has been tested as an example for the "CH_4 + air" mixture, for equivalence ratios $\alpha_{ox} = 0.66;\ 0.85;\ 1.00;\ 1.15; 1.42$ for temperatures $T_{eq,a} = 1600 - 2700$ K at p = 1 atm. The complete combustion mechanism for this propellant is given in [93] and contains 28 species and 131 reactions (see Subsection 3.4.2). The pecified set of analyzed species includes CH_4, O_2, N_2, CO_2, and H_2O (molecular nitrogen is considered as usual to be inert). Threshold values accepted in calculations $\zeta_i \in (\zeta_z, \zeta_v, \zeta_R)$ equal 0.01 or 0.02. Table 3.25 lists the results of calculation of reduction for the C–mechanism at $\alpha_{ox} = 1$ and $\zeta_i = 0.02$ in the range $T_{eq,a} = 2700 \rightarrow 1800$ K. Notations listed in this table stand for the following:

- N_{Rz} – number of reactions remaining after the first step (engagement method, Lz-mechanism)
- N_{Rv} – number of reactions remained after the second step (reduction over species, Lv-mechanism)
- N_{Rr} – number of reactions remained after the third step (reduction over reactions, Lr-mechanism)

Local errors (δ_Z) are between C- and Lz- mechanisms, δ_Z are between Lz- and Lv-mechanisms, δ_R are between Lv- and Lr-mechanisms, and δ_Σ are between C- and Lr-mechanisms.

Local errors are defined by the following formulas:

$$\delta_z = max\left|\frac{\gamma_k(\mathrm{C}) - \gamma_k(\mathrm{Lz})}{\gamma_k(\mathrm{C})}\right|, \delta_v = max\left|\frac{\gamma_k(\mathrm{Lz}) - \gamma_k(\mathrm{Lv})}{\gamma_k(\mathrm{C})}\right|, \tag{3.97}$$

$$\delta_R = max\left|\frac{\gamma_k(\mathrm{Lv}) - \gamma_k(\mathrm{Lr})}{\gamma_k(\mathrm{C})}\right|, \delta_\Sigma = max\left|\frac{\gamma_k(\mathrm{C}) - \gamma_k(\mathrm{Lr})}{\gamma_k(\mathrm{C})}\right|, \tag{3.98}$$

where $\gamma_k = -ln(r_k)$; $k \in CH_4, O_2, N_2, CO_2, H_2O$.

In the case of every point (for example, $\alpha_{ox} = 1$; p = 1 atm; T_0 = 2300 K), residence time τ_p is defined during the course of calculation, while the reduction starts from the C-mechanism (N_{Rc} = 131 reactions). It is evident from Table 3.27 that the main reduction results at the first step when $N_{Rc} - N_{Rz} \approx 80$ reactions at the average local error $\bar{\delta}_z \approx 0.003$ are excluded from the C-mechanism. At the second step, when changeover occurs from the Lz-mechanism to the Lv-mechanism, $N_{Rz} - N_{R_V} \approx 25$ reactions are excluded at the average local error $\overline{\delta_v} \approx 0.03$. At the third step, when changeover occurs from the *Lv* - κ *Lr* – mechanism, $N_{R_V} - N_{Rr} \approx 10$ reactions are excluded at the mean average error $\bar{\delta}_R \approx 0.02$. The total error is rather sufficient and varies in the interval $\delta_\Sigma \approx 0.01 \ldots 0.06$. Once Lr-mechanisms (for $\alpha_{ox} = 1$, and $T_{ap} = 2700$ K $\rightarrow$ 1800 K) are defined, they are combined into a single Gt($\alpha_{ox} = 1$) -mechanism incorporating

Downloaded from https://www.cambridge.org/core. Nottingham Trent University, on 17 Aug 2019 at 02:05:11, subject to the Cambridge Core terms of use, available at https://www.cambridge.org/core/terms. https://doi.org/10.1017/9781108581714.003

Table 3.27 Results of C-mechanism reduction (p = 1 atm, $T_{eq,a} = 2700 - 1800$ K, $\alpha_{ox} = 1$; threshold values $\zeta_z = \zeta_v = \zeta_R = 0.02$

$T_{eq,a}$	T_f	N_{Rz}	N_{Rv}	N_{Rr}	δ_z	δ_v	δ_R	δ_Σ
2700	2435	48	20	10	0.0026	0.017	0.039	0.059
2600	2344	48	20	11	0.0026	0.021	0.024	0.047
2500	2256	50	21	11	0.0013	0.023	0.024	0.048
2400	2166	50	21	11	0.0014	0.027	0.023	0.052
2300	2072	50	21	11	0.0015	0.030	0.024	0.055
2200	1985	49	20	11	0.0028	0.033	0.022	0.059
2100	1892	48	18	11	0.0054	0.035	0.020	0.061
2000	1816	49	19	11	0.0039	0.037	0.021	0.062
1900	1780	47	19	11	0.0030	0.040	0.018	0.061
1800	1725	47	24	13	0.0021	0.005	0.007	0.014

Table 3.28 Reactions of Gt($\alpha_{ox} = 1$)-mechanism at p = 1 atm, $T_{eq,a} = 2700\,\text{K} \rightarrow 1800\,\text{K}$, $\zeta_z = \zeta_v = \zeta_R = 0.02$

Reaction	T_{ap}	Reaction	T_{ap}
$H + O_2 = O + OH$	2700	$CH_4 + H = CH_3 + H_2$*	2700
H_2+ $OH = H_2O + H$	2700	$CH_4 + OH = CH_3 + H_2O$	2700
$OH + OH = H_2O + O$	2700	$CH_3 + O = CH_2O + H$	2700
$H + OH + M = H_2O + M$	2600	$CH_2O + OH = HCO + H_2O$	2700
$H + O_2 + M = HO_2 + M$	1800	$HCO + M = CO + H + M$	2700
$HO_2 + H = OH + OH$*	1800	HCO+H=CO+H_2*	2700
$CO + OH = CO_2 + H$	2700		

* Reactions not included in the Gt-mechanism for $\alpha_{ox} = 1.42$

14 species (H, O, N_2, O_2, OH, H_2, H_2O, HO_2, HCO, CO, CO_2, CH_3, CH_4, CH_2O) and 13 reactions, given in Table 3.28, where T_{ap} is the temperature $T_{eq,a}$ whereat the reaction has been involved for the first time in the Gt($\alpha_{ox} = 1$) -mechanism. Most reactions get involved at $T_{ap} = 2700\,\text{K}$ in compliance with the following rule: if certain reaction is included in Gt-mechanism at whatever temperature T_{ap}, it should be included at other temperatures as well. The obtained mechanism depicts the basic way of the conversion of reactants (CH_4, O_2) into combustion products (H_2O, CO_2) via radicals and intermediate species H, O, OH, HO_2, HCO, CO, CH_3, CH_2O. Alternative ways of combustion products formation proceed via low-rate reactions, which is why these ways are rejected to render the Gt($\alpha_{ox} = 1$)-mechanism not complicated.

Similar results for the Gt-mechanism are obtained at $\alpha_{ox} = 1.42$, p = 1 atm in the same temperature range (with thresholds $\zeta_i = 0.02$). The total error for preset species varies in the range $\delta_\Sigma \approx 0.01 \ldots 0.03$. The Gt-mechanism ($\alpha_{ox} = 1.42$) comprises 10 reactions only (Table 3.28), but includes the same 14 species. Thus, the Gt-mechanisms are not complicated in the case of lean mixtures and at incorporating them in the model of multidimensional flows, the scope of combustion calculations can be reduced compared with the C-mechanism some $\left(\frac{131}{13}\right) \times \left(\frac{28}{14}\right)^3 \approx 80$ times at an

Downloaded from https://www.cambridge.org/core. Nottingham Trent University, on 17 Aug 2019 at 02:05:11, subject to the Cambridge Core terms of use, available at https://www.cambridge.org/core/terms. https://doi.org/10.1017/9781108581714.003

acceptable error of calculation. At calculating the change in the relative scope of calculations, it is assumed in compliance with [73] that this scope is proportional to the number of reactions and the cube of amount of species.

In the case of rich reacting systems ($\alpha_{ox} \leq 1.0$), the Gt-mechanisms render more complicated. Table 3.29 lists the results of reduced mechanism generation for the following conditions: $\alpha_{ox} = 0.66$; $p = 1\,\text{atm}$; $T_{eq,a} = 2400\,\text{K} \rightarrow 1600\,\text{K}$; $\zeta_i = 0.02$. The engagement method (first step) is shown to exclude solely $N_{Rc} - N_{Rz} \approx 50$ reactions with significant local error $\bar{\delta}_z \approx 0.01$ from the C-mechanism.

At the second step of the reduction of species, the $N_{Rz} - N_{Rv} \approx 30$ reactions at average local error $\bar{\delta}_v \approx 0.02$ are excluded from the Lz-mechanism. At the reaction reduction step, $N_{Rv} - N_{Rr} \approx 25$, reactions are excluded at high local error $\bar{\delta}_R \approx 0.06$. The total error for specified species is significant and varies in the range $\delta_\Sigma = 0.02 \ldots 0.09$. Combined Gt($\alpha_{ox} = 0.66$)-mechanism with $\zeta_i = 0.02$ contains 21 species (C, H, O, N_2, O_2, OH, H_2, H_2O, HCO, CO, CO_2, CH, CH_2, CH_3, CH_4, CH_2O, C_2H_2, C_2H_3, C_2H_4, C_2H_5, C_2H_6) and 28 reactions listed in Table 3.30. It is

Table 3.29 Results of C-mechanism reduction ($p = 1$ atm, $T_0 = 2400 \rightarrow 1600\,\text{K}$, $\alpha_{ox} = 0.66$, $\zeta_i = 0.02$

$T_{eq,a}$	T_f	N_{Rz}	N_{Rv}	N_{Rr}	δ_z	δ_v	δ_R	δ_Σ
2400	2236	81	42	17	0.013	0.023	0.037	0.052
2300	2167	80	43	17	0.013	0.022	0.040	0.057
2200	2093	80	42	19	0.014	0.035	0.060	0.081
2100	2015	79	50	21	0.015	0.018	0.089	0.095
2000	1922	75	54	27	0.012	0.013	0.079	0.054
1900	1833	69	50	27	0.005	0.016	0.069	0.049
1800	1738	71	50	27	0.008	0.017	0.068	0.046
1700	1636	74	49	28	0.006	0.019	0.041	0.018
1600	1539	71	47	28	0.011	0.017	0.032	0.017

Table 3.30 Reactions of Gt($\alpha_{ox} = 0.66$) mechanism at $p = 1$ atm, $T_0 = 2400 \rightarrow 1400\,\text{K}$, $\zeta_i = 0.02$

Reaction	$T_{eq,a}$	Reaction	$T_{eq,a}$
$H + O_2 = O + OH$	2400	$CH_2 + OH = CH_2O + H$	2400
$H_2 + O = H + OH$	2200	$CH_2 + OH = CH + H_2O$	2400
$H_2 + OH = H_2O + H$	2400	$CH + H = C + H_2$	2400
$OH + OH = H_2O + O$	2400	$CH + O_2 = HCO + O$	2400
$CO + OH = CO_2 + H$	2400	$C + OH = CO + H$	2200
$CH_4 + M = CH_3 + H + M$	2400	$C + O_2 = CO + O$	2400
$CH_4 + H = CH_3 + H_2$	2400	$CH_3 + CH_3 = C_2H_6$	2000
$CH_3 + H = CH_2 + H_2$	2400	$C_2H_6 + CH_3 = C_2H_5 + CH_4$	2000
$CH_3 + O = CH_2O + H$	2400	$C_2H_5 + M = C_2H_4 + H + M$	2000
$CH_3 + OH = CH_2O + H_2$	2100	$C_2H_4 + H = C_2H_3 + H_2$	2000
$CH_2O + H = HCO + H_2$	2400	$C_2H_3 + M = C_2H_2 + H + M$	2000
$HCO + M = CO + H + M$	2400	$C_2H_3 + H = C_2H_2 + H_2$	2100
$HCO + H = CO + H_2$	2400	$C_2H_3 + O_2 = HCO + CH_2O$	1700
$CH_2 + H = CH + H_2$	2400	$C_2H_2 + O = CH_2 + CO$	2000

Downloaded from https://www.cambridge.org/core. Nottingham Trent University, on 17 Aug 2019 at 02:05:11, subject to the Cambridge Core terms of use, available at https://www.cambridge.org/core/terms. https://doi.org/10.1017/9781108581714.003

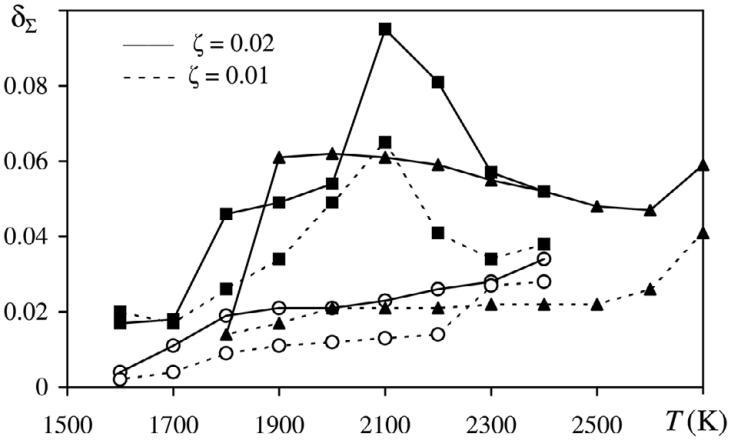

Figure 3.58 Distribution of global errors (δ_Σ) over temperature T_{ap} at different ζ_i $\alpha_{ox} = 0.66$ (■); $\alpha_{ox} = 1.00$ (▲); $\alpha_{ox} = 1.42$ (∘).

known that rich mixtures feature several significant ways forming the main combustion products (H_2O, CO_2) and intermediate species (CO, H_2, etc.). These ways should be allowed for in the performing of correct calculations for obtaining correct results. Therefore, the combined Gt($\alpha_{ox} = 0.66$) mechanism is more complicated than Gt ($\alpha_{ox} > 1.0$). It should be noted that the Gt($\alpha_{ox} = 0.66$) mechanism is formed not only at $T_{eq,a} = 2400\,\mathrm{K} \rightarrow 1600\,\mathrm{K}$, but at other temperatures as well; for example, at $T_{eq,a} = 2700\,\mathrm{K} \rightarrow 1800\,\mathrm{K}$. This means that the combustion scheme varies with the change in temperature.

The application Gt($\alpha_{ox} = 0.66$) mechanism allows to reduce the scope of calculations compared with the C-mechanism $\left(\frac{131}{28}\right) \times \left(\frac{28}{24}\right)^3 \approx 7$ times only. Combining of all Gt mechanisms (for $\alpha_{ox} =$ 0.66; 0.85; 1.00; 1.15; 1.42) allows getting the $G(T, \alpha_{ox})$-mechanism (i.e., reduced global mechanism for the entire area of application) that comprises 34 reactions.

Generally, with the decrease in ζ_i, all errors (including δ_Σ) should decrease. For verification of this trend, calculations have been made for the same area of application but with threshold values $\zeta_i = 0.01$. The results of comparison with global errors at $\zeta_i = 0.02$ are shown in Figure 3.58. As a rule, these errors decrease with the decrease in threshold values. Values δ_Σ decrease for $\alpha_{ox} = 0.66$ in the average approximately 1.5 times at the changeover from $\zeta_i = 0.02$ to $\zeta_i = 0.01$, while for $\alpha_{ox} = 1.00$, it decreases approximately 2.5 times, and for $\alpha_{ox} = 1.42$, approximately 2 times. The maximum error δ_Σ is perceived for the Gt($\alpha_{ox} = 0.66$) mechanism at T_{ap} = 2100 K. However, with the decrease in threshold values, the numbers of reactions and species increase in the reduced mechanisms.

Figure 3.59 compares residence time (for different values of α_{ox}) calculated by C-mechanisms and Gt-mechanisms ($\zeta_i = 0.02$). These times are defined in the course of the calculations so that the reacting system is located in region A near the extinction line. The closeness of appropriate lines indicates that for a given α_{ox}, the reduced

Downloaded from https://www.cambridge.org/core. Nottingham Trent University, on 17 Aug 2019 at 02:05:11, subject to the Cambridge Core terms of use, available at https://www.cambridge.org/core/terms. https://doi.org/10.1017/9781108581714.003

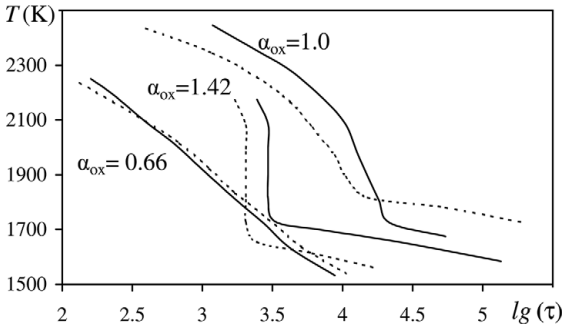

Figure 3.59 Dependence of temperatures T_f as a function of τ_p (residence time in microseconds) for different values of α_{ox}: C-mechanism (- - -); Gt-mechanisms for $\zeta_i = 0.02$ (—).

mechanism reflects the C-mechanism. The mechanism Gt($\alpha_{ox} = 0.66$) is from this point of view the most adequate, while the other mechanisms lead to a notable error.

3.6.3 Technique of Creation of G-Mechanism for PFR by Application of Engagement and Sounding Methods

The PFR scheme is usually used at the analysis of one-dimensional problems of propellant combustion while its initial temperature is higher than that of self-ignition, and combustion proceeds without the formation of the flame front; that is, the reacting system does not allow for conduction and diffusion. It is known that PFR can be represented in Euler coordinates by the series of PSR whereat reactants are fed into the first reactor while combustion products escape from the last reactor. Products of incomplete combustion escaping $(z - 1)$-th reactor are considered as a reactants for z-th reactor. Naturally, the greater the number of PSRs, the more accurate is the simulation of PFR. Let us consider the creation of the Gt-mechanism at α_{ox}, $p = const$ in the rage of reactant initial temperatures $T_{in} = T_1 \ldots T_{nz}$ for several PFRs with different initial temperatures (Figure 3.60).

Lets us assume that the flow in every PFR is isobaric and isothermal while heat released in the course of reactions is discharged through the channel walls. Assume also that the flow velocity in the reactors is V_g = 1 m/s (in this case, the equations for moving PFR and BR become identical). Then, for PFR (composed by the set of PSR) at temperature T_1 ,the L(T_1)-mechanism can be generated for some temperature T_{in}. This L(T_1)-mechanism will consist of L-mechanisms formed in each independent PSR (see Figure 3.60). Then it is required to perform the same procedure for PSR with temperature $T_{in} = T_2$ and generate the L(T_2) mechanism, while proceeding with the formation unless the L(T_n)-mechanism is formed. Now, at the combination of all produced L(T_{in})-mechanisms, the reduced Gt-mechanism can be formed to be applied for the calculation of processes in adiabatic PSRs, not just in isothermal ones.

The reduced L-mechanism in each of sequential PSR is formed in three steps; that is, engagement, species, and reactions sounding (see Subsection 3.5.1) with thresholds

Downloaded from https://www.cambridge.org/core. Nottingham Trent University, on 17 Aug 2019 at 02:05:11, subject to the Cambridge Core terms of use, available at https://www.cambridge.org/core/terms. https://doi.org/10.1017/9781108581714.003

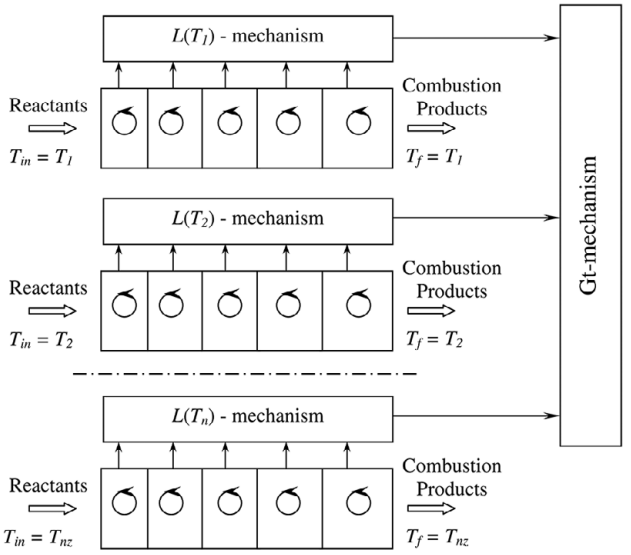

Figure 3.60 Diagram of PFR simulation by the set of PSRs ($T_{in} = const$) and the scheme of Gt-mechanism formation.

$\zeta_{z0}, \zeta_v, \zeta_R$. However, at the final stage, the so-called multistage threshold technique is used [97, 173]. In compliance with this procedure, the low threshold (for example, $\zeta_{R1} = \zeta_R/16$) is first set to perform sounding so that reactions with errors $\delta_R \leq \zeta_{R1}$ are excluded. Then the threshold is increased (for example, $\zeta_{R2} = \zeta_R/8$) and reactions with errors $\delta_R \leq \zeta_{R2}$ are excluded, and so on, unless the desired threshold ζ_R is reached. This procedure results in the increase in the scope of calculations, but, on the other hand, insignificant-influence reactions will not be included in the reduced mechanism with a high probability. Note here that the error δ_R calculated by Formula (3.98) is integral and increases as the reactions are excluded. Note also that a situation may arise when $\delta_R \cong \zeta_R$, which makes even insignificant reactions remain in the reduced mechanism at further sounding.

Apart from integral error, it is possible to calculate the independent errors by the formula:

$$\delta_s = \max \left| \frac{\gamma_k(\mathrm{Lv}) - \gamma_k(\mathrm{Lv} - s)}{\gamma_k(\mathrm{C})} \right| \qquad s = 1 \ldots s_f. \tag{3.99}$$

where s_f is the number of reactions being sounded and $\gamma_k(\mathrm{Lv\text{-}s})$ are logarithmic concentrations of the target species originating in the calculation of reacting system by the Lv-mechanism wherefrom the s-th reaction is withdrawn. These errors reflect the influence of individual reactions on the combustion process. Yet they are not additive with respect to each other and can hardly make the basis for the creation of the reduction procedure, but, nevertheless, they may well be used for illustration of multistage threshold advantages.

Figure 3.61 displays the diagram of independent errors of reactions (δ_s) of a certain hypothetic mechanisms (Figure 3.61a) and the lines of the rise of the integral error δ_R in

Downloaded from https://www.cambridge.org/core. Nottingham Trent University, on 17 Aug 2019 at 02:05:11, subject to the Cambridge Core terms of use, available at https://www.cambridge.org/core/terms. https://doi.org/10.1017/9781108581714.003

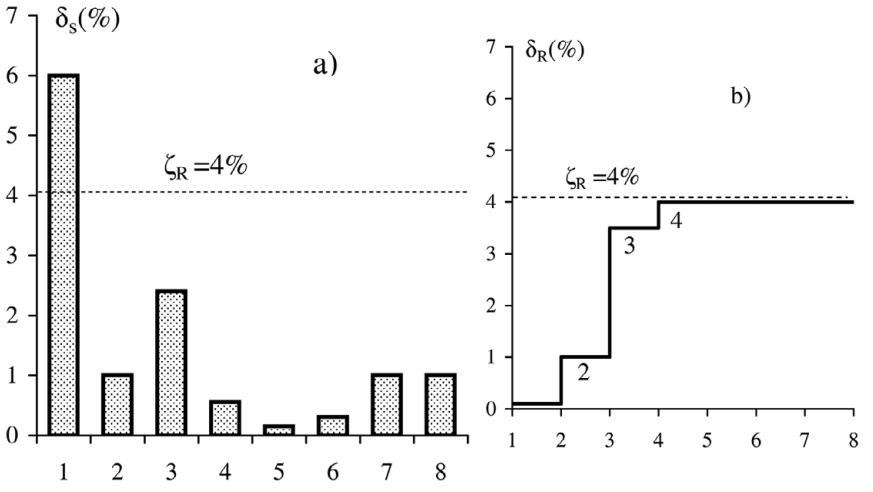

Figure 3.61 Diagram of independent errors of reactions (δ_s) of a certain hypothetic mechanism the line of rise of the integral error δ_R at the one-stage threshold $\zeta_R = 4\% = const$.

the course of reactions sounding at the one-stage threshold $\zeta_R = 4\%$ (Figure 3.61b). Numbers of reactions are shown on the abscissa axis, and it is evident that the first reaction notably influences the combustion characteristics (i.e., $\delta_R \geq \zeta_R$) and is retained in the mechanism. Then the second reaction is sounded and excluded from the mechanism, but the error $\delta_R = 1\%$ originates therein. Then the third reaction is analyzed and also excluded also the mechanism, though it exerts a notable influence ($\delta_s = 2.4\%$) to "form" the error $\delta_R = 1 + 2.4 = 3.4\%$ in the mechanism being reduced. Finally, the fourth reaction of insignificant influence with independent error $\delta_s = 0.55\%$ is sounded and excluded, which brings about the integral error $\delta_R = 3.4 + 0.55 = 3.95\%$. This error corresponds, in fact, to the set threshold $\zeta_R = 4\%$. Therefore, the fifth, sixth, seventh, and eighth reactions are not excluded from the mechanism, despite their insignificant influence on combustion parameters.

Let us consider the mechanism reduction procedure at the reaction sounding step with the same diagram of independent errors but at the stage-wise threshold (Figure. 3.62). First, sounding is performed at low threshold $\zeta_{R1} = 0.5\%$, and it is evident that only the fifth ($\delta_s = 0.15\%$) and sixth ($\delta_s = 0.3\%$) reactions will be eliminated from the mechanism being reduced to form the integral error $\delta_R = 0.15 + 0.3 = 0.45\%$. Other reactions will not be eliminated because of low threshold (see line a in Figure 3.62). Then, the threshold is increased to the value $\zeta_{R2} = 1.0\%$ to start the new sounding; its results are used for excluding only the fourth reaction ($\delta_s = 0.55\%$), while the error $\delta_R = 0.45 + 0.55 = 1.0\%$ reaches the threshold ζ_{R2} by now. The threshold is further increased to the value $\zeta_{R3} = 2.0\%$ to additionally eliminate the second reaction (see line b) from the mechanism. Finally, the threshold increases to the maximum permissible value, $\zeta_{R2} = 4\%$, and, as a result of sounding, the seventh and eighth reactions are excluded with independent errors $\delta_s = 1.0\%$ after the last probing.

Downloaded from https://www.cambridge.org/core. Nottingham Trent University, on 17 Aug 2019 at 02:05:11, subject to the Cambridge Core terms of use, available at https://www.cambridge.org/core/terms. https://doi.org/10.1017/9781108581714.003

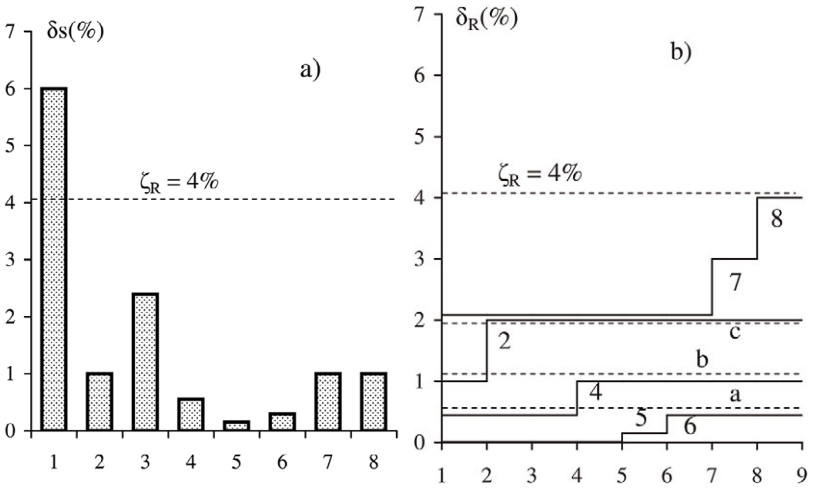

Figure 3.62 Diagram of independent errors of reactions (δ_s) of a certain hypothetic mechanism the line of rise of the integral error δ_R at the multistage threshold (a – $\zeta_{R1} = 0.5\%$; b – $\zeta_{R2} = 1.0\%$; c – $\zeta_{R3} = 2.0\%$).

As a result, at the multistage threshold, six reactions with minor independent errors are excluded from the basic mechanism, unlike the one-stage threshold where three reactions have been excluded – one of them (the third reaction) introducing a notable error in the reduced mechanism. Thus, the application of the multistage threshold allows one to avoid the following errors:

– inclusion of insignificant reactions in the mechanism being reduced
– exclusion of significant reactions from the mechanism being reduced

3.6.4 Example of Mechanism Reduction for Reacting Mixture "Methane + Air" in PFR

In the analyzed example, the C-mechanism (28 species and 131 reactions) cited in previous examples of reduction was used in compliance with algorithm given in Subsection 3.6.3. The Gt-mechanism is formed for $\alpha_{ox} = 0.66$; 1.0; 1.42; p = 1 atm, T_{in} = 1600 – 2400 K with the step $\Delta T = 200$ K. The initial data include the same species: CH_4, O_2, N_2, CO_2, and H_2O. Threshold values are $\zeta_z = 0.02$ for the engagement method and $\zeta_\nu = 0.02$ for sounding. At reaction sounding, the upper threshold is set to $\zeta_R = 0.016$ with the stages $\zeta_{R1} = 0.001$; $\zeta_{R2} = 0.002$; $\zeta_{R3} = 0.004$; $\zeta_{R4} = 0.008$; $\zeta_{R5} = \zeta_R = 0.016$. Residence time in the series of reactors is set in the range of $ln(\tau_p) = (-14), (-13.4), (-12.8), \ldots, (-5.6)$ with the increment $h = 0.6$ (τ_p is given in seconds); that is, the PFR is simulated by the series composed of n_z = 15 PSRs. The resultant Gt-mechanism for the stoichiometric mixture ($\alpha_{ox} = 1.0$) is shown in Table 3.31, where Nr is the number of the reaction in the C-mechanism, $z = (1 \ldots n_z)$ is the number of the reactors wherein the reaction has been detected (that is, included in the reduced mechanism).

Downloaded from https://www.cambridge.org/core. Nottingham Trent University, on 17 Aug 2019 at 02:05:11, subject to the Cambridge Core terms of use, available at https://www.cambridge.org/core/terms. https://doi.org/10.1017/9781108581714.003

Table 3.31 Reduced mechanism and sequence of reactions inclusion at $p = 1$ atm ($\zeta_R = 0.016$), $T_{in} = 2400 \ldots (200) \ldots 1600$ K; $\alpha_{ox} = 1.0$

Nr	Reaction	T_{in}	z	*Nr*	Reaction	T_{in}	z
2*	$H + O_2 = O + OH$	2400	4	38*	$CH_3 + O_2 = CH_3O + O$	2400	5
4*	$H_2 + OH = H_2O + H$	2400	6	39*	$CH_3O + M = CH_2O + H + M$	2400	5
5*	$OH + OH = H_2O + O$	2400	6	47*	$CH_2O + OH = HCO + H_2O$	2400	6
6	$H + OH + M = H_2O + M$	2400	13	48*	$HCO + M = CO + H + M$	2400	6
13*	$H + O_2 + M = HO_2 + M$	1800	13	49*	$HCO + H = CO + H_2$	2400	6
15	$HO_2 + H = OH + OH$	1800	13	58	$CH_2 + OH = CH_2O + H$	2400	6
24*	$CO + OH = CO_2 + H$	2400	6	83*	$CH_3 + CH_3 = C_2H_6$	2000	9
26*	$CH_4 + M = CH_3 + H + M$	2400	4	85*	$CH_3 + CH_3 = C_2H_4 + H_2$	2400	5
27*	$CH_4 + H = CH_3 + H_2$	2400	4	90*	$C_2H_6 + CH_3 = C_2H_5 + CH_4$	2000	9
28*	$CH_4 + O = CH_3 + OH$	2400	5	92*	$C_2H_5 + M = C_2H_4 + H + M$	2000	9
29*	$CH_4 + OH = CH_3 + H_2O$	2400	5	97	$C_2H_4 + O = HCO + CH_3$	2400	6
33*	$CH_3 + O = CH_2O + H$	2400	6	109	$C_2H_2 + O = CH_2 + CO$	2400	6
37	$CH_3 + O_2 = CH_2O + OH$	2400	5				

* Reactions not included in the Gt-mechanism for $\alpha_{ox} = 1.42$

The reduced mechanism starts forming at $T_{in} = 2400$ K, passing sequentially through the reactors from the first to the fifteenth. For PSR, the calculations are performed using the following mechanisms: C, Lz, Lv, and Lr. In the evaluation of the reaction influence at the step of reduction over reactions, the value δ_R is defined by Formula (3.98) to include this reaction in the reaction mechanism if $\delta_R \geq \zeta_R$. It is evident that in the course of the calculation of the processes taking place in the first, second, and third reactors, none of reactions are selected to be included in the Lr-mechanism because the residence time is small (from 0.83 to 2.8 μs) and the concentration of species from their initial list does not, in fact, vary; that is, $\delta_R = \zeta_R$. But the reacting mixture composition starts varying already in the fourth reactor to include three reactions of reactant decomposition in the Lr-mechanism, for which $\delta_R \geq \zeta_R$. The combustion process starts in this reactor to proceed in the fifth and sixth PSRs. Concentrations of the target species vary notably; therefore, meaningful reactions of combustion are detected and selected into the Lr-mechanism (six reactions from the fifth reactor and ten reactions from the six reactor). Important intermediate species involved in these reactions are also included in the reduced mechanism. The species conversion path renders more slanted in the seventh reactor, and other reactions are not detected because the threshold ζ_R, is not overcome. However, residence time increases, which facilitates the detection of slower but important reactions. Henceforth, only one reaction is detected; that occurs in the 13th reactor and exceeds this threshold. As a result, the Lr-mechanism including 20 reactions is formed for $T_{in} = 2400$ K.

Then, the Lr-mechanism is formed for $T_{in} = 2200$ K, which includes the entire set of reactions generated at $T_{in} = 2400$ K. Therefore, a few other reactions (detected as meaningful at $T_{in} = 2200$ K) can be included in this mechanism. However, on passing all 15 PSRs at the indicated temperature, such reactions have not been revealed.

Then, the Lr-mechanism is formed for $T_{in} = 2000$ K. It is evident from Table 3.31 that three reactions are additionally included: 83rd, 90th and 92nd proceeding in the ninth

Downloaded from https://www.cambridge.org/core. Nottingham Trent University, on 17 Aug 2019 at 02:05:11, subject to the Cambridge Core terms of use, available at https://www.cambridge.org/core/terms. https://doi.org/10.1017/9781108581714.003

reactor. Finally, at T_{in} = 1800 K this reduced mechanism is complemented with reactions 13 and 15 occurring in the 13th reactor. Note here that the Gt-mechanism results (at $\zeta_R = 0.016$), which includes 25 reactions. The obtained mechanism reflects the main pass of CH_4, O_2 reactant conversion into combustion products (H_2O, CO_2) via radicals and intermediate species – i.e., CH_3, H, O, OH, CH_3O, CH_2O, HCO, CO. Alternative passes of combustion product formation are implemented via low-rate reactions; therefore, the Gt($\alpha_{ok} = 1$) mechanism is not complicated. The same process has been used to generate the Gt -mechanism at multistage threshold $\zeta_R = 0.008$ and invariable other parameters, including 32 reactions.

Both reduced mechanisms are tested using the one-dimensional adiabatic flow model (2.26, 2.149) of reacting mixture "Methane + Air" at $\alpha_{ok} = 1.00$; p = 1 atm, T_0 = 1600 K. Results of calculations for complete and reduced mechanisms are shown in Figures 3.63 and 3.64. It is evident that parameters of flows for all options are sufficiently close and decrease with the drop in threshold ζ_R of mismatch with the data obtained from the C-mechanism.

It should be underlined that the application of the reduced mechanism obtained by the single PSR scheme (Table 3.28) to the solution of this problem brings about significant errors in the prediction of the parameters of the reacting flow. This discrepancy results from the fact that combustion products in a single PSR are directly mixed with reactants that runs counter to the model of propellant combustion in the PFR. In particular, on comparing Tables 3.28 and 3.31, it should be pointed out that the CH_3O radical, which important at the initial stage of combustion, is absent in the reduced mechanism for the single PSR.

At the same thresholds, quantity and size of reactors the C-mechanism have been reduced at $\zeta_R = 0.016$ for the reacting mixture at $\alpha_{ox} = 1.42$. The resulting Gt-mechanism comprises 21 reactions marked by an asterisk (*) in Table 3.31 and reaction

$$C_2H_4 + OH = CH_2O + CH_3 \tag{3.100}$$

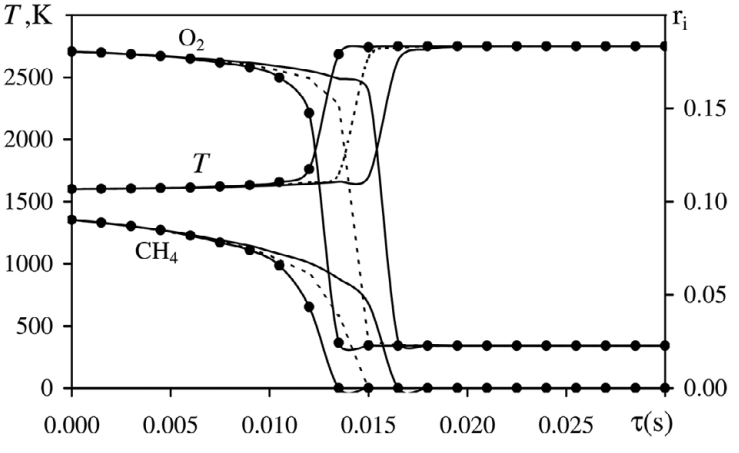

Figure 3.63 Variation of temperature and CH_4, O_2 concentrations (at $\alpha_{ox} = 1.0$; T_0 = 1600 K; p = 1 atm) obtained by complete (•) and reduced (--- $\zeta_R = 0.008$), (— $\zeta_R = 0.016$) mechanisms.

Downloaded from https://www.cambridge.org/core. Nottingham Trent University, on 17 Aug 2019 at 02:05:11, subject to the Cambridge Core terms of use, available at https://www.cambridge.org/core/terms. https://doi.org/10.1017/9781108581714.003

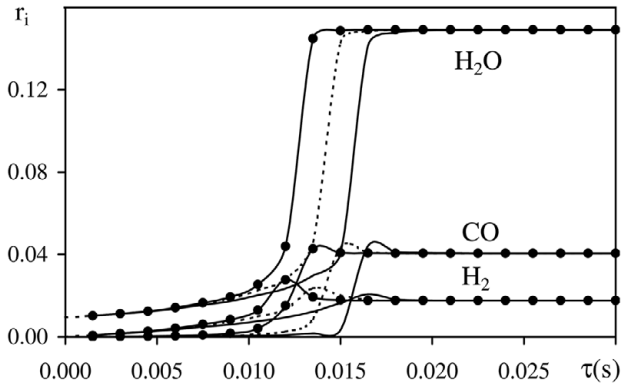

Figure 3.64 Variation of H_2O, CO, and H_2 concentrations (at $\alpha_{ox} = 1.0$; $T_0 = 1600$ K; $p = 1$ atm) obtained by complete (●) and reduced (---$\zeta_R = 0.008$), (—$\zeta_R = 0.016$) mechanisms.

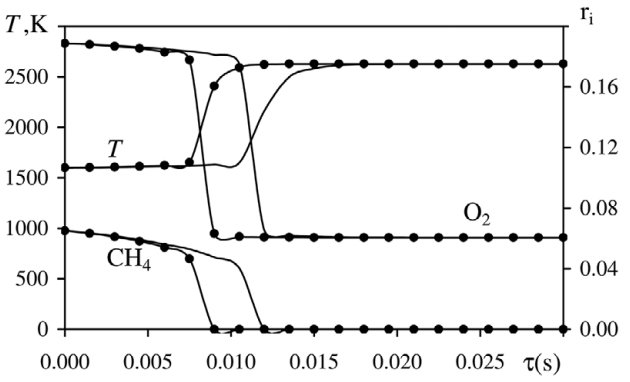

Figure 3.65 Variation of temperature and CH_4, O_2 concentrations (at $\alpha_{ox} = 1.42$; $T_0 = 1600$ K; $p = 1$ atm) obtained by complete (●) and reduced (—$\zeta_R = 0.016$) mechanisms.

It is apparent that this mechanism is simpler compared with the mechanism at $\alpha_{ox} = 1.0$ at the same main scheme of methane conversion:

$$CH_4 \rightarrow CH_3 \rightarrow (CH_2O, CH_3O) \rightarrow HCO \rightarrow CO \rightarrow CO_2 \qquad (3.101)$$

Hydrogen formed here in the interaction with O_2 is converted into water. The Gt ($\alpha_{ox} = 1.42$)-mechanism has no CH_2, C_2H_2, while C_2H_4, C_2H_6 forms as an intermediate species, and some others are insignificant in the ignition process. Figures 3.65 and 3.66 show the comparison of combustion characteristics in the adiabatic reactor for complete and reduced mechanisms. As can be seen, the reduced mechanism satisfactorily predicts the ignition process.

The basic C-mechanism [93] is not that universal one and not recommended for application to $\alpha_{ox} < 0.66$, since in the case of very rich mixtures, the combustion process will be more complicated with the formation of heavy hydrocarbons and soot and can be described by 500 and more reactions [27, 46]. Therefore, for rich mixtures,

Downloaded from https://www.cambridge.org/core. Nottingham Trent University, on 17 Aug 2019 at 02:05:11, subject to the Cambridge Core terms of use, available at https://www.cambridge.org/core/terms. https://doi.org/10.1017/9781108581714.003

Table 3.32 Reduced mechanism and sequence of inclusion of reactions at $\alpha_{ox} = 0.66$; $p = 1$ atm ($\zeta_R = 0,016$), $T_{in} = 2000 \ldots (200) \ldots 1600$ K

Nr	Reactions	T_{in}	*z*	*Nr*	Reactions	T_{in}	*z*
2	$H + O_2 = O + OH$	2000	7	59	$CH_2 + OH = CH + H_2O$	2000	10
3	$H_2 + O = H + OH$	2000	10	68	$CH + H = C + H_2$	2000	10
4	$H_2 + OH = H_2O + H$	2000	10	71	$CH + O_2 = HCO + O$	2000	10
5	$OH + OH = H_2O + O$	2000	10	77	$C + OH = CO + H$	2000	10
10	$H + H + H_2O = H_2 + H_2O$	2000	11	83	$CH_3 + CH_3 = C_2H_6$	2000	9
24	$CO + OH = CO_2 + H$	2000	10	85	$CH_3 + CH_3 = C_2H_4 + H_2$	2000	9
26	$CH_4 + M = CH_3 + H + M$	2000	9	87	$C_2H_6 + H = C_2H_5 + H_2$	1800	14
27	$CH_4 + H = CH_3 + H_2$	2000	9	90	$C_2H_6 + CH_3 = C_2H_5 + CH_4$	2000	9
28	$CH_4 + O = CH_3 + OH$	2000	9	92	$C_2H_5 + M = C_2H_4 + H + M$	2000	9
29	$CH_4 + OH = CH_3 + H_2O$	2000	9	96	$C_2H_4 + H = C_2H_3 + H_2$	2000	10
32	$CH_3 + H = CH_2 + H_2$	2000	11	100	$C_2H_3 + M = C_2H_2 + H + M$	2000	10
33	$CH_3 + O = CH_2O + H$	2000	10	101	$C_2H_3 + H = C_2H_2 + H_2$	2000	10
38	$CH_3 + O_2 = CH_3O + O$	2000	9	104	$C_2H_3 + O_2 = HCO + CH_2O$	1800	13
39	$CH_3O + M = CH_2O + H + M$	2000	9	109	$C_2H_2 + O = CH_2 + CO$	2000	10
45	$CH_2O + H = HCO + H_2$	2000	10	110	$C_2H_2 + O = HC_2O + H$	1800	13
48	$HCO + M = CO + H + M$	2000	10	112	$C_2H_2 + OH = C_2H_2O + H$	1800	15
49	$HCO + H = CO + H_2$	2000	10	116	$C_2H_2O + H = HC_2O + H_2$	1800	15
54	$CH_2 + H = CH + H_2$	2000	10	119	$C_2H_2O + OH = CH_2O + HCO$	1800	15
58	$CH_2 + OH = CH_2O + H$	2000	10	121	$HC_2O + H = CH_2 + CO$	1800	13

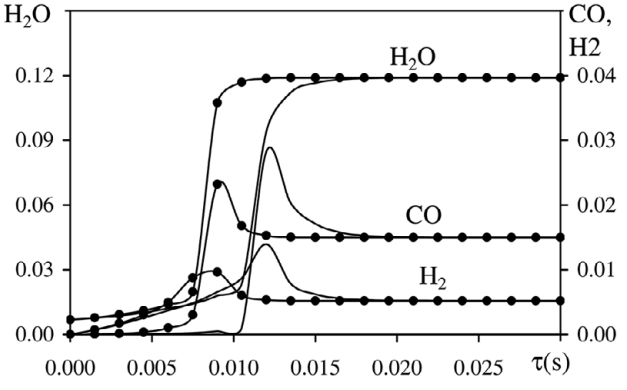

Figure 3.66 Variation of H_2O, CO, H_2 concentrations (at $\alpha_{ox} = 1.42$; $T_0 = 1600$ K; $p = 1$ atm) obtained by complete (•) and reduced (—$\zeta_R = 0.016$) mechanisms.

the C-mechanism has been reduced for $\alpha_{ox} = 0.66$. It has been performed at the same thresholds and sizes of the reactors in the temperature range $T_{in} = 2000$ K … 1600 K with the 200 K step at $\zeta_R = 0.016$. The resulting Gt-mechanism comprises 38 reactions (Table 3.32).

This mechanism is more complicated compared with the mechanism for stoichiometric mixture, though the main methane conversion scheme (3.100) does not vary. However, more significant are reactions with unsaturated hydrocarbons – i.e., soot

Downloaded from https://www.cambridge.org/core. Nottingham Trent University, on 17 Aug 2019 at 02:05:11, subject to the Cambridge Core terms of use, available at https://www.cambridge.org/core/terms. https://doi.org/10.1017/9781108581714.003

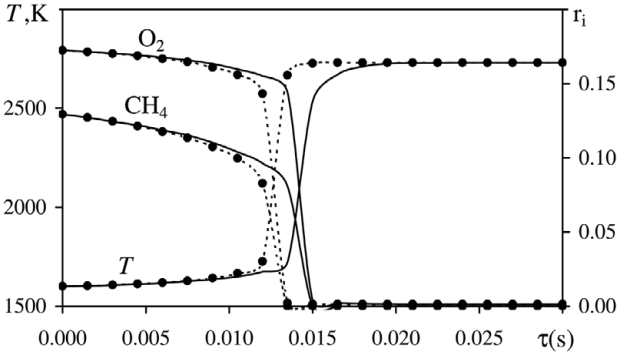

Figure 3.67 Variation of the temperature and CH_4, O_2 concentrations (at $\alpha_{ox} = 0.66$; $T_0 = 1600$ K; $p = 1$ atm) obtained by complete (•) and reduced (— $\zeta_R = 0.016$) mechanisms.

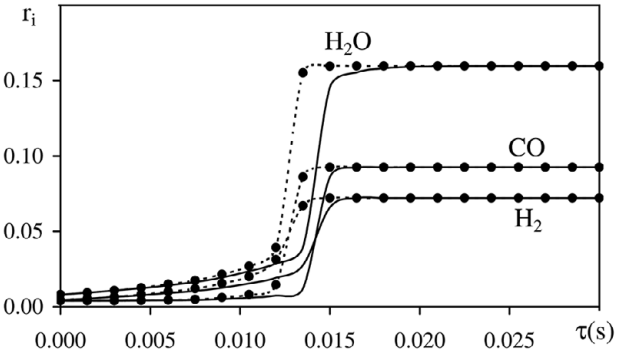

Figure 3.68 Variation of the H_2O, CO, H_2 concentrations (at at $\alpha_{ox} = 0.66$; $T_0 = 1600$ K; $p = 1$ atm) obtained by complete (•) and reduced (—$\zeta_R = 0.016$) mechanisms.

formation precursors – which define the CO and H_2 formation ways; rates of these reactions influence the chemical composition of combustion products. Table 3.30 shows that combustion begins in the seventh reactor wherein the second reaction is selected. The significant fast reactions are included in the reduced mechanism in the ninth and tenth reactors while slow reactions markedly affecting combustion join the reduced mechanism in the eleventh, thirteenth, and fifteenth reactors.

Figures 3.67 and 3.68 show the comparison of combustion parameters in adiabatic reactor for complete and reduced Gt($\alpha_{ox} = 0.66$) mechanisms. The reduced mechanism adequately predicts the ignition process.

3.6.5 Application of Directed Relation Graph with Error Propagation Method and Adaptive Threshold for PSR Scheme

The DRGEP method (see Subsection 3.5.3) is focused on the selection of only unimportant species and the removal them from reaction mechanism along with the reaction involving them. However, after the application of this method, many unimportant

Downloaded from https://www.cambridge.org/core. Nottingham Trent University, on 17 Aug 2019 at 02:05:11, subject to the Cambridge Core terms of use, available at https://www.cambridge.org/core/terms. https://doi.org/10.1017/9781108581714.003

Table 3.33 Reduced L-mechanism after application of the combined DRGEP method and adaptive threshold procedure: basic scheme – PSR; $\alpha_{ox} = 1.0$; $T_0 = 2700$ K; $p = 1$ atm; $\tau_p = 0.39{*}10^{-4}$s. №(C) – reaction number in the basic mechanism

№(C)	Reaction	№(C)	Reaction
1	$H + O_2 = O + OH$	32	$CH_3 + O = CH_2O + H$
2	$H_2 + O = H + OH$	34	$CH_3 + OH = CH_2 + H_2O$
3	$H_2 + OH = H_2O + H$	44	$CH_2O + H = HCO + H_2$
4	$OH + OH = H_2O + O$	46	$CH_2O + OH = HCO + H_2O$
23	$CO + OH = CO_2 + H$	47	$HCO + M = CO + H + M$
26	$CH_4 + H = CH_3 + H_2$	48	$HCO + H = CO + H_2$
27	$CH_4 + O = CH_3 + OH$	50	$HCO + O = CO_2 + H$
28	$CH_4 + OH = CH_3 + H_2O$		

reactions can persist in the mechanism. Therefore, the general algorithm of the reduction is frequently complemented by a procedure of their removal [99, 130, 142]. In particular, the application of the adaptive threshold concept along with parameter $G_i^d = max(Z_{ik})$ allows the removal of individual reactions (see Subsection 3.5.3). To do that, it is necessary to define the coefficient of influence of the i-th specie on the set of target species $K_i^d = 1/G_i^d$. Then, after application of the DRGEP method, reactions are validated by the relation:

$$abc[\nu_{is}(\Omega_s - \Omega_{s+m_c})] \geq K_i^d \zeta_{a0} \Omega_i^{\Sigma} \qquad s = 1 \ldots m_c, \tag{3.102}$$

where ζ_{a0} is the initial threshold for the removal of the reaction, and sum Ω_i^{Σ} is defined by Formula (3.73).

If the reversible s-th reaction satisfies Relation (3.102), then it remains in the mechanism.

The L-mechanism for some point in space $\{\alpha_{ox}, T, p\}$ results from combination of the DRGEP method and the adaptive threshold technique. This reduction procedure requires the minor amount of calculation and can easily be built in the PSR, PFR, and "batch" reactors.

Let us consider the example of reaction mechanism reduction in the PSR for the "CH_4 + air" mixture under conditions given in Subsections 3.5.1–3.5.3. The following threshold parameters are adopted in this example: $\zeta_d = 0.01$, or $\zeta_{a0} = 0.04$. At the first stage – i.e., after the application of the DRGEP method – the reduced mechanism comprises 15 species and 52 reactions. At the second stage – i.e., after the application of the adaptive threshold – the number of species does not decrease, but the number of reaction decreases to 15. This reduced L-mechanism is shown in Table 3.33.

This example and examples described in Subsections 3.5.1–3.5.3 reduce the same mechanism for the PSR scheme but use different reduction procedures. Figure 3.69 shows the comparison of the reduction results obtained at application of these methods.

The reduction methods comparison (m1–m4) reveals the following features:

– (m1) After reduction, the excess species and reactions persist in the reaction mechanism, but this method requires a minor scope of calculation and may be

Downloaded from https://www.cambridge.org/core. Nottingham Trent University, on 17 Aug 2019 at 02:05:11, subject to the Cambridge Core terms of use, available at https://www.cambridge.org/core/terms. https://doi.org/10.1017/9781108581714.003

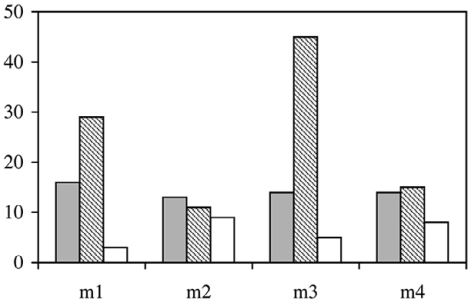

Figure 3.69 Comparison of characteristics of the basic mechanism reduction by different methods. ▭ – number of species; ▨ – number of reactions; ▭ – reduction error (%); m1 – engagement method with adaptive threshold; m2 – method of direct sounding over species and reactions; m3 – DRGEP method; m4 – DRGEP method and adaptive threshold procedure.

readily built in the algorithms of computing the combustion processes in the reactors.

– (m2) This method allows one to reach a high degree of mechanism reduction but requires a significant amount of calculation, and it can hardly be built in the applied models of combustion.
– (m3) The independent application of the DRGEP method leaves many unimportant reactions in the reduced mechanism; therefore, it is advisable to use this method in combination with some procedure of the analysis and reduction of reactions.
– (m4) This combined method provides for a quite acceptable reduced mechanism without a large amount of calculation. Besides, it may be readily built in the applied models of combustion.

Hereinafter, the DRGEP and adaptive threshold method will be used as an illustration of the reduced mechanism formation for chemical nonequilibrium flows in the nozzles.

3.6.6 Reduction of Chemical Mechanisms at Calculating Chemical Nonequilibrium Flows in the Nozzle of a Rocket Engine

The calculation of chemical nonequilibrium processes in nozzles is a traditional problem in the design of these units. Interest stirred by this problem related with seeking new propellants and developing new designs of nozzles has continued unabated [174, 175, 176, 177, 178, 179]. At present, the models used for calculations of such flows (see Section 3.4) are based on a detailed chemical kinetics. For this, a certain reaction mechanism to be built in such model – for example, in the inverse problem of the Laval nozzle (Section 3.4) – is formed. The reaction mechanism is usually a redundant one, and it is advisable to reduce it with the help of one of the developed reduction procedures – in particular, the combination of the DRGEP method and the adaptive threshold procedure may be applied. In the case of rocket engine nozzles, the problem of the reduction of the chemical mechanism possesses the following features:

Downloaded from https://www.cambridge.org/core. Nottingham Trent University, on 17 Aug 2019 at 02:05:11, subject to the Cambridge Core terms of use, available at https://www.cambridge.org/core/terms. https://doi.org/10.1017/9781108581714.003

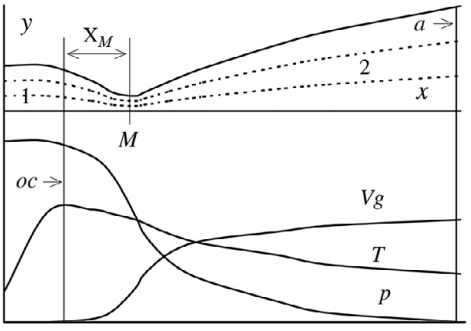

Figure 3.70 Variation of characteristics V_g, T, p in the thrust chamber: 1 – combustion chamber; 2 – nozzle; *oc* – inlet to the nozzle; *M* – minimum section (throat); *a* – outlet section.

- High-temperature equilibrium combustion products of some two-component propellant is fed to the nozzle inlet interpreted as PFR.
- Individual species including more than four atoms are contained in combustion products at high temperatures in extremely low concentrations. This is why such species may be omitted a priori from the basic mechanism of reactions.
- The most important characteristic of nonequilibrium flow is the coefficient of specific impulse losses because of chemical noneqilibrium (ξ_{dq}); at the chemical mechanism reduction, the accuracy of the calculation of this coefficient should remain very high.

Figure 3.70 displays the flow characteristics variation over the nozzle length. To determine the loss coefficient (ξ_{dq}) in the framework of one-dimensional flow, it is necessary to calculate the following:

- ideal specific impulse (I_{sp}^{id}) by the chemical equilibrium flow model
- specific impulse (I_{sp}^{dq}) by the chemical nonequilibrium flow model (see Section 3.4)
- coefficient of specific impulse losses by the formula:

$$\xi_{dq} = \frac{I_{sp}^{id} - I_{sp}^{dq}}{I_{sp}^{id}} \tag{3.103}$$

Equations (1.31, 1.34, and 1.35) are included in the mathematical model of chemical equilibrium flow in the nozzles that are complemented with the following equations:

– isentropic flow

$$S(p, T, r_i) \; - S_{oc} = 0 \tag{3.104}$$

– energy

$$h_p - \frac{\sum H_i r_i}{\mu_m} - \frac{V_g^2}{2} = 0, \tag{3.105}$$

Downloaded from https://www.cambridge.org/core. Nottingham Trent University, on 17 Aug 2019 at 02:05:11, subject to the Cambridge Core terms of use, available at https://www.cambridge.org/core/terms. https://doi.org/10.1017/9781108581714.003

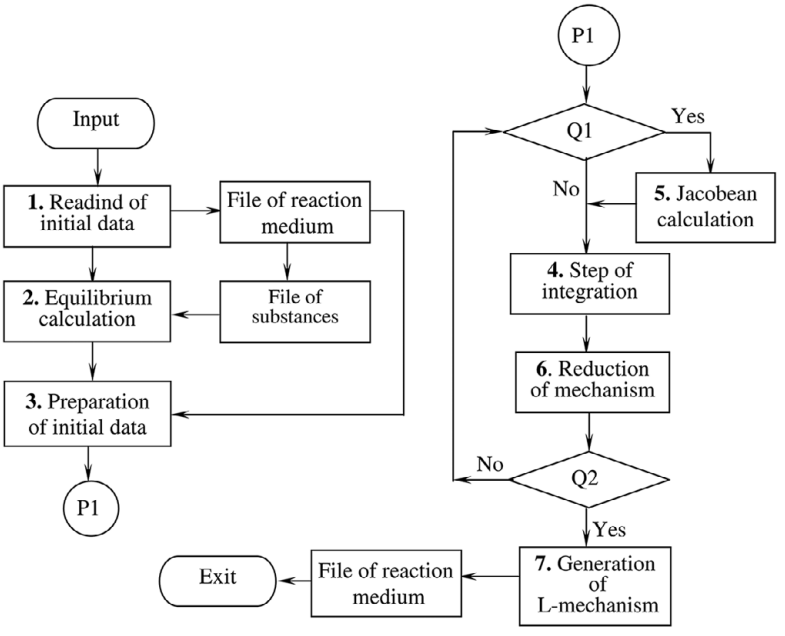

Figure 3.71 Diagram of the algorithm for calculation of flows in the nozzle with the reaction mechanism reduction unit. Q1 – calculate a Jacobian?, Q2 – has final value of the integration interval been reached?

where V_g is flow velocity; h_p is enthalpy of the propellant; H_i is molar enthalpy of the i-th substance; μ_m is the average molecular mass; oc is the entrance to the nozzle; $S(p, T, r_i)$ is molar entropy, a function of the pressure, temperature and working medium composition.

The specific impulse in vacuum is defined by the formula:

$$I_{sp}^{id} = V_{ga} + p_a / \left(\rho_{ga} V_{ga}\right). \tag{3.106}$$

The same formula is applied to calculation of the specific impulse (I_{sp}^{dq}) of chemical nonequilibrium flow described by Equations (3.69; 3.70) at the preset pressure distribution over the nozzle length: $\varphi(x) = -ln(p/p_{oc})$.

The diagram of the algorithm for the computation of one-dimensional flows in nozzles including the reaction mechanism reduction procedure is shown in Figure 3.71.

This algorithm comprises the following units:

1. Reading of initial data:
   - code of reacting medium
   - nozzle shape coordinates (x_k, y_k); α_{ox}
   - stagnation pressure at the entrance to the nozzle (p_{oc})
   - threshold values ζ_d, ζ_{a0}
   - set of target species.

Downloaded from https://www.cambridge.org/core. Nottingham Trent University, on 17 Aug 2019 at 02:05:11, subject to the Cambridge Core terms of use, available at https://www.cambridge.org/core/terms. https://doi.org/10.1017/9781108581714.003

The preset code from is used to select the set of symbols of species and the reaction mechanism (the very same C-mechanism) from the database of the reacting media (see Table 2.1) required for the calculation of both equilibrium and chemical nonequilibrium flows. Besides, the species symbols are used to read off the data from the species database on species thermodynamic properties (see Table 2.2).

2. Calculation of chemical equilibrium flow parameters over the nozzle length $T(x), p(x), V_g(x), r_i(x)$, and specific impulse in vacuum I_{sp}^{id}
3. Determination of the initial data for calculation of chemical noneqilibrium flow characteristics – i.e., formation of coordinating matrices (see Subsection 2.4.1), calculation of rate constants of reverse reactions, the first determination of the Jacobian matrix, etc., as well as the execution of the required operations for further reduction of reaction mechanisms
4. Execution of the step of integration over the nozzle length in compliance with the chemical nonequilibrium flow model (Section 3.4.) and selection of the next integration step (Subsection 2.4.4)
5. Recalculation of the Jacobian matrix in the case of need (Subsections 2.4.3 and 2.4.4)
6. Execution of the reaction mechanism reduction procedure by the DRGEP method with the application of the adaptive threshold procedure
7. Determination of the specific impulse I_{sp}^{dq} and loss coefficient ξ_{dq}, completion of the reduced mechanism generation, and loading of calculated data in the archive

The calculations have been made to exemplify the reactions mechanism reduction for reacting flows in shaped nozzles [160] for the following domain of parameters:

$$\alpha_{ox} = 0.7 \ldots 1.2;\ p_{\text{oc}} = 20 \ldots 100\,\text{atm};\ \ r_m = 0.006 \ldots 0.06\,\text{m}, \tag{3.107}$$

where r_m is the nozzle throat radius.

The reduced G-mechanism covers aforesaid domain. With the change in nozzle size, its shape does not vary while a geometric degree of expansion (relative area) is set constant $f_a = (r_a/r_m)^2 = 50$.

A. Reaction Mechanism Reduction for Reacting Medium C + H + O (Propellant: Kerosene + O_2).

The basic mechanism (C-mechanism) formed for this example (Table 3.34) comprises 16 species and 47 reactions [25, 93].

Let us accept for further comparison the flow mode with parameters $\alpha_{ox} = 1.0$; p_{oc} = 20 atm; r_m = 0.006 m as the basic mode, when chemical noneqilibrium effects become most obvious. The calculation results for this mode have been used (see Table 3.35) to set the values of thresholds ζ_d, ζ_{a0} for the entire region of G-mechanism action (3.107).

Table 3.35 obviously displays that the basic mechanism notable reduction is reached at minor threshold values $\zeta_L = 0.01$, while nine species remain in the L-mechanism:

$$(\text{H}, \text{H}_2, \text{O}, \text{O}_2, \text{CO}_2, \text{H}_2\text{O}, \text{CO}, \text{OH}, \text{HCO}) \tag{3.108}$$

and 13 reactions at very small reduction errors.

Downloaded from https://www.cambridge.org/core. Nottingham Trent University, on 17 Aug 2019 at 02:05:11, subject to the Cambridge Core terms of use, available at https://www.cambridge.org/core/terms. https://doi.org/10.1017/9781108581714.003

Table 3.34 Basic mechanism (C-mechanism) of reactions in combustion products for propellant kerosene + O_2

№ (C)	Reaction	№ (C)	Reaction	№ (C)	Reaction
1	$O_2 + H_2O = HO_2 + OH$	17	$CH + O_2 = CO + OH$	33	$CH_2 + O = CO + 2H$
2	$O_2 + H_2 = 2OH$	18	$CH + O_2 = HCO + O$	34	$CH_2 + OH = H + H_2CO$
3	$H_2 + OH = H_2O + H$	19	$CH_4 + O = CH_2 + H_2O$	35	$CH_2 + O_2 = OH + HCO$
4	$O+H_2 = OH + H$	20	$O_2 + CH_4 = CH_3 + HO_2$	36	$CH_2 + O_2 = H_2 + CO_2$
5	$H+O_2 = OH + O$	21	$CH_4 + M = CH_3 + H + M$	37	$OH + CO_2 = O_2 + HCO$
6	$2OH = H_2O + O$	22	$CH_4 + H = CH_3 + H_2$	38	$HCO + OH = CO + H_2O$
7	$2H + M = H_2 + M$	23	$CH_4 + O = CH_3 + OH$	39	$HCO + M = H + CO + M$
8	$2O + M = O_2 + M$	24	$OH + CH_4 = H_2O + CH_3$	40	$HCO + H = CO + H_2$
9	$H + M + OH = H_2O + M$	25	$OH + CH_3 = H_2O + CH_2$	41	$HCO + O = CO + OH$
10	$O + H + M = OH + M$	26	$CH_3 + H_2CO = CH_4 + HCO$	42	$HCO + O_2 = CO + HO_2$
11	$CO + O_2 = CO_2 + O$	27	$CH_3 + O_2 = OH + H_2CO$	43	$H_2CO + M = HCO + H + M$
12	$CO + OH = CO_2 + H$	28	$CH_3 + O_2 = HCO + H_2O$	44	$H_2CO + OH = HCO + H_2O$
13	$CO + O + M = CO_2 + M$	29	$CH_3 + O = H_2CO + H$	45	$H_2CO + H = HCO + H_2$
14	$CO_2 + H_2 = OH + HCO$	30	$CH_2 + OH = CH + H_2O$	46	$H_2CO + O = HCO + OH$
15	$CO_2 + H = O + HCO$	31	$CH_2 + O = CH + OH$	47	$H_2CO + O_2 = HCO + HO_2$
16	$CH_2 + H = CH + H_2$	32	$CH_2 + O = HCO + H$		

Table 3.35 Size of reduced mechanism for the basic mode and characteristics of the flow at the nozzle exit depending on threshold parameters ζ_d, ζ_{a0} at $\zeta_d = \zeta_{a0} = \zeta_L$ (concentrations of species CO_2, O_2, H_2O, CO are given in mole fractions)

Mechanism	Specie	Number of reactions	T_a(K)	CO_2	O_2	H_2O	CO	$\xi_d(\%)$
C-mechanism	16	47	1515	0.2875	0.0933	0.3447	0.1577	5.213
$\zeta_L = 0.01$	9	13	1515	0.2875	0.0933	0.3447	0.1577	5.215
$\zeta_L = 0.02$	9	13	1515	0.2875	0.0933	0.3447	0.1577	5.215
$\zeta_L = 0.04$	8	10	1501	0.2859	0.0941	0.3435	0.1583	5.329
$\zeta_L = 0.08$	8	10	1501	0.2859	0.0941	0.3435	0.1583	5.329

In particular, for the nozzle exit the following errors result:

– for temperature:

$$\delta_T = \left|T_g(\mathrm{C}) - T_g(\mathrm{L})\right| / T_g(\mathrm{C}) \le 10^{-4} \tag{3.109}$$

– for loss coefficient because of chemical noneqilibrium (ξ_{dq}):

$$\delta_{dq} = \left|\xi_{dq}(\mathrm{C}) - \xi_{dq}(\mathrm{L})\right| / \xi_{dq}(\mathrm{C}) \le 2*10^{-4} \tag{3.110}$$

– for target species:

$$\delta_t = max|r_k(\mathrm{C}) - r_k(\mathrm{L})| / r_k(\mathrm{C}) \le 10^{-4}, k \in \text{target species} \tag{3.111}$$

Downloaded from https://www.cambridge.org/core. Nottingham Trent University, on 17 Aug 2019 at 02:05:11, subject to the Cambridge Core terms of use, available at https://www.cambridge.org/core/terms. https://doi.org/10.1017/9781108581714.003

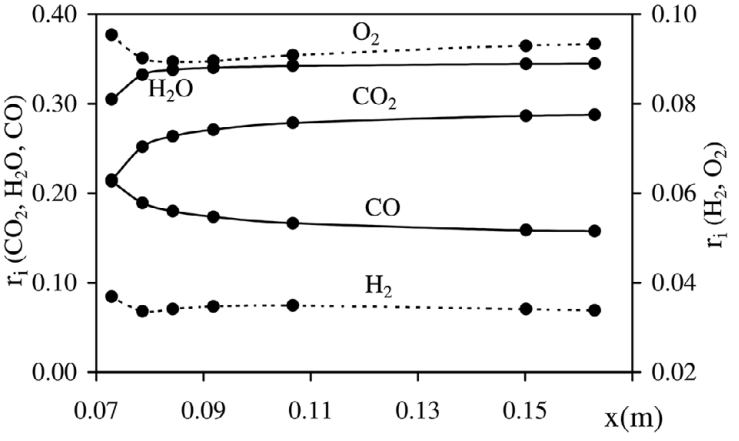

Figure 3.72 Variation of combustion products chemical composition and temperature over the nozzle length for basic and reduced ($\zeta_L = 0.02$) mechanisms; propellant "kerosene + O_2".

Such a significant reduction results from availability of four-atom substances and related radicals in the C-mechanism. These species are unstable at high temperatures, which is why they are contained in the working medium in extremely low concentrations that do not affect the content of target species. Six substances (CH_4, HO_2, CH, CH_2, CH_3, and H_2CO) and 29 reactions related therewith are removed at the first step of the reduction procedure (DRGEP method) as the result. An additional five insignificant reactions are removed at the adaptive threshold step.

At the basic mode, at threshold parameter $\zeta_L = 0.02$, the same reduced mechanism is generated; therefore, the working medium characteristics errors at the nozzle exit remain insignificant. They are insignificant as well over the nozzle length, as seen in Figure 3.72, which displays the combustion products chemical composition variation at calculation by the C- and L-mechanisms.

At thresholds $\zeta_L = 0.04$, the reduced mechanism is generated in basic mode with eight species and 10 reactions when radical HCO and three reactions are removed. Radical removal results in some discrepancy between the results obtained at calculation by C- and L-mechanisms – in particular, $\delta_T \approx 1\%; \delta_{dg} \approx 2\%; \delta_t \approx 1\%$. Therefore, at the generation of L-mechanisms, for other modes of noneqilibrium flow, the thresholds $\zeta_L = 0.02$ have been set. Then, about 40 points $\{\alpha_{ox}; p_{oc}; r_m\}$ have been selected in the domain (3.107); for each of them, the flow parameters have been calculated and L-mechanism has been generated.

Some results obtained with the application of these mechanisms are listed in Table 3.36, where B_i(L), R_s(L) is the number of species and reactions in L-mechanisms and T_a(C), T_a(L), ξ_{dq}(C), ξ_{dq}(L) are parameters at the nozzle exit obtained by the C- and L- mechanisms. Columns 2–7 list characteristics of the L-mechanisms at points $p_{oc} = 20$ atm, $r_m = 0.006$ m in the range of $\alpha_{ox} = 0.7$, to $\alpha_{ox} = 1.2$, with the step $\Delta\alpha_{ox} = 0.1$, while columns 8 and 9 describe the same characteristics at the points:

Downloaded from https://www.cambridge.org/core. Nottingham Trent University, on 17 Aug 2019 at 02:05:11, subject to the Cambridge Core terms of use, available at https://www.cambridge.org/core/terms. https://doi.org/10.1017/9781108581714.003

Table 3.36 Comparison of flow characteristics for combustion products of the propellant kerosene + O_2 at application of the basic and reduced ($\zeta_L = 0.02$) mechanisms

	p_{oc} = 20 atm; r_m = 0.006 m						(3.112a)	(3.112b)
α_{ox}	0.7	0.8	0.9	1.0	1.1	1.2	1.0	1.0
B_i(L)	9	9	9	9	9	9	9	9
R_s(L)	11	12	13	13	14	12	13	11
T_a(C) K	1258	1436	1509	1515	1493	1461	1850	2055
T_a(L) K	1258	1435	1510	1515	1493	1461	1851	2055
ξ_{dq}(C)%	2.372	4.119	5.037	5.213	5.310	5.335	2.362	1.080
ξ_{dq}(L)%	2.383	4.163	4.983	5.215	5.261	5.354	2.369	1.080

Table 3.37 Reduced G-mechanism for combustion products of the propellant kerosene + O_2 for the domain (3.107) of the variation of parameters α_{ox}, p_{oc}, r_m

№(C)	Reaction	№(C)	Reaction	№(C)	Reaction
3	$H_2 + OH = H_2O + H$	8	$2O + M = O_2 + M$	13	$CO + O + M = CO_2 + M$
4	$O + H_2 = OH + H$	9	$H + M + OH = H_2O + M$	14	$CO_2 + H_2 = OH + HCO$
5	$H + O_2 = OH + O$	10	$O + H + M = OH + M$	15	$CO_2 + H = O + HCO$
6	$2O\ H = H_2O + O$	11	$CO + O_2 = CO_2 + O$	39	$HCO + M = H + CO + M$
7	$2H + M = H_2 + M$	12	$CO + OH = CO_2 + H$	40	$HCO + H = CO + H_2$

$$\{\alpha_{ox} = 1.0; p_{oc} = 100 \text{ atm}; r_m = 0.006 \text{ m}\} \tag{3.112a}$$

$$\{\alpha_{ox} = 1.0; p_{oc} = 100 \text{ atm}; r_m = 0.06 \text{ m}\} \tag{3.112b}$$

Each L-mechanism is shown to contain nine species included in the set (3.108) but with the different number of reactions (from 11 to 14) that results from the change in the role of some of them with their subsequent removal (or retention) at the adaptive threshold step. Temperature T_a(L) at the nozzle exit is predicted practically without errors, but minor errors related to the specific impulse loss originate. The maximum discrepancy in this parameter between the C- and L-mechanisms is 1%, which corresponds to the error in specific impulse $\approx 0.05\%$ or, in absolute terms, 1.5 m/s. Combining all generated L-mechanisms, it is possible to get the "global" reduced mechanism (Table 3.37) for the entire domain (3.107).

In compliance with the known rule, the "amount of calculations is proportional to the number of reactions and to the cube of the number of species" [90, 142], it is possible to derive the estimate for the relationship of the amount of calculation by the C- and G-mechanisms:

$$\frac{V(\text{C})}{V(\text{L})} = \left(\frac{47}{15}\right) \times \left(\frac{16}{9}\right)^3 \approx 20. \tag{3.113}$$

The obtained result is not that important for univariate problems because of the extremely short computer time required for their analysis. However, the calculation of

Downloaded from https://www.cambridge.org/core. Nottingham Trent University, on 17 Aug 2019 at 02:05:11, subject to the Cambridge Core terms of use, available at https://www.cambridge.org/core/terms. https://doi.org/10.1017/9781108581714.003

multidimensional reacting flows may take a lot of time [99, 130]. In this case, the application of the developed G-mechanism will allow a notable reduction in time of computation.

B. Reduction Reactions Mechanism for Reacting Medium C + H + O + N (Propellant N_2O_4 + Unsymmetrical Dimethylhydrazine; UDMH)

This reacting system is more complicated than that in the previous example, since at high temperatures, the nitrogen-contained chemical compounds take an active part in chemical reactions. The formed basic mechanism comprises 26 species and 82 reactions [25, 26, 93]. This example aims to create the reduced G-mechanism for the same region (3.107) of changes in parameter α_{ox}, p_{oc}, r_m at the same basic flow mode (α_{ox} = 1.0; p_{oc} = 20 atm; r_m = 0.006 m). However, molecular nitrogen (N_2) is included additionally in the set of target species.

Table 3.38 lists the results of the C-mechanism reduction for the basic mode and flow characteristics at the nozzle exit depending on the threshold values ζ_L. It is obvious that at as early as $\zeta_L = 0.01$, this mechanism reduces to 15 species and 26 reactions at insignificant errors – i.e., $\delta_T \approx 0.1\%$ in temperature, $\delta_t \approx 1\%$ in target species, and $\delta_{dg} \approx 0.07\%$ in specific impulse losses.

It is known that with the increase in thresholds, there is a common trend of the increase in discrepancy between the results obtained by C- and L-mechanisms. However, at $\zeta_L = 0.02$, these errors render very small ($\delta_T \approx 0.01\%$; $\delta_{dg} \approx 0.01\%$; $\delta_t \approx 0.01\%$) though the size of the L-mechanism decreases. In a number of papers – for example, [97] – such fluctuation is considered possible. Let us assume two reactions, R^+ and R^-, involving specie B are in some C- mechanism. Let us assume also that reaction rates $W^+$and W^- have the following properties – i.e.,

1. At the proceeding of reaction R^+, specie B is generated, while in reaction R^-, it is consumed.
2. Reaction rates are interrelated as $|W^+| \approx 1.2|W^-|$.
3. Each of the velocities of these reactions W^+, W^- makes $\approx 1\%$ of the overall rate (W_Σ) of the change in concentration of specie B.

Table 3.38 Sizes of reduced mechanisms for the basic mode and characteristics of the flow at the nozzle exit depending on the value of thresholds $\zeta_d = \zeta_{a0} = \zeta_L$. Propellant N_2O_4 + UDMH; NB – number of substances; NR – number of reactions

Mechanism	NB	NR	T_a(K)	CO_2	O_2	H_2O	CO	NO	ξ_{dq}
C-mechanism	26	82	1187	0.1436	0.0386	0.3731	0.0637	0.0177	6.002
$\zeta_L = 0.01$	15	26	1188	0.1439	0.0383	0.3736	0.0635	0.0178	5.932
$\zeta_L = 0.02$	14	23	1187	0.1436	0.0386	0.3731	0.0637	0.0177	6.013
$\zeta_L = 0.03$	13	17	1181	0.1429	0.0388	0.3730	0.0642	0.0177	6.026
$\zeta_L = 0.04$	12	14	1179	0.1425	0.0392	0.3722	0.0644	0.0178	6.131

Downloaded from https://www.cambridge.org/core. Nottingham Trent University, on 17 Aug 2019 at 02:05:11, subject to the Cambridge Core terms of use, available at https://www.cambridge.org/core/terms. https://doi.org/10.1017/9781108581714.003

Table 3.39 Comparison of the flow characteristics for combustion products of the propellant N_2O_4 + UDMH at application of basic and reduced ($\zeta_L = 0.02$) mechanisms

	p_{oc} = 20 atm; r_m = 0.006 m						(3.112a)	(3.112b)
α_{ox}	0.7	0.8	0.9	1.0	1.1	1.2	1.0	1.0
B_i(L)	14	14	14	14	14	13	15	15
R_s(L)	22	24	21	23	22	22	24	22
T_a(C)	938	1074	1152	1187	1150	1106	1369	1486
T_a(L)	938	1072	1152	1187	1150	1102	1369	1485
ξ_{dq}(C)	1.778	2.928	4.602	6.002	5.493	5.066	3.112	1.670
ξ_{dq}(L)	1.771	2.929	4.650	6.013	5.508	5.146	3.078	1.710

Table 3.40 Reduced G-mechanism for combustion products of the propellant N_2O_4 + UDMH for the domain (3.107) of the variation of parameters α_{ox}, p_{oc}, r_m

№ (C)	Reaction	№ (C)	Reaction	№ (C)	Reaction
3	$H_2 + OH = H_2O + H$	14	$CO_2 + H_2 = OH + HCO$	67	$HNO + OH = NO + H_2O$
4	$O + H_2 = OH + H$	15	$CO_2 + H = O + HCO$	69	$N + OH = NO + H$
5	$H + O_2 = OH + O$	39	$HCO + M = H + CO + M$	71	$N_2O + H = N_2 + OH$
6	$2OH = H_2O + O$	40	$HCO + H = CO + H_2$	72	$HNO + H = H_2 + NO$
7	$2H + M = H_2 + M$	48	$N_2O + M = N_2 + O + M$	74	$NH + NO = N_2O + H$
8	$2O + M = O_2 + M$	49	$N + NO = N_2 + O$	77	$NH + O_2 = HNO + O$
9	$H + M + OH = H_2O + M$	50	$N + O_2 = NO + O$	78	$HNO + M = H + NO + M$
10	$O + H + M = OH + M$	57	$NH + H = N + H_2$	79	$HNO + H_2O = H + NO + H_2O$
12	$CO + OH = CO_2 + H$	64	$NH + OH = N + H_2O$		
13	$CO + O + M = CO_2 + M$	65	$NH + OH = HNO + H$		

Then, at the reduction at threshold $\zeta_L = 0.01$, reaction W^- may be removed, while reaction W^+ is retained in the reduced mechanism. As a result, velocity W_Σ(L) may deviate notably from the value of W_Σ(C) to make the error δ_t increase. But at threshold $\zeta_L = 0.02$, reaction W^+ will be also removed to make velocity W_Σ(L) approach W_Σ(C) and to make the error decrease.

At the generation of the L-mechanism, fluctuations of this kind are encountered infrequently, and, as seen from Table 3.38, at the further increase in the thresholds, the reduced mechanism errors increase. It should be noted that, even at $\zeta_L = 0.04$, discrepancies between the results obtained by the C- and L-mechanisms are insignificant – i.e., $\delta_T = 1.0\%$ in temperature, $\delta_T = 2.0\%$ in target species, and $\delta_{dg} = 0.13\%$ in losses caused by chemical nonequilibrium, which corresponds to the specific impulse error of approximately 4 m/sec.

The thresholds $\zeta_a = \zeta_{a0} = \zeta_L = 0.02$ for the entire region of G-mechanism action have been set proceeding from the results of calculations for the basic flow mode (see Table 3.38). Then, about 40 points $\{\alpha_{ox}; p_{oc}; r_m\}$ have been selected for G-mechanism formation in the domain (3.107). To form the G-mechanism, the L-mechanism was

Downloaded from https://www.cambridge.org/core. Nottingham Trent University, on 17 Aug 2019 at 02:05:11, subject to the Cambridge Core terms of use, available at https://www.cambridge.org/core/terms. https://doi.org/10.1017/9781108581714.003

generated for each of these points. Some results are listed in Table 3.39 with the structure complying with that of Table 3.36. The L-mechanism of the maximum size has been generated at the point (3.112a) and comprises 24 reactions and 15 species:

$$(\mathrm{H}, \mathrm{H_2}, \mathrm{O}, \mathrm{O_2}, \mathrm{CO_2}, \mathrm{H_2O}, \mathrm{CO}, \mathrm{OH}, \mathrm{N}, \mathrm{N_2}, \mathrm{NO}, \mathrm{NH}, \mathrm{HCO}, \mathrm{HNO}, \mathrm{N_2O}) \qquad (3.114)$$

By combining all obtained L-mechanisms, it is possible to form the G-mechanism including the species (3.114) and 28 reactions listed in Table 3.40. This mechanism comprises four reactions more than the maximum L-mechanism, since reactions insignificant for it may be sensitive for the other local mechanisms.

Downloaded from https://www.cambridge.org/core. Nottingham Trent University, on 17 Aug 2019 at 02:05:11, subject to the Cambridge Core terms of use, available at https://www.cambridge.org/core/terms. https://doi.org/10.1017/9781108581714.003

Downloaded from https://www.cambridge.org/core. Nottingham Trent University, on 17 Aug 2019 at 02:05:11, subject to the Cambridge Core terms of use, available at https://www.cambridge.org/core/terms. https://doi.org/10.1017/9781108581714.003

Part II

Mathematical Modeling of Selected Typical Modes of Combustion

Downloaded from https://www.cambridge.org/core. Nottingham Trent University, on 17 Aug 2019 at 03:26:26, subject to the Cambridge Core terms of use, available at https://www.cambridge.org/core/terms. https://www.cambridge.org/core/product/C67CBC56BA48557877829F9CF8A13814

Downloaded from https://www.cambridge.org/core. Nottingham Trent University, on 17 Aug 2019 at 03:26:26, subject to the Cambridge Core terms of use, available at https://www.cambridge.org/core/terms. https://www.cambridge.org/core/product/C67CBC56BA48557877829F9CF8A13814

4 Laminar Premixed Flames: Simulation of Combustion in the Flame Front

4.1 Specific Features of Modeling

The model of the combustion in the flame front is commonly used for the simulation of operating parameters and emission characteristics of combustion chambers of different combustion systems as one of the main simulation fragments in models of premixed flames. The typical scheme of combustion in the flame front was described in the Section 1.1. Combustion in the flame front predetermines to a considerable extent the further afterburning processes and parameters of reacting flows in the combustion unit and combustion products emission. In accordance with the generally accepted definition, the flame front is identified as a thin layer separating an unburned fresh mixture of the reactants from the combustion products wherein maximum gradients of concentrations of the reactants and reaction products are observed (Figure 4.1). Once the fresh mixture is ignited, a resulting premixed flame propagates in the x direction, consuming the unburned mixture. The chemical interaction in the flame front under conditions of intensive self-acceleration of the processes caused by the transfer of both heat and active catalyzing centers from the products of reactions to the unburned fresh mixture.

Working medium parameters in the flame front vary from the parameters of the fresh mixture upstream the flame front to the combustion product parameters downstream the flame front. Therefore, designing the combustion scheme, we can assume that gradients of all parameters in the direction of flame front propagation (axis x) are notably higher than those perpendicular to the flame front propagation (axis y), and we consider the scheme of processes in the flame front as a quasi-one-dimensional model.

The model of the processes in the premixed flame front is an integral part of complex mathematical models used to calculate parameters of reacting mixtures in a variety of combustion units. Also, the model of the flame front can be used for the solution of the so-called reverse problem of chemical kinetics – i.e., for the construction and analysis of chemical reaction mechanisms.

The flame front is laminar in the laminar flow of reacting mixture and turbulent in the turbulent flow. Most reacting flows in practical combustion units are turbulent, where combustion proceeds in the presence of random and rapid fluctuations of the velocity and thermophysical parameters of the reacting mixture [180]. At the same time, an excellent example of a stationary laminar premixed flame may be the Bunsen burner [181].

Turbulence increases the flame speed by a factor of several dozens or even hundreds. Turbulent flame speed, unlike laminar flame speed is determined not only by the

Downloaded from https://www.cambridge.org/core. Nottingham Trent University, on 17 Aug 2019 at 02:03:36, subject to the Cambridge Core terms of use, available at https://www.cambridge.org/core/terms. https://doi.org/10.1017/9781108581714.004

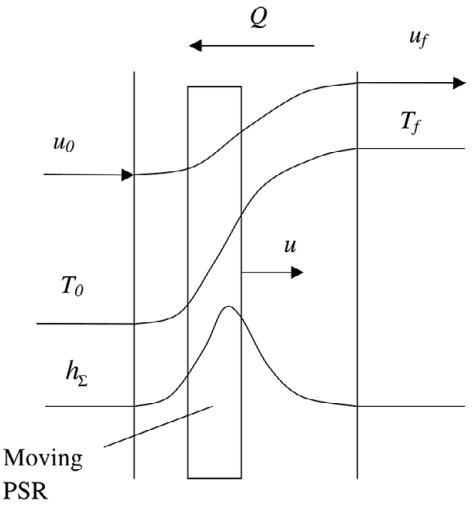

Figure 4.1 Scheme of the processes in the flame front.

chemical composition, temperature, and pressure of the reacting mixture, but also by flow turbulence intensity. Low intensity of the turbulence can lead to the formation of curved laminar flame fronts. In so doing, the turbulent flame can be considered as the set of "micro-laminar" flames. Laminar premixed flame speed (the speed of flame front propagation perpendicular to the front surface), called the "normal" or "fundamental," speed can be seen as a physicochemical constant, which depends on a pressure and temperature. Results of analyses show that laminar premixed flame speed defines, to a considerable extent, the flame front propagation velocity in a turbulent flow, which occurs in the combustion chambers.

In this chapter, we will consider the simulation of the simplest idealized premixed laminar flame front steady propagation in the condition of chemical nonequilibrium behavior in the flame front based on the reactor approach. Existing models of combustion in the flame front can be conventionally divided into following groups:

1. Simplified models [8, 182] exploiting the global chemical kinetics concepts (Section 1.4) of combustion with simultaneous allowance for governing aerothermodynamic processes
2. Semiempirical models [183] supplemented by detailed kinetic schemes (Section 1.3)
3. Models exploiting general conservation laws and basic processes [184], supplemented by detailed chemical kinetics schemes (Section 1.3)
4. Complex models [143, 185, 186] exploiting detailed kinetic mechanisms (Section 1.3) and describing the entire set of aerothermochemical processes.

Every type of models has both advantages and disadvantages.

Thus, given the relative simpleness and possibility of an analytical solution, the disadvantage of the first group of models is the impossibility of a detailed calculation of the composition of combustion products in the flame front that precludes application

Downloaded from https://www.cambridge.org/core. Nottingham Trent University, on 17 Aug 2019 at 02:03:36, subject to the Cambridge Core terms of use, available at https://www.cambridge.org/core/terms. https://doi.org/10.1017/9781108581714.004

of these models to the detailed calculations of chemical composition and especially the prediction of small concentrations – for instance, emission characteristics.

The second group differs in a wider spectrum of possibilities but is limited by a definite set of reacting components and operating parameters. Besides, the models of this group require, as a rule, a preliminary determination of the variation of some aerothermodynamic parameters across the flame front and their application to calculations.

The third group of models can totally be used for the calculation of operating and ecological parameters of combustion units. These models possess a fair degree of accuracy and high efficiency in terms of the required calculation resources. At the same time, an incomplete account of several specific phenomena in some combustion modes can become the source of substantial errors.

At last, the fourth group of models, exploiting the complete kinetic mechanisms, are too complicated for applied problems solution, which results in a long and unstable calculation process, significant constraints as applications are concerned (a limited set of substances and chemical mechanisms, relatively low pressures and temperatures, necessity in individual selection of a number of simulated parameters); i.e., the quality of calculation depends on the qualification of a researcher.

4.2 Convective Model of Combustion Processes in Laminar Flame Front and Impact of Diffusion

A mathematical model of the processes of combustion of premixed reagents in the flame front can be analyzed as one of the applications described in the monograph reactor approach (Sections 1.1 and 1.5) to particular physical processes in propulsion and power generation units. In compliance with the classification given in the Section 4.1, this model relates to the third group; i.e., it assumes the consideration of only the basic processes, governing for this mode, in aggregate with detailed kinetic mechanisms. It rules out the disadvantages of complex models (the fourth group) and, at the same time, predicts the flame characteristics accurately enough.

The physical scheme proceeds from the thermal model of the flame front [187], that is, it does not allows for the diffusion of active particles (active centers) into the fresh mixture but assumes that the combustion is maintained due to conduction from combustion products to the fresh mixture through the flame front.

This assumption seems correct enough upon simulation of the processes at higher pressures, since autocatalytic combustion caused by the diffusion of active centers is observed under isothermal conditions at combustion of strongly diluted mixes at pressures significantly lower than the barometric pressure [8].

Let us write the flame front classical equations:

– Continuity equation:

$$\frac{d(\rho u)}{dx} = 0. \tag{4.1}$$

Downloaded from https://www.cambridge.org/core. Nottingham Trent University, on 17 Aug 2019 at 02:03:36, subject to the Cambridge Core terms of use, available at https://www.cambridge.org/core/terms. https://doi.org/10.1017/9781108581714.004

– Equation of conservation of energy for elementary volume:

$$-c_p\rho u\frac{dT}{dx}+\frac{d}{dx}\left(k\frac{dT}{dx}\right)+\sum R_i\mu_i h_i=0,\quad i=1,2,\ldots,n_b, \tag{4.2}$$

where $c_p\rho u\frac{dT}{dx}$ is the amount of heat for heating up the unburned mixture entering the combustion zone, $\frac{d}{dx}\left(k\frac{dT}{dx}\right)$ is the change of the amount of heat transferred by conduction across the combustion zone in the x direction, and $\sum R_i\mu_i h_i$ is the change of the enthalpy of the reacting mixture in the combustion zone.

By analogy with (4.2), the equation of variation of concentration of specie i is written as follows:

$$\rho u\frac{dr_i}{dx}+\frac{d}{dx}\left(\rho D_{im}\frac{dr_i}{dx}\right)+R_i\mu_i=0,\quad i=1,2,\ldots,n_b, \tag{4.3}$$

where $R_i\mu_i$ is the density of the source of i-th substance resulting from chemical interaction, h_i is the mass enthalpy of i-th substance; H_i is the molar enthalpy of i-th substance, ρ is density, u is linear velocity of the mixture motion, D_{im} is binary diffusion coefficient of i-th substance in gas mixture, k is thermal conductivity, T is temperature, and c_p is the mass specific heat of the mixture.

To confirm the possibility of the application of the thermal model of flame front, let us analyze the dependence of separate terms of Equations (4.1–4.3) on pressure taking into account ideal gas assumption:

1. $\frac{d(\rho u)}{dx}$ is proportional to p
2. $c_p\rho u\frac{dT}{dx}$ is proportional to p
3. $\frac{d}{dx}\left(k\frac{dT}{dx}\right)$ is proportional to p
4. $\sum R_i\mu_i h_i$ is proportional to p^2
5. convective member $\rho u\frac{dr_i}{dx}$ is proportional to p
6. diffusion member $\frac{d}{dx}\left(\rho D_{im}\frac{dr_i}{dx}\right)$ does not depend on p, since

$$D_{im}=0,0266T\frac{\sqrt{T\left(\mu_i+\mu_g\right)/\left(2\mu_i\mu_g\right)}}{\mathrm{p}\sigma_{im}\Omega_{im}}\propto\frac{1}{\mathrm{p}};\quad\text{and}\quad\rho\propto p,$$

where p is pressure, Ω_{im} is the reduced collision integral written for i-th particle and mixture, σ_{im} is collision diameter, and μ_i,μ_g are molecular masses of i substance and mixture, respectively

7. density of the source of i-th substance resulted from chemical interaction of $R_i\mu_i$ is proportional to p^2.

Thus, assuming the generally adopted assumption of barodiffusion as a second-order phenomenon compared to concentration diffusion, it can be ascertained that with an increase in pressure, the influence of diffusion notably decreases to render chemical interaction and convective transfer the governing processes; that is, Equation (4.3) can be transformed to

$$\rho u\frac{dr_i}{dx}+R_i\mu_i=0,\quad i=1,2,\ldots,n_b. \tag{4.4}$$

Downloaded from https://www.cambridge.org/core. Nottingham Trent University, on 17 Aug 2019 at 02:03:36, subject to the Cambridge Core terms of use, available at https://www.cambridge.org/core/terms. https://doi.org/10.1017/9781108581714.004

This is confirmed by papers [188, 189], wherein it is traced that the variation of reaction substance diffusion coefficients does not affect the stoichiometric methane–air flame propagation velocity, whereas the variation of thermal conductivity brings about a significant influence on the combustion normal velocity. Thus, the assumption of thermal mechanism prevalence in propagation of stoichiometric methane–air flame is confirmed.

Let us consider the application of formal chemical kinetics models (Section 1.3.2) for a description of combustion processes in the flame front. In this case, the Maxwell–Boltzmann distribution is considered valid while temperature dependence of the rate constant of chemical reaction is defined by translational energy of relative motion of the reactant particles and described by the Arrhenius equation (1.70).

At the same time, it is known that equilibrium energy distribution over the degrees of freedom of molecules and atoms is disturbed in very fast processes – for example, in shock waves (Section 1.4.3). If relaxation of translational and rotational degrees of freedom occurs in several collisions, then relaxation of vibrational degrees of freedom proceeds in several thousand collisions [190], which can bring about the disturbance of distribution over the vibrational degrees of freedom. In this case, the rate constant differs from its equilibrium value and can be described by various semiempirical relationships [191, 192]. However, variations of the chemical composition and temperature, despite their great gradients in the front, are not so fast, and multiple analyses [143, 186, 190, 193, 194] bring out clearly that vibrational degrees of freedom manage, in fact, to reach equilibrium with translational and rotational degrees of freedom.

4.3 Application of Plug Flow Reactor to the Simulation of Combustion in the Premixed Laminar Flame

This model is based on the basic mathematical apparatus for calculation of nonequilibrium chemical composition for the non-stationary plug flow reactor, which is a version of PFR (Sections 1.1 and 1.5) and assumes the variation of state parameters of the reacting mixture over time, as well as mass exchange with surroundings ($m_i^+ \neq 0; m_i^- \neq 0$). The reactor located between two closely set channel cross sections moves at the gas velocity (Figure 4.1). Here, its main thermodynamic parameters (*V, T,* composition) undergo significant changes.

Known equations of substance and energy conservation and continuity equation written as applied to one-dimensional steady-state flow have been used for the development of one-dimensional model of premixed combustion. Note here that the classical formulation of the problem of premixed flame front simulation [8] is updated and dispose of some features which are not suitable for execution of numerical experiments: the requirement to specify boundary conditions at $x = \pm\infty$; equilibrium of chemical composition of the combustion products on the "hot" boundary of the flame front (the flame front boundary where combustion products attain the equilibrium composition). Besides, some conventional assumptions – like k = const, c_p = const over the flame front – are no longer needed.

Downloaded from https://www.cambridge.org/core. Nottingham Trent University, on 17 Aug 2019 at 02:03:36, subject to the Cambridge Core terms of use, available at https://www.cambridge.org/core/terms. https://doi.org/10.1017/9781108581714.004

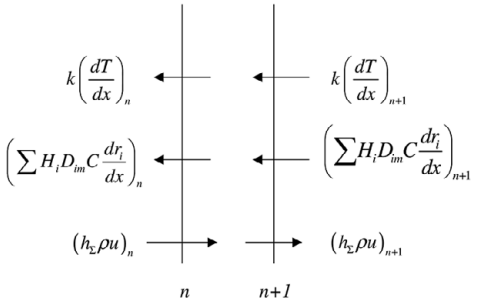

Figure 4.2 Energy transfer diagram in elementary volume of the flame front by conduction.

In developing a physical scheme, it is necessary to mind that neglecting the diffusion term in Equation (4.3) will not permit us to notably reduce the scope of calculations, since it results in the known finite-difference scheme with subsequent solution of a large number of stiff differential equations (see Chapter 3).

This is why the thermal model described in this monograph is presented in a new form, allowing us to notably reduce the scope of calculations, increase the stability of calculations, and expand the range of analyzed propellants and operating parameters. Let us write the energy equation proceeding from the combustion scheme shown in the Figure 4.2, formalizing the energy flows crossing the elementary volume $(n) - (n + 1)$ of a flame front.

Then, with allowance for the steady-state nature of the process for arbitrary elementary volume, we can write

$$(h\rho u)_{n+1} = (h\rho u)_n + k\left(\frac{dT}{dx}\right)_{n+1} + \left(\sum H_i D_{im} C \frac{dr_i}{dx}\right)_{n+1} - \left(\sum H_i D_{im} C \frac{dr_i}{dx}\right)_n - k\left(\frac{dT}{dx}\right)_n. \tag{4.5}$$

$$h_0 \rho_{fr} u_{fr} = h\rho u - k\frac{dT}{dx} - \sum H_i D_{im} C \frac{dr_i}{dx}. \tag{4.6}$$

As shown previously, the influence of $\sum H_i D_{im} C \frac{dr_i}{dx}$ can be neglected. Now, after transforms, we obtain finally

$$k\frac{dT}{dx} = (h - h_{fr})\rho_{fr} u_{fr}, \tag{4.7}$$

where h and h_{fr} are mass enthalpies (the current one and that of the fresh mixture, respectively), fr is the index of belonging to the unburned gas mixture.

It should be noted that energy equation (4.7) is readily reduced to a traditional form (4.2).

Apart from Equation (4.7), the system of equations comprises the equation of variation of gas mixture velocity,

$$F_u \equiv u - \frac{\rho_{fr} u_{fr} R_0 T}{p\mu} = 0, \tag{4.8}$$

Downloaded from https://www.cambridge.org/core. Nottingham Trent University, on 17 Aug 2019 at 02:03:36, subject to the Cambridge Core terms of use, available at https://www.cambridge.org/core/terms. https://doi.org/10.1017/9781108581714.004

as well as the calorific equation relating enthalpy, temperature, and chemical composition of the reacting mixture (2.32a).

The next fragment of the mathematical model of processes in the flame front is composed of the equations of chemical kinetics in Formula (2.30).

Boundary conditions on the "cold" boundary of the flame front (the boundary of the flame front with the fresh mixture of fuel and oxidizer) include the following parameters: chemical composition r_i, enthalpy h_{fr}, and temperature T_{fr} of the fresh mixture of fuel and oxidizer. It is required to preset a minor excess of initial temperature T_0 of T_{fr}, to rule out the condition $x_0 = -\infty$. It is appropriate to set $\Delta T = T_0 - T_{fr}$ within the limits of 5 ... 30 K to avoid a significant error in the results of calculation.

On the "hot" boundary, the following condition should be met:

$$h - h_{fr} = 0, \tag{4.9}$$

which allows eliminate the traditional boundary conditions $\frac{dT}{dx} = \frac{dr_i}{dx} = 0$ at $x = +\infty$.

Upon solving the system of equations with the help of algorithms described in Chapter 3, values of $h(x)$, $T(x)$, and $\gamma_i(x)$, as well as flame propagation velocity u_n, will be defined. The calculation is performed by the iterative method comprising three steps.

a) A certain value of the fresh mixture velocity u_0 is set.
b) The system of equations (4.7), (4.8), (2.30), (2.32a) is integrated.
c) In the course of integration, change of the difference $\Delta h = h - h_{fr}$ is examined. The increase of Δh (curves 1 and 2 in Figure 4.3) means that u_0 exceeds the combustion velocity u_n. If the difference Δh varies with maximum to become less than zero (curve 3), then $u_0 < u_n$. Using these rules allows us to define the value u_n and all required characteristics of the flame front (including emission parameters) in several progressive approximations (steps 1 and 2).

Algorithm and computer code "FRONT" implementing this model are invariant with respect to the set of substances and chemical mechanisms, which allows computation of small concentrations and, as experience shows, features a good stability of calculations.

The combustion model given earlier can be considered as a typical form of combustion in the flame front described in the Section 1.1. It can be used as an independent

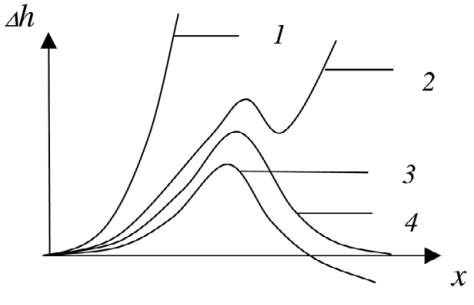

Figure 4.3 Options of the change of mixture enthalpy in the flame front subject to dependence on preset initial velocity of the flame: *1, 2* – $u_0 > u_n$, *3* – $u_0 < u_n$, *4* – $u_0 \approx u_n$.

Downloaded from https://www.cambridge.org/core. Nottingham Trent University, on 17 Aug 2019 at 02:03:36, subject to the Cambridge Core terms of use, available at https://www.cambridge.org/core/terms. https://doi.org/10.1017/9781108581714.004

model for analysis of the features of combustion of various premixed propellants or as a part of more complex models of combustion and flow in energy in propulsion and power generation systems. In this case, it can be used as the source of information on ecological and working properties of combustion products coming from the flame front into the working volumes and ducts of propulsion and power generation units. Its integration into more complex models involves no significant difficulties because of its versatility in terms of chemical kinetics equations (2.30), which are invariant with respect to a set of substances and chemical mechanisms, and which integrate the processes of chemical interaction and mass exchange.

Problems of theoretical model reliability and accuracy testing are analyzed in Section 4.4.

4.4 Examples of Numerical Simulation and Analysis

4.4.1 Combustion of Methane–Air Mixture at Increased Pressures

Selection of methane–air as a propellant for analysis of processes in the flame front is justified by the necessity in testing the proposed thermal model of combustion in the flame front in the combustion units when at high pressures a combustion process is primarily determined by heat transfer and chemical interaction, while the contribution of the diffusion is reduced. This is also due to the increased interest in natural gas as an internal combustion engine fuel. Besides, methane represents a set of ultimate hydrocarbons, whereas basic trends of combustion, including kinetic mechanisms, are typical for the entire group of ultimate hydrocarbons.

Kinetic mechanism for C-H-N-O system is composed proceeding from the analysis of papers [89, 186, 194–202] and, after optimization, can be described by 170 reversible reactions. The signature of this mechanism consists in that it describes the chemical interaction of ultimate hydrocarbon compounds that compose close to stoichiometric fuel–air mixtures. Since the formation of carbon-black particles is not typical for such mixtures in the absence of local fuel-reach zones – potential sources of the formation – carbon-black-formation reactions are not included in the kinetic mechanism. The set of reacting compounds comprises the following species: O, H, N, C, HO_2, OH, H_2, O_2, H_2O, CO, CO_2, CH_4, C_2H_2, C_2H_4, C_2H_6, CH_3, CH_2, CH, C_2H, C_2H_3, C_2H_5, H_2CO, HCO, NH_3, NH_2, NH, HNO, HCN, CN, NCO, HC_2O, C_3H_6, N_2H_2, N_2H, NO, NO_2, N_2O, C_3H_8, C_3H_7, N_2.

Comparison of calculations (Figure 4.4) made according to the model described in Sections 4.2 and 4.3 for the pressure range indicated in the graph with experimental data presented in [143, 196], demonstrates the significant divergence between numerical results and experimental data in the pressure range of up to approximately 4–5 atm.

At higher pressures, divergence of the results is not that significant and is a maximum of 8%–10%. Most likely, this can be explained by the significant influence of diffusion that is possible at comparatively low pressure (refer to the analysis of pressure influence on diffusion processes presented in Section 2.2). Thereby, the application of the thermal

Downloaded from https://www.cambridge.org/core. Nottingham Trent University, on 17 Aug 2019 at 02:03:36, subject to the Cambridge Core terms of use, available at https://www.cambridge.org/core/terms. https://doi.org/10.1017/9781108581714.004

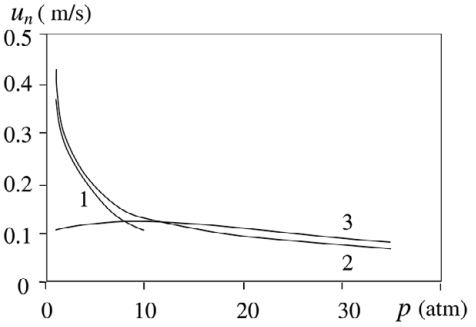

Figure 4.4 Dependence of stoichiometric homogeneous methane–air mixture flame propagation normal speed on pressure at T_{fr} = 300 K: 1 – results of T. P. Coffee, A. J. Kotlar, and M. S. Miller [143]. Reprinted from *Combustion and Flame*, T. P. Coffee, A. J. Kotlar and M. S. Miller, "The Overall Reaction Concept in Premixed, Laminar, Steady-State Flames: II. Initial Temperatures and Pressures," vol. 58, pp. 59–67, 1984, Copyright (1984), with permission from Elsevier; 2 – results of G. E. Andrews, D. Bradley D [196], reprinted from *Combustion and Flame*, G. E. Andrews and D. Bradley, "The Burning Velocity of Methane-Air Mixture," vol. 19, pp. 275–288, 1972, Copyright (1972), with permission from Elsevier; 3 – results of the FRONT-assisted calculation

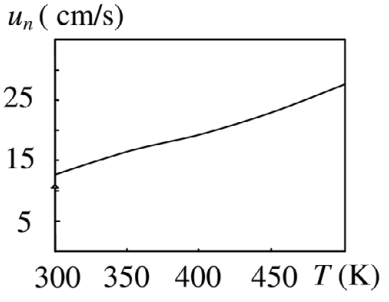

Figure 4.5 Dependence of stoichiometric homogeneous methane–air mixture flame normal speed on initial temperature at p = 10 atm: Δ – experimental values of homogeneous methane–air mixture flame normal velocity obtained by T. P. Coffee, A. J. Kotlar, and M. S. Miller [143]. Reprinted from *Combustion and Flame*, T. P. Coffee, A. J. Kotlar, and M. S. Miller, "The Overall Reaction Concept in Premixed, Laminar, Steady-State Flames: II. Initial Temperatures and Pressures," vol. 58, pp. 59–67, 1984, Copyright (1984), with permission from Elsevier

model of a flame front to aforesaid pressure range can cause notable discrepancies in numerical simulation of combustion process at low pressures. Hereafter, the thermal mechanism starts dominating with the increase in pressure at methane–air flame propagation, which explains a good agreement between experimental and calculated data in the range of p = 5 . . . 50 atm.

Thus, further detailed analyses of the combustion in the laminar flame front of a homogeneous methane–air mixture with application of the model described in Sections 4.2 and 4.3 were performed at high pressures p = 10 atm. Results of these numerical experiments are shown in Figures 4.5–4.10.

Figure 4.5 shows the dependence of homogeneous stoichiometric methane–air flame normal speed on the initial temperature at p = 10 atm and demonstrates a satisfactory

Downloaded from https://www.cambridge.org/core. Nottingham Trent University, on 17 Aug 2019 at 02:03:36, subject to the Cambridge Core terms of use, available at https://www.cambridge.org/core/terms. https://doi.org/10.1017/9781108581714.004

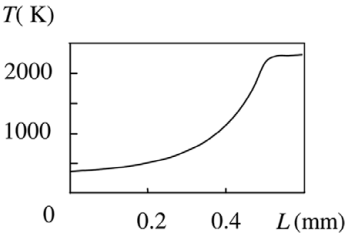

Figure 4.6 Change in temperature of stoichiometric methane–air mixture within the flame front at p = 10 atm, T_{fr} = 300 K.

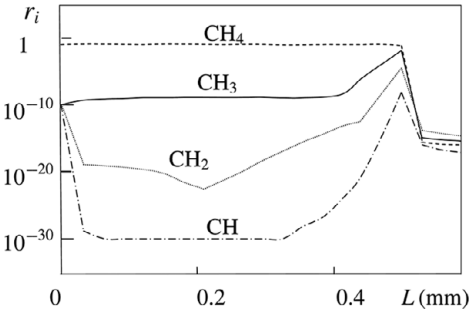

Figure 4.7 Change in concentrations of CH, CH_2, CH_3, CH_4 within the flame front of stoichiometric methane–air mixture at p = 10 atm, T_{fr} = 300 K.

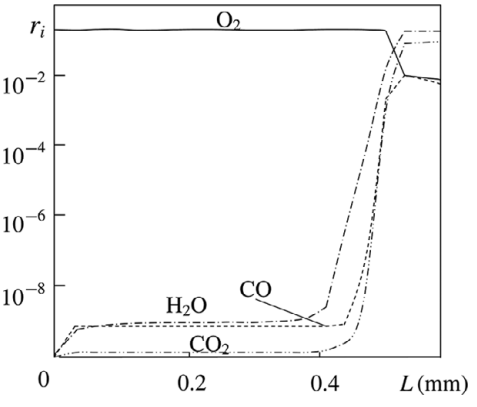

Figure 4.8 Change in concentrations of O_2, CO_2, CO, H_2O within the flame front of stoichiometric methane–air mixture at p = 10 atm, T_{fr} = 300 K.

convergence of calculated speeds with experimental data for homogeneous stoichiometric methane–air mixture obtained by Coffee T. P., Kotlar A. J., Miller M. S. and given in [143].

Analysis of the temperature history (Figure 4.6) and variation of concentration of combustion products of methane–air mixture at p = 10 atm and T_{fr} = 300 K

Downloaded from https://www.cambridge.org/core. Nottingham Trent University, on 17 Aug 2019 at 02:03:36, subject to the Cambridge Core terms of use, available at https://www.cambridge.org/core/terms. https://doi.org/10.1017/9781108581714.004

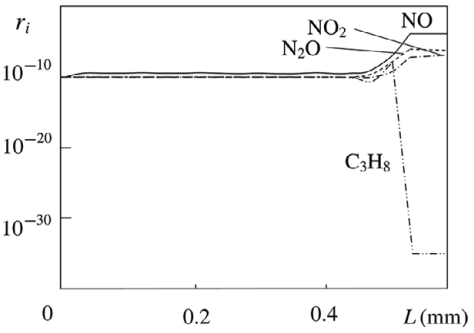

Figure 4.9 Change in concentrations of NO, NO_2, N_2O, C_3H_8 within the flame front of stoichiometric methane–air mixture at p = 10 atm, T_{fr} = 300 K.

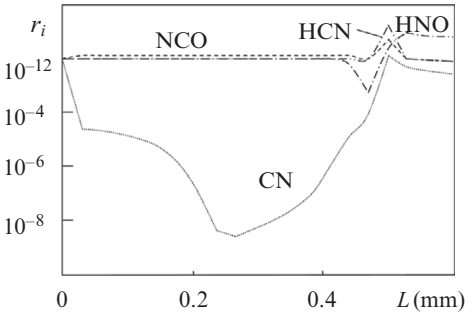

Figure 4.10 Change in concentrations of HNO, HCN, CN, NCO within the flame front of stoichiometric methane–air mixture at p = 10 atm, T_{fr} = 300 K.

(Figures 4.7–4.10) shows intensive hydrocarbons oxidation according to the scheme $C_nH_m \rightarrow CO_2$ in the temperature range of 1200 … 2200 K. A narrow reaction zone (from 4×10^{-4} m to 5×10^{-4} m) is typical for the thermal mechanism of the flame front propagation, which agrees well with data published in [188, 189].

4.4.2 Combustion of Ammonia–Air Mixture

The series of numerical experiments presented in this section reveals the analysis of the combustion characteristics of a homogeneous ammonia–air mixture. The selection of this propellant is justified by the necessity in testing the proposed thermal model of combustion and the possible use of ammonia in combustion units. Thus, for example, it is known [182, 194, 203–210] that one of the efficient methods of nitrogen oxide neutralization in combustion products is the reduction of nitrogen oxides with ammonia. Ammonia–air mixtures are known to burn slowly while standard conditions in air atmosphere do not allow the steady-state diffusion combustion of ammonia that is of interest for the application of the constructed thermal model of combustion in the flame front to these analyses.

Downloaded from https://www.cambridge.org/core. Nottingham Trent University, on 17 Aug 2019 at 02:03:36, subject to the Cambridge Core terms of use, available at https://www.cambridge.org/core/terms. https://doi.org/10.1017/9781108581714.004

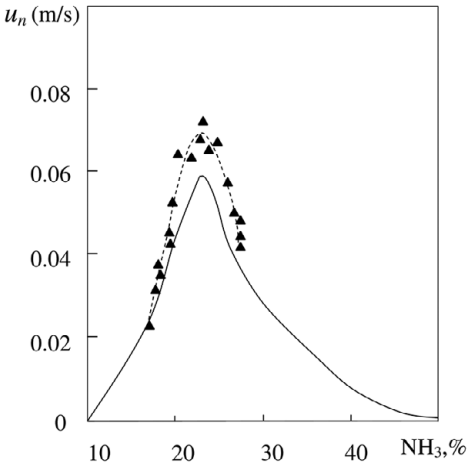

Figure 4.11 Flame normal speed versus NH_3 volume concentration in the air: Δ – results of experiments by V. F. Zakaznov, L .A. Kurshevoy, Z. I. Fedina [211]; ( ) – calculation results.

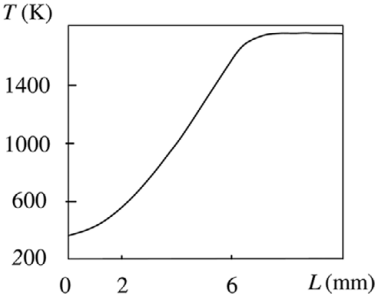

Figure 4.12 Change in ammonia–air mixture temperature in the flame front at T_{fr} = 300 K and standard atmospheric pressure.

Figures 4.11–4.14 show the results of homogeneous ammonia–air mixture laminar flame calculation for T_{fr} = 300 K and standard atmospheric pressure.

A chemical reaction mechanism including 64 reversible chemical reactions was constructed for reacting H-N-O system. The first set of numerical experiments aimed at defining the values of ammonia–air mixture normal speed of flame propagation subject to the content of ammonia in air. Note here that ammonia volume concentration in the mixture varied from 10% to 50%.

Figure 4.11 shows that calculated values of the flame normal speed versus ammonia concentration in the air displays a good agreement with experimental data given in [211]. Numerical analyses brought about the interval of possible combustion (ultimate concentrations of ammonia) of premixed ammonia–air mixture under normal conditions. The minimum concentration of ammonia was found to make 10 ÷ 12%, while the maximum concentration approximated to 45%, as shown in the Figure 4.11.

Downloaded from https://www.cambridge.org/core. Nottingham Trent University, on 17 Aug 2019 at 02:03:36, subject to the Cambridge Core terms of use, available at https://www.cambridge.org/core/terms. https://doi.org/10.1017/9781108581714.004

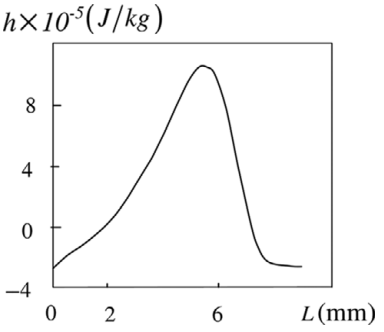

Figure 4.13 Change in ammonia–air mixture enthalpy in the flame front at T_{fr} = 300 K and standard atmospheric pressure.

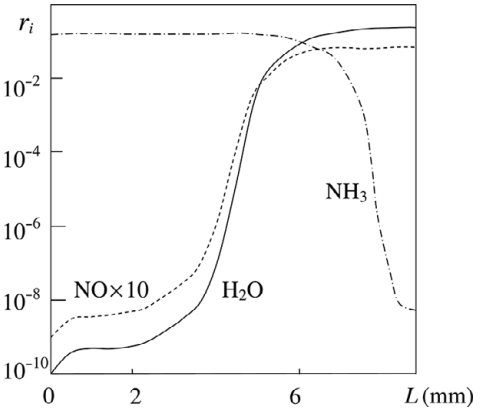

Figure 4.14 Change in NH_3, NO, H_2O concentrations in the flame front at T_{fr} = 300 K and standard atmospheric pressure.

Figures 4.12–4.14 adduce the ammonia–air mixture parameters variation within the flame front, with the mixture containing 17% of ammonia. Thus, Figures 4.12 and 4.13 show the plots of the change of enthalpy and temperature in the flame front at T_{fr} = 300 K and standard atmospheric pressure.

It should be noted that incomplete combustion renders the calculated temperature downstream the flame front lower than the equilibrium temperature by 86 K.

Figure 4.14 displays variation of concentrations of NH_3, H_2O, and NO within the flame front.

On the whole, calculation results exhibit that the constructed model, despite the one-dimensional approximation and single PFR scheme, adequately describes the processes in the premixed flame front and displays sufficient accuracy and reliability. Note that this model can be widely used as both the typical combustion scheme for analysis of processes in the laminar flame fronts and a key element of more complicated models of combustion and flows in combustion units.

Downloaded from https://www.cambridge.org/core. Nottingham Trent University, on 17 Aug 2019 at 02:03:36, subject to the Cambridge Core terms of use, available at https://www.cambridge.org/core/terms. https://doi.org/10.1017/9781108581714.004

4.4.3 Combustion in the Flame Front of Bicomponent Fuel–Air Mixture

Of the various publications on the combustion in the flame front, combustion in the flame front of bicomponent fuel when one component of the fuel features a high combustion rate while another one – a low combustion rate (for example, "H_2+CO" + air or "C_2H_2+NH_3" + air, etc.) – can hardly be found. Obviously, models of the first and second groups (see Section 4.1) are not appropriate for the analysis of such a multi-component fuels. Application of complex models (the fourth group) to this end is problematic as well, since a complex nature of the variation of combustion product concentrations will affect the calculation process stability, and, at the least, raise calculation time.

The model described in Sections 4.2 and 4.3 has been used to perform such numerical experiments. Thus, characteristics of the reacting mixture have been analyzed wherein air makes the oxidizer while the fuel is the mixture of acetylene and ammonia (C_2H_2 + NH_3). The content of acetylene in the fuel was defined by a variable parameter z. Hence, a mixed fuel was presented by $zC_2H_2 + (1 - z)NH_3$.

Calculations have been made for a stoichiometric mixture at the following initial conditions: p = 6 atm, T_{fr} = 300 K. Here, acetylene content in this bicomponent fuel varied in the range of $z = 0 \ldots 1$. Mass stoichiometric ratio k_m^o varied accordingly.

The kinetic mechanism is developed on the basis of the analysis of papers [106, 185, 186, 212, 213] and consists of 124 reversible chemical reactions. The set of reacting components includes the following individual substances: N, N_2, NO, NO_2, NH, NH_2, NH_3, HNO, H_2O_2, N_2O, H, H_2, O, O_2, C, H_2O, CO, OH, CH_2, CH_3, CH_4, HCO, H_2CO, C_2H, HO_2, C_2H_6, C_2H_5, C_2H_3, C_2H_4, C_2H_2, CO_2.

Figure 4.15 shows the dependence of the flame front propagation velocity u_n, temperature downstream the front T_f, and maximum change of enthalpy in the flame front $\Delta h_{\max}$ versus acetylene content in the mixed fuel. The front normal velocity u_n is seen to vary from the pure ammonia–air mixture flame velocity (at $z = 0$) to the values typical for the combustion of pure acetylene–air mixture (at $z = 1$). Because of higher acetylene combustion heat as compared to ammonia, the temperature of combustion products subject to z increase by more than 500 K. Besides, it is interesting to point out

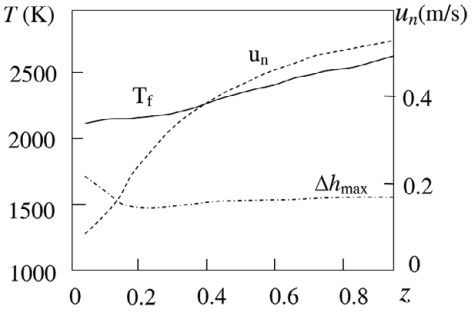

Figure 4.15 Dependence of the flame front characteristics: flame front propagation normal velocity u_n, temperature downstream the front T_f, maximum change of enthalpy in the flame front $\Delta h_{\max}$ on the content of ammonia in the fuel (z).

Downloaded from https://www.cambridge.org/core. Nottingham Trent University, on 17 Aug 2019 at 02:03:36, subject to the Cambridge Core terms of use, available at https://www.cambridge.org/core/terms. https://doi.org/10.1017/9781108581714.004

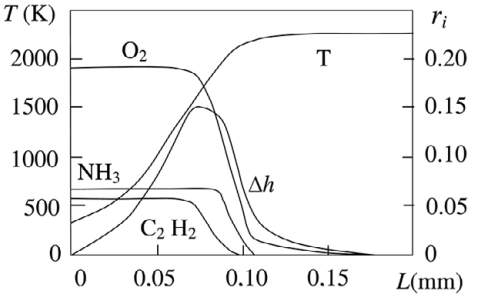

Figure 4.16 Variation of T, Δh_{max}, r_{O_2}, r_{NH_3}, $r_{C_2H_2}$ in the flame front of stoichiometric mixture $(zC_2H_2 + (1 - z)NH_3)$ + air (p = 6 atm, T_{fr} = 300 K, z = 0.45).

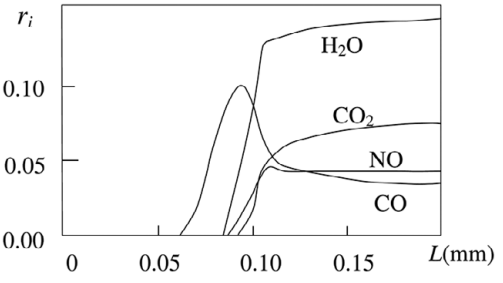

Figure 4.17 Variation of concentrations r_{H_2O}, r_{CO_2}, r_{NO}, r_{CO} in the flame front of stoichiometric mixture $(zC_2H_2 + (1 - z)NH_3)$ + air (p = 6 atm, T_{fr} = 300 K, z = 0.45).

the heightened rise of enthalpy in the flame front of mixture with high concentration of ammonia (z = 0 . . . 0.2).

Figures 4.16–4.18 show the plots of the variation of gas mixture parameters in the flame front (x = 0 ÷ 0.2 mm) for z = 0.45. Thus, Figure 4.16 shows the temperature variation in flame front (T), maximum change of enthalpy in the flame front Δh_{max}, and concentrations of a number of substances r_{O_2}, r_{NH_3}, $r_{C_2H_2}$. The maximum value of the Δh_{max} rise is reached in the area of intensive combustion accompanied by an abrupt decrease in the concentration of the propellant r_{NH_3}, $r_{C_2H_2}$ and corresponds to the inflection point in the graph $T = T(x)$. In this case, the initial components of the fuel intensively interact chemically to be consumed completely in the range of narrow enough zone (x = 0.07 . . . 0.11 mm), and bicomponent fuel $C_2H_2 + NH_3$ can be considered by all parameters as a monocomponent fuel – i.e., we have a "co-combustion" of both components of the fuel. Figure 4.17 shows that an intensive formation of the basic combustion products – i.e., H_2O vapors and carbon dioxide CO_2 – occurs also in this narrow combustion zone.

Decomposition of C_2H_2 in the flame front is accompanied with the intensive carbon monoxide CO formation, its concentration in the range x = 0.07. . . 0.11mm, reaching the maximum ($r_{CO}^{max} \approx 0.1$), which complies with the results of analysis presented in [7]. Henceforth, a considerable portion of carbon monoxide (CO) oxidizes to carbon dioxide (CO_2). Oxidation of ammonia (NH_3) is accompanied with an active formation of nitrogen oxide (NO), which thereafter does not practically decompose.

Downloaded from https://www.cambridge.org/core. Nottingham Trent University, on 17 Aug 2019 at 02:03:36, subject to the Cambridge Core terms of use, available at https://www.cambridge.org/core/terms. https://doi.org/10.1017/9781108581714.004

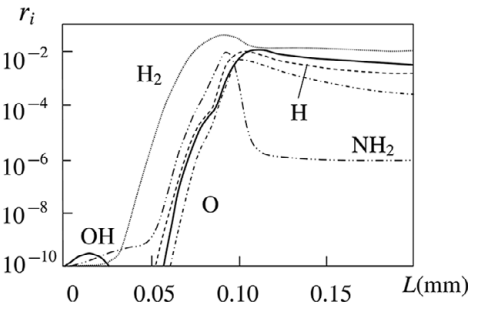

Figure 4.18 Variation of concentrations r_{H_2}, r_{NH_2}, r_H, r_{OH}, r_O in the flame front of stoichiometric mixture $(zC_2H_2 + (1 - z)NH_3)$ + air (p = 6 atm, T_{fr} = 300 K, z = 0.45).

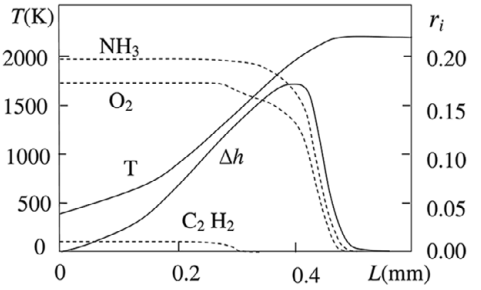

Figure 4.19 Variation of T, Δh_{max}, r_{O_2}, r_{NH_3}, $r_{C_2H_2}$ in the flame front of stoichiometric mixture $(zC_2H_2 + (1 - z)NH_3)$ + air, (p = 6 atm, T_{fr} = 300 K, z = 0.05).

Figure 4.18 shows the change in molecular hydrogen concentration, as well as that of radicals O, H, OH, and NH_2. Radicals O, OH, and H, depicting the intensity of chemical interaction, feature similar graphs of concentrations change over flame front length x. They are formed in the zone of intensive combustion to reach maximum super-equilibrium values ($r_i \approx 0.01$). Radical NH_2 results only from NH_3 pyrolysis and, as an unstable chemical specie, it transforms quickly into the other substances. This explains a pronounced peak of NH_2 concentration. Concentration of molecular hydrogen H_2, a product of C_2H_2 and NH_3 decomposition, also reaches the maximum super-equilibrium values.

Thus, the analysis of parameters shown in the Figures 4.16–4.18 allows us to conclude that at z = 0.45, when acetylene concentration in the fuel is significant, it oxidizes actively with the formation of intermediate components and radicals – which facilitate, in their turn, the intensive decomposition of ammonia (NH_3). In this regard, the behavior of bicomponent fuel in the flame front at z = 0.45 can be considered to be the combustion of the monocomponent propellant.

Figures 4.19–4.21 show the parameters of the reacting mixture at z = 0.05, which corresponds to the following composition of the propellant: 5% C_2H_2 + 95% NH_3 + air at stoichiometric fuel-to-oxidizer ratio.

The behavior of temperature and enthalpy upsurge is similar to that given in Figure 4.16. At the same time, it is evident that acetylene decomposes completely

Downloaded from https://www.cambridge.org/core. Nottingham Trent University, on 17 Aug 2019 at 02:03:36, subject to the Cambridge Core terms of use, available at https://www.cambridge.org/core/terms. https://doi.org/10.1017/9781108581714.004

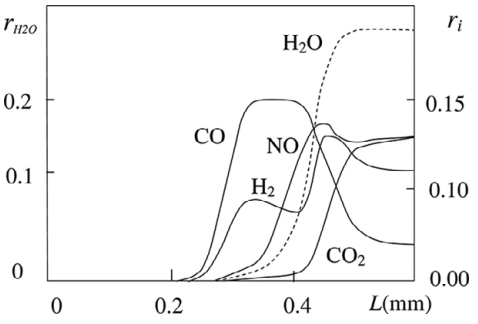

Figure 4.20 Variation of concentrations r_{H_2O}, r_{CO_2}, r_{NO}, r_{CO}, r_{H_2} in the flame front of stoichiometric mixture $(zC_2H_2 + (1 - z)NH_3)$ + air (p = 6 atm, T_{fr} = 300 K, z = 0.05).

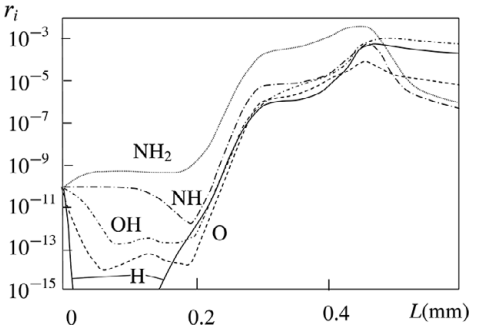

Figure 4.21 Variation of concentrations r_{NH}, r_{NH_2}, r_H, r_{OH}, r_O in the flame front of stoichiometric mixture $(zC_2H_2 + (1 - z)NH_3)$ + air (p = 6 atm, T_{fr} = 300 K, z = 0.05).

over the length x = 0.3 mm, whereas intensive decomposition of ammonia starts at x = 0.4 mm (Figure 4.19).

This results in the development of two interfering combustion zones inside the flame front – that is, the first one in the range of x = 0.25 . . . 0.30 mm, making the acetylene combustion zone, and the second one in the range of x = 0.30 . . . 0.50 mm, making the ammonia combustion zone. Thus, the C_2H_2 combustion in the first zone brings about the formation of separate intermediate components and insignificant growth in the concentration of active radicals O, H, OH, and NH_2, which initiate the start of NH_3 combustion. The NH_3 combustion, in its turn, causes the additional growth in reacting medium temperature and intensifies the heat flux into the first zone of C_2H_2 decomposition. This interaction makes the flame front normal velocity of the fuel consisting of ammonia by 95%, notably exceeding the known values for pure ammonia.

Figure 4.20 shows the variation of concentrations of main combustion products H_2O, CO_2, as well as H_2, CO, NO. Apparently, H_2O starts forming at the end of acetylene decomposition zone. The overall reaction of C_2H_2 oxidation can be described as follows:

$$2C_2H_2 + 3O_2 \Rightarrow 4CO + 2H_2O.$$

Downloaded from https://www.cambridge.org/core. Nottingham Trent University, on 17 Aug 2019 at 02:03:36, subject to the Cambridge Core terms of use, available at https://www.cambridge.org/core/terms. https://doi.org/10.1017/9781108581714.004

However, the main process of water formation results from ammonia combustion and can be described as follows:

$$2NH_3 + O_2 \Rightarrow N_2 + H_2 + 2H_2O.$$

It is obvious that the source of carbon dioxide (CO_2) formation is C_2H_2. But Figure 4.20 shows that, notwithstanding the fact that the complete decomposition of C_2H_2 proceeds in the range of x = 0.25 … 0.3 mm, appreciable formation of CO_2 starts at the distance x = 0.4 mm. A governing factor of such a delay at C_2H_2 decomposition is the CO formation. CO concentration sharply increases at first, but then, because of the lack of radicals, remains constant ($r_{CO} \approx 0.02$) for some length (x = 0.2 … 0.3 mm) required for the accumulation of active radicals. Nitrogen monoxide formation occurs due to interaction of NH_3 with O_2 in the range of x = 0.3 … 0.4 mm, as a result of a "chemical" but not a "thermal" source. This is why the nitrogen oxide concentration in the flame front reaches very high values (r_{NO} = 18,000 ppm) and notably exceeds the equilibrium values (r_{NO}^{eq} = 7700 ppm). However, at the exit from the front, the NO concentration approaches its equilibrium values r_{NO}^{eq}.

In the analysis of characteristics shown in Figure 4.20, it is necessary to pay special attention to the change in concentration of molecular hydrogen H_2, which is bought about by propellant components pyrolysis. As a rule, such substances exhibit the maximum of change in concentration, which describes the combustion intensity. In this case, H_2 concentration curve features two pronounced peaks (Figure 4.20) corresponding to two combustion zones (the first, C_2H_2 combustion; the second, NH_3 combustion). Thus, the r_{H_2} rises initially at decomposition of acetylene in the first zone, but at increased temperatures, H_2 enters into a chemical interaction to down the r_{H_2} concentration. The NH_3 combustion initiated thereafter brings about, again, the abrupt increase in r_{H_2} concentration, which – given the super equilibrium values reached – decreases again at the front exit approaching its equilibrium values.

Distribution of concentration of radicals NH_2, NH, OH, O, H in the flame front at z = 0.05 is shown in Figure 4.21. Practically all of them become relatively significant ($r_{iR} > 10^{-10}$) over the length $x \approx 0.2$ mm and, further, feature similar values:

- The concentration of radicals in the zone of intensive combustion of C_2H_2 (x = 0.2 … 0.3 mm) rises quickly (from $r_{iR} \approx 10^{-10}$ to $r_{iR} = 10^{-6} \ldots 10^{-7}$) and slows down gradually thereafter because of relatively low temperatures (T = 1300 K).
- Concentrations of radicals between the acetylene and ammonia combustion zones do not vary almost to tend to equilibrium in compliance with temperature.
- In the NH_3 combustion zone ($x \approx 0.35 \ldots 0.45$ mm), concentration of radicals rises again from $r_{iR} = 10^{-6}$ to $r_{iR} = 10^{-5} \ldots 10^{-4}$, approaching its super-equilibrium values.
- r_{iR} concentration decreases at the exit from NH_3 combustion zone to tend to equilibrium values and, thus, creates the peak at $x \approx 0.45 \ldots 0.47$ mm.

The most interesting result of these analyses consists in a numerical determination of two combustion zones (separate combustion) at z = 0.05. Individual combustion of each

Downloaded from https://www.cambridge.org/core. Nottingham Trent University, on 17 Aug 2019 at 02:03:36, subject to the Cambridge Core terms of use, available at https://www.cambridge.org/core/terms. https://doi.org/10.1017/9781108581714.004

fuel component occurs in each aforesaid zone. Another interesting result is that in spite of the flame front normal velocities for C_2H_2 and NH_3 differ notably, both fuel components in the analyzed mixture burn out at identical velocity, since even an insignificant concentration of a component burning at higher rate (C_2H_2) generates a portion of radicals that initiate the fast combustion of more stable component (NH_3).

The so-called separate combustion phenomenon is also observed at $z = 0.1$; its characteristics are given in Figures 4.22–4.24. In this mode, acetylene combustion accomplishes in the length approximately $x \approx 0.24$ mm, while ammonia does it in the length $x \approx 0.34$ mm (Figure 4.22). At the same time, the C_2H_2 influence on the flame front parameters is more pronounced than that at $z = 0.05$. It becomes apparent in the distribution of Δh_{max} enthalpy upsurge with a characteristic sagging between combustion zones, not available at $z = 0.05$. Curves of concentration of the main combustion products – nitrogen and carbon oxides as well as active radicals (Figures 4.23, 4.24) – are similar to the previous mode ($z = 0.05$). Besides, more pronounces peaks on the H_2 concentration distribution curve can be isolated, which corresponds to two combustion zones.

Figures 4.25 and 4.26 show the variation of separate parameters the flame front at $z = 0.15$. Here, two combustion zones with similar signatures are also observed.

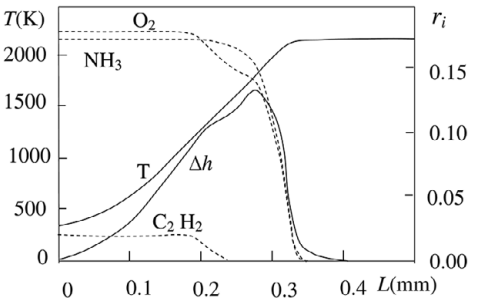

Figure 4.22 Variation of T, Δh_{max}, r_{O_2}, r_{NH_3}, $r_{C_2H_2}$ in the flame front of stoichiometric mixture $(zC_2H_2 + (1 - z)NH_3)$ + air ($p = 6$ atm, $T_{fr} = 300$ K, $z = 0.10$).

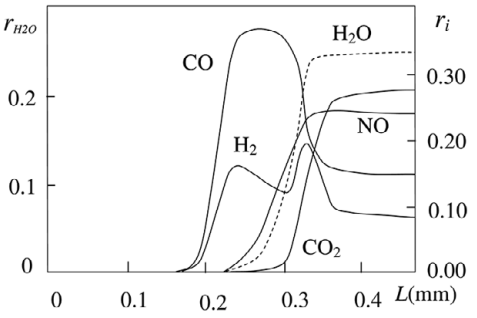

Figure 4.23 Variation of concentrations r_{H_2O}, r_{CO_2}, r_{NO}, r_{CO}, r_{H_2} in the flame front of stoichiometric mixture $(zC_2H_2 + (1 - z)NH_3)$ + air ($p = 6$ atm, $T_{fr} = 300$ K, $z = 0.10$).

Downloaded from https://www.cambridge.org/core. Nottingham Trent University, on 17 Aug 2019 at 02:03:36, subject to the Cambridge Core terms of use, available at https://www.cambridge.org/core/terms. https://doi.org/10.1017/9781108581714.004

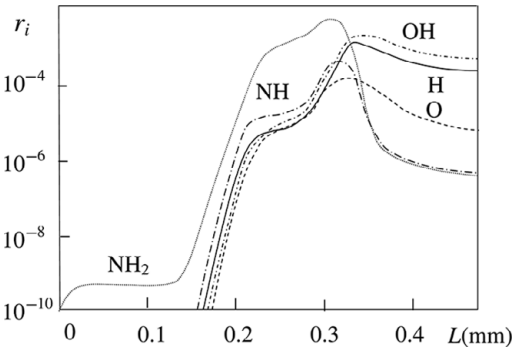

Figure 4.24 Variation of concentrations r_{NH}, r_{NH_2}, r_H, r_{OH}, r_O in the flame front of stoichiometric mixture (zC_2H_2 + (1− z)NH_3) + air (p = 6 atm, T_{fr} = 300 K, z = 0.10).

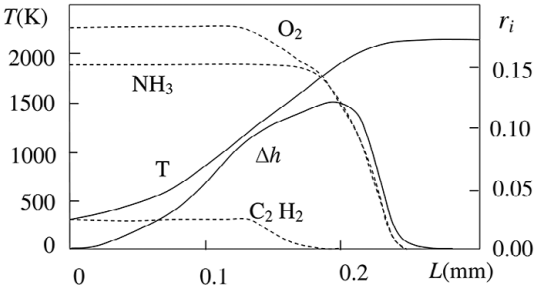

Figure 4.25 Variation of T, Δh_{max}, r_{O_2}, r_{NH_3}, $r_{C_2H_2}$ in the flame front of stoichiometric mixture (zC_2H_2 + (1 − z)NH_3) + air (p = 6 atm, T_{fr} = 300 K, z = 0.15).

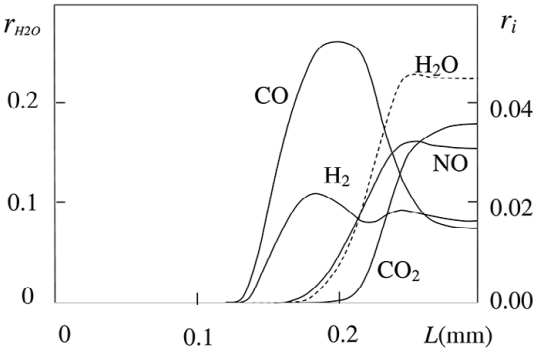

Figure 4.26 Variation of concentrations r_{H_2O}, r_{CO_2}, r_{NO}, r_{CO}, r_{H_2} in the flame front of stoichiometric mixture (zC_2H_2 + (1 − z)NH_3) + air (p = 6 atm, T_{fr} = 300 K, z = 0.15).

At the same time, the combustion zones are practically aligned at $z \geq 0.20$ while the fuel behaves as the multicomponent one and flame front characteristics are similar to those shown in Figures 4.16–4.18 for mode z = 0.45. In this case, the combustion of the mixture with higher content of acetylene and high heat of combustion facilitates the

Downloaded from https://www.cambridge.org/core. Nottingham Trent University, on 17 Aug 2019 at 02:03:36, subject to the Cambridge Core terms of use, available at https://www.cambridge.org/core/terms. https://doi.org/10.1017/9781108581714.004

temperature grows and results in combined and simultaneous combustion. Combustion of stoichiometric mixtures "$_zC_2H_2$ + (1 − z)NH_3+ air" at p = 6 atm, T_{fr} = 300 K was analyzed to reveal the following.

(1) Combustion in the front of bicomponent fuel C_2H_2 + NH_3 at $z \geq 0.2$ occurs in compliance with the scheme typical of multicomponent fuel with appropriate changes in temperature, enthalpy and concentration of combustion products and active radicals.

(2) Two combustion zones are observed at $z < 0.2$: acetylene combustion occurs in the first zone and ammonia combustion proceeds in the second zone. At the same time, both components of the fuel are burned at identical velocity. This results in that the distribution of characteristics over the flame front features some distinctions – e.g., availability of peaks in the history of variation of H_2 concentration and typical sagging in the plots of enthalpy and concentration of intermediate products.

Downloaded from https://www.cambridge.org/core. Nottingham Trent University, on 17 Aug 2019 at 02:03:36, subject to the Cambridge Core terms of use, available at https://www.cambridge.org/core/terms. https://doi.org/10.1017/9781108581714.004

5 Droplets and Particles: Evaporation in High-Temperature Flow and Combustion in Boundary Layers

5.1 Peculiarities of Droplets Evaporation and Combustion

Evaporation and combustion of dispersed propellants in a high-temperature reacting flow are typical for the most diverse propulsion and power generation systems such as internal combustion engines (ICE), combustors of air breathing engines (ABE), combustion chambers of liquid-propellant rocket engines (LPRE), liquid gas generators (LGG), and steam-gas generators (SGG), combustion chambers of furnaces, etc. Liquid-propellant atomization, spray formation, and droplet evaporation processes are seen to bear strong influence on the efficiency of the combustion process and, hence, the operating and ecological parameters of these combustion systems.

Relatively small droplets of a volatile fuel or oxidizer moving in a high-temperature reacting flow have a comparatively small evaporation time that allows to assume immediate droplet evaporation without consideration of detailed processes of droplet heating and evaporation preceding the combustion. For larger droplets of less volatile fuel or oxidizer, droplets evaporation will be a controlling process during combustion. In the present situation, the analysis of the combustion has to begin with a detailed study of the vaporization of a single droplet.

The set of preparatory processes precedes the combustion: atomization, impingement, and evaporation of the propellant injected into a combustion chamber via mixing elements (injector in the ICE cylinder or gas turbine engine [GTE] combustion chamber; injector head in LPRE, LGG, or SGG; injector or system of injectors in the furnace), mixing of vapors, and their ignition. As a rule, these processes occur in the external flow of high-temperature combustion products of already burned-out fuel and oxidizer or in the flow of propellant (fuel or oxidizer) vapors that forms a complicated hydrogasodynamic pattern of two-phase flow of the mixture of combustion products and reactants [1, 214–217]. The main part of these processes proceeds in a comparatively thin nearby surface layer surrounding the propellant or oxidizer droplet, which – if abstracting the dynamic effects brought thereon from an external flow – may be treated as a boundary layer wherein occur the phase transitions, chemical reactions, temperature, enthalpy, chemical composition, other thermodynamic parameters variation, etc. (Figure 5.1).

The thickness of this layer can be tens and hundreds of times smaller than diameter of the droplet proper that, for example, for LPRE equals 25–250 μm. Thus, speaking of the processes in these thin layers, it is possible to operate with the term "processes at the

Downloaded from https://www.cambridge.org/core. Nottingham Trent University, on 17 Aug 2019 at 02:07:06, subject to the Cambridge Core terms of use, available at https://www.cambridge.org/core/terms. https://doi.org/10.1017/9781108581714.005

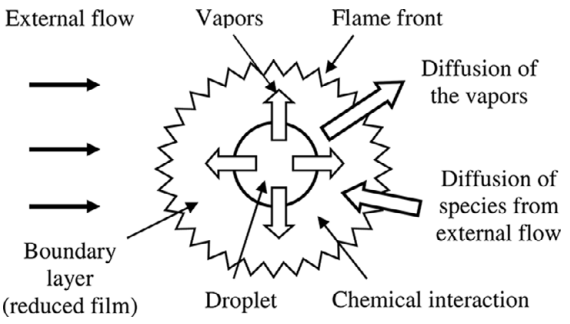

Figure 5.1 Simplified diagram of droplet evaporation in the high-temperature external flow.

microlevel," which corresponds to the division of processes and technologies into nano-, micro-, and macrolevels. The concept of such microlayers surrounding the droplet is surely an idealized one. Unlike the boundary layer formed, for instance, on a long, flat surface of a solid body, the layer around the liquid droplet in a high-temperature flow features less stability in shape and thickness because of the small size of the droplet and high velocities of external flow. Nevertheless, this concept is quite suitable for theoretical comprehension and simulation. In this connection and with a number of assumptions, it may be approximately considered as a certain boundary layer around the droplet evaporating in the external flow. The boundary layer thickness depends on the velocity, temperature, and thermophysical properties of external flow as well as on evaporating fluid parameters and droplet diameter. Parameters of the mixture of gases vary in boundary layer from the parameters of the liquid vapors on the droplet surface up to parameters of the external flow at the boundary. Common interpretation of the boundary layer in the case of droplet evaporation is "reduced film" [8, 11, 55, 57, 218] (see also Chapter 6), wherein gradients of thermophysical parameters are concentrated.

Typical processes accompanying the droplet evaporation in high-temperature gas flow are the following:

- Thermodiffusion, barodiffusion, and concentration diffusion of the propellant vapors and products of the reactions in the boundary layer into the external flow, as well as diffusion of individual substances from the external flow toward the fluid surface
- Heat transfer by conduction, convection, and radiation from the external flow to the droplet surface
- Chemical interaction of vapors with individual substances coming from the external flow
- Droplet heating and, in some cases, thermal decomposition of the liquid propellant.

Frequently, evaporating fluids feature multiphase composition and decompose a fraction at heating. Note here that with time, a redistribution of fractions by densities can be observed. A separate complex of phenomena represents a dynamic state of the liquid phase. These include the deformation, droplet spinning and their secondary atomization, origination of reactive forces at droplet evaporation, and circulating flows

Downloaded from https://www.cambridge.org/core. Nottingham Trent University, on 17 Aug 2019 at 02:07:06, subject to the Cambridge Core terms of use, available at https://www.cambridge.org/core/terms. https://doi.org/10.1017/9781108581714.005

in the droplet. Analysis of each of these processes allows evaluation of the interrelation and mutual influence. Thus, for example, the droplet evaporation rate in the ballasting zone of LGG (a detailed description of the processes in gas generators and issues of simulation and optimization of their parameters are given in Chapter 7) establishes chemical composition of generated gas (combustion products), LGG equivalence ratio, hence, and gas temperature. The evaporation rate, in its turn, depends on the temperature of gas flow and that of droplets, pressure of saturated vapors, relative velocity of droplets, their initial size, and thermophysical properties of gases and fluids. The evaporation rate is significantly influenced by Stefan's flow, originating at variation of steam-gas volume [8, 55, and 57].

If we assume the absence of intensive convective flows in the boundary layer nearby the evaporating droplet surface, then the main driving force of interosculation of individual substances within the limits of this layer is the diffusion.

The processes analyzed in this chapter include a regular assumption of pressure uniformity over the entire working volume of boundary layer. In this connection, the barodiffusion can be assumed as not affecting the processes under consideration. Thermal diffusion is known to have the higher order as compared with concentration diffusion. In this connection, the concentration diffusion only is considered, as a rule, in simulation of diffusion processes. This is why the concentration diffusion causes the origination of diffusion flows of separate substances, thus initiating the "mechanical" variation of composition in the boundary layer – hence, the occurrence of chemical reactions, variation of temperature, and chemical composition of the gas–vapor mixture in the boundary layer.

In case the external gas flow exists at a high temperature of the order of 2500–3000 K and at high pressures, chemical reaction rates may be considered infinitely high while for determination of chemical composition, the chemical equilibrium model and corresponding calculation procedures may be applied. However, a distinctive feature of nearby surface microlayers under consideration is that the mixture temperature therein can vary, in fact, from the droplet surface temperature (for example, some hundreds Kelvin) to that of external flow (for example, some thousands degrees Kelvin). Chemical interaction time in the low-temperature range is known to render comparable with that of the other processes such as diffusion, conduction, etc. Then, at the determination of the gas composition and its thermophysical parameters in the boundary layer, it is expedient to allow for finite chemical reaction rates – that is, to apply the chemical kinetics models and their corresponding calculation procedures.

The given description displays how complicated are aerothermochemical the processes that proceed in boundary layers at the evaporation of dispersed propellants. Simulation of these processes represents an undoubted interest in terms of gaining the new data on the combined occurrence of heat exchange and mass exchange processes with chemical conversions and diffusion at the microlevel – all the more so because the experimental research is extremely intricate in this case. The applied interest of this research consists in the possibility of developing the methods of control and optimization of operational and ecological parameters of the combustion units wherein such evaporation and combustion processes occur.

Downloaded from https://www.cambridge.org/core. Nottingham Trent University, on 17 Aug 2019 at 02:07:06, subject to the Cambridge Core terms of use, available at https://www.cambridge.org/core/terms. https://doi.org/10.1017/9781108581714.005

It has been shown earlier that the reduced film model is a classical one (from the historical standpoint) that allows one to define the rate of steady-state evaporation of fluid from the spherical surface and, in this particular case, from the flat surface, as well as heating of the droplet taking into consideration Stefan's flow . However, this model does not allow estimating actual composition of the reacting gas mixture in reduced film subject to possible chemical reactions of the vapors with external high-temperature gas flow. This model is widely used for calculation of vapor flow rate without allowance for a chemical reaction in the film [8, 11, 55, 57, 101, 218].

Studies related to the simulation of vapor conversion [6, 32, 219, 220] confirm the importance of allowance for chemical interaction of phase transition products and external flow within the boundary layer limits. The separation of a layer around the droplet into oxidizer and propellant zones and operation with integral relationships for calculation of chemical reaction products, considering chemical interaction in the flame front dividing these zones, and describing chemical conversions by global reaction "oxidizer + propellant = reaction products" make a classical approach to simulation. This approach was described by F. A. Williams [6] and successfully used lately by various researchers. Thus, for example, a considerable amount of research of processes occurring above the liquid fuel layer at blowing it with the oxidizer flow was cited in the [219–221].

One of the main directions of such research consists in the acquisition of data on the oxidizer droplet combustion rate in the medium of fuel vapors or fuel droplets in the medium of oxidizer. Detailed analysis of aerothermochemical processes in boundary layer at droplet evaporation with allowance for complex kinetic mechanisms is extremely limited. Thus, for example, the paper [222] represents the results of numerical simulation of the oxygen single-droplet combustion in high-temperature gas flow, yet the reaction mechanism in the boundary layer is described by the global reaction $H_2 + 1/2O_2 \leftrightarrow$ reaction products. Dealing with the problem of allowing for a detailed mechanism of interaction, it is more appropriate to refer to research of aerothermochemistry in boundary layers with phase and chemical conversions performed, for example, by B. Boyarshinov, E. Volchkov et al. [223]. However, these studies relate to the processes in boundary layers on the flat surface that doesn't reflect the specific character of evaporation of dispersed propellant.

A more adequate model of the processes in boundary layers at propellant droplet evaporation in high-temperature reacting flow requires combined allowance for dynamic, diffusion, and heat factors with application of chemical kinetics under conditions of variable chemical composition and properties of reacting medium in the boundary layer and multicomponent diffusion over the thickness of boundary layer that utterly complicates problem analysis.

5.2 Application of Perfectly Stirred Reactor to the Simulation of Evaporation and Chemical Reacting of Dispersed Propellant: Governing Equations

A widespread assumption confirmed experimentally and used for the simulation of droplet evaporation is that of the droplet's temperature invariability over its radius,

Downloaded from https://www.cambridge.org/core. Nottingham Trent University, on 17 Aug 2019 at 02:07:06, subject to the Cambridge Core terms of use, available at https://www.cambridge.org/core/terms. https://doi.org/10.1017/9781108581714.005

which can be considered close to the droplet surface temperature. Evaluation of the analyzed problem complexity and the separate processes' influence allows and even requires accepting a number of extra assumptions:

- The reduced film model used widely enough and successfully in evaporation simulation practices is applied as the boundary layer model.
- The droplet moves in the high-temperature flow at constant velocity and over straightline trajectory.
- Spherical symmetry is applicable.
- All parameters of the gas–vapors mixture (except for pressure, which is uniform) vary in a radial direction from the droplet surface to the outer edge of the boundary layer.
- Parameters at the outer edge of boundary layer approach the values of external flow parameters.
- Heterogeneous reactions on liquid/gas interface are not allowed for;
- External flow is laminar.
- Within the limits of the boundary layer, the substance molecular transfer is effected; its driving force is composed of diffusion and convective transfer caused by Stefan's flow.
- The model allows for concentration diffusion phenomenon only, since thermodiffusion and barodiffusion in similar processes bring about negligibly minor effects, which is a common belief.
- Binary diffusion model is used.
- Gas-phase solubility in the liquid is not allowed for.
- Circulating flows in the droplet are not allowed for.
- Radiation heat transfer is negligibly small as compared with the convective process.

Undoubtedly, some assumptions – such as spherical symmetry, laminar flow, and droplet liner trajectory – idealize the processes under consideration. However, such simplification allows one to pay a deeper attention to simulation of thermochemical and diffusion processes in the boundary layer. A number of specific assumptions related to the mathematical model is given in the following paragraphs along with derivation of specific relationships and equations.

A small thickness of the reaction zone (reduced film) and comparatively low temperatures nearby the droplet surface result in the situation when chemical reaction times increase to become comparable with that of diffusion and convective mass transfer in the boundary layer. A mathematical description of such processes requires application of models and methods of chemical kinetics allowing for finite reactions rates (Sections 1.3 and 2.1). With due allowance for radial variation of parameters in the boundary layer and assumption of spherical symmetry, a reactor approach described in Section 1.5 is considered acceptable for simulation of the reacting vapor–gas mixture parameters' distribution over the boundary layer as well as the chemical nonequilibrium

Downloaded from https://www.cambridge.org/core. Nottingham Trent University, on 17 Aug 2019 at 02:07:06, subject to the Cambridge Core terms of use, available at https://www.cambridge.org/core/terms. https://doi.org/10.1017/9781108581714.005

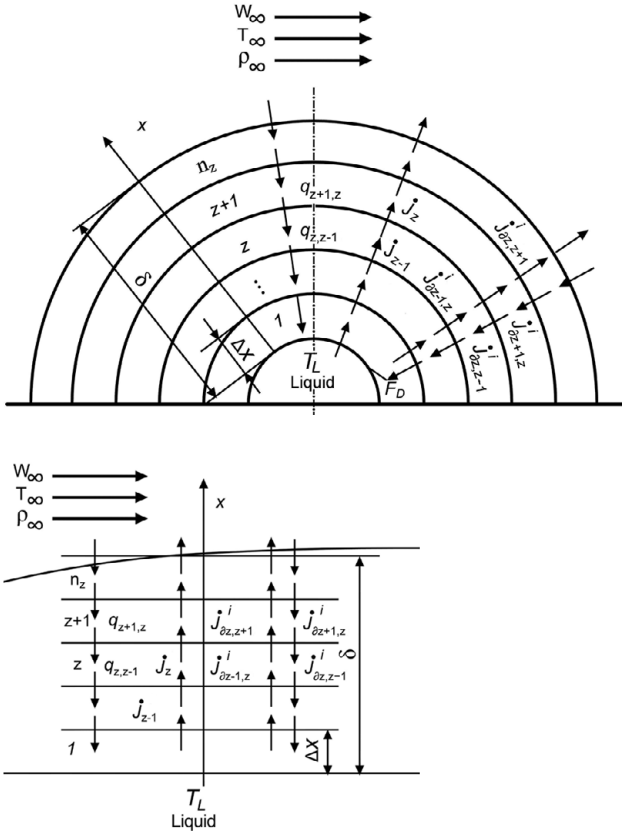

Figure 5.2 Physical diagrams of evaporation of the liquid in reacting gas flow: (a) evaporation from the droplet surface; (b) evaporation from the plane surface of the liquid.

model and original models of mass exchange processes and corresponding basic algorithms (Chapter 2).

Let us consider the boundary layer consisting of a set of interrelated PSRs – i.e., the system of PSRs that represent concentric spherical Δx-thickness layers as a boundary layer surrounding the droplet (Figure 5.2a), or flat Δx-thickness layers in a case of the evaporation from the plane surface of the liquid (Figure 5.2b). In compliance with the previously listed assumptions, one can consider that neighbor reactors exchange mass and energy via molecular diffusion, convection, and conduction. The reactor in contact with interface surface exchanges mass with the droplet (fluid evaporation from the droplet surface) and some amount of heat with the droplet surface, while the reactor in contact with external flow exchanges mass and energy therewith.

In compliance with this diagram, let us write the conservation equations, considering the gas mixture in the reactors as an ideal gas.

Downloaded from https://www.cambridge.org/core. Nottingham Trent University, on 17 Aug 2019 at 02:07:06, subject to the Cambridge Core terms of use, available at https://www.cambridge.org/core/terms. https://doi.org/10.1017/9781108581714.005

Mass conservation equation for reactor z is written as follows:

$$\frac{dM_z}{d\tau} = F_{z-1,z}\dot{J}_{z-1} - F_{z+1,z}\dot{J}_z + F_{z+1,z}\sum_{i=1}^{n}\dot{J}^i_{\partial z+1,z} - F_{z+1,z}\sum_{i=1}^{n}\dot{J}^i_{\partial z,z+1}$$
$$+F_{z-1,z}\sum_{i=1}^{n}\dot{J}^i_{\partial z-1,z} - F_{z-1,z}\sum_{i=1}^{n}\dot{J}^i_{\partial z,z-1} \equiv F_{M_z}, \tag{5.1}$$

where $\dot{J}_{z-1}$ is the mass flux of the vapor–gas mixture coming into reactor z from reactor $z-1$; $\dot{J}_z$ is the mass flux of the vapor–gas mixture coming into reactor $z+1$ from reactor z; $\dot{J}^i_{\partial z+1,z}$ is the mass flux of substance i coming from reactor $z+1$ into reactor z; $\dot{J}^i_{\partial z,z+1}$ is the mass flux of substance i coming from reactor z into reactor $z+1$; $\dot{J}^i_{\partial z-1,z}$ is the mass flux of substance i coming from reactor $z-1$ into reactor z; $\dot{J}^i_{\partial z,z-1}$ is the mass flux of substance i coming from reactor z to reactor $z-1$; $F_{z-1,z}$ is the area of contact surface between reactors $z-1$ and z; $F_{z-1,z}$ is the area of contact surface between reactors $z+1$ and z; and F_{Mz} is the formal notation of the right-hand side of the equation of conservation of mass.

Equation of conservation of energy for reactor z is written as follows:

$$dU_z + pdV_z = dQ_{z-1} - dQ_z + d\sum_{i=1}^{n}Q^i_{\partial z+1,z} - d\sum_{i=1}^{n}Q^i_{\partial z,z+1} + d\sum_{i=1}^{n}Q^i_{\partial z-1,z}$$
$$-d\sum_{i=1}^{n}Q^i_{\partial z,z-1} + dQ_{z+1,z} - dQ_{z,z-1}, \tag{5.2}$$

where dQ_{z-1} is the energy transferred to reactor z from reactor $z-1$ with convective flow of vapor–gas mixture toward the external flow, (J); dQ_z is the energy transferred from reactor z to reactor z + 1 with convective flow of vapor–gas mixture toward the external flow, (J); dU_z is the total energy change in reactor z, (J); pdV_z is expansion work, (J); $d\sum_{i=1}^{n}Q^i_{\partial z+1,z}$; $d\sum_{i=1}^{n}Q^i_{\partial z-1,z}$ is energy transferred into reactor z from reactors $z+1$ and $z-1$ with diffusing substance i, (J); $d\sum_{i=1}^{n}Q^i_{\partial z,z+1}$; $d\sum_{i=1}^{n}Q^i_{\partial z,z-1}$ is energy transferred from reactor z into reactors $z+1$ and $z-1$ with diffusing substance i, (J); $dQ_{z+1,z}$ is amount of heat transferred to reactor s from reactor $z+1$ by conduction, (J); and $dQ_{z,z-1}$ is amount of heat transferred from reactor z into reactor $z-1$ by conduction, (J).

Allowing for $U = H - pV$ (where U is total internal energy and H is total enthalpy) and having made some conversions, write (5.2) as follows:

$$\frac{dH_z}{d\tau} - p\frac{dV_z}{d\tau} - V_z\frac{dp}{d\tau} + p\frac{dV_z}{d\tau} = \dot{m}_{z-1,}h_{z-1} - \dot{m}_z h_z + \sum_{i=1}^{n}\dot{m}^i_{\partial z+1,z}\,h^i_{z+1}$$
$$-\sum_{i=1}^{n}\dot{m}^i_{\partial z,z+1}\,h^i_z + \sum_{i=1}^{n}\dot{m}^i_{\partial z-1,z}\,h^i_{z-1} - \sum_{i=1}^{n}\dot{m}^i_{\partial z,z-1}\,h^i_z + q_{z+1,z} - q_{z,z-1}, \tag{5.3}$$

where $q_{z+1,z}$ is heat transfer rate by conduction to reactor z from reactor $z+1$, (W); and $q_{z,z-1}$ is heat transfer rate by conduction from reactor z to reactor $z-1$, (W).

Downloaded from https://www.cambridge.org/core. Nottingham Trent University, on 17 Aug 2019 at 02:07:06, subject to the Cambridge Core terms of use, available at https://www.cambridge.org/core/terms. https://doi.org/10.1017/9781108581714.005

Owing to ideal-gas assumption and that of droplet steady-state evaporation, the boundary layer thickness – hence, the volume of each reactor – may be considered invariable. In this case, allowing for total enthalpy $H = hM$ and mass flow rate $\dot{m} = \dot{J}F$, and with regard to constant pressure in the reactors, Equation (5.3) may be transformed with application of (5.1) to the following form:

$$\frac{dh_z}{d\tau} = \frac{R_0 T_z}{\mu_z p V_z}\left[\dot{J}_{z-1,}F_{z-1,z}(h_{z-1} - h_z) + \sum_{i=1}^{n}\dot{J}^i_{\partial z+1,z}\,F_{z+1,z}\left(h^i_{z+1} - h_z\right)\right.$$
$$-\sum_{i=1}^{n}\dot{J}^i_{\partial z,z+1}\,F_{z+1,z}\left(h^i_{z+1} - h_z\right) + \sum_{i=1}^{n}\dot{J}^i_{\partial z-1,z}\,F_{z-1,z}\left(h^i_z - h_z\right)$$
$$\left.-\sum_{i=1}^{n}\dot{J}^i_{\partial z,z-1}\,F_{z-1,z}\left(h^i_z - h_z\right) + \dot{q}_{z+1,z}F_{z+1,z} - \dot{q}_{z,z-1}F_{z-1,z}\right] = F_{h_z}, \tag{5.4}$$

where μ_z is the molecular mass of the vapor–gas mixture in reactor z; $\dot{q}_{z+1,z}$ is heat flux by conduction to reactor z from reactor $z + 1$, (W/m^2); and $\dot{q}_{z,z-1}$ is heat flux by conduction from reactor z to reactor $z - 1$, (W/m^2).

It is reasonable that for reactor $z = n_z$ (where n_z is the number of the rector bordering the external flow), Equation (5.4) requires the following substitution: $h_{z+1} = h_\infty$; $\dot{J}^i_{\partial z+1,z} = \dot{J}^i_{\partial\ \infty,z}$; $\dot{J}^i_{\partial z,z+1} = \dot{J}^i_{\partial z,\ \infty}$; $\dot{q}_{z+1,z} = \dot{q}_{\infty,z}$, where symbol ∞ indicates external flow parameters.

On another hand, Equation (5.4) will be written for reactor in contact with the evaporation surface as follows:

$$\frac{dh_1}{d\tau} = \frac{R_0 T_1}{\mu_1 p V_1}\left[\begin{array}{l}\dot{J}_V F_L(h_L - h_1) + \sum_{i=1}^{n}\dot{J}^i_{\partial 2,1}\,F_{2,1}\left(h^i_2 - h_1\right) \\ -\sum_{i=1}^{n}\dot{J}^i_{\partial 1,2}\,F_{2,1}\left(h^i_1 - h_1\right) + \dot{q}_{2,1}F_{2,1}\end{array}\right] = F_{h_1}, \tag{5.5}$$

where $\dot{J}_V$ is vapor mass flux from the droplet surface, h_L is specific enthalpy of liquid, F_L is evaporation surface area, and symbol L designates the evaporating liquid.

Owing to application of the PSR basic model (Section 1.5), equations of chemical kinetics (2.31), normalizing equations (2.157), and caloric (energy) equations (2.149) written for reactors $z = 1 \ldots n_z$, should be added to the system of equations (5.1, 5.4, 5.5).

The system of equations (5.1, 5.4, 5.5, 2.31, 2.149, 2.157) represents mathematical model of thermochemical processes in the boundary layer. Assumption of the droplet stationary evaporation does not contradict with notation of differential equations with time derivatives in their left-hand sides since the system of equations can be solved by ascertaining the method – i.e., by multiple integration of the system of equations to achieve a relative change in the unknown parameters (temperature, enthalpy, chemical composition of the mixture and its mass) in each of the reactors of some predetermined small value.

Downloaded from https://www.cambridge.org/core. Nottingham Trent University, on 17 Aug 2019 at 02:07:06, subject to the Cambridge Core terms of use, available at https://www.cambridge.org/core/terms. https://doi.org/10.1017/9781108581714.005

The previously mentioned "reduced film" model can be used for evaluation of the thickness of layer [8, 11, 57, 101, 218]. In compliance with this model, the diffusion reduced film thickness is calculated from the relationship

$$\delta_D = d_D / Nu_D, \tag{5.6}$$

where d_D is the droplet diameter; Nu_D is the diffusion Nusselt number.

For calculation of Nusselt number in the case of droplet evaporation, one can use the relationship that rendered a classical one for the analysis of this kind [218, 224].

$$Nu_D = 2 + 0.6 Sc^{1/3} \mathrm{Re}^{1/2}, \tag{5.7}$$

where Sc is the Schmidt number.

It is clear from (5.6) and (5.7) that the boundary layer thickness depends, in particular, on external flow parameters, notably decreasing at external flow velocity decrease and reaching its maximum at external flow zero velocity ($\delta_D = d_D/2$). The thickness of each reactor is assumed constant for steady-state evaporation $\Delta x = \delta_D / n_z$.

5.3 Heat and Mass Transfer in Boundary Layer at Evaporation of Single Droplet

One of the most important issues of notation of the left-hand sides of Equations (5.1), (5.4), and (5.5) is the estimation of the evaporation rate from the droplet surface. Since the model examines the steady-state evaporation of a droplet moving at constant velocity over a linear trajectory in high-temperature gas flow, the temperature T_∞, which is notably higher than the boiling temperature ($T_\infty \gg T_b$), the concept of equilibrium evaporation may be used for the droplet evaporation simulation [218]. Following this model vapor mass flux from the droplet surface is defined from the relationship,

$$\dot{j}_V = \frac{k_{V-G} Nu}{c_{pV} d_D} \ln \left[1 + \frac{c_{pV}}{L_V} \left(T_\infty - T_{eq} \right) \right], \tag{5.8}$$

where $c_{pV}, L_V,\ T_{eq}$ are specific heat of the vapor, latent heat of evaporation, and droplet equilibrium temperature, respectively, and k_{V-G} is thermal conductivity of vapor–gas mixture in the boundary layer.

Owing to steady-state evaporation and $T_{eq} \approx T_b$ condition that makes the equilibrium evaporation model attribute and the effect of $T_\infty \gg T_b$, one may suggest that the droplet is heated uniformly to T_{eq}, which equals to boiling temperature T_b.

Mass flux of vapor–gas mixture coming into reactor z from reactor $z - 1$ (as an example) is defined from the continuity equation:

$$\dot{j}_{z-1} = \frac{1}{F_{z-1,z}} \dot{j}_z F_{z,z+1}. \tag{5.9}$$

Downloaded from https://www.cambridge.org/core. Nottingham Trent University, on 17 Aug 2019 at 02:07:06, subject to the Cambridge Core terms of use, available at https://www.cambridge.org/core/terms. https://doi.org/10.1017/9781108581714.005

Given that the vapor mass flux from the droplet surface defined analytically from (5.8), it is possible with the help of (5.9) to determine all convective flow rates between reactors $1 \ldots n_z$ simulating the boundary layer.

For the calculation of diffusion in the boundary layer, it is appropriate to assume that the main mass exchange mechanisms are not violated when evaporation and diffusion are accompanied by chemical reactions. Following the assumption of binary diffusion, Fick's law for *i*th substance is written as follows:

$$\dot{J}^i_{\partial z-1,z} = D^i_{z-1,z}\frac{dC_i}{dx}. \tag{5.10}$$

Integration (5.10) over the reactor thickness results in the expression for mass flux of *i-th* individual substance between reactors $z-1$ and z:

$$\dot{J}^i_{z-1,z} = \frac{pD^i_{z-1,z}\mu_i(r_{iz-1} - r_{iz})}{R_0\bar{T}_{z-1,z}\Delta x}, \tag{5.11}$$

where $D^i_{z-1,z}$ is the binary diffusion coefficient for substance i diffusing from reactor $z-1$ into reactor z and $\bar{T}_{z-1,z}$ is the averaged vapor–gas temperature in reactors z and $z-1$.

Similarly, using the Fourier's law, we obtain the expression for the calculation of heat flux, for instance, from reactor $z+1$ into reactor z:

$$\dot{q}_{z+1,z} = \frac{\bar{k}_{z+1,z}}{\Delta x}(T_{z+1} - T_z), \tag{5.12}$$

where $\bar{k}_{z+1,z}$ is the gas mixture thermal conductivity calculated at average temperature $\bar{T}_{z+1,z}$ in reactors $z+1$ and z.

Analysis of mass exchange processes shows that the problem under consideration features two types of mass exchange processes: mass exchange between the reactors caused by convective mass transfer and mass exchange caused by concentration diffusion. The convective flow initiated by the vapor flow directed from the droplet surface to the external flow will prevail. However, it should be remembered that the processes under consideration relate to processes that occur at microlevel. This means that convective mass flows in the boundary layer may be extremely small and, in principle, comparable with the diffusion mass flows. This is why one cannot neglect diffusion mass exchange.

In compliance with the rules of writing the rate constants of mass supply "reactions" (Section 2.2), the rate constant of convective mass supply of *i*th individual substance from reactor $z-1$ into reactor z is written as follows:

$$k^+_{iz-1,z} = \frac{\dot{m}_{z-1}g_{iz-1}}{\mu_i V_z}, \tag{5.13}$$

where g_{iz-1} is the mass fraction of *i*th individual substance in rector $z-1$, and $\dot{m}_{z-1}$ is the mass flow rate of gas mixture flowing from reactor $z-1$ into reactor z.

Since convective mass discharge from the reactor into another one occurs in concentrations proportional to the gas mixture chemical composition in this reactor and,

Downloaded from https://www.cambridge.org/core. Nottingham Trent University, on 17 Aug 2019 at 02:07:06, subject to the Cambridge Core terms of use, available at https://www.cambridge.org/core/terms. https://doi.org/10.1017/9781108581714.005

thereby, does not change chemical composition in the reactor wherefrom it is discharged, rate constants of mass discharge from the reactor into another one may be omitted from the analysis of right-hand sides of Equations (2.31).

For more detailed explanation of the notation of diffusion mass exchange reaction rate constants (Section 2.2), one should turn to diffusion terms in Equation (5.1). If we consider the flow of ith substance diffusing from reactor $z-1$ into reactor z and vice versa, then the total diffusion flow of this substance between the reactors is written in the following form:

$$F_{z-1,z}\dot{J}^{i}_{\partial z-1,z} - F_{z-1,z}\dot{J}^{i}_{\partial z,z-1} = \dot{m}^{i}_{\partial z-1,z} - \dot{m}^{i}_{\partial z,z-1} \equiv m^{i}_{\partial (z-1,z),(z,z-1)}. \tag{5.14}$$

Or, from the Fick's law,

$$\dot{m}^{\,i}_{\partial z-1,z} - \dot{m}^{i}_{\partial z,z-1} \equiv m^{i}_{\partial (z-1,z),(z,z-1)} = -\frac{D^{i}_{z-1,z}pF_{z-1,z}\mu_i r_{iz-1}}{R_0\bar{T}_{z-1,z}} - \frac{D^{i}_{z-1,z}pF_{z-1,z}\mu_i r_{iz}}{R_0\bar{T}_{z-1,z}}, \tag{5.15}$$

where $\bar{T}_{z-1,z}$ is the temperature averaged over the reactors $z-1$ and z.

The direction of ith individual substance flow will depend on the values of concentrations r_{iz-1} and r_{iz}.

Correspondingly, diffusion mass exchange "reaction" rate depends on the ith substance concentrations in reactors $z-1$ and z and is written in the general form as (see for instance Subsection 2.2.2):

$$W_{i\partial (z-1,z),(z,z-1)} = W^{+}_{iz-1,z} - W^{-}_{iz,z-1}. \tag{5.16}$$

That is, the reaction of ith substance diffusion mass exchange between the reactors $z-1$ and z should be represented by the aggregate of two reactions: zero-order mass supply reaction and the corresponding reaction rate written as (Section 2.2)

$$W^{+}_{iz-1,z} = k^{+}_{i}C^{0}_{i,z-1} = k^{+}_{i}, \tag{5.17}$$

and first-order mass discharge reaction and corresponding reaction rate written as (Section 2.2):

$$W^{-}_{iz,z-1} = k^{-}_{i}C_{iz}. \tag{5.18}$$

In this case, using (5.11) and (5.15)–(5.18) and allowing for the dimension of reaction rate adopted in chemical kinetics (gmol/cm$^3\times$s), we can write (see Section 2.2):

$$W_{i\partial (z-1,z),(z,z-1)} = W^{+}_{iz-1,z} - W^{-}_{iz,z-1} = \frac{D^{i}_{z-1,z}pF_{z-1,z}r_{iz-1}}{V_z\Delta xR_0\bar{T}_{z-1,z}} - \frac{D^{i}_{z-1,z}pF_{z-1,z}r_{iz}}{V_z\Delta xR_0\bar{T}_{z-1,z}}. \tag{5.19}$$

Formulas (5.17)–(5.19), given the allowance for dimensions of the zero- and first-order reaction rates (gmol/cm$^3\times$s and 1/s, respectively), allow an unambiguous representation of the following the mass supply and mass discharge reaction rate constants that govern the diffusion exchange of ith substance between reactors $z-1$ and z:

Downloaded from https://www.cambridge.org/core. Nottingham Trent University, on 17 Aug 2019 at 02:07:06, subject to the Cambridge Core terms of use, available at https://www.cambridge.org/core/terms. https://doi.org/10.1017/9781108581714.005

$$k_i^+ = \frac{D^i_{z-1,z} p F_{z-1,z} r_{i\,z-1}}{V_z \Delta x R_0 \bar{T}_{z-1,z}}; \tag{5.20}$$

$$k_i^- = \frac{D^i_{z-1,z} F_{z-1,z}}{V_z \Delta x}. \tag{5.21}$$

The cited set of the convective and diffusion mass exchange reaction rate constants written for all reactors and species is included in the right-hand sides of Equations (2.31) to formalize the convective and diffusion mass exchange between the reactors simulating the boundary layer and to combine them with rate constants of chemical reactions (Sections 2.1 and 2.2). Thereby, we obtain a closed system of the ordinary differential equations, the solving of which allows the calculation of chemical nonequilibrium composition of reacting gas–vapor mixture, mass, temperature, enthalpy, and any other parameters over the boundary layer thickness.

5.4 Peculiarities of Algorithm: Mathematical Model Testing

Comparison of the results of numerical simulation of processes occurring in thin reacting boundary layers with experimental data makes a complex problem. The main reasons are limited experimental data caused by the complexity of measurements at microlevel as well as an idealization of the previously described model of these processes.

The experience of simulation in the framework of single and multiple reactor models has shown that for maintaining of the basic mathematical description and algorithm and for simulation of stationary problems, it is more reasonable to use the system of equations in non-steady-state form (Section 2.1) and then solve it by the ascertain method. Solving this particular problem is controlled by the temperature and concentration of individual substances setting within the limits of a relative error of these values at integration step ($\varepsilon < 0.001 \ldots 0.002$).

The mathematical model of evaporation from the droplet surface and reacting in the boundary layer described in Sections 5. 2 and 5.3 is a sufficiently universal one and allows simulation of the thermochemical process in different thin layers of reacting gas (for example, calculation of processes in laminar flame fronts, calculation parameters in the boundary layer during the injection of cold gas or liquid at transpiration cooling, etc.). Note here that the previously described basic reactor model and algorithm remain practically unchanged except for the following features.

In calculation of processes in the flame fronts (combustion zones) or at injection of reacting fluid into the boundary layer, quite insignificant changes in the algorithm are necessary that consist in the following:

– The enthalpy of liquid in Equation (5.5) is replaced by the initial enthalpy of gas fed into the thin layer.
– There is no need to calculate the vapor mass flux from the droplet surface, which should be substituted in Equation (5.5) by the mass flux of injected in the boundary layer fluid or component of the propellant coming in the combustion zone.

Downloaded from https://www.cambridge.org/core. Nottingham Trent University, on 17 Aug 2019 at 02:07:06, subject to the Cambridge Core terms of use, available at https://www.cambridge.org/core/terms. https://doi.org/10.1017/9781108581714.005

– Instead of droplet diameter, the boundary layer thickness can be used in calculations, which is set for the analyzed cross section and defined from known relationships of the theory of boundary layers [225], or the flame front thickness, for calculation of combustion.

It is necessary to note once more that the primary focus is on the simulation of chemical interaction in the boundary layers in the development of described models. That is, paying tribute to the importance of detailed simulation of chemical and mass exchange processes, the authors consider gas-dynamic aspects of these problems analyzed in sufficient detail in a great amount of studies and may be taken from there.

Experimental study of the process of evaporation from the droplet surface is an extremely complex task because of the unfeasibility of fixing a separate droplet in gas flow as well as the difficulties associated with measuring vapor flow and concentration of individual substances, temperature, and other parameters within boundary layer, nearby the droplet surface. Therefore, experimental data on evaporation are cited, as a rule, as the integral parameters in a certain volume at evaporation therein from the dispersed liquid phase surface or from the plane surface. This is why most available experimental data on distribution of parameters in boundary layers are obtained for homogeneous (premixed fuel and oxidizer) combustion or diffusion combustion (as a rule, injection of one component in a flow of the other one), such as the experimental data given for instance in [22]. The discussed model allows one to perform numerical studies of such processes.

However, it is more revealing to demonstrate the use of this model for simulation of the evaporation process and chemical interaction of a droplet in a reacting flow. Figure 5.3 shows a comparison of the calculation of dispersed oxygen combustion in the external flow of combustion products of 50% hydrogen + 50% oxygen (mass

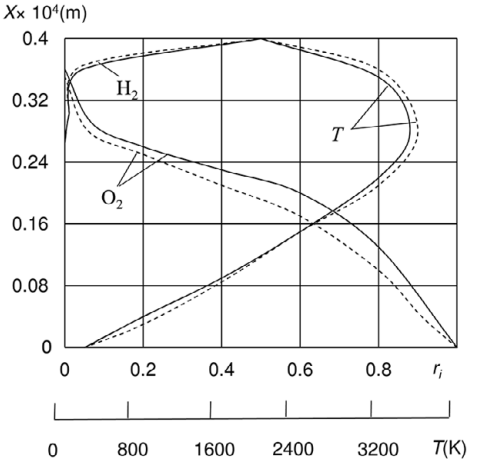

Figure 5.3 Oxygen droplet evaporation into combustion products $O_2 + H_2$ (p = 10.0 MPa, $d_D = 8 \times 10^{-5}$ m): dotted line – numerical data; solid line – calculation with application of PSRs model [226]. From V. I. Naumov, and V. Y. Kotov. "Micro-Scale Investigation of Non-Equilibrium Thermo-Fluid Transport during Droplet Evaporation and Combustion," 43rd Aerospace Science Meeting and Exhibit, AIAA 2005–1431, pp. 1–14, Reno, NV, 2005, reprinted by permission of the American Institute of Aeronautics and Astronautics, Inc

Downloaded from https://www.cambridge.org/core. Nottingham Trent University, on 17 Aug 2019 at 02:07:06, subject to the Cambridge Core terms of use, available at https://www.cambridge.org/core/terms. https://doi.org/10.1017/9781108581714.005

Table 5.1 Chemical mechanism for the calculation of hydrogen-air combustion

Chemical reaction	Chemical reaction
$H + H + M = H_2 + M$	$OH + OH = O + H_2O$
$H_2 + O_2 = OH + OH$	$H + HO_2 = H_2O + O$
$H + OH + M = H_2O + M$	$H + HO_2 = H_2 + O_2$
$H_2 + O = H + OH$	$H + O_2 + M = HO_2 + M$
$H + O_2 = OH + O$	$H_2O + O_2 = OH + HO_2$
$O + O + M = O_2 + M$	$H + HO_2 = OH + OH$
$H + O + M = OH + M$	$O + HO_2 = O_2 + OH$
$OH + H_2 = H_2O + H$	

fractions) under the following conditions: external flow temperature T = 2000 K; pressure p = 10MPa; and equivalence ratio $\alpha_{ox} = 1.0$, with results of numerical simulation [226]. Calculation of evaporation and combustion of oxygen droplet with diameter $d_D = 8 \times 10^{-5}$ m was performed using chemical mechanism given in Table 5.1. Some discrepancies in temperature and concentrations may be explained by the difference in the reaction mechanisms and different approaches to the simulation of evaporation and combustion.

The preceding results and examples of numerical study demonstrated in Section 5.5 show the possibility of model application to the simulation and analysis of thermochemical processes in reacting boundary layers at liquid fuel or oxidizer evaporation and the simulation of the processes in the combustion zones of homogeneous gas mixtures, as well as its integration in complex mathematical models of combustion and flow of reactive mixtures in power generation and combustion units.

5.5 Numerical Simulation and Analysis of the Processes in Boundary Layers at Evaporation and Chemical Interaction

5.5.1 Effect of Chemical Nonequilibrium

This study aimed to determine the degree of chemical reactions influence on parameters of vapor–gas mixtures in the boundary layers and develop practical recommendations for adequate application of various models of chemical composition of reacting mixtures calculation (frozen, equilibrium, and nonequilibrium; see Section 1.3) to the simulation of evaporation and chemical interaction.

The evaluation of influence of reaction kinetics in the boundary layer on vapor–gas mixtures major parameters (temperature and chemical composition) was accomplished on the basis of the following numerical experiments:

1. Evaporation of dispersed liquid oxygen into oxygen and hydrogen combustion products (O_{2L} +$[O_2$+$H_2]_G$)
2. Evaporation of dispersed nitrogen tetroxide (NT), (N_2O_4) into nitrogen tetroxide and unsymmetrical dimethylhydrazine (UDMH), combustion products (N_2O_{4L}+ $[N_2O_4$+$H_2N_2(CH_3)_2]_G$)

Downloaded from https://www.cambridge.org/core. Nottingham Trent University, on 17 Aug 2019 at 02:07:06, subject to the Cambridge Core terms of use, available at https://www.cambridge.org/core/terms. https://doi.org/10.1017/9781108581714.005

3. Evaporation of dispersed liquid oxygen into oxygen and ammonia combustion products (NH_{3L}+[O_2+NH_3]$_G$)

These schemes of dispersed component evaporation and combustion are typical for gas generators, vapor–gas generators, and LPRE combustion chambers. The features of aerothermochemical processes in gas generators, and their simulation and optimization are described in details in Chapter 7.

Calculations were performed for boundary layers of different thicknesses defined by the velocity of external flow and droplet diameters (Section 5.2).

This research assumed the following main parameters to be analyzed:

– boundary layer thickness δ
– maximum difference in the reacting mixture temperature employing frozen and nonequilibrium models ($\max \Delta T^{st}_{f-n}$)
– maximum difference in the "almost stoichiometric" reacting mixture temperature employing frozen and nonequilibrium models ($\max \Delta T^{st}_{f-n}$)
– minimum difference in the mixture temperature employing equilibrium and nonequilibrium models ($\min \Delta T^{st}_{f-n}$)

a Evaporation of Dispersed Liquid Oxygen into Oxygen and Hydrogen Combustion Products

Figures 5.4–5.6 show the results of numerical simulation of the oxygen O_2 droplet with a diameter of 1.0×10^{-4} m evaporation in the flow of [H_2 + O_2]$_G$ combustion products

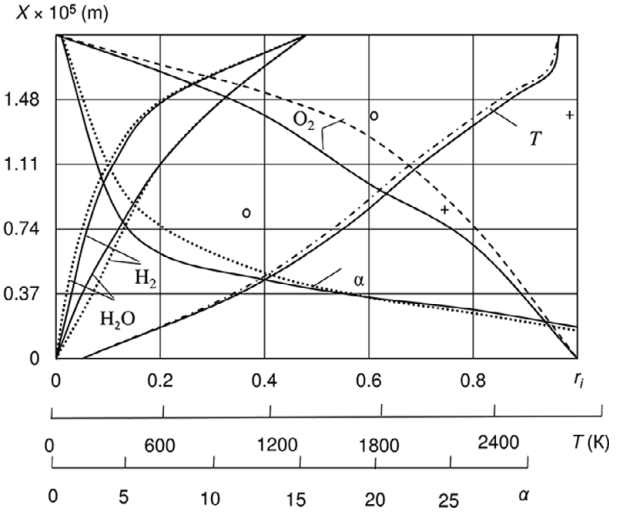

Figure 5.4 Oxygen droplet evaporation in O_2 + H_2 combustion products (W_∞ = 20 m/s, p_∞ = 0.5 MPa): solid line – calculation with allowance for chemical reactions; dotted line – "frozen" calculation; + – equilibrium temperature; o – equilibrium H_2O concentration [226]. From V. I. Naumov and V. Y. Kotov. "Micro-Scale Investigation of Non-Equilibrium Thermo-Fluid Transport during Droplet Evaporation and Combustion," 43rd Aerospace Science Meeting and Exhibit, AIAA 2005–1431, pp. 1–14, Reno, NV, 2005, reprinted by permission of the American Institute of Aeronautics and Astronautics, Inc

Downloaded from https://www.cambridge.org/core. Nottingham Trent University, on 17 Aug 2019 at 02:07:06, subject to the Cambridge Core terms of use, available at https://www.cambridge.org/core/terms. https://doi.org/10.1017/9781108581714.005

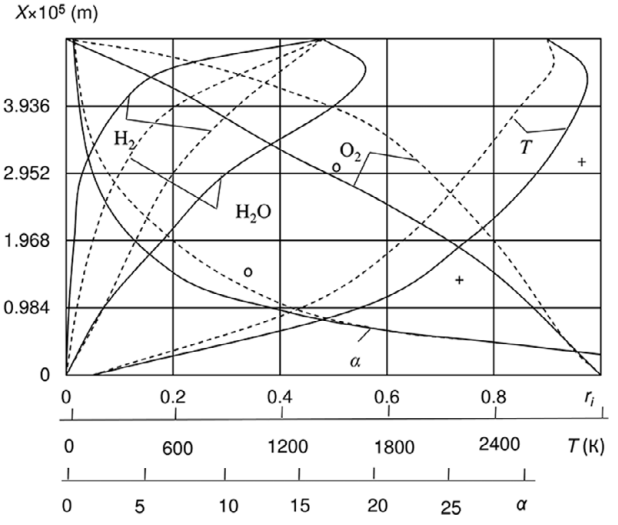

Figure 5.5 Oxygen droplet evaporation in $O_2 + H_2$ combustion products ($W_\infty = 0.002$ m/s, $p_\infty = 0.5$ MPa): solid line – calculation with allowance for chemical reactions; dotted line – "frozen" calculation; + – equilibrium temperature; o – equilibrium H_2O concentration.

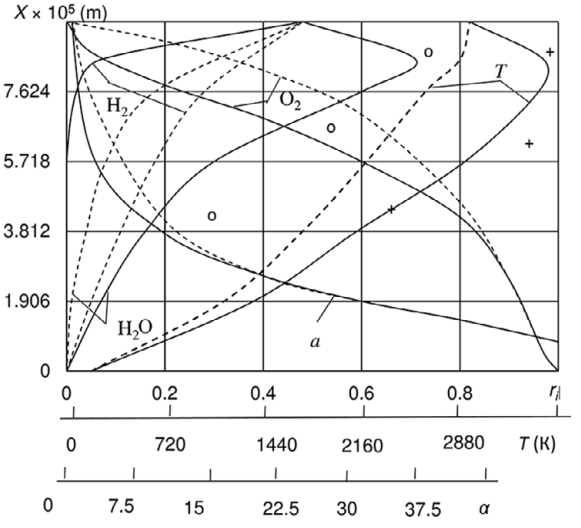

Figure 5.6 Oxygen droplet evaporation in $O_2 + H_2$ combustion products ($W_\infty = 0.002$ m/s, $p_\infty = 5$ MPa): solid line – calculation with allowance for chemical reactions; dotted line – "frozen" calculation; + – equilibrium temperature; o – equilibrium H_2O concentration [226]. From V. I. Naumov and V. Y. Kotov. "Micro-Scale Investigation of Non-Equilibrium Thermo-Fluid Transport during Droplet Evaporation and Combustion," 43rd Aerospace Science Meeting and Exhibit, AIAA 2005–1431, pp. 1–14, Reno, NV, 2005, reprinted by permission of the American Institute of Aeronautics and Astronautics, Inc

Downloaded from https://www.cambridge.org/core. Nottingham Trent University, on 17 Aug 2019 at 02:07:06, subject to the Cambridge Core terms of use, available at https://www.cambridge.org/core/terms. https://doi.org/10.1017/9781108581714.005

Table 5.2 Some results of numerical study of evaporation of dispersed liquid oxygen into oxygen and hydrogen combustion products

Numerical experiment	Parameters: Pressure, p_∞ Velocity, W_∞	Parameters under analysis: Boundary layer (reduced film) thickness δ, m	$max\Delta T_{f-n}$ degrees (%)	$max\ \Delta T^{st}_{f-n}$ degrees (%)	$min\ \Delta T_{e-n}$ degrees (%)
1	p_∞ = 0.5 MPa W_∞ = 20 m/s	1.85×10^{-5}	55 (2.8)	0 (0)	460 (19)
2	p_∞ = 0.5 MPa W_∞ = 0.002 m/s	4.92×10^{-5}	384 (15.3)	175 (5,9)	195 (7)
3	p_∞ = 5 MPa W_∞ = 0.002 m/s	9.53×10^{-5}	763 (23.7)	640 (18.2)	98 (3)

with equivalence ratio $\alpha_{ox} = 0.5$ for the following values of temperature (T_∞), pressure (p_∞) and flow velocity of the external flow (W_∞):

T_∞= 2821 K, p_∞= 0.5 MPa, W_∞= 20 m/s;
T_∞= 2821 K, p_∞= 0.5 MPa, W_∞= 0.002 m/s;
T_∞= 2929 K, p_∞= 5.0 MPa, W_∞= 0.002 m/s.

Chemical mechanism listed in Table 5.1 was used for the calculations. The magnitudes of analyzed parameters are given in Table 5.2.

The analysis of temperature and chemical composition variations of some gas-phase reaction products in the boundary layer (Figures 5.4–5.6) confirms the assumption of significant influence of chemical reactions on parameters of the vapor–gas mixture in the boundary layer. This is observed in the cases when the residence time of vapors and reactants in the boundary layer is comparable to the time of chemical reactions proceeding, which is typical for low velocity of external flow and comparatively small droplet diameters (numerical experiments 2 and 3, Table 5.2). This influence is demonstrated by a notable difference between "frozen" and nonequilibrium temperatures and concentration of evaporation and reaction products in numerical experiments 2 and 3, whereas the difference observed in numerical experiment 1 is less significant. This is also confirmed by the absence of a mixture temperature maximum in numerical experiment 1 (Figure 5.4) and its presence in numerical experiments 2 and 3 (Figures 5.5 and 5.6).

The maximum temperature difference in calculations for "frozen" and nonequilibrium models is reached in numerical experiment 1, approximately in the midplane region of the boundary layer (Figure 5.4), while in the other experiments, the mixture temperature difference was observed in the area of stoichiometric composition of the reaction products (wherein equivalence ratio α_{ox} approaches unity).

The maximum concentration of main reaction product H_2O corresponds also to the temperature maximum in numerical experiments 2 and 3 (Figures 5.5 and 5.6), which, in its turn, complies with the mixture's stoichiometric state.

Downloaded from https://www.cambridge.org/core. Nottingham Trent University, on 17 Aug 2019 at 02:07:06, subject to the Cambridge Core terms of use, available at https://www.cambridge.org/core/terms. https://doi.org/10.1017/9781108581714.005

The temperature maximum in numerical experiments 2 and 3 practically corresponds to its equilibrium values (Figures 5.5 and 5.6), whereas the temperature in the areas with an equivalence ratio larger than unity is somewhat smaller than that for equilibrium values resulting from finite reaction rates. Just the same may be told about both equilibrium and nonequillibrium concentrations of H_2O. It should be noted that the equivalence ratio varies in a very wide range – that is, from its maximum values of the equivalence ratio ($\alpha_{ox} = 30 - 35$) in the in the vicinity of the droplet surface to its minimum at the outer edge of the boundary layer.

With the increase in the boundary layer thickness, the temperature maximum and the maximum concentration of H_2O in the area of stoichiometric composition (α = 1) becomes more vivid (Figures 5.5 and 5.6), whereas the mixture temperature difference in calculation by the equilibrium and nonequillibrium model ($\min \Delta T^{st}_{f-n}$) attains the minimum value.

As seen from Figures 5.5 and 5.6, the pressure's influence on the mixture parameters is practically imperceptible, while the increase in pressure increases only the rates of chemical reactions and shifts the processes toward the equilibrium (which is obvious, for example, from comparison of equilibrium and nonequilibrium temperatures in Figures 5.5 and 5.6). Such behavior complies completely with the concepts of chemical kinetics.

b Evaporation of Dispersed Nitrogen Tetroxide into Nitrogen Tetroxide and Unsymmetrical Dimethylhydrazine Combustion Products

Analysis similar to above described one was accomplished in simulation of nitrogen tetroxide (N_2O) droplet with the diameter of 0.2×10^{-3} m in the products of gas generation "NT+UDMG" $[N_2O_4+H_2N_2(CH3)2]_G$ with equivalence ratio $\alpha_{ox} = 1.5$ at p = 25 MPa and T = 3257 K. These conditions are typical for the evaporation of the droplets of ballasting oxidizer (or fuel) in the secondary zone (ballasting zone) of LPRE two-component gas generators producing gas with considerable excess of oxidizer (or fuel; see Chapter 7) wherein combustion products temperature substantially decreases while the equivalence ratio rises when ballasting with an oxider (or lowers when ballasting with a fuel) substantially as used for the pressurization of LPRE oxidizer and fuel tanks (see Chapter 8) or for generating low-temperature combustion products powering turbines of LPRE turbopumps [160, 215, 227, 228].

The kinetic mechanism given in Table 5.1 was used in calculations with allowance for preliminary NT thermal decomposition by the following scheme:

$$N_2O_4 = 2NO_2; \tag{5.22}$$

$$2NO_2 = 2NO + O_2. \tag{5.23}$$

Results of the analysis are shown in Table 5.4 and in Figures 5.7a, 5.7b, 5.8a, and 5.8b. It follows from the previously described data that, in terms of quality, the pattern of processes in the boundary layer complies with the results of previous research.

Downloaded from https://www.cambridge.org/core. Nottingham Trent University, on 17 Aug 2019 at 02:07:06, subject to the Cambridge Core terms of use, available at https://www.cambridge.org/core/terms. https://doi.org/10.1017/9781108581714.005

Table 5.3 Chemical mechanism

Chemical reaction	Chemical reaction
$CO + OH \leftrightarrows CO_2 + H$	$N + N + M \leftrightarrows N_2 + M$
$N + CO_2 \leftrightarrows NO + CO$	$NO + HO_2 \leftrightarrows NO_2 + OH$
$CO + O + M \leftrightarrows CO_2 + M$	$NO + O + M \leftrightarrows NO_2 + M$
$NO_2 + CO \leftrightarrows NO + CO_2$	$NO_2 + H \leftrightarrows NO + OH$
$O + N_2 \leftrightarrows NO + N$	$NO_2 + O \leftrightarrows NO + O_2$
$NO + O \leftrightarrows N + O_2$	$NO_2 + N \leftrightarrows NO + NO$
$N + OH \leftrightarrows NO + H$	$NO_2 + H_2 \leftrightarrows NO + H_2O$
$NO + NO \leftrightarrows N_2 + O_2$	$N_2O + M \leftrightarrows N_2 + O + M$
$N_2O + O \leftrightarrows NO + NO$	$N_2O + H \leftrightarrows N_2 + OH$
$N + O + M \leftrightarrows NO + M$	$N_2O + O \leftrightarrows N_2 + O_2$
$NO + N \leftrightarrows N_2 + O$	

Table 5.4 Some results of numerical study of evaporation of dispersed nitrogen tetroxide into nitrogen tetroxide and unsymmetrical dimethylhydrazine combustion products

Numerical experiment	Parameters: Pressure, p_∞ Velocity, W_∞	Parameters under analysis			
		Boundary layer thickness δ, m	max ΔT_{f-n} degrees (%)	max ΔT^{st}_{f-n} degrees (%)	min degrees (%)
1	p = 25 MPa	2.916×10^{-6}	130	0	310
	W_∞ = 50 m/s		(15.3)	(0)	(10)
2	p = 25 MPa	4.018×10^{-5}	350	175	110
	W_∞ = 0.1 m/s		(25)	(5.2)	(4)

A peculiarity of this numerical experiment is that in more than 45% of the "thick" boundary layer relative thickness (numerical experiment 2) and about 65% of the "thin" boundary layer relative thickness (numerical experiment 1) the "frozen" temperature is higher than that of gas mixture obtained in the chemical nonequilibrium calculation. This may be explained by the fact that the N_2O_4 decomposition reaction, violently proceeding near the droplet surface, absorbs the heat:

$$N_2O_4 = 2NO_2 - 56,932 \text{ J}$$

while as the temperature increases, the equilibrium of the other reaction

$$2NO + O_2 = 2NO_2 + 112,525 \text{ J}$$

shifts toward decomposition of NO_2 and the corresponding NO formation, which also is accompanied by the heat absorption.

The described chemical conversions explicate a higher "frozen" temperature than that obtained with allowance for chemical reactions. Values of the aforesaid temperatures agree at the distance of about 2.1×10^{-5} m for "thick" and 1.8×10^{-6} m for "thin" boundary layers from the droplet surface that corresponds to a complete decomposition

Downloaded from https://www.cambridge.org/core. Nottingham Trent University, on 17 Aug 2019 at 02:07:06, subject to the Cambridge Core terms of use, available at https://www.cambridge.org/core/terms. https://doi.org/10.1017/9781108581714.005

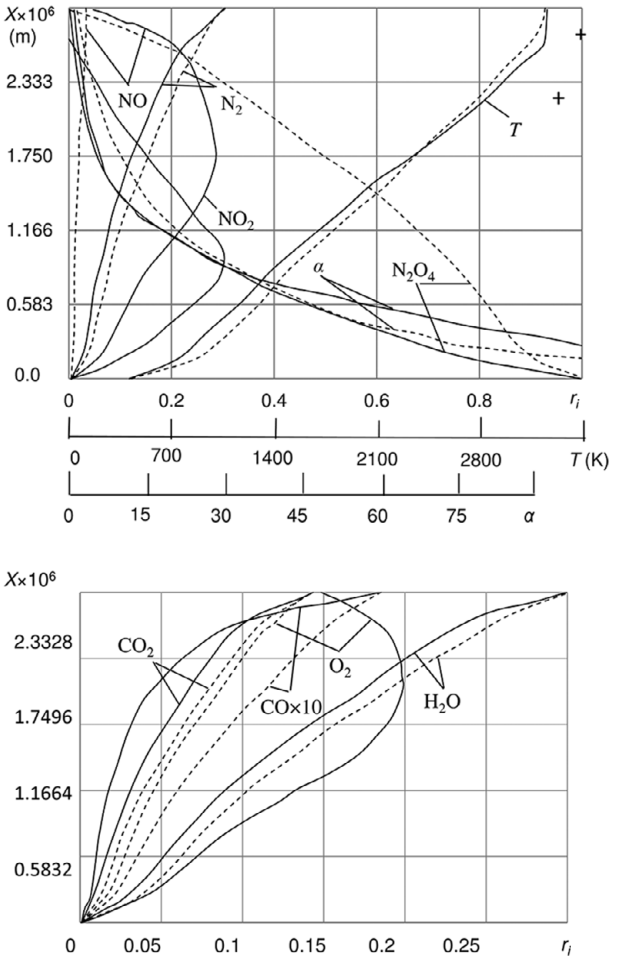

Figure 5.7 a, b NT droplet evaporation into NT+UDMH combustion products (W_∞ = 50 m/s, d_D = 0.2×10^{-3} m): solid line – calculation with allowance for chemical reactions; dotted line – "frozen" calculation; + – equilibrium temperature.

of N_2O_4 in calculations with allowance for chemical reactions (Figures 5.7 and 5.8). Subsequent higher temperatures of the reactive mixture obtained from the calculation with allowance for chemical reactions arise from the total positive thermal effect of the reactions listed in Table 5.3.

c Evaporation of Dispersed Liquid Ammonia into Oxygen and Ammonia Combustion Products

Figures 5.9 and 5.10 and Table 5.5 show the results of the analysis of evaporation of ammonia (NH_3) droplets, 0.3×10^{-3} m in diameter into oxygen and ammonia $[O_2+NH_3]_G$ combustion products with equivalence ratio $\alpha_{ox} = 1.87$ at p = 5 MPa and

Downloaded from https://www.cambridge.org/core. Nottingham Trent University, on 17 Aug 2019 at 02:07:06, subject to the Cambridge Core terms of use, available at https://www.cambridge.org/core/terms. https://doi.org/10.1017/9781108581714.005

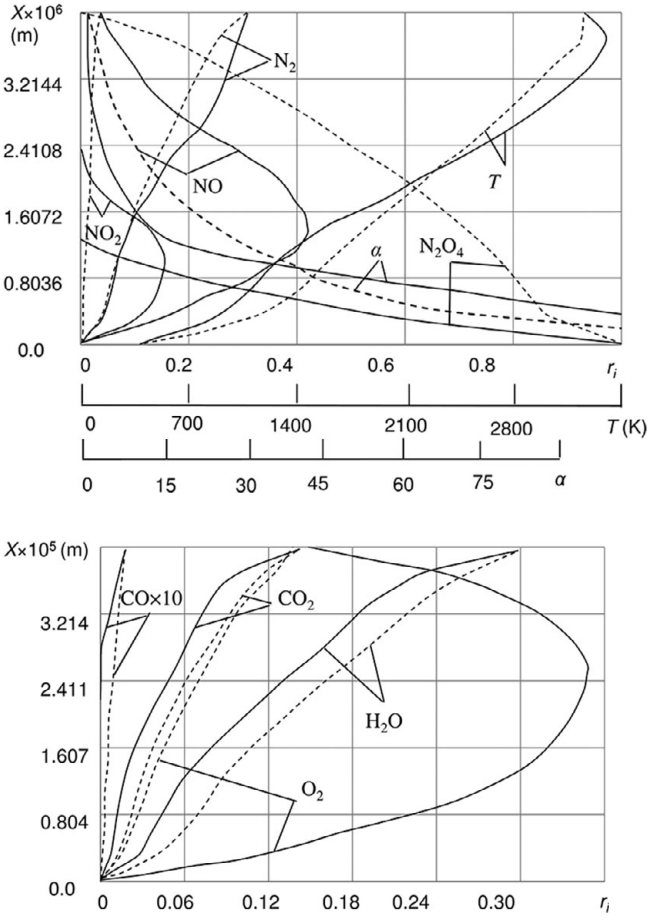

Figure 5.8 a, b NT droplet evaporation into NT + UDMH combustion products ($W_\infty = 0.1$ m/s, $d_D = 0.2 \times 10^{-3}$ m): solid line – calculation with allowance for chemical reactions; dotted line – "frozen" calculation.

$T = 2658$ K at various external flow velocities W_∞. These conditions are typical for the evaporation of the droplets of ballasting fuel in the secondary zone (ballasting zone) of gas generators [160, 215, 227, 228]. The chemical mechanism was formed on the basis of the mechanisms given in Tables 5.1 and 5.3 (except for the reactions involving carbon-bearing molecules) and additional reactions in Table 5.6.

Despite the satisfactory agreement of obtained results and equilibrium values in the region of stoichiometric composition of reacting mixture, a relatively big difference in these values compared with previous calculations should be underlined. This probably testifies to the boundary layer thickness's insufficiency for completion of chemical reactions and reaching chemical equilibrium. This is confirmed by nonequilibrium calculation results approaching equilibrium temperature at the increase in boundary layer thickness.

Downloaded from https://www.cambridge.org/core. Nottingham Trent University, on 17 Aug 2019 at 02:07:06, subject to the Cambridge Core terms of use, available at https://www.cambridge.org/core/terms. https://doi.org/10.1017/9781108581714.005

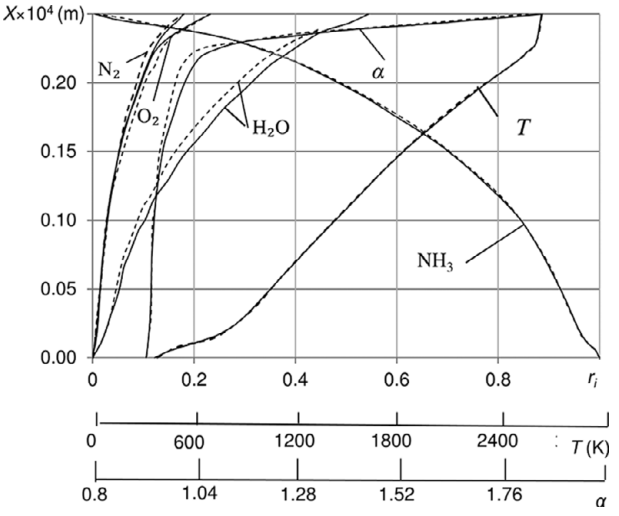

Figure 5.9 Evaporation of ammonia NH_3 droplet into combustion products $NH_3 + O_2$ (W_∞ = 10 m/s, $d_D = 0.3 \times 10^{-3}$ m): solid line – calculation with allowance for chemical reactions; dotted line – "frozen" calculation.

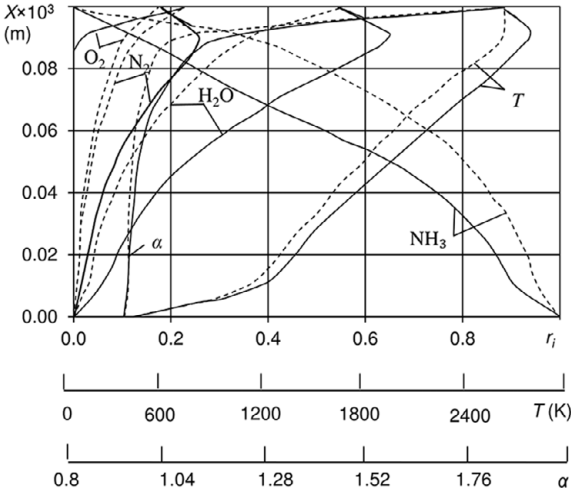

Figure 5.10 Evaporation of ammonia NH_3 droplet into combustion products $NH_3 + O_2$ ($W_\infty = 0.1$ m/s, $d_D = 0.3 \times 10^{-3}$ m): solid line – calculation with allowance for chemical reactions; dotted line – "frozen" calculation.

An analysis of the cited results of the application of equilibrium, nonequilibrium, and "frozen" approaches to different propellant compositions allows us to make the following conclusions:

1. An adequate estimation of parameters of vapor–gas mixtures such as reacting mixtures chemical composition, vapor flow rate, distribution of temperatures, heat

Downloaded from https://www.cambridge.org/core. Nottingham Trent University, on 17 Aug 2019 at 02:07:06, subject to the Cambridge Core terms of use, available at https://www.cambridge.org/core/terms. https://doi.org/10.1017/9781108581714.005

Table 5.5 Some results of numerical study of evaporation of dispersed liquid ammonia into oxygen and ammonia combustion products

Numerical experiment	Parameters: Pressure p_∞ Velocity W_∞	Parameters under analysis: Boundary layer thickness δ, m	max ΔT_{f-n} degrees (%)	max ΔT^{st}_{f-n} degrees (%)	min ΔT_{e-n} degrees (%)
1	p = 5 MPa	0.2516×10^{-4}	24	0	480
	W_∞ = 10 m/s		(1.5)	(0)	(20)
2	p = 5 MPa	0.1002×10^{-3}	253	253	215
	W_∞ = 0.1 m/s		(8.7)	(8.7)	(8)

Table 5.6 Additional reactions

Chemical reaction	Chemical reaction
$NH + OH \leftrightarrows H_2O + N$	$2NH_3 \leftrightarrows 2NH_2 + H_2$
$2NO + O_2 \leftrightarrows 2NO_2$	$NH + NH_3 \leftrightarrows 2NH_2$
$H + NH_3 \leftrightarrows NH_2 + H_2$	$NH + NH \leftrightarrows N_2 + H_2$
$NH_3 + O \leftrightarrows NH_2 + OH$	$NH_2 + O \leftrightarrows NH + OH$

flows, etc., in boundary layer often requires allowing for kinetics of chemical reactions. It follows that, for example, the generally adopted assumption that for the study of the interaction and combustion of $H_2 + O_2$ at close to stoichiometry equivalence ratios, it is always possible to use chemical equilibrium models, is not always valid for analysis of processes at the microlevel. Thus, if the relative velocity of evaporating droplets is high at their small diameters, the calculation of evaporation by the chemical equilibrium model may bring about inadequate results.

2. The total positive thermal effect of chemical reactions significantly intensifies the heat exchange processes in the boundary layer, which is confirmed by the data on vapor flow rate from the droplet surface and values of convective mass flow rates over the boundary layer thicknes, obtained in aforementioned calculations with due allowance for chemical reactions and with the assumption of "frozen" chemical composition (Figures 5.11 and 5.12).

Thus, for example, at oxygen droplet evaporation in $O_2 + H_2$ combustion products at p_∞ = 0.5 MPa and W_∞ = 0.002 m/s (Figure 5.12) calculated with allowance for chemical reactions, the analyzed parameters increase as compared with "frozen" calculation:

– heat flux in the boundary layer: 16%–19%
– convective mass flux in the boundary layer: 20%–25%

Comparing data with similar data for p_∞ = 0.5 MPa and W_∞ = 20 m/s (Figure 5.11) shows that, in the latter case, the difference between "frozen" and equilibrium results is

Downloaded from https://www.cambridge.org/core. Nottingham Trent University, on 17 Aug 2019 at 02:07:06, subject to the Cambridge Core terms of use, available at https://www.cambridge.org/core/terms. https://doi.org/10.1017/9781108581714.005

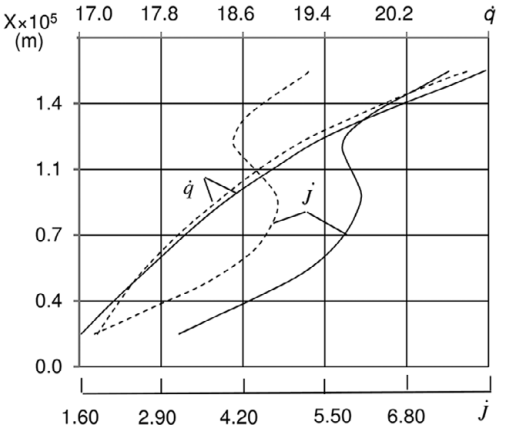

Figure 5.11 Variation of heat flux $\dot{q}$(kJ/m^2×s) and mass flux $\dot{J}$ (kg/m^2×s) at O_2 droplet evaporation into combustion products $O_2 + H_2$ (W_∞ = 20 m/s, p_∞ = 0.5 MPa): solid line – calculation with allowance for chemical reactions; dotted line – "frozen" calculation.

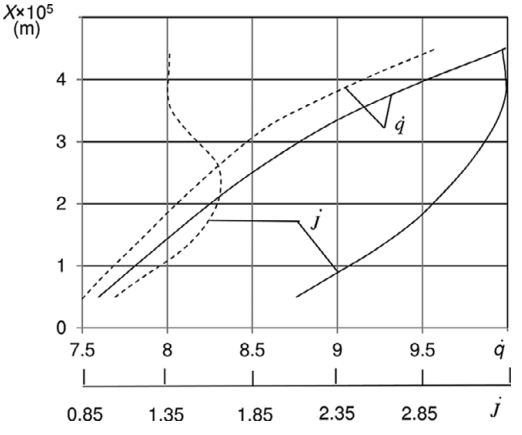

Figure 5.12 Variation of heat flux $\dot{q}$ (kJ/m^2×s) and mass flux $\dot{J}$ (kg/m^2×s) at O_2 droplet evaporation into combustion products $O_2 + H_2$ (W_∞ = 0.002 m/s, p_∞ = 0.5 MPa): solid line – calculation with allowance for chemical reactions; dotted line – "frozen" calculation.

less significant. This may be explained by the notably smaller boundary layer thickness at higher velocities of external flow and, hence, shorter residence time of vapors in the boundary layer, when this time is insufficient for full completion of chemical reactions. Thus, this underlines once more the fact that the application of "frozen" models that are often used in analysis of evaporation can lead to inadequate results at simulating the processes in "thick" boundary layers at low velocities of external flow and with large-diameters odroplets. And, on the contrary, at high velocities of external flow and small diameters of droplets (when boundary layers feature small thickness), "frozen" models can result in sufficiently adequate data.

Downloaded from https://www.cambridge.org/core. Nottingham Trent University, on 17 Aug 2019 at 02:07:06, subject to the Cambridge Core terms of use, available at https://www.cambridge.org/core/terms. https://doi.org/10.1017/9781108581714.005

Proceeding from the analysis of results obtained from numerical experiments for different propellants, it is possible to formulate the following practical recommendations on the application of equilibrium, frozen, and nonequilibrium models to the simulation of processes in boundary layers at interaction of dispersed propellant with external flow.

1. For thin boundary layers forming at high velocities of external flow and small sizes of droplets of dispersed propellant, or, given the absence of valid chemical mechanisms, it is possible to use the "frozen" model and, hence, assume the escape of pure vapors from boundary layer outer edge into external flow.
2. For extremely thick boundary layers forming at low velocities of external flow and comparatively large droplets of dispersed propellant and given a high reaction rates, it is possible to use the equilibrium model. Hence, chemical composition of mixture escaping boundary layer can be considered as equilibrium composition.
3. In the case of boundary layers of notably larger thickness compared with thin boundary layers but insufficient for completion of the basic chemical reactions, to obtain the adequate results, it is required to employ chemically nonequilibrium models to estimate the properties and chemical composition of reacting mixture escaping boundary layer. Otherwise, the error of simulation of parameters may be significant; in the cited examples, it is 15%–35%.
4. In case it is impossible to preliminarily evaluate the influence of the combination of boundary layer thickness, droplet diameters, and reaction mechanisms on the process occurrence intensity, it is more appropriate to use chemically nonequilibrium models of better versatility that can allow one to obtain the adequate results in the entire range of chemical composition variation – from "frozen" to equilibrium.

5.5.2 Study of Propellant Decomposition in Boundary Layer

In the analysis of dispersed propellant combustion in high-temperature chemically active gas flows, the chemical interaction of the reactants in inter-droplet space is usually considered. Here it is usually assumed that either an absence of decomposition of stable propellant components with subsequent vapors getting in the flow or a complete decomposition of chemically unstable propellant components in the boundary layer and getting products of decomposition in the flow. However, as shown in Subsection 5.5.1, more accurate models should include the analysis of evaporation products' chemical conversion within the boundary layer around the droplet. This necessitates the application of models allowing residence time of evaporation products in boundary layer and finite chemical reaction rates.

A typical example of readily decomposing oxidizer is NT. In the calculation of its evaporation, it is traditionally considered that the products of its complete decomposition escape from evaporation surface into working volume, namely nitrogen dioxide (NO_2).

Figure 5.13 shows the results of calculation of evaporation of N_2O_4 droplets of 2×10^{-4} m diameter in the secondary zone of a two-component (NT + UDMH) gas

Downloaded from https://www.cambridge.org/core. Nottingham Trent University, on 17 Aug 2019 at 02:07:06, subject to the Cambridge Core terms of use, available at https://www.cambridge.org/core/terms. https://doi.org/10.1017/9781108581714.005

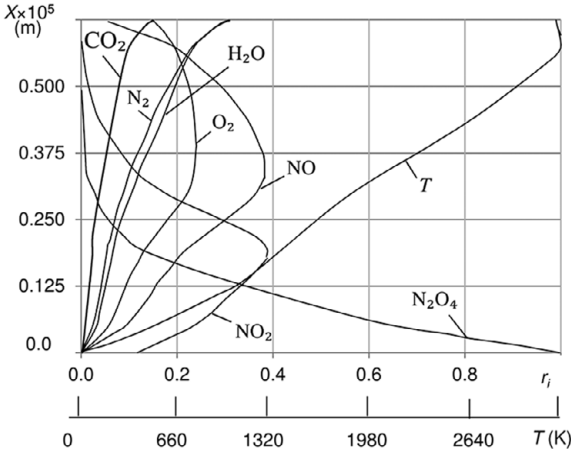

Figure 5.13 Variation of temperature T and concentrations of N_2, NO, NO_2, N_2O_4, O_2, H_2O, CO_2 at NT droplet evaporation into NT + UDMH combustion products ($d_D = 2.0 \times 10^{-4}$ m).

generator, producing gas with excess of oxidizer at the pressure in combustion chamber of 2.5 MPa and combustion products temperature $T = 3257$ K, performed with the help of model described in Sections 5.2 and 5.3.

The diagrams of variation of the main individual substances concentrations shown in Figure 5.13 indicate that decomposition of N_2O_4 vapors getting from the droplet surface occurs, in fact, completely within 60% of the boundary layer simulated by reduced film. Main products of N_2O_4 decomposition in the in the vicinity of droplet surface are NO_2, NO, and O_2. Decomposition of NT proceeds by the mechanism of reactions (5.22) and (5.23) with prevalence of reaction $N_2O_4 \leftrightarrows 2NO_2$, which causes a dramatic increase in NO_2 concentration. At increase in temperature at advance from droplet surface to external surface of reduced film ($T > 1300$ K), a decrease in concentration NO_2 is observed related with increase in the rate of the reaction $2NO_2 \leftrightarrows 2NO + O_2$ forward direction, which is indicated not only by NO concentration maximum at $T \approx 2000$ K, but the O_2 concentration maximum as well.

The variation of vapor–gas mixture composition in upper region of the boundary layer at temperatures higher than 2500 K is influenced by other reactions of chemical mechanism (see Tables 5.1 and 5.3) as well as diffusion between the boundary layer and external flow. Thus, the results of the calculation confirm the data on practically complete decomposition of N_2O_4 at evaporation within the boundary layer, but at the same time, they display that NO_2 is not the stable and sole end product of decomposition fed to the working medium. Influence of kinetics of chemical reactions and diffusion result in that working volume receives about 20% of NO, 22% of N_2, 22% of H_2O, 10% of CO_2, 20% of O_2, and lower concentrations of other individual substances. For analysis of the influence of droplet diameter – hence, boundary layer thickness on the rate of N_2O_4 decomposition – the study of evaporation of N_2O_4 droplets that range from 1.0×10^{-5} m to 1.0×10^{-2} m in diameter was performed at the same values of pressures and temperatures of external flow. Results of calculations made for various

Downloaded from https://www.cambridge.org/core. Nottingham Trent University, on 17 Aug 2019 at 02:07:06, subject to the Cambridge Core terms of use, available at https://www.cambridge.org/core/terms. https://doi.org/10.1017/9781108581714.005

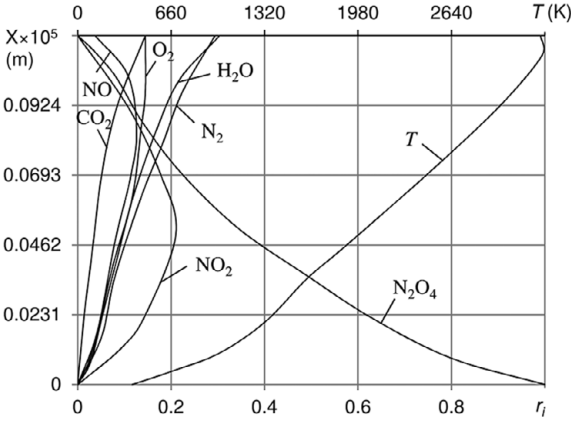

Figure 5.14 Variation of temperature T and concentrations of N_2, NO, NO_2, N_2O_4, O_2, H_2O, CO_2 at NT droplet evaporation into NT + UDMH combustion products ($d_D = 1.0 \times 10^{-5}$ m).

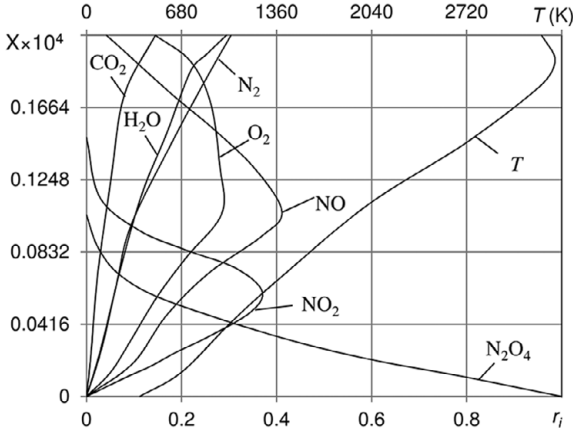

Figure 5.15 Variation of temperature T and concentrations of N_2, NO, NO_2, N_2O_4, O_2, H_2O, CO_2 at NT droplet evaporation into NT + UDMH combustion products ($d_D = 2.0 \times 10^{-3}$ m).

thicknesses of the boundary layer shown in Figures 5.13–5.16 indicate the increase in degree of N_2O_4 decomposition with increase in droplet diameter. Thus, in the discussed example of calculations, the decomposition of NT at droplet diameter $d_D = 1.0 \times 10^{-2}$ is completed at the distance from droplet surface making not more than 30% of the boundary layer thickness, while for droplets of notably smaller diameters ($d_D = 1.0 \times 10^{-5}$), the complete decomposition occurred only at the outer edge of boundary layer because of smaller residence time of vapors in the relatively thin boundary layer. A similar trend is observed for NO_2 decomposition. The difference in the rate of N_2O_4 and NO_2 decomposition results in some diversity (not that significant) in chemical composition of reaction products entering external flow that also follows from Figures 5.13–5.16.

Downloaded from https://www.cambridge.org/core. Nottingham Trent University, on 17 Aug 2019 at 02:07:06, subject to the Cambridge Core terms of use, available at https://www.cambridge.org/core/terms. https://doi.org/10.1017/9781108581714.005

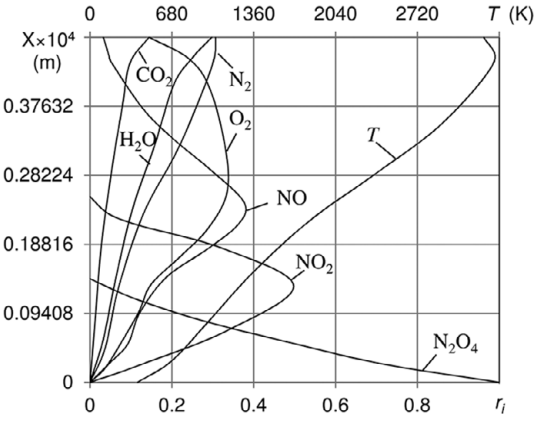

Figure 5.16 Variation of temperature T and concentrations of N_2, NO, NO_2, N_2O_4, O_2, H_2O, CO_2 at NT droplet evaporation into NT + UDMH combustion products ($d_D = 1.0 \times 10^{-2}$ m).

The results of numerical experiments confirm the correctness of the generally adopted model of N_2O_4 complete decomposition in the entire range of droplet diameter variation and the corresponding boundary layer thickness range, displaying the difference in decomposition rates only. At the same time, by the moment of reaction products' escape from boundary layer, NO_2 complete decomposition does not occur even in the case of evaporation of droplets of large diameters. Besides, calculations display a large number of the other reaction products getting into the flow – that is, NO, N_2, O_2. Data of numerical experiments allow, assuming in simulation of N_2O_4 evaporation into high-temperature gas flow, irrespective of droplets dispersion, a complete N_2O_4 decomposition, but with respect to prediction of detailed chemical composition of reaction products, it is recommended to apply a detailed kinetic mechanism (not only reactions of N_2O_4 and NO_2 decomposition) to avoid errors in prediction of composition and properties of evaporation and reacting products entering external gas flow.

A substantially different pattern of chemical interaction is brought about by simulation of N_2O_4 decomposition at its evaporation into low-temperature oxidizing medium ($T = 550$ K), typical, for example, for LPRE tank pressurization (LPRE propellant tank pressurization processes as well as their simulation are described in detail in Chapter 9). Calculations presented below are also made with the help of model described in Sections 5.2 and 5.3.

Figure 5.17 shows the results of calculation of evaporation of NT stored in the LPRE tank, from the NT surface into ullage (gas space) of propellant tank at its pressurization by high-temperature oxidizer-reach (NT+ UDMH) gas generator products at the following parameters of the gas mixture in the ullage: $p = 0.3$ MPa, $T = 550$ K. The purpose of the pressurization system is to control the gas pressure in the ullage. The pressurization system is designed to maintain this ullage at preselected pressure history bounded by propellant feed system requirements and tank structural requirements. The low temperature of the gas mixture in ullage and, hence, low rates of N_2O_4 and NO_2 decomposition make evaporation and chemical interaction in the boundary

Downloaded from https://www.cambridge.org/core. Nottingham Trent University, on 17 Aug 2019 at 02:07:06, subject to the Cambridge Core terms of use, available at https://www.cambridge.org/core/terms. https://doi.org/10.1017/9781108581714.005

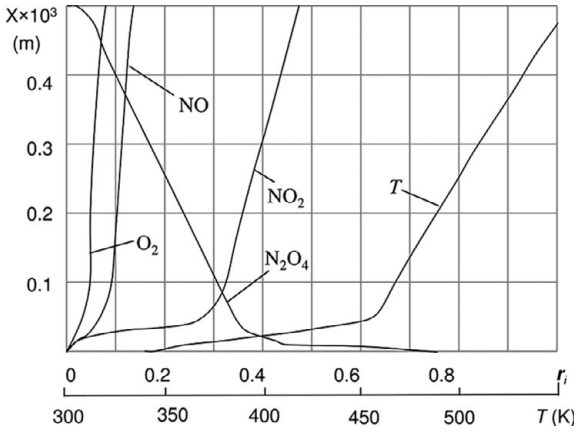

Figure 5.17 Variation of temperature T and concentrations of NO, NO_2, N_2O_4, and O_2 over the thickness of boundary layer at NT evaporation into the ullage of LPRE tank.

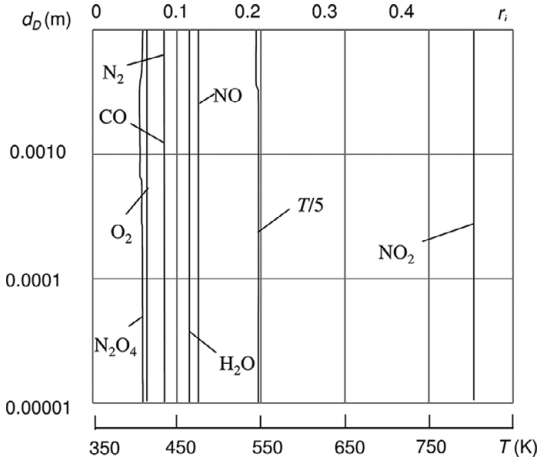

Figure 5.18 Temperature and chemical composition of reaction products at the outer edge of boundary layer at NT evaporation into the ullage of LPRE tank.

layer different from the previously discussed N_2O_4 droplet evaporation in the high-temperature flow in the secondary zone of gas generator.

Figure 5.18 shows chemical composition and temperature of the products of evaporation and reaction at outer edge of boundary layers of different thicknesses. The thickness of the boundary layer above the flat surface of NT is formally reduced here to some conditional droplet diameter to simplify the comparison with calculation results for N_2O_4 droplet evaporation.

As shown in Figure 5.18, the N_2O_4 concentration at the outer edge of the boundary layer of any thickness does not drop below 0.06 for any thickness of the boundary layer. Temperature and concentrations of all substances at the outer edge of boundary layers of

Downloaded from https://www.cambridge.org/core. Nottingham Trent University, on 17 Aug 2019 at 02:07:06, subject to the Cambridge Core terms of use, available at https://www.cambridge.org/core/terms. https://doi.org/10.1017/9781108581714.005

different thickness remain practically invariable, the difference in values being lower than 0.1%. The quantitative composition of substances at the outer surface mainly depends on kinetics of chemical reactions (5.1) and (5.2).

Therefore, at comparatively low temperatures in working volumes of some units of propulsion and power generation systems (for example, LPRE propellant tanks), the assumption of conversion of N_2O_4 into NO_2 in the boundary layer and NO_2 entering the working volume is quite permissible at performing of calculations. Thus, at analyzing the N_2O_4 droplet evaporation into a working medium it is necessary to perform preliminary calculations with application of the developed model of processes in reacting boundary layer to get the valid data on chemical composition and thermodynamic parameters of reaction products escaping boundary layer.

5.5.3 Gas Generator Performance Control by Varying Propellant Dispersion

Prediction of combustion products temperature is one of the main problems of the analysis and optimization of working processes in LPRE units (for example, in combustion chambers of gas generators). Processes occurring in LPRE gas generators, their simulation and optimization are disclosed in Chapter 8. Auxiliary power units, which employ chemical energy of liquid propellant, produce the working medium – generator gas, which is either directly applied to the pressurized propellant-feed systems or enters turbine – which drives the necessary units such as pumps of fuel and oxidizer. The distinction among the processes in gas generators and combustion chambers of LPRE is determined by the need to generate a working medium at relatively low temperature, not exceeding the maximum permissible temperature for the material of the turbine blades or material of walls of propellant tanks. In comparison with temperature upper limit, the lower limit is often determined by minimum permissible values of generator gas efficiency.

One of the most efficient methods of control over gas mixture temperature consists in varying the equivalence ratio α_{ox}, which allows generation of gas with both excess of oxidizer and excess of fuel that dramatically reduce the temperature of combustion products. However, such approach may not be always implemented in practice. For example, at chemical pressurization of fuel tanks (see Chapter 9), varying the value of equivalence ratio is permitted within certain limits only. The aforementioned results of analyses allow assuming, but indirectly, the possibility of control over temperature of vapor–gas mixture escaping boundary layer by adjusting the dispersion of fuel or oxidizer droplets at invariable initial ratios of fuel and oxidizer – i.e., invariable equivalence ratios. To verify this hypothesis, the model and mathematical tool described in Sections 5.2–5.3 was used.

a Evaporation of Ammonia Droplets into Combustion Products of Oxygen and Ammonia

Analysis of variation of working medium temperature for fuel-rich two-component $[(O_2+NH_3)_G + NH_{3L}]$ gas generator operating by two-stage fuel feed diagram (see

Downloaded from https://www.cambridge.org/core. Nottingham Trent University, on 17 Aug 2019 at 02:07:06, subject to the Cambridge Core terms of use, available at https://www.cambridge.org/core/terms. https://doi.org/10.1017/9781108581714.005

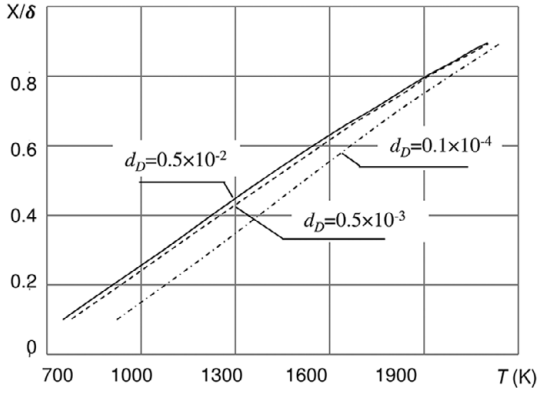

Figure 5.19 Temperature variation over boundary layer relative thickness at evaporation of NH_3 droplets of various dispersion into combustion products of (NH_3 + O_2) [226]. From V. I. Naumov and V. Y. Kotov. "Micro-Scale Investigation of Non-Equilibrium Thermo-Fluid Transport during Droplet Evaporation and Combustion," 43rd Aerospace Science Meeting and Exhibit, AIAA 2005–1431, pp. 1–14, Reno, NV, 2005, reprinted by permission of the American Institute of Aeronautics and Astronautics, Inc

Chapter 8) was performed. The dispersed ammonia NH_{3L} necessary for the lowering of combustion products temperature was injected in the secondary zone of gas generator into the products of (O_2 + NH_3) combustion producing in so-called first zone.

Ammonia dissociation is known to require high energy consumption. As the diameter of droplets increases, the thickness of boundary layer increases. As a consequence, residence time of NH_3 vapors in the boundary layer lengthens, which under certain conditions can cause a more complete decomposition of NH_3. Therefore, it must result in the increase in energy consumption for dissociation and, hence, in some decrease in gas mixture temperature at the boundary layer's outer edge.

To confirm this hypothesis, evaporation of NH_3 droplets in diameter of 0.1×10^{-4} m, 0.5×10^{-3} m, and 0.5×10^{-2} m into (O_2 + NH_3) combustion products with equivalence ratio $\alpha_{ox} = 0.6$ at p = 5 MPa and T = 2168 K was calculated that featured chemically equilibrium composition, which is typical for the first zone of gas generator.

Chemical interaction of vapors of NH_3 with combustion products (O_2 + NH_3) in the boundary layer was simulated with the application of kinetic mechanisms listed in Tables 5.1, 5.3 (except for the reactions involving carbon-bearing molecules), and Table 5.6. The results given in Figure 5.19 illustrate a principal possibility of increasing the temperature by decreasing the NH_3 droplet diameter and, on the contrary, decreasing the temperature by increasing the NH_3 droplet diameter.

The maximum difference in temperature of reacting products coming from the boundary layer outer edge reaches 50 K for the initial data adopted for calculations.

As droplet diameter decreases, temperature and NH_3 concentration increase, which decreases the concentration of the products of its decomposition – i.e., N_2 and H_2 (Figure 5.19). This explains the cause of temperature raise and confirms the correctness of theoretical premises, whereon this calculation experiment was based.

As droplet diameter decreases, not only do the reacting products temperature increases, Reduction of droplet diameter causes not only the combustion products'

Downloaded from https://www.cambridge.org/core. Nottingham Trent University, on 17 Aug 2019 at 02:07:06, subject to the Cambridge Core terms of use, available at https://www.cambridge.org/core/terms. https://doi.org/10.1017/9781108581714.005

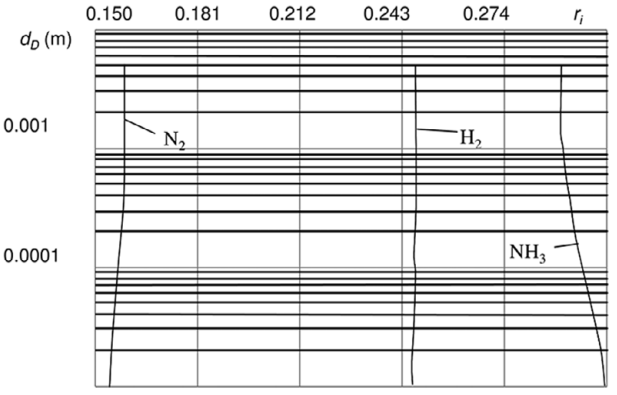

Figure 5.20 Variation of NH_3, N_2, and H_2 concentrations at the outer edge of boundary layer subject to NH_3 droplet diameter [226]. From V. I. Naumov and V. Y. Kotov. "Micro-Scale Investigation of Non-Equilibrium Thermo-Fluid Transport during Droplet Evaporation and Combustion," 43rd Aerospace Science Meeting and Exhibit, AIAA 2005–1431, pp. 1–14, Reno, NV, 2005, reprinted by permission of the American Institute of Aeronautics and Astronautics, Inc

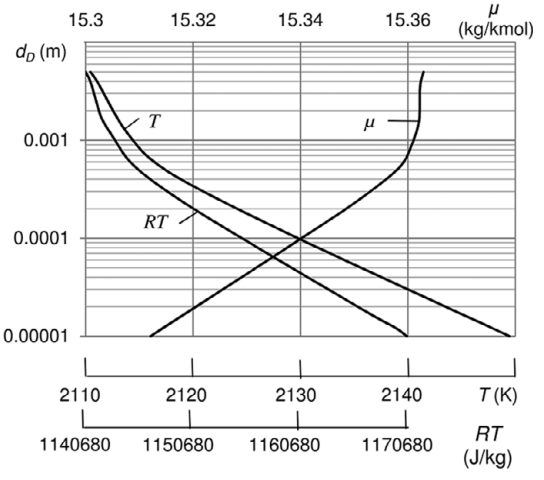

Figure 5.21 Variation of working parameters of reacting mixture at the outer edge of boundary layer subject to NH_3 droplet diameter [226]. From V. I. Naumov and V. Y. Kotov. "Micro-scale Investigation of Non-Equilibrium Thermo-Fluid Transport During Droplet Evaporation and Combustion," 43rd Aerospace Science Meeting and Exhibit, AIAA 2005–1431, pp. 1–14, Reno, NV, 2005, reprinted by permission of the American Institute of Aeronautics and Astronautics, Inc

temperature to increase but also their molecular mass to decrease, which also stipulates an increase in specific working capacity (RT) – one of the most important parameters of gas generator (Figures 5.20 and 5.21).

Thus, at invariable equivalence ratio, it is possible to increase generator-gas-specific working capacity by increasing the droplet dispersion (finer spray) that causes a simultaneous increase in gas mixture temperature and decrease in its molecular mass, which increase the gas constant R.

Downloaded from https://www.cambridge.org/core. Nottingham Trent University, on 17 Aug 2019 at 02:07:06, subject to the Cambridge Core terms of use, available at https://www.cambridge.org/core/terms. https://doi.org/10.1017/9781108581714.005

b Evaporation of Nitrogen Tetroxide Droplets into Combustion Products of Nitrogen Tetroxide and Unsymmetrical Dimethylhydrazine

The possibility of a similar control over vapor–gas mixture temperature is also confirmedby calculations of evaporation of NT droplets of 0.2×10^{-4} m, 0.2×10^{-3} m, and 0.2×10^{-2} m diameter, injected in the products of $(N_2O_4+H_2N_2(CH_3)_2)$ combustion coming from the first zone of $[(N_2O_4+H_2N_2(CH_3)_2)_G+ N_2O_{4L}]$ gas generator. Nitrogen tetroxide injected in combustion products with equivalence ratio $\alpha_{ox} = 1.5$ at p = 25 MPa and T = 3257 K.

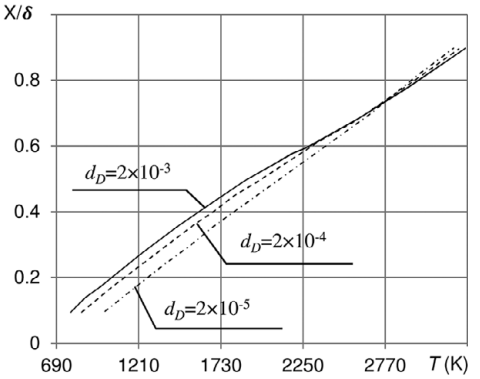

Figure 5.22 Temperature variation over boundary layer relative thickness at evaporation of N_2O_4 droplets of various dispersion into combustion products of $(N_2O_4+H_2N_2(CH_3)_2)$.

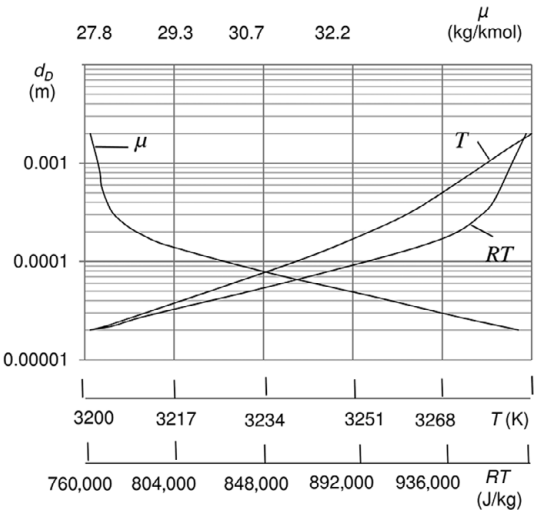

Figure 5.23 Variation of working parameters of reacting mixture at the outer edge of boundary layer subject to N_2O_4 droplet diameter [226]. From V. I. Naumov and V. Y. Kotov. "Micro-Scale Investigation of Non-Equilibrium Thermo-Fluid Transport during Droplet Evaporation and Combustion," 43rd Aerospace Science Meeting and Exhibit, AIAA 2005–1431, pp. 1–14, Reno, NV, 2005, reprinted by permission of the American Institute of Aeronautics and Astronautics, Inc

Downloaded from https://www.cambridge.org/core. Nottingham Trent University, on 17 Aug 2019 at 02:07:06, subject to the Cambridge Core terms of use, available at https://www.cambridge.org/core/terms. https://doi.org/10.1017/9781108581714.005

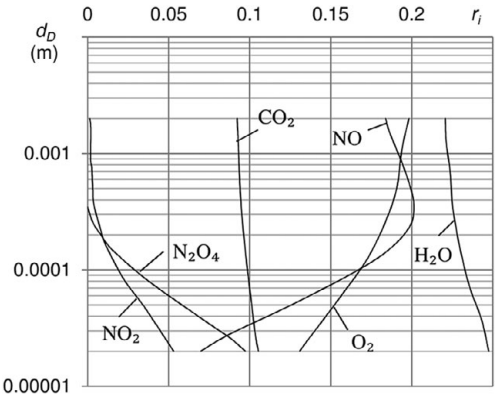

Figure 5.24 Variation of N_2O_4, NO_2, NO, O_2, H_2O, CO_2 concentrations at boundary layer outer edge subject to N_2O_4 droplet diameter [226]. From V. I. Naumov and V. Y. Kotov. "Micro-Scale Investigation of Non-Equilibrium Thermo-Fluid Transport during Droplet Evaporation and Combustion," 43rd Aerospace Science Meeting and Exhibit, AIAA 2005–1431, pp. 1–14, Reno, NV, 2005, reprinted by permission of the American Institute of Aeronautics and Astronautics, Inc

Calculations exploit the kinetic mechanism shown in Table 5.1 and Table 5.3, allowing for preliminary NT decomposition (Reactions 5.22 and 5.23) along with several reactions involving carbon-containing compounds. As follows from Figure 5.22 with the increase of droplet diameter from 0.2×10^{-4} m to 0.2×10^{-2} m, the temperature of the products of decomposition increases by about 80 K. Temperature raise appears to be due to total positive caloric effect of the reactions occurring at evaporation and reacting of N_2O_4 vapors in the boundary layer. The increase in residence time of evaporation and decomposition products in the boundary layer with the increase in droplet diameter facilitates more complete chemical conversions and the emission of greater amount of heat.

The increase in specific working capacity RT (about 30%) of evaporation and reaction products (Figure 5.23) is even more significant. This is mainly explained by the decrease in N_2O_4 and NO_2 concentration (Figure 5.24) – their higher molecular mass, despite a relative low concentration, governing (because the reduction of NT and UDMH concentration) the decrease in total molecular mass of the reacting mixture and increase in gas constant R with increase in droplet diameter (Figure 5.23). The increase in temperature of gas generation products and their gas constant at the increase in droplet diameter causes the rise in the specific working capacity of the products of evaporation and reacting.

Downloaded from https://www.cambridge.org/core. Nottingham Trent University, on 17 Aug 2019 at 02:07:06, subject to the Cambridge Core terms of use, available at https://www.cambridge.org/core/terms. https://doi.org/10.1017/9781108581714.005

6 Models of Droplet Evaporation in Gas Flow

The evaporation of droplets is one of the major stages of the working process that defines the combustion efficiency in the propulsion and power generation systems. Droplets of different sizes moving relative to gas flow and distributed in a complicated manner evaporate in the medium with variable gas dynamic and thermodynamic parameters. The evaporation process is very complicated, which is why whatever actual problem reduces in its theoretical analyses to an approximate model, allowing one to obtain an analytical or numerical solution. For instance, the chemical nonequilibrium model of evaporation of a single-component droplet in high-temperature flow illuminated in Chapter 5 comprises dozens of assumptions. A large number of theoretical and experimental studies are dedicated to the problems of droplets evaporation and combustion.

Historically, mathematical models of combustion of stationary (immovable) droplets of fuel in a gaseous oxidizer environment were developed among the first. These first developments were based on the following governing assumptions: a flame front is formed at a sufficiently large distance from a droplet (Figure 1.6), and chemical transformations are simulated by one or several global reactions [6].

In the working volumes of propulsion systems, the velocities of gas and droplets are different, and a thin boundary layer is formed around each droplet. Under these conditions, a vaporized component enters the boundary layer and, escaping it, burns in a reacting flow.

The first models aimed to calculate the evaporation of droplets of a single-component liquid at pressures lower than the critical pressure of that fluid ($p < p_{cr}$). Such "classic" models (see Section 6.1) are widely used today.

In some types of high-temperature systems, combustion occurs at high pressures ($p > 10$ MPa), while the liquid propellants have small critical pressures. For example, according to [160], methane, oxygen, nitrogen tetroxide, and unsymmetrical dimethylhydrazine have following critical pressures: p_{cr} (CH_4) = 4.5 MPa; p_{cr} (O_2) = 5.05 MPa; p_{cr} (N_2O_4) = 10.1 MPa; p_{cr} ($H_2N_2(CH_3)_2$) = 5.35 MPa. For these conditions, the "classic" model is inadequate. Such conditions require the creation of models of evaporation at high pressures ($p > p_{cr}$) – one of which is presented in Section 6.2.

Another problem to be solved is the use of multicomponent liquid fuels (gasoline, kerosene, fuel oil, etc.). For mathematical modeling of their evaporation, special models of evaporation and heating of multicomponent droplets in a high-temperature gas flow are required. One of them is created by the authors and presented in Section 6.3.

Downloaded from https://www.cambridge.org/core. Nottingham Trent University, on 17 Aug 2019 at 02:08:15, subject to the Cambridge Core terms of use, available at https://www.cambridge.org/core/terms. https://doi.org/10.1017/9781108581714.006

The goal of all three of the previously mentioned models presented in this chapter is to numerically predict the rate of evaporation and the heating rate for a droplet of liquid fuels or oxidizers in a reacting flow. For the solution of these problems, the following governing assumptions have been used:

– The droplet has spherical shape.
– The approximation of the reduced film is valid (see Section 5.1).
– The parameters of external gas flow (T_g, u_g, p_∞) during evaporation of the droplet remain unchanged.

By analogy with the evaporation scheme presented in Chapter 5, the radiant heat transfer, barodiffusion, and thermal diffusion are not taken into account. The other assumptions specific to each evaporation model will be presented in this chapter.

6.1 Classic Model of Droplet Evaporation in Reacting Gase Medium

One of the versions of the classic (regular) model of single-component droplet evaporation was developed in the 1960s [229] and assumed that temperature is uniform over droplet volume but changes with time. The ambient pressure may not be higher than critical pressure of evaporating liquid (p_{cr}).

Chemical reactions do not proceed in the reduced film because of relatively low temperature of the external reacting flow. The evaporation scheme and variation in the parameters along the droplet radius and the thickness of the reduced film are shown in Figure 6.1. The external parameters coincide with parameters on the outer edge of the reduced film (Section 5.1). It is assumed that a droplet already having such a film (δ) is injected in the reacting flow with temperature $T_{d0} \ll T_g$. According to the physical scheme, there are two processes proceeding simultaneously around a droplet (Figure 6.1a):

– flow of evaporated substance with mass flow rate $\dot{m}_V$ through the reduced film
– heat transfer from the environment to the droplet (heat flow $Q(r)$)

In order to reach the ambient temperature, the liquid must first be vaporized with heat consumption $\dot{m}_V L_V$ (see Figure 6.1b) and vapors must be heated up from the temperature T_d to the temperature T_g, which requires the amount of heat $\dot{m}_V c_{pV}\left(T_g - T_d\right)$. This flow is formed under the influence of two factors:

– concentration diffusion due to the difference in partial pressures, $p_{sat} - p_\infty$ (see Figure. 6.1c); and
– Stefan's flow – a convective flow caused by the difference in the densities of the liquid (ρ_{liq}) and the vapor (ρ_V).

Given that ($\rho_{liq} \gg \rho_V$), vapor occupies a larger volume than the evaporated liquid, moves through the reduced film and escapes it, incidentally heating up due to the heat flow Q (r).

Downloaded from https://www.cambridge.org/core. Nottingham Trent University, on 17 Aug 2019 at 02:08:15, subject to the Cambridge Core terms of use, available at https://www.cambridge.org/core/terms. https://doi.org/10.1017/9781108581714.006

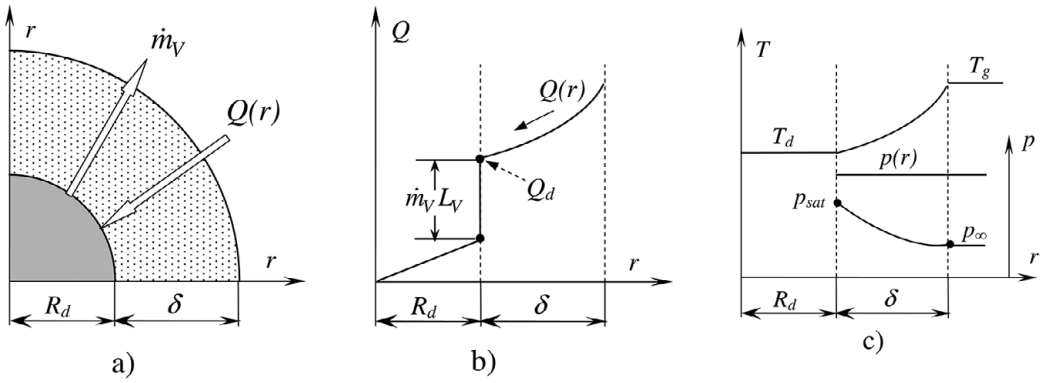

Figure 6.1 Scheme of evaporation of single-component droplet at subcritical pressures: (a) heat and vapor flows in the reduced film; (b) variation of heat flow over the thickness of reduced film and droplet radius; (c) variation of temperature and vapor partial pressure over the thickness of reduced film and droplet radius.

This heat flow, which is created due to the temperature difference $(T_g - T_d)$, in turn, passes through the layer δ in the direction to a droplet (Figure 6.1a). During the heating of a vapor, the latter loses a significant amount of heat and comes to the surface of a droplet having a value Q_d (Figure 6.1b). Then, one part of this heat flow is consumed for evaporation, and the other one is consumed for heating of a droplet itself, raising its temperature. The pressure of a saturated vapor p_{sat} plays an important role (Figure 6.1c). With increasing temperature T_d, the pressure increases, raising the diffusion component of a vapor flow. Then more heat is consumed to heat a vapor, and droplets (Q_d). It is possible that the heat can be consumed entirely on evaporation, and T_d at a certain value of $T_{lim} \approx T_{boil}$ ceases to increase. As a result, stationary (equilibrium) evaporation is established.

On forming the mathematical model of single-component liquid droplet evaporation, the following relations are used:

1. Expression for droplet mass variation at evaporation [8]:

$$\frac{dm_d}{d\tau} = \dot{m}_d = 4\pi R_d^2 \frac{D_{Vm} p \mu_V}{\gamma R_0 T_{gV}} \left(\frac{R_d + \delta}{R_d \delta}\right) ln\left(\frac{p - \gamma p_{sat}(T_d)}{p - \gamma p_\infty}\right), \tag{6.1}$$

where m_d is the droplet mass, $\dot{m}_d$ is the rate of droplet mass reduction ($\dot{m}_d < 0$), $p_{sat}(T_d)$ is the vapor's saturated pressure above the droplet surface, p is the pressure in the external flow, T_d is the droplet temperature, D_{Vm} is the diffusion coefficient of vapor into gaseous medium, p_∞ is the vapor's partial pressure in the external flow, R_d is the droplet radius; T_{Vd} is the average temperature of vapor–gas mixture in the reduced film, $\delta = 2R_d/Nu_D$ is the reduced film thickness (average boundary layer thickness of the droplet in still (unmoving) medium $\delta = R_d$ since $Nu_D = 2$), and γ is the relative variation of droplet volume at evaporation:

$$\gamma = \frac{V_V - V_{liq}}{V_V} = 1 - \frac{\rho_V}{\rho_{liq}}. \tag{6.2}$$

It is evident that at $p < p_{cr}$ parameter $\gamma \approx 1$, since $\rho_V \ll \rho_{liq}$.

Downloaded from https://www.cambridge.org/core. Nottingham Trent University, on 17 Aug 2019 at 02:08:15, subject to the Cambridge Core terms of use, available at https://www.cambridge.org/core/terms. https://doi.org/10.1017/9781108581714.006

2. Assuming that thermal and diffusive reduced film thicknesses are the same ($\delta_T = \delta_D = \delta$), the equation of droplet heating can be written as

$$\frac{dT_d}{d\tau} = \frac{1}{m_d c_{liq}}(\dot{m}_d L_V + Q_d), \tag{6.3}$$

where L_V is the latent heat of vaporization, c_{liq} is the specific heat of liquid, and Q_d is the amount of heat transferred to the droplet surface, which is spent for the droplet evaporation and heating (Figure 6.1b), defined with following equation:

$$Q_d = \bar{k}_{gV}\frac{dT}{dr}4\pi r^2 - \bar{c}_{pV}\dot{m}_V(T - T_d), \tag{6.4}$$

where $\bar{k}_{gV}$ is the average vapor–gas thermal conductivity of vapor–gas mixture in the boundary layer, $\bar{c}_{pV}$ is the average thermal capacitance of the vapor, r is the current radius, $\dot{m}_V$ is the vapor flow rate from the droplet surface ($\dot{m}_V = -\dot{m}_d$), and $T = T(r)$ is the temperature over boundary layer thickness.

Assuming that $Q_d, \dot{m}_V, T_d$ are constant, separating variables r, T and integrating, one can obtain

$$\int_{R_d}^{R_d+\delta} \frac{r^{-2}dr}{4\pi\bar{k}_{gV}} = \int_{T_d}^{T_g} \frac{dT}{Q_d + \bar{c}_{pV}\dot{m}_V(T - T_d)}, \tag{6.5}$$

which results in

$$\frac{1}{4\pi\bar{k}_{gV}}\left(\frac{1}{R_d} - \frac{1}{R_d + \delta}\right) = \frac{1}{\bar{c}_{pV}\dot{m}_V} ln\left(\frac{Q_d + \bar{c}_{pV}\dot{m}_V(T_g - T_d)}{Q_d}\right). \tag{6.6}$$

Using the definition of "conditional reduced film" [229] and the corresponding thickness of conditional reduced film $\delta^* = \frac{R_d\delta}{R_d+\delta} = \frac{R_d}{Nu_D}$ from which it follows that $\frac{1}{R_d} - \frac{1}{R_d+\delta} = \frac{\delta^*}{R_d^2}$, after some transformations, one obtains

$$exp\left(\frac{\dot{m}_V\bar{c}_{pV}\delta^*}{4\pi R_d^2\bar{k}_{gV}}\right) = \frac{Q_d + \bar{c}_{pV}\dot{m}_V(T_g - T_d)}{Q_d}. \tag{6.7}$$

From (6.7):

$$Q_d = \frac{\bar{c}_{pV}\dot{m}_V(T_g - T_d)}{exp\left(\frac{\dot{m}_V\bar{c}_{pV}\delta^*}{4\pi R_d^2\bar{k}_{gV}}\right) - 1}. \tag{6.8}$$

Substituting (6.8) in (6.3) and assuming uniform temperature over droplet volume, we obtain the equation of droplet heating:

Downloaded from https://www.cambridge.org/core. Nottingham Trent University, on 17 Aug 2019 at 02:08:15, subject to the Cambridge Core terms of use, available at https://www.cambridge.org/core/terms. https://doi.org/10.1017/9781108581714.006

$$\frac{dT_d}{d\tau} = \frac{\dot{m}_V}{m_d c_{liq}} \left(\frac{\bar{c}_{pV}\left(T_g - T_d\right)}{exp\left(\frac{\dot{m}_V \bar{c}_{pV}\delta^*}{4\pi R_d^2 \bar{k}_{gV}}\right) - 1} - L_V \right). \tag{6.9}$$

Considering steady-state evaporation ($T_d = T_{lim} = const$), (6.9) can be written as

$$\frac{\bar{c}_{pV}\left(T_g - T_d\right)}{exp\left(\frac{\dot{m}_V \bar{c}_{pV}\delta^*}{4\pi R_d^2 \bar{k}_{gV}}\right) - 1} - L_V = 0 \tag{6.10}$$

Then, from (6.10):

$$exp\left(\frac{\dot{m}_V \bar{c}_{pV}\delta^*}{4\pi R_d^2 \bar{k}_{gV}}\right) = 1 + \frac{\bar{c}_{pV}\left(T_g - T_d\right)}{L_V}. \tag{6.11}$$

It follows from (6.11) that for steady-state evaporation,

$$\dot{m}_V = \frac{4\pi R_d^2 \bar{k}_{gV}}{\bar{c}_{pV}\delta^*} ln\left(1 + \frac{\bar{c}_{pV}\left(T_g - T_d\right)}{L_V}\right). \tag{6.12}$$

6.2 Model of Droplet Evaporation in Reacting Gaseous Medium at High Pressures

In the reacting flow of hot gas at $p \geq p_{cr}$, the droplet temperature (T_d) can reach its critical magnitude. In this case, surface tension approaches zero, which formally can lead to the "explosion" of the droplet. In fact, the droplet continues to exist and vaporize, which may be the result of nonuniform heating. Then the temperature of the droplet surface can approach its critical value while intermolecular forces in inner layers remain significant that allows droplet to exist. Therefore, nonuniform temperature distribution over droplet radius is taking into account at $p \geq p_{cr}$.

The specific feature of the proposed physical scheme consists in nonuniform temperature distribution over the droplet radius with a parabolic pattern of temperature distribution (Figure 6.2):

$$T(r,\tau) = a(\tau) + b(\tau)(r/R_d)^2, \tag{6.13}$$

where $a(\tau), b(\tau)$ are time-dependent parameters describing the droplet center temperature and droplet temperature variation over the radius.

Let us consider the droplet evaporation scheme as the process proceeding in two stages. The droplet is heated at the first stage in compliance with common relationships of non-steady-state heating from initial temperature T_0 to some limit temperature of the surface T_{lim} (close to critical temperature T_{cr} under these conditions). Temperature T_{lim} is defined given the equality of forces of liquid intermolecular cohesion and

Downloaded from https://www.cambridge.org/core. Nottingham Trent University, on 17 Aug 2019 at 02:08:15, subject to the Cambridge Core terms of use, available at https://www.cambridge.org/core/terms. https://doi.org/10.1017/9781108581714.006

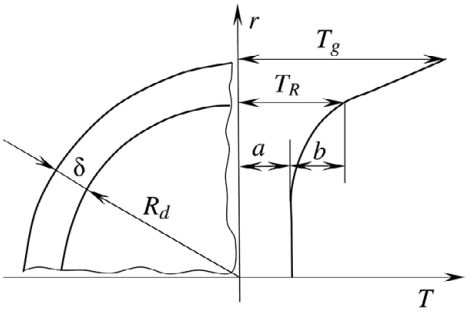

Figure 6.2 Diagram of droplet nonuniform heating (temperature distribution).

aerodynamic forces acting upon the droplet. Fluid droplets feature a spherical shape while the boundary layer there is simulated by the reduced film (see Sections 5.1, 5.2, and 6.1). Errors caused by this assumption are, as a rule, inessential. Besides, the reduced film model shown in Chapter 5 is sufficiently efficient in various computations of droplet evaporation.

The surface temperature that reached the limit value T_{lim} at the second stage remains practically constant, but the droplet inner region is still getting heated. Note here that heat flow toward the droplet surface of constant temperature is used for heating its inner volume and intensive evaporation from the droplet surface. As inner layers reach the limit temperature T_{lim}, the evaporation rate rises to the level that provides a compensation for the amount of heat transferred to the droplet. The droplet surface displaces here inside the droplet toward its center. The increase in the rate of vapor diffusion through the reduced film is caused by a higher concentration of vapors above the droplet surface as compared to the conditions of saturation conditioned by aerodynamic forces destructing the droplet surface layer.

The criteria of the transition to the second stage of evaporation are the temperature T_{lim} and saturated vapor pressure p_{sat}. Thus, the second stage of evaporation begins when saturated vapor pressure p_{sat} reaches current pressure p (to ensure the computation process stability it is helpful to assume that $p_{sat} = 0.9p$), or when the droplet surface temperature is close to critical temperature T_{cr}.

Thus, the mathematical model compiles two stages: non-steady-state, when $T_R \to T_{\lim}$, and steady-state, when $T_R = T_{\lim}$.

For the first stage, the equation of evaporation (6.1) remains almost the same except the term $p_{sat}(T_d)$, which is replaced by $p_{sat}(T_R)$, where $T_R = a + b$ is the temperature of droplet surface (Figure 6.2). This leads to the equation:

$$\frac{dm_d}{d\tau} = 4\pi R_d^2 \frac{D_{Vm} p \mu_V}{\gamma R_0 T_{gV} \delta^*} ln\left(\frac{p - \gamma p_{sat}(T_R)}{p - \gamma p_\infty}\right) = f_{m1}^{\tau}. \tag{6.14}$$

For the second stage, $p_{sat}(T_d)$ is replaced by p_{Vd} (partial pressure on the droplet surface), which can be much higher than p_{sat}. This leads to the equation:

Downloaded from https://www.cambridge.org/core. Nottingham Trent University, on 17 Aug 2019 at 02:08:15, subject to the Cambridge Core terms of use, available at https://www.cambridge.org/core/terms. https://doi.org/10.1017/9781108581714.006

$$\frac{dm_d}{d\tau} = 4\pi R_d^2 \frac{D_{Vm} p \mu_V}{\gamma R_0 T_{gV} \delta^*} ln\left(\frac{p - \gamma p_{Vd}}{p - \gamma p_\infty}\right) = f_{m2}^\tau. \tag{6.15}$$

Equations (6.14) and (6.15) could be combined using generalized designations $p_{sur} \in p_{sat}, p_{Vd}$, and $f_m^\tau \in f_{m1}^\tau, f_{m2}^\tau$.

However, the equation of droplet heating must be completely different because of nonuniform temperature distribution over droplet radius. To derive this equation, let's use the droplet thermal capacitance concept in following form:

$$\Phi_d = m_d \bar{h}_d, \tag{6.16}$$

where $\bar{h}_d$ is mass-averaged droplet enthalpy.

First, let's identify which variables $\bar{h}_d$ depends from. It can be written:

$$\bar{h}_d = \frac{\Phi_d}{m_d} = \frac{\int_0^{R_d} h\big(T_{liq}(a,b,r/R_d)\big)\rho_{liq}(a,b,r/R_d)4\pi r^2 dr}{\int_0^{R_d} \rho_{liq}(a,b,r/R_d)4\pi r^2 dr}. \tag{6.17}$$

Using $\bar{r} = \frac{r}{R_d}$, one can write

$$\bar{h}_d = \frac{R_d^3 \int_0^1 h\big(T_{liq}(a,b,\bar{r})\big)\rho_{liq}(a,b,\bar{r})4\pi \bar{r}^2 d\bar{r}}{R_d^3 \int_0^1 \rho_{liq}(a,b,\bar{r})4\pi \bar{r}^2 d\bar{r}} = f(a,b). \tag{6.18}$$

Integrals in Formula (6.18) can be calculated analytically, but the analytical formula is likely to be complex. So it is better to preliminarily compute h_d in the specified ranges of a and b and then approximate results of the calculations. This problem can be solved using methods of nomographic approximation [145]. The droplet averaged-mass enthalpy $\bar{h}_d$ is set as the approximating polynomial:

$$\bar{h}_d = A + Ba + Cb + Dab + Ea^2 + Fb^2, \tag{6.19}$$

where A, B, C, D, E, and F are approximation coefficients.

Similarly, the following polynomials were obtained for the calculation of average values of density $\bar{\rho}_{liq}$, thermal conductivity $\bar{k}_{liq}$ and thermal capacitance $\bar{c}_{liq}$ of liquid.

It follows from Formulas (6.16) and (6.19) that

$$\Phi_d = m_d \bar{h}_d = m_d\big(A + Ba + Cb + Dab + Ea^2 + Fb^2\big). \tag{6.20}$$

The second equation of mathematical model follows from (6.20):

$$\Phi_d - m_d\big(A + Ba + Cb + Dab + Ea^2 + Fb^2\big) \equiv F_b^\tau = 0. \tag{6.21}$$

Equation (6.21) is written in the form with "zero" right-hand side since in Chapter 8 this equation will be included in the mathematical model of reacting two-phase flows.

Downloaded from https://www.cambridge.org/core. Nottingham Trent University, on 17 Aug 2019 at 02:08:15, subject to the Cambridge Core terms of use, available at https://www.cambridge.org/core/terms. https://doi.org/10.1017/9781108581714.006

The original equation of variation of droplet rate of internal energy variation is written as follows:

$$\frac{d\Phi_d}{d\tau} = Q_d + \left(L_V + h_d^R\right)\frac{dm_d}{d\tau}, \tag{6.22}$$

where h_d^R is mass enthalpy of the fluid at the droplet surface temperature.

Using same transformations that are presented in [229], we obtain:

$$Q_d = \frac{\bar{k}_{gV}}{\delta^*}\left(\frac{\dot{m}_V \bar{c}_{p,gV}\delta^* / \left(\bar{k}_{gV} 4\pi R_d^2\right)}{exp\left(\frac{\dot{m}_V \bar{c}_{p,gV}\delta^*}{\bar{k}_{gV} 4\pi R_d^2}\right) - 1}\right) 4\pi R_d^2 \left(T_g - T_R\right), \tag{6.23}$$

where $\bar{c}_{p,gV}$ is the average specific heat of the vapor–gas mixture.

Substituting (6.14) in the exponent of Equation (6.23) with allowance for $\dot{m}_V = -\frac{d\dot{m}_d}{d\tau}$ gives

$$Q_d = \; -\left(\frac{dm_d}{d\tau}\right)\left(\frac{\bar{c}_{p,gV}\left(T_g - T_R\right)}{exp\left(-K_e ln\left(1 - \frac{p - \gamma p_{sur}}{p - \gamma p_\infty}\right)\right) - 1}\right), \tag{6.24}$$

where $K_e = \frac{D_{Vm} p \mu_V \bar{c}_p}{\bar{k}_{gV} R_0 T_{gV\gamma}}$, and T_{gV} is the average temperature of vapor–gas mixture in the reduced film.

Then rate of droplet internal energy variation $\frac{d\Phi_d}{d\tau}$ is defined from Relation (6.22):

$$\begin{aligned}\frac{d\Phi_d}{d\tau} = & \frac{4\pi R_d^2 K_e \bar{k}_{gV} ln\left[\frac{(p - \gamma p_{sur})}{(p - \gamma p_\infty)}\right]}{\bar{c}_{p,gV}\delta^*} \\ & \times \left(L_V + h_d^R - \frac{\bar{c}_{p,gV}\left(T_g - T_R\right)}{exp\left(-K_e ln\left(1 - \frac{p - \gamma p_{sur}}{p - \gamma p_\infty}\right)\right) - 1}\right) = \mathrm{f}_\Phi^\tau.\end{aligned} \tag{6.25}$$

Equation (6.25) is additional equation of the mathematical model.

For the calculation of the droplet center temperature (a), let us use the well-known heat equation in spherical coordinates:

$$\frac{\partial T}{\partial \tau} = \frac{k_{liq}}{c_{liq}\rho_{liq}}\left(\frac{\partial^2 T}{\partial r^2} + \frac{2}{r}\frac{\partial T}{\partial r}\right), \tag{6.26}$$

where $k_{liq}, c_{liq}, \rho_{liq}$ are thermal conductivity, specific heat, and density of the droplet, respectively.

Then, allowing for (6.13), the temperature of the droplet center (at $r = 0$) is defined from the expression:

Downloaded from https://www.cambridge.org/core. Nottingham Trent University, on 17 Aug 2019 at 02:08:15, subject to the Cambridge Core terms of use, available at https://www.cambridge.org/core/terms. https://doi.org/10.1017/9781108581714.006

$$\frac{da}{d\tau} = \frac{\bar{k}_{liq}}{\bar{c}_{liq}\bar{\rho}_{liq}} \frac{6b}{R_d^2}, \tag{6.27}$$

where parameters $\bar{k}_{liq}, \bar{c}_{liq}, \bar{\rho}_{liq}$ have their mean-integral values.

Equation (6.27) is not completely accurate because of the preliminary approximation of temperature distribution over the droplet radius, but it correctly reflects the influence of R_d and b on the rate of heating the droplet center. Moreover, the rate of evaporation is primarily driven by the amount of external heat transferred to the droplet, which weakly depends on the temperature in the droplet center. Substituting the value of the radius written in terms of droplet mass and density, one can derive a fourth equation of the mathematical model:

$$\frac{da}{d\tau} = \frac{\bar{k}_{liq} 6b}{\bar{c}_{liq}\bar{\rho}_{liq}} \left(\frac{4}{3} \frac{\pi\bar{\rho}_{liq}}{m_d}\right)^{2/3} = f_a^{\tau}. \tag{6.28}$$

Partial pressure of vapors at the first stage of evaporation is taken equal to the pressure of saturated vapors, which is the known function of the droplet surface temperature:

$$p_{sat} = A_p + B_p T_R + C_p {T_R}^2 + D_p {T_R}^3. \tag{6.29}$$

Coefficients A_p, B_p, C_p, and D_p are standard or may be defined with the help of, for example, n-order approximation. At this stage, unsteady heating (up to the temperature T_{lim}) of the droplet and evaporation are taking place; therefore, the mathematical model includes following equation:

$$p_{sat} - A_p + B_p T_R + C_p {T_R}^2 + D_p {T_R}^3 \equiv F_{p1}^{\tau} = 0. \tag{6.30}$$

The second-stage fluid evaporation at constant temperature T_{lim} of the droplet surface (i.e., $r = R_d$) differs in that the heat transferred to the droplet is mainly compensated by mass discharge (evaporation from the droplet surface), but the droplet center goes on being heated. Therefore, allowing for Figure 6.1, the relationship $a(\tau) + b(\tau) = T_R = const = T_{\lim}$ corresponds to the second evaporation stage. Differentiation of this relation gives

$$da/d\tau = -db/d\tau. \tag{6.31}$$

Due to the effect of aerodynamic forces destructing the droplet surface layer, pressure above the droplet surface (p_{Vd}) at the second stage may notably exceed the pressure of saturated vapors p_{sat}. This pressure is unknown and can be defined from the condition of droplet surface temperature constancy, as well as equality of evaporation rate and rate of vapor diffusion through the reduced film, that can be expressed by Equation (6.32), obtained by taking the logarithm and subsequent differentiation of (6.16):

$$ln(\Phi_d) = ln(m_d) + ln(\bar{h}_d), \tag{6.32}$$

$$\frac{1}{\Phi_d}\frac{d\Phi_d}{d\tau} - \frac{1}{m_d}\frac{dm_d}{d\tau} - \frac{1}{\bar{h}_d}\frac{d\bar{h}_d}{d\tau} = 0. \tag{6.33}$$

Downloaded from https://www.cambridge.org/core. Nottingham Trent University, on 17 Aug 2019 at 02:08:15, subject to the Cambridge Core terms of use, available at https://www.cambridge.org/core/terms. https://doi.org/10.1017/9781108581714.006

Substituting $\frac{dm_d}{d\tau}$, $\frac{d\Phi_d}{d\tau}$ in the right-hand sides of Equations (6.14) and (6.25) and expressing $\frac{d\bar{h}_d}{d\tau}$ using (6.19), Equation (6.33) may be written as follows:

$$\frac{1}{\Phi_d} f_\Phi^\tau - \frac{1}{m_d} f_m^\tau - \frac{1}{\bar{h}_d} \frac{d\left(A + Ba + Cb + Dab + Ea^2 + Fb^2\right)}{d\tau} = 0. \tag{6.34}$$

Taking derivative $\frac{d\bar{h}_d}{d\tau}$, one obtains

$$\frac{d\left(A + Ba + Cb + Dab + Ea^2 + Fb^2\right)}{d\tau} = B\frac{da}{d\tau} + C\frac{db}{d\tau} + Db\frac{da}{d\tau} + Da\frac{db}{d\tau} + 2E\frac{da}{d\tau} + 2F\frac{db}{d\tau}. \tag{6.35}$$

With allowance for $da/d\tau = -db/d\tau$, and substituting $\frac{da}{d\tau}$ in the right-hand side of Equation (6.28), one can obtain the algebraic equation:

$$\frac{1}{\Phi_d} f_\Phi^\tau - \frac{1}{m_d} f_m^\tau - \frac{f_a^\tau}{\bar{h}_d}[(B - C) + a(2E - D) + b(D - 2F)] \equiv F_{p2}^\tau = 0. \tag{6.36}$$

It should be noted that parameter p_{Vd} is contained in the expressions f_Φ^τ and f_m^τ. Equations (6.30) and (6.36) are closing equations of mathematical model (6.30) for the first stage and (6.36) for the second stage). Parameters $m_d, \Phi_d, a, b,$ and $p_{sur} \in (p_{sat}, p_{Vd})$ are unknowns in the system of equations (6.15), (6.21), (6.25), (6.28), and (6.30) or (6.36). The system of equations describes the evaporation of single-component liquid droplet with allowance for specific features of the process at subcritical (evaporation first stage) and supercritical (evaporation second stage) conditions.

Parameters of the gas–vapor mixture in the reduced film are required for the calculation of heat and mass transfer between gas and droplets. The method of their calculation is adopted from [166] and expressed by following generalized formula:

$$x_{gV} = \left(1 - \frac{p_{sur}}{2p}\right) x_g + \frac{p_{sur}}{2p} x_V, \quad p_{sur} \in p_{sat}, p_{Vd}, \quad x = c_p, k. \tag{6.37}$$

The diffusion coefficient of vapor into gaseous medium is calculated by formulas of molecular-kinetic theory and defined by the expression [160]:

$$D_{Vm} = 0.0266 \frac{T_{gV}\sqrt{T_{gV}\left(\mu_g + \mu_V\right)/\left(\mu_g \mu_V\right)}}{p\sigma_{gV}^2 \Omega_{gV}^{1,1*}}, \tag{6.38}$$

where $T_{gV} = 0.5\left(T_R + T_g\right)$.

The reduced collision integral is defined from polynomial [13]:

$$\Omega_{gV}^{1,1*} = \sum_p \alpha_p \left(\ln T_{gV}^*\right)^p, \quad p = 0 \ldots 5 \tag{6.39}$$

Downloaded from https://www.cambridge.org/core. Nottingham Trent University, on 17 Aug 2019 at 02:08:15, subject to the Cambridge Core terms of use, available at https://www.cambridge.org/core/terms. https://doi.org/10.1017/9781108581714.006

and constitutes the function of reduced temperature:

$$T^*_{gV} = T_{gV}/(\varepsilon/k)_{gV}. \tag{6.40}$$

The parameters of the potential function of interaction for approximation of intermolecular interaction are defined by the expressions [13, 160]:

$$\sigma_{gV} = 0.5(\sigma_g + \sigma_V), \quad \left(\frac{\varepsilon}{k}\right)_{gV} = \sqrt{\left(\frac{\varepsilon}{k}\right)_g \left(\frac{\varepsilon}{k}\right)_V}. \tag{6.41}$$

The studies of parametric models were done for various liquids. In particular, the study of evaporation of a droplet of liquid ammonia (NH_3) under the influence of a number of parameters was carried out. The study of the impact of the velocity of flow V_g in terms of $\Delta V_{gd} = |V_g - u_d|$ was simulated by $\bar{\delta} = \delta/R_d$, which increases at the decrease of V_g and reaches unity at $V_g = 0$. Figure 6.3 shows the dependences $\bar{m} = m_d/m_{d0} = f(\tau)$ for different values of p_g, where m_{d0} is an initial mass of a droplet. As it is seen, with the increase of pressure p, the gasification rate decreases initially but increases at the final stage. This trend is explained by the increase in the droplet temperature (T_d) with the increase of pressure. Therefore, by the time the temperature T_{lim} is achieved, the droplet (at the high value of pressure) will be heated better and then will evaporate with the higher intensity. As the parameter $\bar{\delta}$ increases, this trend becomes more and more intense, leading to the significant stratification of the droplet gasification curves. When $\bar{\delta} = 1$ (unmoving droplet), a significant congruence of the calculation results, and the data from [230] is observed, confirming that droplet gasification time increases with the increasing pressure.

Also, Figure 6.3 shows the change in the droplet's radius through its gasification. At small values of pressure, this radius could decrease monotonically if the rate of its decrease due to gasification is greater than the rate of its increase caused by the heating of a droplet. At the increasing pressure, the ratio between these rates is changing, and function $R_d(\tau)$ could reach its maximum.

The value $\bar{k}_{liq}$ is not completely predetermined, and, thus, the influence of thermal conductivity $\bar{k}_{liq}$ on the rate of gasification of a droplet was also analyzed. The bottom line is that because of the influence of convective currents in the liquid, the value of $\bar{k}_{liq}$ that determines the heat transfer inside a droplet can be significantly higher than regular molecular thermal conductivity of liquid. Figure 6.4 represents the influence of $\bar{k}_{liq}$ on

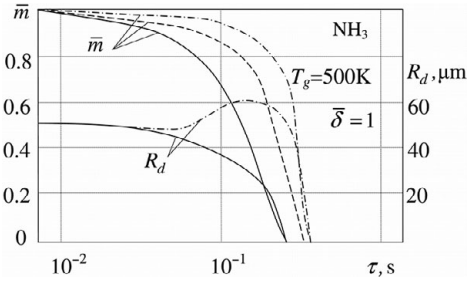

Figure 6.3 Variation of relative mass $\bar{m}$ and radius of ammonia droplet R_d subject to time at different pressures of the gas mixture: (—) $p < p_{cr}$; (---) $p_g = 5p_{cr}$; (–· – ·) $p_g = 50p_{cr}$.

Downloaded from https://www.cambridge.org/core. Nottingham Trent University, on 17 Aug 2019 at 02:08:15, subject to the Cambridge Core terms of use, available at https://www.cambridge.org/core/terms. https://doi.org/10.1017/9781108581714.006

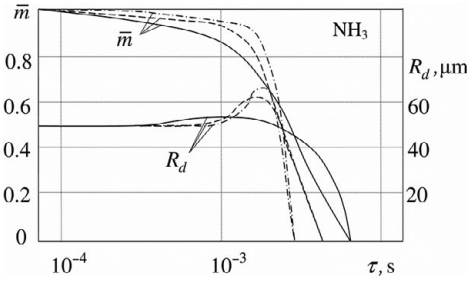

Figure 6.4 Influence of thermal conductivity of the liquid on the nature and time of evaporation: (---) $-\bar{k}_{liq} = 0$; (—) $-\bar{k}_{liq} = 0.37 \frac{W}{m\,K}$; $(-\cdot - \cdot)$ $-\bar{k}_{liq} = 10^3 \frac{W}{m\,K}$; $T_g = 1000$ K; $p = 5p_{cr}$; $\bar{\delta} = 0.03$.

the parameters of gasification of a droplet. The larger $\bar{k}_{liq}$ is, the later T_{lim} is attained on the surface of a droplet, and the more intensive gasification that occurs. As a rule, the time for complete gasification of a droplet decreases as $\bar{k}_{liq}$ increase. Its influence is similar to the influence of pressure, but it is more intense.

At the initial stage of gasification, with the increase of $\bar{k}_{liq}$, more heat is consumed for the droplet heating rather than for gasification. This leads to an increase in maximum value of the droplet radius $R_d(\tau)$, which, when $\bar{k}_{liq} \to \infty$ is approaching $R_d^{max}\left(\bar{k}_{liq} \to \infty\right) = \left(\frac{3m_0}{4\pi\bar{\rho}(T_{lim})}\right)^{1/3}$. The curve $R_d^{max}\left(\bar{k}_{liq} = 0\right)$ estimates to some extent the imperfection of this model. The maximum of the curve is 4% higher than R_d^0. At the same time, when $\bar{k}_{liq} = 0$, the radius of a droplet should decrease monotonically. This insignificant discrepancy is caused by the assumption of a parabolic change of the temperature of a liquid along the radius of a droplet.

6.3 Model of Evaporation of Multicomponent Fluid

Dispersed hydrocarbon propellants used in most propulsion systems feature multicomponent composition, which is why the mechanisms of their evaporation differs from that of single-component fluids. Multicomponent composition of droplets affects not only the evaporation process but also those of gas-phase combustion processes that depend on kinetics of reactions involving evaporating species. Use of models developed for single-component fluids have, as a rule, some constraints on their application to analysis of multicomponent droplets evaporation. This is why the problem of what model may be used for the description of the evaporation of droplets of complex composition becomes of importance.

For example, the model of evaporation and combustion of spherically symmetric multicomponent droplets [231] proceeds from the assumptions of equilibrium evaporation from droplet surface, combustion occurring in the thin flame zone (flame front), heat and mass transfer in liquid phase being governed by diffusion, while heat and mass transfer, in gas phase, is carried out by convection and diffusion. Processes inside the droplet are described by relations of the type of heat equation with displacing boundary

Downloaded from https://www.cambridge.org/core. Nottingham Trent University, on 17 Aug 2019 at 02:08:15, subject to the Cambridge Core terms of use, available at https://www.cambridge.org/core/terms. https://doi.org/10.1017/9781108581714.006

congruent with the droplet surface. The rate of heat transfer by conduction is higher than that of the diffusion mass transfer.

Analyses of droplet evaporation have shown that after beginning evaporation, the droplet surface is rapidly heated to reach almost steady-state temperature. In the course of this time, the liquid evaporates slowly. After heating the surface layer, including a considerable portion of droplet mass, the evaporation rate grows dramatically. Profiles of component concentrations in the droplet follow the variation of temperature. As the droplet surface's steady-state temperature reached, profiles of concentrations become stable. The revealed features of the evaporation process have been allowed for in an approximate analytical model of the evaporation and combustion of a multicomponent droplet [232]. The model describes an equilibrium evaporation of the ideal mixture of liquid components. The dependence of the droplet diameter (d) on evaporation time τ has the form $d^2 = d_0^2 - K\tau$, where K is the evaporation constant.

The droplet surface temperature has been assumed to be a time-invariant magnitude equal to the mixture's average boiling temperature calculated as the combination of boiling temperatures of individual components averaged over their concentrations $\bar{T}_{boil} = \sum_q r_q T_{boil}^q$. The droplet's initial transient heating and gas flow's influence on the evaporation process have not been allowed for.

The intensity of convective flows in the droplet is known to influence the manner of the evaporation process of components. For example, two opposite cases have been analyzed in the paper [233]. In the first case, evaporation has been simulated at the fast internal mixing of components. Volatility of components has made a limiting factor in this case: more volatile components evaporated more quickly. In the second case, with no internal convection, the diffusion of liquid components became the limiting factor while the proportions between concentrations of components approached their constant values.

The external flow of the gas mixture exercises a definite influence on the evaporation of multicomponent droplets. The droplet's motion in the gas flow can make the evaporation features dependent on the ratio between time of heating and time of reaching the equality between phase velocities. If the droplet velocity reaches the gas's local velocity quickly, then a droplet heating becomes the factor defining the character of component evaporation. In this case, the internal circulation intensity drops down to transport the liquid components to the droplet surface mainly by diffusion. At faster heating of the droplet, the internal circulation effect becomes more profound because of the external flow. The transport of more volatile components to the surface is intensified to make evaporation similar to the distillation process.

The multicomponent liquid evaporation model is considered in following manner. The liquid mixture consists of components with nearly identical properties. The liquid also features the properties of the ideal solution of several components with no interaction between them. Raoult's law is observed. Enthalpy of mixing and of volume variation at the mixing of components equals zero. The liquid droplet instantly entrains into gas flow with higher temperature. The gas flow features temperature T_g, velocity u_g, and physical–chemical properties varying over the channel length.

The existence of notable relative velocity causes the intensification of internal circulation in the droplet that precludes stratification of components with different

Downloaded from https://www.cambridge.org/core. Nottingham Trent University, on 17 Aug 2019 at 02:08:15, subject to the Cambridge Core terms of use, available at https://www.cambridge.org/core/terms. https://doi.org/10.1017/9781108581714.006

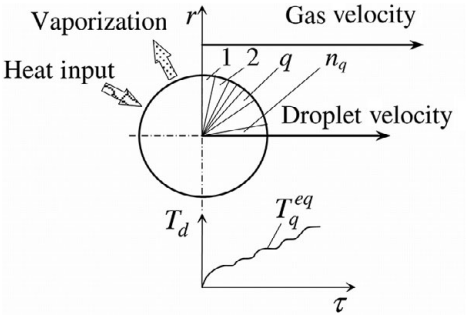

Figure 6.5 Diagram of variation of the temperature of multicomponent droplet at the concurrent evaporation of all components.

densities. At higher gas temperatures, it can be expected that a complete evaporation occurs in a very short time, while redistribution of components concentration over droplet volume would be insignificant. In this connection, it may be assumed that evaporation of all components occurs simultaneously and components are distributed uniformly over the droplet volume (Figure 6.5).

A major part of the heat transferred to the droplet surface at the beginning of the process is consumed for the droplet heating; therefore, the liquid evaporates slowly. After droplet heating, the evaporation of the component with the lowest boiling temperature grows sharply. The amount of heat consumed for evaporation at the stage of equilibrium evaporation (see Equations (5.8) and (6.12)) becomes equal to the amount of heat received by the droplet from the gas mixture. After complete evaporation of the component with the lowest boiling temperature, the fraction of the heat consumed for droplet heating rises again. The droplet temperature increases until the certain value corresponding to equilibrium evaporation of the next component with the lowest boiling temperature of remaining components. During the intensive evaporation of this component, the droplet temperature remains constant in connection with the assumption of equilibrium evaporation. Thus, the droplet evaporation model under consideration is characterized by a stepwise temperature variation with successive vanishing of components that feature different boilint temperatures.

Along with the general assumptions listed in the introduction to this chapter, the mathematical model of evaporation of a multicomponent droplet assumes that fluid temperature is the same over the droplet volume – that is, the droplet is heated uniformly over its radius and, hence, its volume.

It is assumed that initially the droplet features radius R_{d0} and temperature T_{d0}. Also, let's assume that the diffusive Nusselt number (Nu_D) differs from the thermal Nusselt number (Nu_T), thus $\delta_D \neq \delta_T$. Every liquid component is described by individual values of molecular mass μ_q, density ρ_q, latent heat of evaporation L_{qV}, and pressure of saturated vapors $p^0_{q,sat}$. The concentration of liquid components in a droplet is described by mass fraction

$$\bar{m}_q = \frac{m_q(\tau)}{m_{0q}}, \quad q = 1 \ldots n_q, \tag{6.42}$$

Downloaded from https://www.cambridge.org/core. Nottingham Trent University, on 17 Aug 2019 at 02:08:15, subject to the Cambridge Core terms of use, available at https://www.cambridge.org/core/terms. https://doi.org/10.1017/9781108581714.006

where n_q is the number of liquid components, $m_q(\tau)$ is the mass of component q in the droplet at time τ, and m_{0q} is the mass of component q in the droplet at time $\tau = 0$.

The equation describing the variation of mass fraction of the component q in the droplet is presented in the following form:

$$\frac{d\bar{m}_q}{d\tau} = -\frac{\dot{m}_{qV}}{m_{0q}} = -\frac{\dot{J}_q 4\pi r^2 \bar{S}_q}{m_{0q}}, \tag{6.43}$$

where $\dot{m}_{qV}$ is the mass flow rate of component q vapors, $\dot{J}_q$ is the vapor mass flux of component q through the reduced film (δ_D), and $\bar{S}_q$ is the relative area of the droplet conditional surface occupied by component q.

Since the model assumes that liquid components are distributed uniformly over the droplet volume, then the conditional surface area S_q is proportional to volume fraction of component q:

$$S_q = 4\pi R_d^2 \frac{V_q}{V_d} = \frac{4\pi R_d^2}{\frac{4}{3}\pi R_d^3} V_q = \frac{3\bar{m}_q m_{0q}}{R_d \rho_q}. \tag{6.44}$$

The formula for the calculation of relative area of the surface occupied by component q has the following form:

$$\bar{S}_q = \frac{S_q}{4\pi R_d^2} = \frac{3\bar{m}_q m_{0q}}{4\pi R_d^3 \rho_q}. \tag{6.45}$$

To define vapor mass flux $\dot{J}_q$, the equation of binary diffusion with allowance for Stefan flow [8] written for the distribution of diffusing matter in the boundary layer in direction r perpendicular to the droplet surface has been used:

$$\frac{dp_q}{dr} = -\frac{R_0 T}{D_{qm} p \mu_q} \dot{J}_q \left(p - \gamma_q p_q\right), \quad q = 1 \ldots n_q \tag{6.46}$$

where $p_q = f(r)$ is the partial pressure of component q over the thickness of reduced film, D_{qm} is the coefficient of diffusion of component q, and $\gamma_q = \frac{V_{vq} - V_{liq,q}}{V_{vq}}$ is the volume relative variation at evaporation written for each component q.

With allowance for relation between $\dot{m}_{qV}$ and $\dot{J}_q$ in (6.43), the expression (6.46) in integral form is written as follows:

$$\int_{p_{q\,sat}}^{p_{q\infty}} \frac{1}{\left(p - \gamma_q p_q\right)} dp_q = -\frac{\dot{m}_{qV} R_0}{4\pi \bar{S}_q p \mu_q} \int_{R_d}^{R_d + \delta_D} \frac{T}{D_{qm} r^2} dr, \tag{6.47}$$

where $p_{q\infty}$ is the partial pressure of component q in external flow, $p_{q\,sat}$ is the saturated pressure of component q above droplet surface, and δ_D is the diffusive reduced film thickness.

Integration of Equation (6.47) brings about the equation:

$$-\frac{1}{\gamma_q} \ln\left(\frac{p - \gamma_q p_{q\infty}}{p - \gamma_q p_{q,sat}}\right) = \frac{\dot{m}_{qV} R_0}{4\pi \bar{S}_q p \mu_q} \frac{\bar{T}_{gV}}{\bar{D}_{qm}} \left(\frac{1}{R_d + \delta_D} - \frac{1}{R_d}\right), \tag{6.48}$$

Downloaded from https://www.cambridge.org/core. Nottingham Trent University, on 17 Aug 2019 at 02:08:15, subject to the Cambridge Core terms of use, available at https://www.cambridge.org/core/terms. https://doi.org/10.1017/9781108581714.006

where $\bar{T}_{gV}$ is the average temperature of the vapor–gas mixture in the reduced film and $\bar{D}_{qm}$ is the average coefficient of the diffusion of component q into the gas mixture.

The equation for the vapor mass flow of component q from the droplet surface is derived from Equation (6.48):

$$\dot{m}_{qV} = 4\pi R_d^2 \frac{\bar{S}_q p \mu_q \bar{D}_{qm}}{R_0 \bar{T}_{gV}} \left(\frac{R_d + \delta_D}{R_d \delta_D}\right) \frac{1}{\gamma_q} ln\left(\frac{p - \gamma_q p_{q\infty}}{p - \gamma_q p_{q,sat}}\right). \tag{6.49}$$

Reduced film thickness δ_D is defined by Formula (5.6): $\delta_D = 2R_d/Nu_D$.

After substituting (6.49) in (6.43) with allowance for (6.45) and (5.6) and after simple transforms, the final equation for the variation of mass fraction of component q is obtained:

$$\frac{d\bar{m}_q}{d\tau} = -\frac{3}{2} \frac{(Nu_D + 2)\bar{m}_q p \mu_q \bar{D}_{qm}}{R_d^2 \rho_q R_0 \bar{T}_{gV}} \frac{1}{\gamma_q} ln\left(\frac{p - \gamma_q p_{q\infty}}{p - \gamma_q p_{q,sat}}\right). \tag{6.50}$$

It is assumed that droplet temperature variation is defined by conduction in the reduced film while heat transfer from the droplet surface is influenced by flow of the vapors of components:

$$Q_d = \bar{k}_{gV} \frac{dT}{dr} 4\pi r^2 + \sum_q \frac{d\bar{m}_q}{d\tau} m_{0q} \bar{c}_{pq} (T - T_d), \tag{6.51}$$

where $\bar{k}_{gV}$ is the average vapor-gas thermal conductivity over reduced film thickness, $\bar{c}_{pq}$ is the average specific heat of the vapor of component q, and $T = f(r)$ is the vapor-gas temperature over reduced film thickness.

After separation of variables and integration over reduced film thickness, $\delta_T = 2R_d/Nu_T$, where Nu_T is the thermal Nusselt number and δ_T is the thermal boundary layer thickness, one obtains

$$Q_d = \frac{-\sum_q \frac{d\bar{m}_q}{d\tau} m_{0q} \bar{c}_{pq} (T_g - T_d)}{exp\left(\frac{-\sum_q \frac{d\bar{m}_q}{d\tau} m_{0q} \bar{c}_{pq}}{2\pi R_d k_{gV} (Nu_T + 2)}\right) - 1}. \tag{6.52}$$

While heating the evaporating droplet, a certain amount of heat is consumed for compensation of latent heat of evaporation of liquid components L_{qV}, while the droplet temperature variation equation has the following form:

$$\frac{dT_d}{d\tau} = \frac{1}{\sum_q \bar{m}_q m_{0q} \bar{c}_{pq}} \left(\sum_q \frac{d\bar{m}_q}{d\tau} m_{0q} L_{qV} + Q_d\right). \tag{6.53}$$

At equilibrium evaporation of whatever component k, the heat flow rate to the droplet surface equals the sum of the products of evaporation rates and the latent heat of evaporation of liquid components:

Downloaded from https://www.cambridge.org/core. Nottingham Trent University, on 17 Aug 2019 at 02:08:15, subject to the Cambridge Core terms of use, available at https://www.cambridge.org/core/terms. https://doi.org/10.1017/9781108581714.006

Table 6.1 Initial chemical composition of surrogate fuel evaporating into gas flow

Number	1	2	3	4	5	6	7
Component	C_5H_{12}	C_6H_{14}	C_7H_{16}	C_8H_{18}	C_9H_{20}	$C_{10}H_{22}$	$C_{11}H_{24}$
g_q (mass fraction)	0.018	0.051	0.08	0.174	0.464	0.168	0.045

$$Q_d = -\sum_{q\neq k} \frac{d\bar{m}_q}{d\tau} m_{0q} L_{qV} - \frac{d\bar{m}_q}{d\tau} m_{0k} L_{kV}. \tag{6.54}$$

It follows from Equation (6.53) that at this stage,

$$\frac{dT_d}{d\tau} = 0. \tag{6.55}$$

The evaporation rate at equilibrium evaporation of component k is derived from Equation (6.54):

$$\frac{d\bar{m}_k}{d\tau} = -\frac{1}{m_{0k} L_{kV}} \left(\sum_{q\neq k} \frac{d\bar{m}_q}{d\tau} m_{0q} L_{kV} + Q_d \right). \tag{6.56}$$

The current radius of the droplet is calculated according to the known formula for the calculation of spherical volume:

$$R_d = \left(\frac{3}{4\pi} \sum_q \frac{\bar{m}_q m_{0q}}{\rho_q} \right)^{1/3}. \tag{6.57}$$

The velocity variation equation for the droplet in unidirectional gas flow is written on the basis of Newton's second law:

$$\frac{du_d}{d\tau} = \frac{F_x}{\sum_q \bar{m}_q m_{0q}}, \tag{6.58}$$

where F_x is the drag force acting on the droplet moving in gas flow defined by Formula (7.6).

As a result, the mathematical model of multicomponent droplet evaporation includes Equations (6.50) or (6.56); (6.53) or (6.55); (6.57); and (6.58). Unknown parameters $\bar{m}_q, T_d, R_d, u_d$ are used for the simulation of high-temperature heterogeneous reacting flows (see Chapter 7).

Numerical study of the effect of chemical composition of liquid phase on the evaporation process was performed. Parameters of the gas flow remained constant: $T_g = 1000$ K; $p = 0.1$ MPa; $V_g = 20\ m/s$. Calculations were made for a multicomponent (multifractional) mixture of hydrocarbons of various structures that are part of surrogate fuels.

Figure 6.6 illuminates variation of main parameters of the droplet over time: $\bar{m}_q = f(\tau)$, $R_d = f(\tau)$, $T_d = f(\tau)$.

The curves of the variation of relative masses of the fractions of liquid clearly illustrate the nature of evaporation of a multifractional droplet. The volatile compounds

Downloaded from https://www.cambridge.org/core. Nottingham Trent University, on 17 Aug 2019 at 02:08:15, subject to the Cambridge Core terms of use, available at https://www.cambridge.org/core/terms. https://doi.org/10.1017/9781108581714.006

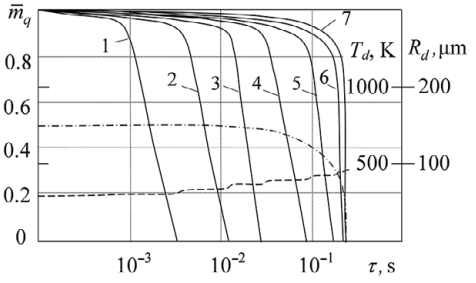

Figure 6.6 Variation of relative masses of fractions $\bar{m}_q$, temperature T_d and droplet radius R_d [(—) $-\bar{m}_q$]; [(---) $-T_d$]; [(—·—·) $-R_d$].

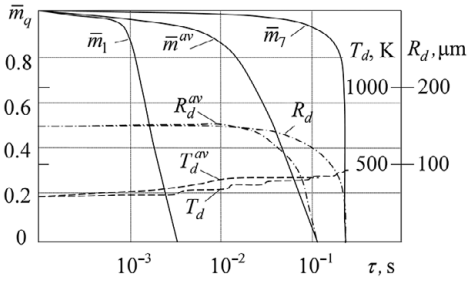

Figure 6.7 Variation of parameters of the droplet composed of seven fractions and homogeneous droplet with properties averaged over the fractions (—) $-\bar{m}_q$; (---) $-T_d$; (—·—·) $-R_d$; *av* – averaged parameters.

evaporate first, then the heavy fractions. The parameters of evaporation of different fractions largely depend on their individual properties: latent heat of evaporation, saturated vapor pressure, boiling point, etc.

At evaporation of droplets of complex composition, the individual fractions have a significant affect over the time and nature of the gasification of other fractions. As is known, liquids evaporate most intensively when reaching an equilibrium temperature. Therefore, when its equilibrium temperature is reached, the fraction begins to evaporate rapidly; causing the reduction to the minimum of the amount of heat consuming for the droplet heating. Consequently, the temperature and the rate of evaporation of the remaining fractions will not change significantly until the evaporating "in equilibrium conditions" fraction disappears. This circumstance does not allow the application of conventional methods for calculating the gasification of homogeneous liquids to the calculation of multifraction liquids, even in the case of averaging the properties of fractions.

Figure 6.7 shows the results of calculations of fractional composition of multifractional liquid (the graph demonstrates the evaporation curves for the first and last fractions) and also for a multifractional liquid – properties of which are averaged over seven fractions. The averaging was carried out by the method proposed in [231]. As can be seen from Figure 6.7, gasification of a droplet of a fractional composition requires much more time. The difference is not only in the absolute values of the time of a

Downloaded from https://www.cambridge.org/core. Nottingham Trent University, on 17 Aug 2019 at 02:08:15, subject to the Cambridge Core terms of use, available at https://www.cambridge.org/core/terms. https://doi.org/10.1017/9781108581714.006

complete evaporation for both cases, but also in the nature of the variation of the main parameters of a droplet: its temperature and radius.

Obviously, when dealing with gas–liquid flows, neglicting the previously features of the evaporation of droplets of multifractional composition could result in significant inaccuracies in calculation of composition and thermo-gasodynamic parameters of the flow as well.

Downloaded from https://www.cambridge.org/core. Nottingham Trent University, on 17 Aug 2019 at 02:08:15, subject to the Cambridge Core terms of use, available at https://www.cambridge.org/core/terms. https://doi.org/10.1017/9781108581714.006

Part III

Simulation of Combustion and Nonequilibrium Flows in Propulsion and Power Generation Systems

Downloaded from https://www.cambridge.org/core. Nottingham Trent University, on 17 Aug 2019 at 03:27:53, subject to the Cambridge Core terms of use, available at https://www.cambridge.org/core/terms. https://www.cambridge.org/core/product/D7299171573E1B0F33612F399FE03C10

Downloaded from https://www.cambridge.org/core. Nottingham Trent University, on 17 Aug 2019 at 03:27:53, subject to the Cambridge Core terms of use, available at https://www.cambridge.org/core/terms. https://www.cambridge.org/core/product/D7299171573E1B0F33612F399FE03C10

7 Simulation of High-Temperature Heterogeneous Reacting Flows

7.1 Features of Physicochemical Processes in Combustion and Flow of Heterogeneous Mixtures

In numerical analyses aimed at developing high-efficiency combustion chambers for various engines and thermal power systems, it is necessary to have an adequate understanding of hydrodynamic and chemical processes related to flowing, mixing, and combustion of two-phase fuels and oxidizers. The occurrence of such processes is described by the availability of zones differing in type, space, and time scale of these processes in the working volume.

The injection of liquid propellants through single injectors (nozzles) or sets of injectors (injector plates) into the combustion chambers of ICE, LPRE, ABE, gas generators, and furnaces may be an illustration of these processes. In the region of injection, the working medium's major characteristics are defined by processes of atomization, fragmentation of droplets, propellant jet impingement, droplet evaporation, possible chemical interaction between hypergolic and non-hypergolic components of propellant, reverse flows affecting the development of multiphase flows, ignition and combustion, etc. (Figure 7.1).

With the flow's further development, the processes of droplet heating and evaporation, turbulent mixing and turbulent diffusion, the ignition of fuel, and oxidizer mixture become the governing processes. The main interrelated processes in the developed combustion zone after a complete evaporation of liquid droplets, as well as gas dynamic processes, are chemical interaction and turbulent diffusion.

In the downstream region, the thermodynamic state of the working medium can approach that of chemical equilibrium, due – as a rule – to high temperatures. However, close to the comparatively cold walls of the combustion chambers, the working medium can have a notably lower temperature and differ markedly from the working medium in a core flow in chemical composition and thermodynamic properties.

Certain difficulties originate in the simulation of flow in the combustion chamber with swirling flow used to enhance the mixing and evaporation of propellant components, to decrease the combustion chamber length, and to equalize the temperature fields, as well as in the simulation of the flow in a channel with sudden expansion used to maintain stable combustion in the combustion chamber. Mathematical modeling acquires a considerable complexity in the simulation of secondary air injection in the dilution zone of ABE through the dilution holes [216, 234] or in the simulation of fuel or oxidizer injection in the ballasting zone of two-zone LGG (Chapter 8, [215]).

Downloaded from https://www.cambridge.org/core. Nottingham Trent University, on 17 Aug 2019 at 02:09:06, subject to the Cambridge Core terms of use, available at https://www.cambridge.org/core/terms. https://doi.org/10.1017/9781108581714.007

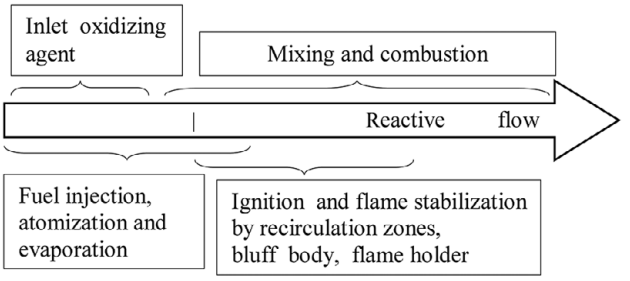
Inlet oxidizing agent
Mixing and combustion
Reactive flow
Fuel injection, atomization and evaporation
Ignition and flame stabilization by recirculation zones, bluff body, flame holder

Figure 7.1 Diagram of physicochemical processes.

Swirling flows differ from non-swirling flows by the existence of the velocity tangential component. Centrifugal forces related to this velocity component should be equalized by the pressure radial gradient that brings about a low pressure near the axis of the combustion chamber. A positive-pressure gradient will act on the working medium near the chamber axis downstream from the swirler. In case the value of this gradient is sufficient for changing the flow impulse axial component sign, then the flow rearrangement results in the development of the reverse flow near the axis. This zone stabilizes and intensifies the combustion process. In a channel with sudden expansion, the development of a flow pattern and combustion process is significantly influenced by the degree of the sudden expansion of the flow channel defining the peripheral recirculation zone size and shape, as well as heat transfer parameters and flame stabilization conditions.

Characteristcis of most combustion chambers or other working volumes of propulsion and power generation units are flows that, with some assumptions, may be considered as flows with prevalence of the axial component of the velocity of gas-phase reacting mixture in a core flow due to the prevailing axial direction of the bulk flow of the working medium. At the same time, as mentioned before, the development of the flow is accompanied by the formation of stable recirculation and mixing zones. Therefore, the processes in working volumes is characterized by gradients of parameters (chemical composition, temperature, etc.) of the working medium. Availability of dispersed evaporating liquid phase in gas flow is possible as well.

Wide ranges of temperature and pressure variation are characteristic in different regions of the flow, subject to the purpose and design of the combustion chambers. A nonequilibrium variation of chemical composition is also inherent in some regions (nearby wall layers, zones of intensive evaporation, and mixing, ballasting zones), and close to chemical equilibrium state is inherent in other regions. A notable degree of flow turbulization is possible. Local zones with an excess of hydrocarbon fuel (if used) can include the condensed soot particles.

It is obvious that the flow and combustion of two-phase mixtures comprises the entire spectrum of complex aerothermochemical processes, which requires the development of reliable and adequate mathematical models since, in the end, the character of the processes defines the operational parameters of propulsion and power generation units.

One of the features of the simulation of high-temperature processes in different combustion chambers is that sometimes with minor variations of working process

Downloaded from https://www.cambridge.org/core. Nottingham Trent University, on 17 Aug 2019 at 02:09:06, subject to the Cambridge Core terms of use, available at https://www.cambridge.org/core/terms. https://doi.org/10.1017/9781108581714.007

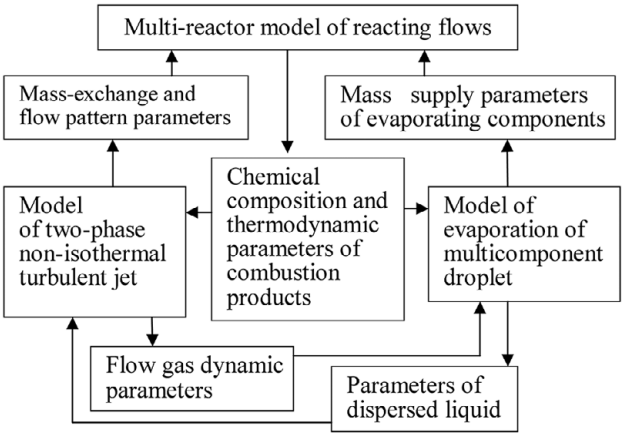
Multi-reactor model of reacting flows
Mass-exchange and flow pattern parameters
Mass supply parameters of evaporating components
Chemical composition and thermodynamic parameters of combustion products
Model of two-phase non-isothermal turbulent jet
Model of evaporation of multicomponent droplet
Flow gas dynamic parameters
Parameters of dispersed liquid

Figure 7.2 Diagram of comprehensive model.

organization, even for the same chamber, essential changes of the physical scheme and mathematical description, as well as subsequent computer code upgrades, may be required. Therefore, a more universal approach to the simulation is the modular principle in which the base model (Section 2.1) may be supplemented by mathematical models of accompanying processes typical for the specific high-temperature unit. An example of such an approach based on the reactor model proposed in Chapter 1 is shown in Figure 7.2.

Here, the model of the system of PSR (Sections 1.1 and 1.5) is applied as the base model. On the basis of the preliminary gas dynamic calculations and analysis, the chamber working volume is split into a series of interrelated reaction volumes (reactors) wherein local homogeneity of the working medium is assumed. The variation of reacting mixture state parameters in every volume is caused by the chemical interaction between the gas mixture components, convective and diffusion heat and mass exchange with neighboring volumes (reactors) and the external medium, heat and mass exchange between the gas phase and the disperse phase, and mass feed of individual components from the evaporation surfaces.

A typical diagram of the working process in a combustion chamber wherein propellant components (oxidizer in the gas phase and fuel in the liquid phase) are injected through the hollow post and sleeve element (single stream-impinging injector) [215] of the injector plate is shown in Figure 7.3.

The analyzed flow region is limited by the axially symmetric surface that may be conditional at the calculation of the flow formed by the set of mixing elements injectors. In this case, for each element, it is supposed that the processes occurring in the flow are identical; therefore, one can consider the flow formed by a single injector. A turbulent jet with different-sized droplets is formed at the injector exit. The gas phase component flows at a high speed while the liquid component flows far more slowly and the differential velocity causes a shear action, which breaks up the liquid stream into droplets. When jets interact with the channel walls and between themselves, regions of recirculation flows are formed.

Downloaded from https://www.cambridge.org/core. Nottingham Trent University, on 17 Aug 2019 at 02:09:06, subject to the Cambridge Core terms of use, available at https://www.cambridge.org/core/terms. https://doi.org/10.1017/9781108581714.007

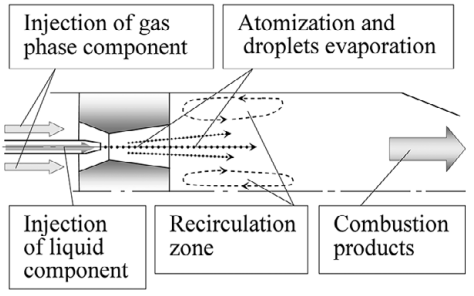

Figure 7.3 Diagram of the processes in combustion chamber.

In the steady-state operating mode, the combustion products are admixed the developed combustion zone by reverse flows to the jet to heat and evaporate the liquid droplets.

Typical modes of working processes are characterized by sufficiently high relative velocities of the liquid droplets. Therefore, that the existence of individual flame fronts around the droplets is unlikely, and that combustion occurs in the interdroplet space, is a regular assumption that is widespread in the simulation of the combustion of dispersed gas–liquid mixtures. Chemical reactions proceed at rates far higher than evaporation rates. This is why evaporation is a constricting process defining the other stages of the working process and its completeness as a whole. With droplet evaporation, the gas mixture temperature varies. Some regions of the flow have relatively low temperatures, which is why chemical equilibrium in the reacting mixture may fail to settle.

Technical problems of the solution of the system of equations that provide the unified description of processes (Section 2.3) are well known; this is why it is advisable to divide the general problem into partial problems corresponding to separate physico-chemical processes.

A complex model integrates the models of three main processes:

– the development of a two-phase turbulent nonisothermal jet;
– the evaporation of multicomponent fluid droplets;
– the chemically reacting flow.

This approach allows a sufficiently efficient allowance for the mutual influence of the governing processes. A general algorithm of the analysis consists in the sequential iterative solution of separate individual problems. Unknown parameters obtained in the solution of the system of equations of every separate model are used as input parameters necessary for calculation of unknown parameters in the other models.

7.2 Model of Two-Phase Nonisothermal Jet in a Channel with Sudden Expansion

The model analyzes the axial-symmetric reacting jet flowing from a single hollow post and sleeve element (stream-impinging injector; Figure 7.4). The flow is assumed to be

Downloaded from https://www.cambridge.org/core. Nottingham Trent University, on 17 Aug 2019 at 02:09:06, subject to the Cambridge Core terms of use, available at https://www.cambridge.org/core/terms. https://doi.org/10.1017/9781108581714.007

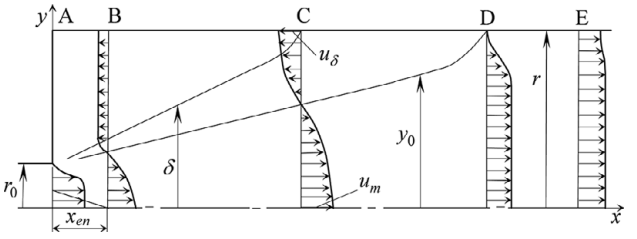

Figure 7.4 Gas mixture flow diagram.

constricted by a conditional cylindrical wall without friction and heat exchange between the flow and the wall. The development of the gas–fluid jet is accompanied by the onset of the steady reverse flow region, the mass supply from evaporating droplets, and the variation of gas temperature and density in axial and radial directions. The gas prevails over the considered volume.

Flow development occurs within the BE main section conditionally divided into three characteristic regions – i.e., BC is the flow separation region, CD is the flow attachment region, and DE is the developed flow region. The reverse flow exists in the separation region near the wall with constant radial velocity varying over the channel length. The flow attachment occurs downstream from cross section C, given the availability of the reverse flow. The velocity changes the direction downstream from cross section D while the flow velocity moves into alignment in the channel cross section. The length of entrance region x_{en} is assumed to be negligibly small compared to the developed region length because of a small diameter of the nozzle compared to the chamber length.

Usually, to calculate turbulent separating flows and jet flows, the Navier–Stokes equations, are used. For example, the paper [235] provides the derivation of continuity and the momentum equations for the adjoined turbulent single-phase flows. Equations describing axial-symmetric flows written in the boundary layer approximation with the application of Cartesian coordinates (x, y) without allowance for body forces have the following form:

$$\frac{\partial}{\partial x}(y\rho u) + \frac{\partial}{\partial y}(y\overline{\rho v}) = 0, \tag{7.1}$$

$$\rho u\frac{\partial u}{\partial x} + \overline{\rho v}\frac{\partial u}{\partial y} = -\frac{\partial p}{\partial x} + \frac{1}{y}\frac{\partial}{\partial y}\left[y\left(\mu\frac{\partial u}{\partial y} - \rho\overline{u'v'} - \overline{\rho' u' v'}\right)\right], \tag{7.2}$$

where ρ, u, v are time-averaged values of density and velocity vector components in the axial (x) and radial (y) directions; ρ', u', v' are turbulent fluctuation terms; p is pressure; μ is dynamic viscosity; and $\overline{\rho v}$ is the reduced notation of the parameter $\rho v + \overline{\rho' v'}$.

Hereinafter, the equations of motion do not allow for fluctuation term $\overline{\rho' u' v'}$, and, as in [235], the abridged notation is used:

$$\tau = \mu\frac{\partial u}{\partial y} - \rho\overline{u'v'}. \tag{7.3}$$

Downloaded from https://www.cambridge.org/core. Nottingham Trent University, on 17 Aug 2019 at 02:09:06, subject to the Cambridge Core terms of use, available at https://www.cambridge.org/core/terms. https://doi.org/10.1017/9781108581714.007

In the formation of continuity and momentum equations with the allowance for a dispersed phase, the following additional assumptions have been used. Liquid component droplets feature a spherical shape. The concept of groups is used for liquid droplets of different sizes. Droplets of each group feature equal parameters – e.g., diameter, temperature, velocity, etc. Coagulation and secondary atomization of droplets during their motion are not allowed. Instant velocities of the dispersed phase equal the averaged values. Turbulent transfer of droplets' mass and droplets' moment of momentum are not taken into account. The gas phase and liquid droplet velocities differ in the initial cross section of the jet. It may be assumed that the evaporation rate is sufficiently high, and then the majority of droplets evaporate within the BD region. This ensures a sufficiently high temperature of the gas mixture in the reverse flow region to facilitate the stable ignition of the injected jet. The reverse flow region has no dispersed liquid phase. Gas mixture state parameters are identical in the entire region of reverse flow.

Continuity and momentum equations of the axial-symmetric two-phase jet are written with due allowance for the interaction between the gas and dispersed phases and liquid droplet evaporation:

$$\frac{\partial}{\partial x}(\rho u c) + \frac{1}{y}\frac{\partial}{\partial y}(y\overline{\rho v}c) = \sum_{sd=1}^{n_s} S_{sd}, \tag{7.4}$$

$$\rho u c\frac{\partial u}{\partial x} + \overline{\rho v}c\frac{\partial u}{\partial y} = -\frac{\partial p}{\partial x} + \frac{1}{y}\frac{\partial}{\partial y}(y\tau c) - \sum_{sd=1}^{n_s}\left(\frac{F_{x\,sd}c_{sd}}{V_{sd}} + S_{sd}(u - u_{sd})\right), \tag{7.5}$$

where ρ is the gas phase density; u, v are gas velocity vector components in the axial and radial directions; c, c_{sd} are the relative volume flow rates of the gas and dispersed phase in the elementary volume; S_{sd} is the amount of substance evaporated from the surface of the sdth group of droplets; n_s is the number of droplet groups; u_{sd} is the axial component of the sdth group droplet velocity; and V_{sd} is the volume of the droplet of the sdth group.

The projection of the vector of force acting on the sdth group droplets is described by the following formula:

$$F_{xsd} = 0.5C_{xsd}\pi R_{sd}^2\rho(u - u_{sd})|u - u_{sd}|, \tag{7.6}$$

where C_{xsd} is the drag coefficient for the droplet of the sdth group, and R_{sd} is the radius of the droplet of the sdth group.

The following ratio is valid for relative volume flow rates of the gas and dispersed phases:

$$c + \sum_{sd=1}^{n_s} c_{sd} = 1. \tag{7.7}$$

In compliance with [53], let us present the profile of shear stress in the jet cross section as a polynomial:

$$\tau = a_0 + a_1 y + a_2 y^2 + a_3 y^3, \tag{7.8a}$$

Downloaded from https://www.cambridge.org/core. Nottingham Trent University, on 17 Aug 2019 at 02:09:06, subject to the Cambridge Core terms of use, available at https://www.cambridge.org/core/terms. https://doi.org/10.1017/9781108581714.007

$$\frac{\partial \tau}{\partial y} = a_1 + 2a_2 y + 3a_3 y^2. \tag{7.8b}$$

Coefficients of the polynomial are defined by the boundary conditions at the jet axis and the external boundary of the layer of mixing:

(a) $\tau = 0$

(b)
$$\left(\frac{\partial \tau}{\partial y}\right)_{y=0} = \rho_m u_m \frac{\partial u_m}{\partial x} + \sum_{sd=1}^{n_s} \left[F_{xsd} \frac{c_{sd}}{V_{sd} c_m} + \frac{S_{sd}}{c_m}(u_m - u_{sd})\right] - \left(\frac{\tau}{y}\right)_{y=0} + \frac{\partial p}{\partial x} \tag{7.9}$$

at $y = 0$;

(c) $\tau = 0$ (d) $d\tau/dy = 0$ at $y = \delta$.

Expression (a) follows from the conditions of symmetry on the jet axis; expression (b) results from Equation (7.5); expressions (c) and (d) are obtained proceeding from the assumption that, for the reverse flow, the Bernoulli equation is obeyed.

If we substitute boundary conditions (7.9) in Formulas (7.8a) and (7.8b), the expression for coefficients of polynomial will result in the following:

$$a_0 = 0, a_1 = \left(\frac{\partial \tau}{\partial y}\right)_{y=0}, a_2 = -\frac{2}{\delta}\left(\frac{\partial \tau}{\partial y}\right)_{y=0}, a_3 = \frac{1}{\delta^2}\left(\frac{\partial \tau}{\partial y}\right)_{y=0}. \tag{7.10}$$

By substituting these coefficients in (7.8a) and performing simple transformations with the application of dimensionless coordinate $\eta = y/\delta$, the expression for the shear stress profile will get the following form:

$$\tau = \left\{\rho_m u_m \frac{\partial u_m}{\partial x} - \left(\frac{\tau}{y}\right)_{y=0} + \frac{\partial p}{\partial x} + \sum_{sd=1}^{s} \left[F_{xsd} \frac{c_{sd}}{V_{sd} c_m} + \frac{S_{sd}}{c_m}(u_m - u_{sd})\right]\right\} \delta \eta (1-\eta)^2. \tag{7.11}$$

The relationship for the profile of average velocity across the flow u depending on the shear stress profile τ can be obtained with the allowance for the Boussinesq hypothesis and the application of the concepts of turbulent and molecular components of kinematic viscosity:

$$\tau = \rho(\nu_t + \nu)\frac{\partial u}{\partial y} = \rho(\nu_t + \nu)\frac{\partial u}{\delta \partial \eta}, \tag{7.12}$$

where ν_t, ν are turbulent and molecular components of kinematic viscosity, respectively.

Equating the left-hand sides of Equations (7.11) and (7.12) results in the following expression:

$$\partial u = \frac{\delta^2}{(\nu_t + \nu)} \left\{\rho_m u_m \frac{\partial u_m}{\partial x} - \left(\frac{\tau}{y}\right)_{y=0} + \frac{\partial p}{\partial x} + \sum_{sd=1}^{n_s} \left[F_{xsd} \frac{c_{sd}}{V_{sd} c_m} + \frac{S_{sd}}{c_m}(u_m - u_{sd})\right]\right\} \times \frac{\eta(1-\eta)^2}{\rho} \partial \eta. \tag{7.13}$$

Downloaded from https://www.cambridge.org/core. Nottingham Trent University, on 17 Aug 2019 at 02:09:06, subject to the Cambridge Core terms of use, available at https://www.cambridge.org/core/terms. https://doi.org/10.1017/9781108581714.007

Integration of Equation (7.13) from 0 to η and from 0 to $\eta = 1$ brings about the following expressions:

$$u - u_m = \frac{\delta^2}{(\nu_t + \nu)} \left\{ \rho_m u_m \frac{\partial u_m}{\partial x} - \left(\frac{\tau}{y}\right)_{y=0} + \frac{\partial p}{\partial x} + \sum_{sd=1}^{n_s} \left[F_{x\,sd} \frac{c_{sd}}{V_{sd} c_m} + \frac{S_{sd}}{c_m} (u_m - u_{sd}) \right] \right\} \times \int_0^{\eta} \frac{\eta}{\rho} (1-\eta)^2 d\eta; \tag{7.14}$$

$$u_\delta - u_m = \frac{\delta^2}{(\nu_t + \nu)} \left\{ \rho_m u_m \frac{\partial u_m}{\partial x} - \left(\frac{\tau}{y}\right)_{y=0} + \frac{\partial p}{\partial x} + \sum_{sd=1}^{n_s} \left[F_{x\,sd} \frac{c_{sd}}{V_{sd} c_m} + \frac{S_{sd}}{c_m} (u_m - u_{sd}) \right] \right\} \times \int_0^{1} \frac{\eta}{\rho} (1-\eta)^2 d\eta. \tag{7.15}$$

Dividing (7.14) by (7.15) will result in the expression describing the velocity profile in the jet cross section:

$$u = u_m + (u_\delta - u_m) \int_0^{\eta} \frac{\eta}{\rho} (1-\eta)^2 d\eta \Big/ \int_0^{1} \frac{\eta}{\rho} (1-\eta)^2 d\eta. \tag{7.16}$$

Application of Equation (7.16) allows us to obtain the following expression of the derivative:

$$\frac{\partial u}{\partial y} = \frac{\partial u}{\delta \partial \eta} = \frac{1}{\delta \rho} (u_\delta - u_m) \eta (1-\eta)^2 \Big/ \int_0^{1} \frac{\eta}{\rho} (1-\eta)^2 d\eta, \tag{7.17}$$

which – along with (7.12) – evaluates the relationship for $\left(\frac{\tau}{y}\right)_{y=0}$:

$$\left(\frac{\tau}{y}\right)_{y=0} = \left(\rho(\nu_t + \nu) \frac{\partial u}{\delta^2 \partial \eta}\right)_{\eta=0} = \frac{1}{\delta^2} (\nu_t + \nu)(u_\delta - u_m) \Big/ \int_0^{1} \frac{\eta}{\rho} (1-\eta)^2 d\eta. \tag{7.18}$$

After substituting (7.18) in (7.15) and simple transformations, the resulting equation describes the gas velocity variation along the jet axis:

$$\frac{\partial u_m}{\partial x} = -\frac{2(u_m - u_\delta)(\nu_t + \nu)}{\rho_m u_m \delta^2 \int_0^1 \frac{\eta}{\rho} (1-\eta)^2 d\eta} - \frac{1}{\rho_m u_m c_m} \left(\frac{\partial p}{\partial x} + \sum_{sd=1}^{n_s} \left(\frac{F_{xsd} c_{sd}}{V_{sd}} + S_{sd} (u_m - u_{sd}) \right) \right). \tag{7.19}$$

The mixing layer boundary δ and reverse flow velocity u_δ written for the streamline on the jet axis are the external parameters in Equation (7.19). To calculate these values, the integral approach may be used. Integral equations of conservation of mass

Downloaded from https://www.cambridge.org/core. Nottingham Trent University, on 17 Aug 2019 at 02:09:06, subject to the Cambridge Core terms of use, available at https://www.cambridge.org/core/terms. https://doi.org/10.1017/9781108581714.007

flow and momentum written with allowance for dimensionless coordinate η, have the following form:

$$2\pi\delta^2\int_0^1\rho uc\eta d\eta+\pi\left(r_k^2-\delta^2\right)\rho_\delta u_\delta=\dot{m}_0+\sum_{sd=1}^{n_s}\left(\dot{m}_{0sd}-\dot{m}_{sd}\right),\tag{7.20}$$

$$2\pi\delta^2\int_0^1\rho u^2c\eta d\eta+\pi\left(r_k^2-\delta^2\right)\rho_\delta u_\delta^2=2\pi r_0^2\int_0^1\rho u_0^2c\eta d\eta+\sum_{sd=1}^{n_s}\left(\dot{m}_{0\,sd}u_{0\,sd}-\dot{m}_{sd}u_{sd}\right),\tag{7.21}$$

where $\dot{m}_0$ is the gas mass flow rate at the entrance to the channel; $\dot{m}_{0sd}, u_{0sd}$ are the mass flow rate and velocity of the droplets of the sdth group at the entrance to the channel; and $\dot{m}_{sd}, u_{sd}$ are the mass flow rate and velocity of the droplets of the sdth group at an arbitrary section of the jet.

The algorithm for the solution of Equations (7.16), (7.19), (7.20), and (7.21) that describes the flow's main parameters – i.e., profile of velocity in cross section $u(\eta)$, velocity at the jet axis u_m, reverse flow velocity u_δ, and thickness of the layer of mixing δ – is given in Section 7.4.

7.3 Multireactor Model of Reacting Flow

In compliance with the scheme of the two-phase nonisothermal jet flowing from the stream-impinging injector (Section 7.2) and the need in simulation of parameters along the jet flow and in the reverse flow region (recirculation zone), the main flow is simulated by the set of PSRs arranged in a series along the flow axis.

The outer boundary of axial reactors in the recirculation zone region (BD) is composed by the line of zero-axial components of the velocities and the channel conditional wall being located beyond the recirculation zone (DE). The recirculation zone is identified by a single annular reactor (R) with its inner boundary aligned with the outer boundary of the axial reactors (Figure 7.5).

Gas phase state parameters' variation in every axial reactor occurs due to evaporation of droplets, chemical reactions, and mass exchange with axial reactors. Mass supply

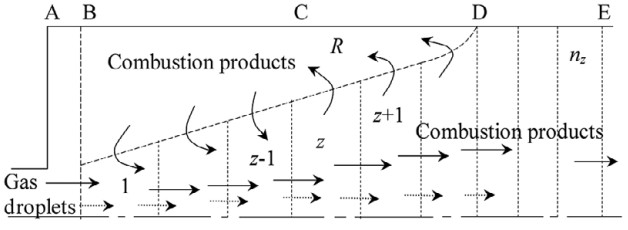

Figure 7.5 Diagram of the arrangement of reactors.

Downloaded from https://www.cambridge.org/core. Nottingham Trent University, on 17 Aug 2019 at 02:09:06, subject to the Cambridge Core terms of use, available at https://www.cambridge.org/core/terms. https://doi.org/10.1017/9781108581714.007

into the annular peripheral reactor (the zone of reverse flow) is carried out from reactors in the flow attachment region (CD) while mass discharge is realized in the flow separation region (BC). Entrainment of liquid drops in the reverse flow region is hardly probable because of the prevailing axial direction of the current. Therefore, the reacting mixture in the annular reactor is considered a homogeneous one.

Unknown parameters for every reactor z in the most general case are considered to be concentrations of individual substances in logarithms of mole fractions γ_{iz} (Section 2.1), mass M_z, enthalpy h_z, and temperature T_z of the reacting mixture.

The basic mathematical model is composed of universal equations of chemical kinetics (2.31) as well as normalizing equations (2.157) and calorific equations (2.149) written for every reactor.

However, the following equations of chemical kinetics differ slightly from Equations (2.31) because of the separation of the terms responsible for chemical reactions and the terms related to mass-exchange reactions.

$$\frac{d\gamma_{iz}}{d\tau} = -\,exp\left(\gamma_{iz}\right)\left(\sum_j \nu_{ij}\Omega_{jz} + S_{iz}^{+}\frac{R_0 T_z}{p_z}, -S_{iz}^{-}\,exp\left(-\gamma_{iz}\right)\right) + \sum_q\left(\sum_j \nu_{qj}\Omega_{jz} + S_{qz}^{+}R_0 T_z/p_z - S_{qz}^{-}\,exp\left(-\gamma_{qz}\right)\right), \tag{7.22}$$

where $\Omega_{jz} = k_{jz}\left(p_z/R_0 T_z\right)^{\bar{m}j}\,exp\left(-\sum_p n_{pj}\gamma_{pz}\right)$;
$z = 1, \ldots, n_z$; n_z is the number of reactors; and S_i^{+}, S_i^{-} are the total rates of mass supply in the reactor and mass discharge from the reactor of specie i, respectively.

The main principles of simulation of mass supply and mass discharge reactions are described in Section 2.2. The total rate of mass supply of the gas mixture in reactor z from neighboring reactors and the external medium is given by

$$S_{iz}^{+} = \sum_{js}\left(\dot{m}_{js,z}^{+} r_{ijs}/\left(\mu_{js}V_z\right)\right)10^{-3}\left[\mathrm{mol/cm^3{\cdot}s}\right], \tag{7.23}$$

where r_{ijs} is the mole fraction of specie i supplied by from the source js.

The rate of the supply of specie i – including evaporation of liquid phase, diffusion, etc. – is given by

$$S_{iz}^{+} = \left(\dot{m}_i^{+}/(\mu_i V_z)\right)10^{-3}\ \ \left[\mathrm{mol}/\left(\mathrm{cm^3{\cdot}s}\right)\right]. \tag{7.24}$$

Bulk consumption of gas mixture $\dot{m}_z$ from reactor z does not affect the variation of concentrations of individual substances in the reactor; therefore, S_{iz}^{-} should be calculated in a case of individual discharge of specie i (for instance, at evaporation or condensation):

$$S_{iz}^{-} = \left(\dot{m}_i^{-}\mu_z/(M_z\mu_i r_{iz})\right)10^{-3}[1/\mathrm{s}]. \tag{7.25}$$

The derivation of equations of accompanying processes (Section 2.1) proceeds from the mass conservation law and the first law of thermodynamics for exposed systems

Downloaded from https://www.cambridge.org/core. Nottingham Trent University, on 17 Aug 2019 at 02:09:06, subject to the Cambridge Core terms of use, available at https://www.cambridge.org/core/terms. https://doi.org/10.1017/9781108581714.007

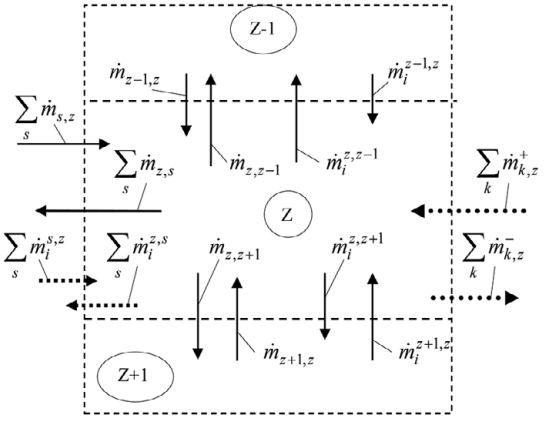

Figure 7.6 Diagram of mass-exchange processes.

with variable mass and volume. In writing the equation of gas mixture mass variation in reactor z, the scheme of mass exchange processes that is used is given in Figure 7.6.

This scheme uses

- $\sum \dot{m}_{s,z}$, $\sum \dot{m}_{z,s}$, $\dot{m}_{z-1,z}$, $\dot{m}_{z,z-1}$, $\dot{m}_{z+1,z}$, $\dot{m}_{z,z+1}$ – gas mixture mass flow rates describing the reactor z mass exchange with the other reactors and environment, where index s indicates both external objects and the other PSRs (apart from $z-1$ and $z+1$ neighboring reactor z)
- $\sum \dot{m}_i^{s,z}$, $\sum \dot{m}_i^{z,s}$, $\dot{m}_i^{z-1,z}$, $\dot{m}_i^{z,z-1}$, $\dot{m}_i^{z+1,z}$, $\dot{m}_i^{z,z+1}$ – mass flow rates of individual substance i caused by evaporation and diffusion
- $\sum \dot{m}_{k,z}^{+}$, $\sum \dot{m}_{k,z}^{-}$ – mass flow rates of dispersed liquid phase in the reactor z and out of the reactor, respectively.

In compliance with the accepted scheme of mass variation equations for gas mixture M_z for every reactor, these feature the following form:

$$dM_z/\mathrm{d}\tau = \sum_{js} \dot{m}_{js,z}^{+} + \sum_{k} \left(\dot{m}_{k,z}^{+} - \dot{m}_{k,z}^{-}\right) + A_z - \dot{m}_z, \tag{7.26}$$

where $\sum_{js} \dot{m}_{js,z}^{+} = \sum_s \dot{m}_{s,z} + \dot{m}_{z-1,z} + \dot{m}_{z+1,z}$; A_z is the term to allow for peculiarities of mass exchange of reactor z with the other reactors and external medium at supply of individual components i;

$A_z = \sum_i \left(\sum_s \dot{m}_i^{s,z} + \dot{m}_i^{z-1,z} + \dot{m}_i^{z+1,z} - \sum_s \dot{m}_i^{z,s} - \dot{m}_i^{z,z-1} - \dot{m}_i^{z,z+1}\right)$; $\dot{m}_z$ is the total mass flow rate of gas mixture from the reactor (without allowance for mass exchange of individual components);

$$\dot{m}_z = \sum_s \dot{m}_{z,s} + \dot{m}_{z,z-1} + \dot{m}_{z,z+1}.$$

The derivation of gas mixture enthalpy variation in reactor z is based on the first law of thermodynamics. In the case of the exposed system of variable mass and volume, the energy conservation law is written as follows:

Downloaded from https://www.cambridge.org/core. Nottingham Trent University, on 17 Aug 2019 at 02:09:06, subject to the Cambridge Core terms of use, available at https://www.cambridge.org/core/terms. https://doi.org/10.1017/9781108581714.007

$$\frac{d(M_z u_z)}{d\tau} = \sum_{js} \dot{m}^{+}_{js,z} h_{js} + \sum_{k} \left(\dot{m}^{+}_{k,z} h^{+}_{k} - \dot{m}^{-}_{k,z} h^{-}_{k} \right) - p_z \frac{dV_z}{d\tau} \pm \frac{dQ_z}{d\tau} + B_z, \tag{7.27}$$

where u_z is the specific internal energy of the gas mixture; h_{js} is the specific enthalpy of the gas mixture fed into reactor z from some source js; h^{+}_{k}, h^{-}_{k} is the specific enthalpy of the dispersed phase at the reactor inlet and outlet, respectively; p_z is gas pressure; V_z is reactor volume; $\frac{dQ_z}{d\tau}$ is quantity of heat received (lost) by the reactor due to conduction; and B_z is the term to allow for energy fed into and discharged from the reactor with the flows of individual substances:

$$B_z = \sum_{i} \left(\sum_{s} \dot{m}^{s,z}_{i} h^{s}_{i} + \dot{m}^{z-1,z}_{i} h^{z-1}_{i} + \dot{m}^{z+1,z}_{i} h^{z+1}_{i} - \sum_{s} \dot{m}^{z,s}_{i} h^{z}_{i} - m^{z,z-1}_{i} h^{z}_{i} - \dot{m}^{z,z+1}_{i} h^{z}_{i} \right).$$

After simple transformations of Equation (7.27) with the application of mass variation equation (7.26) and the differential form of the expression defining the gas mixture's specific enthalpy variation,

$$\frac{du_z}{d\tau} = \frac{dh_z}{d\tau} - \frac{d\left(p_z V_z / M_z\right)}{d\tau}, \tag{7.28}$$

the equation of gas mixture enthalpy variation in reactor z results:

$$\frac{dh_z}{d\tau} = \left(\sum_{js} \dot{m}^{+}_{js,z} \left(h_{js} - h_z\right) + \sum_{k} \left(\dot{m}^{+}_{k,z} \left(h^{+}_{k} - h_z\right) + \dot{m}^{-}_{k,z} \left(h_z - h^{-}_{k}\right) \right) + C_z + V_z \frac{dp_z}{d\tau} \pm \frac{dQ_z}{d\tau} \right) / M_z, \tag{7.29}$$

where $C_z = B_z - A_z h_z$.

Eventually, the kinetic multireactor model is described by the system of equations (7.22), (2.157), (2.149), (7.26), and (7.29). The system of equations is opened to allow supplementation with other accompanying equations to describe the variation of some parameters caused by specific features of processes in the combustion chamber. For example, when necessity in the allowance for pressure variation during combustion, which can be taken as equal for several reactors $p_z = p$ in compliance with the previously described physical scheme, the mathematical model can be supplemented with the algebraic equation for the calculation of gas mixture pressure:

$$p - \left(\sum_{z} M_z \right) / \left(\sum_{z} \left(V_z / R_z T_z \right) \right) = 0. \tag{7.30}$$

The basic model thus supplemented represents a complex model for the calculation of unknowns $X_z = \left[\gamma_{iz}, T_z, M_z, h_z, p\right]$ for every reactor.

Thus, along with some forms of reacting mixture combustion and flow presented in Chapters 4 and 5, the model of heterogeneous reacting flows represents a typical scheme and mathematical model to be used as a basis for simulation of chemically nonequilibrium processes in various combustion units.

Downloaded from https://www.cambridge.org/core. Nottingham Trent University, on 17 Aug 2019 at 02:09:06, subject to the Cambridge Core terms of use, available at https://www.cambridge.org/core/terms. https://doi.org/10.1017/9781108581714.007

7.4 Numerical Study of Heterogeneous Reacting Flows

Calculations start with the analysis of the gas dynamic flow pattern and the calculation of gas dynamic parameters in the region of flow separation. We'll call this stage i. Calculation begins with the determination of parameters in the region of flow separation (Section 7.2). Parameters of the disperse phase and gas temperature distribution are set with the help of approximating relationships on the basis of available experimental or theoretical data. In the first step, the gas flow axial velocity values u_m are considered preset. Velocities of reverse flows u_δ, profile of the velocities across the jet flow $u(\eta)$, and thickness of mixing layer δ (Figure 7.4) are calculated on the basis of axial velocities. Then, the fourth-order Runge–Kutta method with fixed time step (see Section 2.3) is used for the solution of Equation (7.19).

The calculation of integrals in Equations (7.16), (7.20), and (7.21) is performed by the Simpson method. The solution of Equations (7.20) and (7.21) for determination of unknown values δ and u_δ is performed by the method of iterations.

Estimated velocities of the gas and gas temperature distribution are used in the calculation of liquid droplet evaporation (stage ii). Equations describing multicomponent droplet evaporation (Section 6.3) are solved by Pirumov's implicit finite-difference method with application of Newton's iterative scheme (Section 2.3). To determine spatial coordinate of droplet $x(\tau)$ at its motion in the gas flow, the relation $dx = u(\tau)d\tau$ is used.

Relationship $C_x = f_{vap}C_{x0}(Re)$ (where $C_{x0}(Re)$ is the empirical term for the nondeformable spherical particle and f_{vap} is the coefficient allowing for evaporation effects) is usually employed for the calculation of evaporating droplet drag coefficient (Formula 7.6). In most cases, the evaporation of a moving droplet causes the decrease in drag coefficient. Some compensating effect on its actual value is brought about by the droplet deformation that causes the increase in C_x. In the absence of valid information on multicomponent droplet evaporation's influence on drag coefficient, it is appropriate to assume that $f_{vap} = 1$. To define the value $C_{x0}(Re)$, the relation taken in [236] – $C_{x0} = \left(24/Re_d + 5.48/Re_d^{0.573} + 0.36\right)(1 + B_m)^{-0.2}$ – may be used, where B_m is the mass transfer number.

Results of calculations of gas-dynamic parameters (stage i) are used for the conditional separation of the flow into the system of reactors for the determination of mass exchange characteristics between the reactors. The results of the calculation of evaporation (stage ii) are used to determine the mass supply of evaporating components in axial reactors. Then the initial iteration is performed on the basis of calculation of chemical equilibrium composition and temperature. In stage iii, the equations of the reacting mixture parameters' variation in the system of reactors (Section 7.3) are solved by Pirumov's implicit finite-difference method with the application of Newton's iterative scheme (see Section 2.3).

Calculations in stages i, ii, and iii represent a cyclic and iterative process. The necessity of re-execution of every cycle of calculations is defined by the comparison of the results of the current and previous cycles of calculations of unknown parameters such as gas temperature and chemical composition of reacting products at the channel

Downloaded from https://www.cambridge.org/core. Nottingham Trent University, on 17 Aug 2019 at 02:09:06, subject to the Cambridge Core terms of use, available at https://www.cambridge.org/core/terms. https://doi.org/10.1017/9781108581714.007

exit and distance required for complete evaporation of all droplets of liquid component. Calculation terminates when the relative change of these parameters becomes smaller than 1%.

An important problem to be solved by the developed model of evaporation of multicomponent fluid droplets and the reacting flow multireactor model (Sections 6.3 and 7.1–7.3) is the prediction of parameters of the working medium to optimize a combustion chamber's design and operation. For example, the impact of the analysis of geometrical dimensions on the ignition and combustion stability are of undoubted practical interest.

7.4.1 Generation of High-Temperature Gas at the Combustion of Hydrocarbon Fuel; Optimization of Combustion Chamber Parameters

The complex model for the simulation of evaporation of multicomponent fluid and the multireactor model of reacting flows may be exemplified by the application of this model to optimize parameters of the combustion chamber designed for the generation of high-temperature gas at combustion of hydrocarbon fuel with air. The combustion chamber of the heat gas and steam gas generator with an operation scheme corresponding to that given in Figure 7.4 features the following characteristics: inner diameter of combustion chamber – 75 mm; injector nozzle exit diameter – 8 mm, number of injectors – 6, equivalent diameter of conditional channel per single injector – 30.6 mm, conditional channel sudden expansion degree $\bar{r} = r/r_0 = 30.6/8 = 3.825$. Basic operating parameters of the gas generator are the following: flow rate of combustion products – 0.28 kg/s; pressure – 3.5 MPa.

The mixing elements are Laval nozzle–type injectors. Liquid component injection in the air flow in such injectors is arranged in the nozzle throat. The liquid propellant atomization pattern is assumed to be discrete with the division of all droplets into three groups with the following diameters and mass flow rates: $d_1 = 10\ \mu m$, $G_1 = 0.1$; $d_2 = 20\ \mu m$, $G_2 = 0.7$; $d_3 = 70\ \mu m$, $G_3 = 0.2$.

Multicomponent fuel is represented by the mixture (volume concentrations) of methane series of hydrocarbons $C_{10}H_{22}$ – 10%; $C_{11}H_{24}$ – 15%; $C_{12}H_{26}$ – 20%; $C_{13}H_{28}$ – 20%; $C_{14}H_{30}$ – 15%; $C_{15}H_{32}$ – 10%; $C_{16}H_{34}$ – 10%. The kinetic mechanism cited in [55] has been used in the calculations. The reaction mechanism comprised 249 reversible elementary reactions involving 67 species including original reactants and intermediate and final combustion products. The calculations used rate constants involving the species that contained C, H, and O atoms recommended in [22]. The rate constants used in [237] were selected for reactions involving particles of N, O, and H.

Gas temperature variation along the axis of the flow developed by a single injector and the variation of the relative total flow rate of liquid fuel $\bar{m}_\Sigma$ for two chemical interaction models are shown in Figure 7.7. The first study was made on the assumption of chemical equilibrium (line 1). The second study allowed for nonequilibrium variation of the working medium's chemical composition (line 2).

Gas mixture temperature variation along the single injector axis reflects the liquid droplet evaporation pattern and combustion products entrainment from the zone of

Downloaded from https://www.cambridge.org/core. Nottingham Trent University, on 17 Aug 2019 at 02:09:06, subject to the Cambridge Core terms of use, available at https://www.cambridge.org/core/terms. https://doi.org/10.1017/9781108581714.007

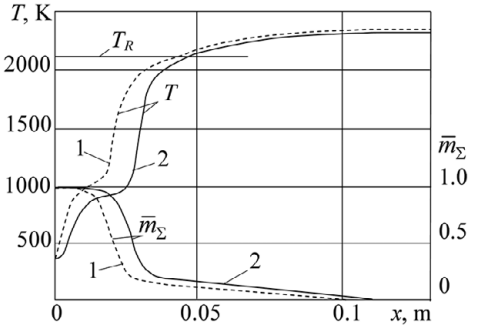

Figure 7.7 Variation of gas temperature and relative flow rate of liquid ($\alpha_{ox} = 1.0; p = 3.5$ MPa); (1) equilibrium calculation; (2) nonequilibrium calculation.

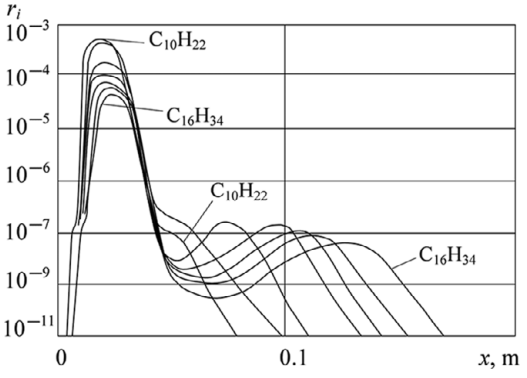

Figure 7.8 Variation of concentration of $C_{10}H_{22}$ ... $C_{16}H_{24}$, r_i – mole fractions.

reverse flow (Figure 7.4) into injected jet. The results of the calculations with the allowance for nonequilibrium chemical reactions display an increase in droplet evaporation time as compared with the results of the equilibrium calculation. The temperature in the region of reverse flow, $T_R = 2111$ K, and the temperature at combustion chamber exit, $T = 2352$ K, practically comply with equilibrium values. The difference in temperatures T and T_R is specified by an incomplete evaporation of droplets within the length of the reverse flow zone; that is, the recirculation region features the excess of oxidizer. Recirculation region relative length $\bar{L}_R = L_R/(r - r_0) = 6.1$. Within this length, about 88% of liquid is vaporized. The completion of the fuel conversion process is observed after the evaporation of the largest droplets.

The change in the content of the evaporation products of fuel multicomponent droplets in the gas mixture is shown in Figure 7.8. An initial increase in concentration of the original species is conditioned by the augmentation of the evaporation process at mixing the injected jet with products fed from the reverse flow region. The maximum concentration of the fuel evaporated products is observed in the region of evaporation of the basic group of droplets ($d_2 = 20$ μm). The sharp decrease in concentration due to reaction of combustion is replaced by a slight increase in concentration because of the evaporation of large droplets ($d_3 = 70$ μm) at the section

Downloaded from https://www.cambridge.org/core. Nottingham Trent University, on 17 Aug 2019 at 02:09:06, subject to the Cambridge Core terms of use, available at https://www.cambridge.org/core/terms. https://doi.org/10.1017/9781108581714.007

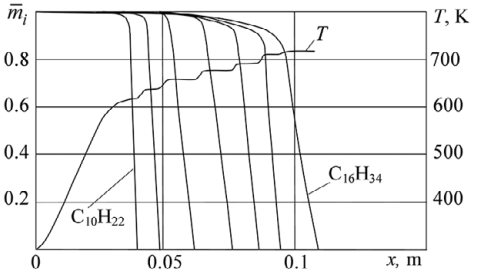

Figure 7.9 Variation of droplet temperature and relative mass content of components in liquid droplet at evaporation (droplet initial diameter of 70 μ*m*).

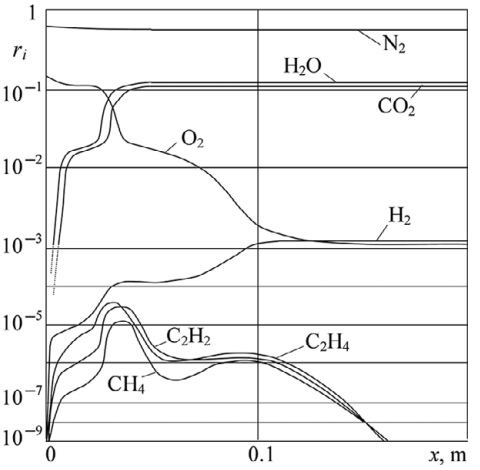

Figure 7.10 Variation of combustion products chemical composition.

$x = 0.07 \ldots 0.13$ m. The sequence of the evaporation of liquid components (Figure 7.9) is displayed in the pattern of concentration variation at the final stage of the combustion (Figure 7.8).

Chemical reactions involving the propellant basic components and their radicals in the gas mixture cause the increase in the content of simple hydrocarbon compounds C_2H_4, C_2H_2, and CH_4 and hydrogen (H_2) (Figure 7.10). The shift in the peak of the concentrations of simple hydrocarbons relative to the maximum concentrations of basic compounds displays the sequence of hydrocarbon formation and decomposition in the mechanism of chemical reactions: $C_nH_m \rightarrow \ldots \rightarrow C_2H_4 \rightarrow C_2H_2 \rightarrow CH_4$.

The content of H_2O and CO_2 corresponds to the combustion process to display rather high combustion completeness of the original and intermediate hydrocarbons.

A comparison of the variation of gas temperature with fluid flow rate (Figure 7.7) demonstrates the intensive combustion of evaporating components. This is first conditioned by the feed of the high-temperature mixture with a high content of active centers OH, O, and H from the reverse flow region (peaks in the region $x \approx 0.01$ m in

Downloaded from https://www.cambridge.org/core. Nottingham Trent University, on 17 Aug 2019 at 02:09:06, subject to the Cambridge Core terms of use, available at https://www.cambridge.org/core/terms. https://doi.org/10.1017/9781108581714.007

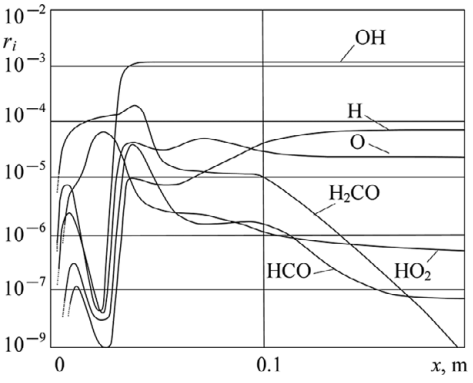

Figure 7.11 Variation of combustion products chemical composition.

Figure 7.11). The high content of hydroxide (OH) and O and H atoms ensures the proceeding of stages of the reaction with high rates and rules out the stage of hydrocarbon low-temperature slow oxidation.

The variation of the concentrations of H_2CO, HCO, and HO_2 confirms their involvement in the reactions as intermediate particles.

It is known that, in the case of homogeneous premixed mixtures the combustion stability increases with the approaching of equivalence ratio to stoichiometric values $(\alpha_{ox} = 1.0)$. Results of numerical analyses of the equivalence ratio influence on the working process show that the stability of combustion of two-phase hydrocarbon–air mixtures can even increase at the shift of original equivalence ratio α_{ox} to the region of range of values smaller than unity and depend on a particular fluid atomization pattern, as well as the mixture composition in the reverse flow zone. Maximum combustion stability is characteristic of the mode where the mixture in the reverse flow region has the maximum possible temperatures at values of equivalence ratio in this region $\alpha_{ox}^{R} = 1$.

The variation of gas mixture equivalence ratio local values along the axis and in the zone of reverse flow is shown in Figure 7.12.

This figure shows that at the original value of equivalence ratio ($\alpha_{ox} \approx 0.8$), the oxidizer-to-fuel ratio in the reverse flow region approaches a stoichiometric value while α_{ox}^{g} on the injector axis after evaporation of the main group of droplets is close to unity, which is a direct consequence of droplet distribution over groups. Therefore, the flow regime at original value of equivalence ratio $\alpha_{ox} \approx 0.8$ is the most favorable for liquid fuel evaporation and ignition conditions at the given atomization pattern and may be recommended for starting the operation of the combustion chamber before onset of the basic regime.

The influence of the atomization pattern on the process of operation has been analyzed at the increase of the major droplet fractions. Analysis of the results makes it clear that at finer atomization combustion, stability increases. At a significant increase in the size of droplets, the length of their zone evaporation increases to increase the probability of combustion blowoff because the temperature decreases in the reverse flow region and combustion conditions deteriorate due to the increase in local values of

Downloaded from https://www.cambridge.org/core. Nottingham Trent University, on 17 Aug 2019 at 02:09:06, subject to the Cambridge Core terms of use, available at https://www.cambridge.org/core/terms. https://doi.org/10.1017/9781108581714.007

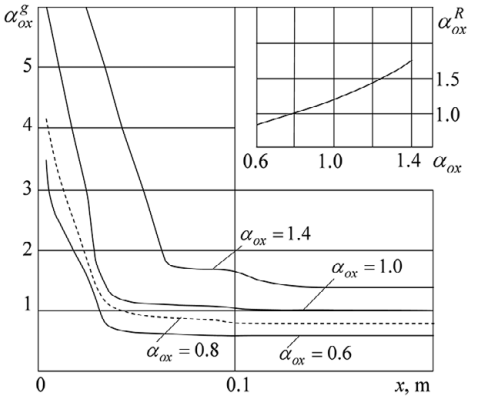

Figure 7.12 Variation of local values of gas mixture equivalence ratio local values along the axis (α_{ox}^{g}) and in the reverse flow zone (α_{ox}^{R}).

the equivalence ratio in the flow attachment region (Figure 7.4). It was also observed that low temperatures over the significant portion of the combustion chamber length at the increase in the fraction of large droplets ($d_1 = 20$ μm, $G_1 = 0.7$; $d_2 = 60$ μm, $G_2 = 0.2$; $d_3 = 80$ μm, $G_3 = 0.1$) cause the reduction in nitrogen oxide concentration (by 12% compared with the basic regime) at the combustion chamber exit.

At the operation of the combustion chamber incorporated with the heat gas or steam gas generator, it is necessary to adjust its efficiency over the wide range. At invariable dimensions of the combustion chamber, a drop in flow rate causes the decrease in pressure. The results of the calculations show that the decrease in pressure causes some rise in the rate of droplet evaporation during their heating. After heating droplets at a lower pressure, the evaporation rate is lower than that at the high pressure. It is conditioned by the fact that at low pressures, droplets are heated to lower temperatures under which the latent heat of evaporation features higher values. The comparison of characteristics of droplet evaporation are shown in Figure 7.13. The main group of droplets ($d_1 = 20$ μm) evaporates in both cases within the recirculation region that ensures gas temperature level, rather high for the stabilization of combustion in the reverse flow region ($T_R \approx T_R$ in basic regime). The pressure drop affects most notably the length of the major droplet evaporation zone; as a result of this, the chamber length required for completion of combustion increases. Therefore, it may be concluded that the optimum chamber length for these conditions and regimes is 0.17–0.18 m.

The influence of the combustion chamber's crosswise dimensions on the working parameters was analyzed proceeding from the results of calculations for two versions of dimensions. In compliance with the first version, the combustion chamber's inner diameter was changed. The dimensions of injectors and their quantity remained unchanged. The degree of sudden expansion $\bar{r}$ was the main factor of variability of geometry. In compliance with the second version, the combustion chamber's diameter did not vary. The injector nozzle's exit diameter and quantity of injectors made the variable parameters selected in the condition $\bar{r}$ = const. The relation of radii at the

Downloaded from https://www.cambridge.org/core. Nottingham Trent University, on 17 Aug 2019 at 02:09:06, subject to the Cambridge Core terms of use, available at https://www.cambridge.org/core/terms. https://doi.org/10.1017/9781108581714.007

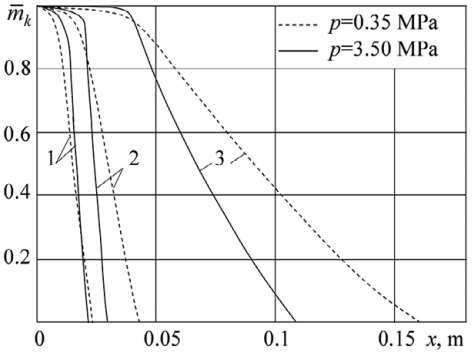

Figure 7.13 Variation of the droplet relative mass.

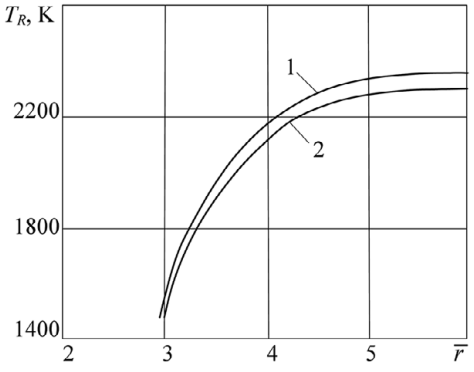

Figure 7.14 Dependence of the temperature in the reverse flow zone on the degree of sudden expansion $\bar{r}$: (1) p = 3.5 MPa; (2) p = 0.35 MPa.

injector nozzle exit $\bar{r}_0 = r_{0,const}/r_0$ ($r_{0,const}$ = 4 mm) was used as the measure of geometry variability.

It was observed that parameters of the state of the mixture in the region of reverse flow bring about the primary effect on the working process at $\bar{r}$ variation. The dependence of gas temperature in the reverse flow region on $\bar{r}$ are given in Figure 7.14.

Gas temperature T_R decreases with a decrease in $\bar{r}$. In the range of values $\bar{r} < 3$, mass feed from the reverse flow region does not ensure conditions required for completion of evaporation of the main group of droplets and the corresponding initiation of the combustion. At gas temperature values about 1500 K in the region of reverse flow, the mixing of products with the air jet ensures the mixture temperature of 600–800 K. At such temperatures, droplet evaporation time increases significantly. Besides, low temperatures result in retardation of reactions of decomposition and combustion of the original species. The generalized effect of these factors promotes the formation of conditions of combustion blowoff. Temperature T_R drop at the decrease in the degree of sudden expansion is caused by the increase in equivalence ratio ($\alpha_{ox}^R > 1$) in the region of reverse flow. The increase in α_{ox}^R is caused by the feed of the mixture with a smaller content of

Downloaded from https://www.cambridge.org/core. Nottingham Trent University, on 17 Aug 2019 at 02:09:06, subject to the Cambridge Core terms of use, available at https://www.cambridge.org/core/terms. https://doi.org/10.1017/9781108581714.007

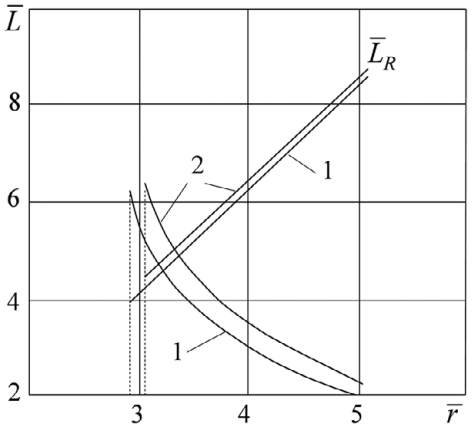

Figure 7.15 Dependence of recirculation region relative dimension $\bar{L}_R$ and those of the main group droplet evaporation section L on degree of sudden expansion $\bar{r}$.

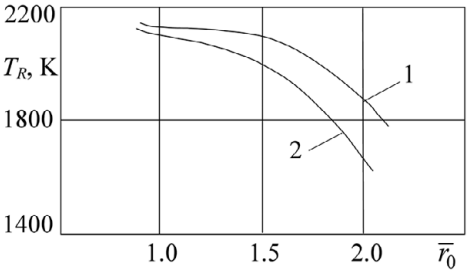

Figure 7.16 Dependence of gas temperature in the region of reverse flow on $\bar{r}_0$: (1) p = 3.5 MPa; (2) p = 0.35 MPa.

evaporated fuel in the region of reverse flow. At $\bar{r} < 3.5$, the length of the zone of evaporation of the main droplet group $\bar{L}$ (Figure 7.15) is larger than that of the recirculation region $\bar{L}_R$ that promotes an even greater increase in α_{ox}^R and a higher probability of combustion blowoff. The increase in pressure intensifies the fuel conversion processes and positively influences the stabilization of combustion.

The results of the calculations at the change in $\bar{r}_0$ are shown in Figures 7.16 and 7.17. To meet the condition $\bar{r}$ = const at the decrease in radius r_0 at the injector nozzle exit, the quantity of injectors n_f is increased respectively (n_f = 6 at $\bar{r}_0$ = 1, n_f = 12 at $\bar{r}_0 = \sqrt{2}$, and n_f = 24 at $\bar{r}_0 = 2$). Numerical experiments show that rather high values T_R required for stabilization of combustion remain at the values $\bar{r}_0 \leq 1.7$. At the increase in $\bar{r}_0$ greater than 1.8, the probability of combustion blowoff is caused by the mixture temperature drop T_R in the region of reverse flow. The reduction of T_R is caused by the influence of the same factors that brought about the decrease in $\bar{r}$.

The optimal quantity of injectors (5 ... 7 for combustion chamber under consideration) can be obtained on the basis of the analysis of influence of geometrical dimensions. The mixture temperature increases in the region of reverse flow at the decrease in

Downloaded from https://www.cambridge.org/core. Nottingham Trent University, on 17 Aug 2019 at 02:09:06, subject to the Cambridge Core terms of use, available at https://www.cambridge.org/core/terms. https://doi.org/10.1017/9781108581714.007

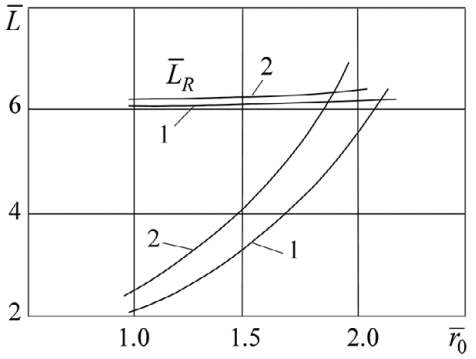

Figure 7.17 Dependence of recirculation zone relative dimensions $\bar{L}_R$ and main droplet group evaporation zone length $\bar{L}$ on $\bar{r}_0$: (1) p = 3.5 MPa; (2) p = 0.35 MPa.

the quantity of injectors that will cause additional difficulties in organizing the cooling of the chamber walls, which reduces its life cycle. Further increases in quantity of injectors increase the probability of combustion blowoff.

7.4.2 Analysis of Combustion of Natural Gas and Air in the Heat Gas Generator Combustion Chamber

The primary purpose of this study is the determination of operating and structural parameters at which maximum completeness of the conversion of the propellant chemical energy is reached and harmful emissions of NO_x, CO, CH_x are minimized. Features of the organization of the combustion process under consideration consist in the following:

- supply pressures of natural gas not greater than 3 kPa
- nominal gas flow rate of 3.6 kg/h
- low values of gage pressures of the air supplied into combustion chamber.

Such parameters are used for the operation of heat gas generators employed for the heating of small industrial premises in the absence of a centralized gas supply.

These features predetermine the selection of procedures aimed at reducing the NO_x emission. First of all, it is appropriate to use stepwise and stage-by-stage fuel combustion in combination with the RQL (Rich–Quenen–Lean) technique and the nonstoichiometric procedure. RQL technology [238] is known to be realized in three stages (in three regions): first, the premixed mixture with a lack of air is combusted; then the combustion products are abruptly diluted with the air; and, finally, the combustion of the mixture with excess oxidizer is completed. The nonstoichiometric procedure of combustion consists in building up separate fuel-rich and fuel-lean zones of combustion and subsequently mixing the combustion products from these zones. The combustion chamber scheme and arrangement of reactors are shown in Figure 7.18.

The combustion chamber's primary components include a frontal device (region A) and a cylindrical tube with a set of holes to supply air in the primary region (B) and

Downloaded from https://www.cambridge.org/core. Nottingham Trent University, on 17 Aug 2019 at 02:09:06, subject to the Cambridge Core terms of use, available at https://www.cambridge.org/core/terms. https://doi.org/10.1017/9781108581714.007

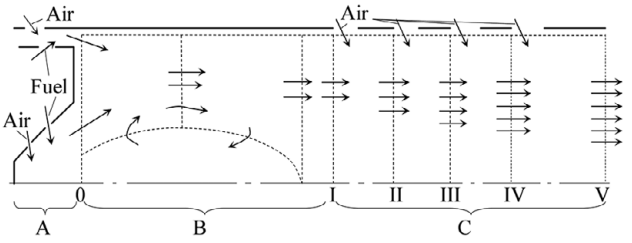

Figure 7.18 Combustion chamber scheme and arrangement of reactors.

secondary region (C). A stable ignition zone is arranged in region A to feed air and fuel (10% of nominal flow rate) with the help of tangential holes. The main fuel portion is fed via the set of stream-impinging injectors in a swirled air co-stream. The combustion of the main amount of air occurs in region B. To decrease the temperature of the combustion products to reduce nitrogen oxide emission, residual air is fed into region C. Note here that the air cools the combustion chamber walls to protect them against overheating and burning. High temperatures in region B facilitate high intensity of fuel combustion and prevent CO emission and unburned hydrocarbons CH_x.

While considering the working process in the combustion chamber, attention has been given to such components as the gas–air jet flow and interaction depending on swirling intensity and combustion zone configuration, ignition of the incoming fresh mixture by feed of high-temperature gas from the active combustion region, and the attainment of the required completeness of combustion with the allowance for constraints on emission of harmful species at the optimal residence time of the mixture.

The general flow pattern is presented as follows (see also Figure 7.18). The reverse flow region originates in the central paraxial region due to lower static pressure caused by centrifugal effect. The reverse flow region exists also in the peripheral region. Thus, two regions may exist, in principle, in the combustion chamber to facilitate the ignition and stabilization of the flame. The central region (zone) of length not greater than $L_R = (0.8 \ldots 0.9)D$ is of importance for flame stabilization.

Optimal reacting mixture residence time in the combustion chamber should be determined at the first stage of the analysis. In this case, the chamber is considered as single PSR. Some of results are shown in the Figures 7.19–7.22.

The obtained results have been compared with those of thermodynamic calculations in the condition of chemical equilibrium. The basic criteria of combustion process completion are minimum of concentrations of CH_x hydrocarbons and mixture temperature T approaching its equilibrium values T^{eq}. Completeness of combustion has been evaluated by the following formula:

$$\eta = 1 - (T^{eq} - T)/T^{eq}.$$

The results of numerical experiments reveal the following:

– Residence time $\tau = \rho V/\left(\dot{m}_{fuel} + \dot{m}_{air}\right)$ whereat completeness of combustion reaches 0.99 comprised about 50 ms.

Downloaded from https://www.cambridge.org/core. Nottingham Trent University, on 17 Aug 2019 at 02:09:06, subject to the Cambridge Core terms of use, available at https://www.cambridge.org/core/terms. https://doi.org/10.1017/9781108581714.007

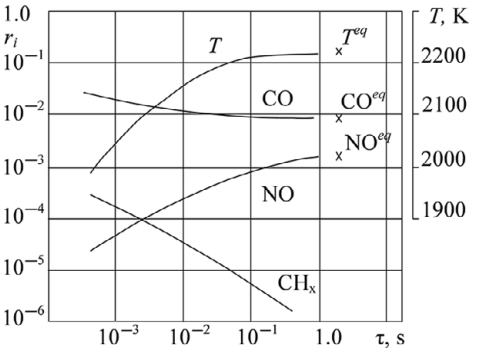

Figure 7.19 Dependence of combustion products temperature and CO, NO, and CH_x concentration on residence time ($\alpha_{ox} = 1.0$).

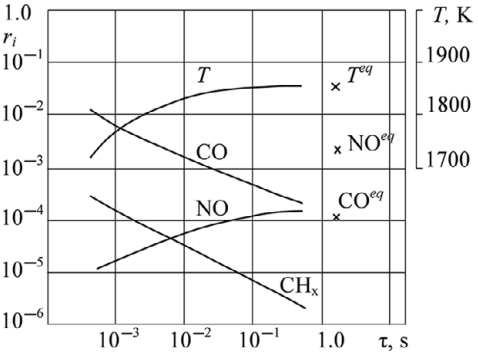

Figure 7.20 Dependence of combustion products temperature and CO, NO, and CH_x concentration on residence time ($\alpha_{ox} = 1.4$).

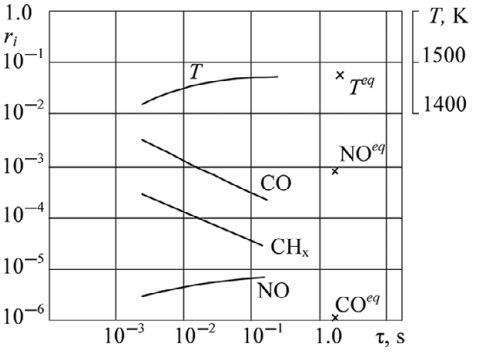

Figure 7.21 Dependence of combustion products temperature and CO, NO, and CH_x concentration on residence time ($\alpha_{ox} = 2.0$).

Downloaded from https://www.cambridge.org/core. Nottingham Trent University, on 17 Aug 2019 at 02:09:06, subject to the Cambridge Core terms of use, available at https://www.cambridge.org/core/terms. https://doi.org/10.1017/9781108581714.007

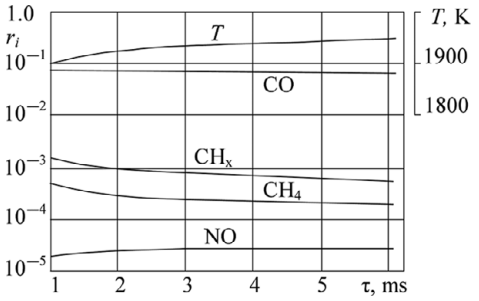

Figure 7.22 Dependence of combustion products temperature and concentration of CO, NO, CH_4, CH_x on residence time ($\alpha_{ox\mathrm{I}} = 0.714$ at the exit of zone 0–I).

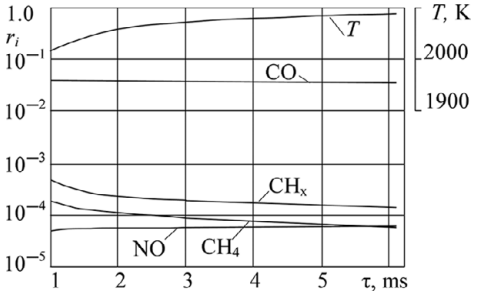

Figure 7.23 Dependence of combustion products temperature and concentration of CO, NO, CH_4, CH_x on residence time ($\alpha_{ox\mathrm{I}} = 0.833$ at the exit of zone 0–I).

- CO concentrations decrease to their equilibrium values – i.e., at oxidizer equivalence ratio $\alpha_{ox} = 1.0$ in time $\tau > 0.1$ ms, while at $\alpha_{ox} = 1.4 \ \ldots \ 2.0$ in time $\tau > 1.0$ s.
- NO concentrations do not exceed 50 ppm at $\alpha_{ox} = 1.0$ and $\tau < 1$ ms, as well as at $\alpha_{ox} = 1.4$ and $\tau < 6$ ms.
- At $\alpha_{ox} = 2.0$ and residence time $\tau < 50$ ms, NO concentrations are not higher than 8–10 ppm.

This is why residence time not greater than 5…7 ms should be maintained for NO concentration limitation. Note here that the expected completeness of combustion is 0.97.

Numerical analyses have been made also for several reaction regions (Figure 7.18): 0–I, I–II, II–III, III–IV, IV–V. Figures 7.22–7.25 show the results of calculations for primary zone (0–I) at different oxidizer-to-fuel flow rate ratios.

The analysis of the results allows one to assume that it is reasonable to limit the reacting mixture residence time in the region (0–I) to $\tau \approx 2 \ \ldots \ 3$ ms. At the increase in residence time, NO concentration goes up, while at its decrease, the completeness of combustion goes down.

Downloaded from https://www.cambridge.org/core. Nottingham Trent University, on 17 Aug 2019 at 02:09:06, subject to the Cambridge Core terms of use, available at https://www.cambridge.org/core/terms. https://doi.org/10.1017/9781108581714.007

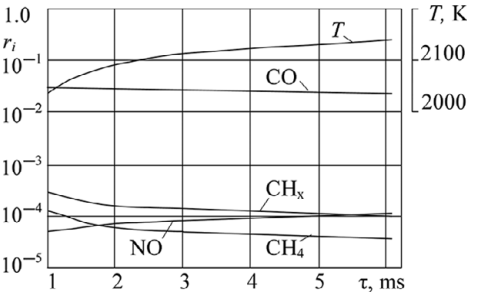

Figure 7.24 Dependence of combustion products temperature and concentration of CO, NO, CH_4, CH_x on residence time ($\alpha_{oxI} = 0.909$ at the exit of zone 0–I).

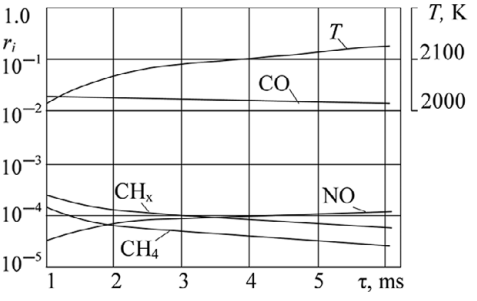

Figure 7.25 Dependence of combustion products temperature and concentration of CO, NO, CH_4, CH_x on residence time ($\alpha_{oxI} = 1.0$ at the exit of zone 0–I).

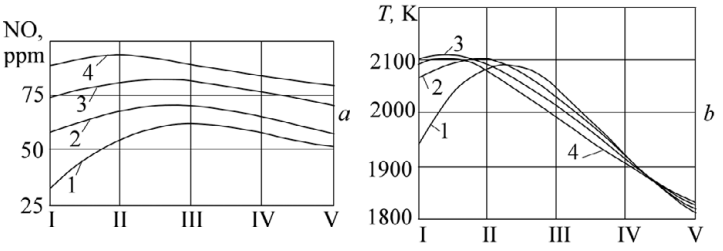

Figure 7.26 NO concentration, combustion product temperature, and equivalence ratio in combustion chamber sections: (1) $\alpha_{oxI} = 0.714$; (2) $\alpha_{oxI} = 0.833$; (3) $\alpha_{oxI} = 0.909$; (4) $\alpha_{oxI} = 1.0$.

Figure 7.26 shows the results of calculations for secondary reaction zones (I–II, II–III, III–IV, IV–V) at the mixing of the combustion products coming from the primary zone (0–I) with the air fed into secondary zone. The results were obtained at different oxidizer equivalence ratio α_{oxI} in region 0–I. Higher NO concentration is observed at the equivalence ratio close to 1.1 in this region.

Downloaded from https://www.cambridge.org/core. Nottingham Trent University, on 17 Aug 2019 at 02:09:06, subject to the Cambridge Core terms of use, available at https://www.cambridge.org/core/terms. https://doi.org/10.1017/9781108581714.007

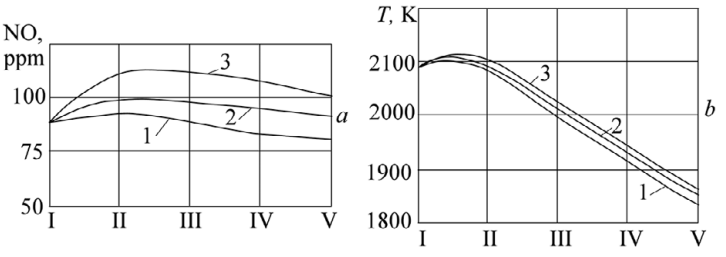

Figure 7.27 Dependence of NO concentration and combustion products temperature on residence time ($\alpha_{oxI} = 1.0$; $\alpha_{oxV} = 1.4$ at the exit of zone IV–V): (1) $\bar{\tau} = 1.0$; (2) $\bar{\tau} = 2.0$; (3) $\bar{\tau} = 3.0$.

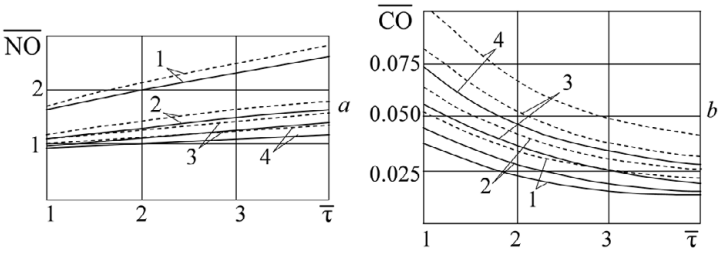

Figure 7.28 Dependence of NO and CO relative concentrations on residence time: (1) $\alpha_{oxI} = 0.714$; (2) $\alpha_{oxI} = 0.833$; (3) $\alpha_{oxI} = 0.909$; (4) $\alpha_{oxI} = 1.0$ (dotted line - $\alpha_{oxV} = 1.3$; solid line - $\alpha_{oxV} = 1.4$).

At the increase in the length of the zone of mixing with secondary air, residence time goes up and higher completeness of combustion is achieved to cause the growth of NO concentrations (Figures 7.27 and 7.28).

The most intensive rise of NO concentrations is observed at the afterburning of fuel-rich mixture (Figure 7.28a) where $\overline{NO} = NO_V/NO_I$; NO_V is the NO concentration at the exit of zone IV–V; NO_I is the NO concentration at the exit of zone 0–I. At the same time, the increase in mixture residence time in the secondary zone facilitates CO oxidation (Figure 7.28b) where $\overline{CO} = CO_V/CO_I$.

Apart from the examined organization of combustion and mixing, the nonstoichiometric procedure of burning was analyzed. In compliance with the design scheme, it was assumed that two regions are initially organized in zone B (Figure 7.18) – that is, peripheral fuel-lean zone $(\alpha_{ox} = 1.25)$ and paraxial fuel-rich zone $(\alpha_{ox} = 0.75)$. The stoichiometric equivalence ratio is established in cross section I when mixing and burning in zone B.

Then, mixture afterburning at the secondary air feed is considered (zone C in Figure 7.18). Results indicate that the nonstoichiometric procedure brings about the reduction in NO emission by about 20%, as shown in Figure 7.29.

Downloaded from https://www.cambridge.org/core. Nottingham Trent University, on 17 Aug 2019 at 02:09:06, subject to the Cambridge Core terms of use, available at https://www.cambridge.org/core/terms. https://doi.org/10.1017/9781108581714.007

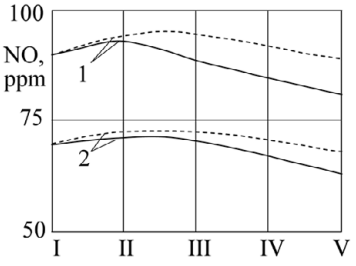

Figure 7.29 Variation of NO concentration in combustion chamber sections: (1) without nonstoichiometric procedure of combustion; (2) with nonstoichiometric procedure of combustion (dotted line – $\alpha_{ox\mathrm{V}} = 1.3$; solid line – $\alpha_{ox\mathrm{V}} = 1.4$).

The preceding examples disclose methods of the employment of models described in Sections 7.2–7.4 to demonstrate the potential of their application to optimization of combustion and flow of two-phase mixtures in combustion and mixing chambers of high-temperature units, as well as to display in the number of cases the importance of allowance for chemically nonequilibrium interaction.

Downloaded from https://www.cambridge.org/core. Nottingham Trent University, on 17 Aug 2019 at 02:09:06, subject to the Cambridge Core terms of use, available at https://www.cambridge.org/core/terms. https://doi.org/10.1017/9781108581714.007

8 Simulation of Two-Phase Flows in Gas Generators of Liquid-Propellant Rocket Engines

8.1 Physical Scheme and Mathematical Model of Two-Phase Flow in Gas Generators

8.1.1 Specific Features of Operation of Liquid-Propellant Rocket Engine Gas Generator

Gas–liquid reacting flows seem to be one of the most complex and, at the same time, most prevalent fields of application for mathematical simulation of high-temperature processes. Of these processes, the phenomena are fluid atomization polydispersity and droplet secondary fragmentation, droplet heating and evaporation, turbulence, reactions in the gas phase, the difference in the velocity between the gas and droplet phases (slip velocity), and the multidimensional nature of fluid flow. Such flows make the core of processes proceeding in combustion chambers of air-breathing jet engines [216, 231, 239, 240], rocket engines [160, 215, 228, 229, 241, 242], gas generator driving turbopumps, pressurization systems of the LPRE propellant tanks [160, 215, 228, 241–243], vapor-gas generators [50, 55, 56], afterburners of air-breathing jet engines [216, 231, 239, 240], and different furnaces [58].

A liquid gas generator (LGG) of rocket engine is a good example of the compilation of all previously listed processes. The gas generator produces the working medium – the generator gas that is either directly applied to the pressurized propellant feed systems and power supplies of servomechanisms or enters turbines that drive the fuel and oxidizer pumps of LPRE [1, 160, 215, 228]. Figure 8.1 shows the schemes of LPRE with a turbopump propellant feed system (a) without generator gas afterburning, and (b) with afterburning. The liquid gas generator (8) produces generator gas – i.e., the working medium for driving the turbine of turbopump unit (9) integrating the turbine with oxidizer and propellant pumps to make the power drive for propellant components feed from fuel (3) and oxidizer tanks (2) into the engine thrust chamber (1). Note here that two-component LGGs use the same propellant components for gas generation that are used for the LPRE. Generator gas used in the turbine is dumping overboard through auxiliary nozzles in a case of engine operation without generator gas afterburning (Figure 8.1a), or, in a case of LPRE operation, with generator gas afterburning (Figure 8.1b), it can be returned to the LPRE thrust chamber as a fuel or oxidizer where the propellant second component (oxidizer or fuel) is injected.

Apart from the turbopump driving, it is possible to employ the liquid gas generators for pressurization of the LPRE propellant tanks to preserve the stability of their structure – that is, the so-called gas generator pressurization system [215, 228]. One

Downloaded from https://www.cambridge.org/core. Nottingham Trent University, on 17 Aug 2019 at 02:10:54, subject to the Cambridge Core terms of use, available at https://www.cambridge.org/core/terms. https://doi.org/10.1017/9781108581714.008

of the simplest purposes of pressurizing the propellants is to supply them from the tanks into the thrust chambers of LPREs. Products of gas generation usually have a relatively high temperature (800–1200 K) and may have both an excess of oxidizer (oxidizer-rich or fuel-lean) and an excess of fuel (fuel-rich or oxidizer-lean). Generator gas is fed into propellant tanks at a controlled pressure: oxidizer-rich gas ($\alpha_{ox} \gg 1$) into the oxidizer tank, and fuel-rich gas ($\alpha_{ox} \ll 1$) into the fuel tank to prevent uncontrolled chemical reactions with propellant component vapors in the gas space of the tank (so-called ullage). Figure 8.1b shows the tank pressurization gas generator system where the gas generator (7) using LPRE propellant components generates the combustion products with an excess of fuel for feeding generator gas into the fuel tank ullage. For oxidizer tank pressurization, this scheme uses the mixing chamber (10), exploiting high-temperature gas that features an excess of oxidizer produced by the turbine of turbopump system and ballasted by liquid oxidizer.

Generator gas physicochemical parameters (temperature, pressure, chemical composition, etc.) are limited by the properties of structural materials and by the type of

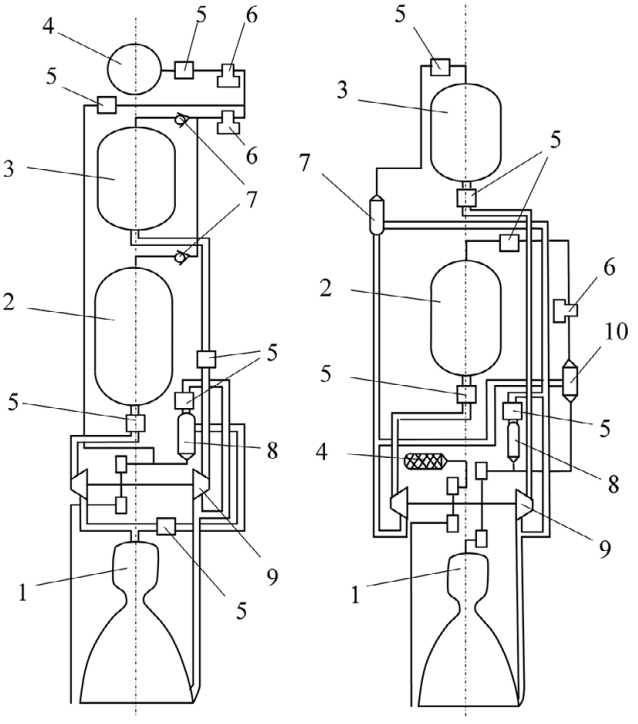

Figure 8.1 Schematic of LRPE with turbopump-pressure feed. (a) without generator gas afterburning: (1) combustion chamber, (2) oxidizer tank, (3) fuel tank, (4) high-pressure compressed gas tank, (5) valve to control fluid flow, (6) pressure reducer, (7) back flow valve, (8) liquid gas generator for turbine driving, (9) turbopump unit; (b) with generator gas afterburning: (1) combustion chamber, (2) oxidizer tank, (3) fuel tank, (4) pyro-starter, (5) valve to control fluid flow, (6) pressure reducer, (7) liquid gas generator for fuel tank pressurization, (8) liquid gas generator for turbine driving, (9) turbopump unit, (10) mixing chamber.

Downloaded from https://www.cambridge.org/core. Nottingham Trent University, on 17 Aug 2019 at 02:10:54, subject to the Cambridge Core terms of use, available at https://www.cambridge.org/core/terms. https://doi.org/10.1017/9781108581714.008

propellant components affected by this gas. Thus, for driving the turbine, the fuel-rich gas generators seem very promising, which is accounted for by the lower corrosive effect of the products of incomplete combustion on structural materials. This allows one to use higher temperatures of fuel-rich gas compared with oxidizer-rich gas. At the same time, hydrocarbon fuels used as the LPRE propellant components can cause soot formation, which imposes significant constraints to the application of fuel-rich gas generators.

In general, on describing the physical–chemical processes in the two-component LGG, it is significant that working processes proceeding therein are like those in the LPRE combustion chamber but with a significant excess of one of the propellant components, which notably complicates the problem of the simulation of these processes. Note here that the process of gas generation can be organized as in a single-zone or two-zone gas generator (Figure 8.2). The combustion of the propellant in a single-zone LGG at a preset equivalence ratio is organized directly near the mixing head (Figure 8.2a). In the two-zone LGG's first zone (nearby mixing head; Figure 8.2b) a high-temperature combustion is organized at the equivalence ratio close to stoichiometric one, and for the simulation of the processes in this zone, chemical equilibrium models described in Section 1.3 may be used. In the second zone (C; Figure 8.2b), ballasting component (fuel for a fuel-rich gas generator or oxidizer for an oxidizer-rich gas generator) is fed to combustion products from the first zone to ensure required temperatures and corresponding concentrations of the gas at the gas generator outlet. Note here that droplets of ballasting component are heated and evaporated while the ballasting component interacts with the combustion products coming from the first zone, thereby reducing the temperature of the working body. Thereupon, it is recommended to apply formal chemical kinetics models (Section 1.3) for the estimation of working medium parameters at relatively low temperatures in the gas generator's second zone. However, in the case of $O_2 + H_2$ propellant, for example, the combustion products are formed at the gas generator exit due to completed physical–chemical conversions; hence, it would be more proper to use chemical equilibrium models for the simulation of the combustion of this propellant.

Since the basic mode of LRPE gas generator operation is the steady-state mode with almost uniform distribution of physicochemical parameters at gas generator exit, the variation of working parameters along gas generator may be well computed with the

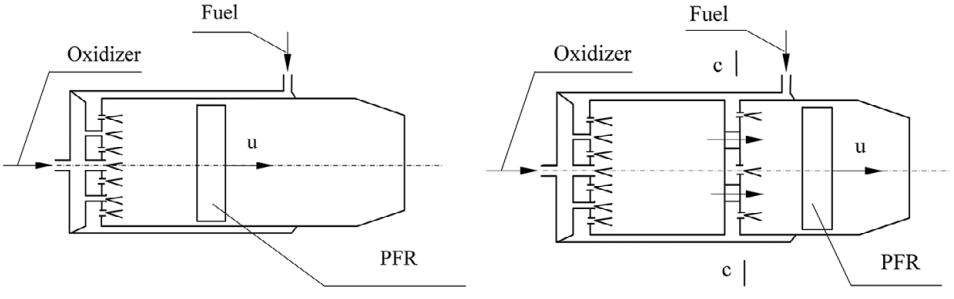

Figure 8.2 Schematic of (a) single-zone generator and (b) two-zone gas generator.

Downloaded from https://www.cambridge.org/core. Nottingham Trent University, on 17 Aug 2019 at 02:10:54, subject to the Cambridge Core terms of use, available at https://www.cambridge.org/core/terms. https://doi.org/10.1017/9781108581714.008

help of the basic physical scheme and mathematical model of PFR (Sections 1.1 and 1.5) of finite thickness moving with the gas flow and bounded along the radius by channel walls (Figure 8.2). As a liquid component (fuel or oxidizer) is injected via the set of atomizers arranged regularly over the unit cross section, and the velocity of the gas flow coming from the first zone can reach essential values, it is only natural to assume a uniform distribution of working medium parameters in the gas generator cross section. With allowance for axisymmetric structure of such units, it may be assumed that working medium parameters vary only in a lengthwise direction – that is, along the x axis. In this case, the model of PFR displacing at the velocity of gas flow allows the tracing of the working medium parameters variation over the length of the gas generator. The difference in gas and droplets velocities is simulated by a continuous feed of droplets and their discharge from the reactor through the transparent walls of the reactor.

The basic mathematical model (Section 2.1), algorithms (Sections 2.2–2.4), and basic software make it possible to develop mathematical models sufficiently efficient for practical application and appropriate computer codes for the computation of reacting gas–liquid flows.

8.1.2 Generalized Mathematical Model of the Reacting Gas–Liquid Flow: Governing Equations

The mathematical model described here for computation of reacting gas–liquid flows using the example of processes in the LPRE two-zone gas generator allows for the following typical factors: polydispersity of droplets atomization, velocity and temperature nonequilibrium of fluid droplets and gas flow, finite rates of chemical reactions, variable channel geometry, non-steady-state and nonuniform droplet heating over its radius, evaporation of homogeneous droplets at subcritical and supercritical pressures, and real properties of vapors. Owing to oxidizer-to-fuel ratio close to the stoichiometric ratio in the gas generator first zone, the chemical equilibrium model has been used for simulation of processes in this zone.

For simulation of the processes in the second zone, given the availability of two-phase flows and owing to the necessity of the simulation of fluid droplets' inflow into PFR and their evaporation in the reactor, the following assumptions may be made.

1. Discrete distribution of droplets over the diameters, which makes it possible to rule out the need of the system of integrodifferential equations in the solution.
2. One-dimensional gas flow and uniform distribution of parameters over the flow cross section.
3. Assumption of the equality of diffusive and thermal Nusselt numbers
4. The reduced firlm model is applicable

As a result, a complex model consists of known equations of two-phase one-dimensional flow [218], equations of the heating and evaporation of droplets, and equations of chemical kinetics written for PFR where independent variable τ must be replaced by axial coordinate x. Some transformations of the equations are needed to reduce and

Downloaded from https://www.cambridge.org/core. Nottingham Trent University, on 17 Aug 2019 at 02:10:54, subject to the Cambridge Core terms of use, available at https://www.cambridge.org/core/terms. https://doi.org/10.1017/9781108581714.008

optimize the computing procedure and make the algorithm and computer code reliable. For this, let's introduce some variables and use some relationships:

- mass of *sd* group of the droplets m_{sd}
- gas mass flow rate $\dot{m}_g$
- mass flow rate of *sd* group of the droplets $\dot{m}_{sd}$
- mass flow rate of working medium $\dot{m}_\Sigma = \dot{m}_g + \sum_{sd} \dot{m}_{sd}$
- velocity of *sd* group of the droplets u_{sd}
- number of droplets of *sd* group in the unit of volume N_{sd}
- flow rate of *sd* group of the droplets trough channel cross section:

$$K_{sd} = N_{sd} u_{sd} F(x) = const \tag{8.1}$$

It needs to be pointed out that this value doesn't vary along the channel.

- relative flow rate of *sd* group of the droplets:

$$\bar{G}_{sd} = m_{sd} K_{sd} / \dot{m}_\Sigma \tag{8.2}$$

- pressure of saturated vapor p_{sat} and partial pressure over the surface p_{Vd}
- index of evaporation:

$$Z_{sd}^2 = \quad - ln\left(1 - \frac{p - \gamma p_{ds}}{p - \gamma p_\infty}\right) \tag{8.3}$$

- relative thermal capacitance of *"sd"* group of the droplets $\bar{\Phi}_{sd} = \Phi_{sd} / \Phi_{sd}^0$, where Φ_{sd}^0 is the initial thermal capacitance of the droplet

The governing equations of the mathematical model and their conversion into the form convenient for the creation of algorithms are as follows (without replacement of ρ_g by $\frac{p\mu_g}{R_0 T_g}$):

1. The equation of droplet motion in the gas unidirectional flow [55] is written as follows:

$$\frac{du_{sd}}{d\tau} = 0.5 C_x \rho_g \frac{\pi R_{sd}^2}{m_{sd}} \left(V_g - u_{sd}\right) \left|V_g - u_{sd}\right|, \tag{8.4}$$

where C_x is the aerodynamic drag coefficient of the particle.
After the replacement of the variables $d\tau = dx/u_{sd}$, $R_{sd} = \left(\frac{3m_{sd}}{4\pi \bar{\rho}_{sd}}\right)^{1/3}$, one can obtain

$$\frac{du_{sd}}{dx} = 0.5 C_x \rho_g \frac{\pi \left(\frac{3m_{sd}}{4\pi \bar{\rho}_{sd}}\right)^{2/3}}{m_{sd} u_{sd}} \left(V_g - u_{sd}\right) \left|V_g - u_{sd}\right|. \tag{8.5}$$

Replacing m_{sd} by $\bar{G}_{sd}$ and using (8.2), equation can be written as follows:

$$\frac{du_{sd}}{dx} = K_{Cx}^{ds} \rho_g \frac{\left(V_g - u_{sd}\right) \left|V_g - u_{sd}\right|}{u_{sd} \left(\bar{G}_{ds}\right)^{1/3}} \equiv f_{Us} \tag{8.6}$$

where $K_{Cx}^{ds} = 0.5\pi C_x \left(\frac{3}{4\pi \bar{\rho}_{sd}}\right)^{2/3} \left(\frac{K_{ds}}{\dot{m}_\Sigma}\right)^{1/3}$.

Downloaded from https://www.cambridge.org/core. Nottingham Trent University, on 17 Aug 2019 at 02:10:54, subject to the Cambridge Core terms of use, available at https://www.cambridge.org/core/terms. https://doi.org/10.1017/9781108581714.008

2. With allowance for (8.3), the original form of the equation of droplets evaporation (6.14) and (6.15) can be written as

$$\frac{dm_{sd}}{d\tau} = -4\pi R_{sd}^2 \frac{D_{mV} p \mu_V}{\gamma R_0 T_{gV} \delta^*} Z^2. \tag{8.7}$$

Replacement of variables τ and R_{sd} gives

$$\frac{dm_{sd}}{dx} = -4\pi \left(\frac{3m_{sd}}{4\pi \bar{\rho}_{sd}}\right)^{2/3} \frac{D_{mV} p \mu_V}{u_{sd} \gamma R_0 T_{gV} \delta^*} Z^2. \tag{8.8}$$

After substitution $m_{sd} = \bar{G}_{sd} \dot{m}_\Sigma / K_{sd}$ and some transformations, one can obtain

$$\frac{d\bar{G}_{sd}}{dx} = -\left(\frac{0.75\bar{G}_{sd}}{\bar{\rho}_{sd}}\right)^{2/3} \left(\frac{\pi K_{sd}}{\dot{m}_\Sigma}\right)^{1/3} \frac{4 D_{mV} p \mu_V}{u_{sd} \gamma R_0 T_{gV} \delta^*} Z_{sd}^2 \equiv f_{Gs}. \tag{8.9}$$

3. With allowance for (8.3), the original equation of variation of droplet thermal capacitance can be written as follows:

$$\frac{d\Phi_{sd}}{d\tau} = -\frac{4\pi R_{sd}^2 K_e k_{gV} Z^2}{\bar{c}_{p,gV} \delta^*} \left(L_V + h_R - \frac{\bar{c}_{p,gV}(T_g - T_R)}{exp\left(K_e Z^2\right) - 1}\right). \tag{8.10}$$

Replacement of variables τ and R_{sd} gives

$$\frac{d\Phi_{sd}}{dx} = -\frac{4\pi \left(\frac{3m_{sd}}{4\pi \bar{\rho}_{sd}}\right)^{2/3} K_e k_{gV} Z^2}{\bar{c}_{p,gV} \delta^* u_{sd}} \left(L_V + h_R - \frac{\bar{c}_{p,gV}(T_g - T_R)}{exp\left(K_e Z^2\right) - 1}\right). \tag{8.11}$$

After m_{sd} and $\Phi_{sd} = \bar{\Phi}_{sd} \Phi_{sd}^0$ replacement and some transformations, one obtains

$$\frac{d\bar{\Phi}_{sd}}{dx} = -\frac{4\pi \left(\frac{0.75\bar{G}_{sd}\dot{m}_\Sigma}{\pi \bar{\rho}_{sd} K_{sd}}\right)^{2/3} K_e k_{gV} Z_{sd}^2}{\bar{c}_{p,gV} \delta^* u_{sd} \Phi_{sd}^0} \left(L_V + h_R - \frac{\bar{c}_{p,gV}(T_g - T_R)}{exp\left(K_e Z_{sd}^2\right) - 1}\right) \equiv f_{\Phi s}. \tag{8.12}$$

4. The original form of the equations of heating of the droplet center can be written as follows:

$$\frac{da_{sd}}{d\tau} = \frac{\bar{k}_{liq}}{\bar{c}_{liq} \bar{\rho}_{sd}} \frac{6 b_{sd}}{R_{sd}^2}. \tag{8.13}$$

Turning to linear coordinates and performing some substitutions, one obtains

$$\frac{da_{sd}}{dx} = \frac{6\bar{k}_{liq} b_{sd}}{u_{sd} \bar{c}_{liq} (\bar{\rho}_{sd})^{1/3} \left(\frac{3\dot{m}_\Sigma \bar{G}_{sd}}{4\pi K_{sd}}\right)^{2/3}} \equiv f_{as}. \tag{8.14}$$

Downloaded from https://www.cambridge.org/core. Nottingham Trent University, on 17 Aug 2019 at 02:10:54, subject to the Cambridge Core terms of use, available at https://www.cambridge.org/core/terms. https://doi.org/10.1017/9781108581714.008

5. After replacing variables Φ_{sd} and m_{sd}, the algebraic equation of droplet thermal capacitance (6.20) can be written as follows:

$$\bar{\Phi}_{sd} - \frac{\bar{G}_{sd}\dot{m}_{\Sigma}}{K_{sd}}\left(A + Ba_{sd} + Cb_{sd} + Da_{sd}b_{sd} + Ea_{sd}^2 + Fb_{sd}^2\right) \equiv F_{bs} = 0. \tag{8.15}$$

6. The model includes two original equations for the index of evaporation calculation. In the first stage, when the temperature of the droplet surface varies from T_0 to T_{lim}, employing (8.3) and (6.29), we obtain

$$Z_{sd}^2 = -ln\left(1 - \frac{p - \gamma\left(A_p + B_pT_R + C_pT_R{}^2 + D_pT_R{}^3\right)}{p - \gamma p_{\infty}}\right). \tag{8.16}$$

Finally Equation (8.16) can be written as follows:

$$Z_{sd}^2 + ln\left(1 - \frac{p - \gamma\left(\begin{matrix}A_p + B_p(a_{sd} + b_{sd}) + C_p(a_{sd} + b_{sd})^2 \\ + D_p(a_{sd} + b_{sd})^3\end{matrix}\right)}{p - \gamma p_{\infty}}\right) \equiv F_{1Zs} = 0. \tag{8.17}$$

In the second stage, when the temperature of the droplet surface remains constant but partial pressure varies, one can use Equation (6.36), written in terms of relative values $\bar{G}_{sd}, \bar{\Phi}_{sd}$ and coordinate x:

$$\frac{1}{\bar{\Phi}_{sd}} f_{\Phi s} - \frac{1}{\bar{G}_{sd}} f_{Gs} - \frac{f_{as}}{\bar{h}_{sd}}\left[(B - C) + a_{sd}(2E - D) + b_{sd}(D - 2F)\right] \equiv F_{2Zs} = 0. \tag{8.18}$$

7. The equation of gas velocity can be obtained from the momentum equation. The following equation can be written for elementary volume [2]:

$$d\left(\dot{m}_g V_g + \sum_{sd} K_{sd} m_{sd} u_{sd}\right) = Fdp, \tag{8.19}$$

where F is the channel cross section area.

Note that the mathematical model of two-phase reactive flows was approached as a "reverse" problem (see Section 3.4) when pressure distribution along the channel $p = p(x)$ is known and specified. Then the cross section area of channel F_{com} should be treated as unknown. Taking the differential with respect to coordinate x, we obtain

$$\dot{m}_g \frac{dV_g}{dx} = F_{com}\frac{dp}{dx} - V_g \frac{d\dot{m}_g}{dx} - \sum_{sd} u_{sd}\frac{d(m_{sd}K_{sd})}{dx} - \sum_{sd} m_{sd}K_{sd}\frac{du_{sd}}{dx}. \tag{8.20}$$

Let us write the expression for calculation of mass flow rate of gas:

$$\dot{m}_g = \dot{m}_{\Sigma} - \sum_{sd} m_{sd}K_{sd}, \tag{8.21}$$

Downloaded from https://www.cambridge.org/core. Nottingham Trent University, on 17 Aug 2019 at 02:10:54, subject to the Cambridge Core terms of use, available at https://www.cambridge.org/core/terms. https://doi.org/10.1017/9781108581714.008

or, allowing for (8.2),

$$\dot{m}_g = \dot{m}_\Sigma \left(1 - \sum_{sd} \bar{G}_{sd}\right). \tag{8.22}$$

Putting (8.22) in (8.20) and allowing for (8.2), one obtains

$$\dot{m}_\Sigma \left(1 - \sum_{sd} \bar{G}_{sd}\right) \frac{dV_g}{dx} = F_{com} \frac{dp}{dx} - \sum_{sd} \left(u_{sd} - V_g\right) \dot{m}_\Sigma \frac{d\bar{G}_{sd}}{dx} - \dot{m}_\Sigma \sum_{sd} \bar{G}_{sd} \frac{du_{sd}}{dx}. \tag{8.23}$$

The area of the channel can be obtained from the continuity equation:

$$\rho_g V_g F_g = \rho_g V_g \left(F_{com} - \sum_{sd} F_{sd}\right) = \dot{m}_\Sigma \left(1 - \sum_{sd} \bar{G}_{sd}\right), \tag{8.24}$$

where the area occupied by droplets is defined by the expression

$$\sum_{sd} F_{sd} = \sum_{sd} \frac{K_{sd} m_{sd}}{\rho_{sd} u_{sd}} = \dot{m}_\Sigma \sum_{sd} \frac{\bar{G}_{sd}}{\rho_{sd} u_{sd}}. \tag{8.25}$$

Putting (8.25) in (8.24) and allowing for the equation of state, we obtain

$$F_{com} = \frac{\dot{m}_\Sigma}{\rho_g V_g} \left(1 + \rho_g V_g \sum_{sd} \frac{\bar{G}_{sd}}{u_{sd} \rho_{sd}} - \sum_{sd} \bar{G}_{sd}\right). \tag{8.26}$$

Putting (8.26) in (8.23) and replacing $\frac{du_{sd}}{dx}$ and $\frac{d\bar{G}_{sd}}{dx}$ with the right-hand sides of Equations (8.6) and (8.9), we obtain final equation for gas velocity:

$$\frac{dV_g}{dx} = \frac{\frac{1}{\rho_g V_g} \left(1 + \rho_g V_g \sum_{sd} \frac{\bar{G}_{sd}}{u_{sd} \rho_{sd}} - \sum_{sd} \bar{G}_{sd}\right) \frac{dp}{dx} - \sum_{sd} \left(u_{sd} - V_g\right) f_{Gs} - \sum_{sd} \bar{G}_{sd} f_{Us}}{\left(1 - \sum_{sd} \bar{G}_{sd}\right)}. \tag{8.27}$$

8. For steady-state adiabatic flow, the original equation of conservation of energy [101] can be written as follows:

$$\dot{m}_g h_g^* + \sum_{sd} K_{sd} m_{sd} h_{sd}^* = \dot{m}_\Sigma h_p = const, \tag{8.28}$$

where h_g^*, h_{sd}^*, h_p are stagnation enthalpies of gas, liquid, and propellant, respectively. It is known that

$$h^* = h + \frac{V}{2}. \tag{8.29}$$

Then, allowing for (8.22) and (8.29), we can write

$$\dot{m}_\Sigma \left(1 - \sum_{sd} \bar{G}_{sd}\right) \left(h_g + \frac{V_g^2}{2}\right) + \dot{m}_\Sigma \sum_{sd} \bar{G}_{sd} \left(\bar{h}_{sd} + \frac{u_{sd}^2}{2}\right) = \dot{m}_\Sigma h_p. \tag{8.30}$$

Downloaded from https://www.cambridge.org/core. Nottingham Trent University, on 17 Aug 2019 at 02:10:54, subject to the Cambridge Core terms of use, available at https://www.cambridge.org/core/terms. https://doi.org/10.1017/9781108581714.008

Finally, we obtain

$$h_g + \frac{V_g^2}{2} + \frac{\sum\limits_{sd} \bar{G}_{sd}\left(\bar{h}_{sd} + \dfrac{u_{sd}^2}{2}\right) - h_p}{1 - \sum\limits_{sd} \bar{G}_{sd}} \equiv F_h = 0. \tag{8.31}$$

In compliance with the basic mathematical model of PFR, the proposed system of equations is supplemented with Equations (2.25) and (3.70) with minor changes.

9. Equations of chemical kinetics written for PFR:

$$\frac{d\gamma_i}{dx} = \frac{1}{V_g}\left(-e^{\gamma_i}\sum_j \nu_{ij}\Omega_j + \sum_q\sum_j \nu_{qj}\Omega_j\right) \equiv f_i^{\gamma}; \quad i,p,q = 1,\ldots,n_b;\ j = 1,\ldots,2m_c + r_c, \tag{2.25}$$

where r_c = 1, and reaction j = $2m_c$ + 1 is reaction of vapor mass feed in the reacting medium.

10. The equation of energy of the gas (calorific equation)

$$h_g - \frac{\sum_i H_i r_i}{\sum_i r_i \mu_i} \equiv F_h = 0. \tag{3.70}$$

The system of equations consists of n_b + 6n_s +3, namely Equations 8.6, 8.9, 8.12, 8.14, 8.15, (8.17 or 8.18), 8.27, 8.31, 2.25, 3.70, where n_b is the number of species and n_s is number of droplets groups and contains the following unknowns: $\gamma_i, \bar{G}_{sd}, u_{sd}, \bar{\Phi}_{sd}, a_{sd}, \mathrm{b}_{sd}, Z_{sd}, V_g, h_g, T_g$. The rest parameters can be obtained from these unknowns.

As it was mentioned earlier, the model belongs to the "reverse problems." However, in general, it is more convenient to represent models of reactive flows in gas generators as a "straight problems" when the variation of cross section area of the channel $F_{va} = F(x)$is known and specified. In this case, it is necessary to preliminarily estimate the value of derivative dp/dx on each integration step so that values of calculated F_{com} and prescribed F_{va} areas will be close to each other.

This derivative is defined by the expression:

$$\frac{dp}{dx} = p\frac{\left\{\begin{array}{l} \dfrac{T_g'}{T_g} - \dfrac{\mu_g'}{\mu_g} - \dfrac{\sum\limits_{sd}\bar{G}_{sd}'}{\left(1 - \sum\limits_{sd}\bar{G}_{sd}\right)} + \left[\dfrac{\rho_g V_g \sum\limits_{sd}\left(\dfrac{\bar{G}_{sd}}{\rho_{sd}u_{sd}}\right)\left(\dfrac{\bar{G}_{sd}'}{\bar{G}_{sd}} - \dfrac{\rho_{sd}'}{\rho_{sd}} - \dfrac{u_{sd}'}{u_{sd}}\right)}{\left(1 - \sum\limits_{sd}\bar{G}_{sd}\right)}\right] \\ -\dfrac{F_{va}' - F_{cor}'}{F_g} + \dfrac{1}{V_g\left(1 - \sum\limits_{sd}\bar{G}_{sd}\right)}\left[\sum\limits_{sd}\left(u_{sd} - V_g\right)\bar{G}_{sd}' + \sum\limits_{sd}\bar{G}_{sd}u_{sd}'\right] \end{array}\right\}}{1 + \dfrac{p}{\left(1 - \sum\limits_{sd}\bar{G}_{sd}\right)V_g}\left(\dfrac{1 - \sum\limits_{sd}\bar{G}_{sd}}{\rho_g V_g} + \sum\limits_{sd}\dfrac{\bar{G}_{sd}}{u_{sd}\rho_{sd}}\right)}, \tag{8.32}$$

where $'$ refers to derivative (for instance, $T_g' = \frac{dT_g}{dx}$).

Downloaded from https://www.cambridge.org/core. Nottingham Trent University, on 17 Aug 2019 at 02:10:54, subject to the Cambridge Core terms of use, available at https://www.cambridge.org/core/terms. https://doi.org/10.1017/9781108581714.008

This formula was obtained by differentiation of the continuity equation with due allowance for (8.6, 8.9, 8.27). The corrective term $F'_{cor} = (F_{va} - F_{cm})/h$ was introduced to avoid the summation of errors in (8.32).

Fluid evaporation is simulated by the "mass feed reaction" (Section 2.2) of the type $\rightarrow H_2O; \rightarrow CH_4$. The rate constant of this reaction has dimension $\left[\frac{gmol}{cm^3 s}\right]$ and is equal to the ratio of gram-moles of vapor feeding into the reactor per unit of time, to the volume of the reactor. During time $\Delta\tau$, between two cross sections of the channel disposed at a distance of $\Delta x$from one another, the following amount of gram-moles of liquid will be vaporized:

$$\dot{m}_\Sigma \left(\sum_{sd} \frac{d\bar{G}_{sd}}{dx} \right) \frac{dx\Delta\tau}{\mu_V}. \tag{8.33}$$

Vaporized liquid will be accepted by the following volume of the gas:

$$F_g dx = \frac{\dot{m}_g dx}{\rho_g V_g}. \tag{8.34}$$

Thus, the rate of the mass feed reaction can be written as follows:

$$W_V^+ = \frac{\dot{m}_\Sigma \left(\sum_{sd} \frac{d\bar{G}_{sd}}{dx} \right) \frac{dx\Delta\tau}{\mu_V}}{\frac{\dot{m}_g dx}{\rho_g V_g}\Delta\tau} = \frac{\dot{m}_\Sigma \left(\sum_{sd} \frac{d\bar{G}_{sd}}{dx} \right) \rho_g V_g}{\dot{m}_\Sigma \left(1 - \sum_{sd} \bar{G}_{sd} \right) \mu_V} = \frac{\rho_g V_g \left(\sum_{sd} \frac{d\bar{G}_{sd}}{dx} \right)}{\left(1 - \sum_{sd} \bar{G}_{sd} \right) \mu_V}. \tag{8.35}$$

With allowance for rate constant dimension of $\left[\frac{gmol}{cm^3 s}\right]$, and keeping in mind that mass feed reaction is a zero-order reaction (Subsection 2.2.2), the corresponding rate constant is written as follows:

$$k_V^+ = \frac{0.001 p \mu_g V_g \sum_{sd} \frac{d\bar{G}_{sd}}{dx}}{\left(1 - \sum_{sd} \bar{G}_{sd} \right) R_0 T_g \mu_V}. \tag{8.36}$$

Parameters of the gas–vapor mixture in the reduced film are required for the calculation of heat transfer and mass transfer between gas and droplets. The method of their calculation is adopted from [244] and expressed by following generalized formula:

$$x_{Vg} = \left(1 - \frac{p_{sd}}{2p} \right) x_g + \frac{p_{sd}}{2p} x_V, \tag{8.37}$$

where $x = \mu, \rho, c_p, \eta, k$.

Following [244], several dimensionless parameters are calculated:

$$\text{-Prandtl number: } Pr = \frac{\eta_{Vg} c_{p\,Vg}}{k_{Vg}}, \tag{8.38}$$

$$\text{-Schmidt number: } Sc = \frac{\eta_{Vg}}{\rho_{Vg} D_{Vg}}, \tag{8.39}$$

$$\text{-Reynolds number: } Re_{sd} = \frac{|V_g - u_{sd}| p \mu_g}{R_0 T_g \eta_g} \sqrt[3]{\frac{6 m_{sd}}{\pi \rho_{sd}}}. \tag{8.40}$$

Downloaded from https://www.cambridge.org/core. Nottingham Trent University, on 17 Aug 2019 at 02:10:54, subject to the Cambridge Core terms of use, available at https://www.cambridge.org/core/terms. https://doi.org/10.1017/9781108581714.008

The Rantz–Marshall relationships are used to define thermal and diffusion Nusselt numbers [244]:

$$Nu_t = 2 + 0.6Pr^{1/3}Re^{1/2}, \tag{8.41}$$

$$Nu_D = 2 + 0.6Sc^{1/3}Re^{1/2}, \tag{8.42}$$

where *Pr, Re, Sc* are calculated at the average temperature of vapor–gas mixture T_{gV}.

For allowance for the sooting process characteristic of fuel-rich gas generators employing hydrocarbon propellant, the presented model uses the "large molecules" method describing the chemical interaction of condensed particles (Section 2.2). Condensed species identified by "large molecules" are known to feature stepwise dependencies of thermodynamic properties on temperature caused by possible polymorphous conversions due to a wide range of temperatures in the process of gas generation. Thereupon, the functional dependence of total enthalpy $H = f(T)$, as well as corresponding values of dissociation and equilibrium constants, may display discontinuities resulting in the divergence of iteration process at integration of equations and, hence, an interruption of computation. To prevent these situations, the model uses a piecewise-linear approximation of indicated thermodynamic functions with the approximation interval decreased to $\Delta T = 100$ K.

The previously described model of two-phase flows in LPRE gas generators allows one to define the generator gas chemical composition, velocity, temperature, and enthalpy as well as propellant component evaporation parameters such as flow rate, temperature, enthalpy and velocity of droplets, and the distance of evaporation of the droplets of different diameters.

8.2 Kinetic Scheme of Soot Formation

Analysis of soot formation is of crucial importance for hydrocarbon propellants combustion in conditions of the excess of fuel when value of equivalence ratio α_{ox} is much lower than stoichiometric one (reducing medium). Control over the soot formation processes unveils, in particular, the possibility of wider use of fuel-rich gas generators that run on hydrocarbon fuels – e.g., methane + oxygen, propane + oxygen, etc.

Many papers deal with the analysis of soot formation – for example, [206, 245–268]. In compliance with up-to-date concepts, soot is a superfine condensed product with particles composed of the aggregate of heavy hydrocarbons with a hydrogen content of 1%–2%. Note here that the ratio between C and H atoms, soot structure, thermodynamic, and thermophysical properties depend not only on temperature but on the prehistory of soot formation as well. Soot formation is known to be a two-stage process – i.e., the formation of nuclei and growth of particles caused by heterogeneous reactions of hydrocarbon decomposition on the surface of these particles. At high temperatures ($T \geq 2500$ K), soot formation can result from the following reactions:

$$CO + CO = C^*_c + CO_2; \quad CO + H_2 = C^*_c + H_2O, \tag{8.43}$$

where c is the substance soot affiliation index and * is the condensate index (in Reactions 8.43, soot is identified by condensed carbon).

Downloaded from https://www.cambridge.org/core. Nottingham Trent University, on 17 Aug 2019 at 02:10:54, subject to the Cambridge Core terms of use, available at https://www.cambridge.org/core/terms. https://doi.org/10.1017/9781108581714.008

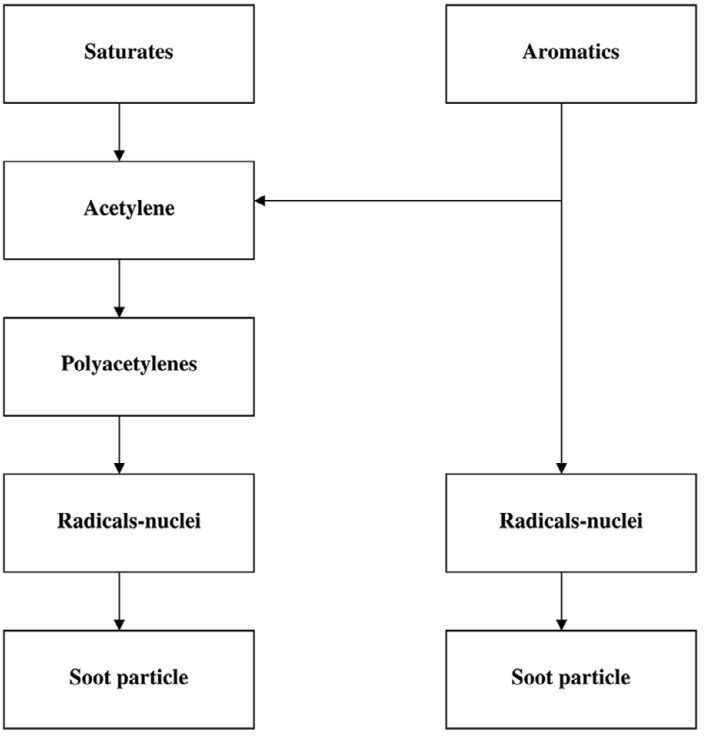

Figure 8.3 Scheme of soot particle formation in fuel-rich gas generator.

Lower temperatures ($T \leq 2000$ K) are generally characteristic of reducing working medium. It has been defined [269, 270] that, under these conditions, the prevailing "construction" material in soot particle formation and growth is composed of polyacetylenes and their radicals (such as C_4H, C_4H_2, C_6H_2, C_6H, C_8H_2, C_8H, etc.).

The generally accepted scheme of soot particle formation in the case of aromatic and saturated hydrocarbons is shown in Figure 8.3.

Polyacetylenes are brought about by the occurrence of chemical reactions in gas phase, for example,

$$C_2H_2 + C_2H_2 = C_4H_3 + H; \quad C_4H_3 + C_2 = C_6H_2 + H. \tag{8.44}$$

Since the number of the types of polyacetylenes formed in gas phase differs subject to process conditions, the soot composition and structure are not the temperature-univocal function.

Besides, the coagulation of polyacetylene molecules with the soot particle is not a completion phase of its formation; the process occurring in the soot particle results in the reconstruction of its structure. Thus, as the particle structure gets more complex and more new hydrocarbons are connected, polyacetylene circuits are closed to make cyclic and polycyclic structures (Diels–Alder reactions [269]). Besides, soot gasification in a reaction with steam and carbon dioxide (the reverse direction of Reactions [8.43]) is also possible. Dehydrogenation (H_2 release) allows one to expect that the hydrogen content in soot would vary subject to temperature and residence time.

Downloaded from https://www.cambridge.org/core. Nottingham Trent University, on 17 Aug 2019 at 02:10:54, subject to the Cambridge Core terms of use, available at https://www.cambridge.org/core/terms. https://doi.org/10.1017/9781108581714.008

The previously described soot formation scheme is complex and ambiguous for strict theoretical description, which is why a number of simplifying assumptions are accepted in the formation of the kinetic scheme of these processes. Simplifications are to be performed to provide for efficient fitting of soot formation mechanisms in algorithms and computer codes for calculation of reducing working medium properties and to reflect the basic soot formation features. These requirements may be efficiently met by applying the LM method adapted to chemical nonequilibrium heterogeneous processes (Section 2.2). Let us assume that soot in the reducing medium (H–C–O) features an unambiguous dependence of enthalpy on temperature, irrespective of a certain ambiguity in composition and the structure of chemical bonds. Note here that soot composition may differ, and it is identified by the aggregate of large molecules formed from polyacetylenes. Let us assume that large molecules of polyacetylenes feature soot thermodynamic properties irrespective of their composition.

Let soot be formed from polyacetylenes and their radicals of the following types: C_4H, C_4H_2, C_6H, C_6H_2. Then, in compliance with accepted assumptions and the proposed model of reactions involving LM (refer to kinetic mechanisms [2.49] and [2.45], Subsection 2.2.1), the soot formation process may be described, for example, as follows:

$$C_4H \rightarrow 0.01(C_4H)^*_c; \quad C_6H \rightarrow 0.01(C_6H)^*_c; \tag{8.45}$$

$$C_6H_2 \rightarrow 0.01(C_6)^*_c + H_2; \quad C_4H_2 \rightarrow 0.01(C_4)^*_c + H_2, \tag{8.46}$$

wherein one large molecule is assumed to include 100 ordinary molecules, * is the large molecule (condensed phase) index, and c is the substance soot affiliation index.

Reactions like (8.45) describe the growth of soot particles via conglomeration of soot particles on an active particle surface, while reactions like (8.46) describe the heterogeneous decomposition of heavy hydrocarbons on the surface of these particles.

In the first stage, soot formation proceeds intensively at an excess of polyacetylenes and their radicals, while Reactions (8.45, 8.46) proceed in the forward direction. Then, in the deficit of molecules making the "construction material" for soot formation, the soot formation stops and the reverse process begins when Reactions (8.45, 8.46) proceed in reverse direction.

The preliminary calculations and analysis of the contribution of separate reactions to the soot formation process demonstrated that immediate act of coagulation (8.46) or heterogeneous decomposition on the particle surface (8.46) occurs practically instantly while limiting for soot formation reactions are those of formation of polyacetylenes and their radicals C_2H_2, C_2H, C_4H_2, C_4H, C_6H_2, C_6H, C_8H_2, C_8H:

$$\begin{array}{ll}
C_2H_2 + M = H + C_2H + M; & C_4H_2 + H = C_4H + H_2; \\
C_2H_2 + H = H_2 + C_2H +; & C_4H + C_2H_2 = C_6H_2 + H; \\
C_2H_2 + C_2H_2 = H + C_4H_3; & C_4H_2 + C_2H = C_6H_2 + H; \\
C_2H_2 + C_2H = H + C_4H_2; & C_6H_2 = C_6H + H; \\
C_2H_2 + H = C_2H_3; & C_6H + C_2H_2 = C_8H_2 + H; \\
H_2 + C_2H = H + C_2H_2; & C_2H + C_6H_2 = C_8H_2 + H; \\
C_4H_3 + M = H + C_4H_2 + M; & C_4H_2 + C_4H = C_8H_2 + H; \\
C_4H_2 + M = C_4H + H + M; & C_8H_2 = C_8H + H.
\end{array} \tag{8.47}$$

Downloaded from https://www.cambridge.org/core. Nottingham Trent University, on 17 Aug 2019 at 02:10:54, subject to the Cambridge Core terms of use, available at https://www.cambridge.org/core/terms. https://doi.org/10.1017/9781108581714.008

This assumption is confirmed by the results of numerical experiment when, at various values of pre-exponential factor $A_j = 10^{12}, \ldots, 10^{16}$ in Arrhenius relationship (1.70) in Reactions (8.45) and (8.46), the soot formation rate remains, in fact, unchanged.

Thus, for calculation of parameters of working medium (H–C–O), the reaction mechanism should be supplemented with polyacetylene formation reactions (8.47) as well as with irreversible Reactions (8.45) and (8.46) describing the soot particle nucleation and growth.

Soot burnout reactions should also be added to the mechanism of chemical reactions. However, in the notable deficit of oxidizer characteristic of fuel-rich gas generators, soot burnout reaction may be neglected.

8.3 Testing the Reaction Mechanisms and Study of Soot Formation in Combustion and Flow of Methane–Oxygen Mixture in Two-Zone Gas Generator

To verify the soot formation model described in Section 8.2, it has been tested for conditions described in [251]. Enriched air (25% O_2 and 75% N_2) and methane are fed to the first zone of test apparatus, simulating gas generator operation (Figure 8.4) at initial temperature $T = 700$ K and equivalence ratio $\alpha_{ox,1} = 1.7$, which corresponds to air-to-methane ratio equal to 27.873 kg/kg. Acetylene C_2H_2 injected into the second zone produces the air-to-acetylene ratio of 3.622 kg/kg to form a reducing medium with high-intensity soot formation. Residence time within the first zone is $\tau_{1R} = 9$ ms and within the second zone is $\tau_{2R} = 8.48$ ms.

Parameters of gas generation in the second zone have been calculated by the model and algorithm described in Section 8.1. Simulation of the combustion in first zone was performed with the chemical equilibrium model.

The reacting mixture comprises the following substances: H, H_2, O, O_2, C, H_2O, CO, CO_2, OH, CH_4, HO_2, CH_2, CH_3, HCO, H_2CO, C_2H, N, N_2, NO, NO_2, C_4H, C_4H_2,

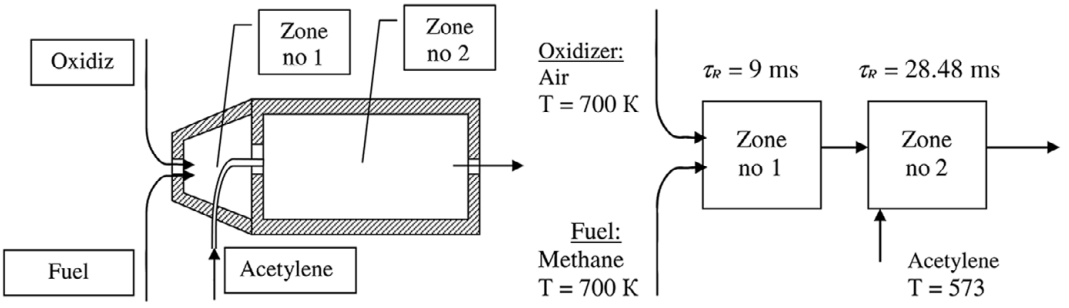

Figure 8.4 (a) Scheme of test apparatus (a) and (b) model of the processes in the of experimental test apparatus [251]. Reprinted from *Combustion and Flame*, vol. 128, M. Balthasar, F. Mauss, A. Knobel, et al., "Detailed Modeling of Soot Formation in a Partially Stirred Plug Flow Reactor," *Combustion and Flame*, vol. 128, pp. 395–409, 2002, Copyright (2002), with permission from Elsevier

Downloaded from https://www.cambridge.org/core. Nottingham Trent University, on 17 Aug 2019 at 02:10:54, subject to the Cambridge Core terms of use, available at https://www.cambridge.org/core/terms. https://doi.org/10.1017/9781108581714.008

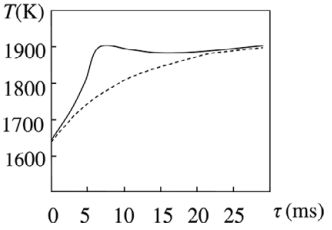

Figure 8.5 Experimental data [251]. (Reprinted from *Combustion and Flame*, vol. 128, M. Balthasar, F. Mauss, A. Knobel, et al., "Detailed Modeling of Soot formation in a Partially Stirred Plug Flow Reactor," *Combustion and Flame*, vol. 128, pp. 395–409, 2002, Copyright (2002), with permission from Elsevier) and calculated values of the temperature of combustion products: ——is T_{exp}; – – – is T_{calc}

C_4H_3, C_2H_6, C_2H_5, C_2H_3, C_2H_4, C_2H_2, HC_4*, where HC_4* is the LM soot particle model prototype. The reaction mechanism of reacting system C–N–H–O was complemented with soot formation sub-mechanism described in Section 8.2.

Figure 8.5 plots the reacting flow calculated and the experimental temperature variation subject to the time of residence of products in the gas generator's second zone. The experimental and calculated temperature at the entrance to the second zone is 1600 K, which corresponds to equilibrium chemical composition at $\alpha_{ox,1}$= 1.7. The feed of acetylene at 573 K is ensured in the same cross section.

For a proper description of mixing the acetylene fed to the second zone with the main flow, it is necessary to have experimental distribution of equivalence ratio α_{ox} at the entrance to second zone. This data is all the more important because this working process implements the transition from the notably lean mixture fed from the first zone via stoichiometric composition to the overly rich flow. However, because of the absence of such data in [251], the mathematical model of the working process under analysis assumes an instant feed and instant mixing of acetylene at the entrance of the second zone and, hence, a uniform initial distribution of concentrations and temperature at the entrance cross section. The forced assumption, unlike finite velocities of mixing, drives one naturally to a certain difference in calculated and experimental values at the second zone's initial section. Further calculations demonstrated about a 5% discrepancy at the second zone's initial section and even the same calculated and experimental temperatures of combustion products at the exit of second zone.

Figure 8.6 shows the curves of soot concentration variation in combustion products expressed in volume fractions r_V. Acetylene feed and mixture enrichment leads to the soot formation via polyacetylenes and their radicals (Section 8.2). The comparison of experimental [251] and calculated data demonstrates their quantitative and qualitative compliance, which allows the model's application for further numerical studies.

The methane–oxygen mixture was considered as another subject of study since the basic mechanisms of soot formation revealed that methane is characteristic of the entire class of saturated hydrocarbons. Methane thermal pyrolysis reactions also are a component of the soot formation mechanism for all alkanes. Besides, methane is one of the widely used and, thanks to its physical and chemical properties, promising fuels.

Downloaded from https://www.cambridge.org/core. Nottingham Trent University, on 17 Aug 2019 at 02:10:54, subject to the Cambridge Core terms of use, available at https://www.cambridge.org/core/terms. https://doi.org/10.1017/9781108581714.008

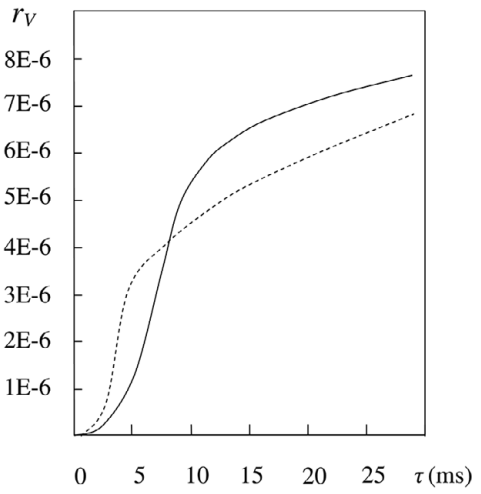

Figure 8.6 Calculated and experimental [251]. (Reprinted from *Combustion and Flame*, vol. 128, M. Balthasar, F. Mauss, A. Knobel, et al., "Detailed Modeling of Soot formation in a Partially Stirred Plug Flow Reactor," *Combustion and Flame*, vol.128, pp. 395–409, 2002, Copyright (2002), with permission from Elsevier) soot volumefraction variation in combustion products: ——— is T_{exp}; – – – is T_{calc}

A set of numerical experiments was performed for the fuel-rich two-zone gas generator running on hydrocarbon propellant; its diagram is presented in Figure 8.2b. At present, the application of fuel-rich gas generators is rather limited because of the increased content of soot in combustion products, which settles on the surface of various units (for example, on turbopump blades) to cause a notable shift from design operating modes.

In calculations, the following operating mode was considered: working medium at the exit from the first zone is in chemical equilibrium at $\alpha_{ox} = 0.6$; $u_g = 150$ m/s. Then liquid methane at temperature $T = 100$ K (if $\alpha_{ox} < 0.6$) or liquid oxygen at temperature $T = 90$ K (if $\alpha_{ox} > 0.6$) is injected in cross section c (Figure 8.2b), subject to the required total equivalence ratio for the gas generator on the whole to develop the gas generator's second zone. The spray spectrum of the injected liquid component is considered monodisperse, the gas generator's second zone length measuring $L = 0.15$ m. A complete set of substances and reactions for reducing medium of methane–oxygen mixture comprises the soot formation sub-mechanism proposed in Section 8.2 and listed in Table 8.1.

The kinetic mechanism comprises reactions of the formation of polyacetylenes and their radicals, C_2H_2, C_2H, C_4H_2, and C_4H, which are soot formation constraints.

The first step of numerical analyses consists in the analysis of the influence of total equivalence ratio (α_{ox}) on the soot formation rate. Figure 8.7 shows the soot formation dependence in the gas generator's second zone on the total equivalence ratio in the range of $\alpha_{ox} = 0.07$–0.6. Soot concentration varies here with the peak in the interval $\alpha_{ox} = 0.25$–0.35 and exceeds 1.3% in mass fractions for accepted conditions.

Downloaded from https://www.cambridge.org/core. Nottingham Trent University, on 17 Aug 2019 at 02:10:54, subject to the Cambridge Core terms of use, available at https://www.cambridge.org/core/terms. https://doi.org/10.1017/9781108581714.008

Table 8.1 Chemical mechanism for reducing medium of methane–oxygen mixture combustion, units: cm^3, mol, s, cal, respectively

$lg A_s^+$	n_s^+	E_s^+	Chemical Reaction
0.1715 E02	0.0 E0	0.88400 E05	$CH_4 + M = CH_3 + H + M$
0.148 E02	0.0 E0	0.73860 E05	$O_2 + H_2O = HO_2 + OH$
0.1388 E02	0.0 E0	0.58590 E05	$O_2 + CH_4 = CH_3 + HO_2$
0.12403 E02	0.0 E0	0.39000 E05	$O_2 + H_2 = 2OH$
0.13382 E02	0.0 E0	0.5200 E04	$H_2 + OH = H_2O + H$
0.12397 E02	0.0 E0	0.7700 E04	$O + H_2 = OH + H$
0.143 E02	0.0 E0	0.16700 E05	$H + O_2 = OH + O$
0.13159 E02	0.0 E0	0.0 E00	$2OH = H_2O + O$
0.15559 E02	0.0 E0	0.0 E00	$2H + M = H_2 + M$
0.15258 E02	0.0 E0	0.0 E00	$2O + M = O_2 + M$
0.16559 E02	0.0 E0	0.0 E00	$H + M + OH = H_2O + M$
0.161615E02	0.0 E00	0.7800 E04	$O + H + M = OH + M$
0.13311 E02	0.0 E00	0.10000 E05	$CH_4 + O = CH_2 + H_2O$
0.11478 E02	0.0 E00	0.2750 E04	$CH_3 + O_2 = H_2CO + OH$
0.1278 E02	0.0 E00	0.0 E00	$OH + CH_3 = H_2O + CH_2$
0.13271E02	0.0 E00	0.4500 E04	$CH_3 + O = H_2CO + H$
0.1378 E02	0.0 E00	0.0 E00	$CH_3 + H_2CO = CH_4 + HCO$
0.1378 E02	0.0 E00	0.0 E00	$CH_3 + HCO = CO + CH_4$
0.1078 E02	0.0 E00	0.0 E00	$CH_2 + O_2 = HCO + OH$
0.1278 E02	0.0 E00	0.2500 E04	$CH_2 + O = HCO + H$
0.1278 E02	0.0 E00	0.0 E00	$CH_2 + H_2O = H_2CO + H_2$
0.1378 E02	0.0 E00	0.4500 E04	$CH_2 + H_2CO = CH_4 + CO$
0.1278 E02	0.0 E00	0.72000 E05	$H_2CO + HCO = CH_3 + CO_2$
0.16698 E02	0.0 E00	0.32000 E05	$H_2CO + M = HCO + H + M$
0.11478 E02	0.0 E00	0.1500 E04	$H_2CO + O_2 = HCO + HO_2$
0.14557 E02	0.0 E00	0.1500 E04	$H_2CO + OH = HCO + H_2O$
0.1378 E02	0.0 E00	0.55000 E04	$H + H_2CO = H_2 + HCO$
0.14926 E02	0.0 E00	0.147 0 E05	$O + H_2CO = OH + HCO$
0.14211 E02	0.0 E00	0.0 E00	$M + HCO = CO + H + M$
0.1378 E02	0.0 E00	0.5000 E04	$OH + HCO = H_2O + CO$
0.1378 E02	0.0 E00	0. 0 E00	$H + HCO = H_2 + CO$
0.1178 E02	0.0 E00	0.7 E04	$O + HCO = OH + CO$
0.1260 E02	0.0 E00	0.2800 E05	$O_2 + HCO = CO + HO_2$
0.1260 E02	0.0 E00	0.4 E04	$O_2 + C_2H_2 = 2HCO$
0.1383 E02	0.0 E00	0.7 E04	$O + C_2H_2 = CH_2 + CO$
0.13 E02	0.0 E00	0.5700 E04	$O_2 + C_2H = HCO + CO$
0.12461E02	0.0 E0	0.2100 E04	$CO + OH = CO_2 + H$
0.1454 E02	0.0 E00	0.920 E04	$CO + O + M = CO_2 + M$
0.1320 E02	0.310 E01	0.2010 E04	$CH_4 + O = CH_3 + OH$
0.354 E01	0.0 E00	0.0 E00	$OH + CH_4 = H_2O + CH_3$
0.130 E02	0.0 E00	0.93200 E05	$CH_2 + CH_4 = 2CH_3$
0.1667 E02	0.0 E00	0.15100 E05	$CH_3 + M = CH_2 + H + M$
0.1486 E02	0.0 E00	0.0 E00	$H + CH_3 = H_2 + CH_2$
0.133 E02	0.0 E00	0.0 E00	$CH_2 + CH_3 = C_2H_4 + H$
0.135 E02	0.0 E00	0.0 E00	$CH_2 + CH_2 = C_2H_2 + H_2$
0.123 E02	0.0 E00	0.26626 E05	$CH_3 + CH_3 = C_2H_6$
0.149 E02	0.0 E00	0.31792 E05	$CH_3 + CH_3 = C_2H_5 + H$

Downloaded from https://www.cambridge.org/core. Nottingham Trent University, on 17 Aug 2019 at 02:10:54, subject to the Cambridge Core terms of use, available at https://www.cambridge.org/core/terms. https://doi.org/10.1017/9781108581714.008

Table 8.1 (*cont.*)

$lg\,A_s^+$	n_s^+	E_s^+	Chemical Reaction
0.160 E02	0.0 E00	0.9370 E04	$CH_3 + CH_3 = H_2 + C_2H_4$
0.1412 E02	0.0 E00	0.6100 E04	$H + C_2H_6 = H_2 + C_2H_5$
0.1326 E02	0.0 E00	0.2450 E04	$O + C_2H_6 = C_2H_5 + OH$
0.1305 E02	0.0 E00	0.21500 E05	$C_2H_6 + OH = C_2H_5 + H_2O$
0.1474 E02	0.0 E00	0.26600 E05	$CH_3 + C_2H_6 = CH_4 + C_2H_5$
0.1467 E02	0.0 E00	0.4860 E04	$C_2H_5 + M = H + C_2H_4 + M$
0.1218 E02	0.0 E00	0.0 E00	$C_2H_5 + O_2 = HO_2 + C_2H_4$
0.1227 E02	0.0 E00	0.79280 E05	$C_2H_5 + H = C_2H_4 + H_2$
0.1747 E02	0.0 E00	0.98160 E05	$C_2H_4 + M = H_2 + C_2H_2 + M$
0.1749 E02	0.0 E00	0.14500 E05	$C_2H_4 + M = H + C_2H_3 + M$
0.1484 E02	0.0 E00	0.2700 E04	$C_2H_4 + H = H_2 + C_2H_3$
0.1335 E02	0.0 E00	0.0 E00	$C_2H_4 + O = CH_3 + HCO$
0.1300 E02	0.0 E00	0.31500 E05	$C_2H_4 + OH = CH_3 + H_2CO$
0.1490 E02	0.0 E00	0.0 E00	$C_2H_3 + M = H + C_2H_2 + M$
0.1300 E02	0.0 E00	0.10700 E06	$C_2H_3 + H = H_2 + C_2H_2$
0.1662 E02	0.32 E01	0.500 E03	$C_2H_2 + M = H + C_2H + M$
0.7760 E01	0.0 E00	0.3700 E04	$C_2H_2 + H = H_2 + C_2H$
0.1372 E02	0.0 E00	0.43000 E05	$C_2H_2 + O = CH_2 + CO$
0.1300 E02	0.0 E00	0.0 E00	$C_2H_2 + C_2H_2 = H + C_4H_3$
0.1360 E02	0.0 E00	0.2392 E04	$C_2H_2 + C_2H = H + C_4H_2$
0.1274 E02	0.0 E00	0.0 E00	$C_2H_2 + H = C_2H_3$
0.1240 E02	0.0 E00	0.59809 E05	$H_2 + C_2H = H + C_2H_2$
0.1600 E02	0.0 E00	0.80144 E05	$C_4H_3 + M = H + C_4H_2 + M$
0.1754 E02	0.0 E00	0.0 E00	$C_4H_2 + M = C_4H + H + M$
0.11 E02	0.0 E00	0.0 E00	$C_4H_2 + H = C_4H + H_2$
0.08 E02	0.0 E00	0.0 E00	$2\,C_4H_2 = HC_4^* + HC_4^* + H_2$
0.08 E02	0.0 E00	0.0 E00	$C_4H_2 + M = HC_4^* + H + M$
0.08 E02	0.0 E00	0.0 E00	$C_4H = HC_4^*$

This is due to intensive methane decomposition at sufficiently high temperatures ($T > 1800$ K), when some portion of methane being converted into soot at thermal pyrolysis. The oxidation reaction impeding this conversion at $\alpha_{ox} < 0.6$ does not, in fact, proceed since the content of molecular and atomic oxygen in the mixture is extremely low.

The decrease in the formation of soot at $\alpha_{ox} < 0.3$ up to practical absence of soot at $\alpha_{ox} < 0.1$ is explained by low temperatures of gas mixture and methane stability under these conditions (for example, at $\alpha_{ox} = 0.07$, and $T = 830$ K).

The maximum output of soot at $\alpha_{ox} = 0.3$, well complying with a series of experimental data [245], and may be explained by an optimum combination of conditions that favor the soot formation, namely the small amount of oxidizer and high temperature facilitating the methane pyrolysis with the formation of soot particles. Besides, the so-called soot formation threshold is traced in the gas generator's second zone at $\alpha_{ox} \approx 0.50$; at the value greater than this threshold, with accepted working process conditions, soot is not practically produced. The decrease in soot formation at $\alpha_{ox} > 0.3$

Downloaded from https://www.cambridge.org/core. Nottingham Trent University, on 17 Aug 2019 at 02:10:54, subject to the Cambridge Core terms of use, available at https://www.cambridge.org/core/terms. https://doi.org/10.1017/9781108581714.008

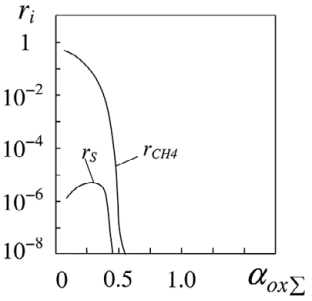

Figure 8.7 Variation of soot and methane concentrations in combustion products subject to the total equivalence ratio $\alpha_{ox\Sigma}$: p = 2 MPa; $\alpha_{ox,1}$ = 0.6.

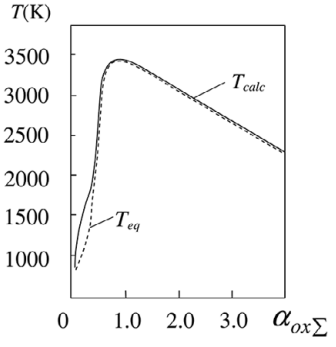

Figure 8.8 Variation of temperature of combustion products subject to total equivalence ratio $\alpha_{ox\Sigma}$; p = 2 MPa; $\alpha_{ox,1}$ = 0.6.

up to the threshold value is explained by the minor consumption of liquid methane fed to cross section c (Figure 8.2b), the presence of some amount of oxidizer, and the prevalence of the reactions of polyacetylene (soot precursor) conversion into stable components like H_2O, CO, and CO_2 over soot formation reactions.

Figure 8.8 shows that during maximum sooting-up conditions at α_{ox} = 0.3, also observed is the maximum excess of nonequilibrium temperature T of combustion products over equilibrium temperature T_{eq}, $\Delta T \approx 400$ K.

At the same time, at minimum sooting-up ($\alpha_{ox} < 0.1$, and $\alpha_{ox} > 0.6$), this difference doesn't exceed 20 K. Pyrolysis at maximum sooting-up accompanied by a notable amount of incomplete combustion products brings about a significant difference in the chemical composition of combustion products (see Table 8.2) from equilibrium composition, which, in its turn, causes a notable difference in gas mixture equilibrium and nonequilibrium temperatures. This confirms the fact that soot is the product of a chemical nonequilibrium, whilst the estimation of working process characteristics at intensive sooting-up, with the use of chemical equilibrium models, may cause a notable error (up to 15%) in calculations of chemical composition and temperature of gas generator combustion products.

Downloaded from https://www.cambridge.org/core. Nottingham Trent University, on 17 Aug 2019 at 02:10:54, subject to the Cambridge Core terms of use, available at https://www.cambridge.org/core/terms. https://doi.org/10.1017/9781108581714.008

Table 8.2 Chemical composition of combustion products at maximum sooting-up conditions

	r_{H_2}	r_{CO_2}	r_{H_2O}	r_{CO}	r_{CH_4}
Equilibrium calculation	0.557	0.0276	0.08336	0.2927	0.0391
Nonequilibrium calculation	0.4477	0.021	0.18	0.274	0.0786

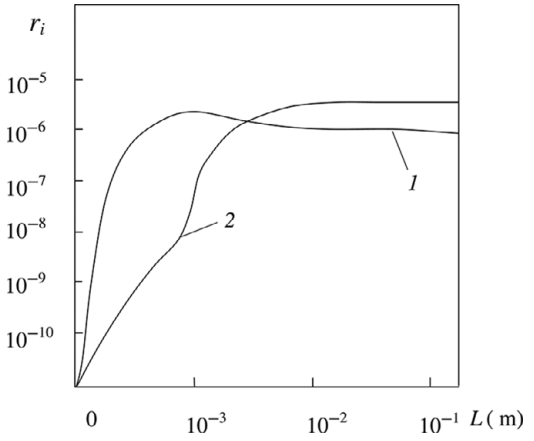

Figure 8.9 Variation of soot concentration in combustion products over the channel length subject to total equivalence ratio $\alpha_{ox\Sigma}$: (1) $\alpha_{ox\Sigma} = 0.07$, $p = 2$ MPa, $\alpha_{ox,1} = 0.6$; (2) $\alpha_{ox\Sigma} = 0.3$; $p = 2$ MPa; $\alpha_{ox,1} = 0.6$.

Figure 8.9 shows the variation of soot concentration over the second zone length for two modes: $\alpha_{ox} = 0.07$, and $\alpha_{ox} = 0.3$. At $\alpha_{ox} = 0.3$, the concentration of soot particles in combustion products over the gas generator length increases monotonically. This is caused by a comparatively slow methane pyrolysis reaction, and even after complete evaporation of methane, one observes a further increase in soot particles concentration from 1.15% to 1.32% in mass fractions.

Different behavior is displayed by the curve of soot concentration variation over the channel length at $\alpha_{ox} = 0.07$. In the initial section of high temperatures (from $T \approx 3000$ K at $\alpha_{ox} \approx 0.6$ to $T \approx 1800$ K at $\alpha_{ox} \approx 0.3$) evaporating methane decomposes with soot formation.

Then, as fuel is heated and evaporated, the gas mixture temperature drops, evaporating methane decomposition terminates, and the increase in soot particles concentration is suspended. Further, only "mechanical" admixing of gas-phase methane occurs to cause, accordingly, the decrease in soot particle concentration in combustion products.

To determine the mixture parameters in the range of $\alpha_{ox} = 0.6 \ldots 4.0$ (at equivalence ratio in gas generator's first zone $\alpha_{ox,1} = 0.6$), the liquid oxygen feed to the gas generator's second zone has been simulated.

Predictably, at $\alpha_{ox} > 0.6$, soot is absent (Figure 8.6), since the "soot formation threshold" has been registered even at $\alpha_{ox} \approx 0.50$. The temperature in this range, in fact, corresponds to its equilibrium values (Figure 8.8). The chemical composition of combustion products does not differ from the equilibrium composition as well

Downloaded from https://www.cambridge.org/core. Nottingham Trent University, on 17 Aug 2019 at 02:10:54, subject to the Cambridge Core terms of use, available at https://www.cambridge.org/core/terms. https://doi.org/10.1017/9781108581714.008

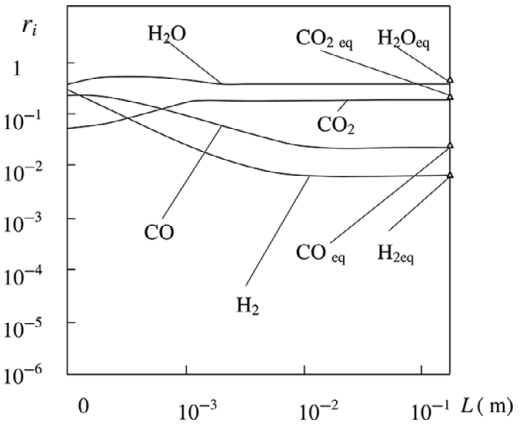

Figure 8.10 Variation of concentration of individual components in combustion products over the channel length, $\alpha_{ox\Sigma} = 2.0$; $p = 2$ MPa; $\alpha_{ox,1} = 0.6$.

(Figure 8.10). Hence, numerical experiments clearly illustrate that for the accepted conditions of the working process in the two-zone gas generator at $\alpha_{ox} > 0.50$, it is expedient to use chemical equilibrium models for the calculation of methane–oxygen mixture parameters.

8.4 Numerical Study of Combustion and Flow of Unsymmetrical Dimethylhydrazine and Nitrogen Tetroxide in Liquid Propellant Rocket Engine Gas Generator

So-called storable (non-cryogenic) propellants – nitrogen tetroxide (NT; N_2O_4) as an oxidizer, and unsymmetrical dimethylhydrazine (UDMH; $H_2N_2(CH_3)_2$), as fuel are widely used in rocket technique [215, 228]. Combustion thermodynamics and the study of chemical interaction and the flow of the previously mentioned fuel and oxidizer in gas generators is covered in a number of papers – for instance [150, 271].

The two-zone oxidizer-rich gas generator running on propellant (NT+UDMH) was selected as the matter to be analyzed with the application of the mathematical model of combustion and flow in gas generators (Section 8.1). Behavior is simulated in the following paragraphs for the case when equilibrium combustion products are generated in the gas generator's first zone with equivalence ratio $\alpha_{ox} = 0.3$. Ballasting liquid-oxidizer NT is fed to equilibrium combustion products (section c in Figure 8.2b) to reach the total gas generator equivalence ratio of 7.0. Such a huge range of "conversion" of the equivalence ratio from 0.3 (lean mixture) into 7.0 (rich mixture) is in some way hypothetical for the operation of gas generators, which as a rule use the dilution of lean mixtures with oxidizer or rich mixtures with fuel, and was chosen in order to show the reliability of the chemical nonequilibrium model and the possibility to simulate combustion and flow of both extremely lean and extremely rich mixtures. The following parameters are accepted for the entrance to the gas generator's second zone in the cross section c:

Downloaded from https://www.cambridge.org/core. Nottingham Trent University, on 17 Aug 2019 at 02:10:54, subject to the Cambridge Core terms of use, available at https://www.cambridge.org/core/terms. https://doi.org/10.1017/9781108581714.008

$u_g = u_{liq} = 10$ m/s, $p = 10$ MPa, $T_c = 1752$ K, $\dot{m}_g = 1.9$ kg/s, $\dot{m}_{liq} = 20.1$ kg/s.

The reaction mechanism consists of 35 reversible chemical reactions and comprises such substances as O, C, H, N, O_2, H_2, OH, H_2O, N_2, NO, NO_2, NH, NH_2, NH_3, CO, CO_2, CH_3, and CH_4.

It is obvious that, at such a high flow rate of ballasting component required for reaching α_{ox} = 7.0 and a relatively low gas temperature, the risk of combustion failure grows dramatically. To prevent such a situation, it is necessary to select an appropriate droplet size distribution and corresponding flow rate for every group of droplets.

Numerical analyses show that in the case of a monodisperse droplets' spray spectrum, the termination of the combustion occurs independently of the diameter of droplets and their velocities u_g and u_{liq}. Hence, to guarantee a stable combustion, it is necessary to create a "special" ion procedure of the atomization of the ballasting component (for instance, provide at least two groups of droplets) that guarantees fast evaporation of the first group of drops, facilitating a certain growth in the mixture equivalence ratio (for example, an increase in α_{ox} from 0.3 to 1.0) even before a high-intensity evaporation of other groups starts. To prove the validity of the hypothesis about possibility of maintaining a stable combustion by control over droplets atomization, it is sufficient to consider two groups of drops with flow rates $\bar{m}_{1\Sigma}$ and $\bar{m}_{2\Sigma}$. The relative flow rate of the first group of drops $\bar{m}_{1\Sigma} = \frac{\dot{m}_1}{\sum_{sd} \dot{m}_{sd}}$ obtained in numerical analysis and, complying with the aforesaid conditions (increase in α_{ox} from 0.3 to 1.0), equals 0.1. Pro tanto, the value of relative flow rate for the second group of drops $\bar{m}_{2\Sigma}$ equals 0.9. Note here that the first group of drops feature a small diameter ($d_1 \leq 30$ μm), while that of the second group drops is notably larger – i.e., $d_2 \leq 500$ μm. This allows one to postpone the process of high-intensity evaporation of the ballasting component (which makes a determinant of the decrease in gas temperature T_g in the second zone) unless the first group of drops evaporates completely to interact with the mixture of combustion products coming from zone 1, hence bringing about a notable increase in the mixture temperature to comparatively high values that guarantee a stable combustion (Figures 8.11–8.13).Then T_g decreases due to ballasting component evaporation and mixing with the gas mixture. Numerical analyses performed for different diameters d_1 and d_2 indicate that the following drop diameter ranges are the most acceptable: d_1 = 20–30 μm, d_2 = 150–200 μm, which is confirmed by curves 1 and 2 shown in Figure 8.11. It should be pointed out that these droplet diameter variation ranges can ensure the continuation of combustion; in addition, they are acceptable in terms of oxidizer droplet diameters and their distribution adopted in gas generator design. In this case, no termination of combustion occurs, and, at the same time, the distance at which ballasting component evaporates completely is notably decreased.

Curve 1 illustrates the termination of combustion (point A). At $d_2 \leq 100$ μm, the second droplet group high-intensity evaporation sets in much earlier, which causes combustion termination. Besides, Figure 8.12 shows that a considerable difference in gas and liquid velocities is the cause of combustion interruption as well (point A), since it initiates the high-intensity, hence notable, decrease in gas temperature ($T_g \leq 1000$ K).

Downloaded from https://www.cambridge.org/core. Nottingham Trent University, on 17 Aug 2019 at 02:10:54, subject to the Cambridge Core terms of use, available at https://www.cambridge.org/core/terms. https://doi.org/10.1017/9781108581714.008

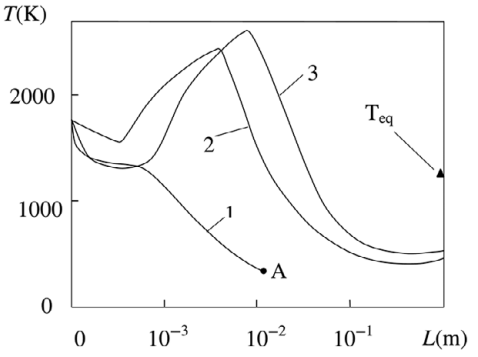

Figure 8.11 Influence of droplet atomization on combustion process, $u_g = u_{liq} = 10$ m/s; (1) $d_1 = 25$ μm, $d_2 = 75$ μm; (2) $d_1 = 25$ μm, $d_2 = 200$ μm; (3) $d_1 = 7$ μm, $d_2 = 300$ μm.

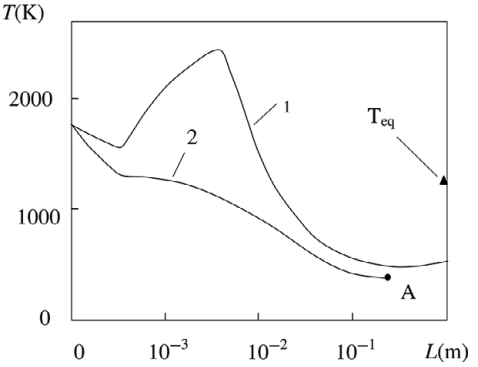

Figure 8.12 Influence of relative velocities of gas and liquid on combustion process, $d_1 = 25$ μm, $d_2 = 200$ μm; (1) $u_g = u_{liq} = 10$ m/s; (2) $u_g = 100$ m/s, $u_{liq} = 50$ m/s.

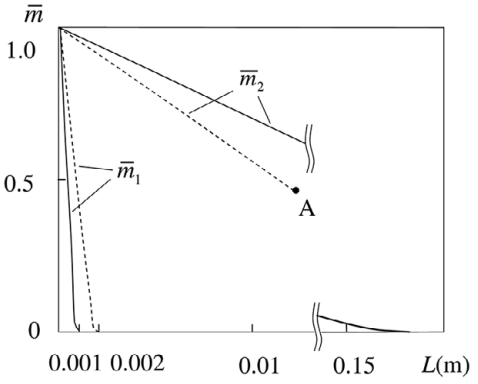

Figure 8.13 Variation of relative mass of droplet groups over the channel length, $d_1 = 25$ μm, $d_2 = 75$ μm; —— $-d_1 = 25$ μm, $d_2 = 200$ μm; $\bar{m}_1 = m_1/m_{1,0}$ $\bar{m}_2 = m_2/m_{2,0}$; $u_g = u_{liq} = 10$ m/s.

Downloaded from https://www.cambridge.org/core. Nottingham Trent University, on 17 Aug 2019 at 02:10:54, subject to the Cambridge Core terms of use, available at https://www.cambridge.org/core/terms. https://doi.org/10.1017/9781108581714.008

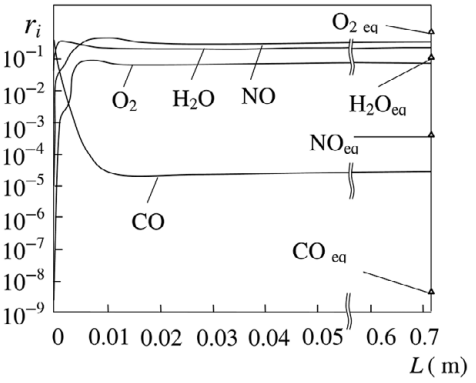

Figure 8.14 Variation of concentrations of individual components of combustion products in gas generator second zone, d_1 = 25 μm, d_2 = 200 μm; $u_g = u_{liq}$ =10 m/s.

Under such conditions (Figure 8.14), the effects of chemical nonequilibrium are most pronounced. Besides, the maximum difference from equilibrium concentrations is observed in CO, NO components that define the gas generator emission characteristics.

The previously described analyses underline the urgency and even the necessity to apply chemically nonequilibrium models for estimation and optimization of gas generator operating parameters, as well as wide possibilities of using even one-dimensional models, provided that chemical nonequilibrium approach and detained kinetic mechanisms are used.

Downloaded from https://www.cambridge.org/core. Nottingham Trent University, on 17 Aug 2019 at 02:10:54, subject to the Cambridge Core terms of use, available at https://www.cambridge.org/core/terms. https://doi.org/10.1017/9781108581714.008

9 Pressurization of Liquid Propellant Rocket Engine Tanks

9.1 Processes in Ullage of Liquid Propellant Tank

Feeding high-pressure gas into the gas space of the tanks filled with liquids and even solids aims to maintain this gas space at a preselected pressure history bounded by tanks' structural requirements or required propellant supply pressures, to prevent propellant pump cavitation, to avoid uncontrolled chemical reactions in gas space, etc. The pressurization process and corresponding pressurization systems are used in diverse technical devices. These include apparatus for chemical technology, oil and ore tankers, aircraft fuel tanks, and propellant tanks of LPREs. Processes related to high-pressure and often high-temperature gas feeding are extremely diversified because of the complex flow patterns of gas in the free space of the tanks, possible heat exchange with structural elements and the propellant, mass exchange caused by the evaporation of liquids, the chemical reactions in gas, and liquid phases.

Because of the processes' versatility, designing these systems requires the development of complex mathematical models incorporating those of varied models of physical and chemical phenomena. These comprise, for example, the LPRE propellant tank pressurization processes.

A necessity in a high-pressure gas feed into gas space, the extra volume of gas above the propellant in sealed tanks called ullages aims to maintain the ullage at a preselected pressure history to feed fuel or oxidizer in the thrust chamber of the engine and prevent a collapse of the thin-walled tank structure. The pressurization system also can be used for secondary purposes such as providing thrust for the space vehicle's trajectory correction, providing thrust for rocket stages separation, operation of servomechanisms, etc. [215, 228, 243, 272, 273].

Diverse LPREs and a variety of liquid propellants – from cryogenic to high boiling – resulted in the development of different pressurization systems varying in pressurizing gas generation schemes in systems of gas feed into the ullage in types of gas diffusers, devices for gas feed into the tank [57, 215, 228, 243, 272, 273]. The following classification of pressurization systems is most common [160, 243]:

a. stored-gas systems that store high-pressure ambient temperature gas in the storage container;
b. evaporated-propellant systems, when vapors of the heated component of the propellant are directed into the same propellant component tank for tank pressurization;

Downloaded from https://www.cambridge.org/core. Nottingham Trent University, on 17 Aug 2019 at 02:12:43, subject to the Cambridge Core terms of use, available at https://www.cambridge.org/core/terms. https://doi.org/10.1017/9781108581714.009

c. gas-generator systems or mixing chambers that employ high-temperature gas generator products (fuel rich or fuel lean) to pressurize fuel or oxidizer tanks (see Chapter 8)

The advantages of the third kind of systems are a high magnitude of the working capacity RT of the gas and the absence of additional storage of the compressed pressurization gas since the gas generator employs LPRE propellant components.

A diagram of the turbopump feed system (Figure 8.1b) with a gas-generator pressurization system is shown in Chapter 8. Turbopump combines the turbine with oxidizer and propellant pumps for propellant component delivery from propellant and oxidizer tanks to the thrust chamber. The gas generator (Figure 8.1b) generates high-temperature, fuel-rich combustion products (as a rule, α_{ox} = 0.3–0.5), while mixing chamber (Figure 8.1b) produces fuel-lean combustion products (α_{ox} = 5–7). The fuel-lean mixture is fed into the ullage of the oxidizer tank and fuel-rich mixture is fed into the ullage of fuel tank to prevent uncontrolled chemical reactions with the vapors of corresponding propellant component.

Working processes in pressurization gas generators and mixing chambers as well as their operation and design do not, in fact, differ from those described in Chapter 8. The pressure in LPRE tanks with turbopump feed system is, as a rule, 20–40 times lower (70–400 kPa) than the pressure in tanks with pressure feed (1–13 MPa), which notably decreases the propellant supply system weight. Besides, the turbopump feed rules out the application of compressed gas storage tank that reduces the system overall weight. This is why this the turbopump feed system is used in modern rocketry, particularly for high-thrust propulsion systems.

Processes taking place in propellant tanks and specifically in the ullages are especially complex in cases where the turbopump feed system is used. This is caused by several factors, including a complex gas-dynamic pattern and heat and mass exchange of high-temperature gas (so-called hot pressurization) with tank structural elements and liquid propellant, which can be both high boiling (for example, UDMH, kerosene, NT) and cryogenic (for example, oxygen, hydrogen, fluorine). The chemical interaction of the generator gas and propellant vapors in the ullage is also typical.

A special place in pressurization schemes is held by the so-called chemical pressurization systems [243] where, unlike in the previously described schemes, fuel-lean generator gas is fed into the fuel tank while fuel-rich generator gas is fed into the oxidizer tank. This allows a vigorous but controlled chemical interaction with propellant component vapors to be maintained, which creates sufficiently high pressures, and hence reduces the pressurization gas consumption, saves propellant, and reduces the weight of the pressurization system.

The development and optimization of pressurization systems, particularly those of systems with turbopump feed, requires the application of complex mathematical models that combine models of gas flow in closed volumes, heat exchange, and phase transitions, with models of chemical reaction in comparatively low-temperature media. Since the entire complex of these processes occurs in the tank ullage, it is expedient to isolate the latter as the simulation entity.

Downloaded from https://www.cambridge.org/core. Nottingham Trent University, on 17 Aug 2019 at 02:12:43, subject to the Cambridge Core terms of use, available at https://www.cambridge.org/core/terms. https://doi.org/10.1017/9781108581714.009

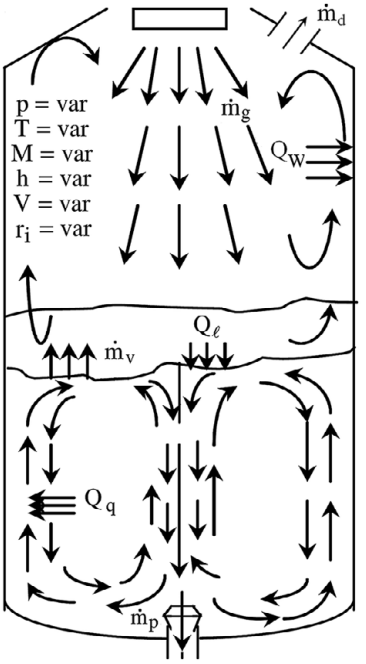

Figure 9.1 Schematic diagram of aerothermochemical processes in liquid-propellant rocket engine tank [274]. From V. Naoumov, "Simulation of High-Temperature Pressurization of the Liquid-Propellant Rocket Tanks," 47th Aerospace Science Meeting Including the New Horizons Forum and Aerospace Exposition, AAA 2009–1600, pp. 1–7, Orlando, FL, 2009, reprinted by permission of the American Institute of Aeronautics and Astronautics, Inc

Before describing the mathematical model, let us analyze main processes that occur in the ullage and liquid propellant during propellant feed system operation accompanied by propellant expulsion and generator gas feed into the ullage (Figure 9.1).

Pressurizing gas flow in the ullage. Features of gas flow in the closed volume of the ullage depend in many ways on the design and arrangement of the gas feed device (diffuser or gas intake), the design, size and shape of the tank, and the dynamics of propellant expulsion. The requirement of a high efficiency of pressurization gas (working capacity, *RT*) and the requirement to protect the tank structure sets its temperature equal to 600–800 K for tanks with high-boiling propellant components and 300–500 K for cryogenic propellants. Thereby, the pressurizing gas flow pattern is influenced not only by mixing the submerged impinging high-temperature jet of pressurizing gas with the low-temperature surrounding mixture in the ullage but also by the Archimedean forces caused by a notable difference in the densities of pressurizing gas and the mixture in the ullage. At a notable difference in densities and temperatures of ullage gas mixture and pressurizing gas, jet velocity is likely to decrease intensively, and the jet undergoes a fast "decay" with complete destruction of the jet flow pattern structure. A study of flow patterns in the ullage [275–277] has shown that the depth of jet penetration in the ullage defines the intensity of heat and mass transfer in

Downloaded from https://www.cambridge.org/core. Nottingham Trent University, on 17 Aug 2019 at 02:12:43, subject to the Cambridge Core terms of use, available at https://www.cambridge.org/core/terms. https://doi.org/10.1017/9781108581714.009

the ullage. High velocities of pressurizing gas feed can cause intensive heat transfer to the walls and other structural elements of the tank and also splashing of liquid propellant that brings about a high intensity of its evaporation. Determination of gas flow characteristics is one of the keystone problems in the calculation of pressurization system parameters.

Pressurizing gas heat exchange with tank walls. The gas flow pattern, its velocity, and the degree of turbulence have a decisive influence on heat exchange processes. Convective heat exchange with tank walls and propellant can vary from free to forced convection subject to gas feed velocity and difference in the temperature of the pressurizing gas and that of the gas mixture in the ullage. At low gas feed velocity and notable differences in temperatures, a significant thermal stratification of the mixture in the ullage can occur to make free convection prevail. At comparatively high velocity and high temperature gradients in the boundary layer on the tank wall, turbulent mixing of gas volumes is caused by turbulent pulsations from high-temperature to low-temperature (near tank walls) regions to bring about not only a transfer of kinetic energy but also a transfer of the heat of chemical reactions. Even without chemical reactions, heat transfer intensification caused by a high degree of turbulence (ε = 40%–50%) was observed [278].

Thermal stratification and circulation of the propellant. Temperature gradient on gas–liquid interface causes a convective heat flow to the propellant surface. Heat propagation deep into component results both from conduction from the propellant surface and circulating convective flows of the liquid caused by pressurization gas impact on the surface. Conduction brings about a thermal stratification of the propellant while convective flows mix the liquid and makes its temperature distribution more uniform. Cryogenic propellant can be also heated up by heat transfer through the tank walls despite a thorough insulation of the walls. Note here that free-convective flow of the liquid directed from the heated walls toward the propellant component surface and, further, along the axis of the tank – from the surface of the propellant deep into the component [243, 273, and 279] – that also facilitates the leveling of the temperature field in the liquid.

Evaporation from the surface of the propellant. Intensive evaporation from the propellant surface can occur at pressurization of tanks with cryogenic and high-boiling propellant by both heated inert gases and gas generation products. Evaporation – particularly evaporation of cryogenic components – can significantly influence the gas thermodynamics in the ullage. At the propellant expulsion, a liquid film can be formed on the walls of the tank to flow down and evaporate, increasing in the amount of vapors in the ullage. Film splashing by pressurizing gas can cause the entrainment of a considerable amount of droplets evaporating in the ullage volume. The boiling of cryogenic propellant generates vapor bubbles flowing toward the surface of the propellant and increases the pressure in the ullage. With pressure exceeding the allowable values, the gas mixture drains through the relief valve in the ambient medium, which finally causes certain losses of the pressurizing gas.

Condensation. Propellant vapors that can be contained in the pressurizing gas are likely to convert into liquid state on the tank wall if its temperature is lower than that of

Downloaded from https://www.cambridge.org/core. Nottingham Trent University, on 17 Aug 2019 at 02:12:43, subject to the Cambridge Core terms of use, available at https://www.cambridge.org/core/terms. https://doi.org/10.1017/9781108581714.009

saturation of component vapors. Condensation can also occur on the propellant surface, liquid film, and, under some conditions – for example, in the presence of condensation centers – in the entire volume of the ullage.

Variation of gas mixture composition in the ullage resulted from chemical reactions. Along with evaporation and condensation, the chemical composition and, hence, thermodynamic properties of the gas mixture in the ullage can be affected by chemical reactions between propellant vapors and pressurizing gas. This is particularly the case in gas generator pressurization systems when chemically active products of gas generation are fed into the propellant tank. That causes chemical reactions, which at previously mentioned pressurization temperatures feature finite rates, thus bringing about the chemical nonequilibrium variation of gas composition in the ullage (see Section 1.3). A fundamental role is played by chemical reactions and, therefore, chemical nonequilibrium in the chemical pressurization systems [273, 275, 277, 279–282].

9.2 Application of Reactor Approach to the Simulation of Pressurization

The involvement of experimental study in the development and optimization of pressurization systems is a generally accepted approach in the creation of rocket technique. However, due to extremely high cost of the experimental study of pressurization systems, the application of mathematical models is highly important at initial stages of systems development.

The diversity of processes described earlier dictates a number of significant assumptions to be used in the development of such models. It is necessary to allow for the fact that unlike the operation of most propulsion and power generation systems, it is impossible to isolate a steady-state process of operation of pressurization systems. Even at a constant rate of propellant expulsion from the tank to the LPRE thrust chamber, the tank gets emptied with a lower of propellant level and a corresponding increase in ullage volume. Note here that a permanent change of the gas flow pattern in the ullage and a corresponding change of velocity field causes a continuous variation of the parameters of heat and mass exchange processes in the ullage and propellant described in Section 9.1. This, in its turn, changes the thermodynamic parameters of the gas mixture in the ullage and the parameters of the propellant, which causes the change in the velocity field and, at times, in flow pattern in the ullage on the whole.

The more common model enabling to accumulate most physical and chemical phenomena described in Section 9.1 is likely to be the turbopump feed system with the application of gas generator pressurization system, which is an integral part of most liquid rocket boosters. With due allowance for relatively low pressurizing gas temperatures and possible proceeding of chemical reactions in the ullage, it is feasible to use the chemical nonequilibrium model (Section 1.4) and the reactor approach (Section 1.5) for the simulation of the processes in the ullage in the conditions of hot pressurization. However, allowing for the key influence of gas flow characteristics in the ullage, the reactor model should be constructed proceeding from the knowledge about the gas flow pattern and velocity fields.

Downloaded from https://www.cambridge.org/core. Nottingham Trent University, on 17 Aug 2019 at 02:12:43, subject to the Cambridge Core terms of use, available at https://www.cambridge.org/core/terms. https://doi.org/10.1017/9781108581714.009

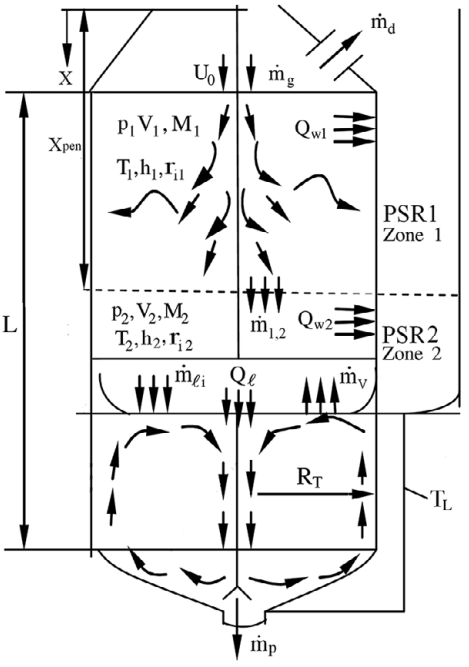

Figure 9.2 Two-zone model of the processes in the propellant tank [274]. From V. Naoumov, "Simulation of High-Temperature Pressurization of the Liquid-Propellant Rocket Tanks," 47th Aerospace Science Meeting Including The New Horizons Forum and Aerospace Exposition, AAA 2009–1600, pp. 1–7,Orlando, FL, 2009, reprinted by permission of the American Institute of Aeronautics and Astronautics, Inc

Based on the analysis of physicochemical processes and using experimental observations [275–277], at least two zones with different state parameters of the gas mixture may be considered in the ullage of the propellant tank. The first zone (zone 1) arranged in the upper part of the ullage is subjected to intensive mixing by pressurizing gas fed into the ullage (Figure 9.2). The second possible zone (zone 2) can originate in the lower part of the ullage during the lowering of the propellant (fuel or oxidizer) level due to the "decay" of pressurizing gas jet under the impact of Archimedean forces (Figure 9.2). A specific feature of the first zone consists in a uniform distribution of temperatures and other parameters over its entire volume, while the second zone differs in a significant distribution (stratification) of parameters and especially gas mixture temperature. Allowing for the fact that liquid-propellant rocket booster tanks, as a rule, featire a cylindrical shape of notably larger axial sizes as compared to radial sizes, the model of the processes in the ullage may be considered a one-dimensional model with parameters varying only along the tank vertical axis. It is obvious that uniform distribution of all parameters of the gas mixture in the first zone may be assumed, and zone 1 may be considered as the non-steady-state PSR (Section 1.5). According to the trend toward stratification of the gas mixture in the lower part of the ullage, which is possible at comparatively low pressurizing gas feed rates and especially at the end of the process of tank emptying, for model simplification it is possible to simulate the

Downloaded from https://www.cambridge.org/core. Nottingham Trent University, on 17 Aug 2019 at 02:12:43, subject to the Cambridge Core terms of use, available at https://www.cambridge.org/core/terms. https://doi.org/10.1017/9781108581714.009

second zone by the single non-steady-state PSR as well, with a certain temperature averaged over the volume as well as other parameters of the state. However, note here that special relations can be used for the determination of thermal stratification of the mixture in zone 2 for the adequate prediction of heat and mass exchange in this zone, since application of the averaged gas mixture temperature for the calculation of heat and mass exchange in the second zone can result in tangible errors.

This model is schematically shown in Figure 9.2, wherein the interface between zone 1 and zone 2 is defined from separate gas dynamic calculations based on the flow pattern of pressurizing gas in a closed volume of the ullage at continuous increase in this volume and under the effect of Archimedean forces acting on the jet until its complete possible decay, which defines the origination of the second zone and following the increase of its volume.

It is obvious that the second zone can either be absent or originate with tank emptying, while the amount of gas in this zone is defined by the overflow of some amount of gas from the first zone and by evaporation of propellant from its surface or condensation of propellant vapors.

Experimental observations have shown that such overflow occurs at low rates comparable with the rate of propellant level lowering at propellant expulsion. This allows one to assume the absence of the gas mixing in the second zone at model construction. The gas mixture mass variation in the first zone is mainly caused by pressurizing gas feed, tank draining, and the gas mixture overflowing to the second zone.

Given the unavailability of the second zone, to these factors is added the evaporation of propellant from its surface or condensation of propellant vapors. Heat exchange processes in the first zone are defined mainly by forced convection while heat exchange in the second zone, as a rule, is a free convective one.

In compliance with the model of two non-steady-state PSRs, the gas mixture in each reactor features different thermodynamic parameters including temperature, enthalpy, density, specific heat, and gas mixture chemical composition. The only exception here is the pressure; instant leveling of the pressure over the entire volume of the ullage seem naturals enough due to relatively low rates of pressurization gas feed and its flow in the volume of the ullage. The volume of reactors varies with tank emptying and variation in depth of pressurization gas penetration into the ullage and ullage volume change because of propellant (fuel or oxidizer) expulsion:

$$dV/dt = \dot{m}_p/\rho_p, \tag{9.1}$$

where V is ullage volume, $\dot{m}_p$ is propellant mass flow rate, and ρ_p is propellant density.

Let us write the following in compliance with the concept of gas mixture mass variation in zones 1 and 2:

$$\frac{dM_1}{dt} = \dot{m}_g\text{-}\dot{m}_{1,2}\text{-}\dot{m}_d + \delta \times \dot{m}_V - \delta \times \sum_i m_{li}, \tag{9.2}$$

$$\frac{dM_2}{dt} = \dot{m}_{1,2} + \dot{m}_V - \sum_i \dot{m}_{li}, \tag{9.3}$$

Downloaded from https://www.cambridge.org/core. Nottingham Trent University, on 17 Aug 2019 at 02:12:43, subject to the Cambridge Core terms of use, available at https://www.cambridge.org/core/terms. https://doi.org/10.1017/9781108581714.009

where M_1 and M_2 are the gas mixture mass in zones 1 and 2, respectively; $\dot{m}_g$ is the pressurizing gas mass flow rate; $\dot{m}_d$ is the gas mixture flow rate through the relief valve; $\dot{m}_{1,2}$ is the gas mixture flow rate from zone 1 to zone 2; $\dot{m}_{li}$ is the flow rate of ith substance condensing on the propellant surface; $\dot{m}_V$ is the vapor flow rate from propellant surface; $\delta = 1$ at the absence of zone 2; and $\delta = 0$ if zone 2 exists.

Equation of energy for zone 1 may be written as follows:

$$\frac{dU_1}{dt} = h_g\dot{m}_g - q_{W1} - h_1\dot{m}_d - p\frac{dV_1}{dt} - h_1\dot{m}_{1,2} + \delta \times \dot{m}_V h_V - \delta \times \sum_i \dot{m}_{li}h_{li} - \delta \times q_l, \tag{9.4}$$

where U_1 is the internal energy of gas mixture in zone 1, h_g is the specific enthalpy of pressurizing gas, h_1 is the specific enthalpy of gas mixture in zone 1, V_1 is the volume of zone 1, p is the pressure in the ullage, q_{W1} is the heat flow rate to the tank walls relating to zone 1, q_l is the heat flow rate to the propellant, h_V is the specific enthalpy of propellant vapors, h_{li} is the specific enthalpy of ith substance condensing on propellant surface, $\delta = 1$ at the absence of zone 2, and $\delta = 0$ if zone 2 exists.

Heat flow rate to the tank walls relating to zone 1 is defined from the relation:

$$q_{W1} = \int_{F_1} \dot{q}_{W1_x} dF_{1_x}, \tag{9.5}$$

where $\dot{q}_{W1_x}$ is the heat flux, F_{1_x} is the elementary area of wall surface, and F_1 is the area of wall surface relating to zone 1.

Using first law of thermodynamics,

$$U_1 = H_1 - pV_1 \quad \text{or} \quad U_1 = h_1M_1 - pV_1, \tag{9.6}$$

it is possible to reduce (9.4) to the following form:

$$\frac{d(h_1M_1)}{dt} - p\frac{dV_1}{dt} - V_1\frac{dp}{dt_1} = \dot{m}_g h_g - q_{W1} - h_1\dot{m}_d - p\frac{dV_1}{dt} - h_1\dot{m}_{1,2} + \delta \times \dot{m}_V h_V - \delta \times \sum_i \dot{m}_{li}h_{li} - \delta \times q_l \tag{9.7}$$

LPREs of the first rocket stages operate mainly in steady-state mode, and at tank emptying, the pressure in the tank is usually maintained as constant. Hereby, pressure variation can be considered a second-order magnitude compared with ullage volume variation. Using this assumption and Equation (9.2), it is possible to reduce (9.7) to the following form:

$$M_1\frac{dh_1}{dt} = \dot{m}_g h_g - q_{W1} - h_1\dot{m}_d - h_1\dot{m}_{1,2} + \delta \times \dot{m}_V h_V - \delta \times \sum \dot{m}_{li}h_{li} - \delta \times q_l - \dot{m}_g h_1 + \dot{m}_{1,2}h_1 + h_1\dot{m}_d - \delta \times \dot{m}_V h_1 + \delta \times h_1 \sum_i \dot{m}_{li} \tag{9.8}$$

Downloaded from https://www.cambridge.org/core. Nottingham Trent University, on 17 Aug 2019 at 02:12:43, subject to the Cambridge Core terms of use, available at https://www.cambridge.org/core/terms. https://doi.org/10.1017/9781108581714.009

or

$$\frac{dh_1}{dt}=\frac{1}{M_1}\left[\dot{m}_g\left(h_g-h_1\right)-q_{W1}+\delta\times\dot{m}_V(h_V-h_1)+\delta\times\left(h_1\sum_i\dot{m}_{li}-\sum_i\dot{m}_{li}h_{li}\right)-\delta\times q_l\right]. \tag{9.9}$$

Energy equation for zone 2 may be written as follows:

$$\frac{dU_2}{dt}=h_1\dot{m}_{1,2}-q_{W2}-p\frac{dV_2}{dt}+\dot{m}_Vh_V-\sum_i\dot{m}_{li}h_{li}-q_l, \tag{9.10}$$

where U_2 is the internal energy of gas mixture in zone 1, V_2 is the volume of zone 2, and q_{W2} is the heat flow rate to the tank walls relating to zone 2.

Similarly to Equation (9.4), it can be transformed to

$$\frac{dh_2}{dt}=\frac{1}{M_2}\left[\dot{m}_{1,2}(h_1-h_2)-q_{W2}+\dot{m}_V(h_V-h_2)+\left(h_2\sum_i\dot{m}_{li}-\sum_i\dot{m}_{li}h_{li}\right)-q_l\right]. \tag{9.11}$$

For both zones, the following equations of state can be written:

$$M_1=pV_1\mu_1/R_0T_1, \tag{9.12}$$

$$M_2=p(V-V_1)\mu_2/R_0T_2, \tag{9.13}$$

where μ_1 and μ_2 are gas mixture molecular mass in zones 1 and 2, respectively.

Since the mixture in zone 2 has averaged temperature T_2, simulation of thermal stratification in this zone requires the ratio, which can be derived from the comparison of this temperature with mass-averaged and volume-averaged temperatures of the gas mixture along with analysis of heat exchange of stratified gas mixture in this zone with tank walls. Let us assume that the gas mixture consists of a set of horizontal layers, each with its own temperature decreasing over the second zone height from temperature T_1 to close to the propellant temperature. Since mixture propagation velocity in zone 2 is defined by mixture flow rate from zone 1, it is possible to write the heat balance equation for zone 2 arbitrary layer on the assumption that the wall ith section corresponding thereto is heated by convection:

$$\dot{m}_{1,2}c_{pi}dT/dt=h_i(T_{x_i}-T_{W_i})2\pi R_Tdx, \tag{9.14}$$

where T_{x_i}, T_{W_i} are temperatures of the gas mixture in ith gas layer and ith section of the wall, respectively; R_T is the tank radius; h_i is the heat transfer coefficient.

Integration of (9.14) from top boundary of zone 2 to arbitrary cross section x gives the following:

$$\frac{T_{x_i}-T_{W_i}}{T_1-T_W}=e^{-A_ix}, \tag{9.15}$$

where $A_i=\dfrac{2\pi R_Th_i}{\dot{m}_{1,2}c_{pi}}$.

Downloaded from https://www.cambridge.org/core. Nottingham Trent University, on 17 Aug 2019 at 02:12:43, subject to the Cambridge Core terms of use, available at https://www.cambridge.org/core/terms. https://doi.org/10.1017/9781108581714.009

The expressions for calculation of mass-averaged temperature, $\bar{T}_M$ and volume-averaged temperature $\bar{T}_V$ of stratified gas mixture can be written as follows:

$$\bar{T}_M = \frac{\int_0^L T_x \left(p\mu_2 / R_0 T_x\right) dx}{\int_0^L \left(p\mu_2 / R_0 T_x\right) dx} = \frac{L}{\int_0^L \frac{dx}{T_x}}, \tag{9.16}$$

$$\bar{T}_V = \frac{\int_0^L T_x dx}{L}, \tag{9.17}$$

where L is the height of zone 2.

Substitute in (9.15) the local values of wall temperature, heat transfer coefficients, and gas mixture specific heat for their averaged values, and substituting this expression in (9.17), one can obtain

$$\bar{T}_V = \frac{\int_0^L [\bar{T}_W + (T_1 - \bar{T}_W) e^{-A \times x}] dx}{L}, \tag{9.18}$$

where $A = \dfrac{2\pi R_T \bar{h}}{\dot{m}_{1,2} \bar{c}_p}$, $\bar{T}_W$ is the average temperature of tank walls in zone 2, and $\bar{c}_p$ and $\bar{h}$ are the average values of specific heat and heat transfer coefficient.

Use (9.15) to find from (9.16) mass-averaged temperature as well:

$$\bar{T}_M = \frac{L}{\int_0^L dx / [\bar{T}_W + (T_1 - \bar{T}_W) e^{-A \times x}]}. \tag{9.19}$$

The integration of (9.19) with allowance for the fact that $\bar{T}_M = T_2$ results in the following expression, hereinafter referred to as "equation of temperatures relation":

$$T_2 = \frac{\bar{T}_W}{1 + \dfrac{1}{A_L} \ln \left[\bar{T}_W / T_1 + \left(1 - \bar{T}_W / T_1\right) e^{A_L} \right]}, \tag{9.20}$$

where $A_L = A \times L$ is the thermal stratification coefficient.

Since pressurizing gas temperature, as a rule, does not exceed 800 K, chemical equilibrium models are not acceptable for the simulation of the chemical interaction in the ullage. Only the model of formal chemical kinetics along with the PSR system scheme (Subsection 1.3.2 and Section 1.5) can be used for an adequate prediction of the reacting mixture composition in the ullage. Thus, the mathematical model is supplemented by equations of chemical kinetics (2.31), normalizing equations (2.157), and calorific (energy) equations (2.149) written both for zone 1 (PSR 1) and for zone 2 (PSR 2).

The availability of mass exchange processes and the necessity in their inclusion in the mathematical model for zones 1 and 2 require the formation of the constants of mass-exchange reactions (Section 2.2) that simulate mass exchange processes in the ullage. These include the following:

Downloaded from https://www.cambridge.org/core. Nottingham Trent University, on 17 Aug 2019 at 02:12:43, subject to the Cambridge Core terms of use, available at https://www.cambridge.org/core/terms. https://doi.org/10.1017/9781108581714.009

- pressurizing gas feed into reactor 1
- gas mixture discharge from reactor 1 to reactor 2
- gas mixture inflow to reactor 2 from reactor 1
- propellant evaporation from the surface to reactor 1 or reactor 2
- condensation of substances on the propellant surface in reactor 1 or 2

In compliance with the rules of mass feed rate constant formation (Section 2.2), these reactions being the zero-order reactions, the rate constants of pressurizing gas feed into reactor 1 (zone 1) are written for each *i*th pressurizing gas substance as

$$k_{ig}^{+} = \frac{\dot{m}_g g_{ig}}{\mu_i V_1 \times 10^3}, \tag{9.21}$$

where g_{ig} is the mass fraction of *i*th substance in pressurizing gas.

Multiplier 10^3 is explained by off-system units using for the dimensions of chemical reaction rates W_i [g-mole/(cm$^3\times$ s)] accepted in chemical kinetics that leads to the off-system dimensions of reaction rate constants depending on the order of these reactions.

The formula for calculation of the rate constants of reactions of discharge from reactor 1 (zone 1) is not considered, since discharge of gas mixture from reactor 1 occurs in concentrations proportional to gas mixture composition in the reactor, hence not influencing the change in chemical composition of the mixture in reactor 1.

Rate constants of mass feed reactions simulating the gas mixture inflow to reactor 2 from reactor 1 are written as

$$k_{i\,1,2}^{+} = \frac{\dot{m}_{1,2} g_{i1}}{\mu_1 V_2 \times 10^3} = \frac{\dot{m}_{1,2} r_{i1}}{\mu_1 (V - V_1) \times 10^3}, \tag{9.22}$$

where r_{i1} is the mole fraction of *i*th substance in zone 1.

Rate constant of mass feed reactions simulating evaporation from the propellant surface into reactor 1 (zone 1) or reactor 2 (zone 2) is written as follows:

$$k_V^{+} = \frac{\dot{m}_V}{\mu_V V_z \times 10^3}, \tag{9.23}$$

where $V_z = V_1$ if zone 2 does not exist, and $V_z = V - V_1$ is zone 2 exists in the ullage.

Condensation of substances on the surface of the propellant in reactor 1 or 2 is described by mass discharge reactions which are the first-order reactions, with the following rate constants:

$$k_{li}^{-} = \frac{\dot{m}_{li}}{\rho_{li} V_z} \tag{9.24}$$

where ρ_{li} is the density of saturated vapors of condensing gas-phase component *i*; $V_z = V_1$ if zone 2 does not exist, and $V_z = V - V_1$ if zone 2 exists in the ullage.

As a rule, condensation of individual substances makes a notably smaller contribution into mass exchange processes compared with propellant evaporation into the ullage, which is why its contribution into mass exchange processes may fully neglected.

Downloaded from https://www.cambridge.org/core. Nottingham Trent University, on 17 Aug 2019 at 02:12:43, subject to the Cambridge Core terms of use, available at https://www.cambridge.org/core/terms. https://doi.org/10.1017/9781108581714.009

System of equations (9.1)–(9.3), (9.9), (9.11)–(9.13), (9.20), (2.31), (2.149) and (2.157) is a closed system of equations and allows, in compliance with the algorithm described in Section 2.4, one to calculate the variation of the following working parameters in zones 1 and 2 during tank pressurization and emptying: gas mixture chemical composition, enthalpy, mass, and temperature, as well as pressure in the ullage, ullage volume, gas mixture flow rate from zone 1 to zone 2, $\dot{m}_{1,2}$, and thermal stratification coefficient A_L.

Specificity of the algorithm of analysis of this problem consists in non-steady-state character of simulated processes and significant time of their occurrence (from hundreds to thousands of seconds). This specificity results in significant calculation time, an increase in stiffness of equations of chemical kinetics, and a decrease in algorithm stability, which can be aggravated at numerical calculation of Jacobian matrix partial derivatives. To avoid this, all partial derivatives are calculated analytically despite some complexity of formulas.

To perform calculations, it is necessary to know some parameters of associated heat and mass exchange processes in ullage and propellant, such as the values of heat flow rates to the tank walls relating to zones 1 and 2, q_{W1} and q_{W2}; the amount of heat transferred to propellant, q_l; the vapor flow rate from the propellant, $\dot{m}_V$; and the averaged temperature of tank wall in zone 2, $\bar{T}_W$.

A preliminary analysis of the behavior of these parameters shows that they can be related to the category of so-called conservative parameters – parameters of accompanying processes that may not be recalculated at every step of the integration of the mentioned system of equations but are redefined outside of the algorithm of the solution of the system of equations with keeping separately calculated magnitudes invariable in the long time interval of integration.

In contrast to these parameters, the gas mixture flow rate through the drain valve (relieve valve, $\dot{m}_d$) may not be reckoned among the conservative magnitudes because it is defined by the difference in the valve setting pressure and the pressure in the ullage included in the list of unknowns calculated at each step of integration.

Let us consider a classical case of gas mixture outflow through the relieve valve arranged at the tank top section and provided with the sensor or the somewhat resilient element opening the relieve valve at the maximum allowable pressure p_{d} in the ullage. It is not difficult to show that the gas mixture flow rate is defined as

$$\dot{m}_d = \gamma \pi D_{valve} S_v \varphi p \sqrt{\mu_1/(R_0 T_1)}, \tag{9.25}$$

[272], where S_v is the valve stroke,

$$S_v = \frac{\pi D_{valve}^2}{4 \times 10^3 G g}(p - p_a), \tag{9.26}$$

where D_{valve} is the valve diameter, G is resilient element stiffness, γ is the gas mixture specific heat ratio, p_a is ambient barometric pressure, $\varphi = \left(\frac{2}{\gamma+1}\right)^{\frac{1}{\gamma-1}} \sqrt{\frac{2\gamma}{\gamma+1}}$ for supercritical gas mixture outflow,

Downloaded from https://www.cambridge.org/core. Nottingham Trent University, on 17 Aug 2019 at 02:12:43, subject to the Cambridge Core terms of use, available at https://www.cambridge.org/core/terms. https://doi.org/10.1017/9781108581714.009

and $\varphi = \sqrt{\frac{2\gamma}{\gamma+1}\left[\left(\frac{p_a}{p}\right)^{\frac{2}{\gamma}} - \left(\frac{p_a}{p}\right)^{\frac{\gamma+1}{\gamma}}\right]}$ for subcritical gas mixture outflow.

Relations (9.25) and (9.26) are substituted in Equation (9.2) to replace gas mixture flow rate $\dot{m}_d$ through the relieve valve.

9.3 Pressurizing Gas Flow and Heat and Mass Exchange in the Ullage

Considering mass flow rates and heat flow rates given in Equations (9.2), (9.3), (9.9), and (9.11) and allowing for the aforesaid comparatively low influence of the condensation process on the mass variation in the ullage, such parameters as pressurizing gas consumption, vapor flow rate from the propellant surface, heat flow rates to the walls of the tank, and heat transferred to the propellant, it is possible to treat them as parameters of accompanying processes that may not be recalculated at every integration step.

As a rule, pressurizing gas consumption is a known value that can be set as

$$\dot{m}_g = f(\tau). \tag{9.27}$$

In most cases for LPRE boosters $\dot{m}_g = const$.

The problem of calculating evaporation from the propellant surface and the amount of heat transferred to the tank walls is related to that of calculating the gas flow in the ullage. In so going, equations of the conservation of mass and energy should be analyzed in combination with gas dynamics equations, while equality of temperatures as well as heat and mass flow rates should be maintained at the gas–liquid interface. However, since characteristics of gas flow in the ullage as well as parameters of heat and mass transfer are conservative, the calculation of heat and mass transfer can be separated from the calculation of gas flow parameters and considered as two isolated problems: the heat and mass exchange problem and the gas dynamic problem. Note here that the analysis of gas dynamic problem allows determining the boundary conditions for solving the heat and mass exchange problems. This approach allows one to solve the problems of heat and mass exchange and gas dynamics in the ullage utilizing simple relations implementing quasi-two-dimensional and even one-dimensional models.

Calculation of Pressurizing Gas Flow

Flow pattern in the closed volume of the ullage is extremely complex for simulation because of the non-steady-state nature of the pressurization process caused by variable volume of ullage, the variation of thermodynamic parameters of gas mixture, and the considerable impact of Archimedean forces on the flow pattern. Non-steady-state aspects can be overcome by the application of the aforesaid assumption about conservatism of variation in parameters of associated gas dynamic and heat and mass exchange processes. The analysis of the complex gas flows in closed volumes can be simplified by considering the set of standard quasi-two-dimensional schemes of flow based on the known design of the diffusers and the methods of pressurizing gas feed into the tank.

Downloaded from https://www.cambridge.org/core. Nottingham Trent University, on 17 Aug 2019 at 02:12:43, subject to the Cambridge Core terms of use, available at https://www.cambridge.org/core/terms. https://doi.org/10.1017/9781108581714.009

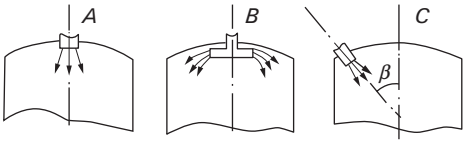

Figure 9.3 Generalized schemes of pressurizing gas feed into the ullage: (A) gas feed trough the cylindrical diffuser arranged on the tank axis; (B) gas feed through the annular gap over tank walls; (C) gas feed trough the cylindrical diffuser aligned at the angle to the tank axis [274]. From V. Naoumov, "Simulation of High-Temperature Pressurization of the Liquid-Propellant Rocket Tanks," 47th Aerospace Science Meeting Including the New Horizons Forum and Aerospace Exposition, AAA 2009–1600, pp. 1–7, Orlando, FL, 2009, reprinted by permission of the American Institute of Aeronautics and Astronautics, Inc

Despite the diversity of the diffusers and their arrangement [273], possible generalized configurations of diffusers and gas feed can be simulated by the conditional schemes shown in Figure 9.3. Pressurizing the high-temperature gas jet escaping from the diffuser exit propagates in the ullage closed volume. As it propagates and increases in diameter, it interacts with the tank walls and propellant surface and – depending on the pressurizing gas temperature and velocity, the shape of the ullage, and the diffuser arrangement – the jet flows over the tank walls or along the tank axis and the propellant surface to form reverse flows along the tank axis or the walls. Also possible is the pressurizing gas flow's decay caused by the impact of Archimedean forces. Formalized flow pattern schemes are shown in Figure 9.4 and systematized by the design of the diffuser and its arrangement.

1. Axial gas feed and related flow patterns (scheme A in Figure 9.3 and schemes A1–A3 in Figure 9.4).
2. Peripheral feed and related flow patterns related (scheme B in Figure 9.3 and schemes B1–B3 in Figure 9.4).

   Schemes A1 and B1 simulate the development of "free" conical and wall jets in the ullage. Schemes A2 and B2, unlike A1 and B1, simulate the development and flow of so-called constrained pressurizing gas jets; further expansion is limited by the reverse flows along tank walls or along of tank.
3. Pressurizing gas feed at the angle to the tank axis (scheme C in Figure 9.3 and schemes C1–C3 in Figure 9.4).

The most probable sequences interpreting flow development with tank emptying and, hence, increase in ullage volume can be the following:

$$A1 \Rightarrow A2 \Rightarrow A3, \tag{9.28}$$

$$A1 \Rightarrow A3, \tag{9.29}$$

$$A2 \Rightarrow A3, \tag{9.30}$$

$$B1 \Rightarrow B2 \Rightarrow B3, \tag{9.31}$$

$$B1 \Rightarrow B3, \tag{9.32}$$

Downloaded from https://www.cambridge.org/core. Nottingham Trent University, on 17 Aug 2019 at 02:12:43, subject to the Cambridge Core terms of use, available at https://www.cambridge.org/core/terms. https://doi.org/10.1017/9781108581714.009

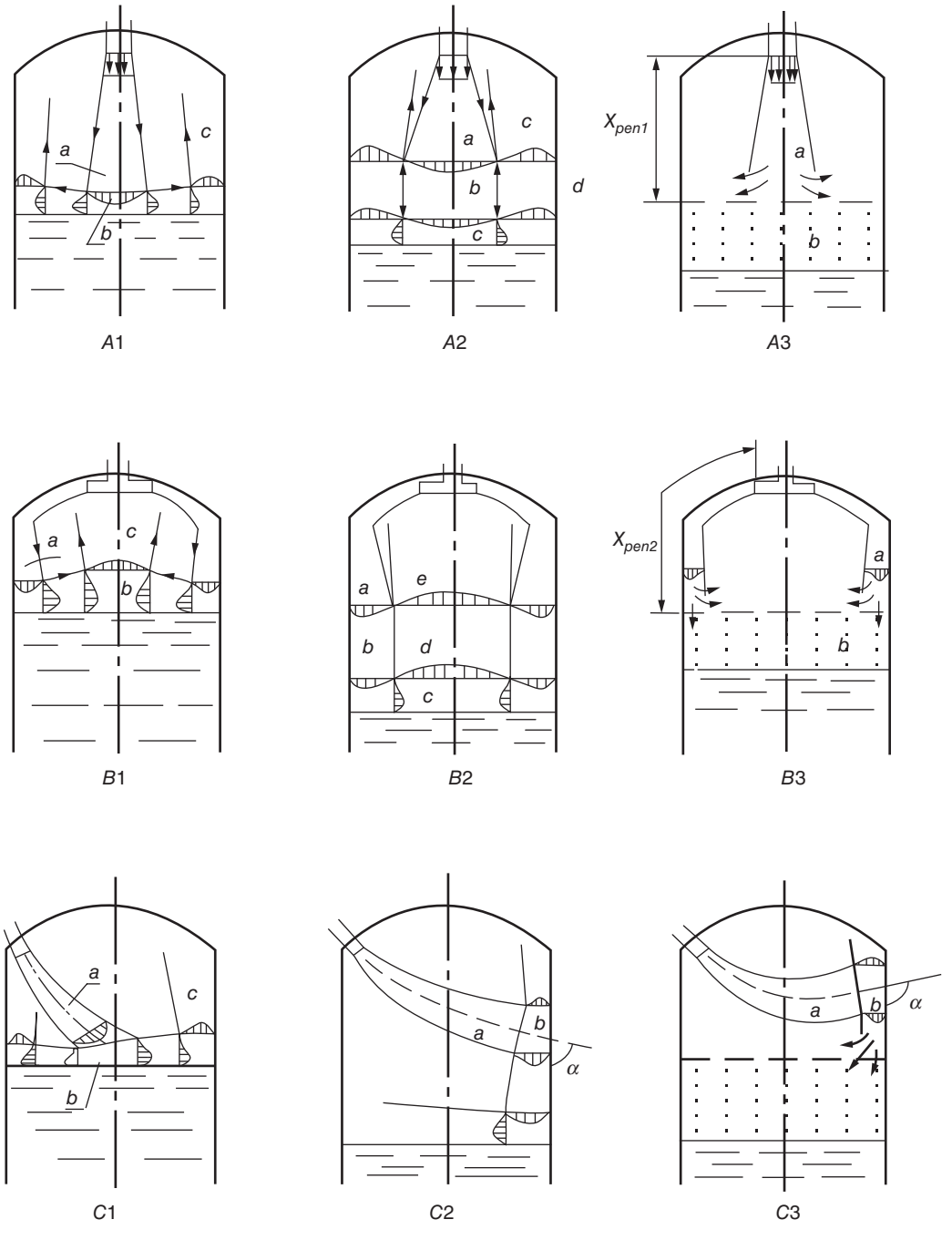

Figure 9.4 Schemes of pressurizing gas flow in the ullage.

Downloaded from https://www.cambridge.org/core. Nottingham Trent University, on 17 Aug 2019 at 02:12:43, subject to the Cambridge Core terms of use, available at https://www.cambridge.org/core/terms. https://doi.org/10.1017/9781108581714.009

$$B2 \Rightarrow B3, \tag{9.33}$$

$$C1 \Rightarrow C2 \Rightarrow C3, \tag{9.34}$$

$$C2 \Rightarrow C3. \tag{9.35}$$

Scheme C is the most conditional out of the proposed schemes because Archimedean force not only causes the reduction of average jet velocity and corresponding slowing down of jet propagation but turns it relative to the tank axis as well. Besides, such pressurization gas feed scheme leads to the three-dimensional flow pattern. Thereby, the main goal of conditional scheme C consists in the determination of tank wall local regions of overheating as well as the boundary between zones 1 and 2 in the case of jet turn caused by Archimedean force.

Schemes A and B are used not only for the determination of jet penetration depth – hence, the boundary between zones 1 and 2 – but also for the calculation of the velocity field in submerged jets flowing over the walls and the propellant surface for the subsequent calculation of heat and mass exchange.

To obtain the required relations, let us examine a set of control volumes near the tank walls and propellant surface assuming axially symmetric flows for schemes A and B and using equations of mass conservation. Since pressurizing gas velocities are relatively low, it is possible to consider the gas to be incompressible

From the consideration of cylindrical control volume ABCD for scheme A1 impingement region (Figure 9.5) due to its small size, the absence of the entrainment of the ambient gas mixture and action of Archimedean forces, it follows that

$$u_{ml} = u_{ms} \quad \text{and} \quad \rho_{ml} = \rho_{ms}, \tag{9.36}$$

where u_{ml}, u_{ms} and ρ_{ml}, ρ_{ms} are axial velocities and densities of the gas in cross sections AD (BC) and AB [57, 101].

Reasoning from mass conservation,

$$\int_0^{r_s} \rho_s u_s 2\pi r dr = \int_0^{l_s} u_l \rho_l \, 2\pi r_s dl, \tag{9.37}$$

where u_l, u_s and ρ_l, ρ_s are local velocities and densities of the gas in cross sections AB and AD (BC), and applying the Schlichting relation [52],

$$\frac{u - u_a}{u_m - u_a} = \left(1 - \eta^{3/2}\right)^2, \tag{9.38}$$

where u_a is the velocity of ambient gas flow, the expression (9.37) is reduced to the following form:

$$r_s \int_0^1 \left(1 - \eta_s{}^{3/2}\right)^2 \eta_s d\eta_s = l_s \int_0^1 \left(1 - \eta_l{}^{3/2}\right) d\eta_l, \tag{9.39}$$

Downloaded from https://www.cambridge.org/core. Nottingham Trent University, on 17 Aug 2019 at 02:12:43, subject to the Cambridge Core terms of use, available at https://www.cambridge.org/core/terms. https://doi.org/10.1017/9781108581714.009

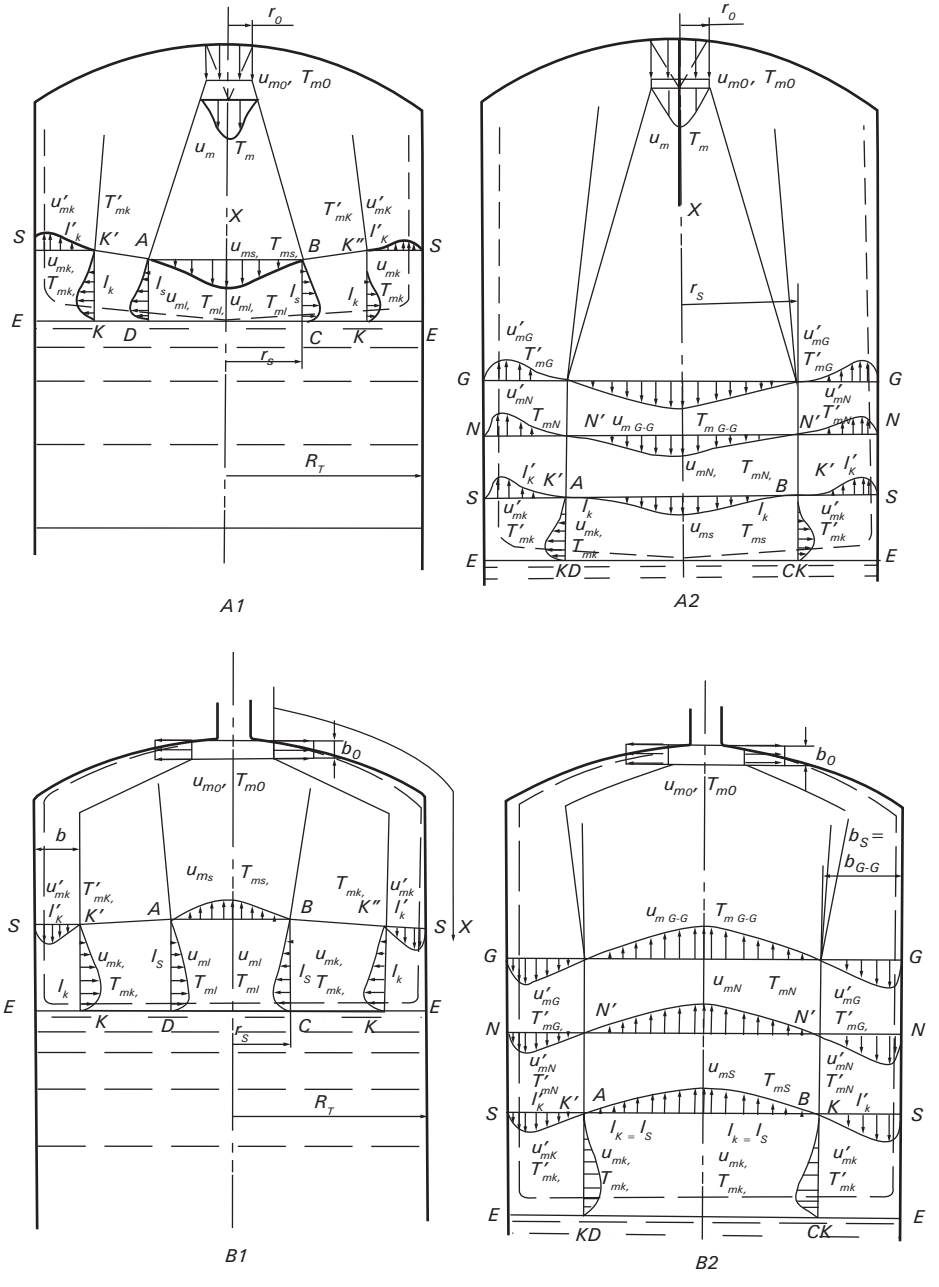

Figure 9.5 Calculation schemes of pressurizing gas flows in the ullage.

Downloaded from https://www.cambridge.org/core. Nottingham Trent University, on 17 Aug 2019 at 02:12:43, subject to the Cambridge Core terms of use, available at https://www.cambridge.org/core/terms. https://doi.org/10.1017/9781108581714.009

where $\eta_s = r/r_s$ and $\eta_l = l/l_s$ are relative coordinates.

By integrating (9.39), we get the expression relating the sizes of control volume ABCD:

$$l_s = \frac{2}{7} r_s. \tag{9.40}$$

Similarly, for cylindrical control volume AB (CK) (KD) of scheme A2 (Figure 9.5), it can be written:

$$\int_0^{l_k} \rho_k u_k 2\pi r_k dl = \int_0^{l'_k} u'_k \rho'_k \, 2\pi (R_T - l) dl, \tag{9.41}$$

where R_T is the tank radius [57, 101].

In using (9.38), it is simple to reduce (9.41) to the following form:

$$l_k \left(R_T - l'_k\right) \int_0^1 \left(1 - {\eta_l}^{3/2}\right)^2 d\eta_l = l'_k R_T \int_0^1 \left(1 - {\eta_{l'}}^{3/2}\right)^2 d\eta_{l'} - \left(l'_k\right)^2 \int_0^1 \left(1 - {\eta_{l'}}^{3/2}\right)^2 \eta_{l'} d\eta_{l'}. \tag{9.42}$$

The integration thereof results in the expression for the calculation of the FK′ segment:

$$l'_k = \frac{(l_k + R_T) - \sqrt{R_T^2 + l_k^2 + 0.8572 R_T l_k}}{0.5714}. \tag{9.43}$$

With conical jet A1 changing over to constricted one (A2), cylinder generatrix AD transforms to K′K, which makes the following equalities valid:

$$l_k = \frac{2}{7} r_s \quad \text{and} \quad R_T = r_s + l'_k. \tag{9.44}$$

Substituting (9.44) in (9.43), we obtain

$$l'_k = 0.1958 R_T, \tag{9.45}$$

$$r_s = 0.8042 R_T. \tag{9.46}$$

Formulas (9.45) and (9.46) define the location of cross section GG wherein the conical jet transforms to the constricted (the so-called closure conditions) relative to the coordinate $x = 0$. The axial velocity of the reverse jet in arbitrary cross section N′N is defined in compliance with the model of the flow (see Formula [9.36]) as

$$u'_{mN} = u_{mN}. \tag{9.47}$$

By applying a similar approach and analysis of control volumes to flow schemes B1 and B2, it is possible to get the relations,

$$l_s = \frac{2}{7} r_s, \tag{9.48}$$

Downloaded from https://www.cambridge.org/core. Nottingham Trent University, on 17 Aug 2019 at 02:12:43, subject to the Cambridge Core terms of use, available at https://www.cambridge.org/core/terms. https://doi.org/10.1017/9781108581714.009

$$l_k = \frac{l'_k\left(R_T - 0.2857l'_k\right)}{R_T - l'_k}, \tag{9.49}$$

and the conditions of closure,

$$l'_k = 0.1958R_T, \tag{9.50}$$

$$r_s = 0.8042R_T. \tag{9.51}$$

Due to the relatively small thickness of free near-by-the-wall jets in area c for the schemes A1 and A2 and area a for the schemes B1 and B2 (Figure 9.4) as compared with the tank radius, the parameters of these jets can be defined by the relations for the calculation of flat jets [52].

As a rule, the velocity of pressurizing gas at the diffuser exit can vary from several meters to some tens of meters a second, while diameters (or gaps) of diffusers vary from several centimeters to tens of centimeters. Rough calculations display that Reynolds numbers at the diffuser exit can vary from 10,000 to 200,000. The pressurizing gas jet may not be classified as a free jet, since it develops in a limited space (closed volume) of the ullage. Thereunder, the transition from laminar to turbulent mode can occur notably earlier than that in free jets but later than for the flows in the channels. This allows the assumption of a mainly turbulent flow and the application of relations as the basis for calculation of the parameters of turbulent axially symmetric and flat jets in areas a of schemes A1–A3 and schemes B1–B3 (Figure 9.4), which were obtained without taking into account the Archimedean forces [52]:

$$c(\bar{x} - \bar{x}_{entr}) = \sqrt{\frac{n_{2u}}{0.134\theta}}\left[\frac{R(z)}{\bar{u}_{m1}} - R(z_0)\right], \tag{9.52}$$

$$c(\bar{x} - \bar{x}_{entr}) = \frac{n_{2u}}{0.136\theta}\left[\frac{P(z')}{\bar{u}^2{}_{m2}} - P\left(z'_0\right)\right], \tag{9.53}$$

where $z = (\theta - 1)K_K\bar{u}_{m1}/2$, $z_0 = (\theta - 1)K_K/2$, $z' = (\theta - 1)K_H\bar{u}_{m2}/2$, $z'_0 = (\theta - 1)K_H/2$;

$$R(z) = \sqrt{1 + 1.49z} - 0.729z \times \arctan\left(1.47 \times \sqrt{1 + 1.49z}\right) - z \times \ln\left|\frac{1 + \sqrt{1 + 1.49z}}{1 - \sqrt{1 + 1.49z}}\right|;$$

$$P(z') = 1 - 0.280z' - 1.720(z')^2 + 0.280(z')^2 \times \ln\left|1 + \frac{1}{z'}\right|;$$

$K_K = 0.745\frac{n_T}{n_{2u}}$; $K_H = 0.86\frac{n_T}{n_{2u}}$; $c = 0.22$; $\bar{x} = \frac{x}{b_0}$; $\bar{x} = \frac{x}{r_0}$ are relative axial coordinates of the flat and axially symmetric jets, respectively, for the fully developed region; $\bar{x}_{entr} = \frac{x_{entr}}{b_0}$; $\bar{x}_{entr} = \frac{x_{entr}}{r_0}$ are relative coordinates of the flat and axially symmetric jets, respectively, for the entry region; r_0 is the diffuser radius (schemes A1 and A2, Figure 9.5); b_0 is the diffuser gap (schemes B1 and B2, Figure 9.5); $\bar{x}_{entr}$ is the entry region relative length; $\bar{u}_{m2} = \frac{u_{m2}}{u_{m20}}$; $\bar{u}_{m1} = \frac{u_{m1}}{u_{m10}}$ are the relative axial velocities of the flat and axially symmetric jets, respectively; $\theta = \frac{T_0}{T}$; T_0; u_{m10}; u_{m20} are the pressurizing gas temperature and velocities at diffuser exit; T is the average gas temperature in the

Downloaded from https://www.cambridge.org/core. Nottingham Trent University, on 17 Aug 2019 at 02:12:43, subject to the Cambridge Core terms of use, available at https://www.cambridge.org/core/terms. https://doi.org/10.1017/9781108581714.009

ullage; and η_{2u} and η_T are the coefficients describing the nonuniformity of temperature and velocity profile at the jet entry region (usually, $\eta_{2u} = \eta_T \approx 1$).

The analysis of $R(z)$ and $P(z')$ shows that these are approximated in the ranges $1 \le \theta \le 7$ and $0 \le \bar{u}_m \le 1$ with error not exceeding 4% by the following relations [57, 101]:

$$R(z) = A_1(\theta)\bar{u}_m + B_1(\theta) \tag{9.54}$$

and

$$P(z') = A_2(\theta)\bar{u}_m{}^2 + B_2(\theta), \tag{9.55}$$

$$\text{where } B_1 = -0.0618\theta + 1.0226 \text{ and } B_2 = -0.0087\theta + 0.9966. \tag{9.56}$$

Substituting (9.54)–(9.56) in (9.52) and (9.53), with allowance for cancellation of the first terms of Formulas (9.54) and (9.55) during transformations, results in

$$u_{m1} = \frac{1.0226 - 0.0618\theta}{0.0805(\bar{x} - \bar{x}_{entr})\sqrt{\theta} + 1.0226 - 0.0618\theta}, \tag{9.57}$$

$$u_{m2} = \sqrt{\frac{0.9966 - 0.0087\theta}{0.0695(\bar{x} - \bar{x}_{entr})\theta + 0.9966 - 0.0087\theta}}. \tag{9.58}$$

It follows from the equation of conservation of momentum

$$\dot{m}u_{av} = \dot{m}_0 u_{av0}, \tag{9.59}$$

where index 0 corresponds to gas parameters at the diffuser exit; u_{av} is the flow rate–averaged jet velocity: $u_{av} = \frac{\int u d\dot{m}}{\dot{m}}$.

With allowance for self-similarity of velocity profiles (as well as those of temperature and concentration of substances) at the jet flow fully developed region, it can be written:

$$\bar{u}_{av} = \frac{u_{av}}{u_{av0}} = \frac{u_m}{u_{m0}} = \bar{u}_m. \tag{9.60}$$

Assuming that self-similarity of velocity profiles set up quickly in the case of submerged jets due to intensive admixture of ambient gas, let us extend Formulas (9.57) and (9.58) to entry regions to use Equation (9.59) wherefrom one can apply (9.57), (9.58), and (9.60) to get

$$\frac{\dot{m}_1}{\dot{m}_{10}} = \frac{0.0805\bar{x}\sqrt{\theta} + (1.0226 - 0.0618\theta)}{1.0226 - 0.0618\theta}, \tag{9.61}$$

$$\frac{\dot{m}_2}{\dot{m}_{20}} = \sqrt{\frac{0.0695\bar{x}\theta + (0.9966 - 0.0087\theta)}{0.9966 - 0.0087\theta}}. \tag{9.62}$$

Let us remember that Formulas (9.57) and (9.58) have been obtained without allowance for effect of Archimedean forces and cannot provide an adequate calculation of the depth of the jets' penetration into the ullage, hence the origination and development of zone 2.

Downloaded from https://www.cambridge.org/core. Nottingham Trent University, on 17 Aug 2019 at 02:12:43, subject to the Cambridge Core terms of use, available at https://www.cambridge.org/core/terms. https://doi.org/10.1017/9781108581714.009

To derive analytical relations for the calculation of submerged jet velocities under effect of Archimedean forces, let us write the momentum conservation equation for jet elementary volume dV with gas variable mass dm:

$$d(u_{av}dm) = -\frac{dm_0}{\rho_0}g(\rho - \rho_0)d\tau, \tag{9.63}$$

where ρ_0 is the pressurizing gas density at the diffuser exit and ρ is the density of gas mixture in the ullage.

After a series of transforms of Equation (9.63) with subsequent application of (9.61) and (9.62), and its further integration [101, 283], it is possible to get the following formulas for the calculation of a relative average velocity of the axially symmetric and flat jets with allowance for Archimedean forces:

$$\bar{u}_{av1} = \sqrt{\frac{1 + K_1 Y_1}{(\bar{x}_1/Y_1 + 1)^2} - K_1 Y_1}, \tag{9.64}$$

$$\bar{u}_{av2} = \sqrt{\frac{1}{(1 + \bar{x}_2 Y_2)}\left\{1 + \frac{4K_2\left[1 - (1 + \bar{x}_2 Y_2)^{3/2}\right]}{3Y_2}\right\}}. \tag{9.65}$$

where $Y_1 = \dfrac{1.0226 - 0.0618\theta}{0.0805\sqrt{\theta}}$; $\quad Y_2 = \dfrac{0.0695\theta}{0.9966 - 0.0087\theta}$;

$$K_1 = g\left(\frac{\rho}{\rho_0} - 1\right)\frac{r_0}{u_{av0}^2}; \quad K_2 = g\left(\frac{\rho}{\rho_0} - 1\right)\frac{b_0}{u_{av0}^2}; \quad \bar{x}_1 = \frac{x_1}{r_0}; \quad \bar{x}_2 = \frac{x}{b_0}.$$

The relative depth of jet penetration into the ullage is defined from (9.64) and (9.65) at $\bar{u}_{av1} = 0$ and $\bar{u}_{av2} = 0$:

$$\bar{x}_{pen1} = Y_1\left[\left(\frac{1}{K_1 Y_1} + 1\right)^{1/2} - 1\right], \tag{9.66}$$

$$\bar{x}_{pen2} = \frac{1}{Y_2}\left[\left(\frac{3Y_2}{4K_2} + 1\right)^{2/3} - 1\right]. \tag{9.67}$$

At the transition of conical jet A1 to constricted jet A2, and of circular free jet B1 to constricted jet B2 (Figures 9.4 and 9.5), the following relation should be obeyed:

$$\dot{m}/u_{av} = \dot{m}_{G-G}/u_{av}\,G - G\; = const, \tag{9.68}$$

where u_{avG-G} and $\dot{m}_{G-G}$ are the average velocity and gas mass flow rate in cross sections GG, wherein conical jets and the jets near the wall transfer into constricted jets.

Using this relation and Equation (9.63), it is possible to get, in a similar way, the analytical relations for the calculation of the relative average velocity of constricted jets with allowance for Archimedean forces:

$$\bar{u}_{av1C}^2 = \sqrt[3]{\bar{u}_{av1G-G}^2\left[\bar{u}_{av1G-G} - \frac{3}{2}K_1(\bar{x} - \bar{x}_{1G-G})\right]}, \tag{9.69}$$

Downloaded from https://www.cambridge.org/core. Nottingham Trent University, on 17 Aug 2019 at 02:12:43, subject to the Cambridge Core terms of use, available at https://www.cambridge.org/core/terms. https://doi.org/10.1017/9781108581714.009

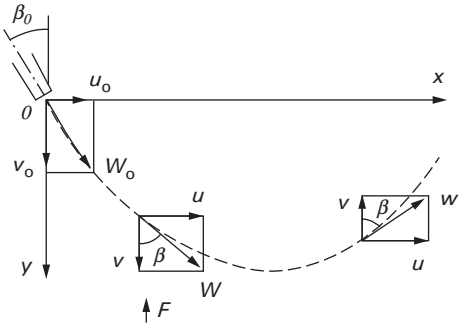

Figure 9.6 Calculation scheme for inclined jet under the effect of Archimedean forces.

$$\bar{u}_{av2C}^2 = \sqrt[3]{\bar{u}_{av2G-G}^2\left[\bar{u}_{av2G-G} - \frac{3}{2}K_2(\bar{x} - \bar{x}_{2G-G})\right]}, \tag{9.70}$$

where $\bar{u}_{av1G-G}$ and $\bar{u}_{av2G-G}$ are the relative average velocities of the jets in cross sections GG for schemes A2 and B2 (Figure 9.5) calculated under conditions specified by (9.45), (9.46), (9.48), (9.49), and (9.50) using Formulas (9.64) and (9.65).

The calculation of parameters of pressurizing gas feed at the angle to the tank axis (scheme C in Figure 9.3 and schemes C1–C3 in Figure 9.4) is complicated by the curvilinear trajectory of the jet and the necessity to consider the variation in value and direction of velocity W in the field of Archimedean forces. Let us write the momentum conservation equation for elementary volume of the jet dV of variable gas mass dm in projection on axis y (Figure 9.6):

$$d(vdm) = -dV_0 g(\rho - \rho_0)d\tau, \tag{9.71}$$

where from

$$\frac{dv}{dx} + v\frac{d(-\ln u)}{dx} - S = 0, \tag{9.72}$$

where $S = \left(\frac{-g}{u_0}\right) \times \left(\frac{\rho}{\rho_0} - 1\right)$.

The integration of Equation (9.72) allows one to obtain the relation for the calculation of the jet velocity vertical component (9.73), the jet trajectory (9.74), and the x-coordinate of the point of jet turn caused by Archimedean forces (9.75):

$$v = uS\left[\frac{tg\,(\pi/2 - \beta_0)}{S} + \frac{1}{u_0 B_1}\left(\frac{C_1 x^2}{2} + B_1 x\right)\right], \tag{9.73}$$

$$y = [\,tg\,(\pi/2 - \beta_0)]x + \frac{S}{u_0 B_1}\left(\frac{C_1 x^3}{6} + \frac{B_1 x^2}{2}\right), \tag{9.74}$$

$$x_{v=0} = -\frac{B_1}{C_1} + \sqrt{\frac{B_1^2}{C_1^2} - \frac{2\,tg\,(\pi/2 - \beta_0)u_0 B_1}{C_1 S}}, \tag{9.75}$$

Downloaded from https://www.cambridge.org/core. Nottingham Trent University, on 17 Aug 2019 at 02:12:43, subject to the Cambridge Core terms of use, available at https://www.cambridge.org/core/terms. https://doi.org/10.1017/9781108581714.009

where $C_1 = \dfrac{0.0805\sqrt{\theta}}{r_0 \sin\beta_0}$; $B_1 = \dfrac{5.6899}{\theta + 6} + 0.1645$.

The value of angle β is defined from

$$\beta = \arctan(u/v). \tag{9.76}$$

Considering that Archimedean force influences only the vertical component of velocity v and the value of angle β but does not affect the value of the horizontal component of velocity u, it will be defined from the following relation:

$$u = \frac{u_0 B_1}{C_1 x + B_1}. \tag{9.77}$$

The obtained relations allow one to calculate the fields of velocities for all considered flow diagrams. Jet gas temperatures are known to vary with gas velocities and can be defined based on the calculated velocities from the known relations for axially symmetric and flat jets [52].

Calculation of Heat Transfer and Mass Transfer

For the calculation of convective heat transfer to the tank's walls, it is expedient to use the known methods of the theory of boundary layers [284, 285] – in particular, the method of integral ratios between the pulses and energy with the application of appropriate laws of friction and heat transfer. This relates to the heat exchange with tank walls for flow schemes A1, A2, B1, and B2 (Figures 9.4 and 9.5) and the portion of the walls flown by the jet in scheme B3. Without analysis of the equation of energy conservation for the turbulent boundary layer, let us write its integral:

$$\mathrm{Re}_T^{**} = \frac{1}{\Delta T}\left\{\frac{1+m}{2\mathrm{Pr}^{0.75}} B \times \mathrm{Re}_{tr} \int_{\bar{x}_{tr}}^{\bar{x}} \psi_t \bar{u}_m \Delta T^{1+m} dx + \left(\mathrm{Re}_T^{**}\Delta T\right)_{x=x_{tr}}^{1+m}\right\}^{\frac{1}{1+m}}, \tag{9.78}$$

where $\mathrm{Re}_T^{**} = \dfrac{u_m \delta_T \rho_m}{\eta_m}$ is the local value of the Reynolds number calculated for the thickness of thermal boundary layer; $\Delta T = T_m - T_W = f(x)$ is the difference of temperatures in boundary layer; Re_{tr}^{**} is the Reynolds number calculated for parameters in the transition cross section; ρ_m and η_m are the axial density and dynamic viscosity of the flat jet near the tank wall; ψ_m is the temperature correction in the heat transfer law; m, B are coefficients depending on the Reynolds number; Tm is the axial temperature of the flat jet nearby the tank wall ($Tm = f(x)$); T^W is the wall temperature ($T^W = f(x)$); and x_{tr} is the transition cross section coordinate.

For the relatively high level of turbulence typical for the gas flow in the closed volume, it is possible to accept that $B = 0.485$ and $m = 0.556$. The value of temperature correction, ψ_m, should differ from generally accepted values [285, 286] and should be selected with allowance for the high degree of turbulence in the ullage closed volume, which is recommended in [53, 287, 288].

Local convective heat flux is defined from a known relation [284] subject to coordinate x (Figure 9.5):

Downloaded from https://www.cambridge.org/core. Nottingham Trent University, on 17 Aug 2019 at 02:12:43, subject to the Cambridge Core terms of use, available at https://www.cambridge.org/core/terms. https://doi.org/10.1017/9781108581714.009

$$\dot{q}_{Wx} = St_x \rho_{mx} u_{mx} \Delta T_x c_{px}, \tag{9.79}$$

where $\Delta T_x = T_{mx} - T_{Wx}$

and

$$St_x = \frac{0.485}{2 \times \mathrm{Pr}_x^{0.75} \left(\mathrm{Re}_T^{**}\right)_x^{0.556}}. \tag{9.80}$$

The complexity of the gas heat exchange with the tank walls in the case of flow schemes A3, B3, and C3 (Figure 9.4) caused by the absence of pressurizing gas flow over the tank walls does not allow one to use methods of boundary layer theory. In this case, the heat flux is defined from Newton's law of cooling:

$$\dot{q}_{Wx} = h_x \Delta T_x, \tag{9.81}$$

where local values of heat transfer coefficient h_x are calculated from relations proven tried and true in the calculation of in-tank processes [101, 289]:

$$Nu = 0.724 K_{T1} Ra_L^{0.09} Ra_D^{0.6}, \tag{9.82}$$

$$Nu = KC_1 Ra_D^{0.59}, \tag{9.83}$$

$$Nu = KC_2 Ra_D^{0.33}, \tag{9.84}$$

where Ra_L is the Rayleigh number calculated for characteristic length L; Ra_D is the Rayleigh number calculated for tank diameter D; $K = 1.473 \times 10^5 Ra_D^{-0.256} K_{T1}^{0.98}$; K_{T1} is the parameter of thermal non-stationarity; coefficients C_1 and C_2 are the functions of the Rayleigh number varying from 10^4 to 10^{12}.

Reverting to mass exchange processes, let us consider the model of evaporation from the propellant surface as the main model, in addition to pressurizing gas feed into the ullage, factor of mass, and thermodynamic parameters variation. As a rule, the liquid film is blown off of the tank walls by the pressurizing gas flow, which allows one to assume its insignificant influence on the evaporation process.

Even considering, as mentioned before, the mass exchange processes apart from the calculation of gas flow parameters, it is required to allow for the necessity in solving the conjugate problem of the evaporation from the propellant surface and the heating of the latter (Figure 9.7). Allowing for prevailing axial symmetry of gas flow in the tank and notably larger axial sizes of tanks relative to their diameters, it is possible to assume a one-dimensional model of evaporation and heating by averaging all parameters over the tank radius.

Assuming the binary diffusion, the equation of the transport of vapors from the propellant surface is written as follows [8, 290]:

$$\dot{J}_1 = -D_{1,2} \rho \frac{d\rho_{10}}{dy} + \rho_1 V \tag{9.85}$$

where $D_{1,2}$ is the binary diffusion coefficient; $D_{1,2} \frac{d\rho_{10}}{dy}$ and $\rho_1 V$ are the diffusion and convective vapor flows, respectively; ρ_{10} is the relative concentration of propellant vapors; and ρ_1 is the concentration of propellant vapors.

Downloaded from https://www.cambridge.org/core. Nottingham Trent University, on 17 Aug 2019 at 02:12:43, subject to the Cambridge Core terms of use, available at https://www.cambridge.org/core/terms. https://doi.org/10.1017/9781108581714.009

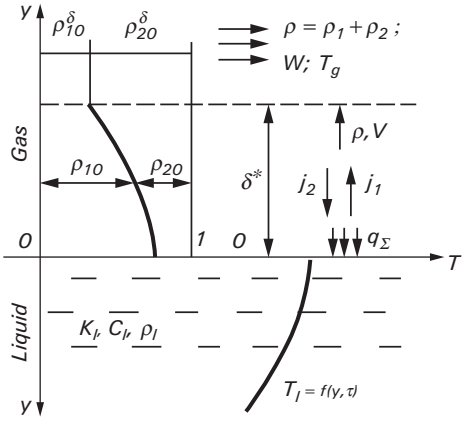

Figure 9.7 Calculation scheme of heat and mass exchange with propellant component surface.

The total gas mixture mass flux to the propellant surface is written as follows:

$$\dot{j}_2 = -D_{2,1}\rho\frac{d\rho_{20}}{dy} + \rho_2 V, \tag{9.86}$$

where $D_{2,1}$ is the binary diffusion coefficient; $D_{2,1}\frac{d\rho_{20}}{dy}$ and $\rho_2 V$ are the gas mixture diffusion and convective flows, respectively; ρ_{20} is the relative concentration of the gas mixture; and ρ_2 is the concentration of the gas mixture.

The total gas mixture mass flux on the propellant surface equals zero:

$$\dot{j}_2 = -D_{2,1}\rho\frac{d\rho_{20}}{dy} + \rho_2 V = 0. \tag{9.87}$$

Parameter V is called "the velocity of Stefan's flow" – that is, the flow of substance perpendicular to the propellant surface [8]. Stefan's flow (see also Chapter 6) is particularly substantial for evaporation and condensation while its velocity does not depend on hydrodynamic conditions and is entirely defined by the conditions of diffusion and stoichiometry of flows. Defining its velocity from (9.97):

$$V = \frac{D_{2,1}}{\rho_{20}}\frac{d\rho_{20}}{dy}_{2,1} = -\frac{D}{1-\rho_{10}}\frac{d\rho_{10}}{dy} \tag{9.88}$$

and substituting it in (9.85), with allowance for the fact that for $D_{1,2} = D_{2,1}$ and $\frac{d\rho_{10}}{dy} = \frac{d\rho_{20}}{dy}$, one can obtain the expressions for the calculation of vapor mass flux with allowance for Stefan's flow:

$$\dot{j}_1 = -\frac{\rho D_{1,2}}{1-\rho_{10}}\frac{d\rho_{10}}{dy}. \tag{9.89}$$

It follows from Formulas (9.88) and (9.89):

$$V = \frac{\dot{j}_1}{\rho} = \frac{R_0 T_g}{p}\dot{j}_1, \tag{9.90}$$

Downloaded from https://www.cambridge.org/core. Nottingham Trent University, on 17 Aug 2019 at 02:12:43, subject to the Cambridge Core terms of use, available at https://www.cambridge.org/core/terms. https://doi.org/10.1017/9781108581714.009

where T_g is the gas temperature near the propellant surface.

Going to relative partial pressures ($p_{10} = p_1/p$) and having performed a series of transforms of expression (9.89), one gets

$$\dot{J}_1 = -\frac{D_{1,2}\mu_1}{R_0 T_g(1-p_{10})}\frac{dp_1}{dy}. \tag{9.91}$$

For further transforms (9.91), it is expedient to use the reduced film model described in Section 5.2 for the simulation of dispersed liquid droplet evaporation. For the flat surface of propellant, the thickness of reduced film wherein concentration and temperature gradients are developed [8] can be selected so that true transport velocity is obtained assuming a solely molecular transport mechanism:

$$\delta_D = d/Nu_D. \tag{9.92}$$

However, unlike Formula (5.6), Relation (9.92) includes d – a certain linear size related with the thickness of pressurizing gas jet (l_s) or (l_k) flowing over the propellant surface (Figure 9.5) – while the Nusselt number is defined from Relations (9.82)–(9.84).

Separating the variables and integrating (9.91) over the reduced film thickness, one gets the expression for the calculation of the vapor mass flux from the propellant surface that can be used for the calculation of condensate mass flux as well:

$$\dot{J}_{V(C)} = -\frac{pD_{1,2}\mu_V}{R_0\bar{T}_{V/G}\delta_D}\ln\left(\frac{p-p_V}{p-p_S}\right), \tag{9.93}$$

where p_V is the partial pressure of propellant vapors in the ullage, $\bar{T}_{V/G} = \frac{T_V+T_G}{2}$ is the vapor–gas mixture average temperature, T_V is the temperature of vapor entraining from the propellant surface, and T_G is the temperature of gas flowing over the propellant surface or the temperature of the gas mixture in the ullage in a case of existence of zone 2 (Figure 9.2).

The binary diffusion coefficient is calculated by the formulas of molecular-kinetic theory and defined by the expression

$$D_{1,2} = 0.0266\frac{\bar{T}_{V/G}\sqrt{\bar{T}_{V/G}\left(\mu_1+\mu_{22}\right)/\mu_1\mu_2}}{p\sigma_{1,2}^2\Omega_{i,j}^{1,1*}}, \tag{9.94}$$

where i and j are gases under consideration (for this particular problem, propellant vapor and gas mixture in the ullage – i.e., $i \equiv V$ and $j \equiv G$) [13, 160].

The reduced integral of collisions is defined from polynomial [13]:

$$\Omega_{i,j}^{1,1*} = \sum_p \alpha_p\left(\ln T_{1,2}^*\right)^p \tag{9.95}$$

and makes the function of reduced temperature [160]:

$$T_{1,2}^* = \bar{T}_{V/G}/(\varepsilon/k)_{1,2}. \tag{9.96}$$

Parameters of the potential function of interaction for approximation of intermolecular interaction are defined by the expressions [13, 160]:

Downloaded from https://www.cambridge.org/core. Nottingham Trent University, on 17 Aug 2019 at 02:12:43, subject to the Cambridge Core terms of use, available at https://www.cambridge.org/core/terms. https://doi.org/10.1017/9781108581714.009

$$\sigma_{1,2} = 0.5(\sigma_1 + \sigma_2), \tag{9.97}$$

$$(\varepsilon/k)_{1,2} = \sqrt{(\varepsilon/k)_1 (\varepsilon/k)_2}. \tag{9.98}$$

Heat flux to the propellant surface through the reduced film is carried by conduction and Stefan's flow:

$$\dot{q}_{\sum} = -\bar{k}_{V/G} \frac{dT}{dy} + \bar{c}_{pV} \rho V (T_l - T), \tag{9.99}$$

where $\bar{k}_{V/G}$ is the thermal conductivity of the vapor–gas mixture; $\bar{c}_{pV}$ is the propellant vapor's specific heat; T_l is the propellant surface temperature; and T is the local temperature in reduced film, varying over its thickness.

By using the expression obtained for the velocity of Stefan flow (9.90) and allowing for $\dot{J}_1 = \dot{J}_{V(C)}$, where indexes V and C denote "vapors" and "condensate," one can obtain

$$\dot{q}_{\sum} = \bar{k}_{V/G} \frac{dT}{dy} + \dot{J}_{V(C)} \bar{c}_{pV} (T - T_l). \tag{9.100}$$

By separating variables, neglecting the dependence of $\bar{k}_{V/G}$ and $\bar{c}_{pV}$ on temperature, and integrating (9.100) over reduced film thickness, one obtains

$$\dot{q}_{\sum} = \frac{\dot{J}_{V(C)} \bar{c}_{pV} (T_G - T_l)}{\exp\left(\dfrac{\delta_D \dot{J}_{V(C)} \bar{c}_{pV}}{\dot{k}_{V/G}} \right) - 1}, \tag{9.101}$$

where T_G is the temperature on the reduced film's outer edge, which – in fact – is that of the gas flowing over the propellant surface, or the gas mixture temperature in the ullage if zone 2 exists (see Figure 9.7).

Considering that the amount of heat transferred to the propellant surface is consumed for both the heating of the propellant and its evaporation, let us write the expression for the calculation of the amount of heat consumed for liquid-propellant heating:

$$\dot{q}_l = \frac{\dot{J}_{V(C)} \bar{c}_{pV} (T_G - T_l)}{\exp\left(\dfrac{\delta_D \dot{J}_{V(C)} \bar{c}_{pV}}{\bar{k}_{V/G}} \right) - 1} - \dot{J}_{V(C)} L_V, \tag{9.102}$$

where L_V is the latent heat of propellant evaporation.

Based on the known amount of heat flux, the simulation of the propellant heating can be considered as a one-dimensional non-steady-state heat diffusion problem:

$$\frac{\partial T}{\partial t} = \frac{k_l}{\rho_l c_l} \frac{\partial^2 T}{\partial y^2}. \tag{9.103}$$

Heat exchange intensification due to propellant circulation caused by the pressurizing gas flow can be allowed for by increasing the value of thermal diffusivity $\frac{k_l}{\rho_l c_l}$.

Downloaded from https://www.cambridge.org/core. Nottingham Trent University, on 17 Aug 2019 at 02:12:43, subject to the Cambridge Core terms of use, available at https://www.cambridge.org/core/terms. https://doi.org/10.1017/9781108581714.009

The described models of the pressurizing gas flow and heat exchange with tank walls along with the heating and evaporation of the propellant give important information required for the calculation of conservative parameters of the accompanying processes included in the system of equations (9.1)–(9.3), (9.9), (9.11)–(9.13), (9.20), (2.31), (2.149), and (2.157) implementing the procedure for their redefinition beyond the process of solving the system of equations and maintaining these conservative parameters invariable at the series of integration steps.

9.4 Numerical Simulation and Optimization of Propellant Tank Pressurization

The comparison of the results of numerical simulation performed by applying the mathematical model (Sections 9.2 and 9.3) with experimental data demonstrate their acceptable coinciding. Examples of this comparison are shown in Figure 9.8, whereby calculation data are compared with experimental data obtained for the pressurization of the tank filled with liquid oxygen by gaseous oxygen. The pressurizing gas is fed through a cylindrical diffuser arranged at the tank's upper bottom (scheme A, Figure 9.5) at the velocities of 32 m/s and 79.2 m/s. Figure 9.9 illustrates the results of this

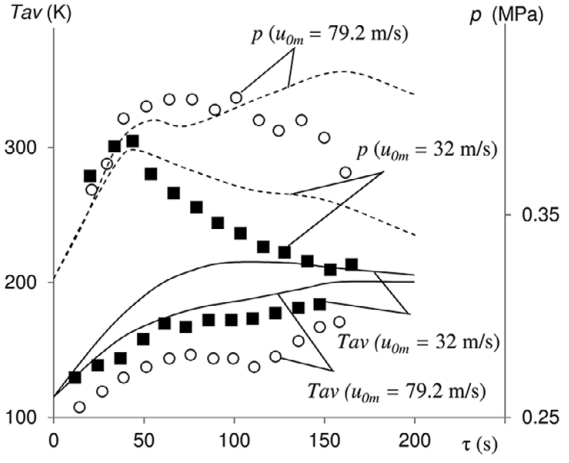

Figure 9.8 Comparison of calculated and experimental pressure and temperature variation in the ullage at pressurization of the tank filled with liquid oxygen by gaseous oxygen at pressurizing gas velocities of 32 m/s – ■ and 79.2 m/s – ○ [274]. From V. Naoumov, "Simulation of High-Temperature Pressurization of the Liquid-Propellant Rocket Tanks," 47th Aerospace Science Meeting Including the New Horizons Forum and Aerospace Exposition, AAA 2009–1600, pp. 1–7, Orlando, FL, 2009, reprinted by permission of the American Institute of Aeronautics and Astronautics, Inc.; [291], from V. I. Naoumov, V. G. Kriukov, and A. L. Abdullin, "Chemical Kinetics Software System for the Propulsion and Power Engineering," 41st Aerospace Science Meeting and Exhibit, AIAA 2003–854, pp. 1–11, Reno, NV, 2003, reprinted by permission of the American Institute of Aeronautics and Astronautics, Inc

Downloaded from https://www.cambridge.org/core. Nottingham Trent University, on 17 Aug 2019 at 02:12:43, subject to the Cambridge Core terms of use, available at https://www.cambridge.org/core/terms. https://doi.org/10.1017/9781108581714.009

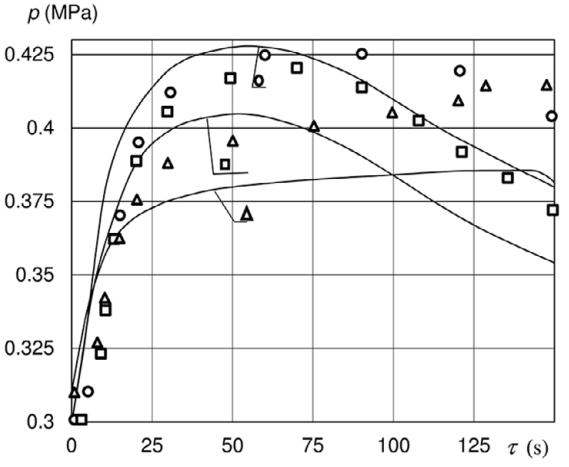

Figure 9.9 Comparison of calculated and experimental pressure variation in the ullage at pressurization of the tank filled with liquid oxygen by helium at pressurizing gas velocities of 70 m/s – □, 76 m/s – ○, and 315 m/s – Δ.

comparison of experimental pressures and calculated pressures at the pressurization of the oxygen tank by helium at the velocities of 70 m/s, 76 m/s, and 315 m/s. It is clear from these figures that divergence between experimental and calculated data increases as the tanks empty. Naturally, at such diversity of aerothermochemical processes taking place at pressurization (Section 9.1) and the application of a one-dimensional mathematical model, it is unlikely to expect an ideal convergence of numerical and experimental results. One of the main reasons of this divergence results from the comparison of calculated parameters with averaged experimental pressures and temperatures of the gas mixture in the tank. It is natural that the accuracy of such averaging decreases with the increase of ullage volume as the tank empties – all the more so that these calculations have been made for the rocket first stage with the tank of about 75 m^3, which coincides with the fact that ullage the volume approaches this value at the end of tank emptying.

Since this comparison considers the pressurizing gases inert with respect to the propellant vapors, Equations (2.31) and (2.157) of mathematical models operate with only "mechanical" (not chemical) variation of the gas mixture composition in the ullage caused by pressurizing gas injection and liquid oxygen evaporation or condensation at the absence of chemical reactions. Resources of the model for the simulation of parameters of whatever pressurization systems at the injection of chemically active gases are given in the following subsection.

9.4.1 Influence of Rates of Chemical Reactions on the Parameters of Gas Mixture in the Ullage

Nitrogen tetroxide (NT, N_2O_4) is a widespread oxidizer often used in rocketry. Widespread propellant used in combination with nitrogen tetroxide is an unsymmetrical dimethylhydrozine (UDMH, $H_2N_2(CH_3)_2$). As a rule, gas-generator systems producing

Downloaded from https://www.cambridge.org/core. Nottingham Trent University, on 17 Aug 2019 at 02:12:43, subject to the Cambridge Core terms of use, available at https://www.cambridge.org/core/terms. https://doi.org/10.1017/9781108581714.009

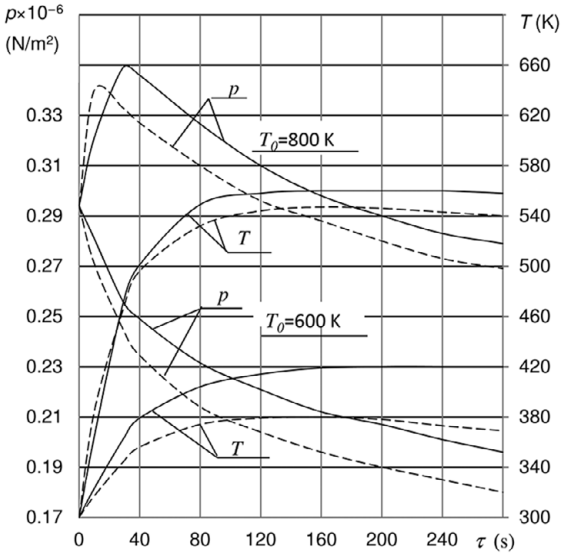

Figure 9.10 Variation of gas mixture parameters at pressurization of the tank with NT; solid line – chemically nonequilibrium calculation, dotted line – frozen calculation.

fuel-lean combustion products (α_{ox} = 5–7) are employed for the pressurization of tanks filled with NT (Section 9.1) to prevent an uncontrolled increase in temperature in the tank ullage. Because of the excess of oxidizing elements at α_{ox} = 5–7, hydrocarbons such as methane are practically absent in the gas mixture. Therefore, the set of individual substances in the ullage of the NT tank may be limited by the following matters: O_2, OH, H_2O, N_2, NO, NO_2, CO, CO_2, HNO_3, N_2O_4 with notable prevalence of NO, NO_2, and N_2O_4 as an evaporation product.

Initial data of the chemical composition of the pressurizing gas and its temperature required for the calculations at such high equivalence ratios are not at equilibrium and may not be obtained from the thermodynamic model. The most likely approach consists in their obtaining proceeding from the calculation of processes in the gas generator with the application of the model described in Chapter 8. Note here that the analysis of the kinetic mechanism in the ullage shows that only two of them prevail:

$$N_2O_4 \Leftrightarrow 2NO_2 + 112.525J, \tag{9.104}$$

$$2NO_2 \Leftrightarrow 2NO + O_2 - 56.932\,J. \tag{9.105}$$

Figures 9.10, 9.12a, and 9.12b display the results of the simulation of pressurization of a 10-meter-high cylindrical tank with NT. Pressurizing gas of two temperature options – i.e., T_0 = 600 K and T_0 = 800 K – is fed into the tank according to scheme A (Figure 9.3).

During the initial stage of tank emptying at the pressurizing gas temperature of 800 K and low temperature in the ullage, the amount of heat transferred to the tank walls is relatively small, which causes an increase of temperature and pressure in the ullage (Figure 9.10). At this stage, the pressurizing gas jet undergoes a substantial effect of the Archimedean force

Downloaded from https://www.cambridge.org/core. Nottingham Trent University, on 17 Aug 2019 at 02:12:43, subject to the Cambridge Core terms of use, available at https://www.cambridge.org/core/terms. https://doi.org/10.1017/9781108581714.009

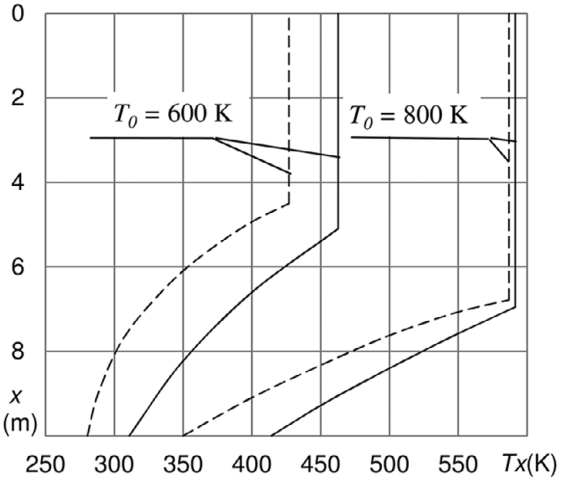

Figure 9.11 Variation of bulk (mass-averaged) temperature of gas mixture over ullage height at the end of tank emptying; solid line – chemically nonequilibrium calculation, dotted line – frozen calculation.

due to the considerable difference between temperatures of the pressurizing gas and the gas mixture (mainly vapors of NT at a temperature of about 300 K) in the ullage. Further, as the gas mixture temperature increases and the effect of Archimedean forces decreases, the velocity of the pressurizing gas reverse flow over the tank walls (scheme A1 and A2, Figure 9.5) increases, and heat transfer to the walls of the tank increases as well. This brings about a certain pressure drop in ullage. At the pressurizing gas temperature of 600 K, the effect of Archimedean force initially is less significant, while the pressurizing gas thermal capacitance is notably smaller than that in the previous case. This results in a less intensive increase in the gas mixture temperature and in continuous reduction of the pressure in the ullage. Note here that, practically, such a pressure drop is unacceptable because it can cause the loss of the tank's structural stability.

Figure 9.11, which demonstrates the gas mixture temperature distribution in the ullage at the end of pressurization and tank emptying, clearly illustrates the effect of Archimedean force and, accordingly, the origination of the gas mixture thermal stratification zone at the bottom of the ullage caused by Archimadian force impact. The so-called frozen version of calculation, where Reactions (9.104) and (9.105) are not allowed for, the gas mixture chemical composition varies only due to the injection of the pressurization gas and NT evaporation is compared in Figure 9.12 with chemically nonequilibrium calculation. The results of the calculation of chemical composition in the ullage at pressurizing gas temperature of 800 K that define the difference in the gas mixture parameters (such as temperature and pressure) are given in Figures 9.12a and 9.12b.

NO concentration in the chemically reacting mixture becomes 3.0–3.5 times lower while the NO_2 concentration is 1.5–2.0 times higher compared to the frozen calculation. Dissociation of N_2O_4 (Reaction [9.104]) results in a notable decrease in its

Downloaded from https://www.cambridge.org/core. Nottingham Trent University, on 17 Aug 2019 at 02:12:43, subject to the Cambridge Core terms of use, available at https://www.cambridge.org/core/terms. https://doi.org/10.1017/9781108581714.009

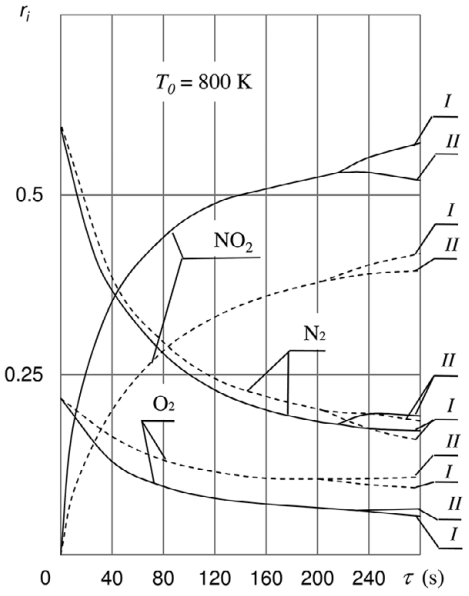

Figure 9.12a Variation of gas mixture chemical composition at pressurization of the tank with NT. Solid line – chemically nonequilibrium calculation, dotted line – frozen calculation; I – chemical composition in zone 1, II – chemical composition in zone 2.

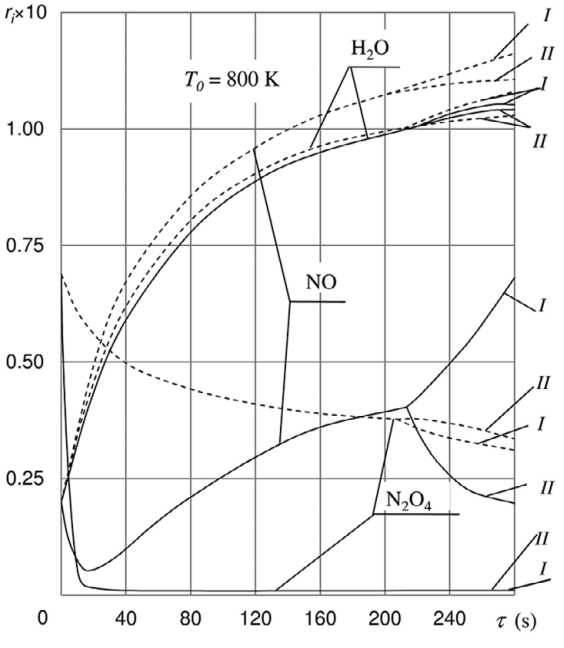

Figure 9.12b Variation of gas mixture chemical composition at pressurization of the tank with NT. Solid line – chemically nonequilibrium calculation, dotted line – frozen calculation; I – chemical composition in zone 1, II – chemical composition in zone 2.

Downloaded from https://www.cambridge.org/core. Nottingham Trent University, on 17 Aug 2019 at 02:12:43, subject to the Cambridge Core terms of use, available at https://www.cambridge.org/core/terms. https://doi.org/10.1017/9781108581714.009

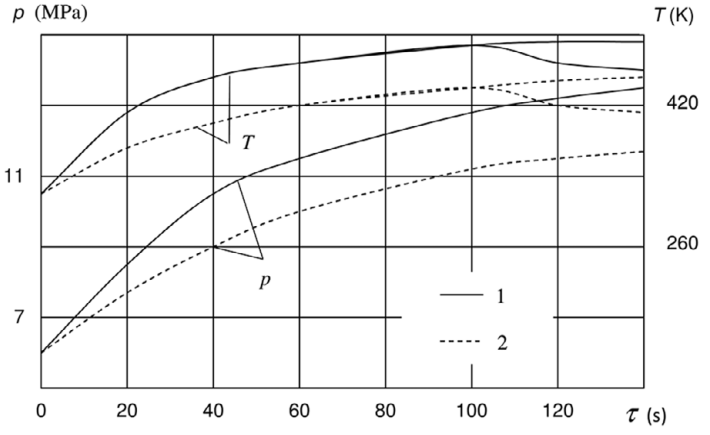

Figure 9.13 Variation of gas mixture parameters at pressurization of the tank with hydrazine. Solid line – chemically nonequilibrium calculation, dotted line – frozen calculation.

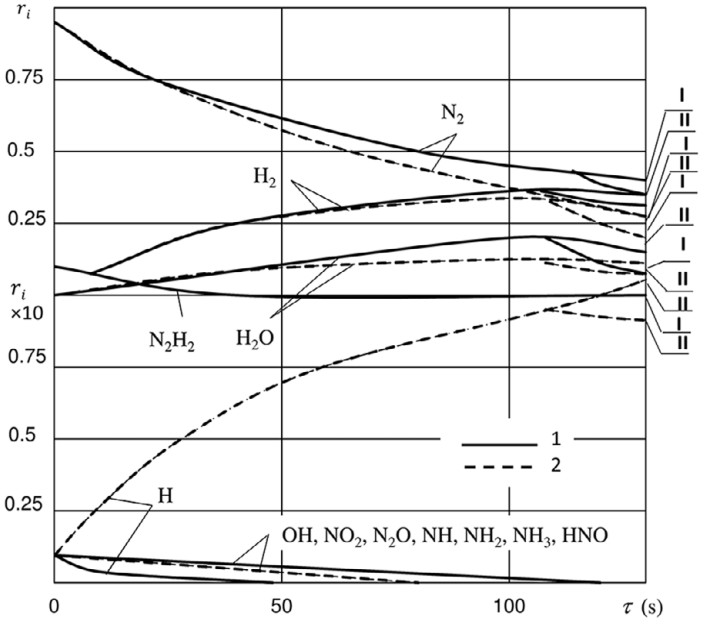

Figure 9.14 Variation of gas mixture chemical composition at pressurization of the tank with hydrazine. Solid line – chemically nonequilibrium calculation, dotted line – frozen calculation; I – chemical composition in zone 1, II – chemical composition in zone 2.

content in the ullage. The comparison of the results of variation of temperature and pressure at chemically nonequilibrium and frozen calculations shows the difference in pressure and temperature reaching 12%. Both chemical nonequilibrium pressure and temperature are higher than their values obtained at frozen calculation. This is explained by the overall positive thermal effect of Reactions (9.104) and (9.105).

Downloaded from https://www.cambridge.org/core. Nottingham Trent University, on 17 Aug 2019 at 02:12:43, subject to the Cambridge Core terms of use, available at https://www.cambridge.org/core/terms. https://doi.org/10.1017/9781108581714.009

With pressurization gas injection into gas ullage, the equilibrium of reaction (9.104) shifts toward formation of NO_2 with the release of some amount of heat evidenced by Figures 9.12a and 9.12b. Endothermic reaction (9.105) brings about a minor influence on temperature variation because of the relatively minor content of N_2O_4 vapors in the ullage (Figure 9.12b).

Similar results are obtained at comparison of chemically nonequilibrium and frozen calculations of the pressurization of the tank with a widespread fuel – hydrazine (N_2H_4, by fuel-rich products of gas generation. The following reaction mechanism was used in chemically nonequilibrium calculation [55]:

$$\begin{array}{l} 2NH_2 \Leftrightarrow N_2H_4; NH + NH_3 \Leftrightarrow N_2H_4; 2NH \Leftrightarrow N_2H_2; 2NH_2 \Leftrightarrow NH_3 + NH; \\ H + NO_2 \Leftrightarrow OH + NO; NH_3 + H \Leftrightarrow NH_2 + H_2; H_2 + OH \Leftrightarrow H_2O + H; \\ HNO + HNO \Leftrightarrow H_2O + N_2O; OH + NH_3 \Leftrightarrow H_2O + NH_2; \\ HNO + HNO \Leftrightarrow 2NO + H_2; OH + NH_2 \Leftrightarrow H_2O + NH; \\ H + H + M \Leftrightarrow H_2 + M. \end{array} \quad (9.106)$$

The difference in temperature and pressure between the calculations with frozen and nonequilibrium parameters reaches 15% (Figure 9.13), which is also explained by the difference in chemical compositions in the ullage caused by effect of chemical nonequilibrium interation (Figure 9.14).

9.4.2 Influence of Temperature and Pressurizing Gas Consumption on the Parameters of Gas Mixture in Ullage

One of the main functions of pressurization systems is to maintain the required pressure in tank ullage. A pressure drop below a definite level can result in the loss of the tank's structural stability. There are two options of getting a required pressure: increasing the pressurizing gas flow rate and increasing the gas temperature. A negative result of the first approach consists in the increase pressurizing gas's required mass, and the second approach can bring about the tank walls' overheating. Figures 9.15 and 9.16 display the results of numerical analyses of the increase in pressurizing gas consumption $\dot{m}_g$ within 0.4 kg/s to 0.6 kg/s at maintaining the invariable pressurizing gas temperature, and the increase in pressurizing gas temperature T_0 within 800–900 K at invariable pressurizing gas consumption, performed for the pressurization of a tank with NT by gas generation products. The variation of pressurization gas flow rate insignificantly influences the gas mixture temperature in ullage but significantly changes the pressure (Figure 9.15), while temperature increase notably raises both the temperature and the pressure in the ullage (Figure 9.16). Because of non-steady-state nature of the pressurization process, an adequate analysis and comparison of the influence of both options on most considerable characteristics of pressurization systems can be performed only on the basis of comparison of some integral parameters – for example, average in-tank pressure during tank emptying. Going to relative parameters, it is possible to evaluate the influence of the increase in pressurizing gas temperature and flow rate on other parameters and to set a certain temperature equivalent of flow rate increase. Figure 9.17 illustrates the example of relative average pressure variation at the increase in pressurizing gas flow rate and

Downloaded from https://www.cambridge.org/core. Nottingham Trent University, on 17 Aug 2019 at 02:12:43, subject to the Cambridge Core terms of use, available at https://www.cambridge.org/core/terms. https://doi.org/10.1017/9781108581714.009

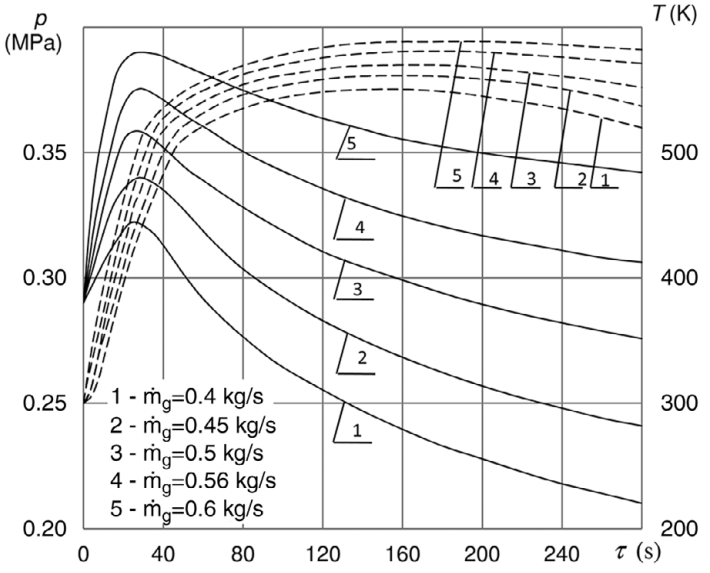

Figure 9.15 Variation of pressure (solid line) and temperature (dotted line) in the ullage at varying pressurizing gas flow rate and invariable pressurizing gas temperature.

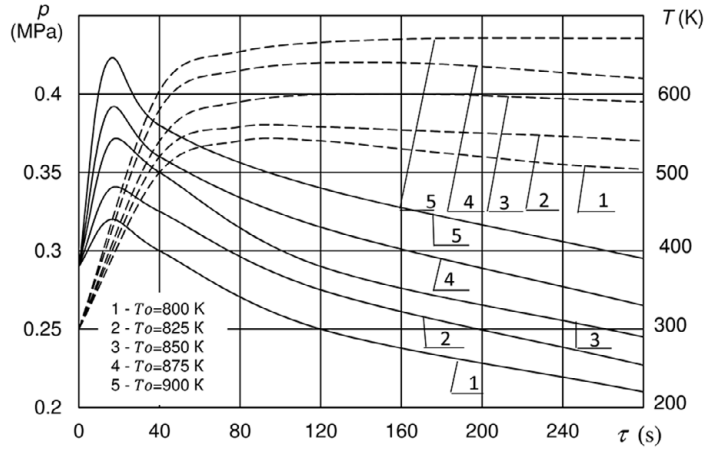

Figure 9.16 Variation of pressure (solid line) and temperature (dotted line) in the ullage at varying pressurizing gas temperature and invariable pressurizing gas flow rate.

temperature. Analyzed values of flow rate and temperature are related to some nominal values taken for reference point: T_{01} = 800 K and $\dot{m}_{g1}$ = 0.4 kg/s. Analysis of the results of numerical experiments in the aforementioned ranges of flow rate and temperature variation displays, for example, that for an increase in average pressure by 30%, it is necessary to raise the pressurizing gas flow rate by almost 40% or the pressurizing gas temperature by only 10%.

Downloaded from https://www.cambridge.org/core. Nottingham Trent University, on 17 Aug 2019 at 02:12:43, subject to the Cambridge Core terms of use, available at https://www.cambridge.org/core/terms. https://doi.org/10.1017/9781108581714.009

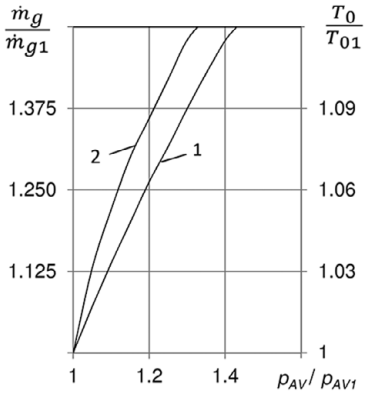

Figure 9.17 Variation of relative pressure subject to relative pressurizing gas flow rate (1) and relative temperature (2).

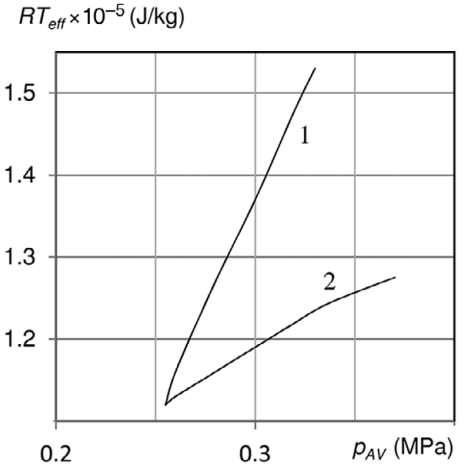

Figure 9.18 Variation of gas mixture effective working capacity: (1) at pressurizing gas temperature increase; (2) at pressurizing gas flow rate increase.

The important working parameter describing the pressurization process efficiency is the gas mixture's effective working capacity in the ullage:

$$RT_{eff} = \frac{pV}{M_{tot}}, \tag{9.107}$$

where p and V are instant pressure in the ullage and ullage volume and M_{tot} is the gas mass consumed for tank pressurization at this time moment.

Results shown in Figure 9.18 display a notable increase in working capacity at the increase in pressurizing gas temperature and an insignificant increase in working capacity at the increase in flow rate. Besides, an increase in the pressurizing gas flow rate causes the increase in pressurization system mass, while the increase in temperature

Downloaded from https://www.cambridge.org/core. Nottingham Trent University, on 17 Aug 2019 at 02:12:43, subject to the Cambridge Core terms of use, available at https://www.cambridge.org/core/terms. https://doi.org/10.1017/9781108581714.009

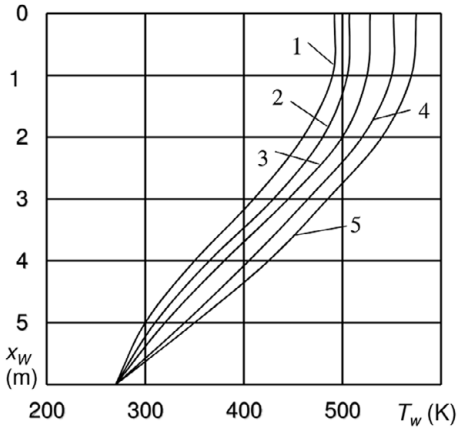

Figure 9.19 Tank wall temperature variation over tank height at complete tank emptying: (1) T_0 = 800 K; (2) T_0 = 825 K; (3) T_0 = 850 K; (4) T_0 = 875 K; (5) T_0 = 900 K.

can simply be brought about by varying the gas generator operating mode (varying the equivalence ratio α). A pressurization temperature increase can have the negative effect of overheating the tank walls and structural elements, as shown in Figure 9.19. The highest temperature of the walls can be observed at the top of the tank, which – particularly at a low velocity of the injection of pressurizing gas – is caused by thermal stratification of gas mixture subjected to the action of Archimedean forces affecting the pressurizing gas jet. These numerical analyses confirm the observations related to gas stratification in the ullage and vividly illustrate the constructiveness of the proposal given in [274, 275, 279] about the reduction of heat transfer to the tank walls through the mixing of the gas in the ullage. Thereby, the distribution of gas mixture temperature and tank walls temperature are leveling off over the tank height.

Further, Subsection 9.4.3 analyzes the method of gas mixing and redistribution of heat flows by optimization of pressurizing gas velocity.

9.4.3 Optimization of Pressurizing Gas Injection Velocity

Pressurizing gas injection velocity defines the intensity of heat and mass exchange processes, hence the performances of pressurization system. This interrelation was confirmed for the first time by an experimental study of pressurization of tanks [276, 277]. Theoretical studies of pressurization of tanks with NT by gas generation products, and the pressurization of oxygen tanks by oxygen and helium vapors revealed a number of options of performance variation at varying the velocities of pressurization gas feed through diffusers (A in Figure 9.3). Results of variation of time-averaged pressures p_{av} (during the entire period of tank emptying) and final pressures p_f (pressures at the end of tank emptying), as well as mass-averaged temperatures in the ullage $T_{M\,av}$ for 10-meter-height tanks with respect to the velocity of injection are shown in Figures 9.20 and 9.21. These results illustrate the existence of maximum values of time-averaged pressures,

Downloaded from https://www.cambridge.org/core. Nottingham Trent University, on 17 Aug 2019 at 02:12:43, subject to the Cambridge Core terms of use, available at https://www.cambridge.org/core/terms. https://doi.org/10.1017/9781108581714.009

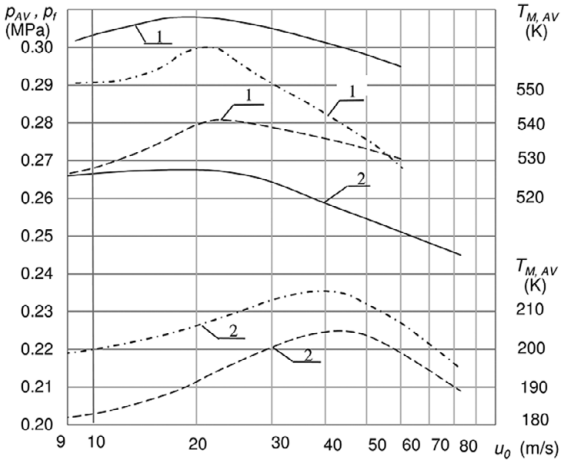

Figure 9.20 Variation of time-averaged pressures (solid line) and final pressures (dotted line) and mass-averaged final temperatures (dot-and-dash line) at NT tank pressurization by products of gas generation (1) and oxygen tank pressurization by vapors of oxygen (2).

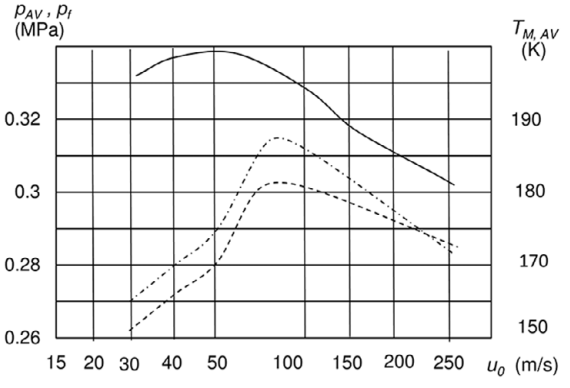

Figure 9.21 Variation of time-averaged pressures (solid line) and final pressures (dotted line) and mass-averaged final temperatures (dot-and-dash line) at oxygen tank pressurization by helium.

final pressures, and mass-averaged final temperatures. These results have an important applied significance because they indicate the possibility of increase in the pressurizing gas's working capacity by the optimization of gas feed velocities at a gas invariable temperature and flow rate (Figures 9.20 and 9.21).

The cause of the existence of maximum values consists in the redistribution of the total amount of heat consumed for the heating up of the tank walls Q_W^{Σ} and propellant Q_l^{Σ} at a variation of pressurizing gas injection velocities, as well as, to some extent, the change of the mass of propellant vapors M^{Σ}. Variations of total values of these parameters (during the entire process of tank emptying) at the pressurization of tanks filled with NT and oxygen (Figures 9.22 and 9.23) show, at definite values of pressurizing gas velocities, a minimum value of the total amount of heat consumed for the

Downloaded from https://www.cambridge.org/core. Nottingham Trent University, on 17 Aug 2019 at 02:12:43, subject to the Cambridge Core terms of use, available at https://www.cambridge.org/core/terms. https://doi.org/10.1017/9781108581714.009

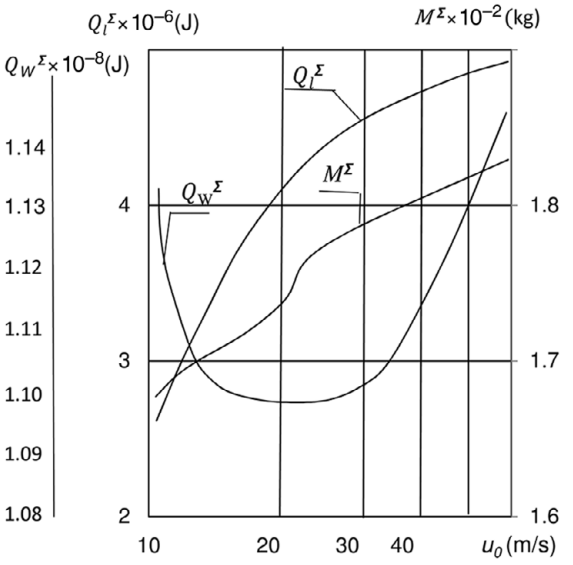

Figure 9.22 Variation of total amount of heat consumed for the heating up to the tank walls, total amount of heat consumed for the heating up of propellant, and total mass of the propellant vapors at pressurization of tank with NT by gas generation products.

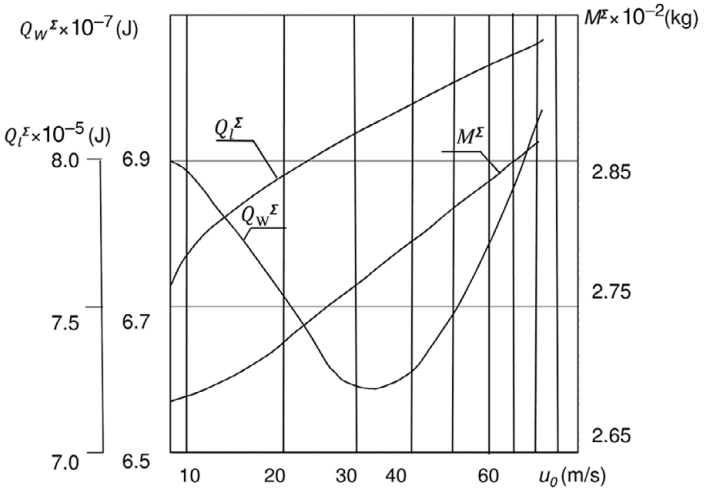

Figure 9.23 Variation of total amount of heat consumed for the heating up of the tank walls, total amount of heat consumed for the heating up of propellant, and total mass of the evaporated propellant at pressurization of tank with oxygen by vapors of oxygen.

heating up of the tank walls. Since the total amount of heat consumed for the heating up of the tank walls is greater by at least an order of magnitude than that consumed for heating up the propellant, it is Q_W^{Σ} that defines an optimum velocity of pressurizing gas. It follows from the comparison of the variation of maximum values of time-averaged

Downloaded from https://www.cambridge.org/core. Nottingham Trent University, on 17 Aug 2019 at 02:12:43, subject to the Cambridge Core terms of use, available at https://www.cambridge.org/core/terms. https://doi.org/10.1017/9781108581714.009

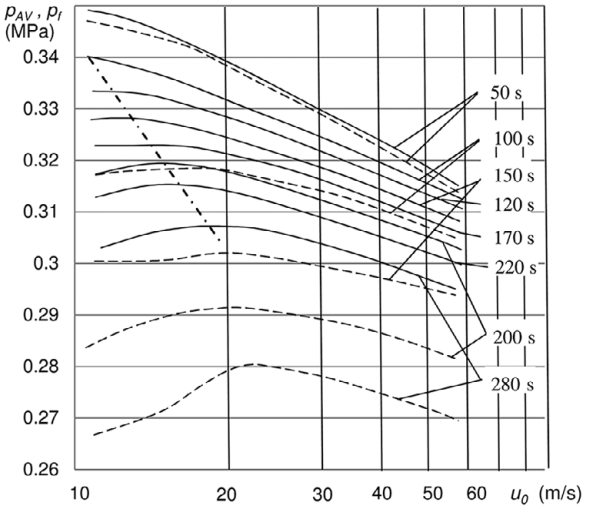

Figure 9.24 Variation of time-averaged pressures (solid line) and final pressures (dotted line) during tank emptying at the pressurization of tank with NT by gas generation products.

pressures, final pressures, and mass-averaged final temperatures and the total amount of heat consumed for the tank walls' heating. Minor differences in the values of optimum velocities corresponding to minimum values of the total amount of heat consumed for the tank walls' heating and optimum velocities corresponding to maximum values of gas mixture performances are explained by an insignificant influence of amount of heat consumed for heating up the propellant.

The nature of this phenomenon follows from the peculiarities of pressurizing gas flow in the tank ullage. The analysis of the gas mixture thermal stratification in the ullage, obtained from numerical experiments, displays that at gas injection velocities lower than optimum values, considerable pressurizing gas jet deceleration occurs as well as its collapse caused by the effect of Archimedean forces. This causes significant gas mixture stratification and a concentration of high-temperature gas in the ullage's top region, which causes the overheating of the tank wall's upper part (Figure 9.4, schemes A3 and B3) due to intensive free convection from the hot gas. At pressurizing gas velocities notably higher that optimum values, heat transfer to the tank walls increases at their blowing by reverse (Figure 9.4, schemes A1 and A2) and forward (Figure 9.4, schemes B1 and B2) flows of high-temperature gas, due to intensive forced convection.

With an increase in the depth of tank emptying, maximum values of time-averaged pressures and maximum values of final pressures decrease and shift to the region of higher pressurizing gas velocities (Figures 9.24 and 9.25). These figures display the results of analysis of the variation of p_{av} and p_f for the same range of pressurizing gas velocity variation. The decrease of p_{av} and p_f, corresponding to optimum velocities of pressurizing gas results from a general trend of a pressure decrease during tank emptying observed from numerical experiments. Note here that the shift of pressurizing gas optimum velocities to the region of their higher values is explained by the increase

Downloaded from https://www.cambridge.org/core. Nottingham Trent University, on 17 Aug 2019 at 02:12:43, subject to the Cambridge Core terms of use, available at https://www.cambridge.org/core/terms. https://doi.org/10.1017/9781108581714.009

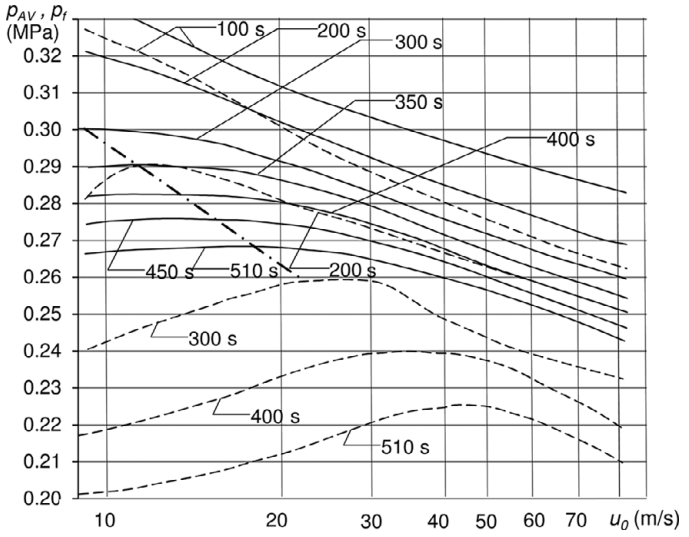

Figure 9.25 Variation of time-averaged pressures (solid line) and final pressures (dotted line) during tank emptying at the pressurization of the tank with oxygen by vapors of oxygen.

in the height of the stratification zone. If the height of the stratification zone exceeds some optimum values depending on pressurizing gas velocity, thermodynamic properties of the gas mixture in the ullage, and some other parameters, values of p_{av} and p_f decrease. Therefore, in order to obtain the maximum pressures at the next time moment of emptying, higher pressurizing gas velocities are required at which the stratification zone has optimum height, or even doesn't exist, which – as was mentioned earlier – depends on thermodynamic properties of the gas mixture in the ullage and some other parameters.

Calculations show that maximum pressure can be reached both at the existence of mixed region only (zone 1) and mixed and stratified regions (zone 1 and zone 2) simultaneously. Note here that the sizes that ensure the most favorable performances of pressurization system depend on the pressurizing gas type and its chemical composition, other conditions being equal. Results of numerical simulation can be used for getting the engineering relations for the prediction of pressurizing gas optimal velocities and maximum pressures in ullages. Thus, for instance, the approximation of the results of numerical experiments of pressurization of the tank of a specific size filled with NT and pressurized by gas generation products and the pressurization of the tank of a specific size filled with oxygen and pressurized by oxygen vapors at invariable propellant flow rate and invariable pressurizing gas inflow rate allow one to use the following relations:

For a tank with oxygen:

$$u_0^{\text{opt}} = 1.5133\text{L} + 3.4518\,\text{m/s} \tag{9.108}$$

$$p_{av}^{\max} = -0.0050L + 0.3610\text{MPa} \tag{9.109}$$

Downloaded from https://www.cambridge.org/core. Nottingham Trent University, on 17 Aug 2019 at 02:12:43, subject to the Cambridge Core terms of use, available at https://www.cambridge.org/core/terms. https://doi.org/10.1017/9781108581714.009

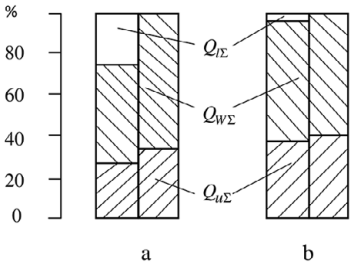

Figure 9.26 Distribution of total amount of heat consumed for the heating up of the tank walls $Q_{W\Sigma}$, total amount of heat consumed for the heating up of the propellant $Q_{l\Sigma}$, and total amount of heat accumulated in the ullage $Q_{u\Sigma}$: (a) pressurization of NT tank by products of gas generation (left column demonstrates the distribution at the beginning of tank emptying and right column demonstrates the distribution at the end of tank emptying); (b) pressurization of oxygen tank by helium (left column demonstrates the distribution at the beginning of tank emptying and right column demonstrates the distribution at the end of tank emptying).

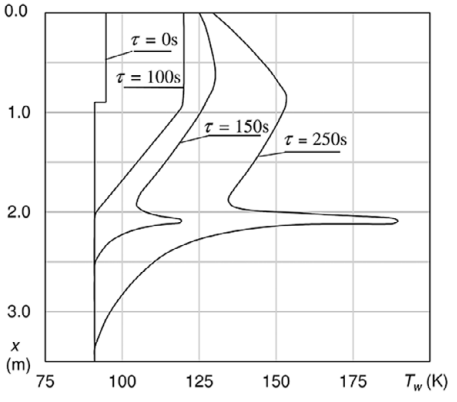

Figure 9.27 Temperature profiles over the wall height at the pressurization of oxygen tank, with the diffuser of the type C, by oxygen vapors [274]. From V. Naoumov, "Simulation of High-Temperature Pressurization of the Liquid-Propellant Rocket Tanks," 47th Aerospace Science Meeting Including the New Horizons Forum and Aerospace Exposition, AAA 2009–1600, pp. 1–7, Orlando, FL, 2009, reprinted by permission of the American Institute of Aeronautics and Astronautics, Inc

For a tank with NT:

$$u_0^{\text{opt}} = 2.1185\text{L} - 4.6882\,\text{m/s} \tag{9.110}$$

$$p_{av}^{\max} = -0.0076L + 0.3488\text{MPa}, \tag{9.111}$$

where L is the tank height.

The determining influence of heat transfer to the tank walls in the distribution of heat flows is clearly illustrated in the graph of the distribution of the total amount of heat consumed for the heating up of the tank walls, the total amount of heat consumed for the heating up of the propellant, and the total amount of heat accumulated in the ullage at the pressurization of the tanks filled with NT and oxygen (Figure 9.26).

Downloaded from https://www.cambridge.org/core. Nottingham Trent University, on 17 Aug 2019 at 02:12:43, subject to the Cambridge Core terms of use, available at https://www.cambridge.org/core/terms. https://doi.org/10.1017/9781108581714.009

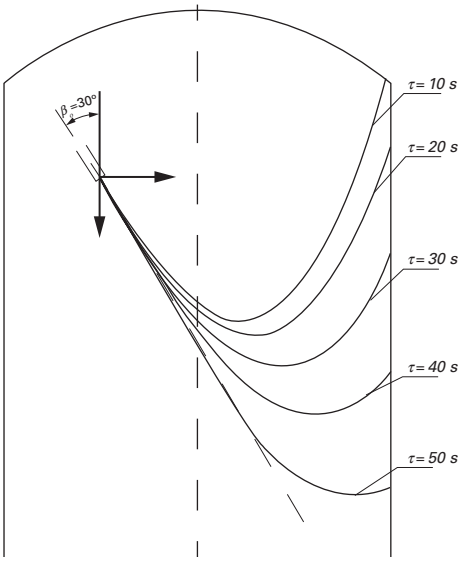

Figure 9.28 Trajectories of the inclined jet at pressurization of the oxygen tank with the diffuser of the type C, by oxygen vapors.

When using the diffuser of the type C (Figure 9.3), a local overheating of the tank wall is especially critical, which is demonstrated by the results of the calculation of emptying of the tank filled with oxygen. Figure 9.27 clearly shows local overheated regions of the tank wall. Figure 9.28 demonstrates corresponding trajectories of the inclined jet and the existence of the areas of jet impingement with the wall, confirming the nature of the development of local overheated regions of the tank wall.

9.4.4 Interchangeability of Pressurization Gases

A possible modification of pressurization systems can require notable variation of pressurizing gas performances up to their replacement. For tanks pressurized by gas generation products, more characteristic is pressurization gas chemical composition variation by varying the equivalence ratio. However, this causes the change of pressurizing gas temperature.

More correct seems to be the analysis of the possibility of replacement of the pressurizing gas maintaining its temperature, which is possible for pressurization systems using a heated gas not reacting with the propellant (that is regular for evaporated-propellant systems and stored-gas systems). Numerical analyses of interchangeability of oxygen, helium, nitrogen, and air at the pressurization of tanks filled with liquid oxygen may be the examples. The conditions of the equality of average $p_{av1} \approx p_{av2} \approx p_{av3}$ and instant $p_1(\tau) = p_2(\tau) = p_3(\tau)$ pressures, required for analysis, were maintained with the accuracy of 1% and 9%, respectively (Figure 9.29).

Downloaded from https://www.cambridge.org/core. Nottingham Trent University, on 17 Aug 2019 at 02:12:43, subject to the Cambridge Core terms of use, available at https://www.cambridge.org/core/terms. https://doi.org/10.1017/9781108581714.009

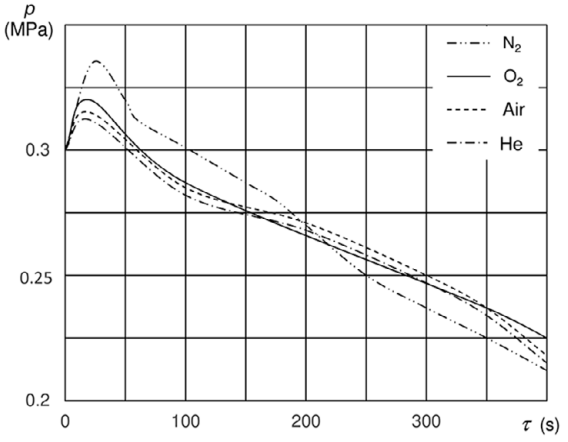

Figure 9.29 Variation of the pressure in the tank ullage at the simulation of pressurizing gases' replacement.

At replacement of pressurization gas x with pressurization gas y, a complete equality of instant and average pressures can be expected at the equality of volume flow rates of these gases:

$$\dot{V}_x = \dot{V}_y \quad \text{or} \quad \frac{\dot{m}_x}{\rho_x} = \frac{\dot{m}_y}{\rho_y}. \tag{9.112}$$

Using the equations of state, Condition (9.112) will be written as follows:

$$\frac{\dot{m}_x}{\dot{m}_y} = \frac{\mu_x}{\mu_y} = \eta_{ideal}. \tag{9.113}$$

The obtained relation of flow rates is an ideal relation because it does not allow for differences in the nature of heat and mass exchange processes for different gases and makes for pressurizing gases under consideration of the following data:

$$\eta_{ideal\ O_2/He} = 8.0; \eta_{ideal\ O_2/N_2} = 1.14; \eta_{ideal\ O_2/Air} = 1.23. \tag{9.114}$$

Actual flow rate ratios can differ from ideal (theoretical) values. Thus, the numerical experiment performed for 10-meter tanks filled with liquid oxygen and equipped with cylindrical 0.006-meter-diameter diffuser brings about the following "real" (actual) ratios:

$$\eta_{real\ O_2/He} = 6.8; \eta_{real\ O_2/N_2} = 1.09; \eta_{real\ O_2/Air} = 1.06. \tag{9.115}$$

Numerical analysis performed in the range of diffuser diameter variation from 0.04 m to 0.1 m and, accordingly, different pressurizing gas velocities, testifies to the change in magnitude $\eta_{real\ x/y}$ at the variation of pressurizing gas velocity (Figure 9.30). For example, at the replacement of oxygen with helium in the limits of diffuser diameter variation from 0.1 m to 0.06 m, which corresponds to a pressurizing gas velocity

Downloaded from https://www.cambridge.org/core. Nottingham Trent University, on 17 Aug 2019 at 02:12:43, subject to the Cambridge Core terms of use, available at https://www.cambridge.org/core/terms. https://doi.org/10.1017/9781108581714.009

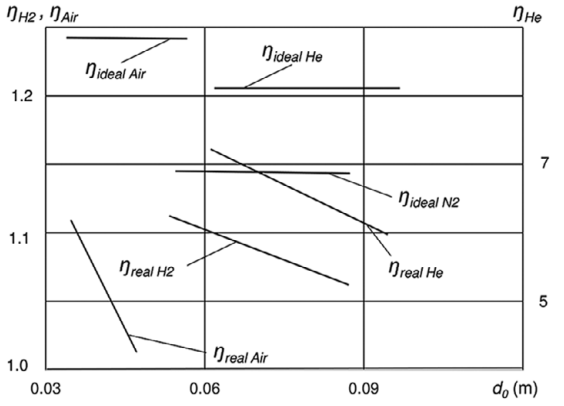

Figure 9.30 Actual and ideal pressurizing gas flow rate ratios at variation of diffuser diameter d_0.

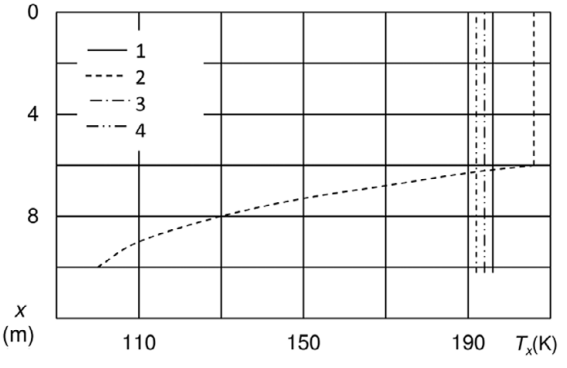

Figure 9.31 Temperature stratification in the ullage at the tank complete emptying: (1) pressurization by oxygen, (2) pressurization by helium, (3) pressurization by nitrogen, and (4) pressurization by air.

variation from 30 m/s to 70 m/s, the actual ratio changes from 6.18 to 6.8. Differences in actual ratios from ideal ones can be explained by different flow patterns of pressurizing gas under conditions of Archimedean forces action, different conditions of heat exchange with tank walls and propellant, different rates of propellant evaporation, etc.

Figure 9.31, for example, displays a different temperature distribution in the ullage for the analyzed gases that is particularly characteristic of the analyzed gases – especially for pressurization by helium, which causes a significant stratification of the gas mixture over the ullage height and subsequently the heat and mass exchange processes differing from other gases. Indeed, if, for example, average pressure variations at the pressurization by helium (Figure 9.32) are considered, then the aforesaid range of pressurization gas velocities (from 30 m/s to 70 m/s) corresponds to the left-hand descending branch of the average pressure variation curve. As diffuser diameter

Downloaded from https://www.cambridge.org/core. Nottingham Trent University, on 17 Aug 2019 at 02:12:43, subject to the Cambridge Core terms of use, available at https://www.cambridge.org/core/terms. https://doi.org/10.1017/9781108581714.009

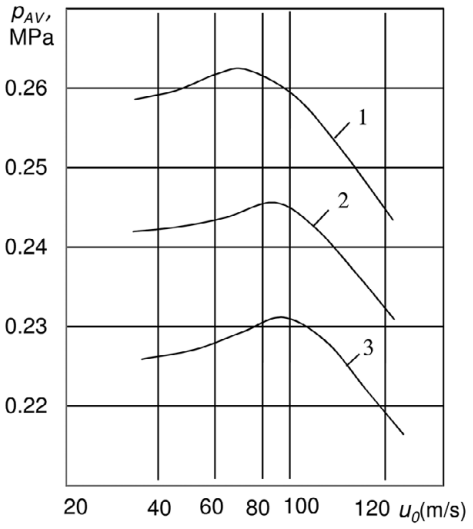

Figure 9.32 Variation of average pressures in the ullage depending on pressurizing gas velocity at different pressurizing gas flow rates: (1) 0.75 kg/s, (2) 0.7 kg/s, and (3) 0.65 kg/s.

increases, gas velocity decreases and shifts from the optimum value (which is approximately 70 m/s). Therefore, for maintaining the required average pressure in the ullage p_{av}, it is necessary to increase the pressurizing gas flow rate, which in its turn causes the decrease in the ratio η_{real}.

Thus, the difference between the ideal and actual ratios is defined not only by the pressurizing gas nature and its thermodynamic properties but also by the pressurizing gas velocity defining the different nature of heat and mass exchange processes in the ullage, and by tank sizes as well.

The analysis of flow rate ratios at the interchange of pressurizing gases is possible only with the help of complex models, such as the model described in Sections 9.2 and 9.3.

Downloaded from https://www.cambridge.org/core. Nottingham Trent University, on 17 Aug 2019 at 02:12:43, subject to the Cambridge Core terms of use, available at https://www.cambridge.org/core/terms. https://doi.org/10.1017/9781108581714.009

10 Combustion and Ionization in Spark Ignition Engines

10.1 Ion Current as a Tool for Engine Performance Control: Specific Features of Ionization

Modeling and numerical simulation of combustion in the cylinders of spark-ignition and compression-ignition internal combustion engines (ICEs) provide a considerable contribution in engines engineering and the optimization of engines performance, efficiency, and emissions. This chapter demonstrates the application of the reactor approach and the chemical nonequilibrium model (Chapters 1–3) to the simulation of combustion in the cylinder of the spark-ignition ICE aiming to predict the variation in ionized particle concentration as control variables. It is known that the combustion of hydrocarbon fuels with oxidizers at high pressures and temperatures is accompanied by the output of some ionized substances. Research on the ionization in flames was started in the mid-1950s for the purpose of optimization of magnetohydrodynamic generators as well as the study of ionized particle formation in combustion products of propulsion systems, particularly in the thrust chambers and exhaust plumes of rocket engines [1, 160, 215, 227, 228]. This study was later extended to the combustion in the ICE for the purpose of employing empirical and theoretical data on the ionization of combustion products for engine performance control intended for the optimization of the combustion process, the reduction of fuel consumption, the reduction of exhaust gas emission, the optimization of the exhaust gas recirculation (EGR) process, etc. [292–305].

The ionization of combustion products in the cylinders of ICEs causes changes in electrical properties of the gas. This allows one to apply the conductivity of the ionized combustion products as a diagnostic parameter for combustion. A regular spark plug can act as an ionization sensor, which can be accomplished by applying a voltage to the spark plug electrodes after the ignition of the air–fuel mixture. Note here that such a low voltage and, hence, a low ion current can be used in combustion diagnostics and feedback control of the parameters governing engine operation [292–295, 300–303, 305]. Measurements of ion current are used for the detection of misfire, engine knock and combustion instability control, spark advance control, equivalence ratio control, and emission control.

Publication [302] represents an example of current measured in an engine along with a pressure variation indicating the energy release by combustion (Figure 10.1). The ion current is measured on the low voltage side of the ignition coil by applying voltage over the spark plug gap [301].

Downloaded from https://www.cambridge.org/core. Nottingham Trent University, on 17 Aug 2019 at 02:14:16, subject to the Cambridge Core terms of use, available at https://www.cambridge.org/core/terms. https://doi.org/10.1017/9781108581714.010

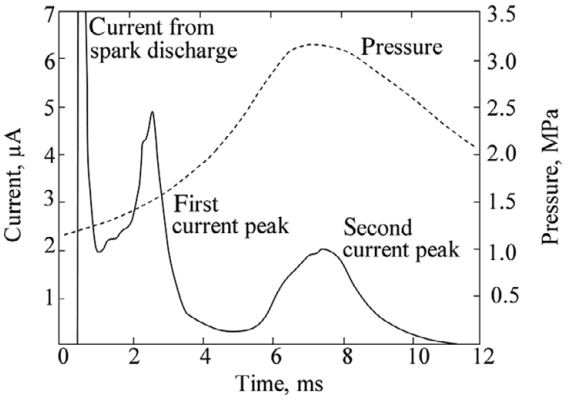

Figure 10.1 Typical ionization sensor current and corresponding pressure measured in an engine [302]. With permission

Three typical ion current peaks were displayed. Citing [302]:

the first peak reflects the flame-initiating spark discharge. In the remaining signal, two parts can be distinguished. The first one is usually attributed to the contact between electrodes and the small flame kernel. In this case, chemi-ionization is considered to be a dominating mechanism for the creation of a conductive channel between the electrodes. The second one, which coincides with the pressure peak, is usually understood to be the result of thermal ionization due to the high temperature in the burned gases [293], although other observations indicate a relation between the contact of the flame with the walls and this signal. [300]

The two last peaks of ion current are of interest for the previously listed diagnostic purposes. Understanding of the nature of these peaks requires the consideration of chemical reactions producing ionized particles.

The experimental and theoretical study of ionization in hydrocarbon–air flames combined with considerations of chemical kinetics [306–310] provides us with following reactions of ionization and their corresponding ionized particles. The most essential ions produced in the reaction zone are the following:

CHO^+, which most probably formed by the reaction of chemi-ionization

$$CH + O = CHO^+ + e. \tag{10.1}$$

H_3O^+ and NO^+, which are most probably formed by charge transfer reactions:

$$CHO^+ + H_2O = H_3O^+ + CO \text{ and} \tag{10.2}$$

$$CHO^+ + NO = NO^+ + HCO. \tag{10.3}$$

The tast two particles are involved in charge recombination reactions:

$$H_3O^+ + e = 2H + OH \text{ and} \tag{10.4}$$

$$NO^+ + e = N + O. \tag{10.5}$$

Thermo ionization + ionization by collision is represented by reaction:

$$NO + M = NO^+ + e + M. \tag{10.6}$$

Downloaded from https://www.cambridge.org/core. Nottingham Trent University, on 17 Aug 2019 at 02:14:16, subject to the Cambridge Core terms of use, available at https://www.cambridge.org/core/terms. https://doi.org/10.1017/9781108581714.010

It was found out that, due to the non-steady-state process in the cylinder of the ICE, small residence time of the working medium in the cylinder and finite values of the rates of reactions of ionization, the application of the chemical equilibrium model for the simulation of combustion sometimes fails to provide reliable data on ionization, which is especially true for the prediction of the first peak of ionization current. At the same time, the equilibrium model can predict the amplitude of the second peak of ion voltage [311]. Bearing in mind that the chemical equilibrium state can be treated as a specific case of the nonequilibrium state when rates of chemical reactions and residence time are high enough to reach chemical equilibrium, the application of the chemical nonequilibrium model to the simulation of combustion and ionization in the cylinder of the ICE would seem to be more appropriate.

10.2 Model of Combustion: Governing Equations and Relations

Since ionization in the engine cylinder occurs during ignition and combustion, the model generally simulates an expansion stroke but also takes into account the last stage of the compression stroke when combustion is initiated at the spark plug by an electrical discharge. A turbulent flame propagates through the premixed propellant – i.e., fuel, air, and residual combustion products – outward from the spark plug electrodes, to reach the walls of the cylinder and possibly the piston surface and then extinguishes [217]. The rapidly increasing volume of the cylinder during the expansion stroke and the corresponding intensive expansion of premixed working medium in the cylinder allow one to assume the uniform distribution of all parameters in the region of the unburned fresh fuel–air–residual combustion products mixture and the uniform distribution of the parameters of the burned mixture as well. Propagating the flame front separates the regions of unburned fresh reactants and the region occupied by the burned mixture. It is also possible to assume that all gradients of parameters of working medium are concentrated in the flame front separating these two regions.

These features of location and interaction of regions (zones) of the unburned and burned mixture and the region of flame propagation are common and well proven for almost all engine combustion chamber geometries and conditions of engine operation [217]. Despite the relative simplicity, this physical diagram can be very helpful in the simulation of combustion chemistry effects. One can see that this approach is similar to the physical scheme of the combustion in the flame front described in Chapter 4.

Based on the previously described processes, it is feasible to use the chemical nonequilibrium model (Section 1.4) and reactor approach (Section 1.5) for the simulation of processes in the cylinder during ignition and combustion. Cylinder volume is split into two reactors (Figure 10.2) to simulate two zones: zone 1 of unburned air–fuel and residual combustion products mixture (u) simulated by PSR of variable volume, and zone 2 of burned mixture (b) simulated by PSR of variable volume as well.

Taking into account the extremely high temperature in the vicinity of the spark plug electrodes at spark discharge, the very short time duration of chemical transformations in this small region, and the extremely small residence time of the reacting mixture

Downloaded from https://www.cambridge.org/core. Nottingham Trent University, on 17 Aug 2019 at 02:14:16, subject to the Cambridge Core terms of use, available at https://www.cambridge.org/core/terms. https://doi.org/10.1017/9781108581714.010

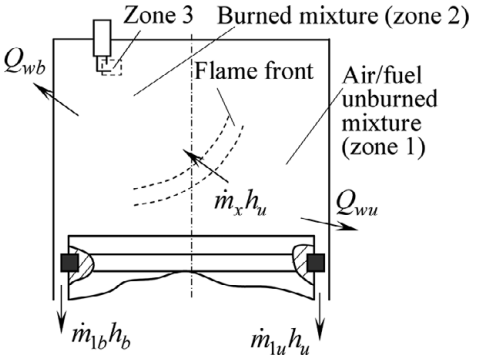

Figure 10.2 Physical diagram of expansion stroke and three-zone model.

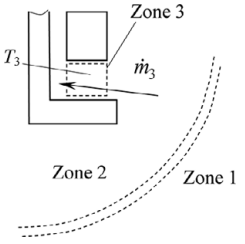

Figure 10.3 Diagram of zones arrangement.

comparable with chemical reactions rates, the third zone is added to zones 1 and 2. The spark kernel (zone 3) is assumed to be a microscopically small fixed-control volume between spark plug electrodes (Figure 10.3). Heat transfer between working medium and spark plug electrodes is taken into account. Mass transfer and heat transfer between kernel and combustion products in zone 2 takes place as well. The working medium continuously flows through this zone from zone 2. As a result, zone 3 has its own parameters (temperature, enthalpy, chemical composition of combustion products, etc.) that differ from the parameters of combustion products in zone 2. It is to emphasize that model of the spark kernel doesn't aim to simulate the initial plasma kernel propagation during the ignition, but simulates the processes in this small volume at the time lapse between two sparks when spark plug electrodes work as a sensor for ion current measurements.

The experience of simulation and numerical study of ionization [311–313] demonstrates the importance of the chemical kinetics application to the simulation of chemical interaction in all zones and, as shown next, provides the possibility for predicting chemical composition and thermodynamic parameters of the working medium including ions and electrons in the condition of small residence time and non-steady-state state nature of the processes in the cylinder of the ICE.

Owing to the application of the PSR basic model (Section 1.5), equations of chemical kinetics (2.31), normalizing equations (2.157) and calorific (energy) equations (2.149) are used as a basic part of the model of thermochemical processes in zones 1 and 2.

Downloaded from https://www.cambridge.org/core. Nottingham Trent University, on 17 Aug 2019 at 02:14:16, subject to the Cambridge Core terms of use, available at https://www.cambridge.org/core/terms. https://doi.org/10.1017/9781108581714.010

While analyzing experimental data and performing theoretical analysis of the specific features of combustion in the kernel, it was observed that the calorific equation for zone 3 can be replaced by special semiempirical equation, which is more convenient for the simulation of thermal processes in such a tiny small region [313]:

$$T_3 - [A_{T3} \cdot T_2 + (1 - A_{T3}) \cdot T_{W3}] = 0, \tag{10.7}$$

where T_3 is the temperature of the working medium in zone 3, T_2 is the temperature of the working medium in zone 2, T_{w3} is the surface temperature of spark plug electrodes, and A_{T3} is the temperature coefficient ($A_{T3} = 0$ for $T_3 = T_{w3}$ and $A_{T3} = 1$ for $T_3 = T_2$) usually varying from 0.7 to 1.0.

The mass flow rate through the electrode gap can be determined from

$$\dot{m}_3 = A_{T3} \cdot \rho_3 \cdot F_3 \cdot v_p, \tag{10.8}$$

where ρ_3 is the density of the working medium in zone 3; F_3 is the cross section area of the "channel" between electrodes; and v_p is the average velocity of the piston.

Taking into account the unburned and burned mixture losses in the ring gaps ($\dot{m}_{1u}$, $\dot{m}_{1b}$), the equations of mass conservation for reactors (zones) 1 and 2 are written as follows:

$$dM_u/d\tau = -\dot{m}_x - \dot{m}_{1u}, \tag{10.9}$$

$$dM_b/d\tau = \dot{m}_x - \dot{m}_{1b}, \tag{10.10}$$

where $\dot{m}_x$ is the mass flow rate defined by the velocity of flame front propagation, index 1 refers to losses through the rings gaps from zones of unburned and burned mixture, M_u is the mass of the unburned mixture in zone 1, and M_b is the mass of burned mixture in zone 2.

In Equations (10.9) and (10.10), $d\tau = d\varphi/(6n)$, where φ is the crank angle and n is the engine speed.

Equations of energy conservation in zones of unburned and burned mixture are written as follows:

$$dU_u + pdV_u = -dQ_u - dQ_{wu}, \tag{10.11}$$

$$dU_b + pdV_b = -dQ_b - dQ_{wb}, \tag{10.12}$$

where dU_u and dU_b are the total energy change in zones of unburned and burned mixture; pdV_u and pdV_b are expansion work; dQ_{wu} and dQ_{wb} are heat transferred to the walls of the cylinder and piston bowl wall; and dQ_u and dQ_b are heat losses through the rings gaps.

Allowing for $U = H - pV$ (where U is total internal energy and H is total enthalpy), assuming a negligibly small amount of losses through the ring gaps and having made some conversions, one can write (10.12) as follows:

$$\frac{dH_b}{d\tau} - p\frac{dV_b}{d\tau} - V_b\frac{dp}{d\tau} + p\frac{dV_b}{d\tau} = \dot{m}_x h_u - q_{wb}. \tag{10.13}$$

Downloaded from https://www.cambridge.org/core. Nottingham Trent University, on 17 Aug 2019 at 02:14:16, subject to the Cambridge Core terms of use, available at https://www.cambridge.org/core/terms. https://doi.org/10.1017/9781108581714.010

Owing to the ideal-gas assumption and allowing for total enthalpy $H = hM$ and mass flow rate $\dot{m} = \dot{J}F$, Equation (10.13) may be transformed with application of (10.10) to the following form:

$$dh_b/d\tau = (\dot{m}_x/M_b)\cdot(h_u - h_b) + (V_b/M_b)\cdot(dp/d\tau) - (q_{wb}/M_b), \tag{10.14}$$

where q_{wb} is the heat flow rate due to convection and radiation to the walls of the cylinder surrounding zone of burned mixture and piston bowl walls; V_b is the volume of the working medium in the zone of burned mixture.

Similarly, considering energy conservation in the unburned zone and taking into account that mass flow from zone 1 into zone 2 doesn't change specific enthalpy in zone 1, one can write for zone of unburned mixture:

$$dh_u/d\tau = (V_u/M_u)\cdot(dp/d\tau) - (1/M_u)\cdot(q_{wu}). \tag{10.15}$$

The equation of state can be written for the zones 1 and 2:

$$p(V_u/(R_uT_u) + V_b/(R_bT_b)) - (M_u + M_b) = 0, \tag{10.16}$$

where R_u and R_b are specific gas constants in the zones of unburned and burned mixtures, respectively.

Newton's law of cooling is used for the calculation of the heat flow rate due to convection to the cylinder walls and piston bowl walls in zones 1 and 2:

$$q_{wz} = h_z F_{wz}(T_z - T_{wz}), \tag{10.17}$$

where $z = 1, 2$ are the number of zones; F_{wz} is the surface area of cylinder walls and piston bowl walls; and $T_z = T_1 \; or \; T_2$ and T_{wz} are temperatures of the cylinder walls or piston bowl walls.

The heat transfer coefficient is defined by the expression [311]:

$$h_z = d^{-0.2}\left(p^2T_z\right)^{0.333}(1 + 1.24u_{av\,s}), \tag{10.18}$$

where $z = 1, 2$; d is the bore diameter; $u_{av\,s} = Sn/30$ is the average velocity of the piston; S is the stroke; and n is the engine speed.

The heat flow rate due to radiation is defined from [314]:

$$q_{rz} = \sigma\varepsilon'_{wz}\varepsilon_z T_z^4, \tag{10.19}$$

where σ is the Stefan–Boltzmann constant; $z = 1, 2$; $\varepsilon_z = \varepsilon_{H_2O} + \varepsilon_{CO_2} - \varepsilon_{H_2O}\varepsilon_{CO_2}$ is emissivity of the working medium in zone z; $\varepsilon'_{wz} = 0.5(\varepsilon_{wz} + 1)$ is effective emissivity of the material of the cylinder wall or material of the piston; and ε_{wz} is emissivity of the material of the cylinder wall or that of the piston.

In order to determine mass flow rate $\dot{m}_x$, originating from the rate of flame front propagation, the three-staged original semiempirical conception of fresh air–fuel mixture burnout in the cylinder of the ICE was developed based on the analysis of experimental data and subsequent numerical approximation [313]. The first stage of combustion corresponds to the burnout of 5%–10% of the fresh air–fuel mixture, the second (main) stage corresponds to the burnout of 65%–85% of the air–fuel mixture,

Downloaded from https://www.cambridge.org/core. Nottingham Trent University, on 17 Aug 2019 at 02:14:16, subject to the Cambridge Core terms of use, available at https://www.cambridge.org/core/terms. https://doi.org/10.1017/9781108581714.010

and the third stage corresponds to the burnout of 100% of the air–fuel mixture. During the stages 1 and 3, the flame propagation is calculated using the Wiebe formula [217]:

$$X_{1,3} = 1 - \exp\left(-k(f/f_b)^{(m+1)}\right), \tag{10.20}$$

where $X_{1,3}$ is the relative mass fraction of burned fresh mixture in the stages 1 and 3; f_b is the duration of the phase of the fresh mixture burnout; $f_b = \varphi_b - \varphi_{ign}$; $f = \varphi - \varphi_{ign}$; φ is the crank angle (CA); φ_{ign} is the timing angle corresponding to the ignition (i.e., to the beginning of stage 1); φ_b is the CA corresponding to complete burnout of the fresh air–fuel mixture); and k, m are adjustable coefficients that depend on the specific engine parameters, those of the fresh air–fuel mixture, and parameters of combustion products.

For stage 2, the relative portion of burnout fresh air–fuel mixture can be calculated using the following relationship:

$$X = a + b\varphi + c\varphi^2. \tag{10.21}$$

Coefficients a, b, and c are calculated using the Wiebe formula at the following boundary conditions:

$X = X_1$ at $\varphi = \varphi_1$, $X = X_2$ at $\varphi = \varphi_2$, and $(\partial X/\partial\varphi)_{\varphi 1}$ calculated using Relationship (10.21) is equal to $(\partial X/\partial\varphi)_{\varphi 1}$ calculated using Wiebe formula (10.20), where φ_1 is the CA corresponding to the end of stage 1; and φ_2 is the CA corresponding to the end of stage 2.

By adding Equations (10.9), (10.10), and (10.14)–(10.16) to Equations (2.31), (2.157) and Equation (2.149), along with the previously listed supplemental relationships, one can obtain the system of equations for simulation of combustion and ionization in the cylinder of the ICE at the end of the compression stroke and during the expansion stroke.

10.3 Ion Current Simulation

The chemical nonequilibrium model (Section 1.4) and previously listed equations give the possibility of predicting the nonequilibrium chemical composition of combustion products, including ions and electrons, as a function of CA and other parameters of the working medium in three zones of the cylinder. Using the calculated concentration of ions, one can find the ion current from following formula:

$$I_e = \dot{J}_e \pi r_e^2, \tag{10.22}$$

where r_e is the radius of the spark plug electrode.

The density of ion current can be obtained from the following relation [315, 316]:

$$\dot{J}_e = \left(n_e e^2 U\right)/(m_e \nu_{eN} d), \tag{10.23}$$

where U is the voltage applied to spark plug electrodes; d is the gap between electrodes; ν_{eN} is the electron-neutral momentum transfer collision frequency; n_e is the density of electrons; and e and m_e are electron charge and electron mass, respectively.

Downloaded from https://www.cambridge.org/core. Nottingham Trent University, on 17 Aug 2019 at 02:14:16, subject to the Cambridge Core terms of use, available at https://www.cambridge.org/core/terms. https://doi.org/10.1017/9781108581714.010

The total electron-neutral momentum transfer collision frequency is defined by the expression [306]:

$$\nu_{eN} = \left(8\sigma_{en}T^2\nu_{ee}\right)/\left(\ln(\Lambda)r_e m_e\right), \tag{10.24}$$

where σ_{en} is the energy-averaged electron-neutral cross section; ν_{ee} is the average electron–electron momentum transfer collision frequency; r_e is the mole fraction of electrons; and $\ln(\Lambda)$ is the logarithm of the ratio of Debye length λ_D to the parameter of scattering b_0 [306].

The average electron–electron momentum transfer collision frequency is calculated as

$$\nu_{ee} = 5n_e T^{-3/2}\ln(\Lambda). \tag{10.25}$$

10.4 Numerical Simulation of Combustion and Ionization

10.4.1 Analysis of Adequacy and Reliability of the Model

The preceding model predicts the chemical composition of combustion products – including ionized substances, pressure, temperature, enthalpy, mass, thermodynamic parameters of the working medium, flame front propagation, convective and radiative heat transfer to the cylinder walls and piston bowl, ion current and voltage as the function of crank angle for any ICE, any kind of fuel, and any value of equivalence ratio, and allows one to perform the numerical study of ICE operation and optimization of the engine operating parameters.

A numerical study was performed for following fuels: the analog of gasoline presented by the conventional formula $C_{7.653}H_{14.884}$ (86% carbon and 14% hydrogen, in mass fractions) and natural gas presented by 96% methane (CH_4) and 4% propane (C_3H_8). The list of substances for the gasoline–air mixture includes 65 substances: Ar, O, H, N, e, C, HO_2, OH, H_2, O_2, H_2O, CO, CO_2, CH_4, C_2H_2, C_2H_4, C_2H_6, C_6H_6, $C_6H_5CH_3$, $C_6H_{11}CH_3$, C_8H_{18}, C_8H_{17}, CH_3, CH_2, CH, C_2H, C_2H_3, C_2H_5, H_2CO, HCO, HC_2O, $C_6H_5CH_2$, C_6H_5CHO, C_6H_5OH, C_6H_5, C_6H_5O, C_6H_5CO, C_5H_4OH, C_5H_4O, C_5H_5O, C_5H_5, $C_6H_{11}CH_2$, C_6H_{12}, C_6H_{11}, $C_6H_{11}CHO$, $C_6H_{11}CO$, $C_6H_{11}OH$, $C_6H_{10}O$, C_3H_6, N_2, N_2H_2, N_2H, NH_3, NH_2, NH, HNO, HCN, CN, NCO, NO, NO_2, N_2O, CHO^+, H_3O^+, and NO^+. The chemical mechanism contains 247 chemical reactions adopted from [306–310] including reactions (10.1)–(10.6) producing ionized substances. The initial chemical composition of gasoline is simulated by octane C_8H_{18}, methylcyclohexane $C_6H_{11}-CH_3$, and toluene $C_6H_5-CH_3$. The list of substances for the natural gas–air mixture consists of 45 substances: Ar, O, H, N, e, C, HO_2, OH, H_2, O_2, H_2O, CO, CO_2, CH_4, C_2H_2, C_2H_4, C_2H_6, CH_3, CH_2, CH, C_2H, C_2H_3, C_2H_5, C_3H_8, C_3H_7, C_3H_6, H_2CO, HCO, HC_2O, N_2, N_2H_2, N_2H, NH_3, NH_2, NH, HNO, HCN, CN, NO, NO_2, N_2O, CHO^+, H_3O^+, and NO^+. The chemical mechanism contains 177 chemical reactions [306–309], including Reactions (10.1), (10.2), (10.4), and (10.6), producing ionized substances.

Downloaded from https://www.cambridge.org/core. Nottingham Trent University, on 17 Aug 2019 at 02:14:16, subject to the Cambridge Core terms of use, available at https://www.cambridge.org/core/terms. https://doi.org/10.1017/9781108581714.010

Numerical experiments were performed for a gasoline engine (stroke = 81 mm, bore = 80 mm, engine speed = 1300–4000 rpm). The results are shown in Figures 10.4–10.9. Figure 10.4 shows the parametric analysis of the influence of temperature coefficient A_{T3} in Relationship (10.7) on the ion voltage variation made for engine 1 and

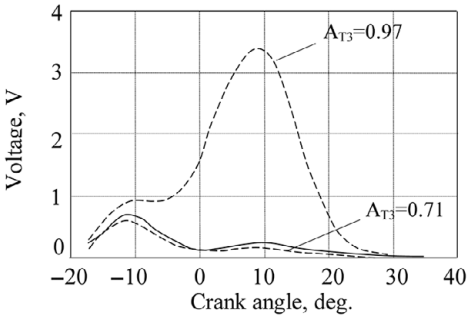

Figure 10.4 Comparison of experimental and calculated ion voltage for different values of temperature coefficient (Engine speed – 1300 rpm, equivalence ratio – 1.0). Solid line – experimental results, dotted lines – calculated data.

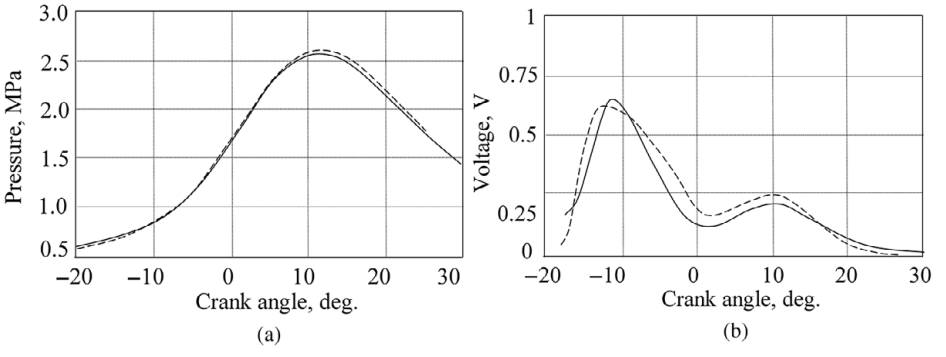

Figure 10.5 Comparison of experimental and calculated (a) pressure and (b) ion voltage (engine speed – 4000 rpm, equivalence ratio – 1.0). Solid lines – experimental results, dotted lines –– calculated data.

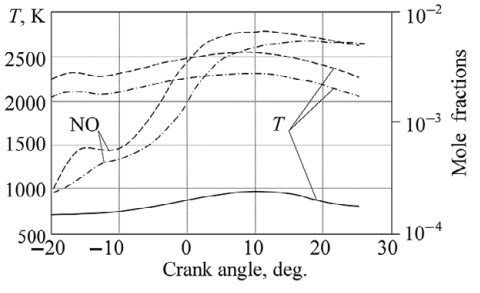

Figure 10.6 Variation in temperature and concentration of NO in zones 2 and 3. (Engine speed – 1300 rpm, equivalence ratio – 1.0). Solid line –– parameters in zone 1, dotted lines – parameters in zone 2, dash-dotted lines – parameters in zone 3.

Downloaded from https://www.cambridge.org/core. Nottingham Trent University, on 17 Aug 2019 at 02:14:16, subject to the Cambridge Core terms of use, available at https://www.cambridge.org/core/terms. https://doi.org/10.1017/9781108581714.010

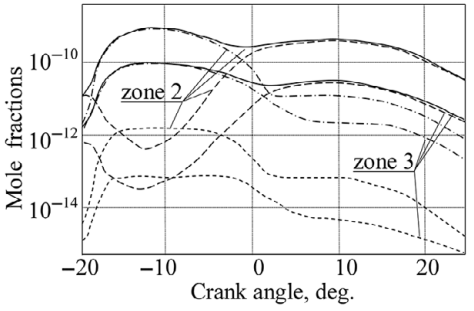

Figure 10.7 Variation of concentration of ions and electrons in zone 2 and zone 3. (Engine speed – 1300 rpm, equivalence ratio – 1.0). Solid lines – electrons, dotted lines – CHO^+, dash-dotted lines – H_3O^+, long-dotted lines – NO^+.

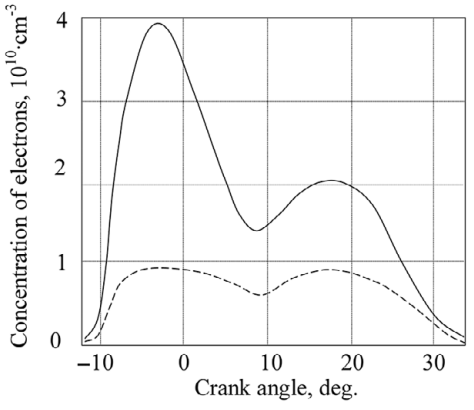

Figure 10.8 Variation in concentrations of electrons in zones 2 (solid line) and 3 (dotted line). Engine speed – 4000 rpm, equivalence ratio – 1.0.

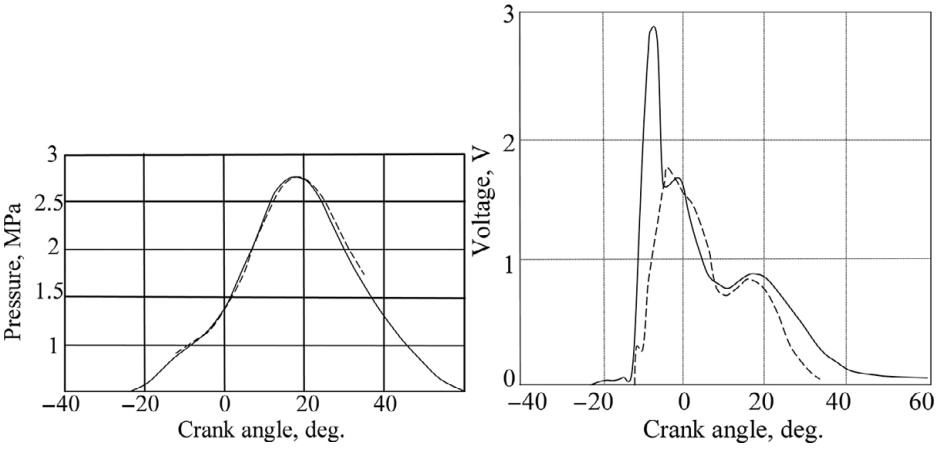

Figure 10.9 Comparison of experimental and numerical parameters. Solid lines – experimental results, dotted lines – calculated data (Engine speed – 4000 rpm, equivalence ratio – 1.0).

Downloaded from https://www.cambridge.org/core. Nottingham Trent University, on 17 Aug 2019 at 02:14:16, subject to the Cambridge Core terms of use, available at https://www.cambridge.org/core/terms. https://doi.org/10.1017/9781108581714.010

demonstrates a satisfactory correlation between experimental and numerical results for $A_{T3} = 0.7$.

It was also shown [313] that best correlation between experimental and numerical data on ion voltage history was obtained at $A_{T3} = 0.71 \ \ldots \ 0.87$. Figures 10.5a and 10.5b demonstrate the results of comparison of numerical calculation and experimental values of pressure and ion voltage. One can find appropriate correlation of calculated pressure and voltage history with experimental data.

Figures 10.6 and 10.7 clearly underline the consistency between temperature history and the history of concentration of H_3O^+, NO, NO^+, and electrons in zones 2 and 3. One can find from Figures 10.6 and 10.7 that first peaks of the temperature observed at the crank angle of $-15^\circ \ldots -12^\circ$ in zones 2 and 3 correspond to the peaks of concentration of electrons in zones 2 and 3. Figure 10.7 shows peaks of concentrations of H_3O^+ at the same value of crank angle. These results confirm the chemical ionization nature of the first peaks of the ion current due to the reaction of chemi-ionization (10.1) and reaction of charge transfer (10.2). The second peak of temperatures in both zones (crank angle = $9^\circ \ldots 11^\circ$) correlates with the second peaks of electrons concentration and concentration of NO^+. Since NO^+ is produced by the reaction of thermal ionization (10.6), peaks of NO concentration temperature (Figure 10.6) correspond to the peaks of concentration of NO^+ in both zones (Figures 10.7).

The preceding study shows the possibility to control in-cylinder temperature using the ion current and specifically its first and second peaks. Also, the second peak value of the ion current can be employed for the control of NO concentration in combustion products.

Figure 10.8 demonstrates the plots of concentrations of electrons calculated in zone 2 and zone 3 for the engine speed of 4000 rpm. The best correspondence of numerical data to experimental results (see the history of pressure and ion voltage in Figure 10.9) was obtained for $A_{T3} = 0.95$. It is reasonable since the rise of engine speed causes the increase of the working media flow rate through the gap between spark plug electrodes $\dot{m}_3$. In this case, the temperature in zone 3 approaches the temperature in zone 2 (the temperature in zone 3 being smaller than that in zone 2 because of heat transfer from the working medium to the electrodes). Equations (10.7) and (10.8) confirm this.

Figure 10.10 shows the results of the calculation of combustion in the cylinder of a six-cylinder natural gas engine of total volume of 8.5 L. A numerical study was performed for the engine speed of 1400 rpm and equivalence ratio of 1.153. Experimental data are averaged over 100 cycles. For analysis of the influence of two different mechanisms of ionization, two numerical experiments have been made separately, taking into account chemi-ionization only (Reactions 10.1, 10.2, and 10.4) and taking into account thermal ionization only (Reactions 10.5 and 10.6). The results given in Figure 10.10b clearly show the responsibility of chemi-ionization for the first peak of ion current and the major contribution of thermal ionization in the generation of the second peak of the ion current.

The preceding study of the combustion and ionization in gasoline and natural gas engines confirms again that the concentration of electrons in zone 3 can be used for the

Downloaded from https://www.cambridge.org/core. Nottingham Trent University, on 17 Aug 2019 at 02:14:16, subject to the Cambridge Core terms of use, available at https://www.cambridge.org/core/terms. https://doi.org/10.1017/9781108581714.010

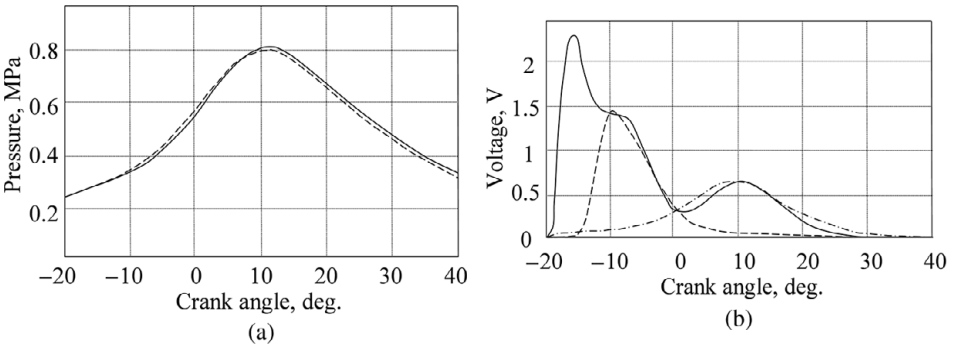

Figure 10.10 Natural gas engine. Engine speed – 1400 rpm, equivalence ratio – 1.153: (a) solid line – experimental pressure, dotted line – calculated pressure; (b) solid line – experimental ion current, dotted line – calculation of ion current using chemi- ionization reaction mechanism only, dash-dotted lines – calculation of ion current using thermal ionization reaction mechanism only. [312]. Republished with permission of SAE International, from V.I. Naoumov, A. V. Demin, and A. B. Sokolov, "Numerical Study and Analysis of Pollutant Production and Emission Control Using Ion Current Prediction in the SI Engine," SAE 2003 World Congress, SAE Technical Paper 2003–01-0724, pp.1–11, 2003; permission conveyed through Copyright Clearance Center, Inc

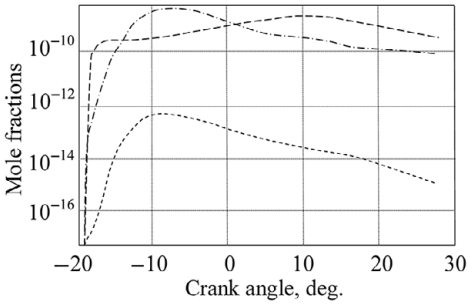

Figure 10.11 Natural gas engine. Engine speed – 1400 rpm, equivalence ratio – 1.153. Variation in concentration of ionized substances, dotted lines – CHO^+, dash-dotted lines – H_3O^+, long-dotted lines – NO^+.

ion current (voltage) calculation with subsequent use of ion current for engine parameters control. Moreover, only the implementation of chemical nonequilibrium model along with the chemi-ionization reaction mechanism provides the possibility to predict the first peak ion current.

The analysis of the contribution of different ions in the first peak of ion current demonstrates the prevailing contribution of CHO^+ in generation of first peak due to Reaction 10.1. A comparison of Figures 10.10 and 10.11 clearly demonstrates this finding. Also, Figures 10.10a, 10.10b, and 10.11 demonstrate precise correspondence of the position (relative to the crank angle) of the second peak of ion current to the peak of concentration of NO^+ and the peak of the pressure that is caused by thermo-ionization.

The same trend can easily be revealed from the results of the calculation of combustion in gasoline engine (Figures 10.12–10.15). One can also find H_3O^+ concentration

Downloaded from https://www.cambridge.org/core. Nottingham Trent University, on 17 Aug 2019 at 02:14:16, subject to the Cambridge Core terms of use, available at https://www.cambridge.org/core/terms. https://doi.org/10.1017/9781108581714.010

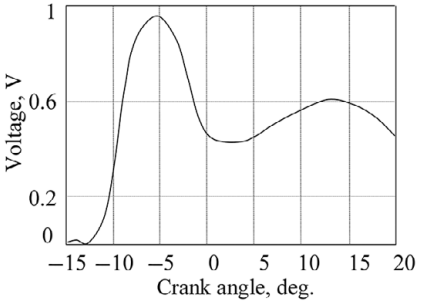

Figure 10.12 Ion voltage variation.

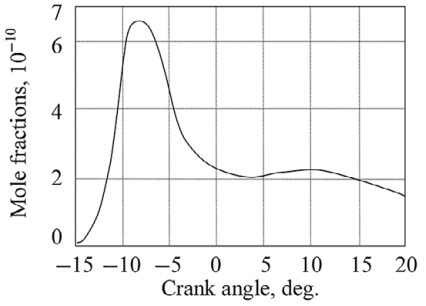

Figure 10.13 Variation of H_3O^+ concentration.

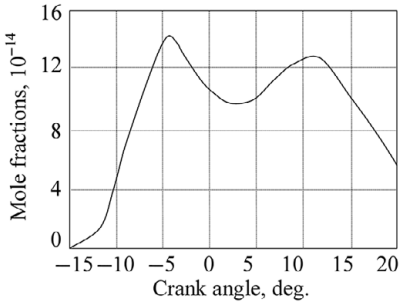

Figure 10.14 Variation in CHO^+ concentration.

peak that corresponds to that of ion current as well; moreover, the concentration of H_3O^+ is much higher compared to that of CHO^+. The matter is that the rate of Reaction (10.2) is much higher than that of Reaction (10.1). That is why the concentration of H_3O^+ is 1000–10,000 times higher than the concentration of CHO^+ and 50–100 times higher than concentration of NO^+.

Similar correspondence between the arrangement of the peaks can be also seen from Figures 10.16–10.21, which represent the results of numerical experiments performed for natural gas engine operating with different values of equivalence ratios.

Downloaded from https://www.cambridge.org/core. Nottingham Trent University, on 17 Aug 2019 at 02:14:16, subject to the Cambridge Core terms of use, available at https://www.cambridge.org/core/terms. https://doi.org/10.1017/9781108581714.010

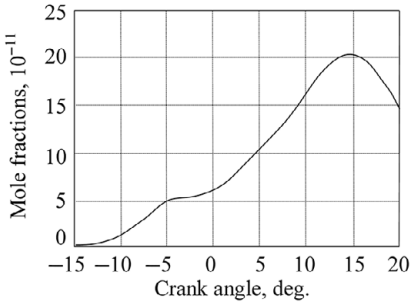

Figure 10.15 Variation in NO^+ concentration.

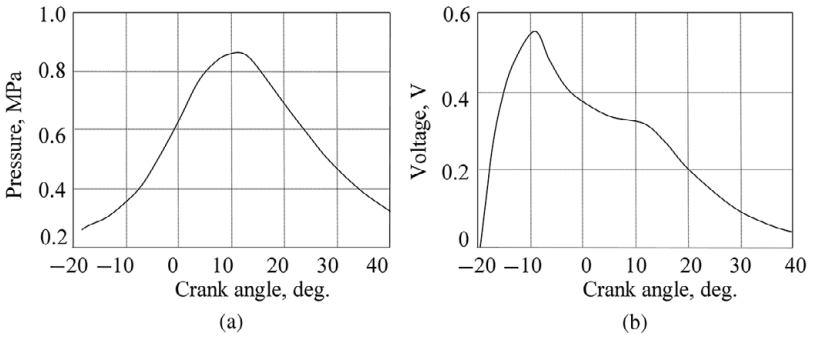

Figure 10.16 Natural gas engine. Engine speed –1450 rpm, equivalence ratio – 0.83. Variation in (a) pressure and (b) ion voltage.

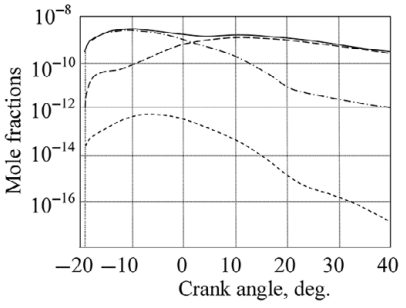

Figure 10.17 Natural gas engine. Engine speed – 1450 rpm, equivalence ratio – 0.83.Variation in concentration of ionized substances. Solid lines – electrons, dotted lines – CHO^+, dash-dotted lines – H_3O^+, long-dotted lines –- NO^+.

10.4.2 The Ion Current Use for the Analysis and Monitoring of Engine Performances

Data presented in Subsection 10.4.1 confirm the reliability of the model of combustion and ionization that provides an opportunity of model application to the prediction and optimization of parameters of the ICE. One of the examples of such an application is the study of the influence of exhaust gas recirculation (EGR) on engine emission characteristics.

Downloaded from https://www.cambridge.org/core. Nottingham Trent University, on 17 Aug 2019 at 02:14:16, subject to the Cambridge Core terms of use, available at https://www.cambridge.org/core/terms. https://doi.org/10.1017/9781108581714.010

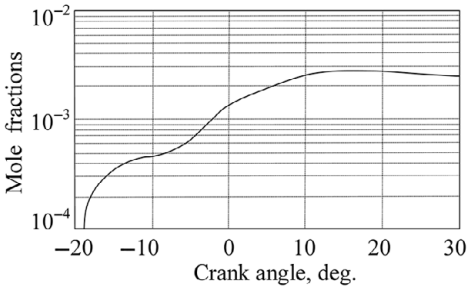

Figure 10.18 Natural gas engine. Engine speed –1450 rpm, equivalence ratio – 0.83. Variation of NO concentration.

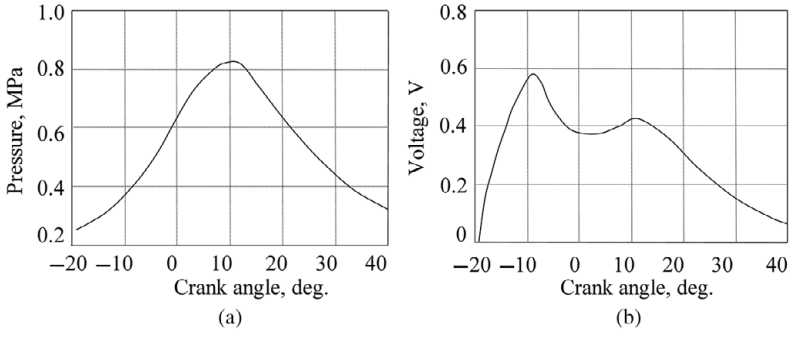

Figure 10.19 Natural gas engine. Engine speed –1420 rpm, equivalence ratio – 1.18. (a) variation of pressure and (b) ion voltage.

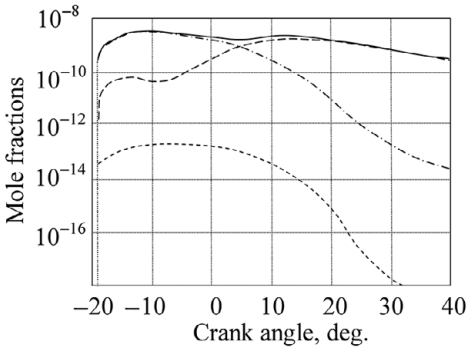

Figure 10.20 Natural gas engine. Engine speed – 1420 rpm, equivalence ratio – 1.18. Variation of concentration of ionized substances. Solid lines – electrons, dotted lines – CHO^+, dash-dotted lines - H_3O^+, long-dotted lines – NO^+.

Numerical experiments presented in Subsection 10.4.1 clearly show the rise of concentration of NO starting from the first peak of the ion current and approaching maximum values of NO concentrations at the second peak of the ion current (Figures 10.16b, 10.18, 10.19b, and 10.21), which indicates the possibility to predict

Downloaded from https://www.cambridge.org/core. Nottingham Trent University, on 17 Aug 2019 at 02:14:16, subject to the Cambridge Core terms of use, available at https://www.cambridge.org/core/terms. https://doi.org/10.1017/9781108581714.010

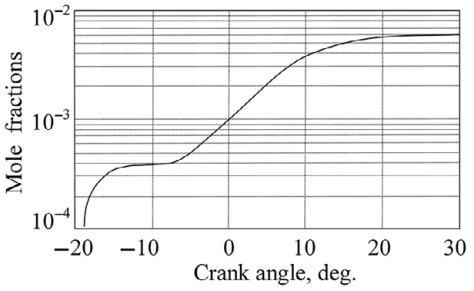

Figure 10.21 Natural gas engine. Engine speed –1420 rpm, equivalence ratio – 1.18. Variation in NO concentration.

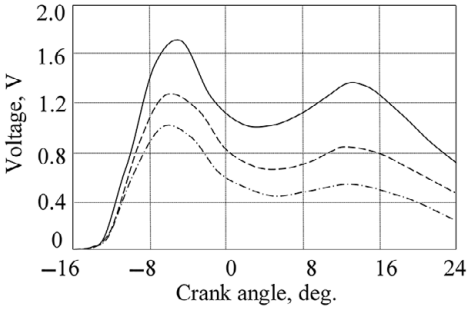

Figure 10.22 Influence of exhaust gas recirculation on the ion voltage in the gasoline engine. Solid line – EGR = 0%, dotted lines – EGR = 7.5%, dash-dotted lines – EGR = 15%.

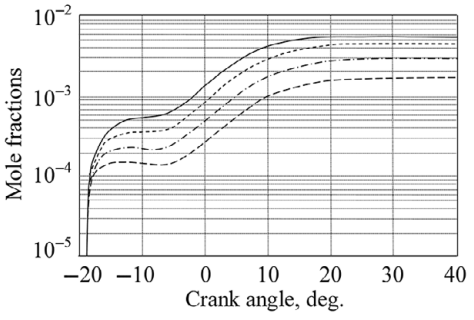

Figure 10.23 Influence of exhaust gas recirculation on the NO concentration in natural gas engine. Solid line – EGR = 0%, dotted lines – EGR = 7.5%, dash-dotted lines – EGR = 15%, long-dotted lines – EGR = 20%.

and control NO emission using measurements of ion current. Calculations performed for different percentages of EGR (Figure 10.22) demonstrate the influence of EGR on the ion voltage that manifests itself in the reduction of ion voltage with the increase in the percentage of exhaust gas recirculation in the cylinder of gasoline engine.

A similar trend was obtained from the numerical simulation of the combustion in natural gas engine. Figure 10.23 shows that an increase of EGR by 20% causes the

Downloaded from https://www.cambridge.org/core. Nottingham Trent University, on 17 Aug 2019 at 02:14:16, subject to the Cambridge Core terms of use, available at https://www.cambridge.org/core/terms. https://doi.org/10.1017/9781108581714.010

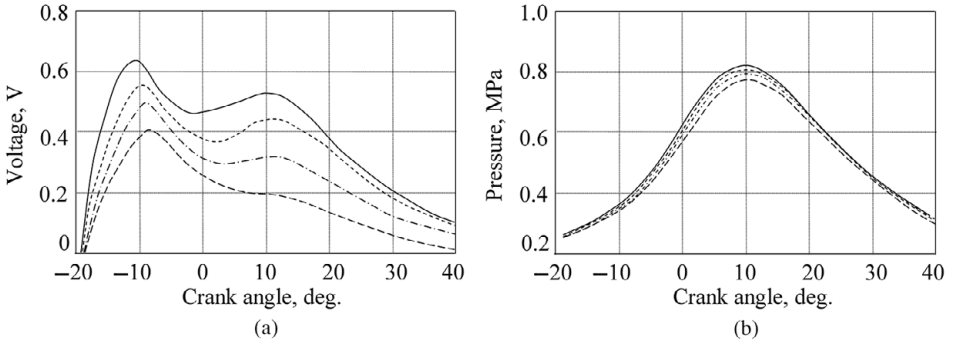

Figure 10.24 Influence of exhaust gas recirculation on (a) the ion voltage and (b) pressure in natural gas engine. Solid line – EGR = 0%, dotted lines – EGR = 7.5%, dash-dotted lines – EGR = 15%, long-dotted lines – EGR = 20%.

250%–300% reduction in NO concentration. As it was with the gasoline engine, the ion voltage is decreasing with the rise in EGR that follows from Figure 10.24a.

The reduction of NO emission can be explained mainly by the reduction in the in-cylinder working medium temperature resulting from its dilution by exhaust gases having relatively low temperatures compared to the temperature in the cylinder. The decrease in temperature leads to the reduction in the rates of reactions of thermal NO production according to the Zeldovich mechanism [316] ($O + N_2 \rightarrow NO + N$ and $N + O_2 \rightarrow NO + O$). This explanation is confirmed by the reduction in overall values of ion voltage with EGR increase as shown in Figures 23 and 10.24a. Also, the reaction of thermal ionization (10.6) clearly shows that a reduction of NO causes a corresponding decrease in the production of electrons that is shown in Figure 10.24a.

It is necessary to point out that, despite the decrease in temperature, the variation in pressure versus crank angle remains almost the same as follows from Figure 10.24b. This phenomenon can be explained by an increased mass of the working medium in the cylinder in the case of injection of a certain percentage of exhaust gases.

This study clearly shows the benefits of the chemical nonequilibrium model's application for adequate simulation of ionization at combustion and the opportunity to monitor engine parameters to ensure the proper engine performances and to assist in malfunction diagnostics.

Downloaded from https://www.cambridge.org/core. Nottingham Trent University, on 17 Aug 2019 at 02:14:16, subject to the Cambridge Core terms of use, available at https://www.cambridge.org/core/terms. https://doi.org/10.1017/9781108581714.010

References

[1] В. Е. Алемасов, А. Ф. Дрегалин, А. С. Черенков. *Основы Теории Физико-химических Процессов в Тепловых Двигателях и Энергоустановках.* Москва: Химия, 2000. [V. Ye. Alemasov, A. F. Dregalin, and A. S. Cherenkov. *Fundamentals of the Theory of Physicochemical Processes in Heat Engines and Power Generation Systems*. Moscow: Chemistry, 2000.]

[2] E. S. Oran and J. P. Boris. *Numerical Simulation of Reactive Flow*. New York: Elsevier, 1987.

[3] N. M. Emanuel and D. G. Knorre. *Chemical Kinetics*. New York: Wiley, 1973.

[4] R. J. Kee, M. E. Coltrin, and P. Glarborg. *Chemically Reacting Flow: Theory and Practice*. Hoboken, NJ: Wiley, 2003.

[5] R. J. Kee, F. M. Rupley, J. A. Miller, et al. *Chemkin Collection, Release 3.7.1: A Software Package for the Analysis of Gas-Phase Chemical and Plasma Kinetics. CHEMKIN Collection, Gas-Phase Kinetics Core Utility Manual; A Software Package for the Analysis of Gas-Phase Chemical and Plasma Kinetics. CHEMKIN Collection, Aurora Application User Manual*. San Diego, CA: Reaction Design Inc., 2003.

[6] F. A. Williams. *Combustion Theory*. 2nd edn. Boulder, CO: Westview Press, 1994.

[7] K. K. Kuo. *Principles of Combustion*. Singapore: J. Wiley & Sons, 1986.

[8] D. A. Frank-Kamenetskii. *Diffusion and Heat Exchange in Chemical Kinetics.* Princeton, NJ: Princeton University Press, 1955.

[9] В. А. Архипов, А. Г. Коротких, А. Т. Парпиев. "Анализ моделей горения частиц порошка алюминия в окислительных средах." *Известия Высших Учебных Заведений. Физика*, Том 55, № 5, стр 18–23, 2012. [V. A. Arkhipov, A. G. Korotkikh, and A. T. Parpiev. "Analysis of the models of combustion of aluminum powder particles in oxidizing environments." *News of the Higher Educational Institutions: Physics*, vol. 55, no. 5, pp. 18–23, 2012.]

[10] В. Ж. Коста, В. Г. Крюков, В. В. Гасилин. "Математическая модель абсорбции окислов серы в реагирующем газоугольном потоке." *Труды Академэнерго*, № 1, стр. 72–88, 2016. [V. Zh. Costa, V. G. Krioukov, and V. V. Gasilin. "A Mathematical Model for the Absorption of Sulfur Oxides in a Reacting Gas-Coal Flow." *Journal Proceedings of Academenergo*, no. 1, pp. 72–88, 2016.]

[11] В. В. Померанцев, К. М. Арефьев, Д. Б. Ахмедов и др. *Основы Практической Теории Горения.* Ленинград: Энергоатомиздат, 1986. [V. V. Pomerantsev, K. M. Arefyev, and D. B. Akhmedov, et al. *Fundamentals of Practical Combustion.* Leningrad: Energoatomizdat, 1986.]

[12] C. L. Mader, *Numerical Modeling of Detonations*. Berkeley, Los Angeles, and London: University of California Press, 1979.

Downloaded from https://www.cambridge.org/core. Nottingham Trent University, on 17 Aug 2019 at 03:56:55, subject to the Cambridge Core terms of use, available at https://www.cambridge.org/core/terms. https://doi.org/10.1017/9781108581714.011

[13] V. E. Alemasov, A. F. Dregalin, A. P. Tishin, et al. *Thermodynamic and Thermophysical Properties of Combustion Products. Volume I*. V. P, Glushko, ed. Moskow: VINITI, 1971. Translated from Russian by Israel Program for Scientific Translations, Jerusalim, 1974.

[14] The National Institute of Standards and Technology (NIST) [Electronic resource]. Retrieved from www.nist.gov.

[15] Л. В. Гурвич, И. В. Вейц, В. А. Медведев и др. *Термодинамические Свойства Индивидуальных Веществ*. Москва: Наука, 1982. [L. V. Gurvich, I. V. Weitz, and V. A. Medvedev, et al. *Thermodynamic Properties of Individual Substances*. Moscow: Science, 1982.]

[16] S. Gordon and B. J. McBride. "Computer Program for Calculation of Complex Chemical Equilibrium Compositions, Rocket Performance, Incident and Reflected Shocks and Chapman-Jouguet Detonations." NASA SP-273 Interim Revision, March 1976. Retrieved from https://ntrs.nasa.gov/archive/nasa/casi.ntrs.nasa.gov/19780009781.pdf.

[17] A. Burcat. "Third Millennium Ideal Gas and Condensed Phase Thermochemical Database for Combustion with Updates from Active Thermochemical Tables." ARGONNE National Laboratory, TECHNION – Israel Institute of Technology ANL-05/20, TAE 960, 2005.

[18] Г. В. Белов, В. С. Иориш, В. С. Юнгман. "Моделирование равновесных состояний термодинамических систем с использованием IVTANTERMO для Windows." *Теплофизика Высоких Температур*, т. 28, № 2, стр. 191–196, 2000. [G. V. Belov, V. S. Yorish, and V. S. Jungman. "Modeling Equilibrium States of Thermodynamic Systems Using IVTANTERMO for Windows." *High-Temperature Thermophysics*, vol. 28, no. 2, pp. 191–196, 2000.]

[19] W. C. Reynolds. "The Element Potential Method for Chemical Equilibrium Analysis: Implementation in the Interactive Program STANJAN, ver. 3." Stanford University, 1986. Retrieved from https://scinapse.io/papers/1097734671.

[20] J. Warnatz, U. Maas and R. W. Dibble. *Combustion: Physical and Chemical Fundamentals, Modeling and Simulation, Experiments, Pollutant Formation*. 4th edn. Berlin: Springer, 2006.

[21] В. Е. Алемасов, А. Ф. Дрегалин, and А. П. Тишин и др. *Термодинамические и Теплофизические Свойства Продуктов Сгорания*. Справочник Том 3. Москва: ВИНИТИ, 1973. [V. Ye. Alemasov, A. F. Dregalin, and A. P. Tishin, et al. *Thermodynamic and Thermophysical Properties of Combustion Products*. vol. 3. Moscow: VINITI, 1973.]

[22] W. C. Gardiner, Jr., ed. *Combustion Chemistry*. New York: Springer-Verlag, 1984.

[23] В. Н. Кондратьев, Е. Е. Никитин. *Кинетика и Механизм Газофазных Реакций*. Москва: Наука, 1974. [V. N. Kondratiev and E. E. Nikitin. *Kinetics and Mechanisms of Gas-Phase Reactions*. Moscow: Science, 1974.]

[24] Е. Т. Денисов. *Кинетика Гомогенных Химических Реакций*. Москва: Высшая школа, 1988. [E. T. Denisov. *Kinetics of Homogeneous Chemical Reactions*. Moscow: High School, 1988.]

[25] В. Н. Кондратьев. *Константы Скоростей Газофазных Реакций*. Справочник. Москва: Наука, 1974. [V. N. Kondratiev. *Rate Constants for Gas-Phase Reactions*. Moscow: Science, 1974.]

[26] "The Master Chemical Mechanism. Version 3.3.1, The MCM Project." University of Leeds, Retrieved from http://mcm.leeds.ac.uk/MCM/project.htt.

[27] N. M. Marinov, W. J. Pitz, C. K. Westbrook, et al. "Aromatic and Polycyclic Aromatic Hydrocarbon Formation in a Laminar Premixed N-Butane Flame." *Combustion and Flame*, vol. 114, pp. 192–213, 1998.

Downloaded from https://www.cambridge.org/core. Nottingham Trent University, on 17 Aug 2019 at 03:56:55, subject to the Cambridge Core terms of use, available at https://www.cambridge.org/core/terms. https://doi.org/10.1017/9781108581714.011

[28] G. P. Smith, D. M. Golden, M. Frenklach, et al. "GRI-Mech Version 3.0," 1999. Retrieved from www.me.berkeley.edu/gri_mech.
[29] A. A. Konnov. "Implementation of the NCN Pathway of Prompt-NO Formation in the Detailed Reaction Mechanism." *Combustion and Flame*, vol. 156, pp. 2093–2105, 2009.
[30] "The Kintecus Simulation Software." Retrieved from www.kintecus.com.
[31] "Computational Fluid Dynamics ANSYS CFX and Fluent CFD Software." Retrieved from https://caeai.com/ansys-software-support.
[32] D. B. Spalding. *Combustion and Mass Transfer*. New York: Pergamon Press, Inc., 1979.
[33] A. M. Eaton, L. D. Smooth, S. C. Hill, et al. "Components, Formulations, Solutions, Evaluation and Application of Comprehensive Combustion Models." *Progress in Energy and Combustion Science*, vol. 25, pp. 387–436, 1999.
[34] T. L. Jiang and H. H. Chiu. "Bipropellant Combustion in a Liquid Rocket Combustion Chamber." *Journal of Propulsion and Power*, vol. 8, no 5, pp. 995–1003, 1992.
[35] G. G. Chernyi, S. A. Losev, S. O. Macheret, et al. *Physical and Chemical Processes in Gas Dynamics: Physical and Chemical Kinetics and Thermodynamics of Gases and Plasmas*, Volume II. Progress in Astronautics and Aeronautics. Paul Zarchan, Editor-in-Chief, AIAA, Volume 197, 2004.
[36] T. P. Coffee, A. J. Kotlar, and M. S. Miller. "The Overall Reaction Concept in Premixed, Laminar, Steady-State Flames. I. Stoichiometries." *Combustion and Flame*, vol. 54, pp. 155–169, 1983.
[37] A. O. Nieckele, M. F. Naccache, M. S. P. Gomes, et al. "Combustion Performance of an Aluminum Melting Furnace Operating with Natural Gas and Liquid Fuel." *Applied Thermal Engineering,* vol. 31, pp. 841–851, 2011.
[38] H. Kobayashi, J. B. Howard, and A. F. Sarofim. "Coal Devolatilization at High Temperatures." Proceedings of 17th International Symposium on Combustion, The Combustion Institute, pp. 411–425, 1976.
[39] С. Т. Суржиков. *Физическая Механика Газовых Разрядов*. Москва: МГТУ им. Н.Э Баумана, 2006. [S. T. Surzhikov. *Physical Mechanics of Gas Discharges*. Moscow: Bauman Moscow Technical University, 2006.]
[40] E. Nagnibeda and E. Kustova. *Nonequilibrium Reacting Gas Flows: Kinetic Theory of Transport and Relaxation Processes*. Berlin and Heidelberg: Springer-Verlag, 2009.
[41] Е. В. Кустова, Г. П. Облапенко, И. З. Шарафутдинов. "Модели колебательной релаксации в неравновесных многотемпературных течениях." *Физико-химическая Кинетика в Газовой Динамике*. Retrieved from http://chemphys.edu.ru/issues/. [E. V. Kustova, G. P. Oblapenko, and I. Z. Sharafutdinov. "Models of Vibrational Relaxation in Non-Equilibrium Multi-Temperature Flows." *Physical-Chemical Kinetics in Gas Dynamics*. Retrieved from http://chemphys.edu.ru/issues/.]
[42] М. Ю. Погосбекян, А. Л. Сергиевская. "Моделирование динамики молекулярных реакций и сравнительный анализ с теоретическими моделями применительно к термически неравновесным условиям." *Физико-химическая Кинетика в Газовой Динамике*, Т. 15, вып. 3, 2014. Retrieved from http://chemphys.edu.ru/issues/. [M. Yu. Poghosbekyan and A. L. Sergievskaya. "Modeling the Dynamics of Molecular Reactions and Comparative Analysis with Theoretical Models as Applied to Thermal Nonequilibrium Conditions." *Physical-Chemical Kinetics in Gas Dynamics*, vol. 15, no. 3, 2014. Retrieved http://chemphys.edu.ru/issues/.]
[43] V. Denis, and L. Vervish. "Turbulent Combustion Modeling." *Progress in Energy and Combustion Science*, vol. 28, pp. 193–266, 2001.

Downloaded from https://www.cambridge.org/core. Nottingham Trent University, on 17 Aug 2019 at 03:56:55, subject to the Cambridge Core terms of use, available at https://www.cambridge.org/core/terms. https://doi.org/10.1017/9781108581714.011

[44] J. G. Blom and J. G. Verwer. "A Comparison of Integration Methods for Atmospheric Transport-Chemistry Problems." *Journal of Computational and Applied Mathematics*, no. 126, pp. 381–396, 2000.

[45] V. R. Katta and W. M. Roquemore. "Numerical Studies on the Structure of Two-Dimensional H2/Air Premixed Jet Flame." *Combustion and Flame*, vol. 102, pp. 21–40, 1995.

[46] R. P. Lindstedt and L. Q. Maurice. "Detailed Chemical–Kinetic Model for Aviation Fuels." *Journal of Propulsion and Power*, vol. 16, no. 2, pp. 187–195, 2000.

[47] W. P. Jones and R. P. Lindstedt. "Global Reaction Schemes for Hydrocarbon Combustion." *Combustion and Flame*, vol. 73, no. 1, 3, pp. 233–242, 1988.

[48] R. A. Yetter, F. L. Dryer, M. T. Allen, et al. "Development of Gas Phase Reaction Mechanisms for Nitramine Combustion." *Journal of Propulsion and Power*, vol. 11, no. 4, pp. 683–697, 1995.

[49] С. Т. Суржиков. "Моделирование радиационно-конвективного нагрева модельных камер ПВРД на водородном и углеводородном топливе." *Физико-химическая Кинетика в Газовой Динамике*, Т. 15, вып. 3, 2014. Retrieved from http://chemphys.edu.ru/issues/. [S. T. Surzhikov. "Simulation of Radiation-Convective Heating of Model Ramjet Cameras on Hydrogen and Hydrocarbon Fuels." *Physical-Chemical Kinetics in Gas Dynamics*, vol. 15, no. 3, 2014. Retrieved from http://chemphys.edu.ru/issues/.]

[50] R. O. Foelsche, J. M. Keen, W. C. Solomon et al. "Nonequilibrium Combustion Model for Fuel-Rich Gas Generators." *Journal of Propulsion and Power*, vol. 10, no. 4, pp. 461–472, 1994.

[51] B. A. Williams and J. W. Fleming. "Comparison of Species Profiles between O_2 and NO_2 Oxidizers in Premixed Methane Flames." *Combustion and Flame*, vol. 100, pp. 571–590, 1995.

[52] G. N. Abramovich. *The Theory of Turbulent Jets.* Cambridge, MA: MIT Press, 1963.

[53] В. Е. Алемасов, Г. А. Глебов, А. П. Козлов и др. *Турбулентные Струйные Течения в Каналах.* Казань: Казанский филиал АН СССР, 1988. [V. Ye. Alemasov, G. A. Glebov, A. P. Kozlov, et al. *Turbulent Jet Flows in Channels*. Kazan: Kazan Scientific Centre of the Russian Academy of Sciences, 1988.]

[54] A. P. Spilimbergo, V. G. Krioukov, and A. V. Fafurin. "Mathematical Modelling of Ethane Pyrolysis in Tube Furnace." *Trends in Applied and Computational Mathematics*, vol. 13, no. 3. pp. 291– 300, 2012.

[55] В. Г. Крюков, В. И. Наумов, А. В. Демин и др. *Горение и Течение в Агрегатах Энергоустановок.* Москва: Янус-К, 1997. [V. G. Krioukov, V. I. Naoumov, A. V. Demin, et al. *Combustion and Flow in Power Generation Systems. Moscow*: Janus-K, 1997.]

[56] V. I. Naumov, V. G. Krioukov, A. L. Abdullin, et al. "Chemical Non-Equilibrium Model for Simulation of Combustion and Flow in Propulsion and Power Generation Systems." ASME International Mechanical Engineering Congress and Exposition, vol. 1, pp. 1–11, Orlando, FL, 2005.

[57] В. Е. Алемасов, А. Ф. Дрегалин, В. Г. Крюков, и др. *Математическое Моделирование Высокотемпературных Процессов в Энергосиловых Установках.* Москва: Наука, 1989. [V. Ye. Alemasov, A. F. Dregalin, V. G. Krioukov, et al. *Mathematical Modeling of High-Temperature Processes in Power Generation Systems.* Moscow: Science, 1989.]

[58] Н. А. Ватолин, Г. К. Моисеев, Б. Г. Трусов. *Термодинамическое Моделирование в Высокотемпературных Неорганических Системах.* Москва: Металлургия, 1994.

Downloaded from https://www.cambridge.org/core. Nottingham Trent University, on 17 Aug 2019 at 03:56:55, subject to the Cambridge Core terms of use, available at https://www.cambridge.org/core/terms. https://doi.org/10.1017/9781108581714.011

[N. A. Vatolin, G. K. Moiseev, and B. G. Trusov. *Thermodynamic Modeling in High-Temperature Inorganic Systems*. Moscow: Metallurgy, 1994.]

[59] В. Г. Крюков, В. И. Наумов, А. Л. Абдуллин, и др. "Математическое моделирование реагирующих течений на базе реакторного подхода." *Физико-химическая Кинетика в Газовой Динамике*, Т. 2. 2004. http://chemphys.edu.ru/issues/2004–2/articles/65/. [V. G. Krioukov, V. I. Naumov, A. L. Abdullin, et al. "Mathematical Modeling of Reacting Flows on the Basis of the Reactor Approach," *Physical-Chemical Kinetics in Gas Dynamics*, vol. 2. 2004.]

[60] V. I. Naumov, V. G. Krioukov, A. L. Abdullin, et al. "Modeling of Combustion and Flow in the Combustors of Rocket Gas Generations." 41st Aerospace Sciences Meeting and Exhibit, AIAA 2003–126, vol. 1, pp. 1–11, Reno, NV, 2003.

[61] Е. В. Аметистов, В. А. Григорьев, Б. Т. Емцев и др. *Тепло- и Массообмен. Теплотехнический Эксперимент*. Москва: Энергоатомиздат, 1982. [Ye V. Ametistov, V. A. Grigoriev, B. T. Yemtsev, et al. *Heat and Mass Transfer: Thermal Engineering Experiment*. Moscow: Energoatomizdat, 1982.]

[62] L. E. Sissom and D. R. Pitts, *Fenômenos de Transporte*. [*Transport Phenomena*.] Rio de Janeiro: Guanabara Dois, 1998.

[63] R. C. Monson, G. J. Germane, A. U. Blackham, et al. "Char Oxidation at Elevated Pressures." *Combustion and Flame*, vol. 100, pp. 669–683, 1995.

[64] H. Nack, R. D. Litt, B. C. Kim, et al. "Coffering Coal with Waste Material." Coal Combustion Congresses, Peking, China. pp. 452–459, 1988.

[65] Z. Ouyang, J. Zhu, Q. Lu, et al. "The Effect of Limestone on SO2 and NOX Emissions of Pulverized Coal Combustion Preheated by Circulating Fluidized Bed." *Fuel*, vol. 120, no. 15, pp. 116–121, 2014.

[66] H. Shirai, M. Ikeda, and H. Aramaki. "Characteristics of Hydrogen Sulfide Formation in Pulverized Coal Combustion." *Fuel*, vol. 113, pp. 114–119, 2013.

[67] H. Liu and B. M. Gibbs. "The Influence of Limestone Addition at Different Positions on Gaseous Emissions from a Coal-Fired Circulating Fluidized Bed Combustor." *Fuel*, vol. 77, no. 14, pp. 1569–1577, 1998.

[68] R. B. Nair, and S. Yavuzkurt. "Modeling Sulfur Dioxide Capture in a Pulverized Coal Combustor." *Journal of Engineering for Gas Turbines and Power*, vol. 119, pp. 291–297, 1997.

[69] M. R. Stouffer, and H. Yoon. "An Investigation of CaO Sulfation Mechanisms in Boiler Sorbent Injection." *AIChE Journal,* vol. 35, pp. 1253–1262, 1989.

[70] W. H. Press, B. P Flinnery, W. T. Vetterling, et al. *Numerical Recipes in C: The Art of Scientific Equation Models by Polynomial Approximation.* Upper Saddle River, NJ: Prentice-Hall, 1988.

[71] J. D. Lambert. *Numerical Methods for Ordinary Differential Systems*. New York: John Wiley & Sons, 1993.

[72] J. C. Butcher. "Numerical Methods for Ordinary Differential Equations in the 20th Century." *Journal of Computational and Applied Mathematics*, vol. 125, pp. 1–29, 2000.

[73] Н. Н. Калиткин. *Численные методы*. Москва: Наука, 1978. [N. N. Kalitkin. *Numerical Methods*. Moscow: Science, 1978.]

[74] J. C. Butcher."Coefficients for the Study of Runge-Kutta Integration Processes." *Journal of Australian Mathematical Society*, vol. 3, pp. 185–201, 1963.

[75] J. C. Butcher. "A Modified Multistep Method for the Numerical Integration of Ordinary Differential Equations." *Journal of Association Computer Mathematics*, vol. 12, pp. 124–135, 1965.

Downloaded from https://www.cambridge.org/core. Nottingham Trent University, on 17 Aug 2019 at 03:56:55, subject to the Cambridge Core terms of use, available at https://www.cambridge.org/core/terms. https://doi.org/10.1017/9781108581714.011

[76] А.Ф. Заусаев. *Разностные Методы Решения Обыкновенных Дифференциальных Уравнений*. Самара: Самарский Государственный Технический Университет, 2010. [A. F. Zausayev. *Difference Methods for Solving Ordinary Differential Equations*. Samara: Samara State Technical University, 2010.]

[77] E. Hairer, and G. Vanner. *Solving Ordinary Differential Equations II*. New York: Springer, 1996.

[78] В. И. Лебедев., А. А. Медовиков. "Явный метод второго порядка точности для решения жестких систем обыкновенных дифференциальных уравнений." *Известия ВУЗов. Математика*, № 9, стр. 55–63, 1998. [V. I. Lebedev and A. A. Medovikov. "Explicit Second Order Accuracy Method for Solving Stiff Systems of Ordinary Differential Equations." *University News: Mathematics*, no. 9, pp. 55–63, 1998.]

[79] Е. А. Новиков. *Явные Методы для Жестких Систем*, Новосибирск: Наука, 1997. [E. A. Novikov. *Explicit Methods for Stiff Systems*. Novosibirsk: Science, 1997.]

[80] Л. М Скворцов. «Явные адаптивные методы численного решения жестких систем», *Математическое Моделирование*, Т.12, № 12, стр. 97– 107, 2000. [L. M. Skvortsov. "Explicit Adaptive Methods for the Numerical Solution of Stiff Systems," Mathematical Modeling, vol. 12, no. 12, pp. 97–107, 2000.]

[81] Л. М. Скворцов. "Простые явные методы численного решения жестких обыкновенных дифференциальных уравнений," *Вычислительные Методы и Программирование*, Т. 9, № 12, стр. 154–162, 2008. [L. M. Skvortsov. "Simple Explicit Methods for the Numerical Solution of Stiff Ordinary Differential Equations," *Computational Methods and Programming*, vol. 9, no. 12, pp. 154–162, 2008.]

[82] C. W. Gear. "The Automatic Integration of Ordinary Differential Equations," *Communication of ACM*, vol. 14, no. 3, pp. 176–180, 1971.

[83] C. W. Gear. "DIFSUB for Solution of Ordinary Differential Equations," *Communication of ACM*, vol. 14, no. 3, pp. 185–190, 1971.

[84] В. И. Камзолов, У. Г. Пирумов. "Расчет неравновесных течений в соплах," *Известия АН СССР. Механика жидкости и газа*, № 6, pp. 25– 33, 1966. [V. I. Kamzolov, and U. G. Pirumov, "Calculation of Non-Equilibrium Flows in Nozzles," *Izvestiya AN SSSR. Fluid and Gas Mechanics*, no. 6, pp. 25–33, 1966.]

[85] U. G. Pirumov, and G. S. Roskyakov. *Gas Flow in Nozzles*. Berlin and Heidelberg: Springer-Verlag, 1986.

[86] C. Burin, R. L., Iskhakova, V. G. Krioukov, et al. "Application of the Spline-Integration Method of for Solving of Chemical Kinetics Equations," *Tendencies in Applied and Computational Mathematics*, vol. 4, no. 3, pp. 313–322, 2003.

[87] A. Durigon, A. L. Abdullin, and V. G. Krioukov. "Method of Spline-Integration: Application in Chemical Kinetic Equations," *XVII Brazilian Congress of Mechanical Engineering*, vol. 1, pp. 1–10, 2003.

[88] S. Sallam. "Stable Quadratic Spline Integration Method for Solving Stiff Ordinary Differential Equations," *Applied Mathematics*, vol. 116, no. 3, pp. 245–255, 2000.

[89] N. M. Marinov, W. J. Pitz, C. K. Westbrook, et al. "Modeling of Aromatic and Polycyclic Aromatic Hydrocarbon Formation in Premixed Methane and Ethane Flame," *Combustion Science & Technology*, vol. 116–117, pp. 211–287, 1996.

[90] S. Kalamatianos, Y. K. Park, and D. G. Vlachos. "Two-Parameter Continuation Algorithms for Sensitivity Analysis, Parametric Dependence, Reduced Mechanisms, and Stability Criteria of Ignition and Extinction," *Combustion and Flame*, vol. 112, pp. 45–61, 1998.

Downloaded from https://www.cambridge.org/core. Nottingham Trent University, on 17 Aug 2019 at 03:56:55, subject to the Cambridge Core terms of use, available at https://www.cambridge.org/core/terms. https://doi.org/10.1017/9781108581714.011

[91] З. С. Андрианова, Е. В. Деюн, Н. Г. Самойленко, и др. "Автоколебания в проточном реакторе идеального смешения с двухстадийной последовательной реакцией," *Химическая Физика*, Т. 28, № 7, pp. 87–93, 2009. [Z. S. Andrianova, E. V. Deyun, N. G. Samoylenko, et al. "Self-Oscillations in a Perfectly Stirred Moving Reactor with a Two-Stage Sequential Reaction," *Chemical Physics*, vol. 28, no. 7, pp. 87–93, 2009.]

[92] J. Ströhle, and T. Myhrvold. "Reduction of a Detailed Reaction Mechanism for Hydrogen Combustion under Gas Turbine Conditions," *Combustion and Flame*, vol. 144, pp. 545–557, 2006.

[93] P. Glarborg, J. A. Miller, and R. J. Kee. "Kinetic Modeling and Sensitivity Analysis of Nitrogen Oxide Formation in Well-Stirred Reactors," *Combustion and Flame*, vol. 65, pp. 177–202, 1986.

[94] J. Li, Z. Zhao, A. Kazakov, and F. Dryer. "An Updated Comprehensive Kinetic Model of Hydrogen Combustion," *International Journal of Chemical Kinetics*, vol. 36, pp. 566–575, 2004.

[95] P. A. Glaude, F. Battin-Leclerc, and R. Fournet. "Construction and Simplification of a Model for the Oxidation of Alkanes," *Combustion and Flame*, vol. 122, pp. 451–462, 2000.

[96] R. C. Brown, C. E. Kolb, R. A. Yetter, et al. "Kinetic Modeling and Sensitivity Analysis for B/H/O/C/F Combination Systems," *Combustion and Flame*, vol. 101, pp. 221–238, 1995.

[97] T. Nagy and T. Turanyi. "Reduction of Very Large Reaction Mechanisms Using Methods Based on Simulation Error Minimization," *Combustion and Flame*, vol. 156, pp. 417–428, 2009.

[98] W. A. Sun, Z. Chen, X. Gou, et al. "A Path Flux Analysis Method for the Reduction of Detailed Chemical Kinetic Mechanisms," *Combustion and Flame*, vol. 157, pp. 1298–1307, 2010.

[99] А. В. Лебедев, М. В. Окунь, А. Е. Баранов, и др. "Упрощение кинетических механизмов физико-химических процессов на основе комбинированных математических методов," *Химическая Физика и Мезоскопия*, Т. 13, № 1, pp. 43–52, 2011. [A. V. Lebedev, M. V. Okun, A. E. Baranov, et al. "Simplification of the Kinetic Mechanisms of Physicochemical Processes Based on Combined Mathematical Methods," *Chemical Physics and Mesoscopy*, vol. 13, no. 1, pp. 43–52, 2011.]

[100] В. Ж.. Коста, В. Г. Крюков. "Математическое моделирование горения распыленного угля в потоке с учетом абсорбции окислов серы," *Физико-Химическая Кинетика в Газовой Динамике*, Институт механики, МГУ, Т. 13, вып. 2, 2012. Retrieved from http://chemphys.edu.ru/issues/. [V. J. Costa and V. G. Krioukov. "Mathematical Modeling of the Combustion of Pulverized Coal in a Stream with Regard to the Absorption of Sulfur Oxides," *Physical with Chemical Kinetics in Gas Dynamics, Institute of Mechanics, Moscow State University*, vol. 13, no. 2, 2012. Retrieved from http://chemphys.edu.ru/issues/.]

[101] А. Ф. Дрегалин, И. А. Зенуков, В. Г. Крюков, и др. *Математическое Моделирование Высокотемпературных Процессов в Энергоустановках*, Казань: Казанский государственный университет, 1985. [A. F. Dregalin, I. A. Zenukov, V. G. Krioukov, et al. Mathematical Modeling of High-Temperature Processes in Power Generation Systems, Kazan: Kazan State University, 1985.]

[102] R. J. Kee, J. A Miller and T. H. Jefferson. *CHEMKIN: A General-Purpose Transportable: Fortran Chemical Kinetics Code Package*, Sandia National Laboratories Report SAND80–8003, 1980.

Downloaded from https://www.cambridge.org/core. Nottingham Trent University, on 17 Aug 2019 at 03:56:55, subject to the Cambridge Core terms of use, available at https://www.cambridge.org/core/terms. https://doi.org/10.1017/9781108581714.011

[103] M. Forsth. "Sensitivity Analysis of the Reaction Mechanism for Gas-Phase Chemistry of H_2 + O_2 Mixtures Induced by a Hot Pt surface," *Combustion and Flame*, vol. 130, pp. 241–260, 2002.

[104] G. D. Byrne and A. M. Dean. "The Numerical Solution of Some Kinetics Models with VODE and CHEMKIN II," *Computers & Chemistry*, vol. 17, no. 3, pp. 297–302, 1993.

[105] C. W. Gear. *Numerical Initial Value Problems in Ordinary Differential Equations*, Englewood Cliffs, NJ: Prentice-Hall, 1971.

[106] C. K. Westbrook and F. L. Dryer. "Chemical Kinetic Modeling of Hydrocarbon Combustion," *Progress. Energy Combustion Sciences*, vol. 10, pp. 1–57, 1984.

[107] "HTU Chemical Reaction and Equilibrium Software HTU."

[108] А. Л. Абдуллин, В. Г. Крюков, К. А. Березовская. "Алгоритм конверсии и передачи информации между базами данных веществ," *Вестник Казанского Технологического Университета*, Т. 16, № 10, pp. 299–303, 2013. [A. L. Abdullin, V. G. Krioukov and K. A. Berezovskaya. "Algorithm for the Conversion and Transfer of Information between Databases of Substances," *Bulletin of Kazan Technical University*, vol. 16, no. 10, pp. 299–303, 2013.]

[109] М. В. Никандрова, В. Г. Крюков, Р. Л. Исхакова. "Аналитическое определение коэффициентов чувствительности реакций для условий реактора идеального смешения," *Физико-Химическая Кинетика в Газовой Динамике*, Т. 4, 2006. [M. V. Nikandrova, V. G. Krioukov, and R. L. Iskhakova. "Analytical Determination of Reaction Sensitivity Coefficients for Conditions of a Perfectly Stirred Reactor," *Physico-Chemical Kinetics in Gas Dynamics*, vol. 4, 2006.]

[110] M. U. Alzueta, R. Bilbao and P. Glarborg. "Inhibition and Sensitization of Fuel Oxidation by SO_2," *Combustion and Flame*, vol. 127, pp. 2234–2251, 2001.

[111] R. P. Dickinson and R. J. Gelinas. "Sensitivity Analysis of Ordinary Differential Equation Systems," *Journal Computer Physics,* vol. 21, pp. 123–143, 1976.

[112] S. H. Lam and D. A. Goussis. "The CSP Method for Simplifying Kinetics," *International Journal of Chemical Kinetics*, vol. 26, pp. 461–486, 1994.

[113] A. Durigon, V. G. Krioukov, and J. C. R. Claeyssen. "Análise da Integração das Equações da Cinética Química com o Uso dos Autovalores do Jacobiano" ["Analysis of the Integration of the Chemical Kinetics Equations with the Use of the Eigenvalues of the Jacobian"], XXV Iberian Latin American Congress on Computational Methods in Engineering, *Recife*, vol. 1, pp. 1–12, 2004.

[114] R. L. Eggels and L. P. H. Goey. "Mathematically Reduced Reaction Mechanisms Applied to Adiabatic Flat Hydrogen/Air Flames," *Combustion and Flame*, vol. 100, pp. 559–570, 1995.

[115] М. В. Никандрова, В. Г. Крюков, Р. Л. Исхакова. "Сокращение механизмов реакций методом «зацепления»," *Физико-Химическая Кинетика в Газовой Динамике*, Т. 5, 2007. [M. V. Nikandrova, V. G. Krioukov and R. L. Iskhakova, "Reduction of Reaction Mechanisms by the 'Engagement' Method," *Physical-Chemical Kinetics in Gas Dynamics*, vol. 5, 2007.]

[116] J. Y. Chen. "A General Procedure for Constructing Reduced Reaction Mechanisms with Given Independent Reactions," *Combustion Science and Technology*, vol. 57, pp. 89 –94, 1988.

[117] R. J. Martin and N. J. Brown. "The Importance of Thermodynamics to the Modeling of Nitrogen Combustion Chemistry," *Combustion and Flame*, vol. 78, pp. 365–376, 1989.

[118] C. K. Westbrook and L. L. Chase. *Chemical Kinetics and Thermochemical Data for Combustion Applications*, Lawrence Livermore Laboratory, UCID-17833, Rev. 3, 1983.

Downloaded from https://www.cambridge.org/core. Nottingham Trent University, on 17 Aug 2019 at 03:56:55, subject to the Cambridge Core terms of use, available at https://www.cambridge.org/core/terms. https://doi.org/10.1017/9781108581714.011

[119] M. W. Chase Jr., C. A. Davies, J. R. Downey, Jr. et al. *JANAF Thermochemical Tables*, 3rd edn., vol. 14, no. 1, 1985. Retrieved from www.scribd.com/doc/173465161/JPCRDS1V14-JANAF-Thermochemical-Tables-3rd-Edition-JPCRD-14-Supplement-No-1–1985.

[120] Л. В. Гурвич, Г. А. Хачкурузов, И. В. Вейц и др. *Термодинамические Свойства Индивидуальных Веществ: Справочник в 2 томах*, Moscow: АН СССР, 1962. [L. V. Gurvich, G. A. Khachkuruzov, I.V. Weitz et al. *Thermodynamic Properties of Individual Substances: A Handbook in 2 Volumes*. Moscow: USSR Academy of Sciences, 1962.]

[121] L. V. Gurvich, I. V. Veyts, and C. B. Alcock. *Thermodynamic Properties of Individual Substances*, 4th edn. New York: Hemisphere Publishing Corporation, vol. 1 in 2 parts, 1989.

[122] В. С. Иориш, Г. В. Белов. "О качестве информации в базах данных по термодинамическим свойствам веществ," *Физико-Химическая Кинетика в Газовой Динамике*, Т. 5, 2007. [V. S. Iorish and G. V. Belov. "On the Quality of Information in Databases on the Thermodynamic Properties of Substances," *Physico-Chemical Kinetics in Gas Dynamics*, vol. 5, 2007.]

[123] V. J. Costa, V. G. Krioukov and C. R. Maliska. "Pulverized Coal Combustion and Its Interaction with Moisture," *Proceedings of 35th National Heat Transfer Conference – NTHC*, Anaheim, CA, vol. 1, 2001.

[124] D. Miller and M. Frenklach. "Sensitivity Analysis and Parameter Estimation in Dynamic Modeling of Chemical Kinetics," *International Journal of Chemical Kinetics*, vol. 15, pp. 677–696, 1983.

[125] H. Rabitz, M. Kramer and D. Dacol. "Sensitivity Analysis in Chemical Kinetics," *Annual Review of Physical Chemistry*, vol. 34, pp. 419–461, 1983.

[126] J. W. Tilden, V. Constanza, G. J. McRae, et al. "Sensitivity Analysis of Chemically Reacting Systems." In *Modeling of Chemical Reaction Systems*, eds. Ebert K. H., Deuflhard P., and Jager W., New York: Springer-Verlag, pp. 69–91, 1981.

[127] V. Constanza and J. H. Seinfeld. "Stochastic Sensitivity Analysis in Chemical Kinetics," *The Journal of Chemical Physics*, vol. 74, pp. 3852–3858, 1981.

[128] R. J. Gelinas and J. P. Vajk. *Systematic Sensitivity Analysis of Air Quality Simulation Models*, Sandia Technical Report PB-80–112162, Science Pleasanton, CA: Applications Inc., 1978.

[129] M. A. Kramer, R. J. Kee and H. Rabitz. *CHEMSEN: A Computer Code for Sensitivity Analysis of Elementary Chemical Reaction Models*, Sandia Technical Report SAND-82–8230, Albuquerque, NM: Sandia National Laboratories, 1984.

[130] L. Tianfeng, J. Yiguang and C. K. Lam. "Complex CSP for Chemistry Reduction and Analysis," *Combustion and Flame*, vol. 126, pp. 1445–1455, 2001.

[131] Г. Николас, И. Пригожин. *Самоорганизация в Неравновесных Системах*. Москва: Мир, 1979. [G. Nicholas and I. Prigogine, *Self-Organization in Nonequilibrium Systems*. Moscow: Mir, 1979.]

[132] Н. С. Пискунов. *Дифференциальное и Интегральное Исчисление для ВТУЗов*, Москва: Физматгиз, 1963. [N. S. Piskunov, *Differential and Integral Calculus for Technical High Schools*, Moscow: Fizmatgiz, 1963.]

[133] J. Stoer and R. Bulirsch. *Introduction to Numerical Analysis*, New York: Springer-Verlag, 1980.

[134] J. H. Wilkinson and C. Reinsch. *Handbook for Automatic Computation. Vol. II: Linear Algebra,* Berlin: Springer-Verlag, 1971.

[135] G. A. Korn and T. M. Korn. *Mathematical Handbook for Scientists and Engineers*, New York: McGraw-Hill, 1961.

Downloaded from https://www.cambridge.org/core. Nottingham Trent University, on 17 Aug 2019 at 03:56:55, subject to the Cambridge Core terms of use, available at https://www.cambridge.org/core/terms. https://doi.org/10.1017/9781108581714.011

[136] F. S. Acton. *Numerical Methods That Work*, New York: Harper and Row, 1970.
[137] N. Peters and R. J. Kee. "The Computation of Stretched Laminar Methane-Air Diffusion Flames Using a Reduced Four-Step Mechanism," *Combustion and Flame*, vol. 68, pp. 17–29, 1987.
[138] U. Maas and S. B. Pope. "Simplifying Chemical Kinetics: Intrinsic Low-Dimensional Manifolds in Composition Space," *Combustion and Flame*, vol. 88, pp. 239–264, 1992.
[139] H. Hiemann, D. Schmidt, and U. Maas. "An Efficient Storage Scheme for Reduced Chemical Kinetics on Orthogonal Polynomials," *Journal of Engineering Mathematics*, vol. 31, pp. 131–142, 1997.
[140] A. T. Norris and S. B. Pope. "Modeling of Extinction in Turbulent Diffusion Flames by the Velocity-Dissipation-Composition PDF Method," *Combustion and Flame*, vol. 100, pp. 211–220, 1995.
[141] Y. Xin, Z. Song, Y. Z. Tan, et al. "The Directed Relation Graph Method for Mechanism Reduction in the Oxidative Coupling of Methane," *Catalysis Today*, vol. 131, pp. 483–488, 2008.
[142] P. Pepiot-Desjardins and H. Pitsch. "An Efficient Error-Propagation-Based Reduction Method for Large Chemical Kinetic Mechanisms," *Combustion and Flame*, vol. 154, pp. 67–81, 2008.
[143] T. P. Coffee, A. J. Kotlar, and M. S. Miller. "The Overall Reaction Concept in Premixed, Laminar, Steady-State Flames: II. Initial Temperatures and Pressures," *Combustion and Flame,* vol. 58, pp. 59–67, 1984.
[144] D. G. Vlachos. "Mathematically Reduced Reaction Mechanisms Applied to Adiabatic Flat Hydrogen/Air Flames," *Chemical Engineering Science*, vol. 51, no. 16, pp. 3979–3993, 1996.
[145] В. Е. Алемасов, Э. А. Даутов, А. Ф. Дрегалин. *Номографическая Аппроксимация Термогазодинамических Параметров Энергоустановок*. Казань: ФЭН, 1993. [V. E. Alemasov, E. A. Dautov, and A. F. Dregalin, *Nomographic Approximation of Thermogasdynamic Parameters of Power Generation Systems*. Kazan: FENG, 1993.]
[146] C. W. Clenshaw. *Chebyshev Series for Mathematical Functions in Mathematical Tables*, vol. 5, London: National Physical Laboratory, H.M. Stationery Office, 1962.
[147] О. В. Бартеньев. *Современный Фортран*, 3-е изд., М: ДИАЛОГ МИФИ, 2000. [O.V. Bartenev, *Modern Fortran*, 3rd edn., Moscow: DIALOG MEPI, 2000.]
[148] Б. У. Керниган, Д. М. Ритчи. *Программирование на Языке С*. Изд. Вильямс, 2016. [Brian W. Kernighan, and Dennis M. Ritchie. *The C Programming Language*. Prentice Hall, 1988.]
[149] В. Е. Алемасов, А. Ф. Дрегалин, А. П. Тишин и др. *Термодинамические и Теплофизические Свойства Продуктов Сгорания*, Справочник. Том 2, Москва: ВИНИТИ, 1973. [V. Ye. Alemasov, A. F. Dregalin, A. P. Tishin, et al. *Thermodynamic and Thermophysical Properties of Combustion Products: Handbook Volume 2*. Moscow: VINITI, 1973.]
[150] V. E. Alemasov, A. F. Dregalin, A, P. Tishin, et al. *Thermodynamic and Thermophysical Properties of Combustion Products: Handbook Volume IV*. ed. V. P., Glushko. Moscow: VINITI, 1973. Translated from Russian by Israel Program for Scientific Translations, Jerusalim, 1976.
[151] В. Е. Алемасов, А. Ф. Дрегалин, А. П. Тишин и др. *Термодинамические и Теплофизические Свойства Продуктов Сгорания, Справочник. Том 5*, Москва: ВИНИТИ, 1973b. [V. Ye. Alemasov, A. F. Dregalin, A. P. Tishin, et al. *Thermodynamic*

Downloaded from https://www.cambridge.org/core. Nottingham Trent University, on 17 Aug 2019 at 03:56:55, subject to the Cambridge Core terms of use, available at https://www.cambridge.org/core/terms. https://doi.org/10.1017/9781108581714.011

and Thermophysical Properties of Combustion Products: Handbook Volume 5. Moscow: VINITI, 1973b.]

[152] В. Е. Алемасов, А. Ф. Дрегалин, А. П. Тишин и др. *Термодинамические и Теплофизические Свойства Продуктов Сгорания, Справочник. Том 6*, Москва: ВИНИТИ, 1973c. [V. Ye. Alemasov, A. F. Dregalin, A. P. Tishin, et al. *Thermodynamic and Thermophysical Properties of Combustion Products: Handbook Volume 6*. Moscow: VINITI, 1973c.]

[153] В. Е. Алемасов, А. Ф. Дрегалин, А. П. Тишин и др., *Термодинамические и Теплофизические Свойства Продуктов Сгорания, Справочник. Том 7*, Москва: ВИНИТИ, 1974a. [V. Ye. Alemasov, A. F. Dregalin, A. P. Tishin, et al. *Thermodynamic and Thermophysical Properties of Combustion Products: Handbook Volume 7*. Moscow: VINITI, 1974a.]

[154] В. Е. Алемасов, А. Ф. Дрегалин, А. П. Тишин и др. *Термодинамические и Теплофизические Свойства Продуктов Сгорания, Справочник. Том 8*, Москва: ВИНИТИ, 1974b. [V. Ye. Alemasov, A. F. Dregalin, A. P. Tishin, et al. *Thermodynamic and Thermophysical Properties of Combustion Products: Handbook Volume 8*. Moscow: VINITI, 1974b.]

[155] Б. И. Соколов, А. С. Черенков, А. И. Саломыков. *Термодинамические и Теплофизические Свойства Твердых Ракетных Топлив и их Продуктов Сгорания: Пособие для курсового и дипломного проектирования*. Москва: Министерство обороны СССР, 1977. [B. I. Sokolov, A. S. Cherenkov, and A. I. Salomykov. *Thermodynamic and Thermophysical Properties of Solid Rocket Fuels and Their Combustion Products: A Manual for Course and Graduation Design Projects*. Moscow: USSR Ministry of Defense, 1977.]

[156] A. L. Abdullin, V. I. Naoumov, and V. G. Krioukov. "Evaluation of Eigenvalues for the Analysis of Combustion and Chemical Non-Equilibrium Flows," AIAA SciTech Forum. 55th AIAA Aerospace Science Meeting, AIAA 20017–0662, Grapevine, TX, pp. 1–12, 2017.

[157] Л. М. Скворцов. "Явные двухшаговые методы Рунге–Кутты," *Математическое Моделирование*, Т. 21, № 9, стр. 54–65, 2009. [L. M. Skvortsov. "Explicit Two-Step Runge–Kutta Methods," *Mathematical Modeling*, vol. 21, no. 9, pp. 54–65, 2009.]

[158] В. Ю. Гидаспов. "Численное моделирование химически неравновесного течения в сопле жидкостного ракетного двигателя," *Вестник МАИ*, Т. 20, стр. 90–97, 2013. [V. Yu. Gidaspov. "Numerical Modeling of Chemical Nonequilibrium Flow in the Nozzle of a Liquid-Propellant Rocket Engine," *MAI Bulletin*, vol. 20, pp. 90–97, 2013.]

[159] С. А. Шустов. "Численное моделирование термогазодинамических процессов в ЖРДМТ с учетом их неидеального протекания," *Вестник МАИ*, Т. 16, № 2. стр. 146–153, 2009. [S. A. Shustov. "Numerical Simulation of Non-Ideal Thermogasdynamic Processes in Micro-Liquid Propellant Rocket Engines," *MAI Bulletin*, vol. 16, no. 2. pp. 146–153, 2009.]

[160] В. Е. Алемасов, А. Ф. Дрегалин, А. П. Тишин. *Теория Ракетных Двигателей*, М.: Машиностроение, 1989. [V. Ye. Alemasov, A. F. Dregalin, and A. P. Tishin. *Theory of Rocket Engines*, Moscow: Mashinostroenie, 1989.]

[161] L. Boccaletto and J. P. Dussauge. "High-Performance Rocket Nozzle Concept," *Journal of Propulsion and Power*, vol. 26, no. 5, pp. 969–979, 2010.

[162] V. G. Krioukov, R. L. Iskhakova, M. Niwa, et al. "Mathematical Modeling of Two-Phase Reacting Flow in Supersonic Nozzle," *XVII Brazilian Congress of Mechanical Engineering*, vol. 1, pp. 1–10, 2003.

Downloaded from https://www.cambridge.org/core. Nottingham Trent University, on 17 Aug 2019 at 03:56:55, subject to the Cambridge Core terms of use, available at https://www.cambridge.org/core/terms. https://doi.org/10.1017/9781108581714.011

[163] М. А. Таймаров, М. Р. Шарипов. “Котёл пульсирующего горения природных и пиролизных газов,” *Вестник Казанского Технологического Университета*, Т. 16, №21, стр.133–135, 2013. [M. A. Taimarov and M .R. Sharipov. “Boiler of Pulsating Combustion of Natural and Pyrolysis Gases,” Bulletin of Kazan Technological University, vol. 16, no. 21, pp. 133–135, 2013.]

[164] Г. И. Павлов, А. В. Кочергин, О. Р. Ситников, и др. “Переработка изношенных шин и резинотехнических изделий в инертную крошку при использовании установок пульсирующего горения,” *Вестник Казанского Технологического Университета*, № 19, стр. 174–179, 2011. [G. I. Pavlov, A. V. Kochergin, O. R. Sitnikov, et al. “Reprocessing Used Tires and Rubber Products Recycling into Inert Crumb Using Pulsating Combustion Installations,” *Kazan Technological University*, no. 19, pp. 174– 179, 2011.]

[165] С. Е. Филиппов, В. М. Ларионов, Д. В. Рукавишников. “Механизмы возбуждения и теоретическая модель вибрационного горения твердого топлива в трубе,” *Проблемы энергетики*, № 1, стр. 20–28, 2006. [S. E. Filippov, V. M. Larionov, and D. V. Rukavishnikov. “Excitation Mechanisms and the Theoretical Model of the Vibration Combustion of Solid Fuel in a Pipe,” *Challenges in Power Engineering*, no. 1, pp. 20–28, 2006.]

[166] Б. В. Раушенбах, *Вибрационное Горение*, М: Государственное издательство физико-математической литературы, 1961. [B. V. Rauschenbakh. *Vibration Combustion*. Moscow: State Publishing House of Physics and Mathematics, 1961.]

[167] A. D. Stazio, C. Chauveau, G. Dayma, et al. “Oscillating Flames in Micro-Combustion,” *Combustion and Flame*, vol. 167, pp. 392–394, 2016.

[168] E. W. Christiansen, C. K. Law, and C. J. Sung. “Steady and Pulsating Propagation and Extinction of Rich Hydrogen/Air Flames at Elevated Pressures,” *Combustion and Flame*, vol. 124, pp. 35–49, 2001.

[169] Ю. К. Карасевич, М. Г.Нейгауз. “Метод отбора определяющих стадий для сложных кинетических схем,” В сб.: Быков В. И. и др. *Прямые и обратные задачи в химической кинетике*, стр. 248–254, 1993. [Yu. K. Karasevich and M. G. Neuhauz. “Method of Selection of Determining Stages for Complex Kinetic Schemes,” In eds. Bykov V. I. et al., *Direct and Inverse Problems in Chemical Kinetics*, pp. 248–254, 1993.]

[170] A. P, Spilimbergo, G. O. Veloso, V. G. Krioukov et. al. “Engagement Method: Application in Area of Alteration of the Parameters of the Reacting Medium,” XXVIII CILAMCE (Iberian Latin American Congress on Computational Methods in Engineering), Porto, Portugal, pp. 1–10, 2007.

[171] В. Г. Крюков, А. Л. Абдуллин, И. И. Сафиуллин. “Метод поэтапного сокращения механизма реакций для сложных реагирующих систем,” *Вестник Казанского Технологического Университета*, Т. 17, № 11, стр. 168–173, 2014. [V. G. Krioukov, A. L. Abdullin, and I. I. Safiullin. “Method of Phased Reduction of the Reaction Mechanism for Complex Reactive Systems,” *Bulletin of Kazan Technological University*, vol. 17, no. 11, pp. 168–173, 2014.]

[172] Edsger W. Dijkstra. *A Discipline of Programming*. Upper Saddle River, NJ: Prentice-Hall Series in Automatic Computation, 1976.

[173] A. P. Spilimbergo, V. G. Krioukov, and I. I. Safiullin. “Redução do Mecanismo de Combustão para Fluxos Reagentes com Base em Reatores Sucessivos” [“Reduction of the Combustion Mechanism for Reactive Flows Based on Successive Reactors”], XXXVI Iberian Latin-American Congress on Computational Methods in Engineering, CILAMCE, November 2015, Rio de Janeiro, Brazil, pp. 1–12, 2015.

Downloaded from https://www.cambridge.org/core. Nottingham Trent University, on 17 Aug 2019 at 03:56:55, subject to the Cambridge Core terms of use, available at https://www.cambridge.org/core/terms. https://doi.org/10.1017/9781108581714.011

[174] D. Bianchi, A. Turchi, F. Nasuti, et al. "Chemical Erosion of Carbon-Phenolic Rocket Nozzles with Finite-Rate Surface Chemistry," *Journal of Propulsion and Power*, vol. 29, no. 5, pp. 1220–1230, 2013.

[175] E. A. Barbour and R. K. Hanson. "Chemical Nonequilibrium, Heat Transfer, and Friction in a Detonation Tube with Nozzles," *Journal of Propulsion and Power*, vol. 26, no. 2, pp. 230–239, 2010.

[176] M. Janbozorgi and H. Metgalchi. "Rate-Controlled Constrained-Equilibrium Modeling of H/O Reacting Nozzle Flow," *Journal of Propulsion and Power*, vol. 28, no. 4, pp. 677–684, 2012.

[177] C. K. Law, "Fuel Options for Next-Generation Chemical Propulsion," *AIAA Journal*, vol. 50, no. 1, pp. 19–36, 2012.

[178] J. M. Powers and S. Paolucci. "Accurate Spatial Resolution Estimates for Reactive Supersonic Flow with Detailed Chemistry," *AIAA Journal*, vol. 43, no. 5, pp. 1088–1099, 2005.

[179] V. R. Katta and W. M. Roquemore. "Calculation of Multidimensional Flames Using Large Chemical Kinetics," *AIAA Journal*, vol. 46, no. 7, pp. 1640–1650, 2008.

[180] C. K. Law. *Combustion Physics*, Cambridge: Cambridge University Press, 2006.

[181] K. W. Ragland and K. M. Bryden. *Combustion Engineering*, 2nd edn. Boca Raton, FL: CRC Press, 2011.

[182] C. J. Sung, C. K. Law and J. Y. Chen. "Augmented Reduced Mechanisms for NO Emission in Methane Oxidation," *Combustion and Flame*, vol. 125, pp. 906 –919, 2001.

[183] J. O. Olsson and L. L. Anderson. "Sensitivity Analysis Based in an Efficient Brute-Force Method, Applied to an Experimental CH_4/O_2 Premixed Laminar Flame," *Combustion and Flame*, vol. 67, pp. 99–109, 1987.

[184] M. Pilawska, C. J. Butler, A. N. Hayhurst, et al. "The Production of Nitric Oxide during the Combustion of Methane and Air in a Fluidized Bed," *Combustion and Flame*, vol. 127, pp. 2181–2193, 2001.

[185] S. Rafael and E. Sher. "Reaction Kinetics of Hydrogen-Enriched Methane-Air and Propane-Air Flame: Stoichiometries," *Combustion and Flame*, vol. 78, pp. 326–338, 1989.

[186] C. K. Westbrook, F. L. Dryer, and R. P. Schuy. "A Comprehensive Mechanism for the Pyrolysis and Oxidation of Ethylene," 19th Symposium on Comustion, pp. 153–166, 1982.

[187] Б. Льюис, Р. Н. Пиз, Х. С. Тэйлор. *Процессы Горения*, Москва: Физ-мат.лит., 1961. [B. Lewis, R. N. Pease, and H. S. Taylor, *Combustion*, Moscow: Physics and Mathematics, 1961.]

[188] S. Fukutani and H. Jinno. "Mechanism of Flame Propagation in Hydrogen-Air and Methane-Air Systems." *Notes on Numerical Fluid Mechanics*, no. 6, pp. 167–181, 1982.

[189] G. Tsatsaronis. "Prediction of Propagating Laminar Flames in Methane, Oxygen, Nitrogen Mixtures," *Combustion and Flame*, vol. 33, pp. 217–239, 1978.

[190] B. Shizgal and M. Karplus. "Nonequilibrium Contributions to the Rate of Reactions: II. Isolated Multicomponent Systems," *The Journal of Chemical Physics*, vol. 54, pp. 4345–4356, 1971

[191] В. А. Щукин. "Явление флуктуационного реагирования в газах," *Рабочие Процессы в Камерах Сгорания Воздушно- Реактивных Двигателей. Межвузовский Сборник*, Казань: Казанский авиационный институт, стр. 4–6, 1987. [V. A. Shchukin. "Phenomenon of a Fluctuating Response in Gases," Processes in the Combustion Chambers of Air-Jet Engines. Kazan: Interuniversity Collection Papers, Kazan Aviation Institute, pp. 4–6, 1987.]

Downloaded from https://www.cambridge.org/core. Nottingham Trent University, on 17 Aug 2019 at 03:56:55, subject to the Cambridge Core terms of use, available at https://www.cambridge.org/core/terms. https://doi.org/10.1017/9781108581714.011

[192] B. Widom. "Reaction Kinetics in Stochastic Models," *The Journal of Chemical Physics*, vol. 55, pp. 44–52, 1971.

[193] G. P. Glass and B. K. Chaturvedi. "The Effect of Vibrational Excitation of H_2 and of OH on the Rate of the Reaction H_2+OH→H_2O+H," *The Journal of Chemical Physics*, vol. 75, pp. 2749–2752, 1981.

[194] J. Levy, B. Taylor, J. Longwell, et al. "C1 and C2 Chemistry in Rich Mixture Ethylene-Air Flames," 19th Symposium on Comustion, pp. 167–169, 1982.

[195] В. Я. Басевич, С. М. Когарко, В. С. Посвянский. "Кинетика реакций при распространении этилено-кислородного пламени," *Физика Горения и Взрыва*, № 2, с. 193–200, 1977. [V. Ya. Basevich, S. M. Kogarko and V. S. Posvyansky, "Kinetics of Reactions during the Propagation of Ethylene-Oxygen Flame," Physics of Combustion and Explosion, no. 2, pp. 193–200, 1977.]

[196] G. E. Andrews and D. Bradley. "The Burning Velocity of Methane-Air Mixture," *Combustion and Flame*, vol. 19, pp. 275–288, 1972.

[197] M.Cathonnet, I. Boettner, and H. James. "Experimental Study and Numerical Modeling of High Temperature Oxidation of Propane and n-Butane," 18th Symposium on Combustion, pp. 903–913, 1981.

[198] M. Caymay and J. Peeters. "The Reaction of Ethane with Atomic Oxygen at T= 600–1030 K," 19th Symposium on Combustion, pp. 51–59, 1982.

[199] J. Levy and A. Sarofim. "Higher Hydrocarbon Combustion: 2. Fuel-Rich C_1/C_2 Mechanism," *Combustion and Flame*, vol. 53, pp. 1–15, 1983.

[200] D. Notzold and J. Algermissen. "Chemical Kinetics of the Ethane – Oxygen Reaction: Part 1; High Temperature Oxidation at Ignition Temperatures between 1400 K and 1800 K," *Combustion and Flame*, vol. 40, pp. 293–313. 1981.

[201] J. Warnatz. "Chemistry of High Temperature Combustion of Alkanes Up to Octane," *20th Symposium on Combustion*, vol. 20, no. 1, pp. 845–856. 1984.

[202] S. J. Ying. "Reduced Chemical Kinetics for Propane Combustion," 28th Aerospace Sciences Meeting, AIAA Paper, no. 0546. pp. 1–9. 1990.

[203] W. Duo, K. Dam-Johansen, and K. Stergaard. "Kinetics of the Gas-Phase Reaction between Nitric Oxide, Ammonia and Oxygen," *The Canadian Journal of Chemical Engineering,* vol. 70, pp. 1014–1020, 1992.

[204] P. Glarborg, K. Dam-Johansen, and J. Miller. "The Reaction of Ammonia with Nitrogen Dioxide in a Flow Reactor: Implications for the NH_2 + NO_2 Reaction," *International. Journal of Chemical Kinetics*, vol. 27, pp. 1207–1220, 1995.

[205] B. Gradon and J. Tomeczek. "Prediction of N_2O and NH_3 in Fuel-Rich Gaseous Flames," *Combustion and Flame*, vol. 126, pp. 1856–1859, 2001.

[206] M. Jodal, T. Lauridsen, and K. Johansen. "NOx Removal on a Coal-Fired Utility Boiler by Selective Non-Catalytic Reduction," *Environmental Progress*, vol. 11, no. 4, pp. 296–301, 1992.

[207] C. C. Schmidt and C. T. Bowman. "Flow Reactor Study of the Effect of Pressure on the Thermal De-NOx Process," *Combustion and Flame*, vol. 127, pp. 1958–1970, 2001.

[208] N. Sullivan, A. Jensen, P. Glarborg, et al. "Ammonia Conversion and NOx Formation in Laminar Coflowing Nonpremixed Methane-Air Flames," *Combustion and Flame*, vol. 131, pp. 285–298, 2002.

[209] J. Tomeczek and B. Gradon. "The Role of N_2O and NNH in the Formation of NO via HCN in Hydrocarbon Flames," *Combustion and Flame*, vol. 133, pp. 311–322, 2003.

[210] V. M. Zamansky, V. V. Lissianski, P. M. Maly, et al. "Reactions of Sodium Species in the Promoted SNCR Process," *Combustion and Flame*, vol. 117, pp. 821–831, 1999.

Downloaded from https://www.cambridge.org/core. Nottingham Trent University, on 17 Aug 2019 at 03:56:55, subject to the Cambridge Core terms of use, available at https://www.cambridge.org/core/terms. https://doi.org/10.1017/9781108581714.011

[211] В. Ф. Заказнов, Л. А. Куршева, З. И. Федина. “Определение нормальных скоростей и критических диаметров гашения пламени аммиачно-воздушных смесей,” *Физика Горения и Взрыва*, Т. 14, № 6, стр. 22–26, 1978. [V. F. Zakaznov, L. A. Kursheva, and Z. I. Fedina. “Study of Normal Velocities and Critical Diameters of Quenching a Flame of Ammonia–Air Mixtures,” *Physics of Combustion and Explosion*, vol. 14, no. 6, pp. 22–26, 1978.]

[212] T. Faravelli, A. Frassoldati, and E. Ranzi. “Kinetic Modeling of the Interactions between NO and Hydrocarbons in the Oxidation of Hydrocarbons at Low Temperatures,” *Combustion and Flame*, vol. 132, pp. 188–207, 2003.

[213] A. Konnov and J. De Ruyck. “Kinetic Modeling of the Decomposition and Flames of Hydrazine,” *Combustion and Flame*, vol. 125, pp. 106–126, 2001.

[214 В.И. Локай, М.К. Максутова, В.А. Струнки. *Газовые турбины двигателей летательных аппаратов*, Москва: Машиностроение, 1996.[V. I. Lokai, M. K. Maksutova, and V. A. Strunkin, *Gas Turbines of Aircraft Engines*. Moscow: Mashinostroenie, 1996.]

[215] G. P. Sutton and O. Bilblarz. *Rocket Propulsion Elements.* 7th edn., Hoboken, NJ: Wiley Interscience, 2001.

[216] A. F. El-Sayed. *Aircraft Propulsion and Gas Turbine Engines*. Boca Raton, FL: CRC Press. Taylor & Francis Group, 2008.

[217] J. B. Heywood. *Internal Combustion Engine Fundamentals*, New York: McGraw-Hill, 1988.

[218] С. М. Ильяшенко, А. В. Талантов. *Теория и расчет прямоточных камер сгорания.* Москва: Машиностроение, 1964. [S. M. Ilyashenko and A. V. Talantov. *Theory and Calculation of Ramjet Engines Combustion Chambers*. Moscow: Mechanical Engineering, 1964.]

[219] И. Н. Зверев, Н. Н. Смирнов. *Газодинамика горения.* Москва: Изд-во МГУ, 1987. [I. N. Zverev and N. N. Smirnov. *Gas Dynamics of Combustion*. Moscow: Moscow State University Publishing House, 1987.]

[220] Н. Н. Смирнов. “Химические реакции и тепломассоперенос в многокомпонентном газе над слоем жидкого горючего,” *Вестник МГУ, Москва. Серия: Математика. Механика,* № 2. стр. 46–55, 1986. [N. N. Smirnov. “Chemical Reactions and Heat and Mass Transfer in a Multicomponent Gas over a Layer of Liquid Fuel,” *Bulletin of MGU, Moscow, Mathematics Series,* no. 2. pp. 46–55, 1986.]

[221] Н. Н. Смирнов. “Горение слоя топлива при обдувании поверхности потоком окислителя,” *Физика Горения и Взрыва*, Т. 18, № 5, стр. 63–70, 1982. [N. N. Smirnov. “Combustion of a Layer of Fuel while Blowing a Surface with an Oxidant Flow,” *Physics of Combustion and Explosion*, vol. 18. no. 5, pp. 63–70, 1982.]

[222] P. Lafon, M. Habiballah, and D. Scherrer. “Lox Droplet Combustion in a High Pressure Hydrogen Atmosphere,” 9th World Hydrogen Energy Conference, Paris, pp. 81–90, 22–25 June 1992.

[223] Б. Ф. Бояршинов, Э. П. Волчков, В. И. Терехов. “Конвективный тепломассообмен при испарении жидкости в газовый поток,” *Известия СО АН СССР. Сер. Техн. Наук*, Т. 16, № 3, стр. 13–22, 1985. [B. F. Boyarshinov, E. P. Volchkov and V. I. Terekhov. “Convective Heat and Mass Transfer at the Evaporation of a Liquid into a Gas Flow,” *News of the Siberian Branch of the USSR Academy of Sciences: Technical Sciences Series*, vol. 16, no. 3, pp. 13–22, 1985.]

[224] W. E. Ranz and W. R. Marshall. “Evaporation from Drops,” *Chemical Engineering Progress*, vol. 48. Part I, pp. 141–146, Part II, pp. 173–180, 1952.

Downloaded from https://www.cambridge.org/core. Nottingham Trent University, on 17 Aug 2019 at 03:56:55, subject to the Cambridge Core terms of use, available at https://www.cambridge.org/core/terms. https://doi.org/10.1017/9781108581714.011

[225] L. G. Loitsyanskiy and R. H. Nunn. *Mechanics of Liquids and Gases.* 6th edn. New York and Wallington: Begell House, 1995.

[226] V. I. Naumov, and V. Y. Kotov. "Micro-Scale Investigation of Non-Equilibrium Thermo-Fluid Transport during Droplet Evaporation and Combustion," 43rd Aerospace Science Meeting and Exhibit, AIAA 2005–1431, Reno, NV, pp. 1–14, 2005.

[227] М. В. Добровольский. *Жидкостные Ракетные Двигатели. Основы Проектирования. Под ред. Д.А. Ягодникова*, 3-е издание. Москва: Издательство МГТУ им. Н.Э. Баумана, 2016. [M. V. Dobrovolsky. Liquid Propellant Rocket Engines: Design Basics. ed. Ye. S. Yagodnikov, 3rd edn. Moscow: Publishing House of Bauman Moscow State Technical University, 2016.]

[228] R. W. Humble, G. N. Henry and W. J. Larson. *Space Propulsion Analysis and Design.* New York: McGraw-Hill, Technology & Engineering, 1995.

[229] P. J. Priem, and M. F. Heidmann. "Propellant Vaporization as a Design Criterion for Rocket-Engine Combustion Chambers," NASA Tech. Rep., R-67, 1960.

[230] А. Червински. "Горение жидких капель при сверхкритических условиях в неподвижной среде," *Ракетная Техника и Космонавтика*, № 8, стр. 1815–1817, 1969. [A. Chervinsky. "Combustion of Liquid Droplets under Supercritical Conditions in a Stationary Medium," *Rocket Technique and Cosmonautics*, no. 8. pp. 1815–1817, 1969.]

[231] C. K. Law. "Internal Boiling and Superheating in Vaporizing Multicomponent Droplets," *AISChe Journal*, vol. 4, no. 24, pp. 626–632, 1978.

[232] C .K. Law and H. K. Law. "A d^2-Law for Multicomponent Droplet Vaporization and Combustion," *AIAA Journal*, vol. 20, no. 4, pp. 522–527, 1982.

[233] C. K. Law. "Multicomponent Droplet Combustion with Rapid Internal Mixing," *Combustion and Flame*, vol. 26, pp. 219–233, 1976.

[234] J. D. Mattingly, and H. von Ohain. *Elements of Propulsion: Gas Turbines and Rockets,* 2nd edn. Reston, VA: American Institute of Aeronautics and Astronautics, 2006.

[235] T. Cebeci and P. Bradshaw. *Physical and Computational Aspects of Convective Heat Transfer*. New York: Springer-Verlag, XII, 1984.

[236] J. Stengele, M. Willmann and S. Wittig. "Experimental and Theoretical Study of Droplet Vaporization in High Pressure Environment," ASME 1997 International Gas Turbine and Aeroengine Congress and Exhibition, ASME Paper 97-GT-151, Orlando, FL, pp. 1–8, 1997.

[237] N. M. Marinov, W. J. Pitz, C. K. Westbrook, et al. "An Experimental and Kinetic Calculation of the Promotion Effect of Hydrocarbons on the NO-NO_2 Conversion in a Flow Reactor," *Symposium (International) on Combustion. Proceedings of the Combustion Institute*, vol. 27, pp. 389–396,. 1998.

[238] A. Ingenito, A. Agresta, R. Andriani, et al. "RQL Combustion as an Effective Strategy to NOx Reduction in Gas Turbine Engines," ASME 2014 International Mechanical Engineering Congress and Exposition, Vol. 1: Advances in Aerospace Technology, Paper No. IMECE 2014–36898. Montreal, Quebec, pp. 1–12, 2014.

[239] G. C. Oates. *Aerothermodynamics of Gas Turbine and Rocket Propulsion*, 3rd edn. Reston, VA: American Institute of Aeronautics and Astronautics, 1997.

[240] R. D. Flack. *Fundamentals of Jet Propulsion Application*. Cambridge: Cambridge University Press. 2005.

[241] V. Yang, M. Habiballah, M. Popp, et al. *Liquid Rocket Thrust Chambers: Aspects of Modeling, Analysis, and Design*. Reston, VA: American Institute of Aeronautics and Astronautics, 2004.

Downloaded from https://www.cambridge.org/core. Nottingham Trent University, on 17 Aug 2019 at 03:56:55, subject to the Cambridge Core terms of use, available at https://www.cambridge.org/core/terms. https://doi.org/10.1017/9781108581714.011

[242] J. Martin and L. Turner. *Rocket and Spacecraft Propulsion*. New York: Springer. 2009.
[243] E. Ring. *Rocket Propellant and Pressurization Systems*. New York: Prentice-Hall. 1964.
[244] Б. В. Раушенбах, С. А. Белый, И. В. Беспалов, и др. *Физические Основы Рабочего Процесса в Камерах Сгорания Воздушно-реактивных Двигателей.* Москва: Машиностроение, 1964. [B. V. Rauschenbach, S. A. Bely, I. V. Bespalov, et al. *Physical Principles of the Working Process in Combustion Chambers of Air-Jet Engines*. Moscow: MachineBuilding, 1964.]
[245] Ф.Г.Бакиров, В.М.Захаров, И.З.Полещук, и др. *Образование и Выгорание Сажи при Сжигании Углеводородных Топлив*, Москва: Машиностроение, 1989. [F. G. Bakirov, V. M. Zakharov, I. Z. Poleshchuk, et al. *Soot Formation and Burnout during the Burning of Hydrocarbon Fuels*. Moscow: MachineBuilding, 1989.]
[246] N. A. Chigier, F. J. Weinberg, C. T. Bowman, et al. "Pollution Formation and Destruction in Flames." In *Progress in Energy & Combustion Science, Vol. 1*, ed. N. A. Chigier, Oxford: Pergamon Press, 1976.
[247] Н. П. Самойлов, Е. И. Игонин, О. А. Кашеваров, и др. *Токсичность Автотракторных Двигателей и Способы ее Снижения*, Казань: КГУ, 1997. [N. P. Samoilov, E. I. Igonin, O. A. Kashevarov, et al. *Ways of Reduction of Toxic Emission of Automotive and Tractor Engines*. Kazan: KSU, 1997.]
[248] Р. М. Петриченко. *Элементы Системы Автоматизированного Проектирования ДВС: Алгоритмы Прикладных Программ*, Ленинград: Машиностроение, 1990. [R. M. Petrichenko. *Elements Internal Combustion Engines Coputer-Aided Design and Algorithms of Applied Computer Codes*. Leningrad: MachineBuilding, 1990.]
[249] J. Andrae, P. Bjornbom, and L. Edsberg. "Numerical Studies of Wall Effects with Laminar Methane Flames," *Combustion and Flame*, vol. 128, pp. 165–180, 2002.
[250] M. Balthasar, F. Mauss, and H. Wang. "A Computational Study of the Thermal Ionization of Soot Particles and Its Effect on Their Growth in Laminar Premixed Flames," *Combustion and Flame*, vol. 129, pp. 204–216, 2002.
[251] M. Balthasar, F. Mauss, A. Knobel, et al. "Detailed Modeling of Soot Formation in a Partially Stirred Plug Flow Reactor," *Combustion and Flame*, vol. 128, pp. 395–409, 2002.
[252] M. Balthasar and M. Kraft. "A Stochastic Approach to Calculate the Particle Size Distribution Function of Soot Particles in Laminar Premixed Flames," *Combustion and Flame*, vol. 133, pp. 289–298, 2003.
[253] A. Beltrame, P. Porshnev, W. Merchan-Merchan, et al. "Soot and NO Formation in Methane–Oxygen Enriched Diffusion Flames," *Combustion and Flame*, vol. 124, pp. 295–310, 2001.
[254] S. J. Brookes and J. B. Moss. "Measurements of Soot Production and Thermal Radiation from Confined Turbulent Jet Diffusion Flames of Methane," *Combustion and Flame*, vol. 116, pp. 49–61, 1999.
[255] S. Hayashi, Y. Hisaeda, Y. Asakuma, et al. "Simulation of Soot Aggregates Formed by Benzene Pyrolysis," *Combustion and Flame*, vol. 117, pp. 851– 860, 1999.
[256] F. Inal and S. M. Senkan. "Effects of Equivalence Ratio on Species and Soot Concentrations in Premixed n-Heptane Flames," *Combustion and Flame*, vol. 131, pp. 16–28, 2002.
[257] J. B. Cuenot, T. Poinsot, and D. Haworth. "Numerical Simulation and Modeling for Lean Stratified Propane-Air Flames," *Combustion and Flame*, vol. 128, pp. 1–21, 2002.
[258] F. Liu, H. Guo, G. J. Smallwood, et al. "The Chemical Effects of Carbon Dioxide as an Additive in an Ethylene Diffusion Flame: Implications for Soot and NOx Formation," *Combustion and Flame*, vol. 125, pp. 778–787, 2001.

Downloaded from https://www.cambridge.org/core. Nottingham Trent University, on 17 Aug 2019 at 03:56:55, subject to the Cambridge Core terms of use, available at https://www.cambridge.org/core/terms. https://doi.org/10.1017/9781108581714.011

[259] M. M. Maricq, S. J. Harris, and J. J. Szente. "Soot Size Distributions in Rich Premixed Ethylene Flames," *Combustion and Flame*, vol. 132, pp. 328–342, 2003.

[260] P. A. Tesner and S. V. Shurupov. "Soot Formation from Acetylene-Benzene Mixture," *Combustion Science and Technology*, vol. 92, pp. 61–67, 1993.

[261] P. A. Tesner and S. V. Shurupov. "Some Physico-Chemical Parameters of Soot Formation during Pyrolysis of Hydrocarbons," *Combustion Science and Technology*, vol. 105, pp. 147–161, 1995.

[262] J. Warnatz, H. Bockhorn, A. Moser, et al. "Expelimental Investigations and Computational Simulation of Acetilene-Oxigen Flames from Near Stoichiometric to Sooting Conditions," 19th Symposium (International) on Combustion. Pittsburg, PA: The Combustion Institute, pp. 197–209, 1982.

[263] C. K. Westbrook and F. L. Dryer. "Chemical Kinetics and Modeling of Combustion Processes," 18th Symposium on Combustion, pp. 749–767, 1981.

[264] C. K.Westbrook, W. Pitz, M. Thornton, et al. "A Kinetic Modeling Study of n-Pentane Oxidation in a Well-Stirred Reactor," *Combustion and Flame*, vol. 72, pp. 45–62, 1988.

[265] F. Xu, A. M. El-Leathy, C. H. Kim, et al. "Soot Surface Oxidation in Hydrocarbon/Air Diffusion Flames at Atmospheric Pressure," *Combustion and Flame*, vol. 132, pp. 43–57, 2003.

[266] F. Xu and G. M. Faeth. "Soot Formation in Laminar Acetylene/Air Diffusion Flames at Atmospheric Pressure," *Combustion and Flame*, vol. 125, pp. 804–819, 2001.

[267] B. Zhao, Z. Yang, M. V. Johnston, et al. "Measurement and Numerical Simulation of Soot Particle Size Distribution Functions in a Laminar Premixed Ethylene-Oxygen-Argon Flame," *Combustion and Flame*, vol. 133, pp. 173–188, 2003.

[268] C. H. Kim, F. Xu, P. B. Sunderland, et al. "Soot Formation and Oxidation in Laminar Flames," 44th AIAA Aerospace Sciences Meeting and Exhibit, AIAA 2006–1508, Reno, NV, pp. 1–17, 2006.

[269] П. А. Теснер. "Образование сажи при горении," *Физика Горения и Взрыва*, № 2, стр. 3–14, 1979. [P. A. Tesner. "Soot Formation in Combustion," *Physics of Combustion and Explosion*, no. 2, p. 3–14, 1979.]

[270] M. Frenklach, S. Taki, M. B. Durgaprasad, et al. "Soot Formation in Shock-Tube Pyrolisis of Acetylene, Allene and 1, 3-Butadiene," *Combustion and Flame*, vol. 54. pp. 81–103, 1983.

[271] И. А. Зенуков, В. Г. Крюков, Т. М. Магсумов. "Методика расчета физико-химических параметров двухфазных потоков," В сборнике: *Тепловые Процессы и Свойства Рабочих Тел Двигателей Летательных Аппаратов.* Казанский авиационный институт: Казань, стр. 71–77, 1980. [I. A. Zenukov, V. G. Kryukov, and T. M. Magsumov. "Method of Calculating the Physicochemical Parameters of Two-Phase Flows." In the collection of publications, *Thermal Processes and Properties of the Working Bodies of Aircraft Engines*. Kazan, Kazan Aviation Institute, pp. 71–77, 1980.]

[272] В. Н. Челомей, Д. А. Полухин, Н. Н. Миркин, и др. *Пневмо-гидравлические Системы Двигательных Установок с Жидкостными Ракетными Двигателями.* Москва: Машиностроение, 1978. [V. N. Chelomey, D. A. Polukhin, N. N. Mirkin, et al., *Pneumo-Hydraulic Systems of Propulsion Systems with Liquid Rocket Engines*. Moscow: MachineBuilding, 1978.]

[273] Н. М. Беляев. *Системы Наддува Топливных Баков Ракет.* Москва: Машиностроение, 1976. [N. M. Belyaev. *Systems of Pressurization of Liquid Rocket Tanks Fuel Tanks*. Moscow: MachineBuilding, 1976.]

Downloaded from https://www.cambridge.org/core. Nottingham Trent University, on 17 Aug 2019 at 03:56:55, subject to the Cambridge Core terms of use, available at https://www.cambridge.org/core/terms. https://doi.org/10.1017/9781108581714.011

[274] V. Naoumov. “Simulation of High-Temperature Pressurization of the Liquid-Propellant Rocket Tanks.” 47th Aerospace Science Meeting Including the New Horison Forum and Aerospace Exposition, AAA 2009–1600, Orlando, FL, pp. 1–7, 2009.

[275] D. W. Kendle. “Ullage Mixing Effects on Tank Pressurization Performance,” *Journal Spacecrafts and Rockets*, vol. 8, no. 9, pp. 990–992, 1977.

[276] К. П. Денисов, А. П. Луковский, Л. П. Леднева. “Экспериментальное исследование влияния скорости ввода газа на тепломассообменные процессы в газовом объеме емкости,” *Известия Высших Учебных Заведений СССР. Авиационная Техника.* № 1, стр. 84–86, 1981. [K. P. Denisov, A. P. Lukovsky, and L. P. Ledneva. “An Experimental Study of the Influence of the Rate of Gas Injection on Heat and Mass Transfer Processes in the Gas Volume,” *News of Higher Educational Institutions of the USSR: Aviation Technique*. no. 1, pp. 84–86, 1981.]

[277] А. А. Козлов, В. Н. Новиков, Е. В. Соловьев. *Системы Питания и Управления Жидкостными Ракетными Двигательными Установками.* Москва: Машиностроение, 1988. [A. A. Kozlov, V. N. Novikov, and E. V. Solovyov. Propellant Supply and Control Systems of Liquid Propellant Rocket Engines. Moscow: MachineBuilding, 1988.]

[278] Г.А. Глебов, А.П. Козлов. “Расчет процесса наполнения емкости сжатым газом,” *Инженерно-Физический Журнал*, Т. 46, № 4, стр. 696–697, 1984. [G. A. Glebov and A. P. Kozlov. “Calculation of the Process of Filling a Container with Compressed Gas,” *Engineering Physics Journal*, vol. 46, no. 4, pp. 696–697, 1984.]

[279] Н. М. Беляев, Е. И. Уваров, Ю. М. Степанчук. *Пневмо-Гидравлические Системы. Расчет и Проектирование.* Москва, Высшая школа, 1988. [N. M. Belyaev, E. I. Uvarov, and Yu. M. Stepanchuk. *Pneumo-Hydraulic Systems: Calculation and Design*. Moscow: High School, 1988.]

[280] E. C. Cady. “An Investigation of Fluorine-Hydrogen Main Tank Injection Pressurization,” *Journal Spacecrafts and Rockets*, vol. 6, no. 11, pp. 1248–1253, 1969.

[281] E. C. Cady and D. W. Kendle. “Vehicle-Scale Investigation of a Fluorine Jet-Pump Liquid Hydrogen Tank Pressurization System,” *Journal Spacecrafts and Rockets*, vol. 10, no. 11, pp. 735–740, 1973.

[282] D. A. Faster and T. C. Howell. “Main Tank Injection for Packaged Liquid Missiles,” 6th Aerospace Sciences Meeting, AIAA Paper, no. 627, New York, pp. 1–11, 1968.

[283] А. Ф. Дрегалин, В. Г. Крюков, В. И. Наумов. “Метод расчета и анализ свойств вертикальной неизотермической струи с учетом выталкивающей силы,” Известия Высших Учебных Заведений СССР. Авиационная Техника, № 1, стр. 29–33, 1983. [A. F. Dregalin, V. G. Krioukov, and V. I. Naumov. “Method of Calculation and Analysis of the Properties of a Vertical Non-Isothermal Jet, Taking into Account Buoyancy Force,” Proceedings of the Higher Educational Institutions of the USSR. Aviation Engineering, no. 1, pp. 29–33, 1983.]

[284] С.С. Кутателадзе, *Основы Теории Теплообмена.* 5-е издание. Атомиздат, 1979. [S. S. Kutateladze, *Fundamentals of Heat Transfer Theory*, 5th edn. Atomizdat, 1979.]

[285] С. И. Исаев, И. А. Кожинов, В. И. Кофанов, и др. *Теория Тепломассообмена.* Москва: Высшая школа, 1979. [S. I. Isaev, I. A. Kozhinov, V. I. Kofanov, et al. *Theory of Heat and Mass Transfer*. Moscow: High School, 1979.]

[286] С.С. Кутателадзе, А.И. Леонтьев. *Турбулентный Пограничный Слой Сжимаемого Газа.* Новосибирск: Изд-во Сиб. отд. АН СССР, 1962. [S. S. Kuataladze and A.I. Leontyev. *Turbulent Boundary Layer of Compressible Gas*. Novosibirsk: Publishing House Sib. Dep. Academy of Sciences of the USSR, 1962.]

Downloaded from https://www.cambridge.org/core. Nottingham Trent University, on 17 Aug 2019 at 03:56:55, subject to the Cambridge Core terms of use, available at https://www.cambridge.org/core/terms. https://doi.org/10.1017/9781108581714.011

[287] Г. А. Глебов, Р. Н. Габитов, В. В. Кузьмин и др. "Течение и теплообмен при взаимодействии турбулетнной осесимметричной струи с поверхностью компонента в топливном баке," В сборнике: *Тепловые Процессы и Свойства Рабочих Тел Двигателей Летательных Аппаратов.* Казань: КАИ, стр. 94–99, 1982. [G. A. Glebov, R. N. Gabitov, V. V. Kuzmin et al. "Flow and Heat Exchange in the Interaction of a Turbulet Axisymmetric Jet with a Component Surface in a Fuel Tank," In the collection of publications, *Thermal Processes and Working Properties of Aircraft Engines*. Kazan: KAI, pp. 94–99, 1982.]

[288] Г. А. Глебов, В. В. Кузьмин, А. Н. Щелков. "Конвективный теплообмен в цилиндрическом канале при вдуве в него турбулентной струи. Течение и теплообмен при взаимодействии турбулентной осесимметричной струи с поверхностью компонента в топливном баке," В сборнике: *Тепловые Процессы и Свойства Рабочих Тел Двигателей Летательных Аппаратов.* Казань: КАИ, стр. 90–93, 1982. [G. A. Glebov, V. V. Kuzmin, and A. N. Shchelkov. "Convective Heat Transfer in a Cylindrical Channel at Turbulent Jet Injection. Flow and heat Transfer in the Interaction of a Turbulent Axisymmetric Jet with the Surface of Component in Fuel Tank. In Collection: thermal Processes and Properties of the Working Bodies of Aircraft Engines. Kazan: KAI, pp. 90–93, 1982.]

[289] Э. К. Калинин, Г. А. Дрейцер, В. В. Костюк и др. *Методы Расчета Сопряженных Задач Тепломассообмена.* Москва: Машиностроение, 1983. [E. K. Kalinin, G. A. Dreitser, V. V. Kostyuk, et al. *Methods for Calculating Conjugate Problems of Heat and Mass Transfer*. Moscow: MachineBuilding, 1983.]

[290] А. В. Лыков. *Тепломассообмен. Справочник. 2-е издание.* Москва: Энергия, 1978. [A. V. Lykov. *Heat and Mass Transfer*, 2nd edn. Moscow: Energy, 1978.]

[291] V. I. Naoumov, V. G. Kriukov, and A. L. Abdullin. "Chemical Kinetics Software System for the Propulsion and Power Engineering," 41st Aerospace Science Meeting and Exhibit, AIAA 2003–854, Reno, NV, pp. 1–11, 2003.

[292] L. Eriksson, L. Nielsen, and J. Nytompt. "Ignition Control by Ionization Current Interpretation," SAE International Congress, SAE Technical Paper 960045, pp. 73–79, 1996.

[293] A. Saitzkoff, R. Reinmann, and T. Berglind. "An Ionization Equilibrium Analysis of the Spark Plug as an Ionization Sensor." SAE International Congress, SAE Technical Paper 960337, pp. 1–13, 1996.

[294] A. Saitzkoff, R. Reinmann, F. Mauss, et al. "In-Cylinder Pressure Measurements Using the Spark Plug as an Ionization Sensor," SAE International Congress, SAE Technical Paper 970857, pp. 1–13, 1997.

[295] R. Reinmann, A. Saitzkoff, and F. Mauss. "Local Air-Fuel Ratio Measurements Using the Spark Plug as an Ionization Sensor," SAE International, SAE Technical Paper 970856, pp. 1–13, 1997.

[296] S. Hajireza, B. Sunden, and F. Mauss. "A Three-Zone Model for Investigation of Gas Behaviour in the Combustion Chamber of SI Engines in Relation to Knock," SAE 1999 World Congress, SAE Technical Paper 1999–01-0219, pp. 1–12, 1999.

[297] M. Hellring, T. Munther, T. Rognvaldsson, et al. "Robust Air-Fuel Ratio Estimation Using the Ion Current and Neural Networks," SAE 1999 World Congress, SAE Technical Paper 991161, pp. 1–12, 1999.

[298] I. Anderson and L. Eriksson. "Ion Sensing for Combustion Stability Control of a Spark Ignited Direct Injected Engine," SAE 2000 World Congress, SAE Technical Paper 01–0552, pp. 1–8, 2000.

Downloaded from https://www.cambridge.org/core. Nottingham Trent University, on 17 Aug 2019 at 03:56:55, subject to the Cambridge Core terms of use, available at https://www.cambridge.org/core/terms. https://doi.org/10.1017/9781108581714.011

[299] L. Person, A. Charlet, P. Higelin, et al. “Limitations of Ionization Current Sensors and Comparison with Cylinder Pressure Sensors,” SAE 2000 World Congress, SAE Technical Paper 2000–01-2830, pp. 1–14, 2000.
[300] S. Yoshiyama, E. Tomita, and Y. Hamamoto. “Fundamental Study on Combustion Diagnostics Using a Spark Plug as Ion Probe,” SAE 2000 World Congress, SAE Technical Paper 2000–012828, pp. 1–15, 2000.
[301] S. Byttner, T. Rognvaldsson, and N. Wickstrom. “Estimation of Combustion Variability Using In-Cylinder Ionization Measurements,” SAE 2001 World Congress, SAE Technical Paper 2001–01-3485, pp. 1–8, 2001.
[302] A. Franke. “Characterization of an Electrical Sensor for Combustion Diagnostics.” Doctoral Thesis. Lund Institute of Technology, 2002.
[303] P. Einewall, P. Tunestal, and B. Johansson. “The Potential of Using the Ion-Current Signal for Optimizing Engine Stability – Comparisons of Lean and EGR (Stoichiometric) Operation,” SAE 2003 World Congress, SAE Technical Paper 2003–01-0717, pp. 1–11, 2003.
[304] M. Thele, S. Selle, U. Riedel, et al. “Detailed Two-Dimensional Numerical Study of Spark Ignition Including Ionization,” SAE 2002 World Congress, SAE Technical Paper 2002–01-1110, pp. 1–10, 2002.
[305] T. Kusuhara, T. Shinkai, K. Yoshida, et al. “Development on Internal EGR Feedback Control Based on Ion Current,” SAE 2017 World Congress, SAE Technical Paper 2017–01-0793, pp. 1–10, 2017.
[306] J. Lawton and F. J. Weinberg. *Electrical Aspects of Combustion*, London: Clarendon Press, 1969.
[307] K. E. Shuler, ed. *Ionization in High-Temperature Gases*. New York and London: Academic Press, 1963.
[308] H. F. Calcote. “Ion Production and Recombination in Fames,” In *8th (International) Symposium on Combustion*. Pittsburgh, PA: The Combustion Institute, pp. 184–199, 1960.
[309] H .F. Calcote. “Ion and Electron Profiles in Fames,” In *9th (International) Symposium on Combustion*. Pittsburgh, PA: The Combustion Institute, pp. 638–658, 1963.
[310] A. B. Fialkov. “Investigations on Ions in Fames,” *Progress in Energy and Combustion Science*, vol. 23, no. 5–6, pp. 399–528, 1997.
[311] V. Naoumov, A. Demin, I. Anderson et al. “Modeling of Combustion and Non-Equilibrium Ionization in Spark Ignition Engines,” SAE 2002 World Congress, SAE Technical Paper 2002–01-0009, pp. 1–8, 2002.
[312] V. I. Naoumov, A. V. Demin, and A. B. Sokolov. “Numerical Study and Analysis of Pollutant Production and Emission Control Using Ion Current Prediction in the SI Engine,” SAE 2003 World Congress, SAE Technical Paper 2003–01-0724, pp. 1–11, 2003.
[313] V. I. Naoumov, A. V. Demin, and A. B. Sokolov. “Three-Zone Model of Combustion and Chemical Non-Equilibrium Ionization in the SI Engine,” SAE 2004 World Congress, SAE Technical Paper 2004–01-0622, pp. 1–10, 2004.
[314] В. И. Алемасов, А. Ф. Дрегалин, А. П.Тишин. *Теория ракетных двигателей*. Москва: Машиностроение, 1969. [V. I. Alemasov, A. F. Dregalin, and A. P. Tishin. *Theory of Rocket Engines*. Moscow: MachineBuilding, 1969.]
[315] M. Mitchner and C. H. Kruger. *Partially Ionized Gases*. New York: Wiley, 1973.
[316] Y. B. Zeldovich, P. Y. Sadonikov, and D. A. Frank-Kamenetskii. *Oxidation of Nitrogen in Combustion*. Translated by M. Shelef. Moscow–Leningrad: Academy of Science of USSR, Institute of Chemical Physics, 1947.

Downloaded from https://www.cambridge.org/core. Nottingham Trent University, on 17 Aug 2019 at 03:56:55, subject to the Cambridge Core terms of use, available at https://www.cambridge.org/core/terms. https://doi.org/10.1017/9781108581714.011

Index

algorithm
  for calculation of processes in single reactor, 88
  of Dijkstra's, 173
  of polynomials conversion, 111
approach
  gas-dynamic, 35
  reactor, 36, 232
Archimedean forces, 352, 354
  action, 339
  effect, 353, 363
  impact on the flow pattern, 346
autooscillation, 104
average mass fraction of condensate, 11

ballasting component, 312, 331
boundary layer, 228, 230
  thickness, 229, 235, 256
Brusselator, 103

catalytic particle (third body), 23
chemi-ionization, 381, 390
CHEMKIN collection, 96
coefficient
  of losses because of chemical noneqilibrium, 153, 195
  stoichiomentric of reaction, 23
collision frequency
  electron–electron momentum transfer, 387
  electron-neutral momentum transfer, 387
combustion, 5
  autocatalytic, 209
  of coal particles, 7
  in the cylinder of spark-ignition ICE, 380
  diffusion, 6
  in the kernel, 384
  of a liquid fuel droplet, 6
  of metal particles, 6
  of multicomponent fuel with air, 296
  of natural gas, 303
  pulsating, 157
  separate, 224
  of solid propellant, 8
  of two-phase mixture, 284
concentration
  mole-mass, 10, 44
  partial molar, 10
condensation of substance, 54
conservative parameters, 345
constant
  of dissociation of individual substance, 13
  of equilibrium of s-th chemical reaction, 26, 77
control
  engine parameters, 391
  in-cylinder temperature, 390
  NO concentration, 390
  NO emission, 395
convection
  to the cylinder walls, 385
  to the piston bowl walls, 385

data base
  BURCAT, 96
  IVTANTERMO, 13
  of substances, 98
  THERMO, 13
  TTR, 12
density
  mixture, 10
  partial, 10
diffuser, 336
  configuration, 347
diffusion
  coefficient, 359
  coefficient of vapor into gaseous medium, 271
  concentration, 229
  mass exchange, 237
  mass exchange reaction rate, 238
discrepancy
  between databases, 117
  in data on substances, 111
discrete distribution of droplets, 313
droplet
  averaged-mass enthalpy, 268
  evaporation, 228, 231, 262, 313
  evaporation rate, 230
  evaporation simulation, 236

Downloaded from https://www.cambridge.org/core. Nottingham Trent University, on 17 Aug 2019 at 03:57:58, subject to the Cambridge Core terms of use, available at https://www.cambridge.org/core/terms. https://doi.org/10.1017/9781108581714.012

heating, 228, 313
thermal capacitance, 268, 315

eigenvalues, 62, 102
calculation, 105, 140
evolution, 142
imaginary, 159
important, 142
of Jacobian matrix, 98, 159
engine
air breathing, 228
emission characteristics, 393
internal combustion, 228
liquid-propellant rocket, 228
enthalpy
of *i*th substance
mass, 11
molar, 11
equation
calorific, 48, 318
Dalton, 17, 19
normalizing, 79
of chemical kinetics of exponential form, 47, 84
of conservation of atom, 17–18
of conservation of energy, 317
of dissociation, 17
of droplet evaporation, 264, 315
of droplet heating, 265, 268
of equilibrium evaporation of *k*-component, 278
of gas velocity, 316
of multicomponent droplet temperature, 277
Ranz–Marshall, 320
errors
in combustion product temperature, 125
in conversion of polynomials, 116
of reapproximation, 113
of reduction in the composition, 169
evaporation
of drops of a single-component liquid, 262
of liquid substance, 54
of multicomponent droplet, 262, 273
stationary (equilibrium), 264
at supercrical pressures, 262
excess
of fuel, 15, 311
of oxidizer, 15, 311
exhaust gas recirculation (EGR), 393
extinction line, 132, 155, 176, 181

feed
at the angle to the tank axis, 347, 355
axial, 347
peripheral, 347
simulation by conditional scheme, 347
flame front, 5, 207, 231, 382
cold boundary, 213
hot boundary, 211
propagation velocity, 384
thickness, 240
fraction
mass, 10, 43
molar, 10, 44
fuel, 14
bicomponent, 220
monocomponent, 221
furnace
radiant tubular, 39, 49

gas generator
liquid, 228, 310
two-zone, 312
gas generator products
fuel lean, 335
fuel rich, 335
gasoline conventional formula, 387

heat transfer
to the propellant surface, 360
to the tank's walls, 356

ion current, 380
density, 386
peaks, 381, 390
simulation, 386
ion voltage
history, 390
peaks, 392
ionization
combustion products, 380
sensor, 380
current, 381
thermal, 381

jet
axially symmetric, 352
flat, 352
inclined, 355
submerged, 353

KINTECUS package, 97

large molecule, 22, 50
latent heat of vaporization, 265
law
Fick, 237
Fourier, 237
of independence of chemical reactions, 26
of limiting transition, 26
mass action, 25
linearization of individual substance enthalpy, 75
linking force, 164, 165, 167
losses through the ring gaps, 384

Downloaded from https://www.cambridge.org/core. Nottingham Trent University, on 17 Aug 2019 at 03:57:58, subject to the Cambridge Core terms of use, available at https://www.cambridge.org/core/terms. https://doi.org/10.1017/9781108581714.012

mass exchange processes, 357
mass feed reaction, 344
matrix
  analytical calculation of partial derivatives, 79
  coordinating, 74
  derivatives of Jacobian, 20, 79
  Jacobian, 64
  Jacobian frozen, 85
method
  Chebyshev, 113
  explicit, 148
    of Euler, 62
    stability, 148
  Gear, 68
  implicit
    of Euler, 63
  Lebedev–Medovikov of second order, 66
  multi-step of Adams, 65
  Newton's, 19
  of direct sounding of species and reactions, 170
  of directed relation graph(DRG), 109
  of DRGEP, 173
  of engagement, 164
  of intrinsic low dimensional manifolds, 110
  of large molecules, 22
  of principal component analysis, 109
  of reaction rates analysis, 108
  of reduction of kinetic mechanisms, 107
  of spline-approximation, 70
  Pirumov, 69
  Runge–Kutta of fourth order, 64
  three-stage one-step of Skvortsov, 67
mixture
  lean, 15
  rich, 15
model
  chemical equilibrium, 16
  of combustion in the flame front, 208
  detailed (formal) chemical kinetics, 16, 23
  of ethane pyrolysis in tubular furnace, 84
  evaporation of single-component droplet, 263
  global kinetics, 16, 32
  heat of flame front, 209
  instant response, 16, 30
  of multicomponent droplet evaporation, 273, 278
  multicomponent fuel, 296
  nonequilibrium chemical kinetics, 16, 33
  of reacting gas–liquid flow, 313
  of supercritical droplet evaporation, 266
  of system of PSR, 285
  system of PSR, 291
  two-phase nonisothermal jet, 286
  two-zone for propellant tank, 339
molecular mass
  working medium, 10

natural gas substances, 387
nozzle
  of aerospace propulsion systems, 152
  chemical nonequilibrium processes, 194
  Laval, 37
  of LPRE, 153
  of SPRE, 155
  subsonic section, 157
number on integration steps
  for explicit scheme, 148
  for implicit scheme, 150
Nusselt number
  diffusive, 236, 275
  thermal, 275

optimization of parameters of ICE, 393
oscillation period, 158
oxidizer, 14

parameters of Arrhenius, 23
  activation energy, 25
  pre-exponential factor, 25
  temperature factor, 25
peak
  of pressure, 381
  of temperature, 390
peak of concentration
  of electrons, 390
  of H3O+, 390–1
  of NO, 390
  of NO+, 390–1
piston
  average velocity, 384
  bowl, 384
Prandtl number, 317
pressure
  of saturated vapor, 264
  supercritical, 313
  partial, 10
pressurization
  chemical, 335
  of LPRE propellant tank, 334
  system, 334
pressurizing gas, 334
  consumption, 346
  feed into reactor, 344
  feed into the ullage, 347
  flow and heat-and-mass exchange, 346
  flow calculation, 346
  flow in ullage, 336, 350

Downloaded from https://www.cambridge.org/core. Nottingham Trent University, on 17 Aug 2019 at 03:57:58, subject to the Cambridge Core terms of use, available at https://www.cambridge.org/core/terms. https://doi.org/10.1017/9781108581714.012

flow pattern in ullage, 338
heat exchange with tank walls, 337
injection velocity, 370
optimal velocity, 374
thermal stratification, 337
pressurizing system
evaporated-propellant, 334
stored-gas, 334
turbopump feed, 335
propellant
atomization, 228
conditional formula, 14–15
cryogenic, 335
enthalpy, 18
evaporation from the surface, 337
high-boiling, 335
solid of rocket engine, 38
tank of LPREs, 334
thermal stratification and circulation, 337
two-component, 14
vapor condensation, 337

rate constant, 23
of forward chemical reaction, 25
reaction
basic of dissociation, 13, 17
of chemi-ionization, 381, 390
elementary, 23
global, 32
of ionization, 381
of ionization charge recombination, 381
of ionization charge transfer, 381
of Lindemann, 28
of mass exchange, 41, 53
mass feed, 317
thermo ionization by collision, 381, 390
reaction mechanism
complete (C-mechanism), 164
global reduced, 164
in the boundary layer, 231
local reduced, 164
reactor
batch (BR), 4
perfectly stirred (PSR), 4, 101, 184
plug flow (PFR), 4, 184
reduced film, 263, 359
model, 231–2
thickness, 236
reduced integral of collision, 359
reduction threshold, 108, 163
adaptive, 167
residence time, 45, 133, 138, 157, 178
Reynolds number, 317, 354

scale thermodynamic, 11
Schmidt number, 236
sensitivity analysis, 98, 126
local, 101
sensitivity coefficients, 101
analytic determination, 127
soot formation, 320, 322
sub-mechanism, 325
threshold, 329
specific heat of substance
mass
at constant pressure, 11
at constant volume, 11
molar
at constant pressure, 11
at constant volume, 11
Stefan's flow, 230–1
velocity, 360
stiffness
artificial, 143
of chemical kinetics equations, 103
stoichiometric ratio of components, 15
mass, 15
molar, 15

tank
draining, 340
emptying, 340
propellant, 311
target species, 108
tested species, 168

ullage, 255, 311, 334, 337–8, 340, 345–6, 348, 353, 362, 364
ullage chemical nonequilibrium of gas composition, 338

Wiebe formula, 386
working capacity, 335, 369
working medium, 253, 257, 283, 296, 310, 322, 382, 384

zone
burned mixture, 382, 385
spark kernel, 383
unburned air-fuel and residual combustion products, 382
unburned mixture, 384

Downloaded from https://www.cambridge.org/core. Nottingham Trent University, on 17 Aug 2019 at 03:57:58, subject to the Cambridge Core terms of use, available at https://www.cambridge.org/core/terms. https://doi.org/10.1017/9781108581714.012

Downloaded from https://www.cambridge.org/core. Nottingham Trent University, on 17 Aug 2019 at 03:57:58, subject to the Cambridge Core terms of use, available at https://www.cambridge.org/core/terms. https://doi.org/10.1017/9781108581714.012